



University  
of Glasgow

Seat, Han Cheng (2001) Growth and characterisation of single-crystal fibres for sensing applications. PhD thesis

<http://theses.gla.ac.uk/6926/>

Copyright and moral rights for this thesis are retained by the author

A copy can be downloaded for personal non-commercial research or study, without prior permission or charge

This thesis cannot be reproduced or quoted extensively from without first obtaining permission in writing from the Author

The content must not be changed in any way or sold commercially in any format or medium without the formal permission of the Author

When referring to this work, full bibliographic details including the author, title, awarding institution and date of the thesis must be given

**GROWTH AND CHARACTERISATION OF SINGLE-  
CRYSTAL FIBRES FOR SENSING APPLICATIONS**

**Han Cheng Seat**

**Thesis submitted for the degree of Doctor of Philosophy  
Department of Mechanical Engineering  
The University of Glasgow  
June, 2001**

©Han Cheng Seat 2001



## Abstract

The laser heated pedestal growth technique has been successfully employed to grow pure and doped sapphire crystal fibres for characterisation as suitable sensor materials. Source materials used were polycrystalline and crystalline sapphire rods while fibres with typical diameters in the range 80 – 170  $\mu\text{m}$  were grown. Pure sapphire fibres, both *a*- and *c*-axis, were found to grow easily with no complications such as melt instability. *C*-axis fibre growth was readily initiated while *a*-axis fibres required an appropriate *a*-axis oriented seed crystal. Dip-coating has been used to prepare suitably coated sapphire source rods for growth into doped fibres. Doped fibres grown included  $\text{Cr}^{3+}$ ,  $\text{Er}^{3+}$ ,  $\text{Er}^{3+}:\text{Yb}^{3+}$  and  $\text{Yb}^{3+}:\text{Er}^{3+}:\text{Al}_2\text{O}_3$ ,  $\text{Er}^{3+}:\text{Yb}^{3+}:\text{Al}_2\text{O}_3$  fibres have been prepared with approximately equal concentration of both dopants while a 10:1  $\text{Yb}^{3+}$  to  $\text{Er}^{3+}$  concentration ratio was used for preparing  $\text{Yb}^{3+}:\text{Er}^{3+}:\text{Al}_2\text{O}_3$  fibres. Ruby fibres were also found to grow easily although brownish-green deposits have been observed on some of these fibres. Large transmission losses have been found in fibres with these deposits. Acid cleaning was not effective in removing these deposits, suggesting that they have diffused beneath the surface of the fibres. This was attributed to the condensation of chromium oxide on the fibre surface during growth. Growth of rare earth-doped fibres was initially problematic due to the constant breaking-off of the crystallising fibres from the melt. This was thought to be due to the flexibility of the small diameter source fibres used as well as the high concentration levels of doping. Replacing these small fibres with larger source rods thus permitted RE-doped fibres with relatively good optical quality to be grown. Fibres were grown with typical growth rates of 0.5 – 1 mm/min.

The fluorescence characteristics of doped fibres were investigated for their dependences on physical influences, mainly temperature and strain. The fluorescence lifetime of  $\text{Cr}^{3+}:\text{Al}_2\text{O}_3$  fibres was found to be highly temperature dependent but only slightly sensitive to uniaxial strain effects. The lifetime behaviour as a function of temperature was also found to be in good agreement with theory. Lineshifts of the ruby R-lines were also investigated as possible temperature sensing mechanisms but were found to exhibit less sensitivity in comparison to the

lifetime. In addition, the R-lines were found to be relatively insensitive to tensile strain.

Rare earth-doped sapphire fibres have been found to exhibit simultaneous emission in the infrared and visible spectral regions and were characterised mainly for temperature sensing applications. Intense upconversion in the green and red was observed in all RE-doped fibres, with the strongest emission obtained from equally  $\text{Er}^{3+}:\text{Yb}^{3+}$ -codoped samples. This was attributed to the high dopant concentration levels (~10 – 12 at. %) used and led to a significant reduction in the primary emission intensity at ~1530 nm. Both the green and red upconversion emissions were found to exhibit sharp, narrow-band structures, indicating the highly crystalline nature of these RE-doped fibres. The upconversion emission was studied using the fluorescence intensity ratio technique and ratios between the sharp lines in both spectral regions were fitted with models obtained from published work with varying degrees of agreement. This implied complex transition processes in the higher energy levels of these fibres. Although no data is currently available on transition dynamics of RE ions incorporated into  $\text{Al}_2\text{O}_3$  fibres using melt growth techniques, it is suggested that further studies are required to better understand the transition dynamics as well as to obtain a better model to describe these characteristics. Singly  $\text{Er}^{3+}$ -doped fibres were found to have relatively weak emissions in both the visible and infrared, and have been investigated to temperatures below ~800 K. Equally codoped fibres were found to emit strongly both in the visible and infrared, due to more efficient energy transfer by the sensitising  $\text{Yb}^{3+}$  ions. The green and red upconversion intensity ratios and intensities have been investigated for high temperature sensing above 1000 K. Their respective lifetimes were also found to be highly non-exponential and, hence, not suitable for sensing unless a more suitable model could be employed to better fit their decay times. Relatively strong lines in the 1000 nm region have been obtained from fibres doped with very high  $\text{Yb}^{3+}$  concentrations. The intensity ratio technique was also applied to characterise the temperature dependence of the 1025 and 996 nm lines. However, due to spectral overlapping with the tail of the pump source, the IR signals from these fibres were found to be dominated by noise from the laser at elevated temperatures.

*C*- and *a*-axis sapphire fibres were used for temperature and bend studies based on their polarimetric properties. *C*-axis fibres were found to be relatively insensitive to both effects while *a*-axis fibres exhibited slightly higher sensitivities. However, scrambling of the linearly polarised input lightwave by the fibres walls while propagating along these fibres was found to be a major problem affecting the signals of interest.

## Acknowledgements

I would, first of all, like to thank Dr. J. H. Sharp, my supervisor, for giving me the opportunity to pursue this research at a level which is intellectually challenging and equally interesting. Throughout the course of this project, Jim has always been understanding, supportive and patient. He was approachable and ready to discuss problems. Jim has guided me through several difficult phases of the project and was always open to suggestions concerning the technical aspects of work. I have gained much in terms of knowledge and experience in experimental research while working with him. His openness and willingness to teach have benefited me greatly and taught me to approach a potential problem from different angles. Without his constant encouragement and guidance, this work would not have come to a conclusion. Also, my stay in department would not have been so stimulating. Thank you.

I would also like to express my appreciation of those who have in some way contributed to the success of this work over the last three years. In particular, Dr. Ian Watson is thanked for being interested in my progress and concerned in my general well-being. His kindness and humour is always a source of comfort in trying times. Ian Peden was never short of advice when it came to some programming difficulties I encountered while writing the control software for the laser heated pedestal growth station. He could always be counted on to initiate anyone towards the advantage of computer programming and a lively discussion on any subject. George Falconer is thanked for helping to put my sometimes incomprehensible technical drawings through the queue as quickly as possible. The other technicians, Brian, Dennis, John, Vic and Allan are thanked for getting all the rush jobs I required done without having to go through "official" channels and the technical advice given freely. Their friendship is well appreciated.

I would also like to thank my office-mate, Boon Kiat, whom I often had to bother when my computer experienced the occasional "hiccups" and crashed, for the many help he has offered. He has been supportive of my situation and has always tolerated

my sometimes excessive nature. Those sleepless nights in the office spent typing on the computer would be much more unbearable without his company and the discussions we had while enjoying a break from work.

Due acknowledgement is also given to the CVCP and Glasgow University, without whose scholarship (ORS) and grant, this work would not have been realised.

I would also like to dedicate this thesis to my parents and parents-in-law for all the encouragement they have given throughout these years of my education.

Finally, I would like to give my utmost appreciation and thanks to my wife, Emmanuelle, who has continually given me her moral and financial support, always been encouraging and understanding throughout these past three or so years which I spent in Glasgow and for always believing in me. *Sans toi cette thèse n'aurait pas été possible. Merci.*

# CONTENTS

**Abstract**

**Acknowledgements**

## **Chapter 1 – Introduction**

1.0	Research Context	2
-----	------------------	---

## **Chapter 2 – Introduction to Single-Crystal Fibre Sensors**

2.0	Introduction to single-crystal fibres	5
2.1	Applications of single-crystal fibres	9
2.2	Introduction to fibre optic sensing	11
2.3	Fundamental principles of FOS	15
2.3.1	Intensity-based sensors	18
2.3.2	Interferometric sensors	28
2.3.3	Distributed and multiplexed sensing systems	34
2.3.4	Fibre Bragg gratings and sensors	39
2.3.5	Fluorescence-based fibre optic sensors	54
2.3.6	Crystal fibre sensors	61
2.4	References to <b>Chapter 2</b>	70

## **Chapter 3 – Laser Heated Pedestal Growth of Crystal Fibres**

3.0	Introduction	85
3.1	Overview of available growth methods	85
3.1.1	Capillary shaping from melts	87
3.1.2	Drawing down and micro-pulling down (DD and $\mu$ -PD) Methods	89
3.1.3	Micro-Czochralski ( $\mu$ -CZ) method	89
3.1.4	Internal crystallisation method (ICM)	90
3.1.5	Laser heated pedestal growth	94
3.2	The laser heated pedestal growth technique	96
3.3	Laser heated pedestal growth system and design considerations	100
3.3.1	Heat source	113

3.3.2	Fibre pull and source feed systems	117
3.3.3	Laser beam focusing optics	124
3.3.4	Growth chamber	127
3.3.5	Vibration-isolated optical bench	127
3.4	Fibre growth	128
3.5	References to <b>Chapter 3</b>	148

#### **Chapter 4 – Fibre Characterisation and Experimental Techniques**

4.0	Introduction	154
4.1	Fibre diameter measurements	154
4.1.1	Diameter measurement experiment	155
4.1.2	Results and Discussion	158
4.2	Loss measurements and scattering losses	161
4.2.1	Experiment on loss measurements	161
4.2.2	Results and Discussion	164
4.3	Coupling of sapphire to silica fibres	167
4.3.1	Experiment	167
4.3.2	Results and Discussion	172
4.4	Absorption spectra measurements	176
4.4.1	Experiment	176
4.4.2	Results and Discussion	180
4.5	Fluorescence spectra measurements	186
4.5.1	Experiment	186
4.5.2	Results and Discussion	189
4.6	Fluorescence lifetime measurements	196
4.6.1	Experiment	196
4.6.2	Results and Discussion	199
4.7	References to <b>Chapter 4</b>	202

#### **Chapter 5 – Ruby-based Crystal Fibre Sensors**

5.0	Introduction	206
5.1	Theory of temperature and deformation influences on the fluorescence characteristics of ruby	210
5.1.1	Temperature dependence	210
5.1.2	Dependence on physical deformations (high pressure and stress)	219

5.2	Absorption and fluorescence spectra of ruby single-crystal fibres	222
5.3	Temperature sensing experiments	225
5.3.1	Fluorescence lifetime decay of single-crystal ruby fibres	225
5.3.1.1	Experiment	226
5.3.1.2	Results and Discussion	230
5.3.2	Wavelength shifts of ruby fibre R-lines with temperature	243
5.3.2.1	Experiment	243
5.3.2.2	Results and Discussion	246
5.4	Strain measurement experiments	258
5.4.1	Fluorescence lifetime decay of ruby fibres	258
5.4.1.1	Experiment	258
5.4.1.2	Results and Discussion	262
5.4.2	Wavelength shifts of ruby fibre R-lines	267
5.4.2.1	Experiment	267
5.4.2.2	Results and Discussion	270
5.5	References to <b>Chapter 5</b>	275

## **Chapter 6 – Rare Earth-based Crystal Fibre Sensors**

6.0	Introduction	281
6.1	Rare earth $\text{Er}^{3+}$ and $\text{Yb}^{3+}$ ions in $\text{Al}_2\text{O}_3$ and upconversion processes	290
6.2	Temperature sensing based on $\text{Er}^{3+}$ , equally $\text{Er}^{3+} + \text{Yb}^{3+}$ -codoped and high $\text{Yb}^{3+}$ + low $\text{Er}^{3+}$ -codoped $\text{Al}_2\text{O}_3$ fibres	302
6.2.1	Temperature sensing with $\text{Er}^{3+}:\text{Al}_2\text{O}_3$ fibres	305
6.2.1.1	FIRs of green upconversion and IR emission for temperature sensing	305
6.2.1.2	Experiments	307
6.2.1.3	Results and Discussion	311
6.2.2	Temperature sensing with equally $\text{Er}^{3+} + \text{Yb}^{3+}$ -codoped $\text{Al}_2\text{O}_3$ fibres	323
6.2.2.1	Temperature dependence of green and red upconversion FIRs	324
6.2.2.2	Experiments on green and red FIRs	326
6.2.2.3	Results and Discussion	328
6.2.2.4	Temperature sensing based on upconversion intensity of equally codoped $\text{Er}^{3+} + \text{Yb}^{3+}:\text{Al}_2\text{O}_3$ fibres	337
6.2.2.5	Experiment on intensity-based temperature sensor	338
6.2.2.6	Results and Discussion	341
6.2.2.7	Temperature dependence of the green and red	

	upconversion decay lifetimes	348
	6.2.2.8 Lifetime experiment	349
	6.2.2.9 Results and Discussion	352
6.2.3	Temperature sensing with high $\text{Yb}^{3+}$ + low $\text{Er}^{3+}$ : $\text{Al}_2\text{O}_3$ fibres	357
	6.2.3.1 Temperature dependence of IR FIR of highly $\text{Yb}^{3+}$ : lowly $\text{Er}^{3+}$ : $\text{Al}_2\text{O}_3$ fibres	358
	6.2.3.2 Experiment on temperature dependence of infrared FIR of high $\text{Yb}^{3+}$ : low $\text{Er}^{3+}$ : $\text{Al}_2\text{O}_3$ fibres	359
	6.2.3.3 Results and Discussion	361
	6.2.3.4 Temperature dependence of the FIRs of upconversion emission in the green and red from high $\text{Yb}^{3+}$ : low $\text{Er}^{3+}$ -codoped $\text{Al}_2\text{O}_3$ fibres	366
	6.2.3.5 Experiment on temperature dependence of green and red upconversion FIRs from high $\text{Yb}^{3+}$ : low $\text{Er}^{3+}$ : $\text{Al}_2\text{O}_3$ fibres	376
	6.2.3.6 Results and Discussion	367
6.3	References to <b>Chapter 6</b>	374

## Chapter 7 – Sapphire Fibre-based Polarimetric Sensors

7.0	Introduction	382
7.1	Fundamental principles of polarimetry-based sensing	387
7.2	Polarimetric sensing with sapphire fibres	391
7.3	Temperature sensing experiments	392
	7.3.1 Temperature sensing with <i>c</i> -axis sapphire fibres	393
	7.3.2 Results and Discussion	398
	7.3.3 Temperature sensing with <i>a</i> -axis sapphire fibres	402
	7.3.4 Results and Discussion	406
7.4	3-point bending of sapphire fibres	410
	7.4.1 3-point bending of <i>c</i> -axis sapphire fibres	411
	7.4.2 Results and Discussion	414
	7.4.3 3-point bending of <i>a</i> -axis sapphire fibres	418
	7.4.4 Results and Discussion	420
7.5	References to <b>Chapter 7</b>	427

## Chapter 8 – Conclusions and Future Work

8.0	Conclusions	431
8.1	Future Work	439

**APPENDIX A**

442

**APPENDIX B**

448

## List of Figures

### Figure

- 2.1 Extrinsic FOS
- 2.2 Intrinsic FOS
- 2.3 Axial Displacement (Transmissive)
- 2.4 Radial Displacement (Transmissive)
- 2.5 Schematic Diagram of a Frustrated Totally Internal Reflection Sensor
- 2.6 Simple Reflective Sensor using Fibre Bundle
- 2.7 Reflective Sensor with Movable Reflector and Separate Fibres
- 2.8 Schematic Diagram of a Reflective Sensor using Directional Coupler
- 2.9 Example of a Microbend Sensor
- 2.10 Basic Grating Sensor (Radial Displacement)
- 2.11 Intensity-modulated Sensor based on Evanescent Effect
- 2.12 Intensity-based Sensors using Fluorescence from Fibres
- 2.13 "Crossed-Over" Compensating Technique
- 2.14 Partially Reflecting Mirror used in Referencing Scheme
- 2.15 Fibre optic Mach-Zehnder Interferometer
- 2.16 Fibre optic Michelson Interferometer
- 2.17 A Basic Fabry-Pérot Interferometer
- 2.18 A Basic Polarimetric Sensor
- 2.19 A Basic Distributed Sensing Configuration
- 2.20 A Basic Time Division Multiplexing Sensor
- 2.21 Schematic of a common Fibre Bragg Grating
- 2.22 A Schematic Diagram of a Blazed Grating
- 2.23 A Schematic Diagram of a Chirped Grating
- 2.24 Schematic of a Strain and Temperature FBG Sensor
- 2.25 Spliced Different-Diameter Gratings
- 2.26 Tunable Filter for Scanning FBG Returned Signals
- 2.27 Interferometric Interrogation of FBG Wavelength Shift
- 2.28 Spectroscopic Technique for Wavelength Shift Detection with CCD Array
- 2.29 Basic FBG Laser Sensor Configuration
- 2.30a Schematic diagram of a Fibre Optic Sensor based on Blackbody Radiation
- 2.30b Blackbody Sensor Head using High Temperature Radiation Film
- 2.30c Blackbody Sensor Head (made by doping end of sapphire fibre or by attaching radiating crystal)
- 2.31 Schematic Diagram of a Sapphire-based FP Sensor
  - (a) Schematic of Sapphire IFPI Sensor Head
  - (b) Schematic of Sapphire EFPI Sensor Head
- 2.32 Schematic of a Sapphire Polarimetric Sensor
  
- 3.1a Crystal Growth from Melts with the aid of Capillary Shapers
- 3.1b Schematic of Bridgman Growth of Crystal Fibres
- 3.2 Schematics of drawing down (left) and micro-pulling down (right) methods
- 3.3 Schematic of micro-Czochralski method

- 3.4 Illustration and schematic of the internal crystallisation method (ICM) for fibre growth
  - (a) Assembly of foils and wires/fibres
  - (b) Finished matrix with multiple channels
  - (c) Cross section of fibre by the ICM
  - (d) Fibre production by the ICM with seed crystal
- 3.5 Schematic of laser heated pedestal growth (LHPG) method
- 3.6 Manipulation of laser beam
- 3.7 Schematic of orthogonal viewing system (dashed lines indicate on-going work)
- 3.8a End taper grown from 170  $\mu\text{m}$  sapphire fibre
- 3.8b Magnified view of taper
- 3.8c In-line taper taken with cross-polarisers
- 3.9a Forward light scattering by large diameter fibre (fringes close together)
- 3.9b Forward light scattering by smaller diameter fibre (fringes apart)
- 3.10 Laser scanning system based on 4f principle
- 3.11a Illustration of pulse counting
- 3.11b Schematic of shadow pulse counting process
- 3.12a Oscilloscope trace of a 250  $\mu\text{m}$  fibre
- 3.12b Oscilloscope trace of 130  $\mu\text{m}$  fibre
- 3.13 Schematic of LHPG station
- 3.14a Graph of stabilised laser power with a step change in power illustrated
- 3.14b Monitoring hysteresis of laser output power
- 3.15a Photograph of pull stage
- 3.15b Photograph showing pin chuck securely holding fibre
- 3.16a Photograph of feed system
- 3.16b Variation in feed and pull velocities at growth rate of 0.75 mm/min
- 3.17a Schematic of reflexicon unit (right) and output beam intensity profile (left)
- 3.17b Burn mark from reflexicon
- 3.17c Photograph of reflexicon unit
- 3.18a Photograph of a *c*-axis sapphire fibre
- 3.18b Photograph of an *a*-axis sapphire fibre
- 3.19 Crystallising fibre during LHPG
- 3.20 Diameter variation of sapphire fibre
- 3.21 Example of chromium oxide coated source rod
- 3.22 EMPA scan of  $\text{Cr}^{3+}:\text{Al}_2\text{O}_3$  fibre cross-section along orthogonal axes
- 3.23 Examples of *c*-axis ruby fibres
- 3.24a Uncoated sapphire source rod
- 3.24b  $\text{Er}_2\text{O}_3$  coated source rod
- 3.24c  $\text{Yb}_2\text{O}_3 + \text{Er}_2\text{O}_3$  coated source rod ( $\sim 10:1$  concentration ratio)
- 3.24d  $\text{Nd}_2\text{O}_3$  coated source rod
- 3.25a  $\text{Er}^{3+}:\text{Al}_2\text{O}_3$  fibre
- 3.25b High  $\text{Yb}^{3+} + \text{low Er}^{3+}:\text{Al}_2\text{O}_3$  fibre
- 3.25c  $\text{Er}^{3+} + \text{Yb}^{3+}:\text{Al}_2\text{O}_3$  fibre
- 3.26a Schematic of crystallising RE-doped fibre
- 3.26b Photograph of crystallising RE-doped fibre
- 3.27a Examples of YSZ fibre/rods produced by LHPG
- 3.27b Large diameter variation along fibre due to fluctuating laser power
- 3.27c Cross sectional view of YSZ fibre/rod
- 3.27d Defects in YSZ fibre

- 4.1 Schematic of fibre diameter measurement using eye-piece and graticule with optical microscope
- 4.2 Diameter variations of *c*- and *a*-axis sapphire fibres
  - (a) *C*-axis fibre grown from 130  $\mu\text{m}$  source
  - (b) *A*-axis fibre grown from 325  $\mu\text{m}$  source
- 4.3 Schematic of ruby fibre loss measurement experiment
- 4.4 Basic principle employed in ruby absorption and geometric loss measurements
  - 4.5a Butt-coupling employing tapered sleeve
  - 4.5b Fusion splicing of two different materials
  - 4.6 Schematic of butt-coupling experiment
  - 4.7 Damage incurred to end of sapphire fibre subjected to fusion splicing
  - 4.8 Splicing of sapphire to silica fibres using  $\text{CO}_2$  laser
  - 4.9 Schematic of absorption spectra experiment
  - 4.10a Visible spectrum of Schott KLT-1500-T lamp
  - 4.10b IR spectrum of KLT-1500-T lamp
  - 4.11 Visible absorption spectrum of ruby fibre and bulk ruby crystal
  - 4.12a Visible absorption spectrum of  $\text{Er}^{3+}:\text{Al}_2\text{O}_3$  fibre (doped tip)
  - 4.12b IR absorption spectrum of  $\text{Er}^{3+}:\text{Al}_2\text{O}_3$  fibre (doped tip)
  - 4.13a Visible absorption spectrum of  $\text{Yb}^{3+}$ -sensitised  $\text{Er}^{3+}:\text{Al}_2\text{O}_3$  fibre
  - 4.13b IR absorption spectrum of  $\text{Yb}^{3+}$ -sensitised  $\text{Er}^{3+}:\text{Al}_2\text{O}_3$  fibre
  - 4.14 Visible absorption spectrum of  $\text{Yb}^{3+}:\text{Er}^{3+}:\text{Al}_2\text{O}_3$  fibre
  - 4.15 Schematic of fluorescence spectra experiment
  - 4.16 Fluorescence spectrum of ruby fibre
  - 4.17a Upconversion spectrum of  $\text{Er}^{3+}:\text{Al}_2\text{O}_3$  fibre (doped tip)
  - 4.17b IR fluorescence spectrum of  $\text{Er}^{3+}:\text{Al}_2\text{O}_3$  fibre (doped tip) pumped by laser diode at 960 nm
  - 4.18a Upconversion spectrum of  $\text{Er}^{3+} + \text{Yb}^{3+}$  codoped  $\text{Al}_2\text{O}_3$  fibre
  - 4.18b IR fluorescence spectrum of  $\text{Er}^{3+} + \text{Yb}^{3+}$  codoped  $\text{Al}_2\text{O}_3$  fibre
  - 4.19a Upconversion spectrum of  $\text{Yb}^{3+}:\text{Er}^{3+}:\text{Al}_2\text{O}_3$  fibre
  - 4.19b IR fluorescence spectrum of  $\text{Yb}^{3+}:\text{Er}^{3+}:\text{Al}_2\text{O}_3$  fibre
  - 4.20 Schematic of experimental set-up for measuring fluorescence lifetime of doped fibres
    - 4.21a Fluorescence lifetime decay of ruby fibre at room temperature
    - 4.21b IR fluorescence lifetime decay of  $\text{Er}^{3+}:\text{Yb}^{3+}:\text{Al}_2\text{O}_3$  fibre at room temperature (pump  $\lambda = 965$  nm)
    - 4.21c Green upconversion lifetime decay  $\text{Er}^{3+}:\text{Yb}^{3+}:\text{Al}_2\text{O}_3$  fibre at room temperature (pump  $\lambda = 965$  nm)
- 5.1a Transmission type sensor
- 5.1b Reflection type sensor
- 5.2 A simplified energy-level diagram for ruby
- 5.3 A simplified Tanabe-Sugano diagram for ruby
- 5.4 A two-level model for ruby
- 5.5 A simplified single configurational coordinate model for studying the temperature dependence of ruby fluorescence decay time
- 5.6 Absorption spectra of ruby SCF and bulk ruby rod
- 5.7 Fluorescence spectra of ruby fibre and bulk ruby rod

- 5.8 Experimental set-up used for determining lifetime of ruby fibre as a function of temperature
- 5.9 Falling edge of the modulated Ar<sup>+</sup> laser signal at 514.5 nm
- 5.10a Ruby fibre lifetime decay at room temperature (292 K)
- 5.10b Lifetime decay at 373 K
- 5.10c Lifetime decay at 374 K
- 5.10d Lifetime decay at 473 K
- 5.10e Lifetime decay at 573 K
- 5.10f Lifetime decay at 673 K
- 5.10g Lifetime decay at 773 K
- 5.10h Lifetime decay at 873 K
- 5.10i Lifetime decay at 923 K
- 5.11 Temperature dependence of ruby fibre fluorescence lifetime
- 5.12 Temperature dependence of fluorescence lifetime of ruby fibre and bulk ruby rod
- 5.13 Single configurational coordinate model for ruby fibre
- 5.14 Sensitivity curve of SCC model
- 5.15 Experimental set-up for determining wavelength shifts of ruby fibre R-lines as function of temperature
- 5.16 Shift of ruby fibre R-lines with temperature
- 5.17a Absolute R<sub>1</sub> and R<sub>2</sub> lineshifts of ruby fibre with temperature
- 5.17b Relative R<sub>1</sub> and R<sub>2</sub> lineshifts of ruby fibre with temperature
- 5.18 Ruby fibre spectrum at 823 K
- 5.19a Calibration curves of R<sub>1</sub> and R<sub>2</sub> lines from 291 to 623 K
- 5.19b Calibration curves of R<sub>1</sub> and R<sub>2</sub> lines from 673 to 973 K
- 5.20a Determination of wavelength coefficient from straight line fit as a function of temperature (291 to 623 K)
- 5.20b Determination of wavelength coefficient from straight line fit as a function of temperature (673 to 973 K)
- 5.21 Photograph of strain testing device used in experiment
- 5.22 Experimental set-up for determining fluorescence lifetime of ruby fibre as a function of uniaxial tensile strain
- 5.23 Ruby fibre lifetime decay at 0 strain ( $\delta L = 0 \mu\text{m}$ )
- 5.24 Ruby fibre lifetime decay at 8110  $\mu\text{e}$  ( $\delta L = 100 \mu\text{m}$ )
- 5.25a Fluorescence lifetime decay of ruby fibre as a function of uniaxial strain
- 5.25b Comparison of strain and temperature dependence of ruby fibre fluorescence lifetime
- 5.26 Experimental set-up for determining R-lineshifts of ruby fibre as a function of uniaxial tensile strain
- 5.27a Relative shift in R-lines as a function of uniaxial strain
- 5.27b Wavelength shift in R-lines as a function of uniaxial strain
- 5.28 Unstrained and highly-strained ruby fibre fluorescence spectra
  
- 6.1a Schematic energy level diagram of Er<sup>3+</sup> ions
- 6.1b Schematic energy level diagram of Yb<sup>3+</sup> ions
- 6.1c Schematic energy level diagram of Er<sup>3+</sup> + Yb<sup>3+</sup> codoped system
- 6.2a Schematic diagram of sequential two-photon absorption upconversion process
- 6.2b Schematic diagram of cooperative energy transfer upconversion process
- 6.2c Schematic diagram of photon avalanche upconversion process

- 6.3 SEM image of  $\text{Er}^{3+}$ -doped tip in  $\text{Al}_2\text{O}_3$
- 6.4 Visible absorption spectrum of  $\text{Yb}^{3+}:\text{Er}^{3+}:\text{Al}_2\text{O}_3$  fibre
- 6.5 IR fluorescence lines used in FIR temperature measurements ( $\text{Er}^{3+}:\text{Al}_2\text{O}_3$  fibre)
- 6.6 Green upconversion spectrum of  $\text{Er}^{3+}:\text{Al}_2\text{O}_3$  fibre (doped tip)
- 6.7 Schematic of experimental set-up for upconversion detection of  $\text{Er}^{3+}$ -doped tip  $\text{Al}_2\text{O}_3$  fibre
- 6.8 Schematic of experimental set-up for IR signal detection of  $\text{Er}^{3+}:\text{Al}_2\text{O}_3$  fibre (doped length  $\sim 20$  mm)
- 6.9a Green intensity ratios,  $\text{FIR}_{g12} - \text{FIR}_{g15}$ , as a function of temperature ( $\text{Er}^{3+}$ -doped tip  $\text{Al}_2\text{O}_3$  fibre)
- 6.9b Green intensity ratios,  $\text{FIR}_{g23} - \text{FIR}_{g25}$ , as a function of temperature ( $\text{Er}^{3+}$ -doped tip  $\text{Al}_2\text{O}_3$  fibre)
- 6.9c Green intensity ratios,  $\text{FIR}_{g34} - \text{FIR}_{g45}$ , as a function of temperature ( $\text{Er}^{3+}$ -doped tip  $\text{Al}_2\text{O}_3$  fibre)
- 6.10a Modelling of green upconversion  $\text{FIR}_{g12}$  ( $I_{540\text{nm}}/I_{541.5\text{nm}}$ ) using **Eq. 6.1** ( $\text{Er}^{3+}$ -doped tip  $\text{Al}_2\text{O}_3$  fibre)
- 6.10b Modelling of green upconversion  $\text{FIR}_{g15}$  ( $I_{540\text{nm}}/I_{541.5\text{nm}}$ ) using **Eq. 6.1** ( $\text{Er}^{3+}$ -doped tip  $\text{Al}_2\text{O}_3$  fibre)
- 6.11a Infrared  $\text{FIR}_{\text{IR}12} - \text{FIR}_{\text{IR}14}$  as a function of temperature ( $\text{Er}^{3+}:\text{Al}_2\text{O}_3$  fibre)
- 6.11b Infrared  $\text{FIR}_{\text{IR}23} - \text{FIR}_{\text{IR}24}$  as a function of temperature ( $\text{Er}^{3+}:\text{Al}_2\text{O}_3$  fibre)
- 6.12a Modelling of infrared  $\text{FIR}_{\text{IR}12}$  ( $I_{1511.5\text{nm}}/I_{1523\text{nm}}$ ) using **Eq. 6.1** ( $\text{Er}^{3+}:\text{Al}_2\text{O}_3$  fibre)
- 6.12b Modelling of infrared  $\text{FIR}_{\text{IR}13}$  ( $I_{1511.5\text{nm}}/I_{15473\text{nm}}$ ) using **Eq. 6.1** ( $\text{Er}^{3+}:\text{Al}_2\text{O}_3$  fibre)
- 6.13 Additional visible lines of laser diode at 960 nm
- 6.14 Narrow-line structures of green upconversion emission ( $\text{Er}^{3+}:\text{Yb}^{3+}:\text{Al}_2\text{O}_3$  fibre)
- 6.15 Narrow-line structures of red upconversion emission ( $\text{Er}^{3+}:\text{Yb}^{3+}:\text{Al}_2\text{O}_3$  fibre)
- 6.16 Schematic of experimental set-up for visible signal detection of  $\text{Er}^{3+} + \text{Yb}^{3+}:\text{Al}_2\text{O}_3$  fibre (doped length  $\sim 20$  mm)
- 6.17a FIRs ( $\text{FIR}_{g12} - \text{FIR}_{g15}$ ) of green upconversion as a function of temperature ( $\text{Er}^{3+} + \text{Yb}^{3+}:\text{Al}_2\text{O}_3$  fibre)
- 6.17b FIRs ( $\text{FIR}_{g23} - \text{FIR}_{g25}$ ) of green upconversion as a function of temperature ( $\text{Er}^{3+} + \text{Yb}^{3+}:\text{Al}_2\text{O}_3$  fibre)
- 6.17c FIRs ( $\text{FIR}_{g34} - \text{FIR}_{g45}$ ) of green upconversion as a function of temperature ( $\text{Er}^{3+} + \text{Yb}^{3+}:\text{Al}_2\text{O}_3$  fibre)
- 6.18a FIRs ( $\text{FIR}_{r12} - \text{FIR}_{r15}$ ) of red upconversion as a function of temperature ( $\text{Er}^{3+}:\text{Yb}^{3+}:\text{Al}_2\text{O}_3$  fibre)
- 6.18b FIRs ( $\text{FIR}_{r23} - \text{FIR}_{r25}$ ) of red upconversion as a function of temperature ( $\text{Er}^{3+}:\text{Yb}^{3+}:\text{Al}_2\text{O}_3$  fibre)
- 6.18c FIRs ( $\text{FIR}_{r34} - \text{FIR}_{r45}$ ) of red upconversion as a function of temperature ( $\text{Er}^{3+}:\text{Yb}^{3+}:\text{Al}_2\text{O}_3$  fibre)
- 6.19a Thermal model of green  $\text{FIR}_{g25}$  ( $I_{541\text{nm}}/I_{550\text{nm}}$ ) and  $\text{FIR}_{g35}$  ( $I_{542.5\text{nm}}/I_{550\text{nm}}$ ) based on **Eq. 6.1** ( $\text{Er}^{3+}:\text{Yb}^{3+}:\text{Al}_2\text{O}_3$  fibre)
- 6.19b Thermal model of red  $\text{FIR}_{r25}$  ( $I_{654\text{nm}}/I_{670\text{nm}}$ ) and  $\text{FIR}_{r35}$  ( $I_{657.5\text{nm}}/I_{670\text{nm}}$ ) based on **Eq. 6.1** ( $\text{Er}^{3+}:\text{Yb}^{3+}:\text{Al}_2\text{O}_3$  fibre)
- 6.20 Schematic of experimental set-up for measurement of upconversion intensity in  $\text{Er}^{3+} + \text{Yb}^{3+}:\text{Al}_2\text{O}_3$  fibre (doped length  $\sim 20$  mm)

- 6.21a Green upconversion intensity as a function of temperature ( $\text{Er}^{3+}:\text{Yb}^{3+}:\text{Al}_2\text{O}_3$  fibre)
- 6.21b Red upconversion intensity as a function of temperature ( $\text{Er}^{3+}:\text{Yb}^{3+}:\text{Al}_2\text{O}_3$  fibre)
- 6.21c Sensitivity curves of red and green upconversion intensity as a function of temperature ( $\text{Er}^{3+}:\text{Yb}^{3+}:\text{Al}_2\text{O}_3$  fibre)
- 6.22 Intensity ratio of red to green upconversion as a function of temperature ( $\text{Er}^{3+}:\text{Yb}^{3+}:\text{Al}_2\text{O}_3$  fibre)
- 6.23a Lifetime decay of green upconversion at 323 K ( $\text{Er}^{3+}:\text{Yb}^{3+}:\text{Al}_2\text{O}_3$  fibre)
- 6.23b Lifetime decay of red upconversion at 323 K ( $\text{Er}^{3+}:\text{Yb}^{3+}:\text{Al}_2\text{O}_3$  fibre)
- 6.24 Schematic of upconversion lifetime decay measurement technique in  $\text{Er}^{3+} + \text{Yb}^{3+}:\text{Al}_2\text{O}_3$  fibre (doped length  $\sim 20$  mm)
- 6.25 Temperature dependence of green upconversion lifetime decay ( $\text{Er}^{3+}:\text{Yb}^{3+}:\text{Al}_2\text{O}_3$  fibre)
- 6.26 Temperature dependence of red upconversion lifetime decay ( $\text{Er}^{3+}:\text{Yb}^{3+}:\text{Al}_2\text{O}_3$  fibre)
- 6.27 Schematic set-up for infrared fluorescence intensity ratio detection in high  $\text{Yb}^{3+}$ : low  $\text{Er}^{3+}:\text{Al}_2\text{O}_3$  fibre (doped length  $\sim 20$  mm)
- 6.28 Modelling the temperature dependence of infrared FIR ( $I_{1025\text{nm}}/I_{996\text{nm}}$ ) of  $\text{Yb}^{3+}:\text{Er}^{3+}:\text{Al}_2\text{O}_3$  fibre using Eq. 6.3
- 6.29 Temperature dependence of IR fluorescence at 292, 373 and 473 K
- 6.30 Modelling the green FIR<sub>g15</sub> ( $I_{532.8\text{nm}}/I_{544\text{nm}}$ ) of  $\text{Yb}^{3+}:\text{Er}^{3+}:\text{Al}_2\text{O}_3$  fibre as a function of temperature
- 6.31a Red FIRs of  $\text{Yb}^{3+}:\text{Er}^{3+}:\text{Al}_2\text{O}_3$  fibre as a function of temperature (FIR<sub>r12</sub> – FIR<sub>r15</sub>)
- 6.31b Red FIRs of  $\text{Yb}^{3+}:\text{Er}^{3+}:\text{Al}_2\text{O}_3$  fibre as a function of temperature (FIR<sub>r23</sub> – FIR<sub>r25</sub>)
- 6.31c Red FIRs of  $\text{Yb}^{3+}:\text{Er}^{3+}:\text{Al}_2\text{O}_3$  fibre as a function of temperature (FIR<sub>r34</sub> – FIR<sub>r45</sub>)
- 6.31 Modelling the red FIR<sub>r25</sub> ( $I_{654.6\text{nm}}/I_{672.2\text{nm}}$ ) and FIR<sub>r35</sub> ( $I_{659.6\text{nm}}/I_{672.2\text{nm}}$ ) of  $\text{Yb}^{3+}:\text{Er}^{3+}:\text{Al}_2\text{O}_3$  fibre as a function of temperature
  
- 7.1 Schematic of experimental set-up for measurement of Stokes parameters as a function of temperature (*c*-axis sapphire fibre)
- 7.2 Schematic of experimental set-up for measurement of orthogonal intensities of output lightwave as a function of temperature (*c*-axis sapphire fibre)
- 7.3 Retardation of *c*-axis  $\text{Al}_2\text{O}_3$  fibre as a function of temperature
- 7.4 Ratio of orthogonally polarised components of light from *c*-axis  $\text{Al}_2\text{O}_3$  fibre as a function of temperature
- 7.5 Schematic of experimental set-up for measurement of Stokes parameters as a function of temperature (*a*-axis sapphire fibre)
- 7.6 Schematic of experimental set-up for measurement of orthogonal intensities of output lightwave as a function of temperature (*a*-axis sapphire fibre)
- 7.7 Retardation of *a*-axis  $\text{Al}_2\text{O}_3$  fibre as a function of temperature
- 7.8 Ratio of orthogonally polarised components of light from *a*-axis  $\text{Al}_2\text{O}_3$  fibre as a function of temperature
- 7.9 Schematic of experimental set-up for measurement of orthogonal intensities of output lightwave for 3-point bending tests (*c*-axis sapphire fibre)
- 7.10a Calculated difference-over-sum ratio for 1 mm bending (*c*-axis sapphire fibre)

- 7.10b Calculated difference-over-sum ratio for 2 mm bending (*c*-axis sapphire fibre)
- 7.11 Schematic of experimental set-up for measurement of orthogonal intensities of output lightwave for 3-point bending tests (*a*-axis sapphire fibre)
- 7.12a Calculated difference-over-sum ratio for 1.4 mm bending (*a*-axis sapphire fibre)
- 7.12b Calculated difference-over-sum ratio for 2 mm bending (*a*-axis sapphire fibre)
- 7.12c Calculated difference-over-sum ratio for 0.5 mm bending (*a*-axis sapphire fibre)
- 7.12d Comparison of  $R_{\text{bend}}$  values for 0.5, 1 and 2 mm bending tests

## List of Tables

### Table

- 3.1 Proportion of dopant-liquid mixtures used for dip coating source fibres/rods
- 4.1 Diameter variation of sapphire fibres (*c*- and *a*-axes)
- 4.2a Absorption loss for *Spec11* (without acid cleaning)
- 4.2b Absorption loss for *Spec11* cleaned with acid
- 4.3 Absorption loss for *Spec19* without HCl acid cleaning
- 4.4 Properties of sapphire and silica
- 4.5 Losses due to coupling between sapphire and silica fibres
- 4.6 Laser sources employed for fluorescence studies
  
- 5.1 Measured lifetime as a function of temperature
- 5.2 Fitted parameters for SCC model
- 5.3 Comparison of measured and calculated lifetimes using SCC model
- 5.4a Fitted parameters for R<sub>1</sub> and R<sub>2</sub> lineshifts from 291 to 623 K
- 5.4b Fitted parameters for R<sub>1</sub> and R<sub>2</sub> lineshifts from 673 to 823 K
- 5.5a Measured and calculated shifts for R<sub>1</sub> position
- 5.5b Measured and calculated shifts for R<sub>2</sub> position
- 5.6a Wavelength coefficients of R<sub>1</sub> line
- 5.6b Wavelength coefficients of R<sub>2</sub> line
- 5.7 Lifetime decay of ruby fibre as a function of applied strain (Gauge length = 12.3 mm)
- 5.8 Relative positions of R-lines with applied strain (Gauge length ~6 mm)
  
- 6.1 Some upconversion laser crystals
- 6.2 Some basic properties of RE erbium and ytterbium elements
- 6.3 Denotation of green and infrared fluorescence intensity ratio (FIR) of singly Er<sup>3+</sup>-doped Al<sub>2</sub>O<sub>3</sub> fibre
- 6.4 Fit parameters of visible FIRs using thermal population model, **Eq. 6.1** (Er<sup>3+</sup>:Al<sub>2</sub>O<sub>3</sub> fibre)
- 6.5 Fit parameters of infrared FIRs using thermal population model, **Eq. 6.1** (Er<sup>3+</sup>:Al<sub>2</sub>O<sub>3</sub> fibre)
- 6.6 Denotation of green and red fluorescence intensity ratio (FIR) of Er<sup>3+</sup>:Yb<sup>3+</sup>-codoped Al<sub>2</sub>O<sub>3</sub> fibre
- 6.7 Fit parameters of green FIRs using thermal population model, **Eq. 6.1** (Er<sup>3+</sup>:Yb<sup>3+</sup>-codoped Al<sub>2</sub>O<sub>3</sub> fibre)
- 6.8 Fit parameters of red FIRs using thermal population model, **Eq. 6.1** (Er<sup>3+</sup>:Yb<sup>3+</sup>-codoped Al<sub>2</sub>O<sub>3</sub> fibre)
- 6.9a Comparison of experimental and exponentially-fitted data in green upconversion intensity changes with temperature (Er<sup>3+</sup>:Yb<sup>3+</sup>:Al<sub>2</sub>O<sub>3</sub> fibre)
- 6.9b Comparison of experimental and exponentially-fitted data in red upconversion intensity changes with temperature (Er<sup>3+</sup>:Yb<sup>3+</sup>:Al<sub>2</sub>O<sub>3</sub> fibre)
- 6.10 Lifetime decay of green upconversion in Er<sup>3+</sup>:Yb<sup>3+</sup>:Al<sub>2</sub>O<sub>3</sub> fibre

- 6.11 Lifetime decay of red upconversion in  $\text{Er}^{3+}:\text{Yb}^{3+}:\text{Al}_2\text{O}_3$  fibre
- 6.12 Fit parameters of IR FIRs based on **Eq. 6.3** (high  $\text{Yb}^{3+}$ : low  $\text{Er}^{3+}:\text{Al}_2\text{O}_3$  fibre)
- 6.13 Comparison of measured and fitted infrared FIRs based on **Eq. 6.3** (high  $\text{Yb}^{3+}$ : low  $\text{Er}^{3+}:\text{Al}_2\text{O}_3$  fibre)
- 6.14 Fit parameters of green FIRs using thermal population model, **Eq. 6.1** (high  $\text{Yb}^{3+}$ : low  $\text{Er}^{3+}:\text{Al}_2\text{O}_3$  fibre)
- 6.15 Fit parameters of red FIRs using thermal population model, **Eq. 6.1** (high  $\text{Yb}^{3+}$ : low  $\text{Er}^{3+}:\text{Al}_2\text{O}_3$  fibre)
  
- 7.1a Retardation of *c*-axis sapphire fibre as a function of temperature
- 7.1b Difference-over-sum ratio,  $R(T)$ , of *c*-axis sapphire fibre as a function of temperature
- 7.2a Retardation of *a*-axis sapphire fibre as a function of temperature
- 7.2b Difference-over-sum ratio,  $R(T)$ , of *a*-axis sapphire fibre as a function of temperature
- 7.3a Results of 1 mm 3-point bend test of *c*-axis sapphire fibre
- 7.3b Results of 2 mm 3-point bend test of *c*-axis sapphire fibre
- 7.4a Results of 1 mm 3-point bend test of *a*-axis sapphire fibre
- 7.4b Results of 2 mm 3-point bend test of *a*-axis sapphire fibre
- 7.4c Results of 0.5 mm 3-point bend test of *a*-axis sapphire fibre

# Chapter 1 – Introduction

## 1.0 Research Context

## Chapter 1 – Introduction

### 1.0 Research Context

Most fibre optic sensing systems have utilised conventional glass fibres as sensing elements. This can result in limitation of certain parameters of interest such as temperature, strain, stress and bending to a lower sensing and/or dynamic range due to the intrinsic physical properties of glasses. While crystalline materials have also been employed as sensing elements in some fibre optic sensing schemes, most have been based on small crystal sections cut from bulk materials. Means then have to be found so that these crystalline probes could be securely connected or coupled to other fibres or materials which serve as the delivery/collection media for the light source. However, many crystalline materials have interesting properties which are often superior to those of glasses or glass-based fibres. Some examples are sapphire, yttria and yttria-stabilised zirconia which have very high melting points, strength and relatively good optical transmission properties. It would thus be highly advantageous if such crystalline materials can be grown in fibre form in order to make them compatible in size to conventional optical fibres so that they could be easily integrated with current glass fibre technologies and components.

This project thus aims to utilise the laser heated pedestal growth method to grow single-crystal fibres of pure and doped sapphire in order to study their temperature, strain and bending-related characteristics/behaviours so that they can be exploited as sensor materials.

This thesis is divided into eight chapters together with two appendices. **Chapter 2** gives an introduction to single-crystal fibres and some of their common applications. A review of current fibre optic sensing is then undertaken with emphasis placed on those sensing techniques which would most likely be employed in this project. Fibre optic sensors based on crystalline materials are then discussed.

In **Chapter 3**, an overview of current crystal fibre grow techniques is given. The design and construction of the laser heated pedestal growth technique are then discussed together with proposals for two automatic diameter

measurement/monitoring systems which could be integrated with the fibre growth controlling programme to form a feedback loop. A procedure for ensuring uniform coating of source rods with dopant materials is established and the growth characteristics of various crystal fibres are also discussed.

In **Chapter 4**, the crystal fibres which have been grown are characterised. Absorption and fluorescence measurements are carried out for doped fibres. Coupling of pure sapphire fibres to silica fibres is also investigated since certain crystal fibre probes are relatively short (<50 mm) and may need a longer light delivery and collection silica fibre.

The temperature and strain dependencies of ruby fibres are studied in **Chapter 5** based on the fluorescence characteristics of the fibre through its fluorescence lifetime decay and lineshift. Models are also used for describing the experimental data. In particular, the temperature-lifetime profile is seen to fit the theory rather well.

In **Chapter 6**, the emission characteristics of rare-earth doped sapphire fibres are studied as a function of temperature. Infrared fluorescence and upconversion emission are observed from singly  $\text{Er}^{3+}$ -doped  $\text{Al}_2\text{O}_3$ ,  $\text{Er}^{3+} + \text{Yb}^{3+}$ -codoped (with approximately equal RE contents) and high  $\text{Yb}^{3+} + \text{low Er}^{3+}$ -codoped  $\text{Al}_2\text{O}_3$  crystal fibres. The fluorescence intensity ratio (*FIR*) technique has been employed to relate the both the IR and upconversion emissions to temperature.

**Chapter 7** investigates the naturally birefringent nature of pure *a*- and *c*-axis sapphire fibres in order to exploit them for fibre optic sensing applications. Both retardation of transmitted light through the two types of fibres as well as the orthogonally polarised intensities of transmitted light are monitored with respect to changes in temperature and bending.

**Chapter 8** concludes the entire project and offers some recommendations for further improvements to the laser heated pedestal growth system for producing longer fibres with smaller diameter variations as well as the ability to grow other higher melting point materials. Field trials are also proposed as the next step in employing these crystal fibres for sensing applications.

## **Chapter 2 – Introduction to Single-Crystal Fibre Sensors**

- 2.0 Introduction to single-crystal fibres**
- 2.1 Applications of single-crystal fibres**
- 2.2 Introduction to fibre optic sensing**
- 2.3 Fundamental principles of FOS**
  - 2.3.1 Intensity-based sensors
  - 2.3.2 Interferometric sensors
  - 2.3.3 Distributed and multiplexed sensing systems
  - 2.3.4 Fibre Bragg gratings and sensors
  - 2.3.5 Fluorescence-based fibre optic sensors
  - 2.3.6 Crystal fibre sensors
- 2.4 References to Chapter 2**

## Chapter 2 – Introduction to Single-Crystal Fibre Sensors

### 2.0 Introduction to single-crystal fibres

Also known as “whiskers” in materials science, single-crystal fibres have rather remarkable properties, both optical and mechanical, which have seen many of them in use in numerous optical and structural applications. The bulk of such applications has largely been in the areas of solid state laser devices, non-linear optics, modulators, switches, amplifiers, optical parametric devices, high power beam delivery and beam delivery in medicine. Only very recently have they been utilised for specialised fibre optic sensing schemes. Rigorous research on single crystal fibres has only been actively pursued over the last two to three decades due mainly to the unavailability of suitable growth techniques in producing crystalline materials in fibre form before this period. Their mechanical and optical properties are often superior to those of glass-based materials and, often, of their bulk-grown counterparts. Unlike glass fibres, single-crystal fibres (SCFs) exhibit a sharp liquid-solid phase transition and through the use of appropriate growth techniques, together with the small dimensions (generally in the  $\mu\text{m}$  region), fibres with little or almost no internal defects can be produced, offering the possibility of high crystalline perfection and near-theoretical strength.

Initial research on single-crystal fibres, however, was mainly concentrated on materials science and structural applications [2.1] due to the great interest in their potentially excellent mechanical properties such as high strength, chemical inertness and high temperature resistance. For example, sapphire fibres, with an ultra-high yield strength of  $>1$  GPa, a modulus of  $\sim 400$  GPa and a high melting point ( $\sim 2323$  K), were recognised early as suitable for structural reinforcement. Again, it was not until the early 1970s that techniques to fabricate these fibres in high quality were developed but due to the high cost involved in producing long lengths and large amounts of these fibres for use as structural reinforcements, research in this area declined. The development of more easily fabricated and cheaper structural reinforcing replacements also contributed to this drop in interest in single-crystal fibres for structural applications.

The search for new electro-optic, solid-state tunable laser and waveguiding materials in the 1970's (in parallel with fibre optic telecommunications) led to renewed efforts being made in single-crystal fibre research. With the advent of optical communications, many applications required crystalline materials but until this period, single-crystals in fibre form were unavailable. Their attractive optical properties such as wide transparency, suitability of dopant incorporation, high crystalline perfection, high achievable energy densities and optical gain, and large non-linear coefficients have also allowed various other electro-optic and device applications. One such material which can be grown as crystal fibres is lithium niobate [2.2], both doped and undoped, which has been intensely studied and which finds potential application in nonlinear optical, surface acoustic wave devices, waveguiding and photorefractive storage, the last of these properties having major commercial implications. The ability to produce single crystalline materials in fibre form with controlled diameter and uniformity in composition thus makes them compatible with existing glass-based fibre optic technologies, giving the combined benefits of an electro-optic material with the useful light guiding properties of a fibre.

In the development of novel optical fibre sensor materials based on fluorescence, speed and efficiency are of outmost importance since it is generally the case that the host material itself has been selected while suitable dopants have to be identified and incorporated which can interact with the physical parameters of interest such as temperature, strain, stress, pressure, etc. Although single-crystal fibres used in sensing applications may not require the same level of doping or very low transmission loss as in, for example, a solid state laser material, a relatively high level of crystal quality and physical perfection is still desired. This process of fabricating high quality optical single crystalline materials in fibre form can be easily achieved through the use of the laser heated pedestal growth technique.

Intense effort was carried out in the early 1970's to find suitably efficient and cost-effective techniques in producing single-crystal fibres. Although C. V. Boys [2.3, 2.4] historically produced very fine fibres made of quartz which were approximately 90 feet in length and 0.25 microns in diameter by cementing one end of a thin quartz rod to a straw arrow, heating the middle of the rod with an oxyhydrogen flame while

hand-holding the other end and firing the arrow with a crossbow, these fibres were not considered to be single-crystals; although it was found that they exhibited very high tensile strength. The first genuine efforts in producing single-crystal fibres can be attributed to LaBelle and Mlavsky [2.5], who, in 1967 successfully grew continuous sapphire "whiskers" from the melt (through a floating disc-like orifice) with diameters ranging from 0.05 to 0.50 mm. The fibres produced were mostly *c*-axis oriented sapphire filaments pulled with an apparatus similar to a Czochralski crystal puller at rates of up to 150 mm/min. RF heating was used and the source was melted in a molybdenum crucible. LaBelle and Mlavsky [2.6] later improved their technique to include a rigid tubular molybdenum capillary orifice from which they were able to pull sapphire filaments several hundred feet long and 0.1 to 0.5 mm in diameter with relatively high pulling rates (up to 50 mm/min). This capillary tube, which was attached to the bottom of a molybdenum crucible, allowed the melt to rise through it by virtue of surface tension and capillary action, and acted as a thermomechanical stabiliser for the molten source material. By controlling the temperature of the top of the tube close to the melting point of sapphire, single crystal fibres of this material could then be pulled from the melt. The authors were able to pull filaments which were then subsequently used for reinforcement agents in structural composites. The capillary-aided crystal fibre growth technique was further refined by LaBelle [2.7] in 1971 into the Edge-Defined Film-Fed Growth (or EFG) with which fibres, filaments and crystals of complex shapes can be grown.

1970 saw the first use of the laser as heat source for crystal growth. Gasson and Cockayne [2.8] demonstrated the use of 2 large CO<sub>2</sub> lasers (maximum individual output power rated at 400 W) as the heat source to grow single crystals of various oxide materials. The beams from the two lasers were first independently directed by concave mirrors to focus onto the surfaces of a source and seed rod respectively, which then melted and expanded to join and form a stable molten zone. Crystal growth was then achieved by downward translation of both rods with rotation of the holding chucks and the laser beams finally deflected to focus on the same level of the molten zone. With efficient absorption of the 10.6 μm radiation from the lasers, they were able to grow single crystals of Al<sub>2</sub>O<sub>3</sub>, CaZrO<sub>3</sub>, MgAl<sub>2</sub>O<sub>4</sub> and Y<sub>2</sub>O<sub>3</sub> approximately 5 mm in diameter with melting temperatures in the range of 2323 to 2723 K with some success. These crystals can hardly be considered as fibres,

although their crystalline states had been determined as single crystal but this work marked the first instance when lasers were used in a zone-refining crystal growth effort. Of the crystals studied, both  $\text{Al}_2\text{O}_3$  and  $\text{Y}_2\text{O}_3$  are known laser materials. Cockayne *et al.* [2.9] later used a DC laser system instead of an AC system in the zone-refining technique mentioned above [2.8] to reduce the peak laser power incident upon the molten zone and, hence, the loss of material by evaporation during crystal growth.

The method of Gasson and Cockayne [2.8] was later adapted and modified in 1975 by Burrus and Stone [2.10] into a two beam  $\text{CO}_2$  laser-heated floating zone pedestal growth technique with the aim of growing communications fibre-optic compatible single crystalline laser devices in fibre form. Rotation of the source/seed-holding chucks was also employed to enable symmetric heating. The source rods used in their work were cut from bulk grown materials and were of a much smaller dimension compared to earlier work (~2 mm square cross-section). Using a thin platinum wire dipped into the laser-heated molten zone and pulling upwards, they were able to pull laser-quality single-crystal Nd:YAG fibres 50  $\mu\text{m}$  in diameter and ~20 cm long. Room temperature cw laser action was demonstrated in 0.5 - 1 cm long samples of these fibres. Using the same two-beam laser-heated float zone technique, Burrus and Coldren [2.11] later grew single-crystal sapphire-clad ruby ( $\text{Cr}:\text{Al}_2\text{O}_3$ ) fibres for studies in waveguiding of acoustical energy by varying the concentration of  $\text{Cr}^{3+}$  ions in the core region. The outer sapphire cladding was realised through a re-growth using the same crystal fibre growing apparatus but this time, only the surface of a previously grown ruby fibre was melted by proper focusing of the laser beams and the use of reduced laser power. This allowed the Cr concentration in the surface layer to be reduced drastically, forming, effectively, a sapphire-clad ruby-cored crystal fibre. Continuous laser operation of a single-crystal ruby fibre grown by the laser-heated float zone technique at room temperature was also demonstrated in 1978 [2.12]. The small cross-sectional area of a fibre geometry and, thus, an increased surface-to-volume ratio leads to an increased cooling efficiency. The authors were thus able to obtain continuous laser action from *c*-axis oriented 35 - 50  $\mu\text{m}$  diameter single-crystal ruby fibres pumped by a Kr laser. The reduced Cr concentration of 0.02 wt. % (compared to conventional ruby laser rods at 0.05 wt. % Cr concentration) used in their samples allowed reduced absorption and

the consequent heating effects during laser action without having the need to increase the pump power at threshold.

One of the major advances in crystal fibre growth occurred in the early 1980s when a group at Stanford University [2.13, 2.14], having realised the potential of laser heating in the growth of single-crystal fibre materials for device applications, carried out further development of the earlier floating zone technique and arrived at what is now commonly referred to as the laser-heated pedestal growth (LHPG) technique. They made major changes to the design of the beam positioning mirrors to include novel focusing optics for axially symmetric heating of the melt. Similar to the float zone growth, no crucible was required, hence, little or no impurity contamination from secondary phase components was possible. With symmetric heating of the source rods and the large temperature gradients afforded by laser heating, very high purity and optical quality single-crystal fibres could be produced. The Stanford Group also included a diameter measurement system [2.15] to monitor and control diameter fluctuations to less than 0.1% and a belt drive feed/pull system for fibre growth limited only by the length of the source material/rod. Within a short period of time the group was able to demonstrate the versatility of the laser-heated pedestal technique by growing a very wide variety of optical, electro-optical, superconducting and magnetic materials in high quality, single-crystal fibre form for a wide range of applications [2.16]. One of the major advantages of this technique is that it permits a small quantity of starting/source materials to be used for growing into single-crystal fibres before any bulk crystal or mass production is initiated. This is of considerable economic importance when expensive compounds, such as scandium, are to be studied. Currently, a few groups in America, Europe and China have also adopted the laser-heated pedestal growth method in the pursuit of novel high performance laser, optical and electronic materials.

## **2.1 Applications of single-crystal fibres**

The main areas of applications for optical single-crystal fibres include miniature solid-state lasers, guided-wave nonlinear optics and, recently, fibre optic sensing; particularly for hostile environments.

One of the most important areas of research in single crystal fibres has been the studies and development of solid-state laser materials and crystal fibre lasers. Although in terms of wavelength coverage, crystalline fibres may not offer any significant advantage compared to glass-based fibre lasers, they do, however, offer the potential of higher optical damage threshold and, because of their intrinsic properties, many crystal fibres can have better mechanical strength. The high damage threshold can mean the use of fewer amplification centres with higher input power while the mechanical advantage would aid the handling and processing of these fibres. Laser crystals with fibre geometry also offer the possibility of direct in-line optical processing when incorporated into existing fibre optic communications configuration rather than having to undergo the complicated and high-loss optical/electronic and electronic/optical signal conversion used in current opto-electronic processing schemes.

Since single-crystal fibres can be considered as quasi-unidimensional (typical diameters in the range of 3 - 500  $\mu\text{m}$ ) and can offer other possibilities in the areas of nonlinear optical interaction due to their waveguiding fibre geometry. Since the efficiency of many nonlinear optical interactions is inversely proportional to the square of the beam diameter or, in another way, directly proportional to the optical intensity [2.17], for a given optical power, the small physical dimensions over extended lengths in these crystalline fibres mean that they could offer a dramatic increase in nonlinear efficiency and optical gains when compared to bulk counterparts. Moreover, most, if not all, of the crystal fibres can be appropriately doped with the right impurities to produce the desired optical properties. An example is the barium metaborate ( $\text{BaB}_2\text{O}_4$ ) single-crystal fibres grown by the laser-heated pedestal growth method [2.18] to allow phase matching for harmonic generation from 200 to 1500 nm because of its large nonlinear second harmonic generation coefficients, wide optical transparency, large birefringence and low dispersion.

There is also considerable interest in growing high temperature superconducting ceramics in single-crystal fibre forms for property characterisation studies. These materials are difficult to grow because of their incongruent melting behaviour but in single-crystal fibre form, they have near-theoretical properties and grown along the

proper crystallographic orientation, they could be used for enhancing the critical current density and operational efficiency [2.19, 2.20].

Another area of application for single-crystal fibres can be found in passive optical devices such as waveguides, filters, polarisers and isolators. It is very difficult to grow single-crystal fibres with lengths typical of those glass-based optical fibres – the longest reported single-crystal fibres grown to date are only several metres in length. Coupled to the wide transparency range afforded by many crystalline materials, the high optical damage thresholds, mechanical strength, chemical inertness and non-toxicity of single-crystal sapphire fibres (for example) mean they are very suitable for high power beam delivery of Nd:YAG lasers, beam delivery systems for medical operations at the Er:YAG wavelength and in fibre optic sensors. In materials science, however, there is still great interest in growing new materials in single-crystal form for property evaluation and to study their fundamental behaviours such as solidification, morphology and formation of ferroic domains, eutectic phases and defect densities. LHPG offers a quick and efficient way of fabricating these new materials in very small dimensions so that their near-ideal properties can be evaluated instead of those filled with defects and crystal deformation typical of bulk crystals.

A relatively recent application has seen single-crystal fibres utilised in fibre optic sensors mainly for measurements of high temperatures. In many of the sensors reported to date, sapphire fibres have been used as the sensing probes because of their favourable material properties. As shall be seen in later sections, SCFs have been used as fibre optic sensors in many configurations: black-body, intrinsic Fabry-Pérot interferometry, extrinsic Fabry-Pérot interferometer and fluorescence [2.21, 2.22, 2.23, 2.24, 2.25, 2.26].

## **2.2 Introduction to fibre optic sensing**

Fibre optic (FO) sensors have been studied for more than three decades. Since the first experimental trials in laboratories in the early 1970's, the interest in this technology has been maintained up to the present time. This is due to the potentially significant contributions that fibre optic sensors can provide for both research and

industry: fibre optic-based sensors are lightweight and small in size generally, immune to electromagnetic interference (EMI), require no electrical power at the sensing point and, hence, can be used in explosion-risk environments, permit access into normally inaccessible areas, have high accuracy, provide secure data transmission, are easily multiplexable and are, generally, immune to radio-frequency interference [2.27]. Some typical physical parameters which can be measured with fibre optic sensors include light intensity, displacement or position (both linear and angular), temperature, pressure, strain, flowrate, magnetic and electric fields, acoustic field and rotation (fibre optic gyroscopes).

Fibre optic technology has revolutionised the telecommunications industry by providing superior performance with constant improvements at lower costs than most alternative approaches [2.28]. FO sensing may be considered a "spin-off" from the telecommunications industry; this has resulted in optical fibres designed mainly for communications being utilised in many FO sensing schemes. However, the substantial knowledge of the underpinning science gained in telecommunications has enabled ease of modification of the relevant optical properties of these fibres for use as fibre optic sensors [2.29, 2.30]. The progress in fibre optic telecommunications technology also provides continuous development and availability of related FO components and materials at lower costs. Laser diodes, which were too expensive for many academic research laboratories two decades ago, are now easily available and at a tiny fraction of their original costs. The high demand for specialised optical fibres [2.31] for FO sensing and the continued refinement in their fabrication techniques also mean that they now cost less and are widely available. The same can be said of optical detector and receiver units, important for good signal detection and recovery.

The recognition of large areas of opportunity and the high potential of replacing many of the existing alternative sensors has led to intense effort being made in the investigation, research and development of fibre sensors. Many sensor schemes remain lab-based but commercial products are beginning to emerge and are currently available in the market. They include the simple intensity-based sensors like the *AccuFiber* and *Luxtron* temperature sensors, the *Photenetics* multiparameter sensor for temperature, pressure and refractive index measurements, the *CDI* chemical

sensor, the *Babcock and Wilcox* pressure sensors and the *York Technology* distributed temperature sensor system. However, due to the limited, low volume markets currently available, FO sensing technology is generally more costly than their conventional counterparts although, as these sensors gain increasing market acceptability, unit cost should be reduced. This low demand has led to the creation of niche markets with specialised applications and needs: examples are multiplexing of FO-based sensors, requiring ultra-sensitive, electrically passive sensor heads, and OTDR (optical time-domain reflectometry), requiring highly-accurate pulse generators, advanced Q-switched laser sources and high performance detection and signal processing components. Another niche application in which conventional sensor technologies are almost impractical to implement is in the structural strain monitoring field where spatially mapped sensors can be embedded in the superstructures using the novel fibre optic Bragg grating technology [2.32, 2.33].

Fibre optic sensors face very keen competition from conventional sensors, which provide considerable sensing capabilities and, generally, good accuracy but there will always be certain sensing applications in which these conventional sensors are inadequate. These include sensing in very hostile thermochemical and thermonuclear environments, temperature sensing in very high electromagnetic and radio-frequency fields, the aerospace industry (weight and size considerations) and high-speed high-data rate distributed sensing application. Furthermore, there has been a healthy increase in commercial interest in using fibre optic sensing techniques with applications to the civil and, especially, military sectors. Large structures such as bridges, buildings, boilers, pressure vessels and even aircraft operating close to their performance limits are important areas which require constant monitoring and control in order to ensure that potential failure can be predicted and does not occur before their anticipated useful life. Here, fibre optic distributed sensing can play a critical role in offering the possibility of monitoring the potential problem areas and, hence, allowing replacements of the faulty components before failure can occur. This can be achieved with multiple sensing heads/tips positioned along the desired measurement areas or through the use of multiple Bragg gratings with different written wavelengths along one length of optical fibre. For example, the monitoring of bridge decks for chlorine corrosion has recently been demonstrated by embedding multiple fibre sensing tips in the reinforced concrete structure [2.34].

The military sector, a major consumer of fibre optic technology, has seen an increasing trend in the commissioning, studies and field trials of important fibre optic sensing schemes. Most major trials involve the implementation of fibre optic sensors on a large scale into new or existing systems, which have previously utilised conventional sensors. Several fly-by-light (FBL) programs [2.35] have been commissioned both by industries and governments to study the possibility of incorporating fibre optics sensors and fibre optic data links to replace existing electrical/electronic data transmission links and sensors on both commercial and military aircraft. Remote actuators and hardware generally require several levels of redundancy to enforce the required safety level and could thus become cumbersome while electrical transmission links, unless heavily shielded, are targets for strong electromagnetic and radio-frequency interferences, and lightning strikes. Failures in such devices often have catastrophic effects and can be avoided by the incorporation of fibre sensors and fibre links to augment or replace current components. Certain commercial aircraft have already adopted the fibre optic gyroscopes (FOGs) as primary or secondary navigation systems while Japanese rockets have been launched since 1991 with the aid of FOGs [2.36]. Field trials have also been performed on naval vessels where the potential failure of any one of the numerous shipboard cables, equipment and sensors would endanger the crew and the vessel as a whole. Hence, stringent monitoring and control are required to ensure their functionality. Incorporation of an integrated fibre optic multiplex system, with a bank of fibre optic shipboard sensors (for monitoring the numerous onboard functions) and data transmission lines ensures freedom from EMI, very high speed sensing operation and high data transmission rate; speed being an important factor for target detection, weapons fire-control and the basic defence of a ship in the event of an external threat to the vessel. Integrated systems also allow automated testing and calibration of the installed fibre sensors and data links [2.37]. One particularly attractive advantage, in purely military terms, when using fibre optic technology in control systems for military jet aircraft and naval vessels is protection from the extreme electromagnetic pulse generated by a nuclear or thermonuclear explosion. Incidentally, single-crystal sapphire fibres would be ideal as the optical fibre data transmission lines and links since sapphire is extremely radiation-hard whereas glass can become opaque when exposed to high levels of radiation. Finally, another major military application is the

deployment of large fibre optic hydrophone arrays for sensitive detection of both underwater and surface movements. The use of fibre optic sensors in chemical and biochemical applications for measuring various parameters has also been increasing in recent years [2.38].

Although the limited market has hindered the commercialising of many fibre optic sensor products, the measurability of theoretically any physical parameters, the continuous improvement and development of existing and novel sensing schemes and the potential advantages exhibited by FO sensing over traditional sensors remain the major driving force in the search for new and wider applications area for this class of sensor.

### **2.3 Fundamental principles of FOS**

The conversion of one type of signal into another is the essence of any sensor system. In the case of fibre optic sensing, input parameters such as changes in temperature, stress, strain, acceleration, angular position and displacement, PH level, pressure, etc., duly called the measurands, can be manipulated to produce corresponding changes in the characteristics of light transmitted along the fibre. For example, the phase, frequency, intensity or polarisation of the light wave may be modulated [2.39]. FO sensors are devices whereby the properties of light guided within an optical fibre is modified or modulated due to the various external influences such as:

- 1) physical,
- 2) chemical,
- 3) biological and
- 4) biomedical effects

There are two distinct ways in which optical fibres are used in measuring environmental influences: extrinsic and intrinsic techniques. The former is distinguished by sensing taking place in a region outside the fibre. Here, light is guided along a length of optical fibre to the measurement point and allowed to exit

the fibre, the light being modulated in a separated zone by the measurand before being re-launched into either the same or a different optical fibre to be detected.

In intrinsic fibre sensors, the guided electromagnetic wave is modulated within the fibre at the measurement point and, after modulation by the physical parameter, continues to propagate along the same fibre at the end of which the signal is detected and processed. Sensing therefore takes place within the fibre itself. This is also commonly known as "all-fibre" sensing. In other fibre sensors, the guided light can be made to couple to the measurand via the evanescent field. This sensor type is midway between the two distinct categories but may be classified as extrinsic. **Figures 2.1** and **2.2** are schematic representations of the extrinsic and intrinsic sensors respectively.

Some techniques commonly used in extrinsic sensing include reflection and transmission, total internal reflection (TIR), gratings, fluorescence and evanescence, while intrinsic techniques are generally based on Rayleigh and Raman scatterings, microbending, mode coupling and interferometry

It is not within the scope of this thesis to describe the whole range of fibre optic sensors already available or currently being developed although a brief discussion on the basic principles will be outlined in the subsequent sections.

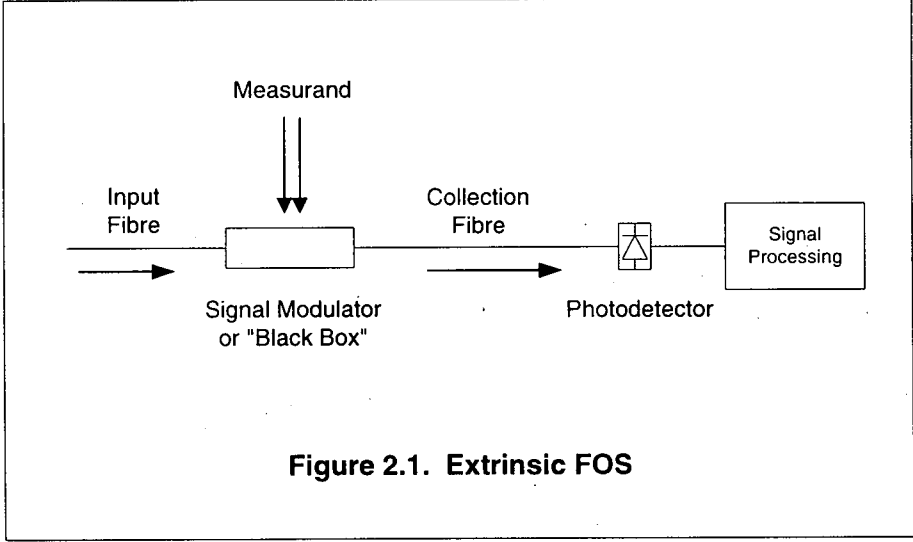


**Figure 2.1. Extrinsic FOS**

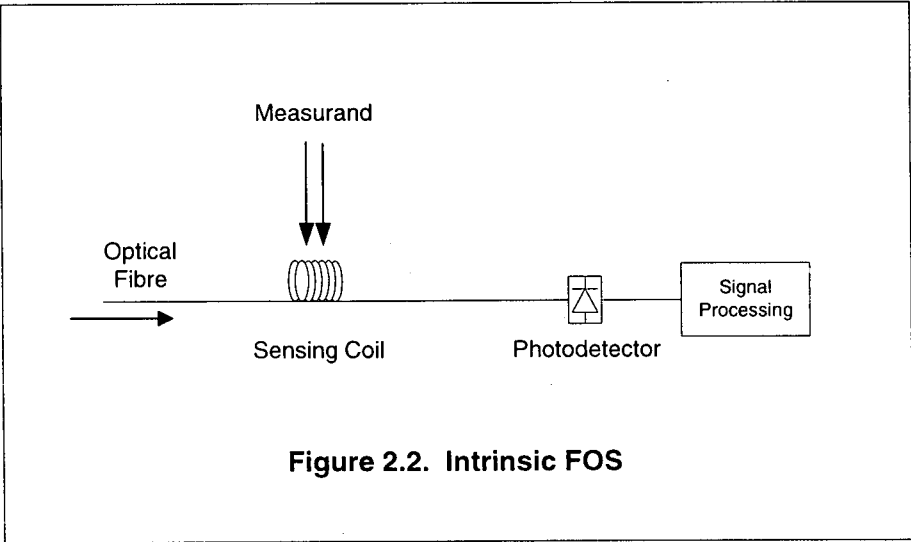


**Figure 2.2. Intrinsic FOS**

### 2.3.1 Intensity-based sensors

Fibre optic sensing can be based upon various sensing configurations, the simplest being intensity-based sensors. This is also known as the optical intensity or amplitude modulated sensor. In such a configuration, light guided along an optical fibre, either in an intrinsic or extrinsic sensor, is modulated in its intensity which offers both simplicity and potential low cost in their manufacture as only the amplitude of the intensity is detected (which can be easily measured using a simple photodetector). Some commonly used concepts in such intensity-based sensors are transmission, reflection and microbending although other concepts such as absorption, scattering, optical gratings, etc., may be used. The two figures below show some of the concepts used, which could be further expanded to produce high performance sensors (**Figures 2.3** and **2.4**). These are transmissive sensors where the light path is interrupted by a separation of the input and collecting fibres. Axial movement of one fibre with respect to the fixed input fibre changes the light intensity arriving at the photodetector, thus giving an indication of axial displacement (**Figure 2.3**). The second figure (**Figure 2.4**) shows that an upward or downward movement of the movable fibre can give a measure of radial displacement due to the corresponding changes in the captured intensity.

The frustrated total internal reflection concept is shown in **Figure 2.5** when two angled fibre ends are brought together from a certain distance apart. This couples the light intensity from the transmitting fibre to the receiving fibre, resulting in a sensor with a very high sensitivity [2.27]. Moreover, if the refractive index of the surrounding medium is changed to approach that of the fibre core, some of the intensity is lost through light propagating out of the fibre and the photodetector thus detects a reduction in the signal. In this way liquid level, pressure and refractive index measurements are possible.

The reflective concept shown in **Figures 2.6**, **2.7**, and **2.8** are commonly used in intensity-based FO sensors due to its simplicity, accuracy and potential low cost. In **Figure 2.6**, a bundle of two fibres is used, one fibre for transmitting light to the reflecting surface while the other collects the reflected intensity and guides it back to the photodetector. Hence, depending on the relative distance between the fibres and

the reflector, the detected light intensity will change accordingly. **Figure 2.7** shows the same concept used in reflective sensing except that the two fibres used for delivery and collection are separated while in **Figure 2.8**, a single directional coupler with 3 fibres is used. The transmitted light is allowed to pass through the coupler to the probe and to the reflecting surface. The reflected signal is collected by another fibre without interfering with the transmitted signal.

A typical microbending sensor is shown in **Figure 2.9** where a force, pressure or displacement, due to a change in a physical parameter, can be introduced. This causes a decrease in the amount of light reaching the detector because of signal loss through the fibre wall when it is subjected to bending. The sensitivity of this type of sensor can be increased by introducing more pressure points in the transducer and reducing their spacings. Such a configuration has a closed optical path and with properly selected claddings, can be used for sensing applications in dirty or hostile environments.

The use of gratings in a fibre optic sensor (**Figure 2.10**) can help increase the sensitivity of the sensor by producing a maximum intensity within one grating spacing instead of having the fibres move a one-diameter distance. Rotational measurement (example torque, radial velocity) can also be carried as well with the proper configuration. In such a sensor, the sensitivity is determined by the grating with and spacing, which can be increased at the expense of the dynamic range.

In an evanescent-based sensor, light intensity is made to cross-couple from one optical fibre to another (**Figure 2.11**). Parameters such as the wavelength of light, relative index of refraction of the surrounding medium, distance between the two fibre cores and the interaction length affect the extent of this cross-coupling mechanism. Hence, temperature, strain, pressure, wavelengths and refractive index measurements are possible measurands for such a sensing concept.

Fluorescence-based sensors (**Figure 2.12**) can be used in applications for measuring temperature, viscosity, humidity and so on [2.38]. They operate on the principle of a reagent material interacting with the incident light and emitting the absorbed light at a longer wavelength. The fibre used for this type of sensing can be coated or, more

commonly, doped with an impurity which is sensitive to the measurand in question. Erbium, neodymium and chromium are examples of impurities which, when incorporated into the appropriate fibre materials, are highly sensitive to changes in temperature. Intensity-modulated sensors based on the fluorescence effect have been widely investigated and used for chemical sensing, measurement of food processes and in medical applications [2.40, 2.41]. Fluorescence-based sensors will be further discussed in **Section 2.3.5**.

Intensity-based sensors have a drawback in that, due to the unavailability of a reference arm or system, there exists an error in the output signal as a result of changes in the optical source intensity. Such erratic changes thus give rise to a random fluctuation of the modulated output signal (there is an error even under no measurand influence) during detection, resulting in inherent inaccuracies. These changes can be due to an unstable (or drifting) source, ageing external influences, loose connectors and fibre leads [2.42, 2.43, 2.44]. This problem has been investigated by various groups and a simple self-compensation technique has been proposed by Gilles *et al.* [2.45] using a “balanced” sensor approach whereby the two light paths are “crossed-over” at the detector. They used two transmitters and two receivers in this approach and, after correcting for output variation due to the d.c. offsets in the detector amplifiers and the transmitters not switching off, were able to obtain a constant output signal within a  $\pm 1\%$  accuracy up to a 20 dB level change (of the lines, transmitters and amplifiers). **Figure 2.13** shows their self-compensating approach, where  $T_{xi}$  are the transmitters,  $P_i$  their corresponding outputs,  $R_{xi}$  the d.c. offsets,  $G_i$  the gains from the two respective amplifiers,  $L_a$  the loss through the sensor,  $L_i$  the attenuation of the optical paths to the sensor head,  $L_{ij}$  the cross-over attenuation. The final output from the amplifiers after correction is given by

$$V = \frac{V_{13}'}{V_{23}'} \times \frac{V_{24}'}{V_{14}'} \quad (2.1)$$

where  $V_{13}' = V_{13} + \beta V_{23} + R_1$  (2.2)

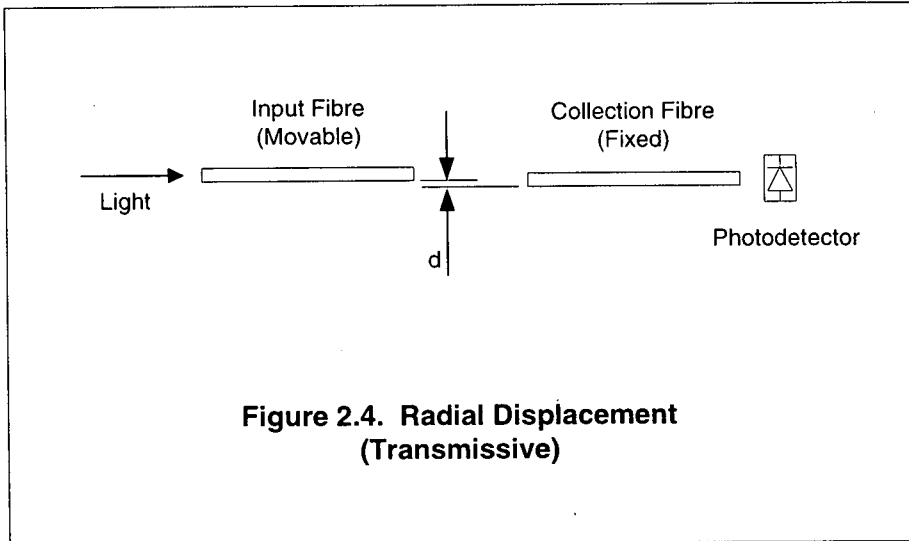
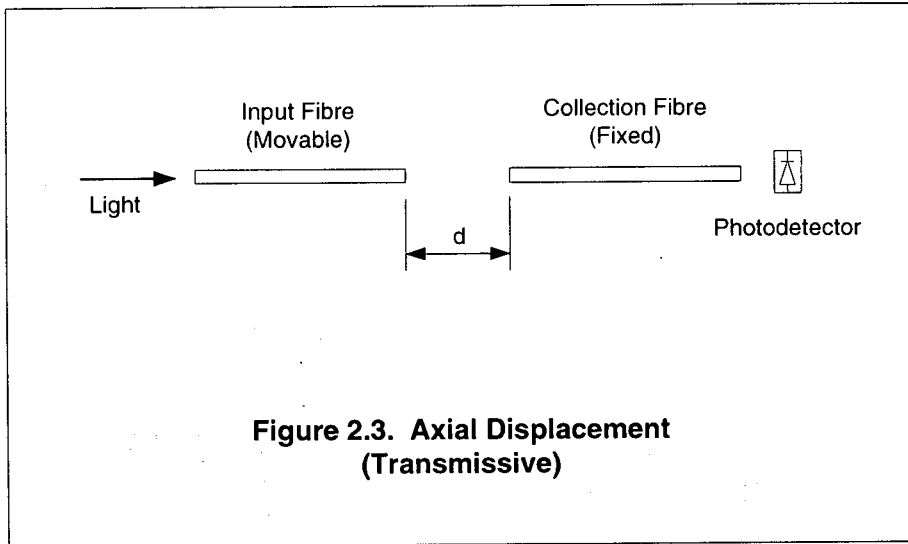
$$V_{23}' = V_{23} + \alpha V_{13} + R_1 \quad (2.3)$$

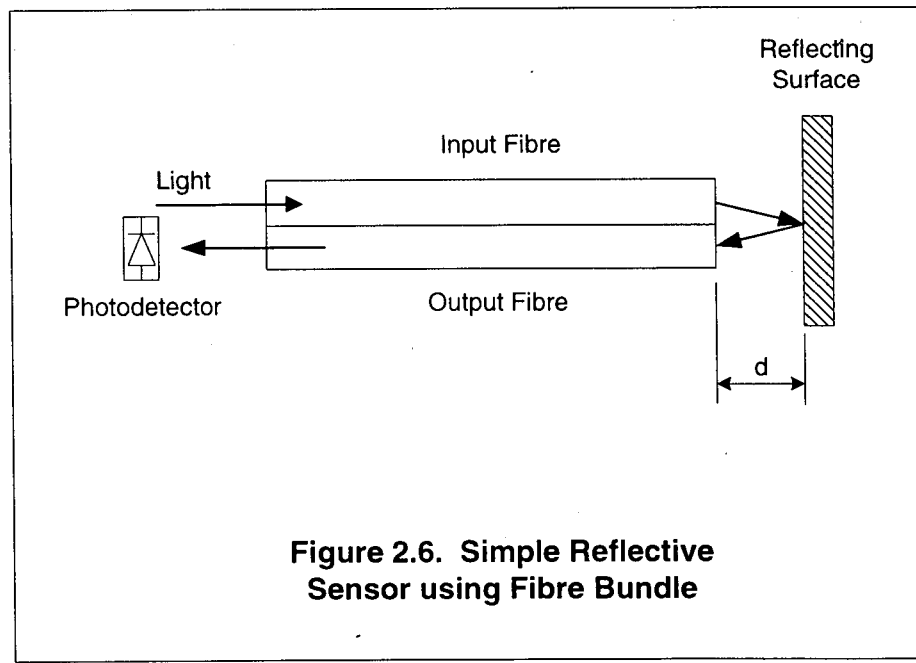
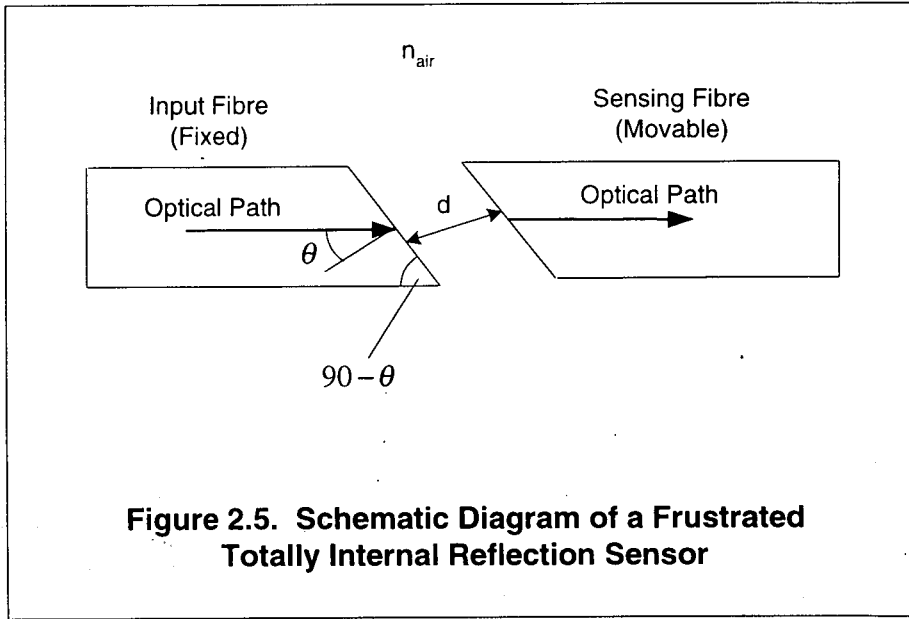
$$V_{14}' = V_{14} + \beta V_{23} + R_2 \quad (2.4)$$

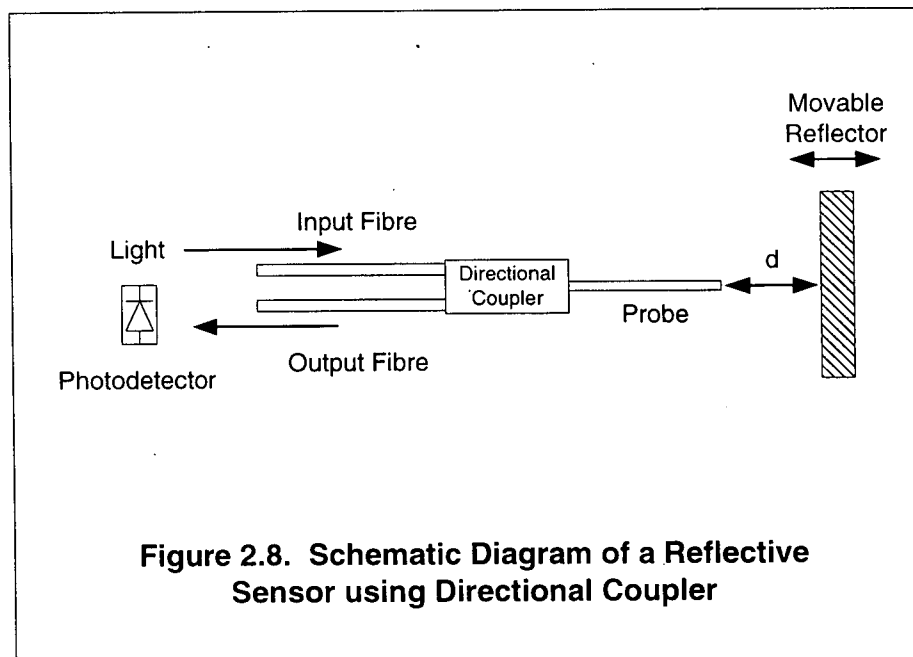
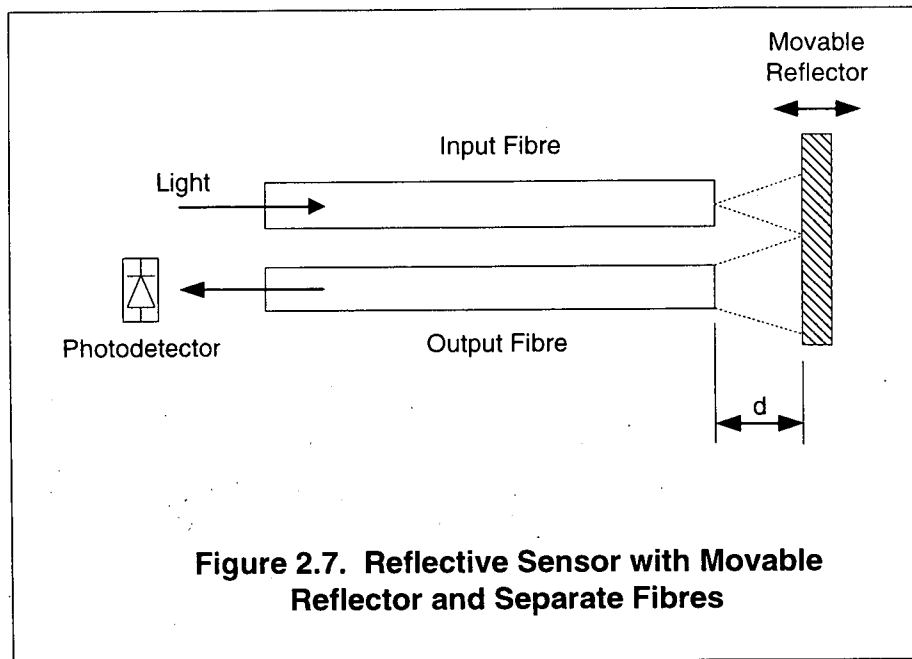
$$V_{24}' = V_{24} + \alpha V_{14} + R_2 \quad (2.5)$$

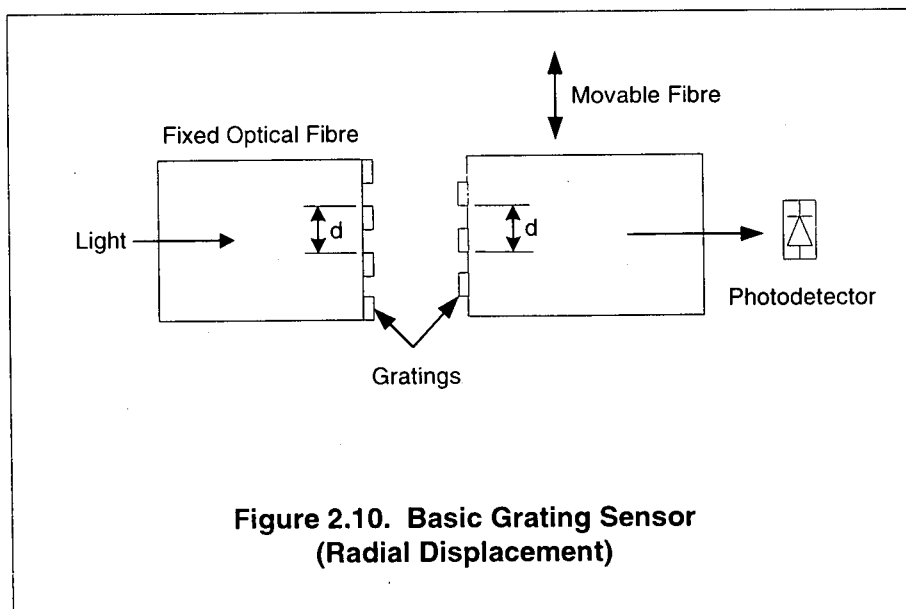
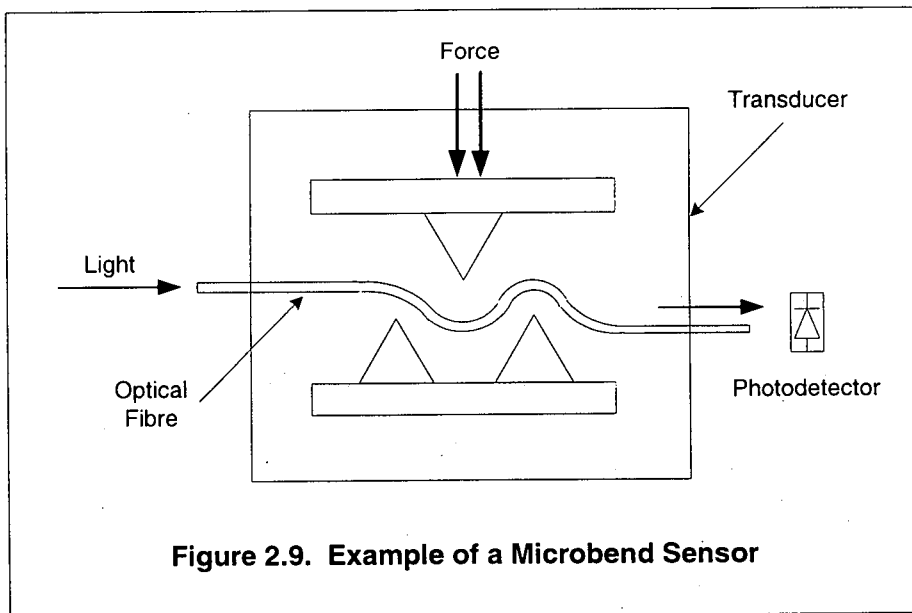
$R_1$  and  $R_2$  are the d.c. offsets on  $R_{x1}$  and  $R_{x2}$ ,  $\alpha P_1$  and  $\beta P_2$  are the output powers from the two transmitters in the "off" condition, respectively. This technique has also been suggested by Murtaza and Senior [2.46]. Senior *et al.* [2.47] also reported on a referencing scheme in which a partially reflecting mirror was constrained to move parallel along two GRIN (graded index) rod lens couplers (**Figure 2.14**) in which some light was reflected back into the emitting lens while about 20% of this emitted light was transmitted through the mirror. This maintains a constant equivalent ratio of the reflected to transmitted intensities even when fluctuations of the input optical source are introduced into the system. Hence, while the reflected power varies with the distance,  $d$ , of the mirror relative to the emitting face, the fraction of the transmitted power collected at the other lens remains constant. Measurements showed that a 3 dB change in the input power produced only a 0.5% variation in the output voltage.

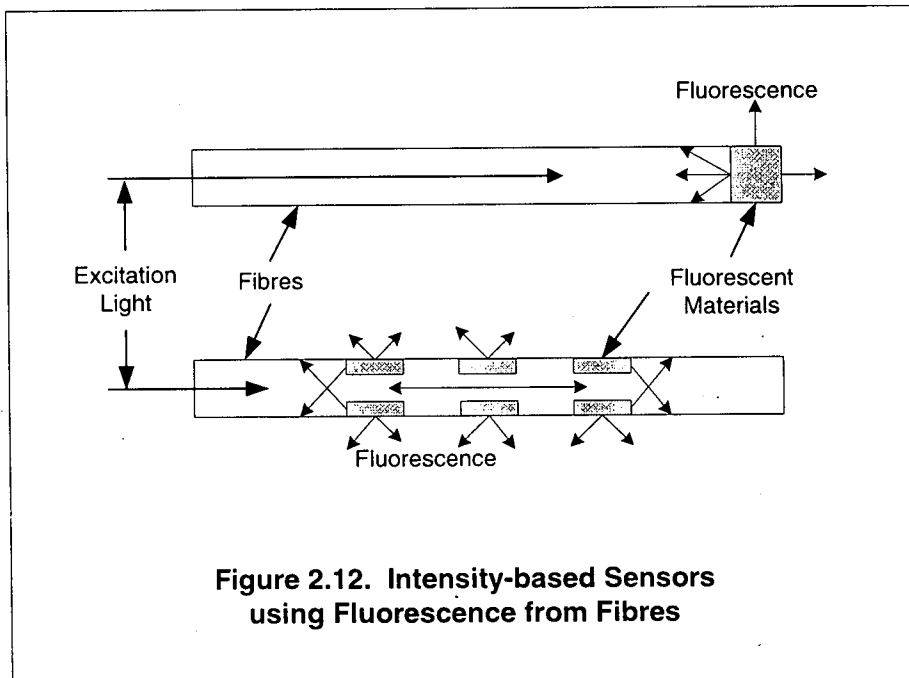
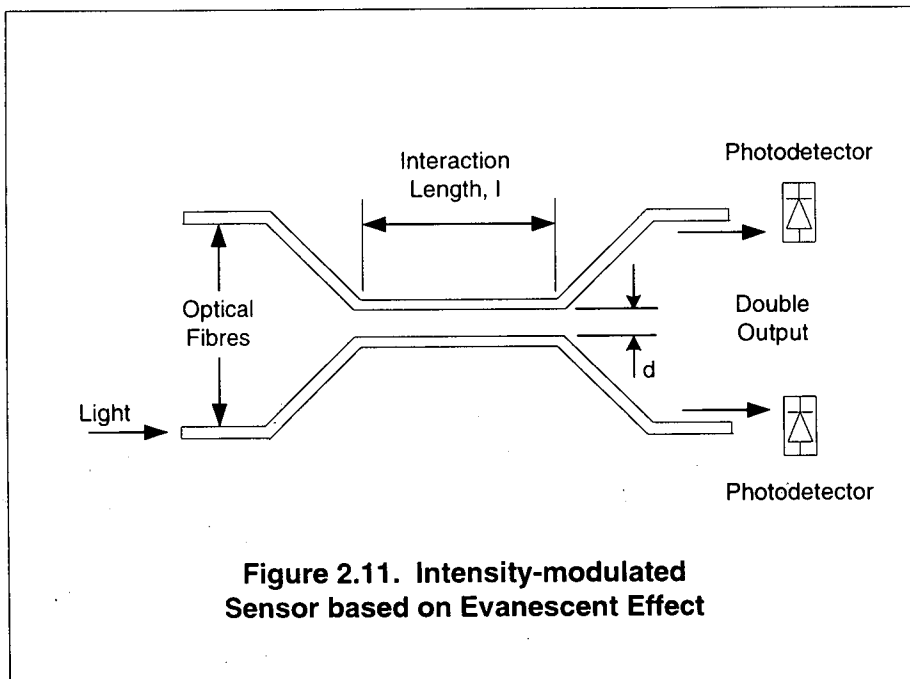
Although the problem of referencing still exists in intensity-based sensors, their obvious simplicity, good accuracy, low weight and potential low cost make them attractive research and development entities. Many such sensors are currently commercially available: many intensity-modulated sensors have emerged from the laboratories into commercial products for sensing of various parameters such as temperature, strain, displacement (linear and angular) and stress. Various companies are currently supplying off-the-shelf fibre optic sensors (for example, the MTI 2000 Fotonic Sensor from *Mechanical Technology Inc., New York*, for displacement and vibration measurements). An important application of this type of sensors is in the field of aircraft flight control where they are used to maintain overall system integrity and aircraft safety [2.48].

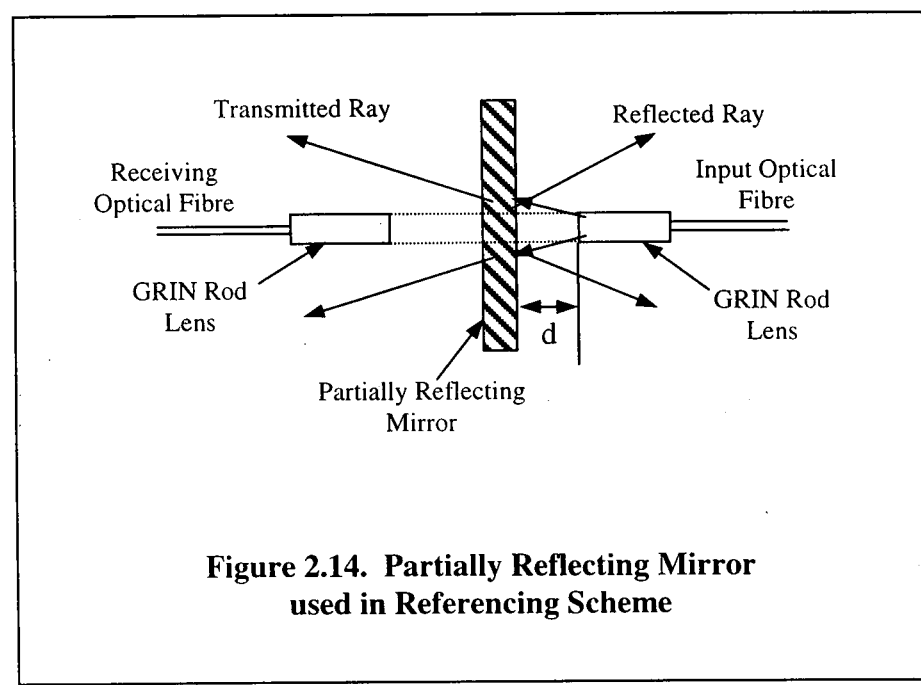
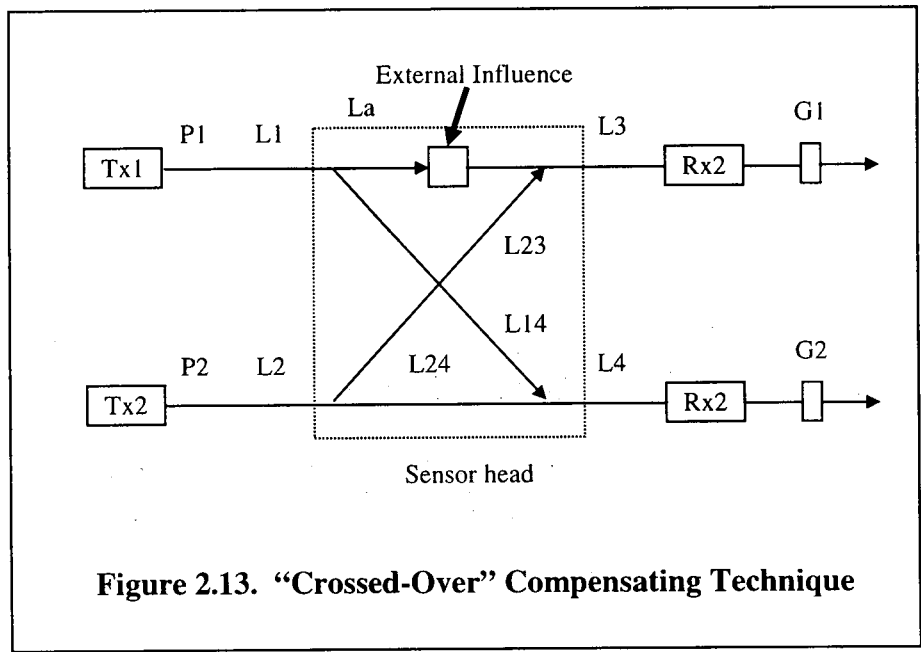












### 2.3.2 Interferometric sensors

Interferometric techniques form the basis of many fibre optic sensor configurations which have attracted researchers because of the extremely high sensitivity and resolution which can be attained [2.32]. Interferometry can be loosely classified under several configurations: namely, two-beam interferometry, two-beam reciprocal interferometry, multiple beam interferometry and differential interferometry, in which both single mode (or monomode) and multi-mode fibres have been employed.

The Mach-Zehnder and Michelson interferometers are the most widely used two-beam configurations and can be used to form very accurate and sophisticated fibre optic sensors. A fibre optic equivalent of these two interferometers is shown in **Figures 2.15** and **2.16**, respectively.

In the Mach-Zehnder configuration, a 3 dB coupler splits the input light into two beams, one in the sensing arm (which is modulated by the measurand) and the other the reference which is "shielded" from any environmental influence. The modulated signal and the reference signal are then recombined by another coupler, detected and amplified before further processing is carried out. The modulation of the beam can be in terms of its phase, intensity, state of polarisation, and frequency, which in turn result from the path length change between the two fibre arms.

In the basic Michelson configuration shown in **Figure 2.16**, light from a laser source is again split into two beams via a directional coupler and sent into the sensing and referencing fibres. The difference here is that both the lightwaves are reflected back through the referencing and sensing fibres by mirrored surfaces at the fibre ends and recombined by the coupler before the detection is performed. One problem which may arise is if the returned signal reaches into the laser source, this can produce instability in laser output and may be avoided by the use of an optical isolator.

The Mach-Zehnder and Michelson interferometers are very versatile and flexible instruments in terms of their geometrical arrangements. The signal detected by a photodetector at the output fibre is routed through demodulation schemes to extract the various modulated properties. The phase of the guided wave is the most

commonly modulated property [2.49] in both the Mach-Zehnder and Michelson interferometers. A comparison of the phases of the modulated and reference signals will yield the required phase change which corresponds to the specific parameter being measured. A large variety of physical parameters have been measured by such interferometric sensors including strain, temperature, magnetic and electric fields and acoustic sensing. Measurements of a specific parameter would ideally be made using fibre sensitive to that parameter only. However, commonly, there is difficulty in distinguishing between, for example, the strain-induced effect and a temperature-induced effect, leading to complexities in signal processing and/or sensor design

Common to both the Mach-Zehnder and Michelson interferometric sensors is the optical phase shift which can be given as [2.49]

$$\phi = nkL \quad (2.6a)$$

or

$$\phi = \frac{2\pi nL}{\lambda} \quad (2.6b)$$

where  $n$  is the refractive index of the fibre core,  $k$  the wavenumber (or  $2\pi/\lambda$ ) and  $L$  the length of the fibre. With the Michelson interferometer, the phase shift is  $2\phi$ . By differentiating this term, the fractional phase change can be obtained as

$$\frac{d\phi}{\phi} = \frac{dn}{n} + \frac{dk}{k} + \frac{dL}{L} \quad (2.7a)$$

or

$$\phi + \Delta\phi = \frac{2\pi}{\lambda} [nL + n\Delta L + L\Delta n] \quad (2.7b)$$

where  $dn/n$  and  $dL/L$  are terms dependent on the changes in the physical parameters being measured. It is thus evident that physical parameters such as pressure, strain,

stress, temperature and magnetic field influence the phase change,  $d\phi$ , through changes in the fibre's refractive index and physical length. In a practical sensor, these terms are maximised to increase their sensitivity with respect to the measured parameter(s). The basic equations shown above must be expanded in such a way as to sensitise them according to the specific measurement requirements. The  $dk$  term is related to any wavelength change associated with the light source, and is useful when considering phase noise and some demodulation processes [2.49]. Components such as beam splitters or couplers are also an important consideration in these types of sensor because their power coupling efficiency influences fringe visibilities given by the equation:

$$V = \frac{(I_{\max} - I_{\min})}{(I_{\max} + I_{\min})} \quad (2.8)$$

Environmental effects on these components can change fringe visibility. However, using this technique, potential problems such as thermal drifts in the detection and demodulation system and source fluctuations may be reduced. Moreover, with accurate set-up of these sensors and careful selection of the detection and signal processing schemes, phase shifts of  $\sim 10^{-6}$  radians are detectable, corresponding to a path length change of  $\sim 10^{-13}$  m, assuming that the optical paths of the two fibre arms are matched to within 1 mm [2.27, 2.49].

The most basic interferometer associated with multiple-beam interferometry is the Fabry-Pérot interferometer as shown in **Figure 2.17**. No reference fibre is required and the interference is obtained from multiple partial reflections of the input beam. This can be produced by well cleaved fibre ends. There is partial reflection of the input light back to the source. The light is then partially reflected by the second reflective surface, resulting in multiple reflections within the interferometer cavity. This action amplifies the phase difference and provides a very high sensitivity. This type of interferometer generally has twice the sensitivity of other interferometers and it is widely used in multiplexed [2.32, 2.40, 2.50], distributed and point sensing applications [2.51].

Differential interferometers are those in which the light coupled into the optical fibre sensor populates two eigenmodes of the waveguide and is usually known as a polarimetric sensor [2.52]. In such a device (**Figure 2.18**), the change in the state of polarisation (SOP) of the two orthogonally propagating eigenmodes within the fibre is effected by an external influence such as temperature, strain, bending or other effects. Light launched into the fibre is generally either linearly polarised or polarised randomly. The modulated signal can then be detected either in an intrinsic or extrinsic fibre optic sensor configuration. The measured parameter can be encoded as a change in intensity, wavelength or phase. Polarimetric sensing is further treated in **Section 2.3.6** in which crystal fibre sensors are also discussed.

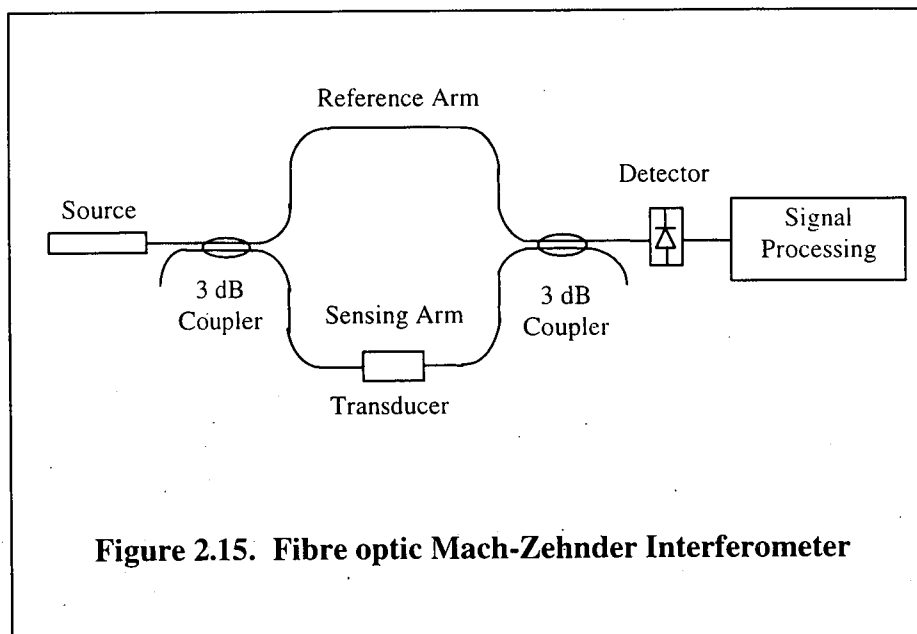


**Figure 2.15. Fibre optic Mach-Zehnder Interferometer**

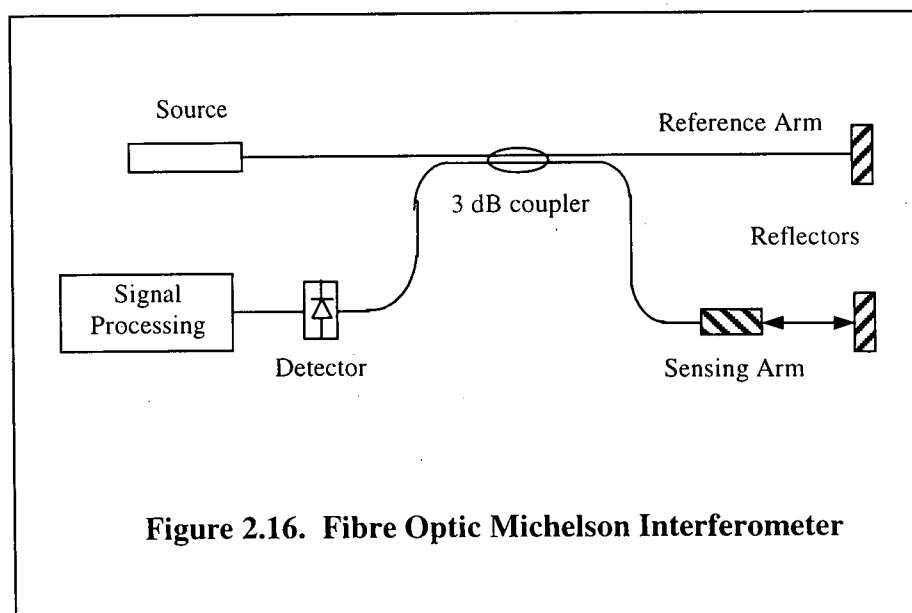
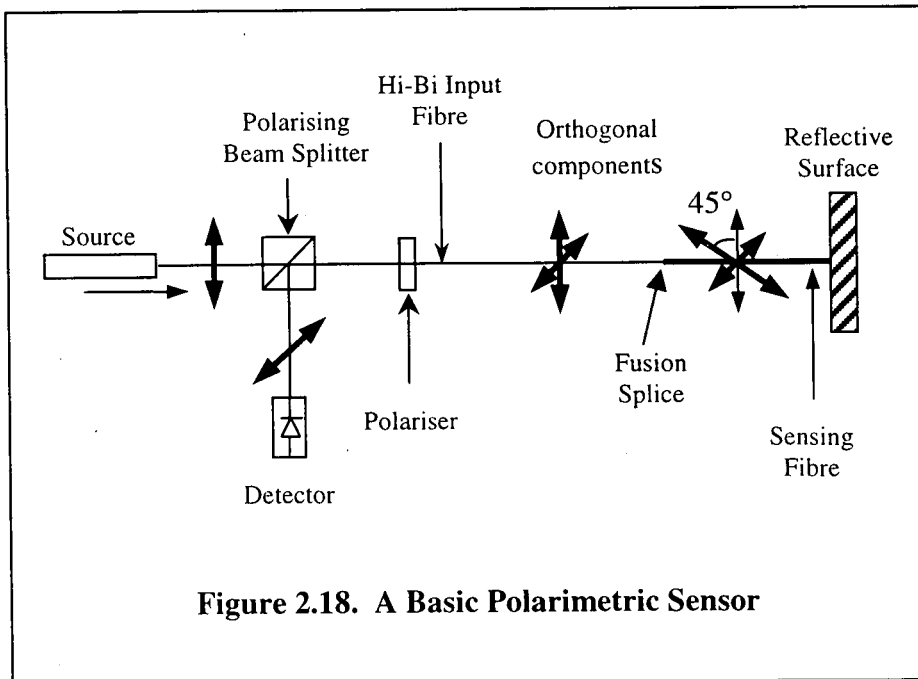
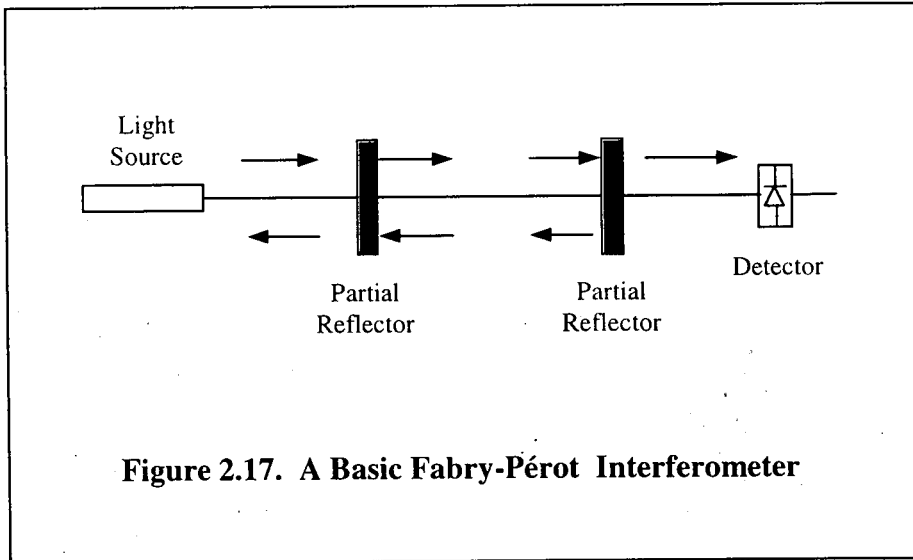


**Figure 2.16. Fibre Optic Michelson Interferometer**



### 2.3.3 Distributed and multiplexed sensing systems

Optical fibre technology has provided an important ability to enable long-range sensing in which a physical parameter is measured as a function of the linear position along the fibre length, usually through some forms of optical time domain reflectometry (OTDR) and/or time division multiplexing. In OTDR schemes, pulsed signals from the laser source driven by a time delay generator are launched into a long fibre link. Several sensitised regions can be incorporated along the fibre or the whole fibre length can be made sensitive to the target parameter(s). The reflected or backscattered signal is detected and demodulated after a certain time delay relative to the input pulse. The value of each individual signal detected is thus directly related to the specific location along the fibre link. This technique is initially used in the telecommunications industry for fault location and signal diagnostics along long lengths of fibre links [2.53]. A basic OTDR scheme is shown in **Figure 2.19**. An almost proportional decrease in the signal is thus obvious the further along the fibre the lightwave is reflected due to the intensity loss as a function of distance. The precision of such a system and the separation between two measurement points are determined by the pulse width of the input signal as well as the bandwidth of the detection unit. Measurement of amplitude and phase modulated signals both in the linear mode (where the returned signal to the OTDR is at the same frequency as the input frequency) or non-linear mode (where the frequencies of the returned signal and input light are different) is possible and is usually based on some loss or scattering mechanisms. Hence, a large number of point sensors distributed over a wide region can be multiplexed onto a single optical fibre, providing a class of sensors which is unique to this technology and which is practically impossible to implement using conventional sensing techniques. The number of sensing elements used in distributed sensing has seen a steady increase from the normal two or more elements from *GEC Research (Marconi Research Centre)* to a 10,000 elements distributed sensor system by York Technology. Other parameters such as stress, strain, pressure and temperature can also be measured in OTDR techniques [2.32, 2.54, 2.55] and the recent introduction of the in-fibre Bragg grating sensors has led to the ability to monitor large structures such as bridges and buildings [2.56].

Polarisation-optical time domain reflectometry (POTDR), a variant of the OTDR, has been the first distributed system used to measure the polarisation state of the backscattered light as a function of time [2.57] in which the state of polarisation can be mapped along the fibre position according to the various measurands (strain, pressure, magnetic fields, etc.) to which the polarisation is sensitive. In the published research on POTDR techniques, Luo *et al.* [2.33] have shown the use of high-birefringence optical fibre in a distributed strain sensing system to detect the mode coupling of the two propagating eigenmodes in a hi-bi fibre. Good resolution was obtained in that work even though the test fibre length was only 70 m. Both interferometry and optical path scanning have been used in their study to detect the fault location and its magnitude (strain). Shatalin *et al.* [2.58] also investigated the interferometric OTDR technique to determine the form and location of external phase disturbances along a fibre to allow for a more accurate (spatially) and higher resolution DOFS (distributed optical fibre sensor) system.

Raman and Brillouin scatterings [2.59] arise from nonlinear effects and can cause significant losses in an optical fibre at high input power densities. Raman scattering occurs when the incident light is scattered due to thermal vibration of the molecules of the glass material while Brillouin scattering is related to the bulk vibration of the optical fibre glass material. The frequency of the scattered light from these two mechanisms is thus different from that of the input light source. Both Raman and Brillouin scatterings, originating from thermally driven molecular and bulk vibrations, respectively, are temperature sensitive. The Raman scattering effect has been successfully used to develop distributed temperature sensors by companies such as York Technology and makes use of the detection of the anti-Stokes backscattered light to measure temperature change, through the ratio of the anti-Stokes to Stokes intensity in the backscattered light given as [2.32, 2.60]

$$R_r = \left( \frac{\lambda_s}{\lambda_a} \right)^4 \exp\left( -\frac{hc\Delta\nu}{kT} \right) \quad (2.9)$$

where  $R_r$  is the ratio of anti-Stokes to Stokes backscattered intensity,  $\lambda_s$  and  $\lambda_a$  the wavelengths of the lower photon energy (Stokes or longer wavelength) and higher

photon energy (anti-Stokes or shorter wavelength), respectively,  $h$  is Planck's constant,  $c$  the velocity of light,  $\Delta\nu$  the frequency shift from the interrogating frequency,  $k$  is Boltzmann's constant and  $T$  the absolute temperature. The anti-Stokes band is used here because of its higher temperature sensitivity than the Stokes band [2.54].

The Brillouin scattering process is similar to Raman scattering in that upper and lower sidebands are formed, but with a smaller frequency shift from the incident light frequency, and with an acoustic phonon generated instead of an optical phonon. The frequency shift,  $\nu_B$ , is given by

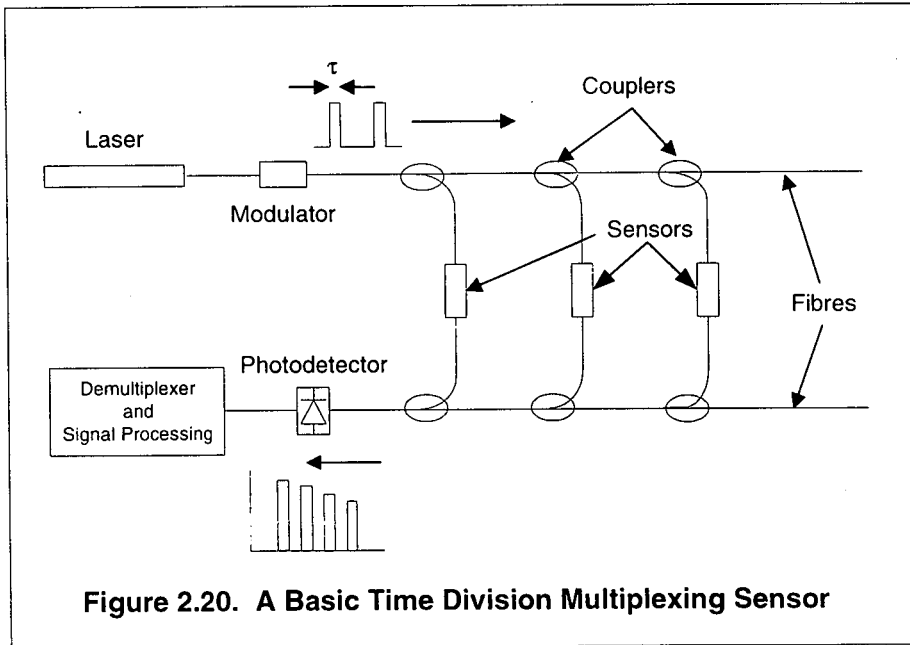
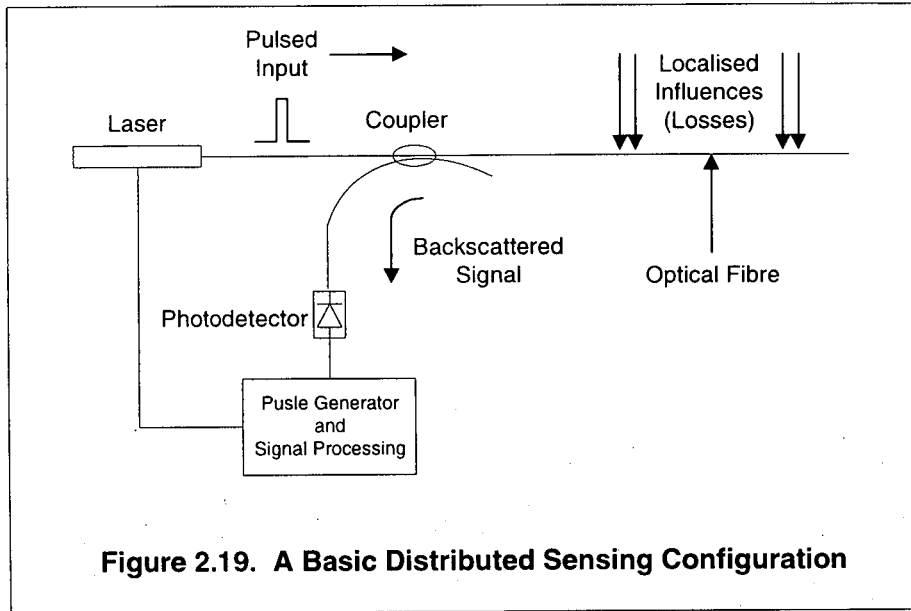
$$\nu_B = \frac{2nV_a}{\lambda} \quad (2.10)$$

where  $n$  is the fibre refractive index,  $V_a$  the sound velocity in glass and  $\lambda$  the wavelength of the incident light. With Brillouin optical time domain reflectometry (BOTDR) approach using Brillouin-induced gain mechanism, Bao *et al.* [2.61] were able to demonstrate a distributed temperature sensing (DTS) system with a resolution of  $\pm 1$  °C and a spatial resolution of 10 m at a sensing range of 22 km. Other DTS systems based on a similar mechanism have also been reported with relatively good temperature and spatial resolutions [2.62, 2.63].

Frequency and time division multiplexing (FDM and TDM) techniques are commonly used in multiplexed sensing to integrate a large number of sensors which can be supported by a single fibre. A basic TDM sensing configuration is shown in **Figure 2.20**. The sensors multiplexed onto the collection fibre link can be intensity-based, interferometric sensors or of any other configuration. Other division multiplexing techniques involve wavelength, coherence, polarisation and spatial multiplexing. The diverse range of applications with such techniques includes underwater acoustic sensor systems or hydrophones [2.64], industrial process control sensing, and chemical, environmental and structural sensing [2.65]. The use of Bragg gratings based on an interferometric configuration with wavelength division multiplexing (WDM) has also been investigated [2.66] and such a sensor can be used

to measure load, strain, temperature and vibration in manufacturing processes or in structures such as bridges, buildings and tunnels.

The attractiveness of distributed and multiplexed sensing is such that a wide range of almost any physical or chemical parameters can be measured. In particular, this technique can be employed to sense either the same or various parameters over a very large area with relatively high accuracy and precision. An example is the Flame Quality Analyser [2.67] used for quasi-simultaneous measurement of temperature and intensity profiles of flames in industrial boilers using two-colour pyrometry. This enables measurement of up to 30 spatially separated points by multiplexing the 30 fibre optic sensor probes onto a single optical fibre link. Acquisition and display of the measured parameters are provided by a computer although this system can also be interfaced with other monitoring and control systems.



### 2.3.4 Fibre Bragg gratings and sensors

Of the most recent developments in fibre optic components, the development of in-fibre Bragg gratings (FBGs) has been one of the most exciting developments in both optical telecommunications and sensing [2.51, 2.68]. Bragg gratings are produced by a refractive index change in the core of an optical fibre due to absorption of UV (ultraviolet) light. Generally, two UV beams are combined to produce an interference pattern which is then imaged onto the fibre core. The resulting change in refractive index establishes a phase structure having the same spatial period as the interference pattern. This gives rise to the characteristic grating structure. Gratings can be used to reflect, disperse or filter light within the fibre core. Low losses can be achieved and bulk optics like mirrors, beamsplitters and diffraction gratings, may be avoided [2.68]. Fibre Bragg gratings are rather easily manufactured and relatively inexpensive devices. Their operation can be described using coupled-wave theory where the incident light is coupled at each grating plane into a backward propagating mode. This condition is satisfied when the Bragg matching condition is met, defined by the wavelength of the Bragg grating [2.51, 2.68]. A schematic of a typical fibre Bragg grating is shown in **Figure 2.21**.

The first observations of permanent refractive changes in the core structure of germanosilicate fibres were reported by Hill and co-workers [2.69, 2.70] when they launched 488 nm light into a fibre from an argon ion laser. Due to the Fresnel reflection from both polished ends of the fibre, an interference pattern in the form of a standing wave was formed within the core, resulting in a periodic grating structure being formed. This had the same spatial periodicity as the interference pattern. This structure was found to be permanent but weak and led to the laser light being reflected as the structure gained in strength. The process was self-organised since the periodic refractive index structure was formed spontaneously and at the saturation level, the maximum reflectivity was reached. A narrowband reflective filter was thus obtained. Photosensitivity of the fibre glass material was the attributed reason behind this novel discovery.

The discovery of photosensitivity in optical fibres was only further developed when Meltz *et al.* [2.71] reported a new side writing technique about a decade. Since then

several grating inscribing techniques [2.72, 2.73] have been developed and they include the interferometric, phase mask, point-by-point and mask image fabrication techniques. Both amplitude-splitting interferometry, in which the inscribing beam from a UV laser is split into two equal intensity beams and recombined to form an interference pattern over the core of the target fibre, and wavefront-splitting interferometry, using prisms and Lloyd's mirrors to spatially split the writing beam into two by refraction and total internal reflection, have been used in the interferometric technique. Amplitude-splitting has the advantage of being able to inscribe Bragg gratings of any wavelengths while the main disadvantage arises from sensitivity to mechanical vibrations due to the focusing and positioning optics involved. With wavefront-splitting, since only a prism or Lloyd's mirror is used, the associated sensitivity to vibration is much reduced. Temperature-induced distortion of the wavefronts due to convection currents is also reduced since the focusing prism or mirror can be positioned close to the target fibre and rotation of the optics can be easily carried out, which is attractive for varying the angle of the interference pattern. A disadvantage though is the length of grating that can be fabricated; this is limited to half the beam width.

The phase masking process is one of the principle techniques used for producing fibre Bragg gratings because of its simplicity and high reliability [2.68]. Here, the UV radiation is passed through a diffractive mask made by etching a silica substrate, which is maximised in its first order diffraction and placed in contact with the fibre. The diffraction thus interferes within the fibre core to produce a periodic refractive index modulation in the glass to form Bragg gratings. This has the advantage that the grating pitch is not dependent on the writing wavelength, but only on the pitch of the phase mask (i.e. half the pitch of the phase mask).

In the point-by-point technique, a focused beam from the UV laser is made to traverse along the longitudinal axis of the fibre core, inducing localised refractive changes one step at a time [2.68]. The distance moved by the focused beam thus corresponds to the pitch ( $\Lambda$ ) of the Bragg grating produced. Since the beam, focusing parameters and motion can be controlled easily, this constitutes a flexibility in allowing the grating length, pitch and other parameters to be varied as required.

The mask image projection technique uses an amplitude rather than a phase mask with a series of lines opaque to the writing beam [2.68]. The transmitted beam is then imaged onto the fibre core by high-resolution focusing optics. This technique is simple to implement and various Bragg grating structures can be fabricated by simply changing the image mask.

Various laser sources (emitting in the UV region) may be used for successfully producing Bragg gratings with this technique. Examples are KrF excimer lasers, dye lasers, frequency-doubled Ar lasers and quadrupled Nd :YAG [2.68]. The excimer laser has emerged as one of the most important laser sources for use in fabricating Bragg gratings in optical fibres with many groups [2.74, 2.75] investigating narrowing the laser output linewidth since this inherently leads to higher output intensity and, more importantly, to the possibility of inscribing higher frequency Bragg gratings. Othonos and Lee [2.76] have recently demonstrated the possibility of narrowing the KrF excimer laser linewidth to  $\sim 4$  pm and obtained sufficient coherence from its output by modifying the laser cavity to include two etalons and an aperture while others have reported advances in fabricating FBGs with 100% reflectivity using single excimer lasers [2.77], contributing to the production/fabrication of high quality, low loss, reliable and relatively low cost FBGs. These lasers are capable of operating at or very close to the peak absorption centres of the silicate-based fibres, and have good temporal and spatial coherences, together with high average powers. They are very attractive sources since long gratings can also be written (due to the high coherence). Some high energy pulsed sources can also enable single-pulse grating writing and may be used to write gratings onto fibres during the fibre drawing process: this may be very advantageous when producing Bragg gratings (or even long period gratings) for large sensing arrays in multiplexed systems.

Bragg gratings are backward-coupling devices in which a forward propagating mode is coupled into the same backward propagating mode when the Bragg condition is met while other wavelengths/modes pass through without any coupling. Typical Bragg grating periods are of the order of  $1 \mu\text{m}$  down to several tens of nm. There is another variant of the Bragg grating: the long period grating (with grating periods on the order of 0.1 to 1 mm), which is a forward coupling-device acting as an attenuator

rather than a reflector, hence producing loss bands at specific wavelengths. Although less attention has been given to long period gratings, these devices can be useful for determining or differentiating wavelength shifts due to strain-induced effects from that due to temperature [2.78]; they are reported to have a larger temperature response as compared to the FBGs and a correspondingly lower strain response. Most of the published research is based on the normal or conventional Bragg reflector, but there also exists several Bragg structures with various specialised uses, particularly in telecommunications requiring erbium-doped fibre amplifiers. The two most common ones are the blazed and chirped types of Bragg gratings, with their schematic representations being shown in **Figures 2.22** and **2.23**.

Bragg gratings consist of periodic changes in the refractive index of the fibre core where the phase fronts are perpendicular to the fibre axis and the grating planes are spatially constant. Guided light is scattered at each plane and if the Bragg condition is not met, the reflected light from each plane becomes out of phase and cancels out. When the Bragg condition is satisfied, the back reflected light adds constructively (superimposition) with its centre wavelength determined by the Bragg wavelength. The wavelength encoded nature of the returned signal after reflection from the Bragg grating is thus a narrowband signal dependent on the Bragg wavelength given as [2.32]

$$\lambda_B = 2n\Lambda \quad (2.11)$$

where  $n$  is the effective index of the fibre core and  $\Lambda$  the grating pitch or period. Such a returned signal is not directly dependent on the variation in the input optical source, hence, any source power variation will not be directly transferred to the wavelength-encoded signal and the bandwidth of this reflected signal is largely dependent on the grating length [2.79]. Thus, the application of strain, temperature or pressure will cause a physical change of the Bragg grating, resulting in a shift in the grating period. The main advantage of these Bragg grating sensors over other interferometric or intensity-based techniques is the linearity of response which can be obtained as well as other qualities such as stability, compactness and low insertion

losses [2.68]. As such, the relationship of the Bragg wavelength change with respect to a physical parameter can be described as

$$\frac{1}{\lambda_B} \cdot \frac{\partial \lambda_B}{\partial A} = \frac{1}{n} \cdot \frac{\partial n}{\partial A} + \frac{1}{L} \cdot \frac{\partial L}{\partial A} \quad (2.12)$$

where  $\lambda_B$  is the Bragg wavelength,  $\partial \lambda_B / \partial A$  the change of Bragg wavelength with any physical parameter,  $n$  the effective refractive index of the fibre core,  $L$  the grating length and  $\partial L / \partial A$  the change of grating length with respect to the parameter change. Of all the parameters, FBG sensors have mainly been applied in temperature and strain (**Figure 2.24**) sensing of different types of structures and multiplexing of a large number of these sensors enables a powerful sensing tool to be realised. The strain-induced wavelength shift of an FBG along the fibre axis can be given as [2.72, 2.80]

$$\Delta \lambda_{BS} = \lambda_B (1 - \rho_e) \Delta \epsilon_z \quad (2.13)$$

where  $\Delta \lambda_{BS}$  is the wavelength shift,  $\lambda_B$  is the Bragg wavelength,  $\Delta \epsilon_z$  is the applied longitudinal strain and  $\rho_e$  is the effective strain-optic coefficient given by

$$\rho_e = \frac{n^2}{2} [\rho_{12} - \nu(\rho_{11} + \rho_{12})] \quad (2.14)$$

$\rho_{11}$  and  $\rho_{12}$  are the strain-optic components,  $n$  is the refractive index and  $\nu$  Poisson's ratio of the glass material. Hence, measuring this shift in Bragg wavelength will allow the induced strain values to be determined.

The temperature-induced wavelength shift,  $\Delta \lambda_{BT}$ , due to a temperature change of  $\Delta T$ , can be given as

$$\Delta \lambda_{BT} = \lambda_B (\alpha + \zeta) \Delta T \quad (2.15)$$

where  $\alpha = (1/\Lambda)(\partial\Lambda/\partial T)$  is the thermal expansion coefficient of the fibre and  $\zeta = (1/n)(\partial n/\partial T)$  is the thermo-optic coefficient. Such terms can be measured independently before the fibre is used for any Bragg grating configuration.

In the case of pressure-induced wavelength change,  $\lambda_{BP}$ , the Bragg ( $\lambda_B$ ) wavelength-pressure relationship can be given as [2.80]

$$\Delta\lambda_{BP} = \lambda_B \left[ -\frac{(1-2\nu)}{E} + \frac{n^2}{2E}(1-2\nu)(2\rho_{12} + \rho_{11}) \right] \Delta P \quad (2.16)$$

where  $E$  is the Young's modulus of the fibre and  $\Delta P$  the change in pressure. As can be seen from the above equations, all physical parameters have a relatively important effect on the refractive index and grating period properties on which the Bragg wavelength shift is highly dependent. This thus reinforces the wavelength-encoded nature of the returned signal as the sensed information is directly detected as a wavelength change or shift. Hence, the source power variation, coupling losses, etc., are not directly transferred into the output signal. However, the signal detection and recovery units for measuring and resolving the wavelength shifts must be highly sensitive.

Sensors based on fibre Bragg gratings have received considerable attention due to their capability in measuring a diverse range of parameters like strain, temperature, pressure and even electric current. However, research has mainly been concentrated in using FBGs as sensors for measuring mechanical deformations such as bending and strain, and for monitoring the health of large civil structures like bridges, roads, lock-gates for waterways, underground tunnels and airframes, etc. A very attractive advantage of using Bragg gratings, as mentioned earlier, is the linearity of response of the Bragg wavelength shift to the measured parameters along with the possibility of multiplexing many of these gratings at various points on the surface or within a structure.

The use of in-fibre Bragg gratings for strain measurements have been demonstrated by various groups. Since fibre optic sensors do not have any great effect on the

structural integrity of concrete or composite materials, O'Dwyer *et al.* [2.81] used FBGs which were embedded in a carbon fibre reinforced composite to monitor its real-time strain characteristics during the curing process. This enabled them to study the internal stresses built up within the material, which is directly related to the different thermal expansion coefficients of the various fibres/resin matrix of the composite material. The axial and radial strains sustained by a gun barrel during the firing of a projectile were also studied with the help of Bragg gratings configured for measuring strain with the aim of improving the weapon's performance [2.82]. The temperature of liquid fuel tanks used for launching space vehicles has also been monitored using fibre Bragg gratings [2.83]. Since the liquid fuel used is always maintained at a very low temperature, there is a need to ensure the safe functioning of the tanks containing it and the reusability of these tanks after recovery, both for safety requirements and cost effectiveness.

One main disadvantage of FBG sensors, which is also common to all other fibre optic sensors, is the difficulty and, hence, complexity in differentiating between the strain and temperature dependence of the returned signals. Considerable work has been focused on differentiating these effects with many groups proposing simultaneous measurement schemes [2.84, 2.85, 2.86, 2.87]. Patrick and Vohra [2.78] recently reported on a dual measurand technique where a long period grating (LPG) was incorporated in line with two FBGs to simultaneously measure temperature and strain, while Song *et al.* [2.88] demonstrated the use of spliced different-diameter fibre gratings where the relative wavelength change of the two gratings is independent of temperature change and is only affected by the applied strain. In the analysis, it was found that the spliced different-diameter fibres with gratings have the same response to temperature-induced change but the response due to the applied strain is different. The fibre diameters were 135  $\mu\text{m}$  and 165  $\mu\text{m}$  with two gratings written at 1549.3 nm and 1546.4 nm, respectively. By heating the fibre up to  $\sim 100^\circ\text{C}$ , the wavelength shifts in both gratings showed an identical response of  $10.65 \pm 0.005 \text{ pm} / ^\circ\text{C}$ , while the strain sensitivities for the two gratings were found to differ by  $0.6 \text{ nm} / \mu\epsilon$ . **See Figure 2.25.** In another work, Song *et al.* [2.89] also reported on the simultaneous measurement of temperature and strain using two Bragg gratings embedded in series in a silica glass tube, with one of the gratings

configured to respond only to temperature while the other responds to both strain and temperature. A similar technique has also been reported elsewhere [2.90]. Previous work on the differentiation of temperature-induced from strain-induced responses used a dual wavelength technique [2.91, 2.92] with gratings of two different wavelengths collocated at the same point.

The use of fibre Bragg grating sensors can play a critical role in monitoring and maintaining the structural integrity of civil structures [2.93] since deformations such as cyclic straining and bending in these structures are potential threats to the safety of the users. Since the early 1990's, fibre optic sensors based on Bragg gratings have seen a growing application in this field of sensing. Moreover, the ability to multiplex Bragg grating sensors has enabled applications ranging from monitoring bending stresses in simple cantilever beams to measuring strains and temperatures in aircraft bodies [2.94, 2.95, 2.96, 2.97, 2.98].

Although the main uses of FBGs are in the field of strain and temperature sensing for structures and structural materials, other applications for fibre Bragg grating sensing have also been found and they include shape and vibration sensing [2.99], high frequency ultrasonic field detection in medical applications (ultrasound surgery, hyperthermia, lithotripsy, etc.) [2.100, 2.101] and high-voltage sensing [2.102]. Many other sensing applications using fibre Bragg gratings will in the near future be found. The use of long period gratings for fibre optic sensing has been discussed by Bhatia [2.103].

With the use of quasi-distributed, multi-point and distributed sensing, some forms of multiplexing are required. These techniques have been detailed in several articles [2.80, 2.104]. The main techniques involved are wavelength division multiplexing (parallel, series, with tuneable filters and crosstalk-free approaches), time division multiplexing (TDM), spatial division multiplexing (SDM) and a combination of two or more of these schemes. A 2D multiplexing technique can also be realised by combining in parallel and/or in series the three main approaches. With wavelength division multiplexing [2.105, 2.106], each of the gratings is written at a different wavelength so that they do not overlap each other. By having another FBG in the receiving fibre, tunability of the detected signals/wavelengths is provided by

stretching this FBG. The wavelength shift due to the parameter(s) at various sensing points can then be traced and processed. In TDM [2.107], the returned signals from any adjacent FGB sensors are delayed over a specific time by the use of fibre delay lines. The signals are then detected with specific temporal delays corresponding to the delays caused during propagation along the returned routes and this delay can be provided by a high-speed optical or electrical switch. For applications requiring independent multi-point sensing, the spatial division multiplexing technique [2.108] is used. The point sensors used generally have identical characteristics and can normally be interchanged or easily replaced.

Several interrogation techniques exist for measuring the small Bragg wavelength shifts of FBGs due to influences by temperature or strain. Most use a broadband light source with a spectrum which covers that of the FBG elements and the narrow-linewidth returned signal reflected by the gratings is detected through various schemes such as optical filtering, tuneable filter tracking and interferometric detection.

In optical filtering, a broadband source is launched into the FBG sensor and the reflected signal is fed into a filter to be compared to the direct reference signal fed directly into the detection path via a coupler. The two signals are then detected and their ratio forms the output to be processed. Tuneable filter tracking involves Fabry-Pérot filters, acousto-optic filters and FBG-based filters, to pass one narrowband of the returned signal for each FBG sensor element. Tuning the filter thus provides a scanning action over which the light reflected from the different wavelength FBG elements are detected as wavelength encoded signals (**Figure 2.26**).

With interferometric detection, the input signal, reflected from an FBG element, is encoded from a wavelength term into a phase term. Consequently, the detected phase,  $\Delta\phi$  is directly associated with the Bragg wavelength shift,  $\Delta\lambda_B$ , given by the equation

$$\Delta\phi = \left( \frac{2\pi nd}{\lambda_B^2} \right) \Delta\lambda_B \quad (2.17)$$

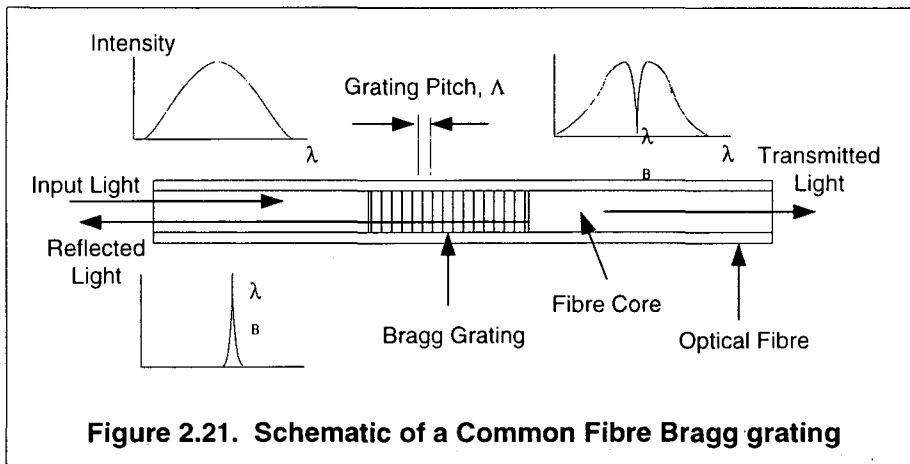
where  $n$  is the effective index,  $\lambda_B$  is the grating wavelength and  $nd$  the optical path imbalance. The interferometer used in such techniques is an unbalanced one (See **Figure 2.27**) whose optical path difference (OPD) must be less than the coherence length of the grating reflected signal. Various phase demodulation techniques can thus be employed to detect the final phase shift. Postulated strain resolutions are in the picostrain/ $\sqrt{\text{Hz}}$  order [2.32]. Temperature measurements are also possible using the interferometric technique [2.109]. Another possible interrogation technique is based on spectroscopic schemes, where the most basic one uses a simple dispersive element such as a diffraction grating to disperse the input wavelengths onto an array of CCDs, in which each CCD element corresponds to an individual wavelength. Hence, a Bragg wavelength shift will be indicated by the shift of the signal from one CCD element to another (**Figure 2.28**).

Fibre Bragg gratings have also been used as reflectors in fibre lasers to be used as tuneable single frequency laser sources as well as for high resolution strain and temperature monitoring [2.110, 2.111, 2.112]. See **Figure 2.29**. An in-fibre cavity is created if two identical FBGs are written onto a section of optical fibre as shown in the figure.

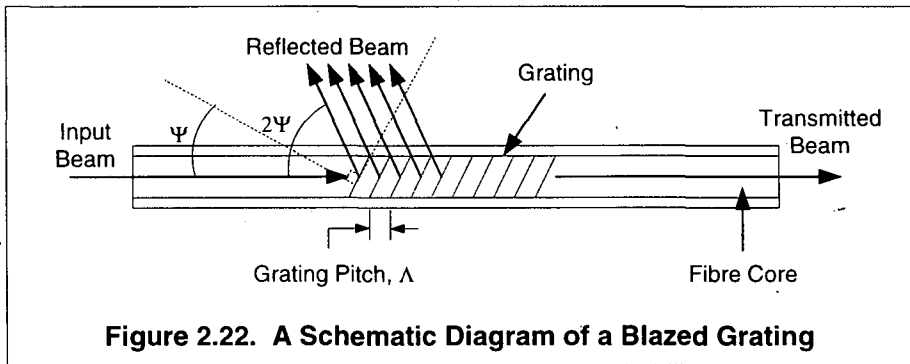
Besides FBG lasers, the introduction of the fibre Bragg grating has also enhanced many communications and sensing applications by allowing novel components/devices to be produced [2.51, 2.113]. They have been used in conjunction with diode lasers to produce stabilised single frequency laser sources, mode-locked lasers (by modulating the laser at a frequency determined by the grating position relative to the laser output and the Bragg grating), and have been used to enhance erbium-doped fibre amplifier (EDFA) performance.

Although the inscription of Bragg gratings in single crystal fibres by the mentioned techniques has not been reported yet, Fejer [2.15] demonstrated that with the appropriate diameter control system, uniform surface relief structures with constant pitch and the desired length can be produced in sapphire fibres. With the high modulus (hence high stiffness) and favourable mechanical properties of many SCFs, in-fibre Bragg gratings written or fabricated in them could provide even higher

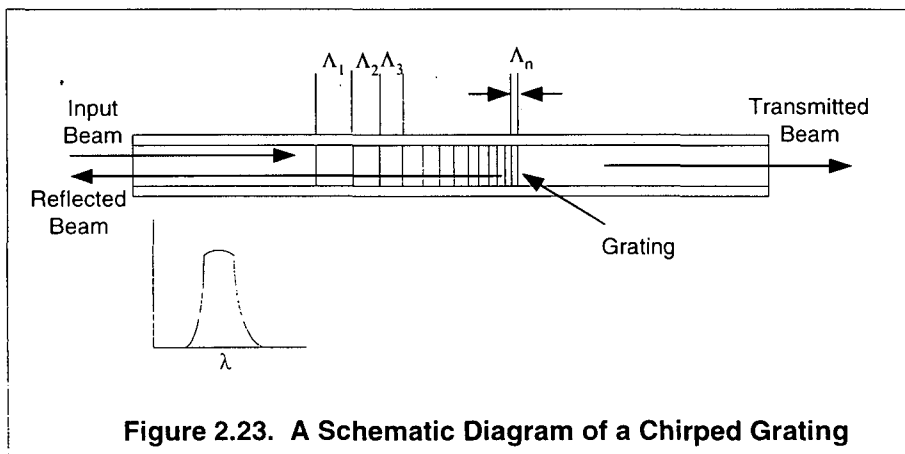
sensitivity and/or measurement range. Moreover, SCFs can allow sensing to be carried out in extremely harsh environments unsuitable for conventional FBGs.



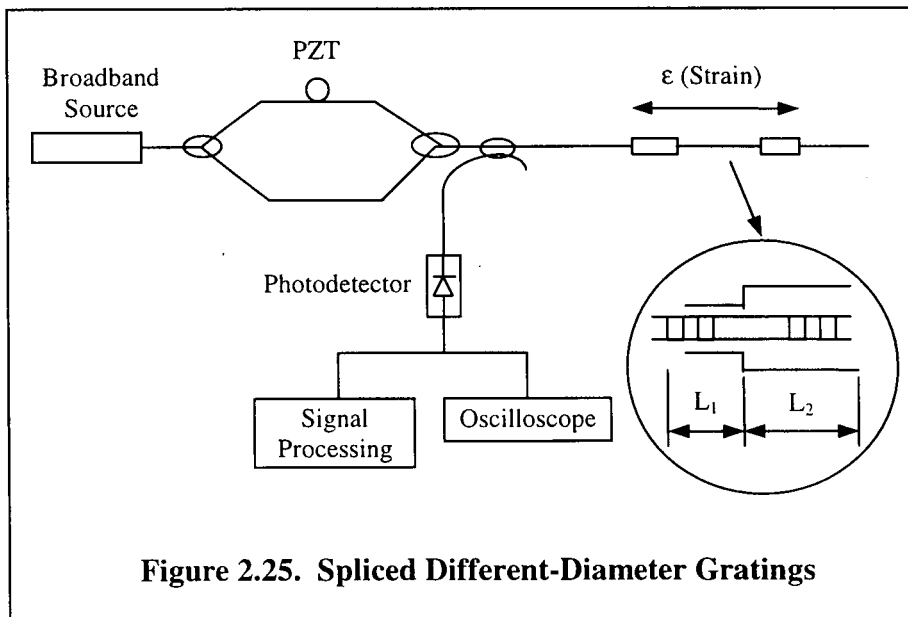
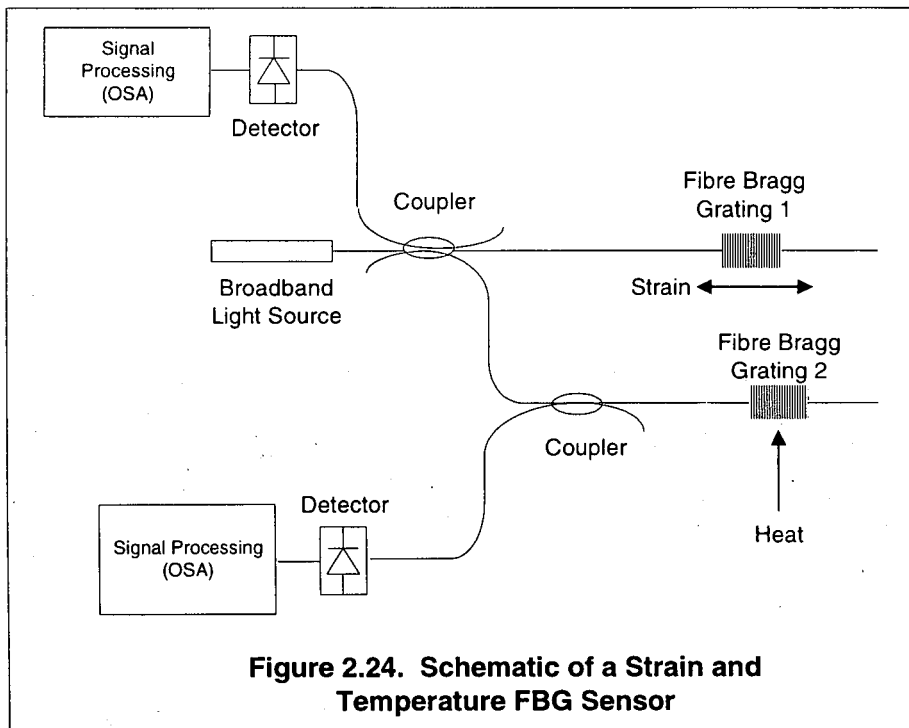
**Figure 2.21. Schematic of a Common Fibre Bragg grating**

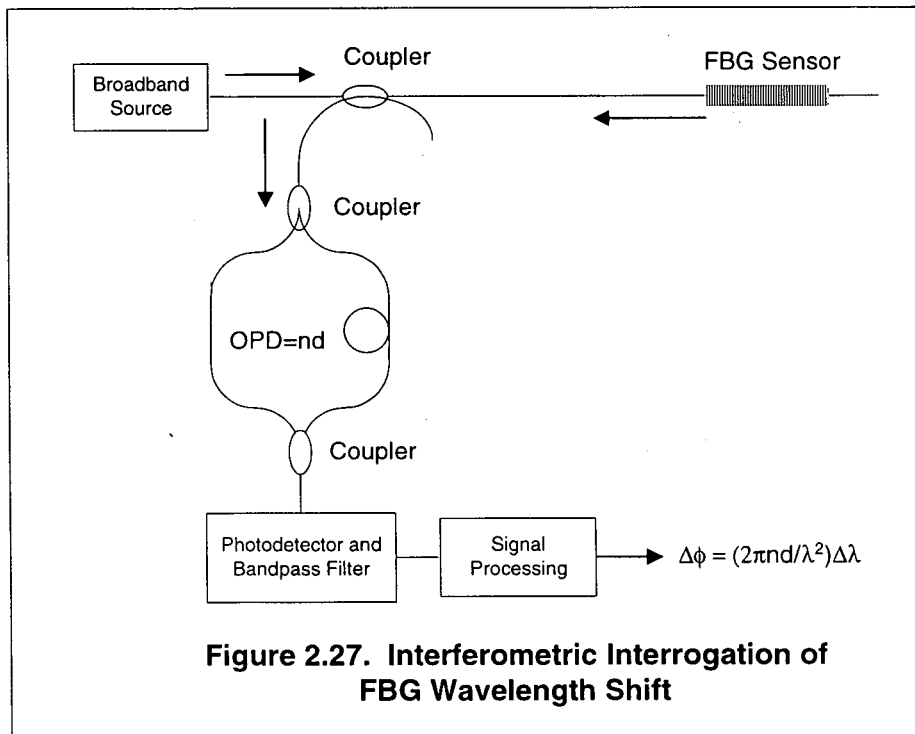
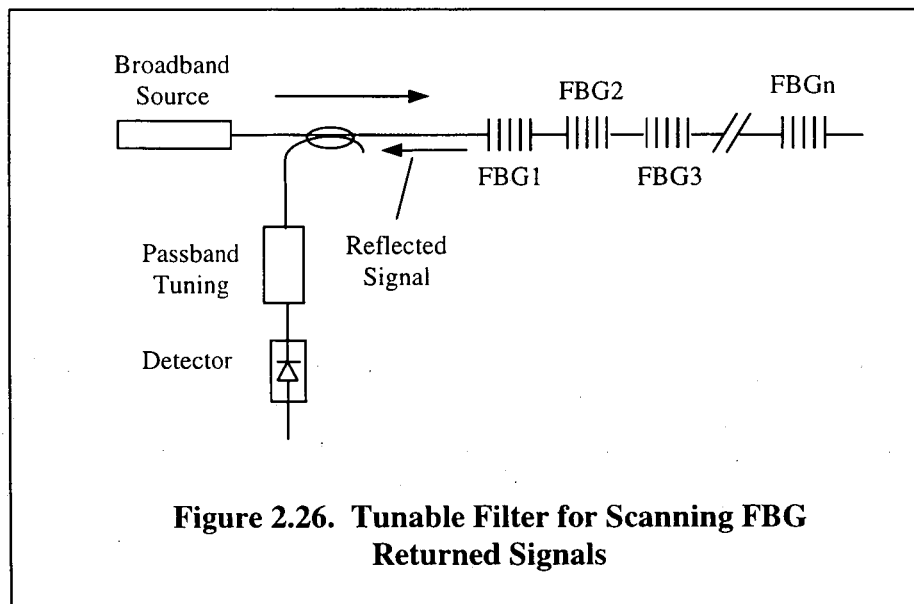


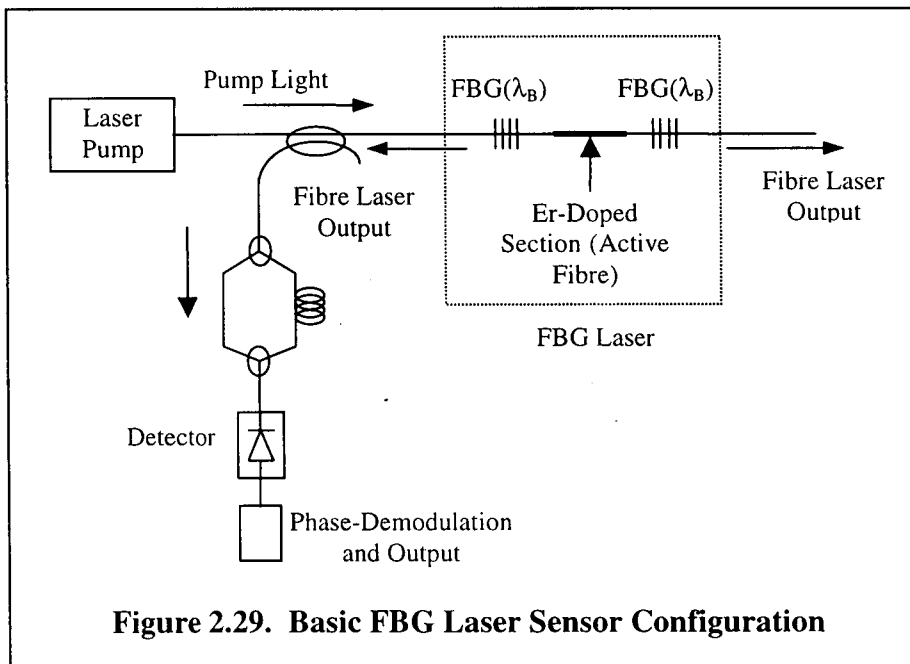
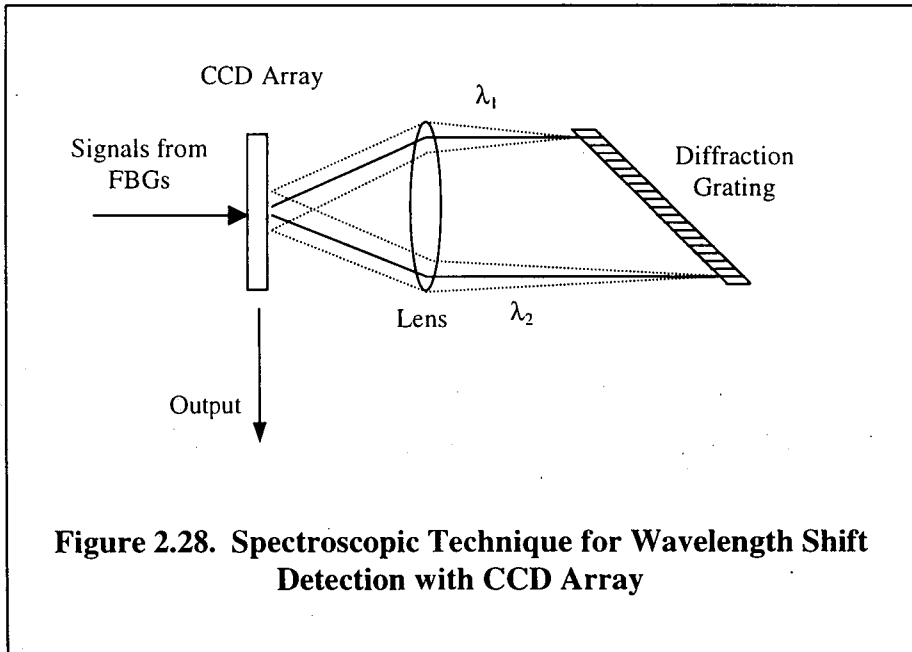
**Figure 2.22. A Schematic Diagram of a Blazed Grating**



**Figure 2.23. A Schematic Diagram of a Chirped Grating**







### 2.3.5 Fluorescence-based fibre optic sensors

Fluorescence-based fibre optic sensing techniques may be classified under a special category of intensity-based sensing in that the unique property of fluorescence lifetime decay is relatively independent of source intensity. With its associated intrinsic or extrinsic sensing configuration, fluorescence-based sensors provide a very attractive scheme upon which various physical parameters can be measured with relatively good accuracy. Temperature, together with pressure form some of the most important and commonly measured parameters in fluorescence-based fibre optic sensing [2.114, 2.115, 2.116] although other parameters such as fluid viscosity, humidity, pH levels, etc. [2.38] have also been investigated.

Fluorescence is the emission of light from a material which has been excited by source(s) of electromagnetic radiation. The choice of excitation source used to induce fluorescence emission is dependent upon the absorption spectrum of the particular fluorescent material. This can span across the ultraviolet, visible and/or infrared spectral regions. The absorption spectrum thus indicates the various spectral regions in which an "active" material can be excited to release fluorescent radiation. After being excited to a higher energy level, the fluorescence emission takes a certain time to spontaneously decay to its ground state and this is characterised by a fluorescence lifetime or decay time. The fluorescence lifetime varies widely in different materials and is an intrinsic property of the particular material used and the particular energy levels. In the case of ruby, it is generally sensitive to temperature over a certain range and has been found to be relatively less sensitive to other physical effects such as pressure and strain [2.25, 2.117]. Similar characteristics have also been found in silica fibres doped with rare-earth erbium and ytterbium [2.118, 2.119]. In principle, fluorescent materials which exhibit a dependency on the parameter to be measured can be exploited as a sensor probe in a fluorescence-based fibre optic sensing configuration. These encompass both transition metal and rare earth ions which can be doped into either glass or crystalline hosts.

The choice of sensor material is dependent on the dopants or impurities selected. While many active dopants can be easily excited to induce fluorescence in various host materials, the concentration of such ions incorporated can play an important role

in determining the final fluorescence characteristics. Beyond a critical level, this can result in a reduction of the fluorescence intensity leading to a subsequent decrease in the observed fluorescence lifetime [2.120], an effect known as concentration quenching. The lifetime decay of transition metal ions such as  $\text{Cr}^{3+}$  in  $\text{Al}_2\text{O}_3$  [2.121] and rare-earth ions such as  $\text{Nd}^{3+}$ ,  $\text{Er}^{3+}$  or  $\text{Er}^{3+} + \text{Yb}^{3+}$  in both glass and crystal hosts [2.122, 2.123, 2.124] have been reported to be dependent on the concentration levels. It is thus important to select sensor materials with levels of active ions sufficiently high enough to achieve efficient fluorescence characteristics but without the onset of concentration quenching, where possible.

The use of fluorescence intensity as a measure of a particular physical parameter such as temperature may lead to ambiguities in the true representation of the measured value since other non-thermal effects like source instability, fibre bending, detector drift and external light leakage into the system, can also induce fluctuations in the measured intensity. Referencing, through the use of one or more wavelengths from the fluorescence spectrum, can be used to overcome this difficulty although use of such techniques generally leads to the increase in cost in terms of additional detector(s), signal processing and associated optics like filters and lenses involved. This can be a disadvantage when commercialisation of a sensor based on intensity measurements is to be considered or realised.

However, monitoring of the fluorescence lifetime decay may offer a more efficient solution since only a single parameter, the lifetime,  $\tau$ , is measured. Moreover,  $\tau$  is intrinsic to a particular material and is therefore independent of the exact intensity level. Nevertheless, sensor materials having relatively long lifetimes are desired to enable ease of detection with inexpensive and widely available electronic components but this generally leads to low bandwidth. For most fluorescent materials with doping below the critical concentration level, the fluorescence lifetime can be treated as a single or quasi-single exponential decay process. This assumption allows a number of signal processing schemes to be employed.

Some commonly used techniques are two point pulse measurements [2.125], pulse integration [2.126], digital curve fitting with DSPs [2.127] and the phase modulation technique [2.128].

In the pulse measurement technique, the fluorescence decay immediately after the termination of the excitation source is measured in which the decaying curve is indicative of the fluorescence lifetime. The intensity levels at two fixed points along the exponential decay curve are compared and from the time interval  $(t_2 - t_1)$  between these two intensity points, the time constant or lifetime,  $\tau$ , can be inferred according to the following expression:

$$I(t) = I_0 \exp[-(t_2 - t_1)/\tau] \quad (2.18)$$

where  $I(t)$  is the fluorescence intensity at time  $t$  and  $I_0$  the intensity at time  $t_1$ . This is a simple and inexpensive method to implement but measurement at only two points along the decay curve can lead to limitations in accuracy and precision. The integrating method may be used to improve the precision of the fluorescence lifetime of the pulse technique. Integration of the signal takes place at two fixed time periods,  $T_1$  and  $T_2$ , after the start of the trigger at a preset level of the measured fluorescence intensity. Taking into account the noise and dc baseline offsets by integrating over the same two fixed periods during which time the fluorescence signal has decayed to zero, the lifetime can be obtained from the following

$$\frac{A - C}{B - D} = \frac{1 - e^{-T_1/\tau}}{1 - e^{-T_2/\tau}} \quad (2.19)$$

where  $A, B, C, D$  are the integrated areas under the decay curve,  $T_1$  and  $T_2$  the two integration periods, and  $\tau$  the desired fluorescence lifetime of the sensor.

The digital curve fitting technique involves the use of high speed digital signal processors to capture/sample a part of the decay curve. Exponential curves are then fitted to this signal by means of least-square curve fitting in which the slope of the fitted curve is proportional to the fluorescence lifetime. The dc offset which occur during data acquisition can be overcome by using a three-parameter least-square curve fit. The use of DSPs in such curve fitting procedures can offer accurate

dedicated lifetime measurement but because of the inherent numerical curve fitting involved, a relatively long signal processing time can be expected.

Phase modulation techniques can offer high levels of accuracy and precision when used for measuring lifetime decay. They are generally insensitive to both ac noise and dc offsets since the fluorescence signal is forced to lag behind the excitation source by a phase shift,  $\phi$ , through the following expression

$$\tan \phi = 2\pi f\tau \quad (2.20)$$

where  $f$  is the modulation frequency and  $\tau$  the required fluorescence lifetime. Hence, measurement of  $\phi$  gives a direct measure of the lifetime of the particular material. This technique involves measuring the fluorescence signal during the excitation process and is thus highly sensitive to external noise such as the leakage of the excitation source to the detection circuit. A high resolution counter must also be used to monitor the small shifts in phase. However, it is an accurate lifetime processing technique and can be suitable for use in precision measurements.

The phase-locked detection scheme demonstrated by Zhang *et al.* [2.129] may be deemed as highly appropriate for measuring the change in lifetime associated with exponentially decaying fluorescence signals because of its accuracy and high speed response. It is similar to the phase modulation technique already discussed in that the fluorescence signal lags the excitation signal by a certain phase and the measured lifetime is converted into a repetitive signal whose period is directly proportional to the desired lifetime itself. The repetitive signal is also fed back into the circuitry to serve as the modulation signal, in effect, creating a feedback loop, and the whole system functions in an identical manner to a lock-in amplifier with high signal-to-noise ratio coupled with the ability to track fluctuating signals to within a certain bandwidth. The fluorescence lifetime,  $\tau$ , may then be inferred from measurement of the in-phase and quadrature phase sensitive detectors (PSDs) and calculated according to the expression [2.130]

$$\tau = \frac{\tan \phi}{\omega} = \left( -\frac{y_q}{y_i} \right) \frac{1}{\omega} \quad (2.21)$$

where  $\phi$  is the phase lag with respect to the modulation frequency,  $\omega$  the radian frequency of the modulation signal,  $y_q$  and  $y_i$  the outputs of the quadrature and in-phase detectors respectively. A category of detection schemes based on the PLD has also been proposed by Zhang *et al.* [2.130] with either sinusoidal or pulse (rectangular or square-wave) modulation of the excitation signal. The advantages of pulse modulation being the ability to achieve a higher signal-to-noise ratio and its simplicity to be utilised. A PLD scheme with two reference signals generated by the use of two mixers/comparators has also been introduced to reduce or eliminate the problem of excitation light leakage at the photodetector associated with PLD schemes having only a single reference signal [2.130]. On the assumption that the fluorescence signals are exponentially or almost exponentially decaying, such PLD schemes can be employed to measure the desired lifetime values with good accuracy, resolution and repeatability.

In principle, any material whose fluorescence characteristics exhibit a dependence on one of the many physical influences may be employed as a sensor material. Fluorescent materials doped with  $\text{Cr}^{3+}$  ions have been widely investigated over the past two decades due to the large amount of data already available concerning their properties [2.131, 2.132]. Several have evolved into sensor materials largely from their initial employment as laser materials, with ruby being one such example [2.133] where energy level transitions have been widely studied. Its fluorescence characteristics (lifetime decay, linewidth and R-line position) have been found to be sensitive to temperature, pressure and compressive stresses [2.116, 2.131, 2.132, 2.134]. Other  $\text{Cr}^{3+}$ -doped materials have been investigated for thermometric applications and they include the laser crystal, alexandrite ( $\text{Cr}^{3+}:\text{BeAl}_2\text{O}_4$ ) [2.135, 2.136], for temperature sensing up to  $\sim 973$  K,  $\text{Cr}^{3+}:\text{LiSrAlF}_6$ , another laser material, for biomedical temperature sensing up to  $\sim 373$  K [2.137, 2.138] and olivine crystals ( $\text{Cr}^{3+}:(\text{Mg,Fe})\text{SiO}_4$ ) for the temperature region of 77 to 370 K [2.139]. In all of these Cr-based sensing schemes, the fluorescent crystals were attached to the excitation and delivery optical fibre(s), usually silica-based, by means of adhesives

and, thus, requiring a sheath to be used to protect the rather delicate assembly of fibre and sensor material. This can lead to reduced frequency response of the sensor probe and complication over the choice or shape of sheaths to be employed. However, the various Cr-doped materials discussed above can be employed for thermometric applications over separate temperature regions from ~77 to 973 K. The limiting temperature for ruby is ~873 K beyond which the fluorescence intensity is drastically reduced for any reasonably accurate lifetime measurements to be made, while alexandrite may be employed to a slightly higher temperature before its fluorescence signal, too, becomes too weak to be measured.

In order to extend the range of temperature to beyond 1000 K, where other important processes (for example, within an internal combustion engine or the turbine jet engine) can be accurately monitored, a different set of fluorescent materials incorporating active agents which can withstand such temperature limits should be selected. Suitable dopants include erbium, ytterbium, thulium and neodymium ions. Rare earth ions such as these undergo many fluorescent transitions when appropriately excited [2.140]. Besides the usual fluorescence emission which can be used as an indication of temperature, upconversion, with several emissions throughout the visible and/or near infrared spectral regions, also allows a variety of sensing schemes to be realised where the physical parameters need not be confined to temperature. Although lifetime measurements can be effected using the techniques available, ratiometric techniques utilising the various lines from the upconverted and fluorescence emissions can also be realised easily. Moreover, the constant progress in fibre optic telecommunications also means that the associated optical devices such as sensitive photodetectors, mirrors and lenses will become more widely available at a lower cost.

Well-known for signal amplification in telecommunications applications in the 1550 nm band as erbium-doped fibre amplifier (EDFA),  $\text{Er}^{3+}$ -doped glass fibres have been studied for thermometric purposes and strain measurements up to ~1373 K and ~2500  $\mu\epsilon$  [2.118, 2.141, 2.142].  $\text{Er}^{3+}$ -based fibre sensors can thus be considered as a "spin-off" of the optical communications industry and are favourable since they can be pumped with high-powered near-infrared and infrared laser diodes which are now widely available. Another important advantage is the low-loss spectral window near

the 1500 nm region, and this renders sensors based on  $\text{Er}^{3+}$  systems attractive since they may be used in conjunction or in parallel with other communications-based  $\text{Er}^{3+}$  systems. Moreover, depending on the concentration level, the infrared fluorescence lifetime of  $\text{Er}^{3+}$ -doped fibres can be extended into the millisecond region [2.142], making the detection of this parameter more efficient and less costly. The green upconverted transitions of  $\text{Er}^{3+}$ -doped silica fibres have been used in an intensity ratiometric configuration to measure temperature [2.143], while co-doped fibres, with sensitiser ions such as  $\text{Yb}^{3+}$  ions allowing the  $\text{Er}^{3+}$  based system to be efficiently pumped near the infrared, have also been reported [2.144]. These thermometric applications are based on the green emission of the active fibre utilising the intensity of two lines from the emitted upconversion in a ratiometric form. The use of  $\text{Nd}^{3+}$ -doped silica fibres or crystals ( $\text{Nd}^{3+}:\text{YVO}_4$  and  $\text{Nd}^{3+}:\text{KGW}$ ) can offer a relatively high temperature sensing limit of  $\sim 1300$  K but suffers from ambiguities since the fluorescence lifetime increases non-monotonically with temperature [2.145]. This effect is even more accentuated when  $\text{Nd}^{3+}:\text{YAG}$  fibres are used [2.123]. Singly-doped  $\text{Yb}^{3+}$  fibres based on glass hosts have been used to measure temperature and strain simultaneously [2.119, 2.146] but suffer from the need to be annealed [2.147] to achieve consistent and reproducible results. With thulium-doping, temperature excursion beyond  $\sim 1400$  K may be achieved [2.148, 2.149] but again, the sensor probe in the form of a  $\text{Tm}^{3+}$ -doped silica fibre has to be annealed. Moreover, due to the relatively low  $\text{Tm}^{3+}$  concentration level used, a minimum length constant has to be determined in order to achieve the appropriate signal-to-noise ratio (SNR) and stable operation.

Most, if not all, of these fluorescence-based silica glass fibre sensors are easy to realise due to the wide range of commercially available doped fibres. However, they all suffer from the disadvantage of requiring heat treatment in order to produce stabilised results. This in turn reflects the susceptibility of damage of the silica fibres to high temperatures as well as the ease with which these fibres, stripped of their protective coating layer, can be broken. A recommendation would be to employ crystalline materials in fibre form which can be relatively easily doped with the required rare earth elements and which can tolerate the high temperature levels or deformations to be measured.

### 2.3.6 Crystal fibre sensors

The limitations imposed by glass-based fibres, especially in the area of fibre optic temperature sensing, has led to the search for more robust and stable systems based on other high temperature materials. Generally, most glass-based systems are limited to temperatures up to ~700 K while others based on silica fibres may be used up to ~1200 to 1300 K. For applications where temperatures higher than 1300 K are to be measured, these “conventional” fibres cannot be used. Suitable replacements must thus be found for this important temperature region.

In initial studies, sensors were either intrinsic and/or extrinsic fibre Fabry-Pérot interference devices for temperature and strain measurements [2.21, 2.22]. The fluorescence emission, both lifetime decay and wavelength shift, of appropriately doped single crystal fibres has also been investigated for temperature and strain dependencies. Fluorescence characteristics are attractive since they are not highly dependent on power fluctuations of the pump source, usually a laser diode, and generally, these fibres can be fabricated from materials which have already been well studied and characterised.

One of the earliest reported use of a crystalline high temperature probe by Dils [2.23] involve the use of single crystal sapphire fibres coated with high temperature metallic films. These sensing tips acted as small blackbody cavities from which radiation emitted at high temperature can be accurately measured within a specific emission spectral band. The coated temperature probes have been employed in high temperature tests up to ~2300 K, near the melting point of the sapphire fibres. Over the last decade, several fibre optic sensing schemes based on crystalline materials have been proposed and demonstrated to extend the temperature and strain sensing limits posed by glass-based sensors [2.21, 2.22, 2.24, 2.25, 2.26, 2.150, 2.151, 2.152, 2.153, 2.154, 2.155, 2.156, 2.157, 2.158, 2.159, 2.160, 2.161, 2.162]. While most of the work involved the use of pure sapphire fibres and/or rods [2.21, 2.22, 2.151, 2.152, 2.154, 2.155, 2.157, 2.158] for temperature and strain monitoring in extreme conditions, transition metal-doped sapphire fibres such as ruby [2.24, 2.25, 2.163] and rare earth-doped YAG [2.26, 2.156] employing temperature-dependent fluorescent mechanisms have also been investigated. Recently, single crystal

zirconia [2.164] fibres have been grown using the LHPG technique to exploit their potential as extreme temperature sensors up to ~2573 K [2.161].

The early demonstration on the practicality of a metal-coated high temperature sapphire sensor [2.23] based on radiation from blackbody cavities has led to interesting work on other high temperature blackbody sensors [2.153, 2.159] employing the basic Planck's equation for blackbody emission tailored to meet the emission conditions of the cavities. However, metallic films have the tendency of being oxidised at such high temperatures and have to be coated with a protective film of dielectric material. Work by Wang and Wu [2.159] has recommended the use of ceramic films made up of nanoparticles of high temperature materials to remove the oxidation characteristics associated with metallic coatings. Although useful in monitoring temperatures up to the melting point of sapphire, purely radiation-based blackbody sensors suffer from the disadvantage that relatively high temperatures are required before any reasonable amount of radiation intensity can be measured. Further work on this type of sensor employed a cross-referencing technique in which the doped end-section (with  $\text{Cr}^{3+}$ ) of a sapphire fibre was used to measure the lower temperature range from ~300 to 700 K using the temperature-dependent fluorescence decay time of the ruby section [2.160]. For higher temperature ranges up to ~2100 K, a miniblackbody was constructed by coating the same doped-section to form a cavity from which blackbody radiation can then be used, in effect, producing a single temperature probe for a wide sensing range. The main problem associated with such a probe construction is one of absorption of the fluorescence signal by the blackbody cavity whereby the resulting detected fluorescence can be drastically reduced [2.160]. However, it is an attractive sensor in which higher temperature ranges than 2100 K may be realised by the use of crystalline materials with a higher melting point than sapphire. Recently, a high temperature sensor with operating characteristics similar to blackbody sensors has been reported in which high melting point rare earth films attached to a high temperature crystal fibre were used in contact measurement of a sample temperature [2.162]. Not requiring knowledge of the emissive properties of the measured sample used, it relies on the narrow emission bands exhibited by these rare earths. Although it is an attractive alternative since many rare earth materials have high melting points it does, however, require a layer of protective shielding in the form of a thin platinum foil to block out radiation from

the emitting sample at high temperature. **Figures 2.30** illustrate the schematics of radiation-based probe construction.

With high melting point crystalline hosts, the limits of temperature sensing can be extended. Crystalline materials form one of the most appropriate sensor materials for temperature sensing applications since refractive oxides such as  $\text{Al}_2\text{O}_3$ ,  $\text{Y}_2\text{O}_3$  and  $\text{Y}_2\text{O}_3\text{-ZrO}_2$  have melting points beyond 2300 K, and recently can be fabricated in fibre form with some levels of ease. As for the fluorescent sensing tips, these can easily be grown by incorporating suitably high melting point fluorescent species. Besides ruby fibre sensors [2.24, 2.25], a high temperature sensor using YAG fibres doped at one end with rare earth  $\text{Er}^{3+}$  ions has recently been reported [2.26] for use up to  $\sim 1500$  K. Rare earth doped crystal fibres are attractive for temperature sensing applications not only because of their relatively high melting points but also because of the sharp emission lines which can be efficiently pumped with widely available and relatively inexpensive high powered laser diodes. The Er:YAG work [2.26] utilised the first-excited state fluorescence decay rate at  $1.6 \mu\text{m}$  from the  ${}^4\text{I}_{13/2} \rightarrow {}^4\text{I}_{15/2}$  transitions and discussed the limitations of the sensor when losses due to competing upconversion processes occur. Signal loss due to upconversion can be avoided by having low dopant concentration levels as well as low pump power.

The selection of a high temperature crystalline fibre will depend on the required operating regime. The  $\text{Al}_2\text{O}_3$  (or sapphire) fibre is a relatively well-established system due its favourable properties and offer very attractive alternatives to glass fibres in FO temperature and strain sensing applications. As with glass-based sensors, the many sensing principles and techniques may be transferred to crystal fibre-based systems. The main disadvantages at the moment, however, remain the difficulty in producing crystalline sapphire fibres in lengths which are comparable to glass-based fibres and the relatively high propagation losses along these fibres due to the lack of cladding. However, for many sensing applications, lengths in the several cm regions should normally be sufficient.

**Figures 2.31** illustrate both the intrinsic and extrinsic sapphire fibre Fabry-Pérot (FP) interferometric (IFPI or EFPI) devices used for both temperature and strain sensing [2.21, 2.22]. As discussed above, FP sensors are known to be highly sensitive to

parameters such as temperature, strain, pressure and acoustic waves and, hence, are suitable for temperature and strain sensing applications [2.165]. In the IFPI sensor (**Figure 2.31a**), a sapphire fibre polished at both ends was spliced to a silica fibre to form the FP cavity [2.21]. Reflections from the silica-sapphire splice ( $R_1$ ) and the far end of the sapphire fibre ( $R_2$ ) resulted in interference patterns being produced with a phase difference,  $\Delta\phi$ , between the two reflections which can be given as [2.21]

$$\Delta\phi \cong \frac{4\pi}{\lambda_o} [n\Delta L + L\Delta n] \quad (2.22)$$

where  $\lambda_o$  is the wavelength of the laser source used,  $n$  the refractive index of sapphire and  $L$  the cavity length. The change in this length,  $\Delta L$ , and the change in the index,  $\Delta n$ , are dependent on physical influences such as temperature and strain and can thus be used as a measure of these parameters.

The sapphire EFPI sensor, as shown in **Figure 2.31b**, consists of a lead-in sapphire fibre, with both ends polished, and another sapphire fibre (target sapphire) with just one end polished both of which are arranged within a sapphire capillary to form an air gap or low-finesse FP cavity. Reflections from the lead-in sapphire/air gap boundary and from the target sapphire again produce an interference wave with intensity,  $I$ , which can be given as [2.154]

$$I = I_o \cos\left[\frac{4\pi d}{\lambda}\right] \quad (2.23)$$

where  $I_o$  is the maximum output intensity,  $d$  the length of the FP cavity and  $\lambda$  the laser wavelength. Monitoring this intensity gives an accurate measure of the cavity length, which in turn, is highly sensitive to parameters such as temperature and strain. Reflection from the far end of the target sapphire is eliminated by shattering that end while reflection from the input end of the lead-in fibre can be reduced by polishing it at an angle relative to the longitudinal axis of the fibre. Any effect due to reflections from these two surfaces can thus be minimised in this way. Sapphire IFPI

sensors have been used for investigating temperatures up to 1770 K [2.21] while extrinsic ones were more commonly employed for strain measurements in high temperature environments [2.22, 2.151, 2.154].

The basic principles of a fibre optic polarimetric sensor have been clearly outlined and discussed by Spillman [2.166] in which the states of polarisation (SOP) of a light beam propagating along a length of fibre subjected to physical influences can be used as a measure of these influences. The Poincaré sphere may be used to qualitatively represent the four component Stokes vector which define the SOP of light while, quantitatively, both Mueller and Jones calculus may be easier to use given that the optical elements employed in a polarimetric sensing technique are simply represented by matrices. While both approaches have their own benefits, the Mueller calculus is generally better suited to situations where intensity variations are measured and Jones calculus employed when measurements of phases are required. The four components can thus be given by [2.166]

$$S_0 = A_x^2 + A_y^2 \quad (2.24)$$

$$S_1 = A_x^2 - A_y^2 \quad (2.25)$$

$$S_2 = 2A_x A_y \cos \delta \quad (2.26)$$

$$S_3 = 2A_x A_y \sin \delta \quad (2.27)$$

where  $A_x$  is the amplitude of light polarised in the x-direction,  $A_y$  the amplitude of light polarised in the y-direction and  $\delta$  the phase difference or retardation between these two amplitude components.

The measurements of the above parameters can, in theory, be easily carried out by the use of appropriate optical elements such as polarisers and other polarising optics while the sensing fibre, acting as the retarder, can be made sensitive to the measurand. The monitored signals may be encoded in the form of intensity and/or wavelength variations from which the desired values with respect to the sensed measurand can be extracted. An illustration of a simple polarimetric sensor can be seen in **Figure 2.32** in which polarised light entering a fibre is caused to alter its SOP

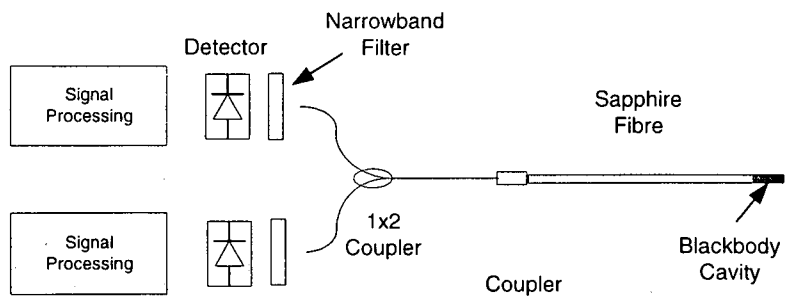
by a physical influence. The x and y component amplitudes are then measured in terms of their respective intensities and the change in their ratio may be taken as a measure of the monitored parameter.

In one of the very few reports on a sapphire-based polarimetric sensor, a birefringence-balanced device was demonstrated [2.21]. Two sapphire rods with their fast and slow axes set orthogonal to one another were butted together in a sapphire capillary to form the sensing head. Light polarised  $45^\circ$  to the input sapphire rod was launched into the sensor and the reflected signal, which was temperature-dependent, from the second rod was monitored for temperatures up to  $\sim 1770$  K. In order to minimise errors due to source fluctuations in any general polarimetric sensor, the difference-over-sum technique may be used and can be given as

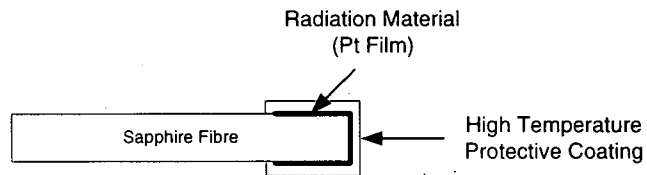
$$V = \frac{I_+ - I_-}{I_+ + I_-} \quad (2.28)$$

This results in a ratio,  $V$ , which is a function of temperature, strain or any other parameters monitored.  $I_+$  and  $I_-$  are the intensities of the orthogonal light components, either in the x or y direction.

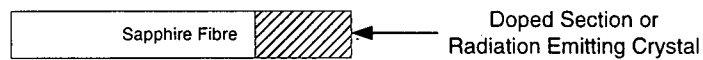
One of the implicit aims of a fibre optic sensor, or indeed of any general sensor systems, is to continuously extend the limit of the sensing range/capacity. Sapphire makes attractive high temperature and strain-temperature sensor materials but can only be employed up to or near its melting point of  $\sim 2300$  K. Recently, another crystalline material has been grown in fibre form [2.164] and has been experimentally demonstrated as a high temperature sensor in the range from  $\sim 1470$  to  $2570$  K [2.161]. The material of concern in that work was a  $Y_2O_3$ - $ZrO_2$  (yttria-stabilised zirconia) crystal fibre used as a blackbody cavity sensor in which the ratio of two narrowband emissions was monitored as a function of temperature – also known as the two-colour technique.  $Y_2O_3$ - $ZrO_2$  has a melting point in excess of  $2950$  K and, potentially, can be used for measuring temperature up to this limit. It is also mechanically stable at such high temperatures but YSZ fibres have been found to crack during growth [2.164] due to the very large temperature gradient produced by localised heating of the fibre.



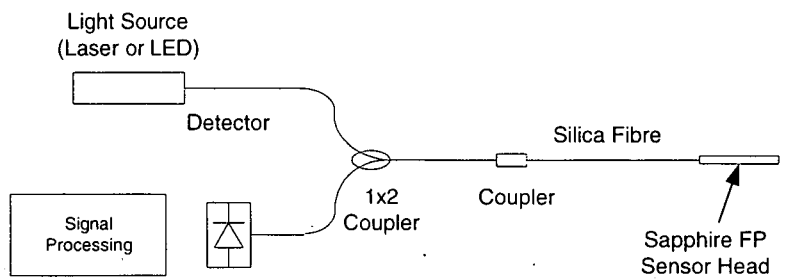
**Figure 2.30a. Schematic diagram of a Fibre Optic Sensor based on Blackbody Radiation**



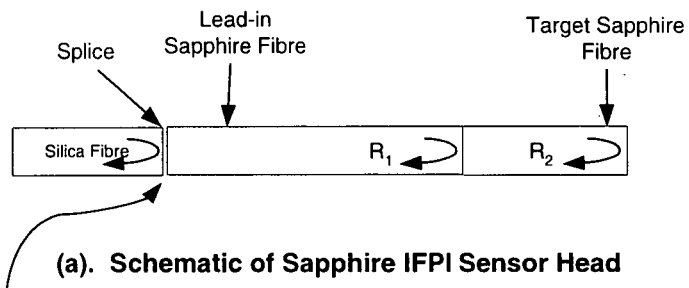
**Figure 2.30b. Blackbody Sensor Head using High Temperature Radiation Film**



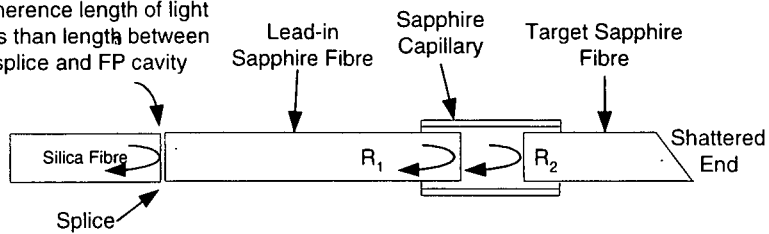
**Figure 2.30c. Blackbody Sensor Head (made by doping end of sapphire fibre or by attaching radiating crystal)**



**Figure 2.31. Schematic Diagram of a Sapphire-based FP Sensor**



Reflection from splice reduced by ensuring coherence length of light less than length between splice and FP cavity



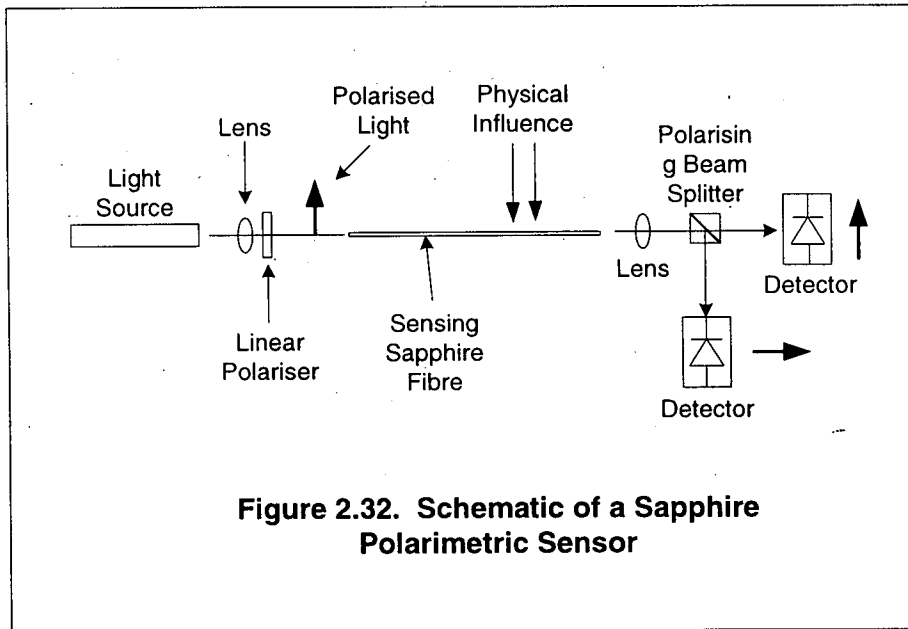


**Figure 2.32. Schematic of a Sapphire Polarimetric Sensor**

## 2.4 References to Chapter 2

- 2.1 A. I. Mlavsky and H. E. LaBelle, Jr., *Growth of Continuous Whiskers from the Melt* in: *Whisker Technology*, A. P. Levitt (Ed.), John Wiley & Sons, Inc., New York, 121, 1970
- 2.2 P. Rudolph and T. Fukuda, *Fiber Crystal Growth from the Melt*, *Crys. Res. Technol.*, **34**(1), 3, 1999
- 2.3 J. T. Stock, *Sir Charles Vernon Boys, Guardian of the Flame*, *Bull. Sci. Instrum. Soc.*, **23**, 2, 1989
- 2.4 C. V. Boys, *On the Production, Properties, and some suggested Uses of the Finest Threads*, *Proc. Phys. Soc.*, **9**, 8, 1887
- 2.5 H. E. LaBelle, Jr. and A. I. Mlavsky, *Growth of Sapphire Filaments from the Melt*, *Nature*, **216**(5115), 574, 1967
- 2.6 H. E. LaBelle, Jr. and A. I. Mlavsky, *Growth of Controlled Profile Crystals from the Melt: Part I – Sapphire Filaments*, *Mat. Res. Bull.*, **6**, 571, 1971
- 2.7 H. E. LaBelle, Jr., *Growth of Controlled Profile Crystals from the Melt: Part II – Edge-Defined Film-Fed Growth*, *Mat. Res. Bull.*, **6**, 581, 1971
- 2.8 D. B. Gasson and B. Cockayne, *Oxide Crystal Growth Using Gas Laser*, *J. Mater. Sci.*, **5**, 100, 1970
- 2.9 B. Cockayne, D. B. Gasson and N. Forbes, *Further Developments in Oxide Crystal Growth Using Gas Lasers*, *J. Mater. Sci.*, **5**, 837, 1970
- 2.10 C. A. Burrus and J. Stone, *Single-Crystal Fiber Optical Devices: A Nd: YAG Fiber Laser*, *Appl. Phys. Lett.*, **26**(6), 318, 1975
- 2.11 C. A. Burrus and L. A. Coldren, *Growth of Single-Crystal Sapphire-Clad Ruby Fibers*, *Appl. Phys. Lett.*, **31**(6), 383, 1977
- 2.12 C. A. Burrus and J. Stone, *Room-Temperature Continuous Operation of a Ruby Fiber Laser*, *J. Appl. Phys.*, **49**(6), 3118, 1978
- 2.13 M. M. Fejer, J. L. Nightingale, G. A. Magel and R. L. Byer, *Laser-Heated Miniature Pedestal Growth Apparatus for Single-Crystal Optical Fibers*, *Rev. Sci. Instrum.*, **55**(11), 1791, 1984
- 2.14 R. S. Feigelson, *The Laser-Heated Pedestal Growth Method: A Powerful Tool in the search for New High Performance Laser Crystals* in: *Tunable Solid State Lasers*, P. Hammerling, A. B. Budgor and A. Pinto (Eds.), Springer-Verlag, Berlin, 129, 1985

- 2.15 M. M. Fejer, *PhD Thesis*, Stanford University, 1986
- 2.16 R. S. Feigelson, *Opportunities for Research on Single-Crystal Fibers*, Mater. Sci. & Eng., **B1**, 67, 1988
- 2.17 R. S. Feigelson, *Growth of Fiber Crystals in: Crystal Growth of Electronic Materials*, E. Kaldis (Ed.), Elsevier, Amsterdam, 127, 1985
- 2.18 D. K. Tang, R. K. Route and R. S. Feigelson, *Growth of Barium Metaborate ( $BaB_2O_4$ ) Single Crystal Fibers by the Laser-Heated Pedestal Growth Method*, J. Cryst. Growth, **91**, 81, 1988
- 2.19 G. W. Qiao, J. S. Zhang, J. G. Huang, M. Jiang, Y. L. Ge, Y. Z. Wang and Z. Q. Hu, *An Investigation of Melt-Textured High  $T_C$  Superconductor Wires made by Laser Heated Pedestal Growth Technique*, Phys. C, **162-164**, 907, 1989
- 2.20 R. Guo, A. S. Bhalla and L. E. Cross,  *$Ba(Mg_{1/3}Ta_{2/3})O_3$  Single Crystal Fiber grown by the Laser Heated Pedestal Growth Technique*, J. Appl. Phys., **75**, 4704, 1994
- 2.21 A. Wang, G. Z. Wang, S. Gollapudi, R. G. May, K. A. Murphy and R. O. Claus, *Advances in sapphire optical fiber sensors*, Proc. SPIE, **1798**, 56, 1992
- 2.22 A. Wang, S. Gollapudi, R. G. May, K. A. Murphy and R. O. Claus, *Sapphire optical fiber-based interferometer for high temperature environmental applications*, Smart Mater. Struct., **4**, 147, 1995
- 2.23 R. R. Dils, *High-temperature optical fiber thermometer*, J. Appl. Phys., **54**(3), 1198, 1983
- 2.24 H. C. Seat, J. H. Sharp, Z. Y. Zhang and K. T. V. Grattan, *Single-Crystal Ruby Fibres for Fluorescence-based Temperature Sensing*, Paper presented at Sensors and their Applications X (Cardiff, Wales), 219, 1999
- 2.25 J. H. Sharp and H. C. Seat, *Temperature and Strain Characteristics of Ruby Fibre Fluorescence Emission*, Proc. SPIE, **4185**, 54, 2000
- 2.26 D. M. Henry, J. H. Herringer and N. Djeu, *Response of 1.6  $\mu m$  Er:  $Y_3Al_5O_{12}$  Fiber-Optic Temperature Sensor up to 1520 K*, Appl. Phys. Lett., **74**(23), 3447, 1999
- 2.27 D. A. Krohn, *Fiber Optic Sensors: Fundamentals and Applications (2<sup>nd</sup> Ed.)*, ISA, North Carolina, 1992
- 2.28 E. Udd, *The Emergence of Fiber Optic Sensor Technology in: Fiber Optic Sensors: An Introduction for Engineers and Scientists*, E. Udd (Ed.), John

- Wiley & Sons, Inc., New York, 1, 1991
- 2.29 R. Yamauchi, K. Himeno, T. Tsumanuma and R. Dahlgren, *Specialty Fibers for Sensors and Sensor Components*, Proc. SPIE, **2292**, 328, 1994
- 2.30 V. P. Martinelli and J. F. Wahl, *Optical Fiber Design Considerations for Fiber-Optic Sensors*, Proc. SPIE, **2292**, 361, 1994
- 2.31 P. E. Sanders, *Specialty Optical Fiber Products for Sensor Applications*, Proc. SPIE, **2292**, 316, 1994
- 2.32 A. D. Kersey, *A Review of Recent Developments in Fiber Optic Sensor Technology*, Opt. Fiber. Technol., **2**, 291, 1996
- 2.33 F. Luo, J. Liu and S. Chen, *Fiber Optic Distributed Sensing Scheme for Monitoring Structural Strain and Deformation*, Opt. Eng., **36**(5), 1548, 1997
- 2.34 P. L. Fuhr, D. R. Huston and B. MacCraith, *Embedded Fiber Optic Sensors for Bridge Deck Chloride Penetration Measurement*, Opt. Eng., **37**(4), 1221, 1998
- 2.35 E. L. Moore, S. D. Kingma, M. B. Miller and N. E. Lewis, *Integration Accomplishment of the Fiber Optic Control System Integration (FOCSI) Program*, Proc. SPIE, **2292**, 113, 1994
- 2.36 K. Hotate, *Fiber Sensor Technology Today*, Opt. Fiber Technol., **3**, 356, 1997
- 2.37 W. F. Hamann and H. A. Glick, *Integrated Diagnostics for Navy Fiber Optic Systems*, Proc. SPIE, **2594**, 2, 1996
- 2.38 G. Boisdé and A. Harmer (Eds.), *Chemical and Biochemical Sensing with Optical Fibers and Waveguides*, Artech House, Boston, 1996
- 2.39 B. Culshaw, *Basic Concepts of Optical Fiber Sensors* in: *Optical Fiber Sensors: Principles and Components*, Vol. I, J. Dakin and B. Culshaw (Eds.), Artech House, Boston, 9, 1988
- 2.40 E. Udd, *An Overview of Fiber-Optic Sensors*, Rev. Sci. Instrum., **66**(8), 4015, 1995
- 2.41 A. M. Smith, *Technology Overview: Optical Fibre Biological and Chemical Sensors* in: *Fibre Optic Sensors: A 2-Day Workshop of the Instrum. Sci. and Technol. Group of the IOP*, Glasgow, 23, 1987
- 2.42 J. D. Place, *A Fibre Optic Pressure Transducer Using a Wavelength Modulation Sensor*, Proc. SPIE, **522**, 219, 1985
- 2.43 G. L. Mitchall, *Intensity-Based and Fabry-Pérot Interferometer Sensors* in: *Fiber Optic Sensors: An Introduction for Engineers and Scientists*, E. Udd

- (Ed.), John Wiley & Sons, Inc., New York, 139, 1991
- 2.44 J. M. López-Higuera, *Optical Sensors? Fundamentals, Current Situation and Future Trends in Optical Sensors*, Servicio de Publicaciones de la Universidad de Cantabria, Cantabria, 1998
- 2.45 I. P. Gilles, D. Uttam, S. McNeil and B. Culshaw, *Self-Compensating Technique for Remote Fibre Optic Intensity Modulated Transducers*, Proc. SPIE, **522**, 233, 1985
- 2.46 G. Murtaza and J. M. Senior, *Schemes for Referencing of Intensity-Based Optical Sensor Systems* in: *Optical Fiber Sensor Technology*, K. T. V. Grattan and B. T. Meggitt (Eds.), Cambridge University Press, Cambridge, 383, 1995
- 2.47 J. M. Senior, S. D. Cusworth, N. G. Purrow and A. D. Muirhead, *An Extrinsic Optical Fibre Sensor Employing a Partially Reflecting Mirror*, Proc. SPIE, **522**, 204, 1985
- 2.48 P. T. Gardiner and R. A. Edwards, *Fibre Optic Position Sensors for Aircraft Flight Control Systems* in: *Fibre Optic Sensors: A 2-Day Workshop of the Instrum. Sci. and Technol. Group of the IOP*, Glasgow, 115, 1987
- 2.49 A. Dandridge, *Fiber Optics Sensors Based on the Mach-Zehnder and Michelson Interferometers* in: *Fiber Optic Sensors: An Introduction for Engineers and Scientists*, E. Udd (Ed.), John Wiley & Sons, Inc., New York, 271, 1991
- 2.50 D. A. Jackson, *Overview of Fibre Optic Interferometric Sensors* in: *Fibre Optic Sensors: A 2-Day Workshop of the Instrum. Sci. and Technol. Group of the IOP*, Glasgow, 1, 1987
- 2.51 J. Dakin and B. Culshaw (Eds.), *Optical Fiber Sensors: Applications, Analysis, and Future Trends*, Vol. IV, Artech House, Boston, 1997
- 2.52 J. D. C. Jones, P. Akhavan, D. A. Jackson, M. Corke and A. D. Kersey, *Single-Mode Fibre-Optic Sensors*, Proc. SPIE, **522**, 196, 1985
- 2.53 M. K. Barnoski and S. M. Jensen, *Fiber waveguides: a novel technique for investigating attenuation characteristics*, Appl. Opt., **15**(9), 2112, 1976
- 2.54 A. H. Hartog, *Distributed Fiber-Optic Sensors* in: *Optical Fiber Sensor Technology*, K. T. V. Grattan and B. T. Meggitt (Eds.), Chapman & Hall, London, 347, 1995
- 2.55 R. Rathod, R. D. Pechstedt, D. A. Jackson and D. J. Webb, *Distributed*

- Temperature-Change Sensor Based on Rayleigh Backscattering in an Optical Fiber*, Opt. Lett., **19**(8), 593, 1994
- 2.56 Y. J. Rao, N. Fisher, P. Henderson, V. Lecoche, C. N. Pannell, D. J. Webb and D. A. Jackson, *Recent Developments in Fibre Optic Sensors for Point and Distributed Sensing in Large Structures*, Proc. SPIE, **3483**, 138, 1998
- 2.57 A. J. Rogers, *Distributed and Multiplexed Sensor Systems in: Fibre Optic Sensors: A 2-Day Workshop of the Instrum. Sci. and Technol. Group of the IOP*, Glasgow, 55, 1987
- 2.58 S. V. Shatalin, V. N. Treschikov and A. J. Rogers, *Interferometric Optical Time-Domain Reflectometry for Distributed Optical-Fiber Sensing*, Appl. Opt., **37**(24), 5600, 1998
- 2.59 E. Hecht and A. Zajac, *Optics*, Addison-Wesley, London, 1980
- 2.60 A. D. Kersey, *Distributed and Multiplexed Fiber Optic Sensors in: Fiber Optic Sensors: An Introduction for Engineers and Scientists*, E. Udd (Ed.), John Wiley & Sons, Inc., New York, 325, 1991
- 2.61 X. Bao, D. J. Webb and D. A. Jackson, *22 km Distributed Temperature Sensor Using Brillouin Gain in an Optical Fiber*, Opt. Lett., **18**, 522, 1993
- 2.62 X. Bao, J. Dhliwayo, N. Heron, D. J. Webb and D. A. Jackson, *Experimental and Theoretical Studies on a Distributed Temperature Sensor Based on Brillouin Scattering*, IEEE J. Lightwave Technol., **13**(7), 1340, 1995
- 2.63 V. Lecoche, D. J. Webb, C. N. Pannell and D. A. Jackson, *Brillouin Based Distributed Fibre Sensor Incorporating a Brillouin Laser*, Proc. SPIE, **3483**, 156, 1998
- 2.64 P. J. Nash, G. A. Cranch, L. K. Cheng, D. de Bruijn and I. Crowe, *32-element TDM Optical Hydrophone Array*, Proc. SPIE, **3483**, 238, 1998
- 2.65 A. D. Kersey, *Multiplexing Techniques for Fiber Optic Sensors in: Fiber Optic Sensors: Applications, Analysis and Future Trends*, Vol. IV, J. Dakin and B. Culshaw (Eds.), Artech House, Boston, 369, 1997
- 2.66 K. P. Koo and A. D. Kersey, *Bragg Grating-Based Laser Sensors Systems with Interferometric Interrogation and Wavelength Division Multiplexing*, IEEE J. Lightwave Technol., **13**(7), 1243, 1995
- 2.67 H. R. Carter and R. T. Bailey, *Flame Quality Analyzer for Temperature Measurement and Combustion Control*, Sensors, **5**(1), 23, 1988
- 2.68 P. St. J. Russell and J. L. Archambault, *Fiber Gratings in: Optical Fiber*

- Sensors: Components and Subsystems*, Vol. III, J. Dakin and B. Culshaw (Eds.), Artech House, Boston, 9, 1997
- 2.69 K. O. Hill, Y. Fujii, D. C. Johnson and B. S. Kawasaki, *Photosensitivity in Optical Fiber Waveguides: Application to Reflective Filter Fabrication*, *Appl. Phys. Lett.*, **32**(10), 647, 1978
- 2.70 B. S. Kawasaki, K. O. Hill, D. C. Johnson and Y. Fujii, *Narrow-band Bragg reflectors in optical fibers*, *Opt. Lett.*, **3**(2), 66, 1978
- 2.71 G. Meltz, W. W. Morey and W. H. Glenn, *Formation of Bragg Gratings in Optical Fibers by a Transverse Holographic Method*, *Opt. Lett.*, **14**, 823, 1989
- 2.72 A. Othonos, *Fiber Bragg Gratings*, *Rev. Sci. Instrum.*, **68**(12), 4309, 1997
- 2.73 A. Inoue, M. Shigehara, M. Ito, M. Inai, Y. Hattori and T. Mizunami, *Fabrication and Application of Fiber Bragg Grating*, *Optoelectronics: Devices and Technologies*, **10**(1), 119, 1995
- 2.74 T. J. McKee, *Spectral-Narrowing Techniques for Excimer Laser Oscillators*, *Can. J. Phys.*, **63**, 214, 1985
- 2.75 M. C. Gower, C. Williams, P. Apte and P. T. Rumsby, *Efficient Line Narrowing and Wavelength Stabilization of Excimer Lasers*, *Proc. SPIE*, **1835**, 98, 1993
- 2.76 A. Othonos and X. Lee, *Narrow Linewidth Excimer Lasers for Inscribing Bragg Gratings in Optical Fibers*, *Rev. Sci. Instrum.*, **66**(5), 3112, 1995
- 2.77 J. L. Archambault, L. Reekie and P. St. J. Russell, *100% Reflectivity Bragg Reflectors Produced in Optical Fibers by Single Excimer Pulses*, *Elect. Lett.*, **29**, 453, 1993
- 2.78 H. J. Patrick and S. T. Vohra, *Fiber Bragg Grating with Long Period Fiber Grating Superstructure for Simultaneous Strain and Temperature Measurement*, *Proc. SPIE*, **3483**, 264, 1998
- 2.79 P. J. Moreira, L. A. Ferreira, J. L. Santos and F. Farahi, *Extended Range Interrogation Scheme for Fibre Bragg Gratings Using a Multimode Laser Diode*, *Proc. SPIE*, **3483**, 278, 1998
- 2.80 Y. J. Rao, *In-Fibre Bragg Grating Sensors*, *Meas. Sci. Technol.*, **8**, 355, 1997
- 2.81 M. J. O'Dwyer, G. M. Maistros, S. W. James, R. P. Tatam and I. K. Partridge, *Relating the State of Cure to the Real-Time Internal Strain Development in a Curing Composite Using In-Fibre Bragg Gratings and*

- Dielectric Sensors*, Meas. Sci. Technol., **9**, 1153, 1998
- 2.82 S. W. James, R. P. Tatam, S. R. Fuller and C. Crompton, *Monitoring Transient Strains on a Gun Barrel Using Fibre Bragg-Grating Sensors*, Meas. Sci. Technol., **10**, 63, 1999
- 2.83 M. B. Reid and M. Ozcan, *Temperature Dependence of Fiber Optic Bragg Gratings at Low Temperatures*, Opt. Eng., **37**(1), 237, 1998
- 2.84 Y. L. Lo, *Using In-Fiber Bragg-Grating Sensors for Measuring Axial Strain and Temperature Simultaneously on Surfaces of Structures*, Opt. Eng., **37**(8), 2272, 1998
- 2.85 A. Vengsarkar, W. Michie, L. Jankovic, B. Culshaw and R. Claus, *Fiber Optic Sensor for Simultaneous Measurements of Temperature and Strain*, Proc. SPIE, **1367**, 249, 1990
- 2.86 W. Michie, B. Culshaw, R. Roberts and R. Davidson, *Fiber Optic Techniques for Simultaneous Measurement of Strain and Temperature Variations in Composite Materials*, Proc. SPIE, **1588**, 342, 1991
- 2.87 Y. J. Rao, P. J. Henderson, D. A. Jackson, L. Zhang, and I. Bennion, *Simultaneous Strain, Temperature and Vibration Measurement Using a Multiplexed In-Fiber Bragg Grating/Fiber Fabry-Perot Sensor System*, Elect. Lett., **33**, 2063, 1997
- 2.88 M. Song, B. Lee, S. B. Lee and S. S. Choi, *Interferometric Temperature-Insensitive Strain Measurement with Different-Diameter Fiber Bragg Gratings*, Opt. Lett., **22**(11), 790, 1997
- 2.89 M. Song, S. B. Lee, S. S. Choi and B. Lee, *Simultaneous Measurement of Temperature and Strain Using Two Fiber Bragg Gratings Embedded in a Glass Tube*, Opt. Fiber Technol., **3**, 194, 1997
- 2.90 F. M. Haran, J. K. Rew and P. D. Foote, *A Strain-Isolated Fibre Bragg Grating Sensor for Temperature Compensation of Fibre Bragg Grating Strain Sensors*, Meas. Sci. Technol., **9**, 1163, 1998
- 2.91 M. G. Xu, J. L. Archambault, L. Reekie and J. P. Dakin, *Discrimination Between Strain and Temperature Effects Using Dual-Wavelength Fiber Bragg Grating Sensors*, Elect. Lett., **30**, 1085, 1995
- 2.92 G. P. Brady, K. Kalli, D. J. Webb, D. A. Jackson, L. Zhang and I. Brennon, *Recent Developments in Optical Fibre Sensing Using Fibre Bragg Gratings*, Proc. SPIE, **2839**, 8, 1996

- 2.93 M. H. Maher, K. Tabrizi, J. D. Prohaska and E. Snitzer, *Fiber Bragg Gratings for Civil Engineering Applications*, Proc. SPIE, **2682**, 298, 1996
- 2.94 P. Ferdinand, O. Ferragu, J. L. Lechien, B. Lescop, S. Magne, V. Marty, S. Rougeault, G. Kotrotsios, V. Neuman, Y. Depeursinge, J. B. Michel, M. Van Uffelen, D. Varelas, H. Berthou, G. Pierre, C. Renouf, B. Jarret, Y. Verbandt, W. Stevens, M. R. H. Voet and D. Toscano, *Mine Operating Accurate STABILity Control with Optical Fiber Sensing and Bragg Grating Technology: The European BRITE/EURAM STABILOS Project*, IEEE J. Lightwave Technology, **13**(7), 1303, 1995
- 2.95 R. L. Idriss, M. B. Kodindouma, A. D. Kersey and M. A. Davis, *Multiplexed Bragg Grating Optical Fiber Sensors for Damage Evaluation in Highway Bridges*, Smart Mater. Struct., **7**, 209, 1998
- 2.96 S. Huang, M. M. Ohn, M. LeBlanc and R. M. Measures, *Continuous Arbitrary Strain Profile Measurements with Fiber Bragg Gratings*, Smart Mater. Struct., **7**, 248, 1998
- 2.97 M. Bugaud, P. Ferdinand, S. Rougeault, V. Dewynter-Marty, P. Parneix and D. Lucas, *Health Monitoring of Composite Plastic Waterworks Lock Gates Using In-Fibre Bragg Grating Sensors*, Smart Mater. Struct, **9**, 322, 2000
- 2.98 K. Wood, T. Brown, R. Rogowski and B. Jensen, *Fiber Optic Sensors for Health Monitoring of Morphing Airframes: I. Bragg Grating Strain and Temperature Sensor*, Smart Mater. Struct., **9**, 163, 2000
- 2.99 M. A. Davis, A. D. Kersey, J. Sirkis and E. J. Friebele, *Shape and Vibration Mode Sensing Using a Fiber Optic Bragg Grating Array*, Smart Mater. Struct., **5**, 759, 1996
- 2.100 N. E. Fisher, J. Surowiec, D. J. Webb, D. A. Jackson, L. R. Gavrilov, J. W. Hand, L. Zhang and I. Bennion, *In-Fibre Bragg Gratings for Ultrasonic Medical Applications*, Meas. Sci. Technol., **8**, 1050, 1997
- 2.101 M. W. Hathaway, N. E. Fisher, D. J. Webb, C. N. Pannell, D. A. Jackson, L. R. Gavrilov, J. W. Hand, L. Zhang and I. Bennion, *Combined Ultrasound and Temperature Sensor Using a Fibre Bragg Grating*, Opt. Commun., **171**, 225, 1999
- 2.102 M. Pacheco, F. Mendoza Santoyo, A. Méndez and L. A. Zenteno, *Piezoelectric-Modulated Optical Fibre Bragg Grating High-Voltage Sensor*, Meas. Sci. Technol., **10**, 777, 1999

- 2.103 V. Bhatia, *Applications of Long-Period Gratings to Single and Multi-Parameter Sensing*, Opt. Express, **4**(11), 457, 1999
- 2.104 Y. J. Rao and D. Jackson, *Recent Progress in Multiplexing Techniques for In-Fibre Bragg Grating Sensors*, Proc. SPIE, **2895**, 171, 1996
- 2.105 G. B. Havsgard, K. Pran, S. Knudsen, P. O. Baalerud, G. W. Wang, S. T. Vohra, M. A. Davis, A. Dandridge and A. E. Jensen, *Composite Plate Drop Test Using a 16-Channel Fibre Bragg Grating Strain Sensor System*, Proc. SPIE, **3483**, 195, 1998
- 2.106 V. A. Handerek, *Optical Fiber Bragg Grating: A New Sensor Multiplexing Tool*, Sensor Rev., **18**, 39, 1998
- 2.107 R. S. Weis, A. D. Kersey and T. A. Berkoff, *A Four-Element Fiber Grating Sensor Array with Phase-Sensitive Detection*, IEEE Photon. Technol. Lett., **6**, 1469, 1994
- 2.108 Y. J. Rao, B. A. Hurle, K. Kalli, G. Brady, D. J. Webb, D. A. Jackson, L. Zhang and I. Bennion, *Spatially-Multiplexed Fiber-Optic Interferometric and Grating Sensor System for Quasi-Static Absolute Measurements*, Proc. 11<sup>th</sup> Int. Conf. On Optical Fiber Sensors, 666, 1996
- 2.109 A. D. Kersey and T. A. Berkoff, *Fiber Optic Bragg Grating Differential Temperature Sensor*, IEEE Photon. Technol. Lett., **4**, 1183, 1993
- 2.110 K. P. Koo and A. D. Kersey, *Fiber Laser Sensor with Ultrahigh Strain Resolution Using Interferometric Interrogation*, Elect. Lett., **31**, 1180, 1995
- 2.111 A. D. Kersey, K. P. Koo and M. A. Davis, *Fiber Optic Bragg Grating Laser Sensors*, Proc. SPIE, **2292**, 102, 1994
- 2.112 C. G. Wallace, A. Othonos and D. Uttamchandani, *Fibre Bragg Grating Based Laser Sensor*, Proc. SPIE, **2509**, 48, 1995
- 2.113 J. Dakin and B. Culshaw (Eds.), *Optical Fiber Sensors: Components and Subsystems*, Vol. III, Artech House, Boston, 1997
- 2.114 K. T. V. Grattan and Z. Y. Zhang, *Fiber Optic Fluorescence Thermometry*, K. T. V. Grattan and A. Augousti (Eds.), Chapman and Hall, London, 1995
- 2.115 K. T. V. Grattan, *The use of fibre optic techniques for temperature measurement*, Measure. Control, **20**, 32, 1987
- 2.116 R. A. Forman, G. J. Piermarini, J. D. Barnett and S. Block, *Pressure Measurement Made by the Utilization of Ruby Sharp-Line Luminescence*, Science, **176**, 284, 1972

- 2.117 Y. Sato-Sorensen, *Measurements of the lifetime of the ruby  $R_1$  line under high pressure*, J. Appl. Phys., **60**(8), 2985, 1986
- 2.118 A. Arnaud, D. I. Forsyth, T. Sun, Z. Y. Zhang and K. T. V. Grattan, *Strain and temperature effects on erbium-doped fiber for decay-time based sensing*, Rev. Sci. Instrum., **71**(1), 104, 2000
- 2.119 T. Sun, Z. Y. Zhang, K. T. V. Grattan and A. W. Palmer, *Intrinsic strain and temperature characteristics of Yb-doped silica optical fibers*, Rev. Sci. Instrum., **70**(2), 1447, 1999
- 2.120 K. T. V. Grattan and Z. Y. Zhang, *Fiber Optic Fluorescence Thermometry: An Introduction* in: *Fiber Optic Fluorescence Thermometry*, K. T. V. Grattan and A. Augousti (Eds.), Chapman and Hall, London, 1, 1995
- 2.121 S. P. Jamison and G. F. Imbusch, *Temperature dependence of the luminescence from heavily doped ruby*, J. Lumin., **75**, 143, 1997
- 2.122 K. T. V. Grattan, A. W. Palmer and C. A. Wilson, *A miniaturised microcomputer-based neodymium 'decay-time' temperature sensor*, J. Phys. E, **20**, 1201, 1987
- 2.123 K. T. V. Grattan, J. D. Manwell, S. M. L. Sim and C. A. Wilson, *Lifetime investigation of fluorescence from neodymium: yttrium aluminium garnet at elevated temperatures*, Opt. Commun., **62**(2), 104, 1987
- 2.124 R. Scheps, *Upconversion Laser Processes*, Prog. Quant. Electron., **20**(4), 271, 1996
- 2.125 K. T. V. Grattan and A. W. Palmer, *A fiber optic temperature sensor using fluorescence decay*, Proc. SPIE, **492**, 535, 1984
- 2.126 R. R. Sholes and J. G. Small, *Fluorescent decay thermometer with biological applications*, Rev. Sci. Instrum., **51**(7), 882, 1980
- 2.127 M. Sun, *Fiber optic thermometry based on photoluminescent decay times* in: *Temperature – Its Measurement and Control in Science and Industry*, Vol. 6, Part 2, Am. Inst. Phys., New York, 715, 1992
- 2.128 K. T. V. Grattan, R. K. Selli and A. W. Palmer, *Ruby decay-time fluorescence thermometer in a fiber-optic configuration*, Rev. Sci. Instrum., **59**(8), 1328, 1988
- 2.129 Z. Zhang, K. T. V. Grattan and A. W. Palmer, *A novel signal processing scheme for a fluorescence based fiber-optic temperature sensor*, Rev. Sci. Instrum., **62**(7), 1735, 1991

- 2.130 Z. Zhang, K. T. V. Grattan and A. W. Palmer, *Phase-locked detection of fluorescence lifetime*, Rev. Sci. Instrum., **64**(9), 2531, 1993
- 2.131 W. H. Fonger and C. W. Struck, *Temperature dependences of Cr<sup>3+</sup> radiative and nonradiative transitions in ruby and emerald*, Phys. Rev. B, **11**(9), 3251, 1975
- 2.132 Z. Zhang, K. T. V. Grattan and A. W. Palmer, *Temperature dependences of fluorescence lifetimes in Cr<sup>3+</sup>-doped insulating crystals*, Phys. Rev. B, **48**(11), 7772, 1993
- 2.133 J. R. Izatt, R. C. Mitchell and H. A. Daw, *Thermal Dependence of Ruby Laser Emission*, J. Appl. Phys., **37**(4), 1558, 1966
- 2.134 Q. Ma and D. R. Clarke, *Stress Measurement in Single-Crystal and Polycrystalline Ceramics Using Their Optical Fluorescence*, J. Am. Ceram. Soc., **76**(6), 1433, 1993
- 2.135 A. T. Augousti, K. T. V. Grattan and A. W. Palmer, *A Laser-Pumped Temperature Sensor Using Fluorescent Decay Time of Alexandrite*, IEEE J. Lightwave Technol., **LT-5**(6), 759, 1987
- 2.136 Z. Zhang, K. T. V. Grattan and A. W. Palmer, *Fiber-optic high-temperature sensor based on the fluorescence lifetime of alexandrite*, Rev. Sci. Instrum., **63**(8), 3869, 1992
- 2.137 Z. Zhang, K. T. V. Grattan and A. W. Palmer, *Sensitive Fibre Optic Thermometer Using Cr:LiSAF Fluorescence For Bio-Medical Sensing Applications*, Proc. 8<sup>th</sup> Opt. Fiber Sensor Conf., Monterey, CA, 93, 1992
- 2.138 Z. Zhang, K. T. V. Grattan and A. W. Palmer, *Cr:LiSAF fluorescence lifetime based fiber optic thermometer and its applications in clinical RF heat treatment*, Proc. SPIE, **1885**, 300, 1993
- 2.139 V. C. Farnicola, Z. Zhang and K. T. V. Grattan, *Fiber optic thermometry based on Cr-fluorescence in olivine crystals*, Rev. Sci. Instrum., **68**(6), 2418, 1997
- 2.140 M. J. Weber (Ed.), *CRC Handbook of Laser Science and Technology*, Vol I, CRC Press, Inc., Boca Raton, Florida, 1982
- 2.141 Z. Y. Zhang, K. T. V. Grattan, A. W. Palmer, B. T. Meggitt and T. Sun, *Fluorescence decay-time characteristics of erbium-doped optical fiber at elevated temperatures*, Rev. Sci. Instrum., **68**(7), 2764, 1997
- 2.142 Z. Y. Zhang, K. T. V. Grattan, A. W. Palmer, B. T. Meggitt and T. Sun,

- Characterization of erbium-doped intrinsic optical fiber sensor probes at high temperatures*, Rev. Sci. Instrum., **69**(8), 2924, 1998
- 2.143 E. Maurice, G. Monnom, D. B. Ostrowsky and G. W. Baxter, *High Dynamic Range Temperature Point Sensor Using Green Fluorescence Intensity Ratio in Erbium-Doped Silica Fiber*, IEEE J. Lightwave Technol., **13**(7), 1349, 1995
- 2.144 P. V. dos Santos, M. T. de Araujo, A. S. Gouveia-Neto, J. A. Medeiros Neto and A. S. B. Sombra, *Optical Thermometry Through Infrared Excited Upconversion Fluorescence Emission in  $Er^{3+}$ - $Yb^{3+}$ -doped Chalcogenide Glasses*, IEEE J. Quant. Electron., **35**(2), 395, 1999
- 2.145 Z. Y. Zhang, K. T. V. Grattan, A. W. Palmer and B. T. Meggitt, *Potential for temperature sensor applications of highly neodymium-doped crystals and fiber at up to approximately 1000 °C*, Rev. Sci. Instrum., **68**(7), 2759, 1997
- 2.146 S. A. Wade, G. W. Baxter, S. F. Collins, K. T. V. Grattan and T. Sun, *Simultaneous strain-temperature measurement using fluorescence from Yb-doped silica fiber*, Rev. Sci. Instrum., **71**(6), 2267, 2000
- 2.147 T. Sun, Z. Y. Zhang, K. T. V. Grattan and A. W. Palmer, *Ytterbium-based fluorescence decay time fiber optic temperature sensor systems*, Rev. Sci. Instrum., **69**(12), 4179, 1998
- 2.148 Z. Y. Zhang, K. T. V. Grattan, A. W. Palmer and B. T. Meggitt, *Thulium-doped intrinsic fiber optic sensor for high temperature measurements (>1100 °C)*, Rev. Sci. Instrum., **69**(9), 3210, 1998
- 2.149 Z. Y. Zhang, K. T. V. Grattan and B. T. Meggitt, *Thulium-doped fiber optic decay-time temperature sensors: Characterization of high temperature performance*, Rev. Sci. Instrum., **71**(4), 1614, 2000
- 2.150 Q. Zheng and K. Torii, *Response of Optical Fiber Thermometer with Blackbody Cavity Sensor (Aiming to Measure the Gas Temperature inside Internal Combustion Engine)*, JSME Int. J. Series B, **37**(3), 588, 1994
- 2.151 R. Claus, K. Murphy, R. May, A. Wang, G. Wang, T. Tran, J. Greene, M. Alcook and J. E. Coate, *Sapphire Fiber Strain Gage for Static and Fatigue Measurements*, Proc. SPIE, **2360**, 384, 1994
- 2.152 T. Tran, J. Greene, M. Alcook, K. Murphy, R. May, A. Wang, G. Wang, R. Claus and J. E. Coate, *High temperature sapphire extrinsic fizeau interferometer for strain measurements on silicon carbide materials*, Proc.

SPIE, **2072**, 177, 1994

- 2.153 Y. Shen, Y. Wang, L. Ye and Z. Ding, *Study on the doped crystal fiber high temperature sensor*, Proc. SPIE, **2292**, 421, 1994
- 2.154 V. Bhatia, K. A. Murphy, R. G. May, R. O. Claus, T. A. Tran, J. A. Greene and J. E. Coate, *High Temperature Sapphire Optical Fiber Interferometric Strain Sensor*, High Temp. and Mater. Sci., **35**, 31, 1996
- 2.155 L. Ye and Y. Shen, *Development of a sapphire fiber thermometer using two wavelength bands*, Proc. SPIE, **2895**, 393, 1996
- 2.156 Z. Zhang, J. H. Herringer and N. Djeu, *Monolithic crystalline fiber optic temperature sensor*, Rev. Sci. Instrum., **68**(5), 2068, 1997
- 2.157 H. Xiao, W. Zhao, R. Lockhart, J. Wang and A. Wang, *Absolute Sapphire Optical Fiber Sensor For High-Temperature Applications*, Proc. SPIE, **3201**, 36, 1997
- 2.158 R. Götz, B. Mizaikoff and R. Kellner, *Application of Sapphire Fibres to IR Fibre-optic Evanescent Field Gas Sensors*, Mikrochim. Acta (Suppl.), **14**, 833, 1997
- 2.159 Y. Wang and X. Wu, *Application of Nanopowder to High Temperature single Crystal Fiber Sensor*, J. Mater. Sci. Technol., **13**, 364, 1997
- 2.160 Y. Shen, L. Tong, Y. Wang and L. Ye, *Sapphire-fiber thermometer ranging from 20 to 1800 °C*, Appl. Opt., **38**(7), 1139, 1999
- 2.161 L. Tong, Y. Shen, L. Ye and Z. Ding, *A zirconia single-crystal fibre-optic sensor for contact measurement of temperatures above 2000 °C*, Meas. Sci. Technol., **10**, 607, 1999
- 2.162 D. L. Chubb and D. S. Wolford, *Rare earth optical temperature sensor*, Rev. Sci. Instrum., **71**(5), 2233, 2000
- 2.163 Y. Shen, Y. Wang, L. Tong and L. Ye, *Novel sapphire fiber thermometer using fluorescent decay*, Sensors and Actuators A, **71**, 70, 1998
- 2.164 L. Tong, *Growth of high-quality  $Y_2O_3$ - $ZrO_2$  single-crystal optical fibers for ultra-high-temperature fiber-optic sensors*, J. Cryst. Growth, **217**, 281, 2000
- 2.165 T. Yoshino, K. Kurosawa, K. Itoh and T. Ose, *Fiber-optic Fabry-Perot interferometer and its applications*, IEEE J. Quant. Electron., **QE-18**, 1624, 1982
- 2.166 W. B. Spillman, Jr., *Multimode Polarization Sensors in: Fiber Optic Sensors: An Introduction for Engineers and Scientists*, E. Udd (Ed.), John Wiley &

Sons, Inc., New York, 181, 1991

## **Chapter 3 – Laser Heated Pedestal Growth of Crystal Fibres**

### **3.0 Introduction**

### **3.1 Overview of available growth techniques**

- 3.1.1 Capillary shaping from melts
- 3.1.2 Drawing down and micro-pulling down (DD and  $\mu$ -PD) methods
- 3.1.3 Micro-Czochralski ( $\mu$ -CZ) method
- 3.1.4 Internal crystallisation method (ICM)
- 3.1.5 Laser heated pedestal growth

### **3.2 The laser heated pedestal growth technique**

### **3.3 Laser heated pedestal growth system and design considerations**

- 3.3.1 Heat source
- 3.3.2 Fibre pull and source feed systems
- 3.3.3 Laser beam focusing optics
- 3.3.4 Growth chamber
- 3.3.5 Vibration-isolated optical bench

### **3.4 Fibre growth**

### **3.5 References to Chapter 3**

## **Chapter 3 – Laser Heated Pedestal Growth of Crystal Fibres**

### **3.0 Introduction**

A brief review of the available crystal fibre growth methods is undertaken to select the most appropriate growth technique for the current requirements. Considerations are also given to the various important growth parameters and discussed in conjunction with the selected growth method, the laser heated pedestal growth technique, with a view to producing high quality crystal fibres of pure and doped sapphire, in particular, and YSZ (yttria-stabilised zirconia) for characterisation as suitable fibre optic sensors. The fibre growth process, which is directly related to the equipment employed, determines the final quality of the fibres produced hence, optimum usage of these parameters must be taken into account. A list of growth methods currently used for growing single crystal fibres is also discussed. Unlike fibres which have been employed for laser studies/materials and other non-linear device applications, where stringent dimensional uniformity and control are essential, fibres for sensors can generally tolerate a certain level of geometrical and dimensional defects such as small diameter variations, etc.

### **3.1 Overview of available growth methods**

The growth of single-crystal fibres (SCFs) for passive, active and nonlinear optical applications has been well documented over the last three decades. Materials grown in single-crystal fibre form can have near-theoretical properties (high strength, for example) due to the small dimensions and reduced defects associated with the fibre geometry. Indeed, the first major applications considered for such fibres were in structural reinforcement where continuous lengths of polycrystalline sapphire fibres were grown from the melt [3.1]. With a melting point of ~2320 K, high strength, high mechanical stability at elevated temperatures, and its chemical inertness, sapphire, in fibre form was considered potentially highly suitable for such an application. The combination of attractive mechanical properties and the waveguiding nature of a fibre geometry in SCFs can offer superior characteristics when compared to glass fibres. Generally, these are wide optical transparency, high

optical damage threshold and, hence, high achievable energy densities, high optical gains and large nonlinear coefficients [3.2, 3.3].

Recent research in SCFs has been driven by new requirements for novel optical materials for use in optical storage, harmonic generation, superconductivity, IR laser beam delivery and solid state lasers [3.4]. In many optical applications, stringent demands are placed on crystal fibres to be grown with high dimensional uniformity and optical quality in order to reduce transmission losses as well as to prevent the formation of both internal and external defects which would then limit their usefulness. Diameter variation is a major factor directly affecting the quality of a crystal fibre. Although the diameter tolerances depend on the desired optical interaction and application, variations on the order of 1 – 2 % should be adequate for fibre optic sensing applications where typical fibre lengths used can be in the region of 50 to 100 mm.

It is relatively easy to achieve good diameter control and, hence, tight tolerancing in glass fibres since the high viscosity exhibited by molten glass materials allows any perturbation imparted to the growing fibre (via vibration and/or shocks) to be absorbed and dampened. Perturbations will thus be drawn out into low frequency diameter variations with small amplitudes. In crystals, however, where a sharp liquid/solid phase transition exists, the molten zone is highly susceptible to perturbations and any disturbance to the molten zone or growth interface will, generally, result in relatively large variations being imparted to the as-grown fibre diameter. Hence, fabrication of single-crystal fibres requires methods which are considerably different from that used to pull glass fibres. Important considerations thus have to be given to the various growth parameters, such as melt stability, molten zone length, growth environment (since even convective cooling currents can lead to non-uniform cooling of the fibre as it is drawn), the stability of the heat source, heating power required as well as the source feed and fibre pull rates.

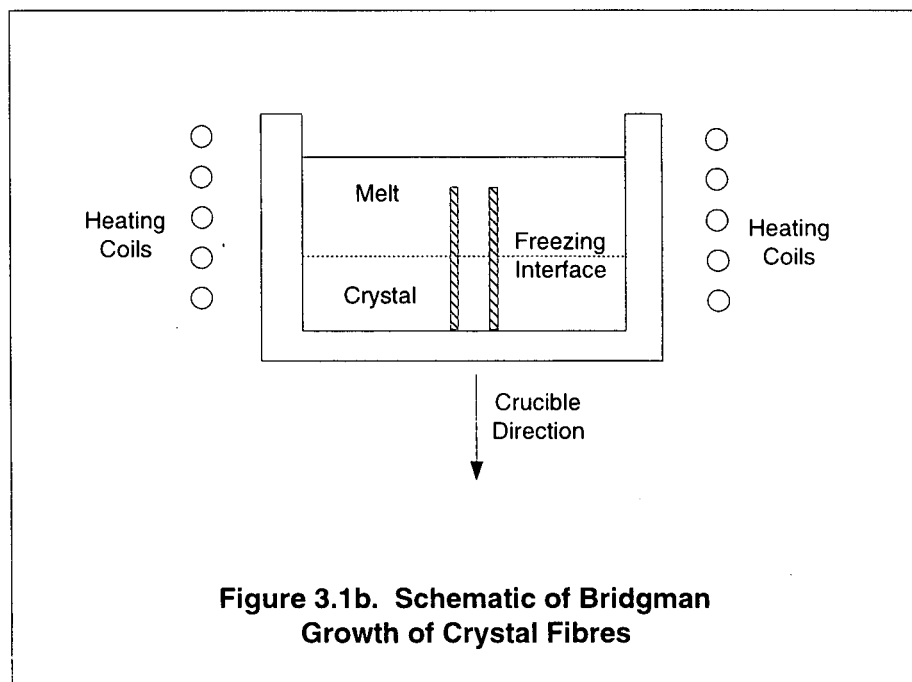
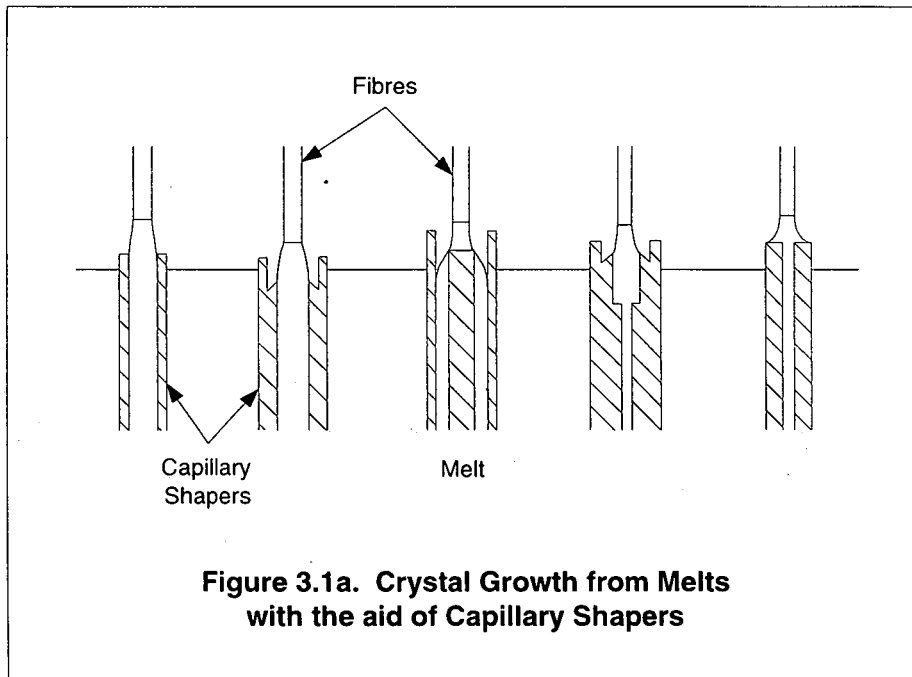
Several methods exist for the growth of single crystal fibres. The large majority of these involve crystal fibre growth from the melt and the most commonly used techniques are briefly summarised below. One observation to note is that all these methods, with the exception of two, require the use of a crucible and /or a furnace.

Hence, the crucible/container materials must be carefully chosen to be compatible with the material to be grown so that there is no chemical reaction between them which may result in impurities being transferred to the growing fibres.

### 3.1.1 Capillary shaping from melts

The main principle behind this technique involves the use of a shaper in the form of capillary tubes inserted into a melt [3.5]. The profiles of the tubes then define the geometry of the crystal pulled. The most basic growth profile is defined by contact between the melt and the walls of the shaper/capillary while other melt schemes can be realised by using capillaries with different edges as shown in **Figure 3.1a**. With shaped growth, the main growth mechanism is determined by the ability of the melt to wet the edge of the capillary, which will result in a stable meniscus angle from which stable growth can then be commenced [3.6]. A variant of this growth method includes the edge-defined film-fed growth (EFG)/Stepanov technique which has been successfully commercialised and employed, mainly, in growing sapphire crystal fibres by *Saphikon, Inc.* [3.7]. Crystal fibres of KRS-5 (thallium bromoiodide) for the delivery of IR wavelengths have also been grown using this technique [3.8]. The Bridgman growth technique is also included here since shapers in the form of capillary tubes are also used [3.9]. It is illustrated in **Figure 3.1b** where the crucible is lowered through a set of heating coils. This causes the melt to undergo a solid/liquid interface when the melt is lowered through a temperature gradient. The capillaries employed define the dimension of the final crystal fibre grown and thus have to be chosen to ensure chemical compatibility and match the thermal coefficients of the desired growth material(s).

With such crystal growth techniques involving capillary shapers, both materials for the crystal and the shapers must be matched so that no reaction and, hence, contamination occur between them. The fibre diameter is controlled by either the internal walls of the capillary shaper used or the meniscus angle of the wet between the melt and the edge of the shaper. The uniformity of the fibre diameter is therefore intrinsically determined by the tolerancing and smoothness of these parameters. The melting point of the shapers may also impose a limit on the type of materials which can be grown.



### 3.1.2 Drawing down and micro-pulling down (DD and $\mu$ -PD) methods

These two methods are basically the same technique used for crystal fibre pulling although they have been given different names by various authors [3.10, 3.11]. A schematic of the principle behind the DD and  $\mu$ -PD methods is shown in **Figure 3.2**. A crucible contains the melt which can be heated by several types of heat sources. The source material is introduced from the top of the growth apparatus while the crystal fibre is pulled in a downward direction. A seed crystal with the desired crystallographic orientation is attached to a puller and moved vertically up to enable contact to be made with the molten source material which flows through an orifice/aperture at the bottom of the crucible. Fibre growth then takes place when the puller is withdrawn at a constant rate in the downward direction. The growth chamber may be flushed with inert gas when materials which are highly oxidising are being grown.

Such techniques employ crucibles to contain the melt hence, the reaction between the crucible material and the melt has to be carefully considered and the fibre dimensions are largely determined by the choice of aperture used as well as the wetting conditions. Contamination may also be a problem if residues from previous growth were not properly removed. With a relatively large melt volume involved in such growth methods, the Marangoni effect [3.12] may cause a degradation in the quality of grown fibres [3.13, 3.14, 3.15]. Although initially conceived to grow doped  $\text{LiNbO}_3$  [3.10, 3.13, 3.14], where compositional uniformity can be tightly controlled, such techniques have been extended to grow crystal fibres of  $\text{Bi}_4\text{Ge}_3\text{O}_{12}$  (scintillator in high energy physics) [3.16], silicon (device applications) [3.11],  $\text{Si}_{1-x}\text{Ge}_x$  (analysis) [3.15],  $\text{K}_3\text{Li}_2(\text{Ta, Nb})_5\text{O}_{12}$  (ferroelectrics) [3.17], some rare earth-doped crystal fibres (optoelectronics) [3.18], eutectic fibres for structural applications [3.19, 3.20] and nonlinear garnets for Faraday isolators [3.21].

### 3.1.3 Micro-Czochralski ( $\mu$ -CZ) method

In  $\mu$ -CZ growth [3.22], the source material is melted in an appropriate crucible in which a heater is embedded. The melt volume is generally small so as to reduce

thermal convection currents in the melt which would otherwise lead to complications in growing crystal fibres. It also provides better control of the melt temperature since melt and crucible/heater are in close contact. A microprotrusion is cast into the crucible to act as a starting point from which crystal growth can be effected. The growth of any fibre is determined by the ability of the melt to wet this protrusion. An oriented seed crystal can then be dipped into the melt at this point and pulled into a crystal fibre at relatively high rates. **Figure 3.3** shows a schematic of the  $\mu$ -CZ method. As in all crystal growth methods requiring crucibles/containers and/or capillary shapers, the chemical matching of the melt and crucible is an important factor to be considered so that little or no contamination of the grown fibre occurs. Another limitation of this method is the maximum temperature which can be realised and this is determined by the heater/crucible material. The micro-Czochralski method was originally used for growing single crystal  $\text{LiNbO}_3$  fibres [3.22] but has also been employed in the growth of crystalline Bi-Sr-Ca-Cu-O fibres for use as high temperature superconducting materials [3.23].

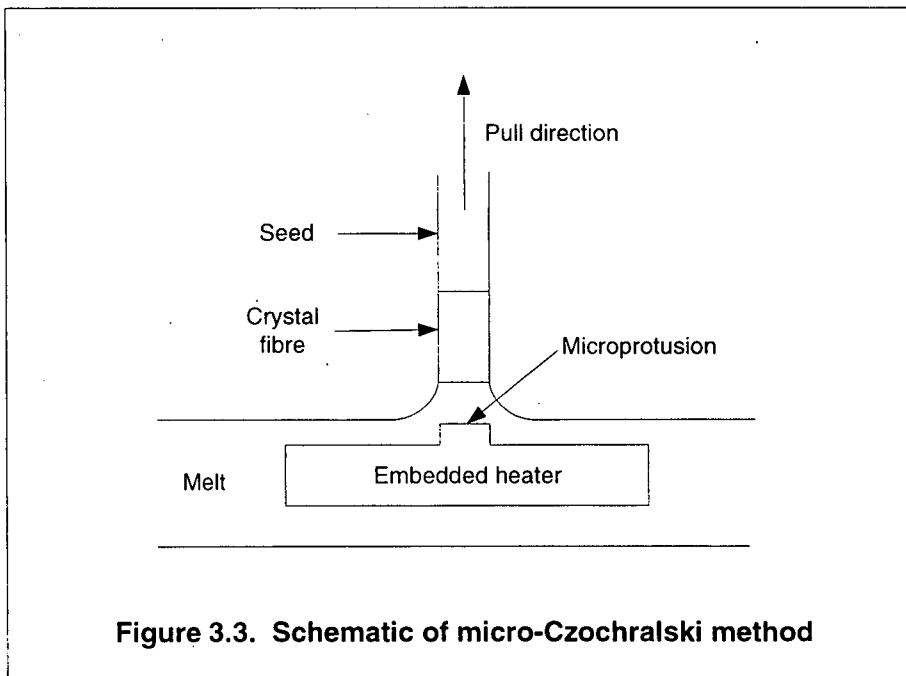
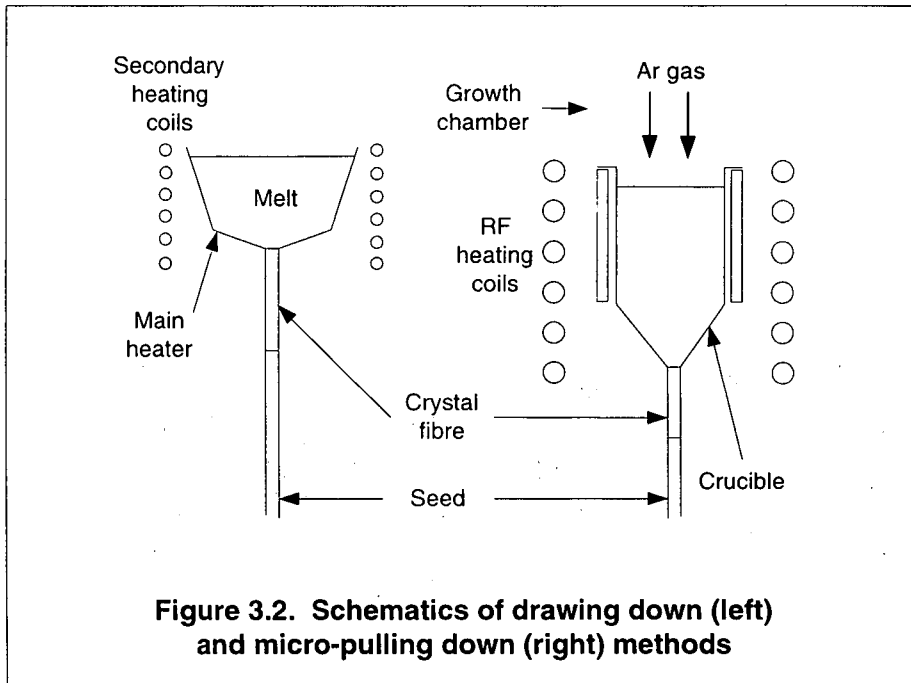
#### **3.1.4 Internal crystallisation method (ICM)**

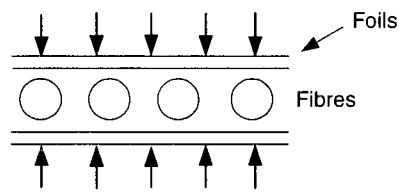
The ICM is a relatively new crystal growth technique originally conceived for fabricating composite fibres in large quantities for use in structural applications [3.24, 3.25, 3.26]. It is based on the crystallisation of the melt within the volume of a suitable matrix to form continuous strands of fibres. A schematic of this technique is shown in **Figures 3.4**. To enable continuous crystal fibre growth, a matrix with prefabricated continuous cylindrical channels is employed. This can be achieved by winding an assembly of foils and wires of the same material onto a mandrel, shown in **Figure 3.4a**, to form a block of an appropriate size which is then subjected to diffusion bonding under certain temperature-pressure-time conditions. Diffusion bonding bonds the foils and wires together and isolates the neighbouring wires from the melt during fibre growth, yielding continuous cylindrical channels within the matrix. The final structure of the finished matrix is shown in **Figure 3.4b**.

For fibre growth to be achieved, the matrix must be kept at a higher temperature than that of the melt and there must be good wetting between the matrix channels and melt. Crystallisation into fibres is achieved by infiltration of the melt into the

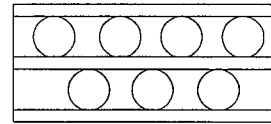
continuous channels and moving the matrix through two temperature zones to provide overcooling. The initial section of the melt which has been moved into the cooler second zone and crystallised will, thus, act as seed for rest of the fibres growing in the channels. Extraction of the fibres is done by dissolving the matrix in acids or suitable solvents. Although polycrystalline crystal fibres are generally produced with ICM [3.24, 3.25], an oriented seed crystal located at the top of the matrix may be used to initiate single-crystal fibre growth [3.27]. An illustration of ICM is shown in **Figure 3.5c** while a typical shape of the fibre cross-section can be seen in **Figure 3.5d**. This technique has been used almost uniquely to produce sapphire crystal fibres with intended applications in high temperature composite matrix and structural reinforcements [3.24, 3.25, 3.27].

Although mass production of crystal fibres is technically possible, several significant limitations do exist when using this technique. Since fibre growth occurs within a matrix, both fibre and matrix materials must be carefully matched for chemical inertness and, to a more significant extent, to ensure compatible thermal expansion coefficients so that little internal stress is imparted to the fibres upon crystallisation. Materials which can be grown with ICM are limited by the melting points of both the crucible and matrix used while diameter control is determined by the uniformity of the channel/wire dimensions used in the fabrication of the matrix, which could be significant since the as-grown fibres are relatively long.

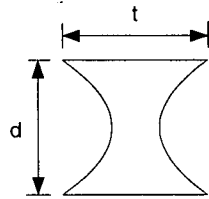




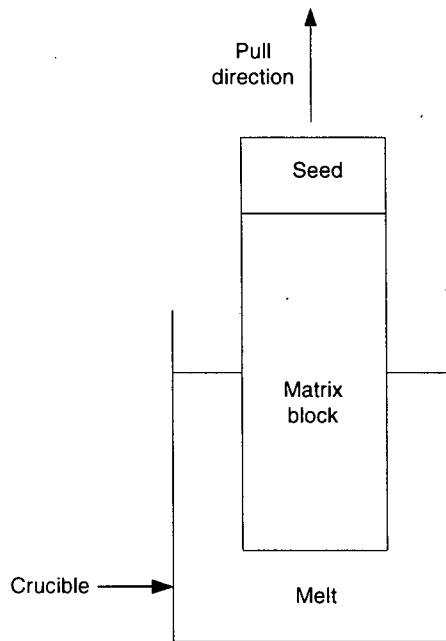
(a) Assembly of foils and wires/fibres



(b) Finished matrix with multiple channels



(c) Cross section of fibre by the ICM



(d) Fibre production by the ICM with seed crystal

**Figures 3.4. Illustration and schematic of the internal crystallisation method (ICM) for fibre growth**

### 3.1.5 Laser heated pedestal growth (LHPG)

This technique [3.28, 3.29] is a variant of the float zone method in which no crucible/container is required. The melt sits suspended between the source rod and seed crystal, as shown in **Figure 3.5**. Heating is provided by laser radiation which is focused onto the top of the source rod, turning it into a hemispherical molten zone. An oriented seed crystal which will determine the crystallographic orientation of the grown fibre is then dipped into this molten zone to initiate growth and withdrawn at a constant rate,  $V_{\text{pull}}$ . Simultaneously, the source rod is fed into the molten zone at a rate,  $V_{\text{feed}}$ , which is, generally, slower than that of the seed crystal. Conservation of mass then results in a diameter reduction of the growing fibre, giving the characteristic shape of the molten zone as shown in **Figure 3.5**. It can also be seen that the laser focal spot and, consequently, the molten zone remain fixed during the fibre growth process.

With laser heating and the focusing optics used in LHPG, a very large variety of materials can be grown. Moreover, fibres with any desired diameters, in general, have also been demonstrated, the smallest reported crystal fibre being 3  $\mu\text{m}$  in diameter [3.30]. The starting materials required in the LHPG method are small and fibres can be pulled at rates up to 3 mm/min or more. A wide range of materials have been grown, including refractory oxides, fluorides, high melting point metals and semiconductors, high temperature superconducting ceramics, garnets and niobates. A list of all the materials which have been grown by this method to date can be seen in **Appendix A**. The LHPG is the crystal growth method selected in this work and, hence, will be further discussed in the next section.

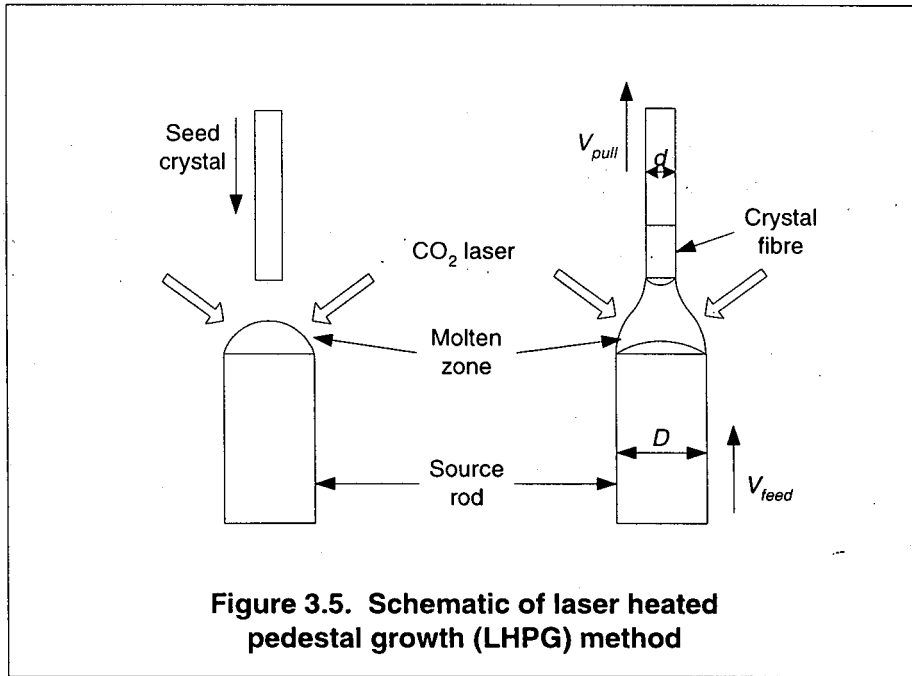


**Figure 3.5. Schematic of laser heated pedestal growth (LHPG) method**

### 3.2 The laser heated pedestal growth technique

As is rather obvious from the growth techniques discussed earlier, with the exception of the LHPG, the other methods all require a crucible to heat and contain the melt. The types of crystal fibres which can be grown are thus dependent on the crucible/melt compatibility. The LHPG method is one of the primary techniques for single crystal fibre growth which does not involve contact between the melt and a crucible. The molten zone is held in place in the laser focus by surface tension and it is very similar to the laser heated float zone technique (laser float zone is generally used for growing bulk crystals).

In LHPG, the primary laser beam is expanded and split into a hollow cylindrical tube of radiation with relatively uniform intensity distribution. This is possible with the aid of novel beam guiding optics which have been developed by researchers at Stanford University [3.28], who, upon recognising the huge potential available from single crystal fibres of various materials, undertook a research program to investigate and establish a versatile crystal fibre growth system which is now commonly known as laser heated pedestal growth (LHPG). From the optics, cylindrical beam is then reflected by a coated plane mirror oriented at an angle of  $45^\circ$  from the horizontal onto a parabolic mirror which finally focuses the beam tightly into a small spot to provide melting of the tip of a source rod. The spot size in this work has been estimated to be  $\sim 22.5 \mu\text{m}$ . This approach thus reduces or eliminates any contamination which might be transferred from a crucible into the grown fibre (although some contamination may occur via impurities attached to or in the source material) together with the added advantage of symmetric heating of the molten zone. Hence, high purity optical crystal fibres can be grown. A schematic of the LHPG optics is shown in **Figure 3.6**.

Several attractive features are associated with crystal fibre fabrication by LHPG. Laser heating provides a clean source of radiation and the maximum temperature that can be attained (when very high melting point materials are grown) depends, in practice, on the available power from the laser employed. This suggests that very large temperature gradients are possible at the solid/liquid interface [3.29], which, in turn, allow crystal fibres to be grown at relatively fast rates in comparison with other

crystal growth methods and with higher dopant levels. Typical growth rates are in the 1 mm/min region. Phomsakha *et al.* [3.31] have reportedly grown high quality sapphire SCFs at ~20 mm/min by modifying the beam shaping optics and growing under an inert gas-atmosphere while even higher growth rates up to ~40 mm/min are possible although at such high growth rates, supercooling will lead to significant internal scattering defects [3.30]. When investigating novel devices, speed is an important factor and a high turn-over rate is desired so that a wide range of different materials can be grown into SCFs for characterisation studies. In this work, growth rates of the order of 1 mm/min are used. Hence, for sensing fibres with lengths of 50 to 100 mm, typical times required to pull each fibre are from ~50 to 100 min. In this way, 4 to 5 fibres can be grown per day.

For material development, it is highly desirable that only small amounts of starting materials be used before a programme of bulk crystal growth is initiated. This is an important consideration when expensive materials, such as scandium compounds, are being studied. The source materials used in LHPG, normally in the form of square or round rods, are typically in relatively small quantities (compared to other crystal growth techniques) hence, excessive costs can be avoided. Moreover, to be compatible with current glass fibre technology, single-crystal fibres can be grown with diameters in the range of 130  $\mu\text{m}$  or smaller. It should be noted that the choice of fibre diameter is arbitrary, however, and it is dependent on the application requirement(s). Besides the very high crystalline perfection which can be achieved, internal crystal defects (such as grain boundaries, dislocations and multiple domains, etc.) can also be minimised [3.2, 3.4]. With the small diameter of the growing fibre, defects which are not aligned exactly along the fibre axis will quickly grow out of the crystal. Likewise any defects present during the initial seeding stage. The relationship between defect densities present in a growing crystal, the growth parameters such as temperature gradients, thermal expansion coefficient, and the crystal diameter has been studied by Tsvinskiy [3.32] and Inoue and Komatsu [3.33] who found that very low defect densities can be achieved as the crystal diameter is reduced dramatically. Hence, good quality optical single crystal fibres can be expected with the LHPG method.

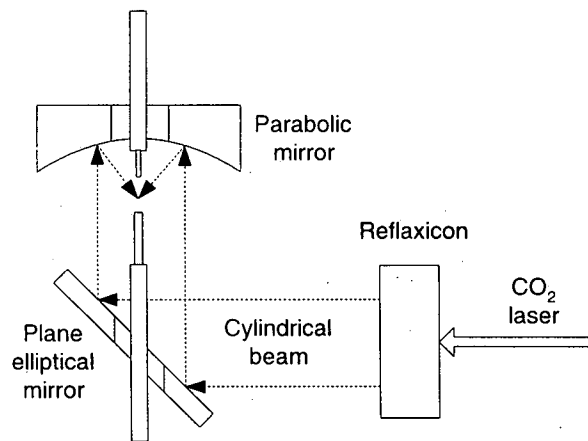


**Figure 3.6. Manipulation of laser beam**

An additional advantage of this growth technique is the possibility of growing a very wide range of materials. By establishing LHPG, Feigelson and fellow researchers at Stanford University [3.4] were able to quickly demonstrate the versatility of this technique by growing a wide range of materials, from congruently and incongruently melting crystals to oxides, fluorides, eutectics, semiconductors and metals. The range of materials which can be grown by LHPG has rapidly increased and **Appendix A** lists all the SCFs which have been grown to date. Various methods can also be employed in the preparation of source materials for growth into crystal fibres [3.2, 3.34], further enhancing the versatility of this technique. For device applications, source materials in the form of square or round rods, cut from bulk or poly-crystals, present the most convenient way of crystal growth. Source rods can also be prepared from a stoichiometric mixture of constituent powders which can be hot or cold-pressed and sintered, and then cut into the desired dimensions. With this simple technique, one potential problem lies in the ability in achieving source rods of sufficient density, which, during fibre growth may result in voids or bubble formation. Incorporation of dopant materials can be through the above technique or a simpler way can be employed in which a coating of dopant(s) is coated onto the surface of the source rod. This can be achieved by vapour deposition of the required dopant(s) onto the rod surface, painting a slurry of dopant powder onto it or by dip-coating the rod into a dopant-liquid suspension. The latter methods do not allow good control of the dopant concentration levels in the as-grown fibre, which is required when producing laser or non-linear optical devices. Dip-coating has been used in this work for the growth of sensing fibres where control of the impurity levels is not as critical.

The problems associated with LHPG must also be considered, the most significant being the ability to maintain a constant uniformity of the fibre diameter which can be considered as the most important effect leading to severe scattering losses [3.28, 3.30, 3.35, 3.36, 3.37]. Sources of diameter fluctuations can be attributed to laser source instability, vibration and friction introduced by both the pull and feed systems, convective cooling currents in the surroundings, vibration introduced by the laser cooling system and any other externally-induced perturbations. In LHPG, a stable molten zone, and hence, melt shape, is required for the growth of crystal fibres with uniform diameters [3.29].

The available laser power will ultimately determine the maximum temperature limit of the molten zone, which will, in turn, determine the type of materials that can be grown. The emission wavelength of the laser employed can also play an important role when growing different materials which efficiently absorb laser radiation in certain wavelength regions. The CO<sub>2</sub> laser selected as the heat source in this work limits growth to materials which absorb strongly at ~10.6 μm. These include most refractory oxides, some fluorides, certain eutectics, semiconductors, superconductors and metals [3.4]. Another disadvantage of the LHPG technique is that materials with very high vapour pressures cannot be easily grown due to preferential evaporation of one or more of the constituents [3.34]. This has been observed during the growth of Ni and Zr-doped Gd<sub>3</sub>Ga<sub>5</sub>O<sub>12</sub> (GGG) garnets in which Ga loss occurred even under reactive atmospheric conditions [3.38] but has been overcome by using excessive Ga contents in the source rod constituents [3.39]. Single-crystal LiTaO<sub>3</sub> fibres have also been observed to exhibit this characteristic where the Li<sub>2</sub>O compound evaporated during crystal growth [3.40], which could also be linked to the high melting point of the source material.

### **3.3 Laser heated pedestal growth system and design considerations**

The LHPG system used in this work is based largely on that established at Stanford University [3.28]. Besides the major considerations which have to be given to the growth system in order to ensure minimal variation in the crystal fibre diameter, it is also important that the system be straightforward and easy to use, where source material/rod preparation time can be minimised so that approximately 4 to 5 fibres can be grown in a day. The relatively high growth rates (~1 mm/min region) used permit this aim to be achieved easily. In relation to this, it is important that for stable growth of a crystal fibre, the growth process, principally the molten zone shape and the alignment of the source rod and growing fibre, must be allowed to be observable whereupon, any corrective actions may be taken should any of these parameters require adjustment.

A viewing system, shown in **Figure 3.7**, comprising conventional optics which allows the growing fibre and, more importantly, the molten zone to be observed from

orthogonal directions has been constructed. To be able to record the melt and growth process for later studies, one of the views can be split and sent to a video camera. The alignment of the source rod and seed fibre, and the positioning of these two into the fixed laser focus at the initial seeding stage are also facilitated by the viewing system. A visible He-Ne laser aligned co-linearly with the invisible CO<sub>2</sub> laser allows the fixed focal point of the parabolic mirror to be determined easily during the initial positioning/seeding stage.

Software control of the growth system has been developed rather than hardware control in order to allow easy integration and manipulation of the various components and growth parameters during fibre growth. These growth parameters would include, principally, the source rod feed rate, fibre pull rate, and stability of laser power which will lead to a stable molten zone and relatively constant melt shape. Consequently, the feed and pull motors, and the laser power have to be carefully monitored and controlled. Besides providing integration of the parameters mentioned, computer control also permits rapid future modification should a need arise to include additional components. Moreover, it is also quicker to implement. To fulfil this goal, where many independent parameters are involved, a PC operating under Microsoft Windows NT was chosen. The controlling program for the LHPG system has been written in Delphi (version III), an object-oriented software development package and was designed to be as user friendly as possible. The control programme has been included as **Appendix B**. Three of the most important features are the pull rate, feed rate and diameter reduction ratio settings. A certain level of flexibility has been built into the program to allow the user to maintain one of these parameters constant while changing another. The computer then calculates the third parameter. The laser power, another critical factor, has recently been integrated into computer control; it can easily be set and monitored from the program. Positioning of both the source rod and seed fibre vertically ( $z$ -axis) and horizontally ( $x$ - and  $y$ -axes) to enable alignment with the fixed laser focus is also computer-controlled. The ability to induce controlled diameter variation, in the form of tapers, during fibre growth has been considered an attractive option since an increased sensitivity, advantageous in fibre optic sensing, can be obtained in the tapered region [3.41], tapers are also potential insertion components for high power fibre-to-fibre and/or laser-to-fibre couplings [3.42] and can also offer a higher

reflectance at its tapered end in multimode crystal fibres as compared to conventionally polished fibres without tapers. End and in-line step tapers can be fabricated by keying-in the desired taper length and percentage diameter reduction while sinusoidal variations, which can result in either a Bragg reflector or long-period grating, were considered easier to fabricate by modulating the laser power. **Figures 3.8** show some examples of tapers incorporated in crystal fibres.

Open-loop growth, without the integration of a diameter monitoring system, does not, in general, allow fibres to be produced with very high diameter tolerances but with high quality and precision drive motors the fibre diameter variation can be reduced to a certain level. It should be noted that closed-loop control of both the pull and feed motors as well as the laser power has been employed in the growth system. Variations of diameter in the region of 1 – 2 % have been achieved in sapphire fibres and although not sufficiently tight enough for nonlinear and optical interaction applications, they are considered sufficient for sensing applications. Fejer *et al.* [3.28] have shown that active diameter monitoring and control during crystal growth are important contributions to the obtaining of fibres with constant diameter. A closed-loop diameter measurement system has been constructed by Fejer and colleagues at Stanford University [3.43] based on tracking the forward-scattered fringe and has been employed during the production of single crystal sapphire fibres by LHPG where diameter variation was reportedly better than 0.5 % [3.44].

For the duration of this work, diameter monitoring schemes have been investigated based on two approaches. In the first approach, the principle of Fraunhofer diffraction was used, in which the forward-scattered light was tracked [3.45]. Light from a laser is scattered when it is obstructed in its path by a small object, in this case, a fibre. This results in an array of interference maxima and minima being produced together with a central bright spot when the diffraction pattern is projected onto a screen some distance away from the scattering fibre. This pattern is passed through a slit with fixed width and the spot from the second maxima projected onto a position sensitive detector (PSD). The second maxima was tracked since the position of the central bright fringe will not change with respect to changes in fibre diameter. Hence, any change in the fibre diameter will result in a change in the position of the spot due to the second maxima along the length of the PSD, determined by the

voltage output from the detector. This is a simple and effective technique which could be easily incorporated into the main LHPG control program but it has one serious drawback. The PSD allows only one fringe of light to be incident upon it, otherwise errors would be incurred with multiple spots. Hence, a fixed slit width was used which allowed only one single fringe to be transmitted. As the fibre diameter increases or decreases, the fringe pattern will contract or expand, respectively. The second maxima is then observed to move and its position can be used as a measure of the fibre diameter. A major problem then arises when the fringe pattern is too closely spaced together or spread too wide, in which case, either two or more fringes are incident on the PSD or the tracked fringe has moved beyond the slit and no light falls onto the PSD. **Figures 3.9** illustrate the basic principle of this technique as well as the problem encountered.

Another diameter measurement system was pursued concurrently [3.46, 3.47, 3.48]. This technique is shown in **Figure 3.10**. Its advantage lies in the simplicity of design and makes use of commercially (and widely) available optics, hence, cost is not a major deterrent. The relatively simple design relies on the "4f" principle in which the resulting radiation/shadow is scanned across a photodetector. Monochromatic light (from a 2 mW HeNe laser) is expanded and collimated onto a mirror attached to a scanning galvanometer which sweeps the beam through an arc. The scanning beam is focused at the focal plane of the first lens (focal length ~200 mm) onto the fibre. In the presence of a fibre, this beam is blocked and no light will be transmitted, thus a "shadow" results. The minimum spot size which is focused onto the fibre is estimated to be ~8  $\mu\text{m}$  and is sufficiently small for monitoring the diameters of fibres to be grown in this application. A second lens, with similar focal length to the first lens, then collects the image in the form of a shadow and collimates it onto a large area detector. Two inexpensive photodetectors, placed in between the two lenses, are used to activate the start-stop counters on an electronic board. This board has been built to provide the following features. As the scanning beam sweeps across the start detector (1), a start counter is activated and a 1 MHz quartz oscillator starts counting the time it takes for one complete sweep, i.e., until the beam reaches the second detector (2), in which the counting process is terminated. This is known as the scan time. Almost simultaneously, after triggering the start counter, the scanning beam would have reached the first edge of the fibre placed in the lens' focal plane, the time

it takes being dependent on the galvanometer sweep frequency. A shadow is then cast onto the "shadow count" photodetector, at which point another counter is activated and starts counting the length of time the scanning beam takes to sweep across the fibre diameter (also known as the shadow count). At the second edge (the exit edge) of the fibre, laser light is re-cast onto the shadow photodetector. The shadow count is terminated at this point. The counting of the scan time, however, ceases only when the scanning beam strikes the second (or stop) detector. The clock pulses from the two sets of counters are then ready to be transferred to a computer to be processed. With the use of a 1 MHz oscillator, each clock pulse corresponds to 1  $\mu$ s, a reasonably high resolution. **Figure 3.11a** illustrates the pulse counting principle while **Figure 3.11b** shows the breakdown of the various counting processes involved. One inconvenience of this method is the requirement of an already known calibrated fibre/wire diameter for an initial calibration.

**Figures 3.12a** and **3.12b** show the oscilloscope traces using this system for two different fibre diameters (250 and 130  $\mu$ m respectively). The smallest diameter which can be detected with this system is  $\sim$ 25  $\mu$ m, near the minimum spot size of the focused beam, where large errors were incurred. For a test fibre of 120  $\mu$ m, a system resolution of  $\sim$ 5  $\mu$ m has been obtained although for larger diameters, better resolution can be achieved. Also, for an out-of-focus tolerance of  $\sim$  $\pm$ 10  $\mu$ m, implying that the fibre has moved out of the beam focus, an accuracy of  $\sim$ 95 % can still be obtained from the system.

The diameter measurement system using forward light scattering, in which the second or arbitrary maxima was monitored/tracked has proven rather difficult to implement as well as time consuming. Further, ambiguities arising when fibres with large diameters are to be monitored reduce system reliability. The second diameter monitoring system is a more attractive option, being cheaper and less complicated, in principle, to implement. This system is currently under development and it is hoped to be incorporated into the main LHPG program in the not-too-distant future. The integration of diameter monitoring will enable full closed-loop feedback control of the fibre diameter during growth and allow parameters such as feed rate, pull rate and laser power to be adjusted accordingly.

In view of the importance in having a stable melt zone to enable stable fibre growth and good dimensional tolerance, the following sub-sections will discuss the most significant growth parameters and their influences on the melt stability during fibre growth. An overview schematic of the LHPG station is illustrated in **Figure 3.13**.

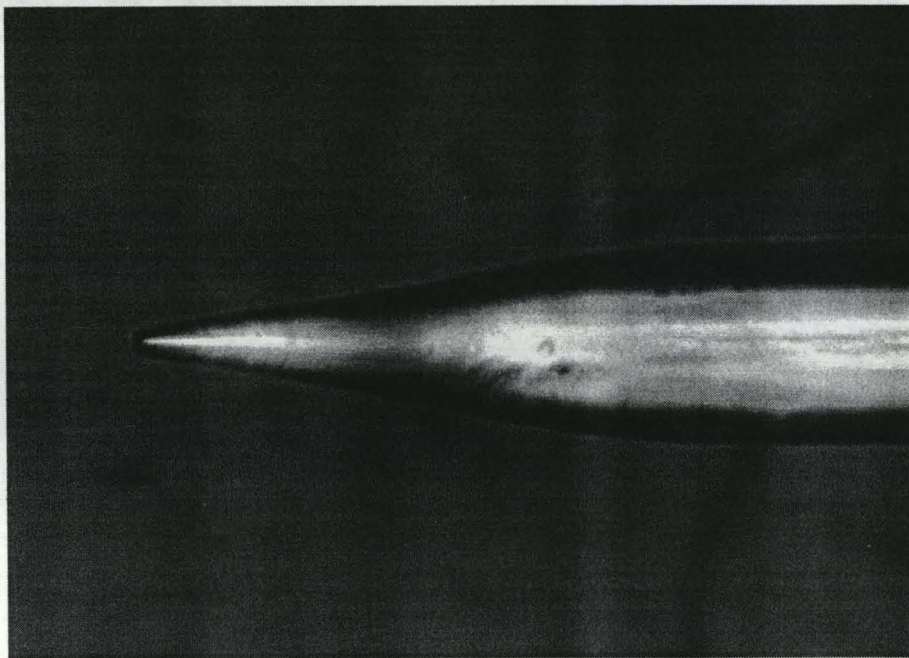
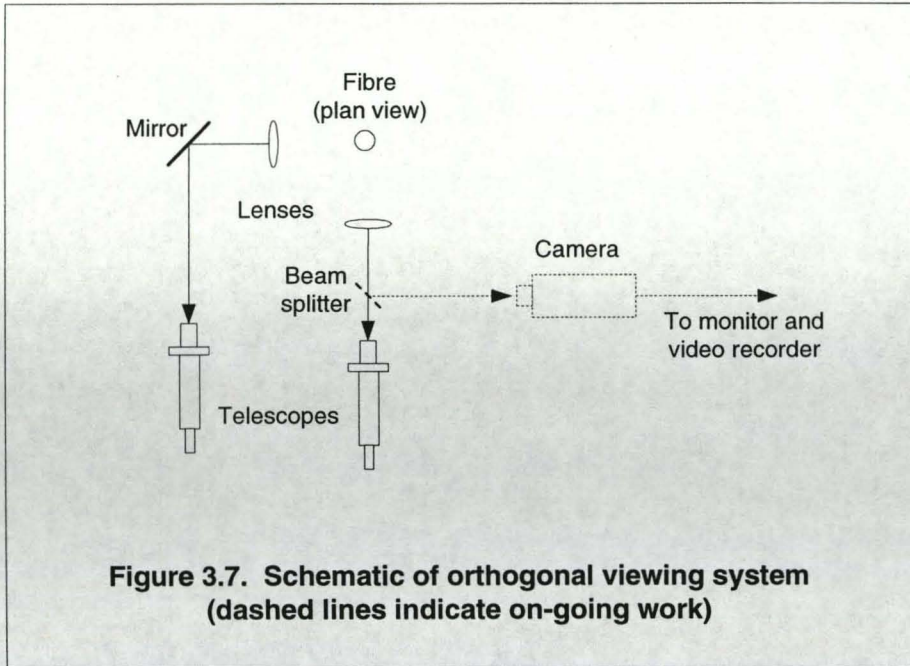
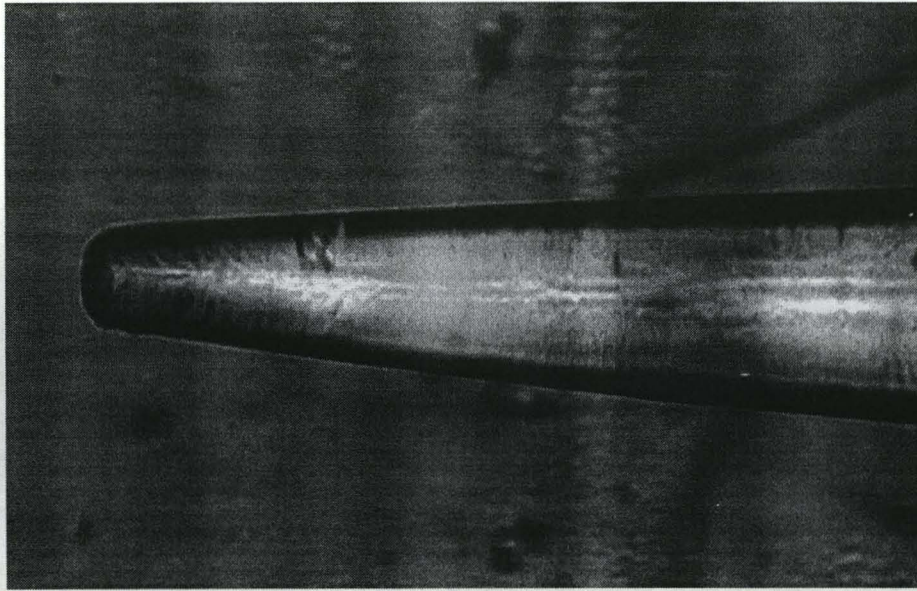
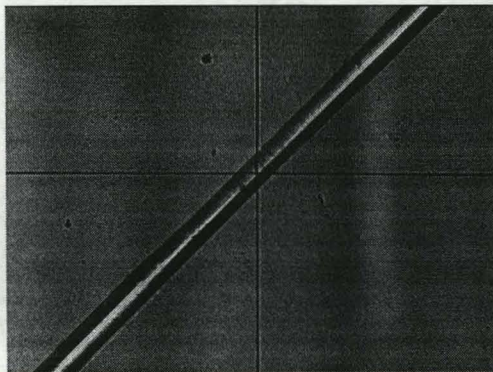


Figure 3.8a. End taper grown from 170  $\mu\text{m}$  sapphire fibre



**Figure 3.8b. Magnified view of taper**



**Figure 3.8c. In-line taper taken  
with cross-polarisers**

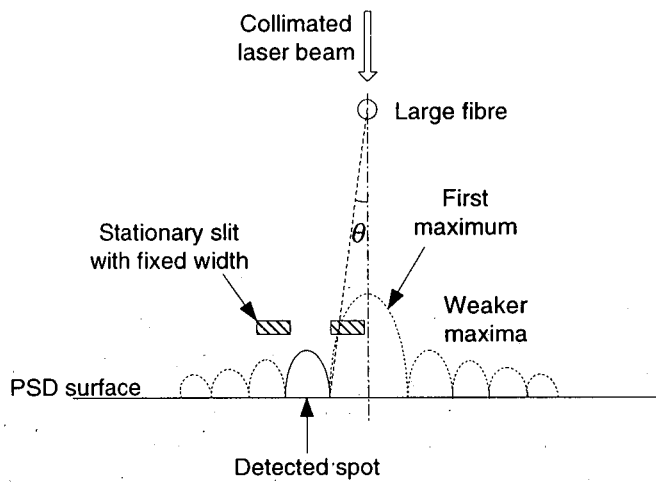


**Figure 3.9a. Forward light scattering by large diameter fibre (fringes close together)**

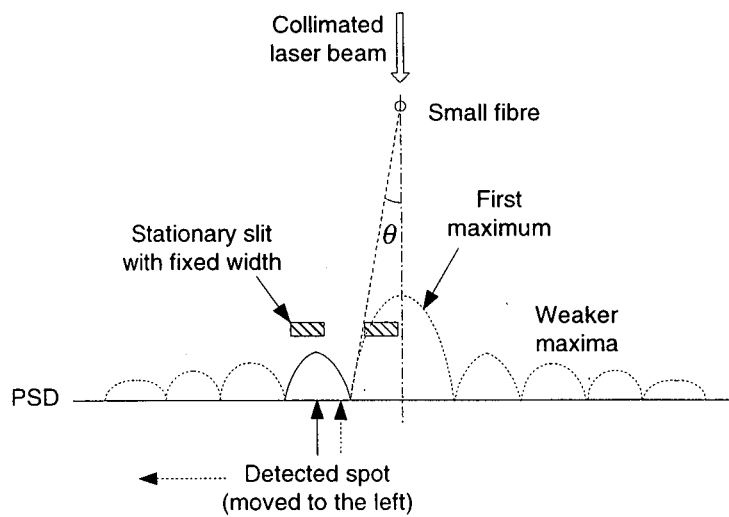


**Figure 3.9b. Forward light scattering by smaller diameter fibre (fringes apart)**

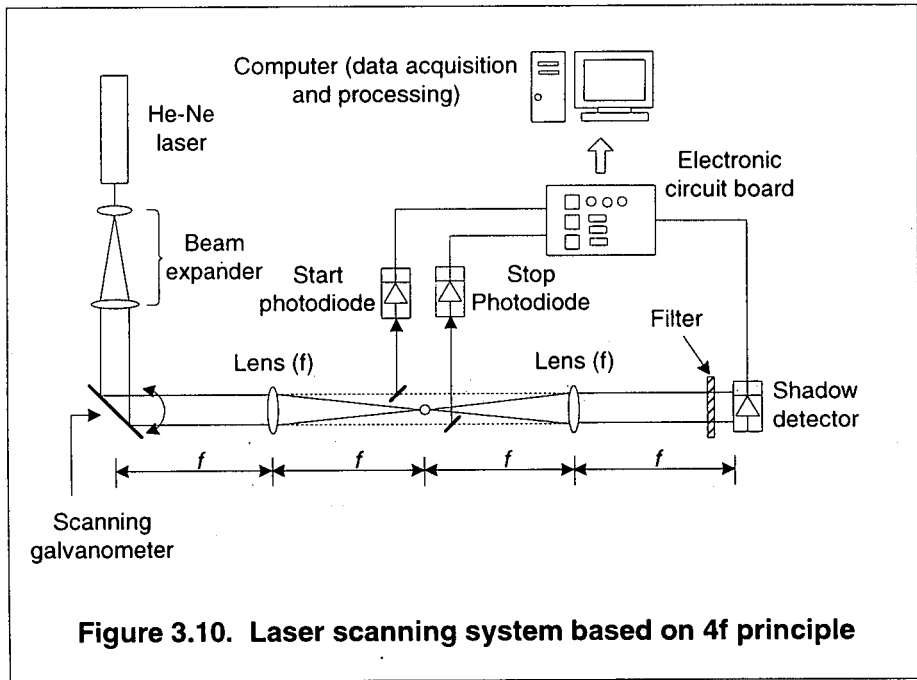


**Figure 3.10. Laser scanning system based on 4f principle**

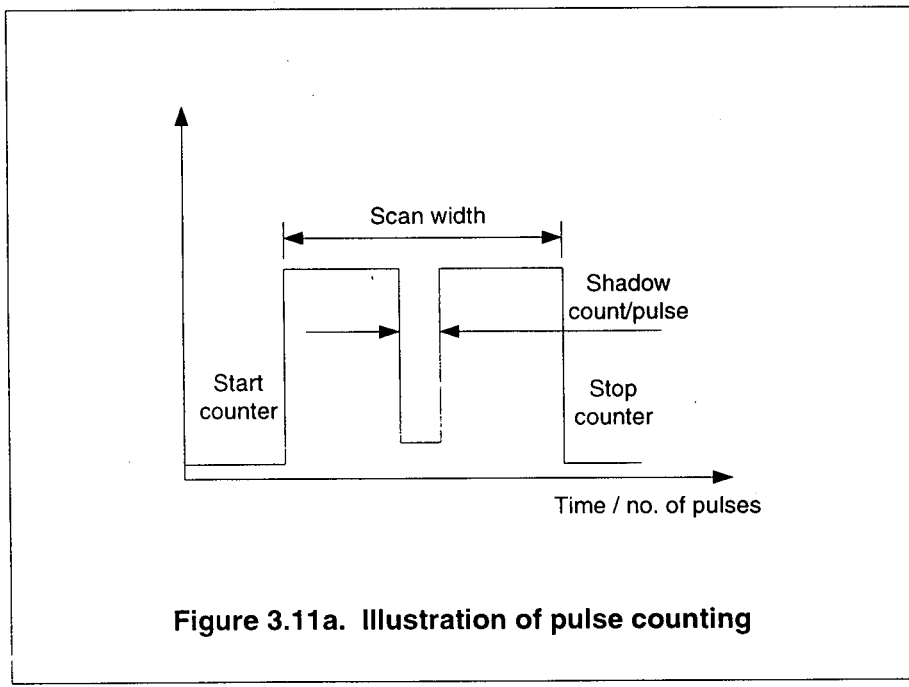


**Figure 3.11a. Illustration of pulse counting**

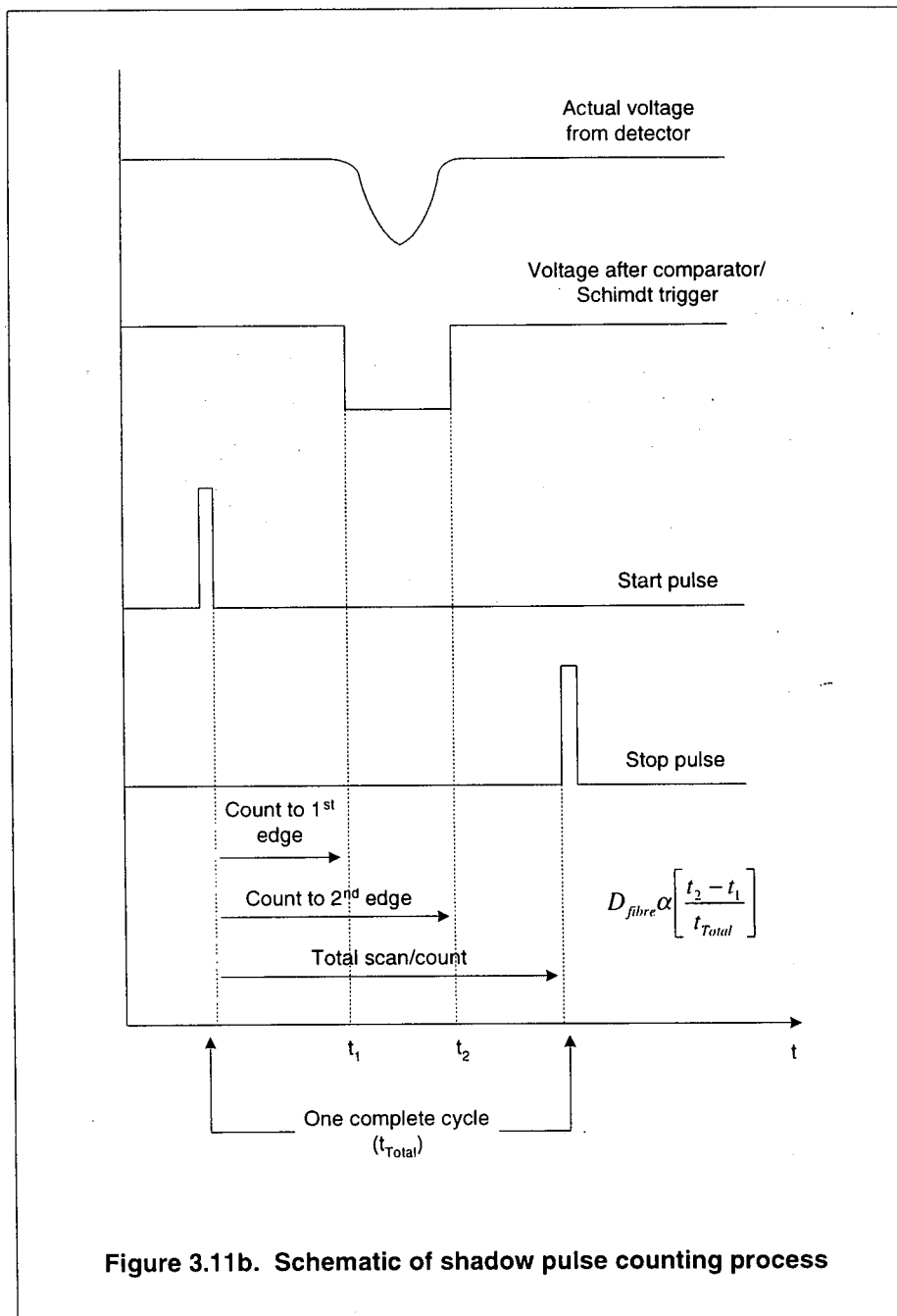


Figure 3.11b. Schematic of shadow pulse counting process

Figure 3.12a. Oscilloscope trace of a 250  $\mu\text{m}$  fibre

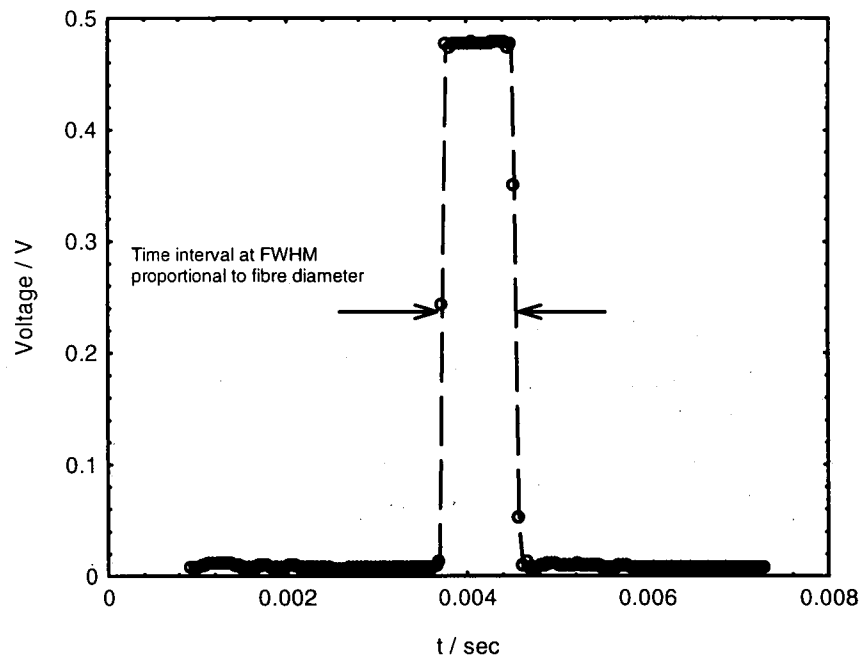
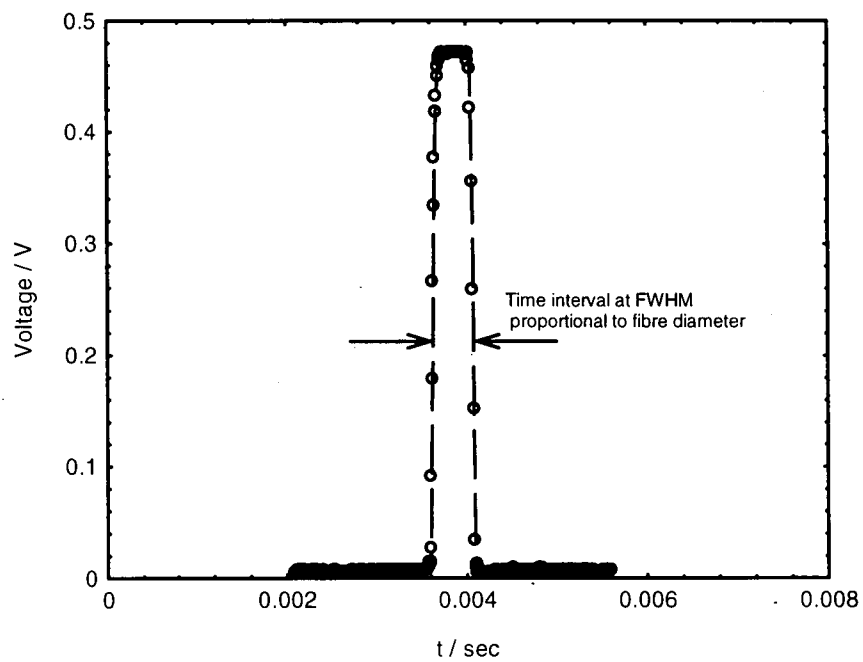


Figure 3.12b. Oscilloscope scan of 130  $\mu\text{m}$  fibre



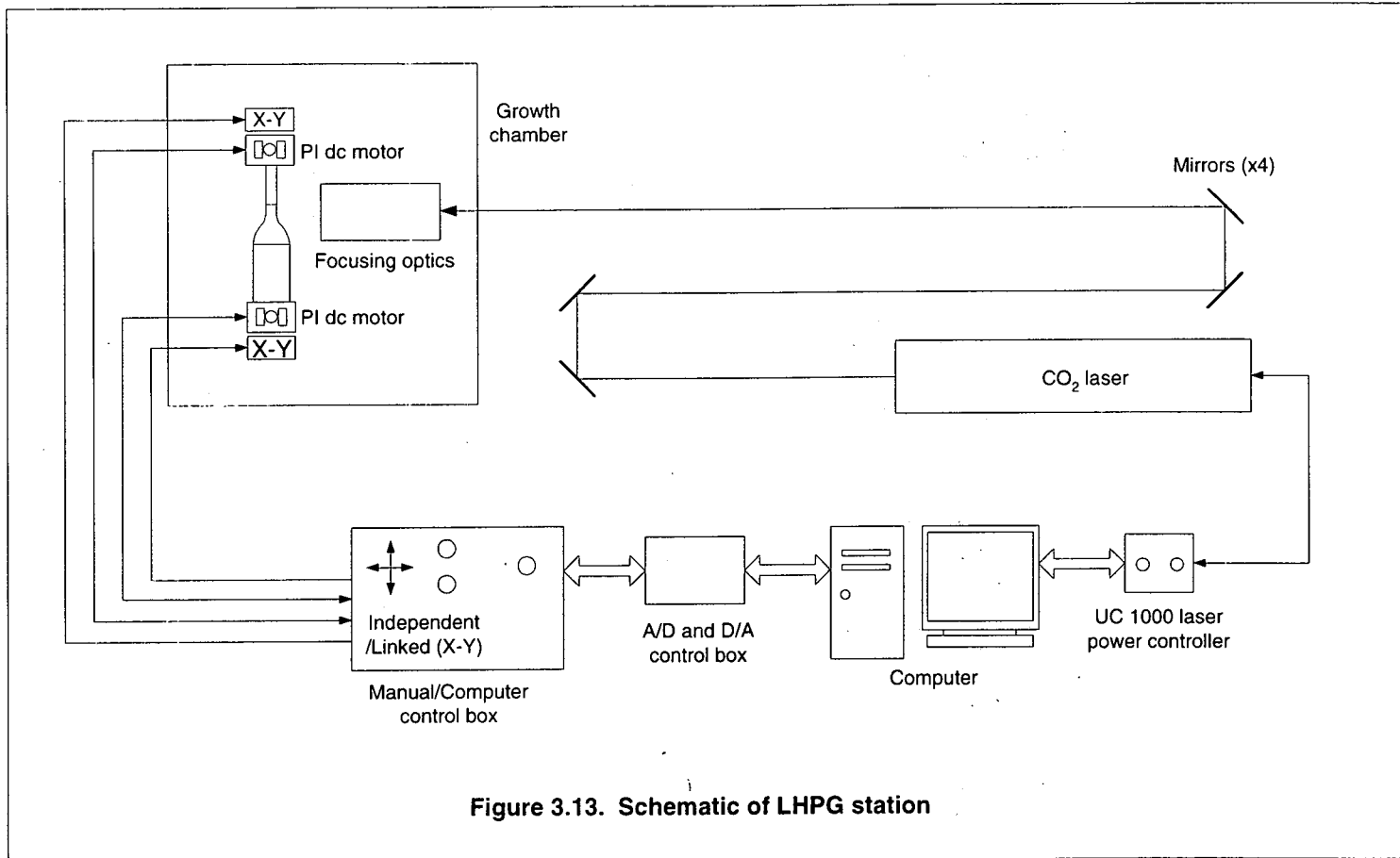


Figure 3.13. Schematic of LHPG station

### 3.3.1 Heat source

Source power fluctuation plays a major role in contributing to variations in diameter of the as-grown crystal fibre. These variations generally lead to high losses (normally through surface scattering effects), resulting in high transmission loss fibres. It has been reported [3.29] that the stability of the molten zone shape influences the temperature distributions during growth and this directly affects the diameter variations in a crystallising fibre due to external perturbations, hence, a melt height-to-fibre diameter ratio in the region of  $\sim 3$  (for sapphire fibre growth) has been proposed as an optimum condition for a stable molten zone to pull fibres with little variations along its diameter. This is directly related to the incident heating power from the laser and during fibre growth, it has been observed that the melt shape is highly dependent on the amount of heating power used. Hence, for ensuring a certain level of diameter uniformity in the crystal fibre throughout its entire length, the control of this heat source power variation is an important parameter and should be kept as constant as possible at the desired power setting.

The laser selected for this work is a *Synrad, Inc.* Series 48 CO<sub>2</sub> laser with a maximum output power rating of 28 W. It is a sealed-tube device and requires no external CO<sub>2</sub> gas supply, hence, it is free from jitter. RF excitation, at 45 MHz, is employed in the laser cavity to provide good discharge stability, output power control and modulation. High laser power stability is achieved with the aid of a *Synrad, Inc.* UC-1000 laser controller and is quoted at  $\pm 2\%$  in closed-loop operation. Approximately 8% of the output laser beam is sent to a thermopile detector, amplified and compared to the set power by the controller to main constant average power. This is the active laser power feedback unit. However, from cold-start, a power fluctuation of  $\sim 10\%$  is expected and a warm-up period of 20 to 30 min is used before fibre growth commences. **Figure 3.14a** shows the time evolution of the laser power level typically used during crystal growth. A step change in power output is also included to illustrate laser stability after warming-up is performed. The laser power with control voltage has also been examined for hysteresis effects; both the incremental and decremental changes in power are shown in **Figure 3.14b**. In order to facilitate computer control of the laser power, a duplicate of the UC-1000 controller was constructed with further modification to permit control from an

*Amplicon Liveline* PCI 726 D/A card installed in the computer. A 4 to 20 mA current input to the laser controller has been employed as a control signal, isolated from surrounding electrical interferences. The new controller allows the original closed-loop feedback power monitoring unit to operate since most of the electronic circuits have been retained. It also allows selection between manual and remote (computer) control of the various laser features. Computer control of the laser power has been considered advantageous since it renders the power profile/cycle more convenient to programming, particularly when deliberate variation of the laser power is used to produce grating structures, tapers and other novel fibre features.

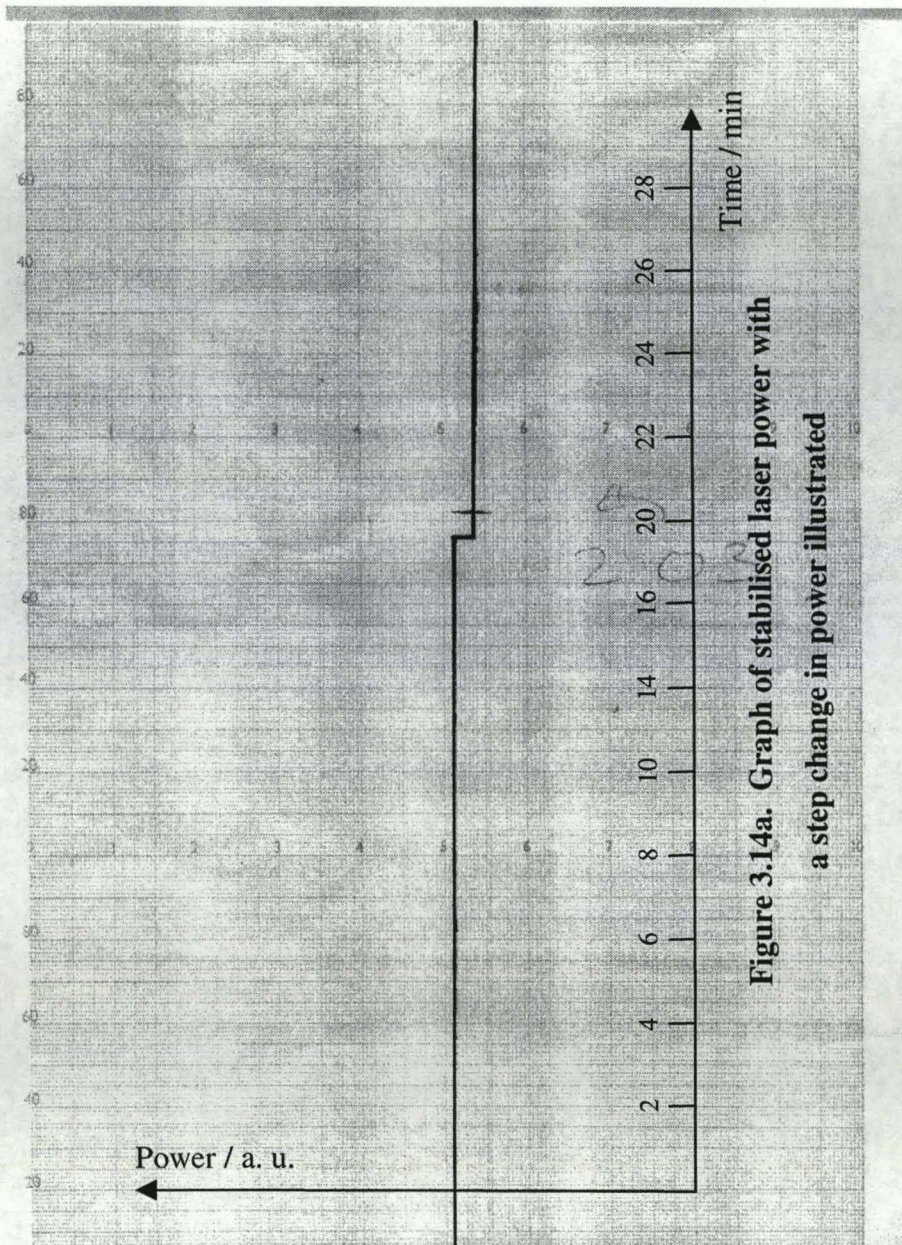
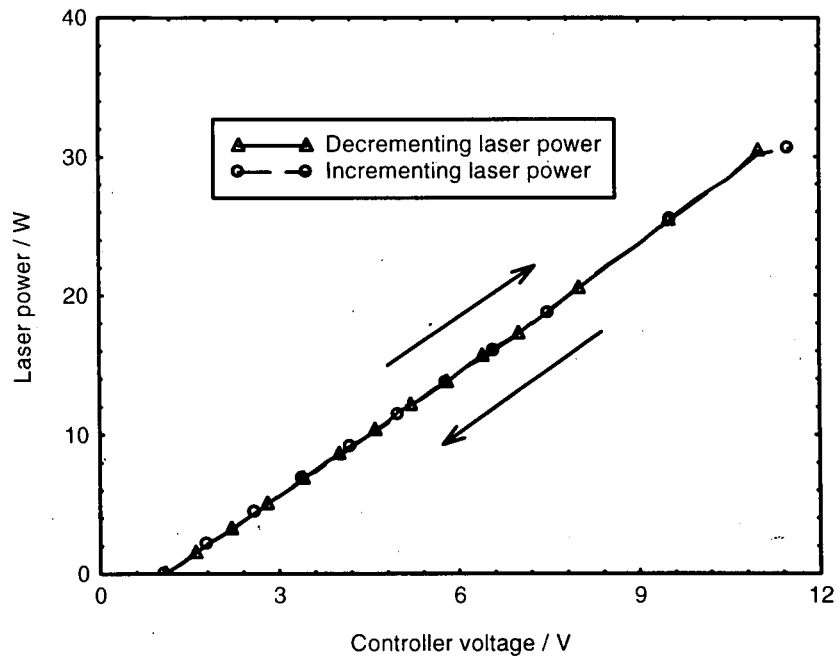


Figure 3.14a. Graph of stabilised laser power with a step change in power illustrated

Figure 3.14b. Monitoring hysteresis of laser output power



### 3.3.2 Fibre pull and source feed systems

Large variations in the pull rate during fibre growth will, obviously, result in variation being transmitted to the fibre diameter via an "unstable" molten zone. Given that crystalline materials generally have a much lower level of viscosity when molten in comparison to glass-based materials and are thus more susceptible to external perturbations, considerable efforts must be exercised in the choice and design of a drive motor for pull system. *Physik Instrumente* C136.10 series DC motors with attached integrated differential encoder drives have been selected as the drives for both the pull and feed systems. The rotary encoder drive has a resolution of 2000 pulses per revolution. The C136.10 motor unit is equipped with a backlash-free gearbox (reduction ratio of ~29.642) and is capable of a maximum speed of 3.3 revolution per second with a quoted resolution of 0.006 degrees per pulse. Thus one output spindle revolution is obtained by moving through ~59284 input encoder pulses. This results in an error of  $\sim\pm 1$  pulse, equivalent to a percentage error of  $\sim 3.4 \times 10^{-3} \%$ . The C136.10 motors are computer controlled via a high performance two-channel C842.2 DC motor controller card (also from *Physik Instrumente*) with onboard digital PID control. It is important to note that stepper motors have been considered as inappropriate since they would not be able to provide the smooth translation/motion required (for both the source rod and seed fibre).

It was decided to run the DC motor (pull system) at its mid-operating speed so that the percentage velocity error can be minimised. Although stable single crystal sapphire fibre growth by the LHPG is possible even at pull rates above 8 mm/min [3.49], those fibres have been grown under active diameter control. In this work, however, pull rates in the region of 1 mm/min have been chosen. This presents little difficulty in programming/configuring the C136.10 pull motor to operate at a rate close to its mid-range of ~90 000 pulses/s. The pull rates can, of course, be increased to 2 or 3 mm/min although care has to be taken in order not to exceed the maximum operating speed of the dc motor when running at mid-velocity ranges (maximum speed ~195600 pulses/s). A precision 80:1 reduction gearbox from *RS Components* has been selected to perform the task of reducing the output velocity of the dc motor into actual desired values. The output spindle from the motor was attached to this gearbox while the output spindle from the latter was, in turn, connected to a *Time &*

*Precision* model A1512K Unislide with a 1 mm pitch leadscrew and a total stroke of 266 mm.

The maximum length of fibre that can be pulled is limited to ~236 mm, which is also the useful range of the Unislide. For material property studies and fibre lasers, fibre lengths of a few centimetres should be sufficient while for sensing applications, longer fibres in the tens of centimetre range or longer are desirable, although not essential. Modification work is currently underway to enable extended growth of crystal fibres by the use of a belt drive system. The main advantage of this system is that the length of crystal fibres which can be grown is only limited by the length of the source material. "Unlimited" growth can be easily achieved by changing the velocity mode profile from the present one used to one with a continuous profile (*Velocity* mode) simply through the controlling program. With velocity mode profiling, the original travel limit of the C136.10 (at  $\pm 1,073,741,823$  pulses) may be overcome together with the possibility of being able to change the subsequent velocity "on-the-fly" to induce desired fibre characteristics such as tapers and surface relief features. This is possible because the controller card is double-buffered, allowing simultaneous motor controlling commands to be stored while the present command is being performed. Operating in this mode also ensures the "smoothness" or continuity of the motor motion over the travel limit imposed by other velocity mode profiles.

In tests carried out on the movement of the Unislide, a minor reduction of the desired pull velocity has been observed using a frequency counter (*5001 Universal Counter-Timer* from *RS Components*). This occurred towards the two extreme edges of the slide range (~5 mm from each edge) and is attributed to the friction generated by the carriage or slider towards the two ends. This problem has been overcome by using only 220 mm of the useful range so that the carriage is ~8 mm from each edge of the Unislide. In doing so the maximum length of fibre which can be grown is limited to ~220 mm. However, the linear translation velocity of the slider, converted from the monitored encoder pulses of the encoder drive, was found to vary by less than 1 %. Due to feedback control of the C136.10 unit, the encoder drive and, hence, the DC motor, is sensitive to friction and other mechanical loading disturbance to the

translation of the slide. A photograph of the fibre pulling stage is shown in **Figure 3.15a**.

To hold the seed crystal/fibre, a miniature pin chuck with four retaining was used as shown in **Figure 3.15b**. It was aligned co-linearly with and screwed onto one end of a solid brass rod. By tightening the chuck jaws, a seed fibre can thus be securely held in place and in a true vertical to the longitudinal axis of the rod. This can then be translated vertically along the Unislide for the seeding stage to occur before initiating the crystal fibre growth. To align the seed fibre relative to the fixed laser focus the entire pull stage has been mounted onto a pair of cross-stacked side-driven linear positioners which provides  $x$ - $y$  translation.

An identical high precision dc motor (*Physik Instrumente* C136.10 model) was also selected as the feed motor for translating the source rod into the laser focus to maintain a constant melt zone. The motor rotation has to be translated into a linear movement at a rate governed by the desired source-to-fibre diameter reduction ratio, which owing to mass conservation, is given as

$$\frac{V_{pull}}{V_{feed}} = \left(\frac{D}{d}\right)^2 \quad (3.1)$$

where  $V_{pull}$  is the fibre pull rate (in mm/min),  $V_{feed}$  the source rod feed rate (also in mm/min),  $D$  the diameter of the source rod and  $d$  the desired fibre diameter. Hence, depending on the diameter reduction ( $D/d$ ) required, either the pull or feed rate can be specified by the user while the control software calculates the other, or vice-versa. An optimum reduction ratio in the region of 3 has been recommended [3.28] as values larger than this may result in growth instability and larger diameter fluctuation while smaller values may require more steps/regrowths to reach the desired fibre diameter.

Using the ratio given above, the feed rate is reduced by a factor of 9 relative to that of the pull motor. A precision gearhead with a 320:1 reduction ratio was selected to couple the feed C136.10 unit and the another Unislide from *Time & Precision*. In

this way, the DC motor can be run approximately at its mid-operating speed without compromising too much in terms of velocity errors. The A1506V model Unislide has an effective stroke of 114 mm and a leadscrew with a pitch of 0.5 mm. To avoid the problem associated with friction generated by the carriage/slider, a useful range of ~70 mm was used, which would also limit the source rod to approximately this length. This has no serious consequence at the moment since the length of fibre grown is also directly proportional to the square of the diameter reduction ratio, and using a ratio of 3, the source rod should only be approximately 25 mm for a required fibre length of 220 mm.

A miniature pin chuck, identical to that used for the pull system, was used to hold the source rod in a stable grip. The chuck was attached to one end of a stainless steel shafting rod and aligned co-linearly. The shafting rod was in turn attached to the carriage/slider of the Unislide with smooth vertical movement afforded by two accurately machined guide holes at both ends of the slide. Two cross-stacked, side-driven linear positioners, onto which the motor, gearhead, slide and associated gearing components were mounted, provided *x-y* translation capability for alignment requirements. The whole assembly is shown in **Figure 3.16a** while the stability of the feed and pull motors is illustrated in **Figure 3.16b**.

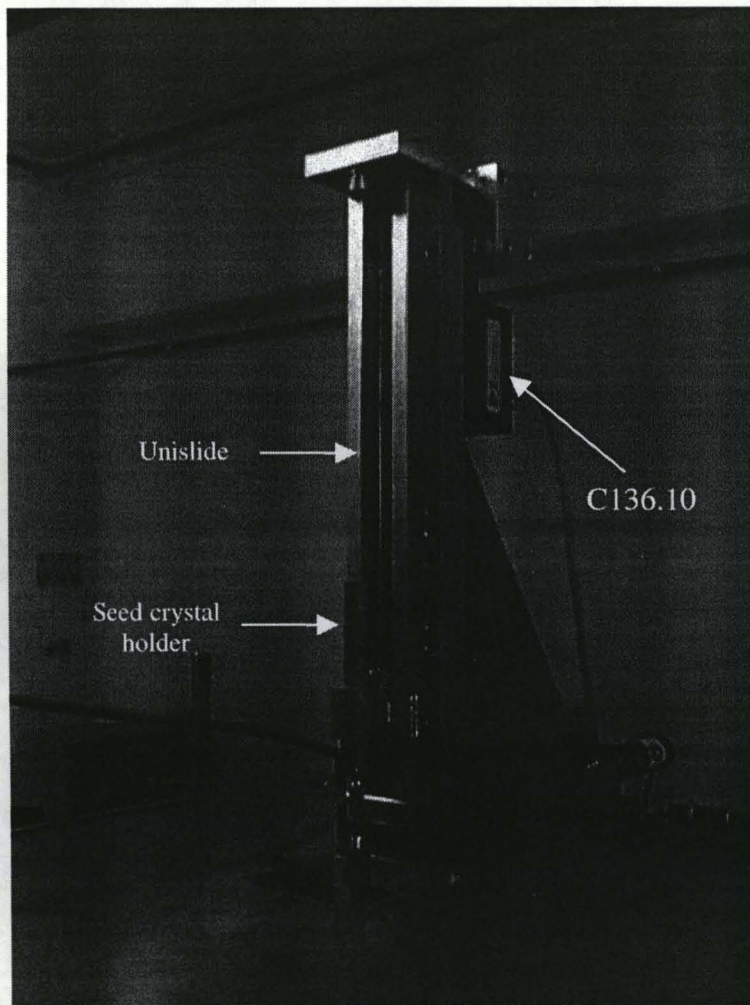


**Figure 3.15a. Photograph of pull stage**

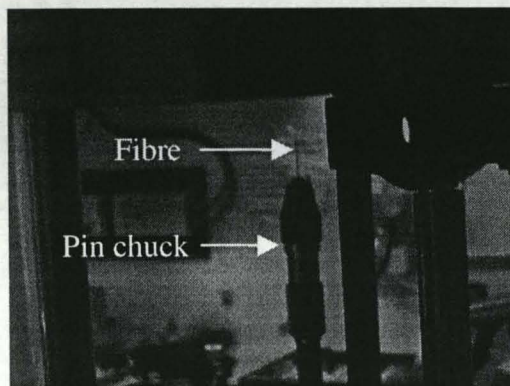


**Figure 3.15b. Photograph showing pin chuck securely holding fibre**

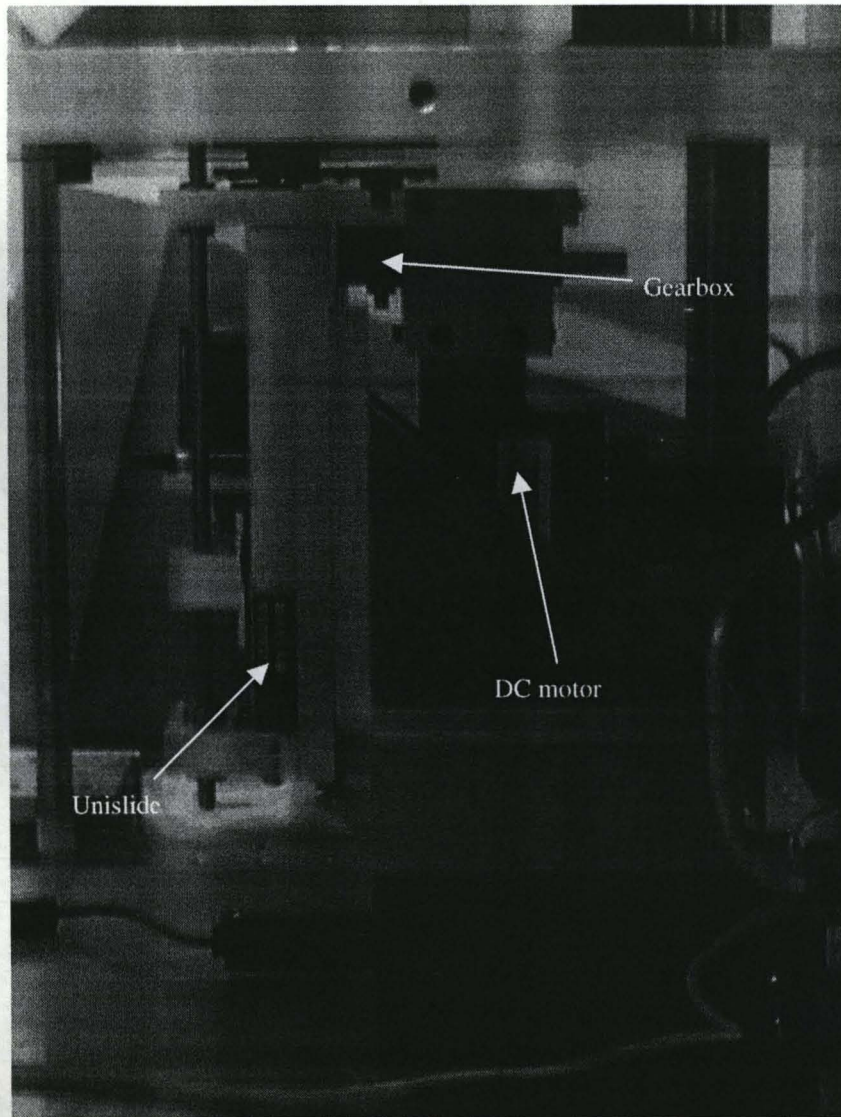
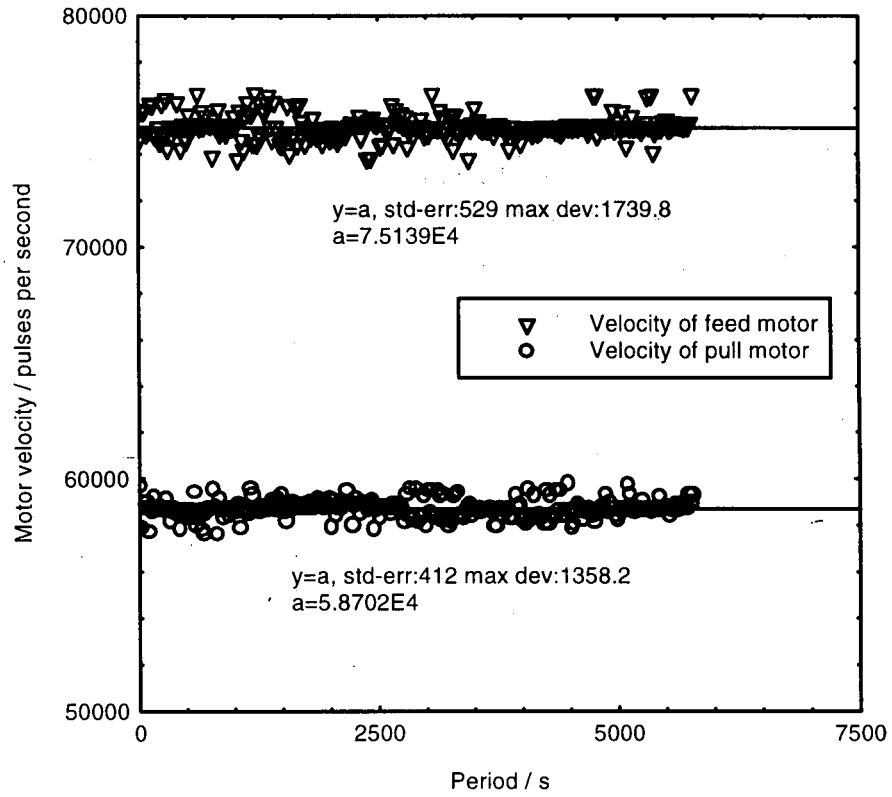


**Figure 3.16a. Photograph of feed system**

Figure 3.16b. Variation in feed and pull velocities at growth rate of 0.75 mm/min



### 3.3.3 Laser beam focusing optics

As has been discussed earlier, symmetrical heating is one of the most critical factors in enabling good crystal growth since it gives rise to a stable molten zone and shape. Hence, a way of ensuring this must be implemented with the CO<sub>2</sub> laser heat source. The output beam from the laser is expanded by allowing it to travel a certain distance depending on the beam divergence of the laser. A set of four gold-coated mirrors was used to deflect and direct the laser beam through a ZnSe window into a reflexicon. Designed by Fejer and colleagues at Stanford University [3.28, 3.29], this novel beam-manipulating element consists of two gold-coated cones, one positioned inside the other as shown in **Figure 3.17a**. The inner cone deflects incoming laser radiation symmetrically onto the outer cone which, in turn, reflects the beam into a ring of cylindrical output radiation. The output from the reflexicon may be approximated as a "hollow" Gaussian beam with a ring of equal intensity distribution [3.29]. A burn mark of the CO<sub>2</sub> laser from this element is shown in **Figure 3.17b**, the "shadows" in the burn mark due to the support structures of the inner cone, while a photograph of the reflexicon can be found in **Figure 3.17c**. A plane elliptical mirror (gold-coated) reflects this radiation onto a parabolic mirror which then focuses the rays into a tight axially symmetric spot size more than sufficiently small (~22.5 μm) to melt a source rod the size of ~130 μm. The use of the reflexicon can thus ensure axi-symmetric heating of the source rod with very few or no hot spots occurring in the molten zone. Indeed, the smallest diameter fibres grown to date using this system have been 80 μm sapphire and ruby fibres.

To aid in the adjustment of both the source and seed into the fixed focus, a He-Ne laser has been co-linearly aligned with the CO<sub>2</sub> laser through a set of beam combiners/splitters to enable visual inspection of this process.

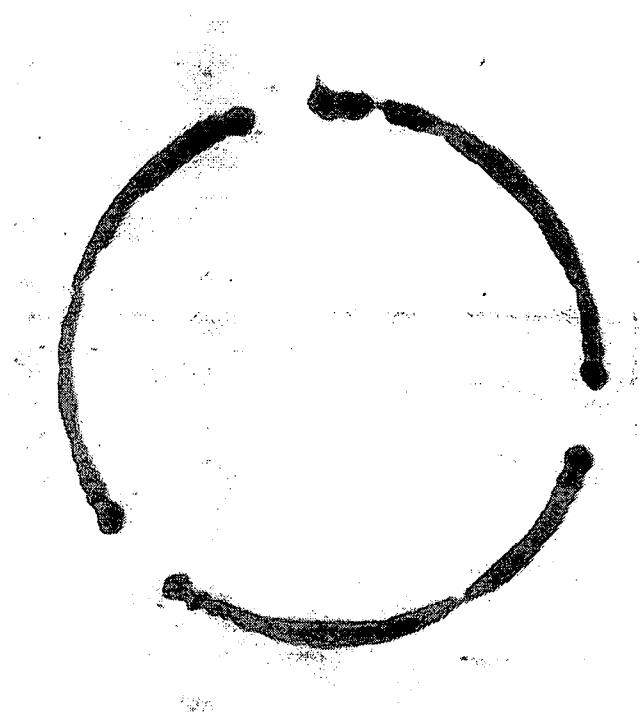
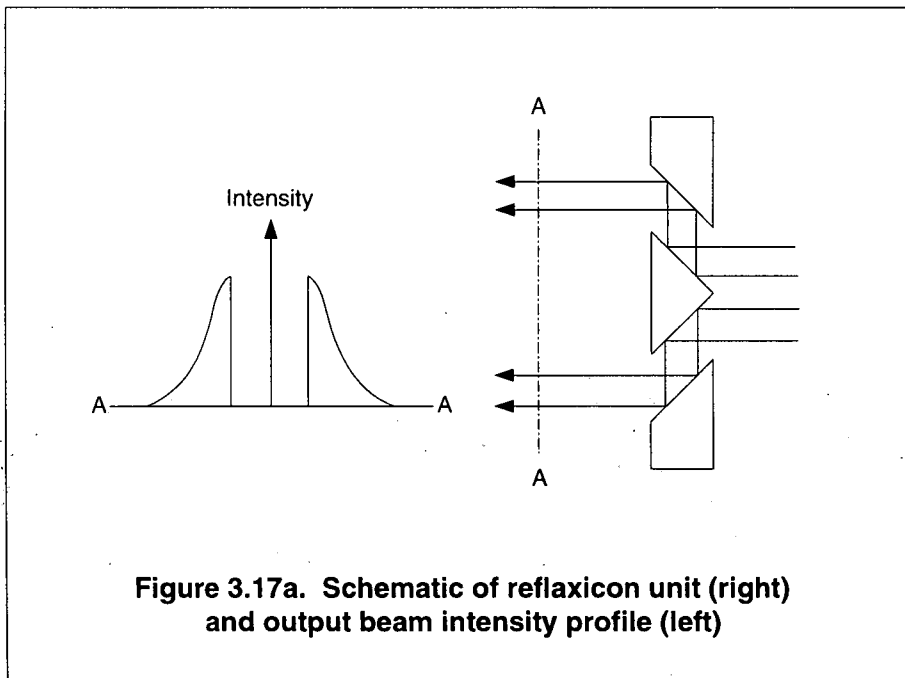


**Figure 3.17b. Burn mark from reflexicon**



**Figure 3.17c. Photograph of reflexicon unit**

### 3.3.4 Growth chamber

Crystal growth takes place inside an enclosed chamber which not only acts as a safeguard against stray CO<sub>2</sub> radiation while growth is in process but, more importantly, also prevents unwanted cooling of the melt by the surrounding air currents. It also allows close observation of the growth. As the enclosed chamber may be partially evacuated or over-pressured with some inert gas, impurities which may attach onto the surface of the source rod can be greatly reduced. In this way, other difficult materials having incongruent melting behaviours can also be grown. Throughout the course of this work, almost all the fibres grown were based on Al<sub>2</sub>O<sub>3</sub> hosts and, hence, no vacuum or inert gases were required.

### 3.3.5 Vibration-isolated optical bench

Unwanted vibration, which will most likely be coupled to the melt, is reduced by mounting only the components critical to the crystal growth process onto a pneumatically-damped optical bench. This isolates the melt from any unwanted vibration or perturbation, which is regarded as one of the most important factors in obtaining a fibre with good dimensional geometry. However, with the present growth system, a tiny amount of vibration may be introduced due to contributions from the pull and feed motors. This type of vibration is high frequency noise which may be coupled directly to the melt and hinder the growth of good quality crystal fibres. It can, however, be damped by the use of high gearing ratios in both the pull and feed drive systems. The microprocessor, laser cooling unit, manual control box (for x-y positioning) and other related components are not placed on this bench, although the cooling tubes and circulating water for the CO<sub>2</sub> laser may be another tiny source of vibration.

### 3.4 Fibre growth

The growth of various types of fibres is discussed in this section while the rest of the experimental techniques used in the characterisation of the crystal fibres fabricated by the LHPG technique are described in **Chapter 4**.

Potential materials for extreme sensing conditions (such as very high temperature, strain, pressure, stress, etc.) should, in principle, have very good mechanical characteristics and be highly stable in such intended environments. Glass fibres, although favourable since they are commercially and widely available at relatively low costs, are limited to the range of "normal" sensing applications because of their inherent physical properties. To date, most crystalline fibres grown in this study have  $\text{Al}_2\text{O}_3$  as the crystal host, with various active impurities/dopants incorporated. These doped fibres include  $\text{Cr}^{3+}:\text{Al}_2\text{O}_3$ ,  $\text{Er}^{3+}:\text{Al}_2\text{O}_3$ ,  $\text{Er}^{3+} + \text{Yb}^{3+}:\text{Al}_2\text{O}_3$  (with approximately equal concentrations of both  $\text{Er}^{3+}$  and  $\text{Yb}^{3+}$ ) and  $\text{Yb}^{3+} + \text{Er}^{3+}:\text{Al}_2\text{O}_3$  (where the  $\text{Yb}^{3+}$  to  $\text{Er}^{3+}$  content is  $\sim 10:1$ ). In addition, pure sapphire fibres, in both *c*- and *a*-axis orientations have been grown. *C*-axis sapphire fibres have rounded hexagonal cross-sections, as shown in **Figure 3.18a** while **Figure 3.18b** shows an *a*-axis fibre whose cross-section resembles an oblong shape with two parallel sides and two rounded edges. Among these, pure sapphire and ruby fibres have been found to grow most easily and readily from polycrystalline and monocrystalline source rods. **Figure 3.19** shows a video image of a growing sapphire fibre using the laser heated pedestal growth process where the diameter reduction ratio is  $\sim 2.5$ .

Sapphire ( $\text{Al}_2\text{O}_3$ ) has been chosen for this work mainly because of its attractive properties. It absorbs  $\text{CO}_2$  radiation efficiently, has high melting point, good optical transparency (0.3 to 4  $\mu\text{m}$ ), good mechanical properties, can be easily doped and it is considered an easy material to grow as fibres. For the growth of pure sapphire crystal fibres, source rods with diameters of 130, 325 and 425  $\mu\text{m}$  have been employed, although with the smallest diameter source, pull rates used were typically 0.5 mm/min or slower. At faster pull rates, relatively large variations of the crystallising fibre diameter have been observed due to the high flexibility of the small diameter source. With larger source rods which are more rigid, typical rates used were between 0.75 and 1 mm/min. Fibres grown were found to be relatively

free from large amplitude high frequency diameter variations. The thinner fibre, being more flexible than the larger ones, is thus more susceptible to perturbations and slight misalignment of the source and seed with respect to the fixed laser focus spot. It also breaks off easily from the melt when the pull rate is increased to  $\sim 1$  mm/min. **Figure 3.20** shows typical diameter variations of a sapphire fibre pulled from a  $325 \mu\text{m}$  source fibre at  $\sim 0.75$  mm/min and measured with the eyepiece-graticule technique. The standard deviation is less than 0.5 % while the maximum deviation from the mean diameter is  $\sim 2$  %. In a normal sapphire fibre growth, laser power is increased up to the point when a stable hemispherical molten zone is formed. A seed crystal, in the form of a sapphire fibre (either polycrystalline or single crystal), is dipped into the melt and withdrawn into a fibre. Since it is difficult to inhibit single-crystal fibre growth, *c*-axis sapphire SCFs can be easily grown. For *a*-axis fibres, a suitably oriented seed crystal has been used to initiate growth. Fibres in both orientations have thus been grown this way with lengths ranging from  $\sim 20$  to 220 mm. No complications or melt instabilities have been observed while growing this material.

In the current work, various dopants have been used as active impurity materials from which the fluorescence characteristics of as-grown fibres were investigated as a function of the sensed physical parameters, namely temperature and strain. Fibres of sapphire (both poly- and mono-crystalline) were first dipped into a well-agitated suspension of impurity materials in aqueous solution. Following this, the coated source fibres were then subjected to heat treatment employing a flame (from a bunsen burner, gas lighter or an oxy-acetylene flame) to heat the samples until visible powdered layers on the surface of the sapphire source fibres/rods have been realised. This is a relatively convenient and fast way to obtain doped fibres but it has the disadvantage of producing unknown or uncontrollable doping levels in the final fibres. Although the proportion of impurity-to-water mixture (in weight) for the various dopants employed has been monitored, no realistic control of their concentration levels can actually be exerted since not all of the coatings on the source rod surface are incorporated into the molten zone. It can only be assumed that the doping level is almost or approximately proportional to the number of coating layers applied.

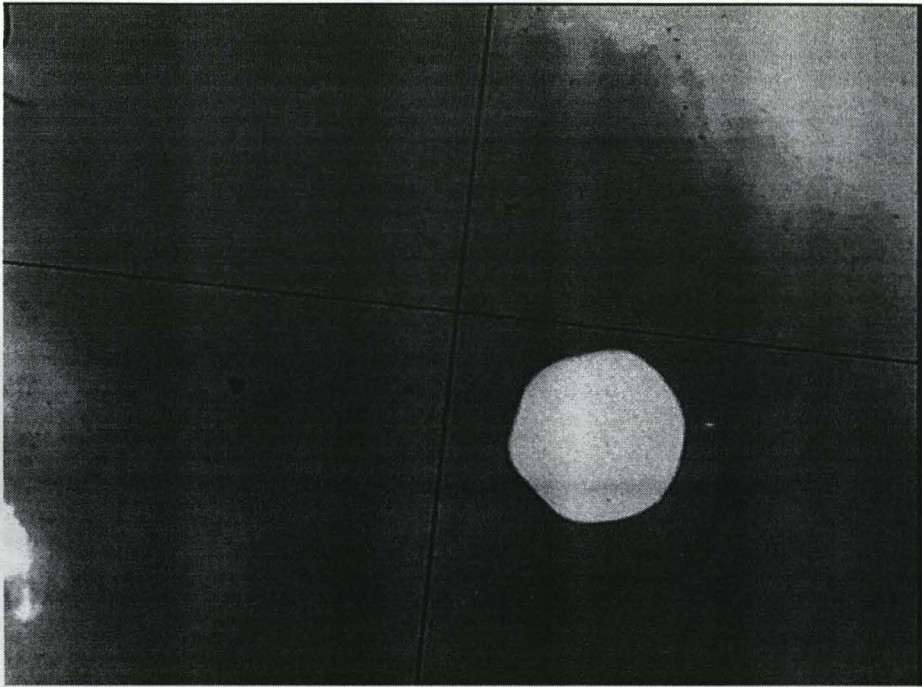


**Figure 3.18a. Photograph of a c-axis sapphire fibre**

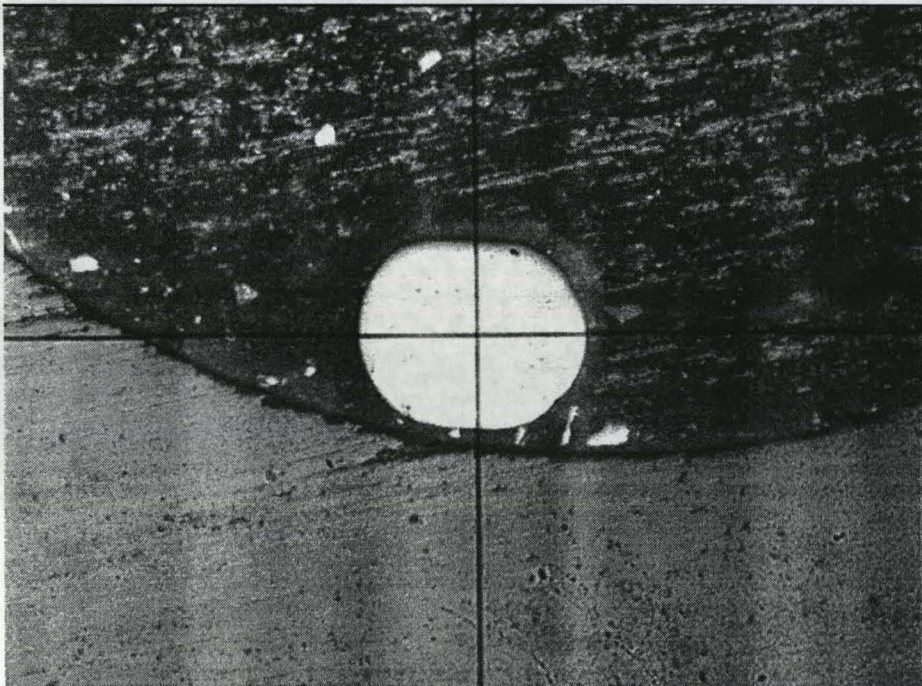


**Figure 3.18b. Photograph showing an a-axis sapphire fibre**

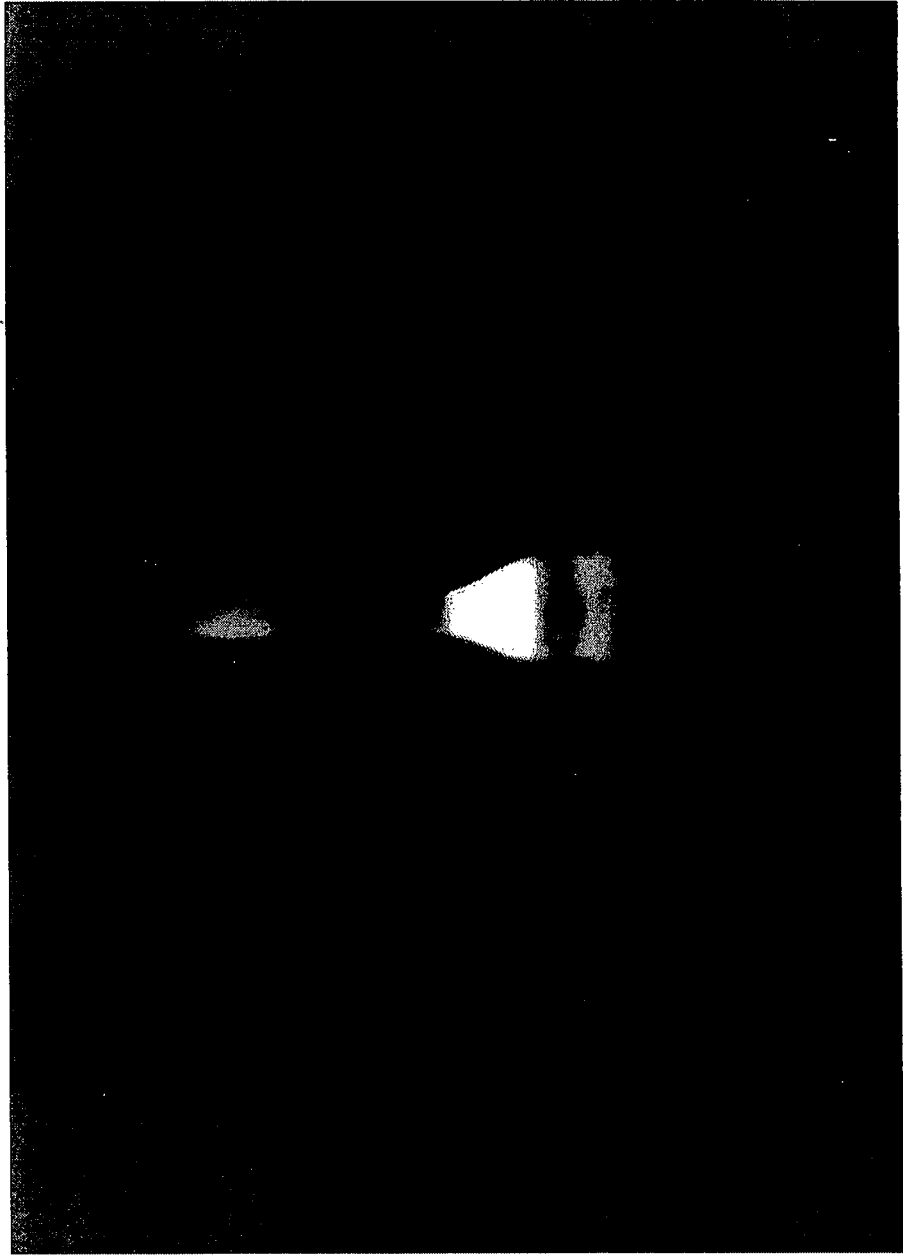
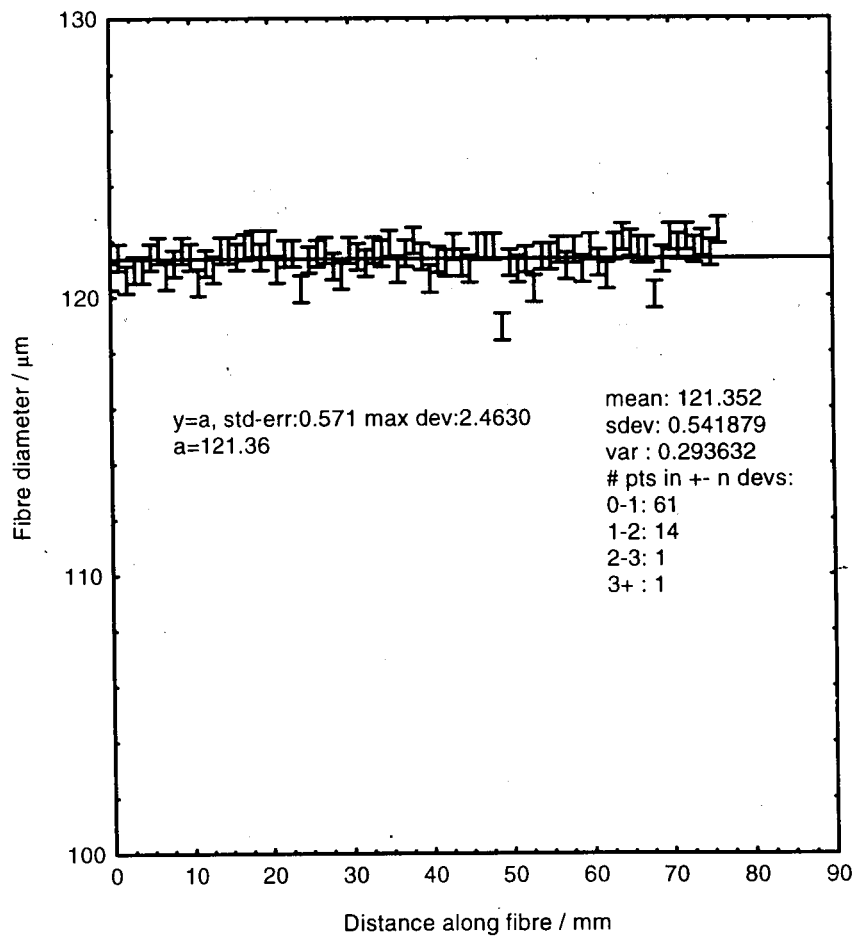


**Figure 3.19.** Crystallising fibre during LHPG

Figure 3.20. Diameter variation of sapphire fibre



As a general procedure, all source fibres/rods were first “decontaminated” by cleaning with acetone; they were then dip-coated and heat-treated three times, and immediately mounted onto the pin chuck of the feed system within the enclosed growth chamber to prevent accidental environmental contamination.

For the growth of ruby ( $\text{Cr}^{3+}:\text{Al}_2\text{O}_3$ ) fibres, the sapphire source rod was coated and heat-treated as described above, until a hard greenish layer of  $\text{Cr}_2\text{O}_3$  was formed on its surface. **Figure 3.21** shows a typical coated source rod. Note the relatively uniform coating and layer thickness. The proportion of the chromium oxide-to-water mixture has been maintained at  $\sim 1$  g  $\text{Cr}_2\text{O}_3$  to 7.5 g water. Ruby fibres have been found to grow easily and in a stable manner using LHPG, without any complications. The only “abnormality” observed during growth was the formation of a layer of brownish-green deposit on the fibre surface. This likely arose from the evaporation and subsequent condensation of chromium and its oxide from the melt during laser heating. It has been thought that a high concentration of dopant could be incorporated into the  $\text{Al}_2\text{O}_3$  host fibre this way but EPMA (electron probe micro-analysis) scans of a fibre cross-section revealed a doping level of  $\sim 0.1$  % Cr. This, however, is still twice the concentration level ( $\sim 0.05$  %) commonly found in ruby laser crystals [3.50]. **Figure 3.22** shows a cross-sectional scan of the doping concentration obtained by EMPA while **Figure 3.23** shows some examples of c-axis ruby fibres grown.

Doping sapphire fibres with rare earth (RE) ions presented a more difficult task. It has been reported that due to the similar cubic crystal structure between rare earths such as  $\text{Er}_2\text{O}_3$  and  $\text{Al}_2\text{O}_3$ , high doping levels greater than 1 % can be achieved [3.51] with trivalent Er ions. It should thus also be possible, in principle, when doping with other RE ions having similar cubic structures to achieve similar doping levels. However, it should be noted that doping of RE ions have generally been performed in thin  $\text{Al}_2\text{O}_3$  films using high-energy electron beam ion implantation [3.52], pulsed laser deposition [3.53], chemical vapour deposition [3.54] and molecular beam epitaxy [3.55], most commonly for telecommunications applications in planar waveguides. No report has yet been published on RE doping in  $\text{Al}_2\text{O}_3$  fibres under any melt growth methods.

Sapphire fibres have been singly doped and co-doped according to the following RE ion combinations:  $\text{Er}^{3+}:\text{Al}_2\text{O}_3$ ,  $\text{Yb}^{3+} + \text{Er}^{3+}:\text{Al}_2\text{O}_3$  (~10:1  $\text{Yb}^{3+}$  to  $\text{Er}^{3+}$  ratio) and  $\text{Er}^{3+} + \text{Yb}^{3+}:\text{Al}_2\text{O}_3$  (~1:1 ratio), with trivalent  $\text{Yb}^{3+}$  serving as sensitizers for more efficient energy transfer for the co-doped fibres. The same dip-coating and heating procedure was adopted. A pinkish layer was observed on fibres coated with  $\text{Er}_2\text{O}_3$ , while coating with both  $\text{Yb}_2\text{O}_3 + \text{Er}_2\text{O}_3$  and  $\text{Er}_2\text{O}_3 + \text{Yb}_2\text{O}_3$  resulted in whitish layers being formed on the surface of the source rods. Examples of some RE oxide coated source rods can be seen in **Figures 3.24**. The dopant(s)-to-water proportion for erbium oxide, ytterbium + erbium oxide and erbium + ytterbium oxides are 0.5 g : 7.5 g, 0.72 + 0.07 g : 7.5 g and 0.5 + 0.5 g : 7.5 g respectively. **Table 3.1** lists the dopant-to-water mixtures for all dopants used for fabricating doped fibres. Some examples of the dip-coated source rods are shown in **Figures 3.24**.

Initial attempts to grow  $\text{Er}^{3+}$ -doped sapphire fibres employed 130  $\mu\text{m}$  source rods. While it was relatively easy to form a molten zone as well as initiating the seeding process, the crystallising fibres broke off from the melt at various stages throughout the growth, at lengths between 2.5 and 25 mm. All these fibres were pulled at rates of 0.2 mm/min or slower. The critical "break-off" lengths were not constant while the crystallising fibres were observed to be transparent during the growth process, hence, no reasonable conclusion can be drawn from the segregation coefficient, time constant and length. However, from the observation of a sapphire fibre doped at the tip with  $\text{Er}^{3+}$ , a light pinkish colour can clearly be seen under microscope inspection. It can be assumed that with such a high dopant concentration used, all the  $\text{Er}^{3+}$  ions segregated within the melt and have not been withdrawn into the resulting fibre, hence, no substitutional replacement of the Al atoms occurred. Similar difficulties were encountered when growing co-doped ( $\text{Er}^{3+} + \text{Yb}^{3+}$  and  $\text{Yb}^{3+} + \text{Er}^{3+}:\text{Al}_2\text{O}_3$ ) fibres from 130  $\mu\text{m}$  source rods, the only difference being the relatively constant critical lengths of these samples. Most of the crystallising fibres broke off from the melt after a short length of ~5 mm and the samples were transparent when observed, during and after growth. Pull rates of 0.15 mm/min and slower have been used for the growth of the co-doped samples.

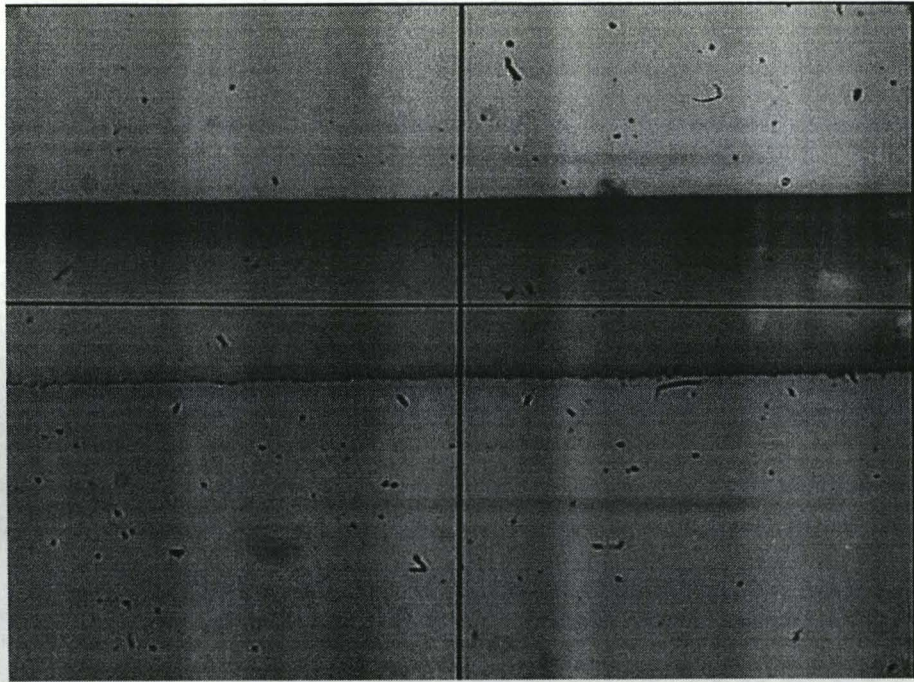
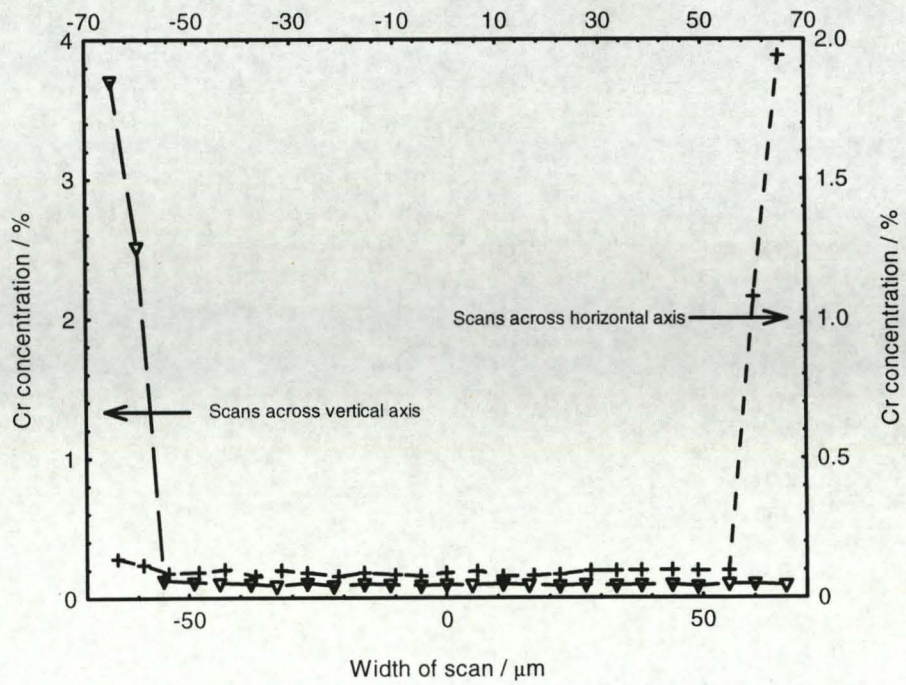
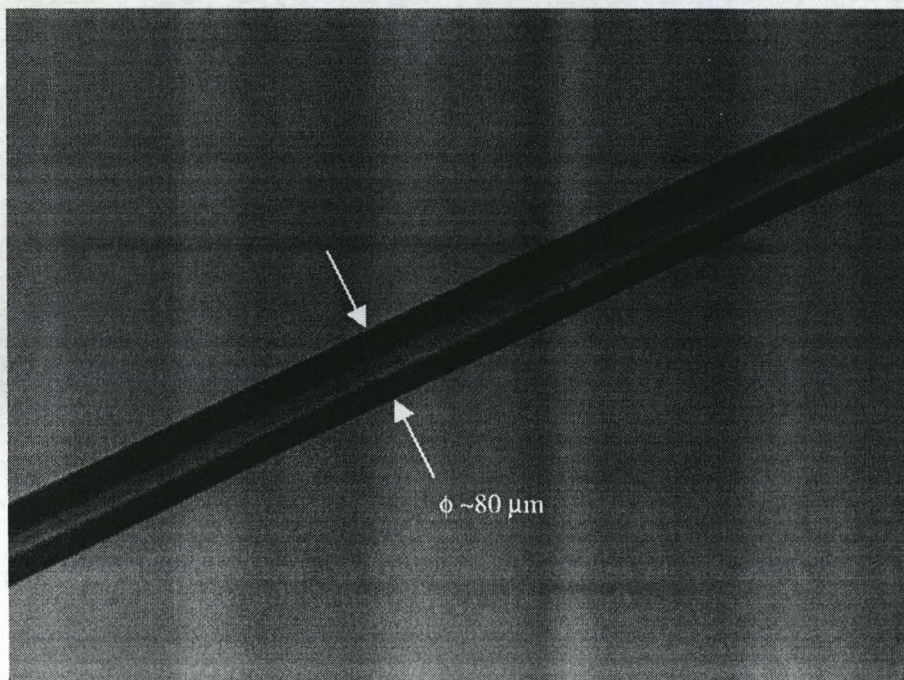
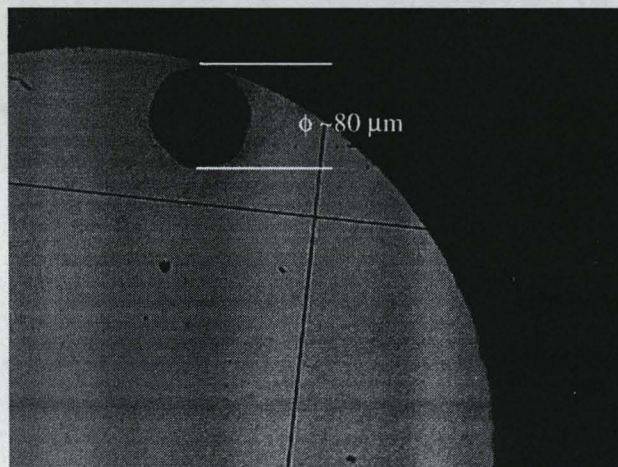
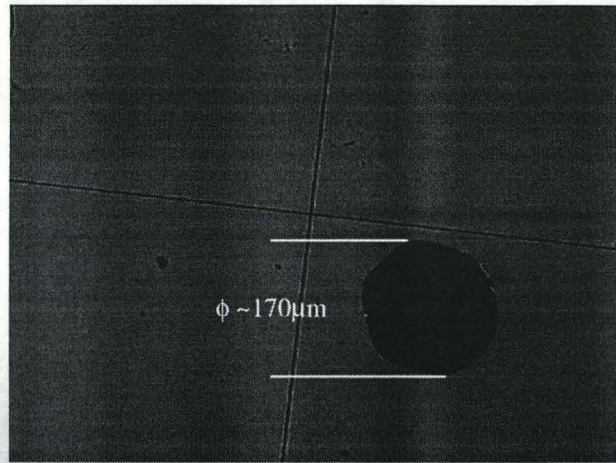


Figure 3.21. Example of chromium oxide coated source rod

Figure 3.22. EMPA scan of  $\text{Cr}^{3+}:\text{Al}_2\text{O}_3$   
fibre cross-section along orthogonal axes





**Figure 3.23. Examples of c-axis ruby fibres**

**Table 3.1. Proportion of dopant-liquid mixtures used for dip coating source fibres/rods**

Dopants	Dopant weight / g	Distilled water / g
$\text{Cr}_2\text{O}_3$	1.0	7.50
$\text{Er}_2\text{O}_3$	0.5	7.50
$\text{Yb}_2\text{O}_3 + \text{Er}_2\text{O}_3$	0.72 + 0.07	7.50
$\text{Er}_2\text{O}_3 + \text{Yb}_2\text{O}_3$	0.5 + 0.5	7.50

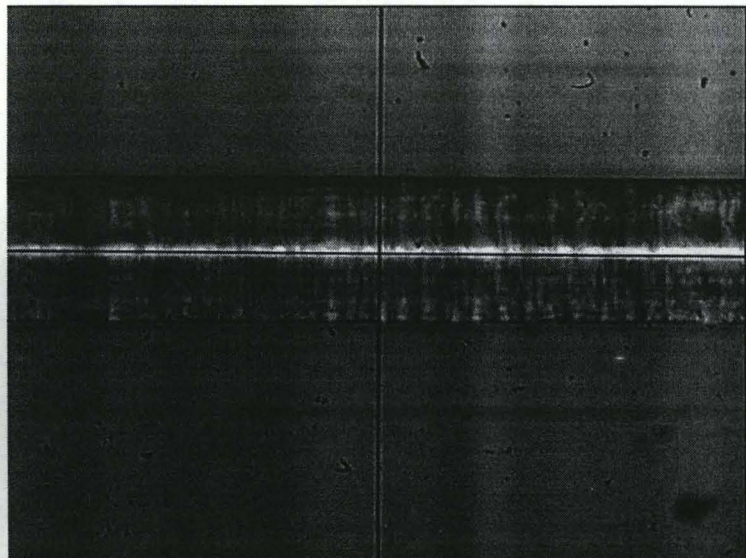


**Figure 3.24a. Uncoated sapphire source rod**

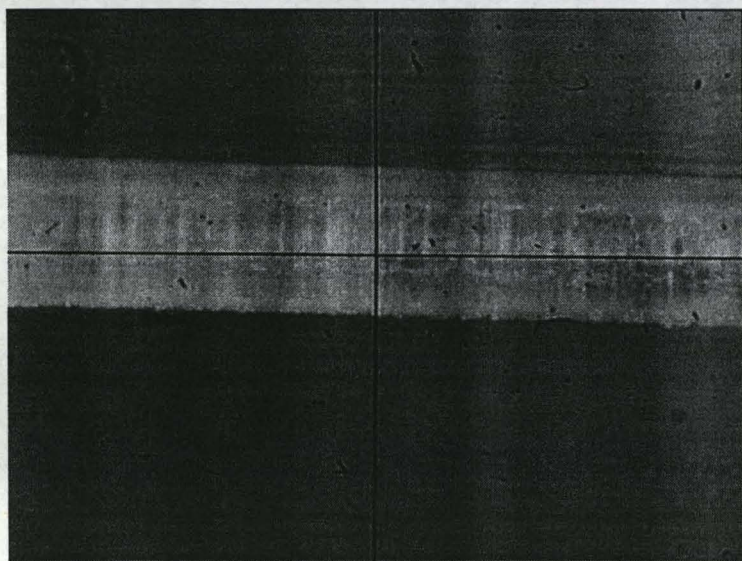


**Figure 3.24b. Er<sub>2</sub>O<sub>3</sub> coated source rod**

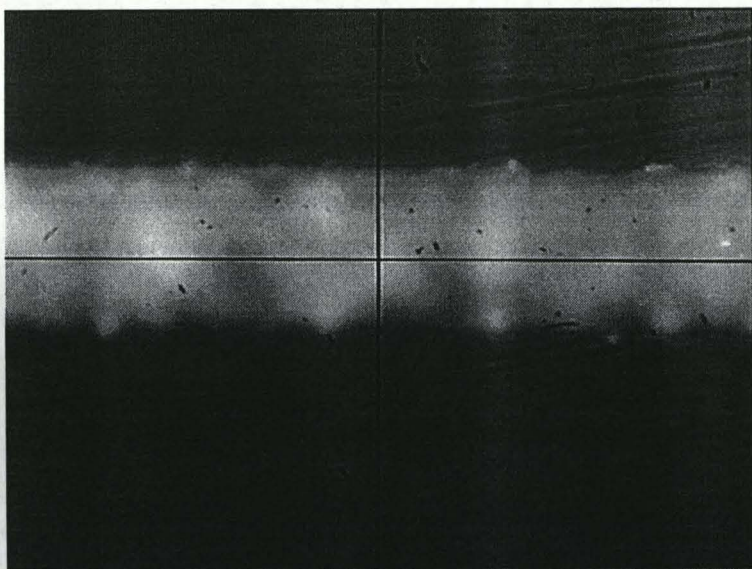


**Figure 3.24c. Yb<sub>2</sub>O<sub>3</sub> + Er<sub>3</sub>O<sub>2</sub> coated source rod (~10:1 concentration ratio)**

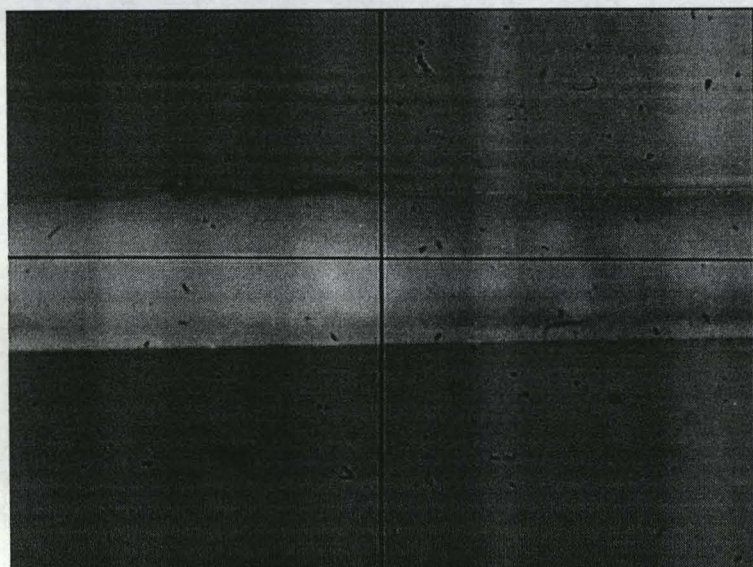


**Figure 3.24d. Nd<sub>2</sub>O<sub>3</sub> coated source rod**

The high beam energies employed during ion implantation of thin  $\text{Al}_2\text{O}_3$  films with RE ions may easily facilitate the doping process, rendering the target films highly soluble or porous to the impurities. Melt growth, on the other hand, involves entirely different doping characteristics and the following reasons are postulated for the ineffective growth of RE-doped sapphire fibres using LHPG. The pull and feed have been recorded by the controlling software and found to be relatively constant at their respective velocities. This should thus not have any significant effect on the breaking-off of the crystallising fibres from the melt. However, the slow pull rates used throughout crystal growth may have caused the RE impurities to accumulate in the molten zone instead of being pulled/diffused into the fibre. In addition, such rates could also have resulted in preferential evaporation of the rare earth coatings from the source rod surface and the remaining amounts which might have accumulated in the melt. Indeed, by increasing the laser power initially to melt the tip of the source rod into its characteristic hemispherical shape, the adjacent RE oxide coatings were observed to be burnt off rather suddenly by the intense focused heat. This has been attributed as one of the reasons for the short fibre lengths which can be pulled using  $130\ \mu\text{m}$  source rods. The RE oxides used were very fine particles and, thus, form dense coating layers. Although it has not been recorded on video, the burning-off process has been observed to cause large perturbation in terms significant vibration to the source rod, in particular to the molten zone. With such a small source rod and its inherent flexibility, this inevitably led to disturbance of the otherwise stable molten zone and, subsequently, resulted in the seed or crystallising fibre breaking off from the melt. Another reason could be the larger atomic/ionic radii of RE ions compared to  $\text{Al}^{3+}$ , in which case, there would be much difficulty in the former replacing the latter ions substitutionally within the crystal lattice. More significantly, however, the high concentrations of REs used in this study could, more likely, have resulted in changes to the melt dynamics which directly affected the stability of the melt, making it difficult to sustain stable fibre growth. This problem was also thought to be further compounded by the small source rods (hence, small melt volumes) and low growth rates utilised. No published data, however, is currently available on melt growth of RE-doped sapphire fibres.

By employing larger diameter ( $325\ \mu\text{m}$ ) source rods which are much stiffer, the vibration of the melt due to burning-off effect of the coatings was drastically

reduced. In fact, no detectable perturbation has been visually observed after the source rod changeover. This is likely due to the larger available melt volume of the rods, hence, the dopants are effectively more dilute. However, above a certain concentration level, the dopant(s) could still lead to destabilisation of the melt by changing the melt/fluid properties such as surface tension. Although evaporation from the coated layers still occurred, the melt (and molten zone shape) was observed to be stable and a layer of dopant(s) could still be seen being fed into the melt as the source rod was translated upwards into the laser focus. Dipping an oriented seed crystal (c-axis sapphire for growing RE-doped fibres, in most cases) into the molten zone, fibres doped with  $\text{Er}^{3+}$ ,  $\text{Yb}^{3+} + \text{Er}^{3+}$  and co-doped with  $\text{Er}^{3+} + \text{Yb}^{3+}$  have been grown, with typical pull rates of  $\sim 0.75$  mm/min.  $\text{Er}^{3+}$ -doped and  $\text{Er}^{3+} + \text{Yb}^{3+}$  co-doped fibres were found to exhibit an almost translucent crystal structure while the highly  $\text{Yb}^{3+}$ -codoped with low  $\text{Er}^{3+}:\text{Al}_2\text{O}_3$  fibres were observed to be relatively transparent. **Figures 3.25** show examples of as-grown RE-doped sapphire fibres.

For fibre optic sensing applications, it was thought that a monolithic crystal fibre, consisting of a short section which has been doped with active ions together with a continuous longer sapphire section, would be the most practical approach. The doped section can be used as the sensor probe with the longer sapphire portion serving as the delivery fibre, so that any coupling required between conventional glass fibres and the sensing crystal fibre can be effected a distance away from the sensed parameter(s). For an all-fibre optic sensing configuration, this type of arrangement would thus serve to reduce degradation to the glass/crystal fibre coupling/interface. Fabrication of such a fibre can be easily carried out without having to join one sapphire fibre to another, separately doped fibre as has been reported [3.56, 3.57], where dimensional continuity may be poor. A short portion of the source rod can be coated, depending on the desired length of the doped fibre to be grown. The source rod can then be securely attached to a pin chuck, with the coated section at the top. This will enable the doped fibre section to be pulled first before the pure sapphire fibre. Mounting the coated section below (in the opposite direction, vertically) will thus allow a relatively long fibre of pure sapphire to be pulled first before the coated section. The latter technique has been employed throughout RE-doping in this work.

Sapphire fibres of diameters between 130 and 170  $\mu\text{m}$  with one end section doped have been observed to grow readily. The pure sapphire sections were, generally, of good diameter uniformity and were crystal clear/transparent. When the coated sections were fed into the melt, the stable growth was maintained. However, the cooling fibre away from the melt zone appeared slightly opaque through the viewing optics, which could be due to precipitation of the RE dopant(s) upon cooling, but under microscopic observation, these fibres were of a more translucent (than opaque) nature. This would suggest that a considerably high level of dopant concentration had been achieved. **Figures 3.26** illustrate the LHPG growth of RE-doped sapphire fibres. Further, if the coated layers were too thick, the fibre was observed to thicken at the solid/liquid interface and slight variation in its diameter occurred. Hence, the 3 coatings applied during the fabrication of doped source fibres have been found to be the optimum thickness, in which highly doped fibres with relatively little diameter variation can be grown. The main disadvantages in using this doping technique remain the difficulty in obtaining a very distinct boundary/interface between the doped and undoped fibre sections as well as the lack of control, or rather the repeatability, of the dopant concentration level.

Yttria-stabilised zirconia ( $\text{Y}_2\text{O}_3\text{-ZrO}_2$ ), also known as YSZ, have been investigated in this work and found to be relatively difficult to grow into fibres. The extremely high melting point of this material ( $\sim 3000\text{ K}$ ) required a much larger amount of heating power than is currently available from the *Synrad, Inc.*  $\text{CO}_2$  laser (maximum power  $\sim 30\text{ W}$ ). Although attempts to grow YSZ fibres have utilised the laser at its maximum power output, this has been found to be barely sufficient, considering the relatively large source rods used ( $\sim 1\text{ mm}$ ). At full power, the laser output has been found to oscillate with low frequency (in the CLL mode), resulting in fibres containing uneven diameter distributions throughout the whole fibre length. Using the laser at maximum output in the CLH mode resulted in high frequency power variation, hence, only the CLL mode has been used. The stability of the laser output has been quoted by the manufacturer for up to a maximum power cycle of 95 %. Due to the high power used, white powdery deposits have been found to settle on the mirrors, pin chucks and crystallising fibres. YSZ is known as a difficult material to grow and heating the tip of the source rod into the typical hemispherical shape required a period of a few seconds. This molten zone has been observed to expand

and contract relative to the oscillating laser power. More importantly, it could be due to the low concentration level of the stabilising yttrium-oxide within the source material, which has been quoted at ~3 mol. %, and the large thermal gradients across the molten zone, leading to the build-up of large residual thermal stress [3.58, 3.59]. It could be that the use of a more powerful CO<sub>2</sub> laser would overcome these problems and permit growth of good quality fibres of this material. **Figures 3.27** show examples of yttria-stabilised zirconia fibres grown by LHPG in this work.

Finally, the as-grown crystal fibres have to be processed before they can be employed in any sensing applications. The first 3 – 4 mm of all the fibres were cut using a diamond scribe (and broken off) before they were polished with an *Ultra Tech Mfg., Inc.* fibre polishing machine. The cut-offs were required since it generally took a short distance (of several fibre diameters) once crystal growth had been initiated before equilibrium and, hence, stable fibre growth, was reached [3.29]. This would indicate that the first few millimetres of the as-grown fibre had uneven diameter variations. The cut fibres were aligned co-linearly with the longitudinal axis of thick-wall glass capillaries used as supports and held securely with the aid of some quartz wax during polishing. The wax was first melted and, by capillary action, drawn up through the capillary bore. For cutting down materials to ensure a relatively flushed plane between the fibre and capillary ends, coarse grit SiC grinding pads (Grit 800 and 1200) have been used. Subsequent polishing steps utilised Al<sub>2</sub>O<sub>3</sub> polishing pads in the following order: 30 µm, 12 µm, 3 µm and 1 µm. Generally, 3 µm polishing has been considered sufficiently fine to enable transmission, reflection and collection of light signals into and out of the fibres, since these fibres are not used for the highly critical laser and nonlinear interaction applications. In this work, most of the crystal fibres used for fluorescence sensing have been polished down to 3 µm while for the more critical application of polarimetric sensing, 1 µm lapping has been employed. Once processing has been accomplished, the fibres were then ready for characterisation studies.

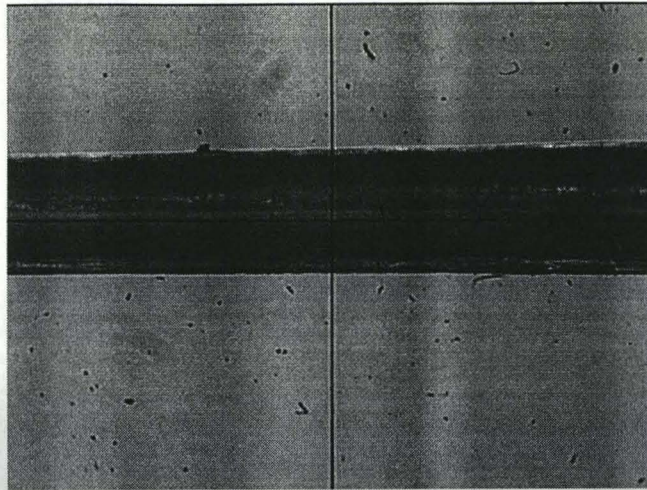


Figure 3.25a. Er<sup>3+</sup>:Al<sub>2</sub>O<sub>3</sub> fibre

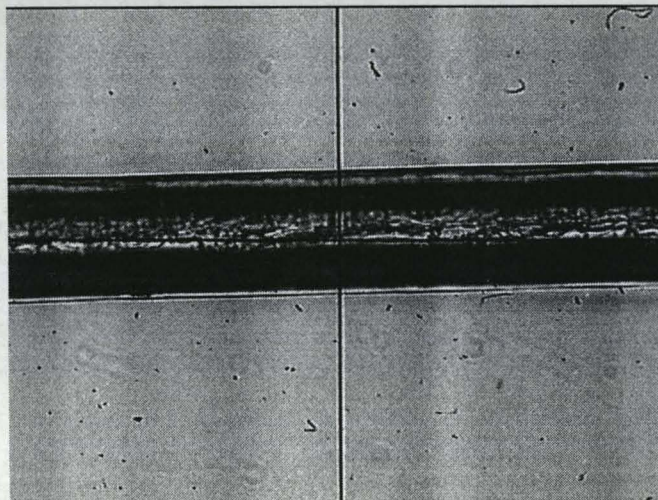


Figure 3.25b. High Yb<sup>3+</sup> + low Er<sup>3+</sup>:Al<sub>2</sub>O<sub>3</sub> fibre

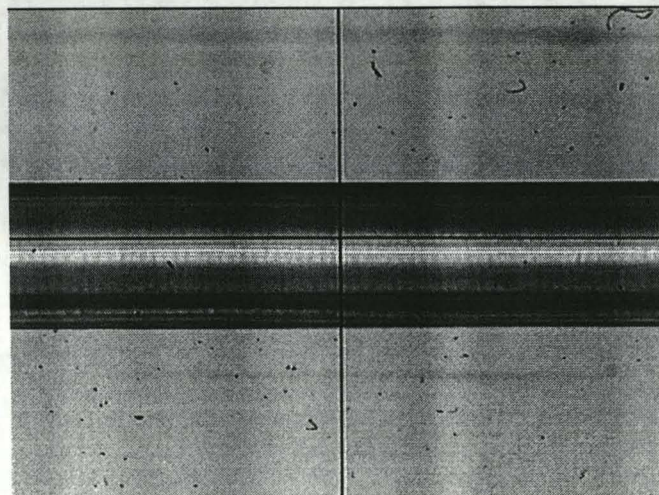
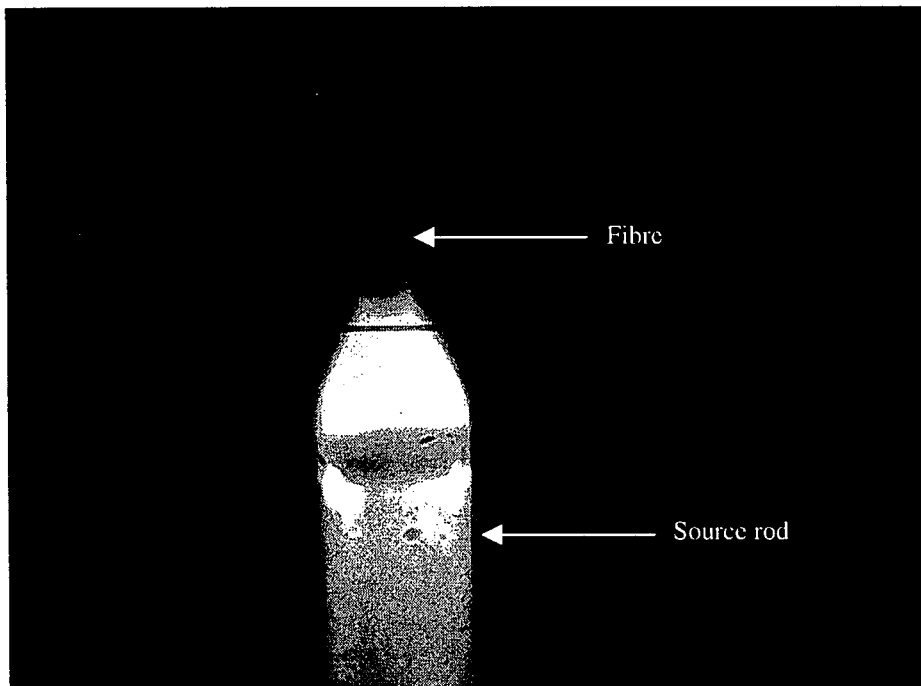
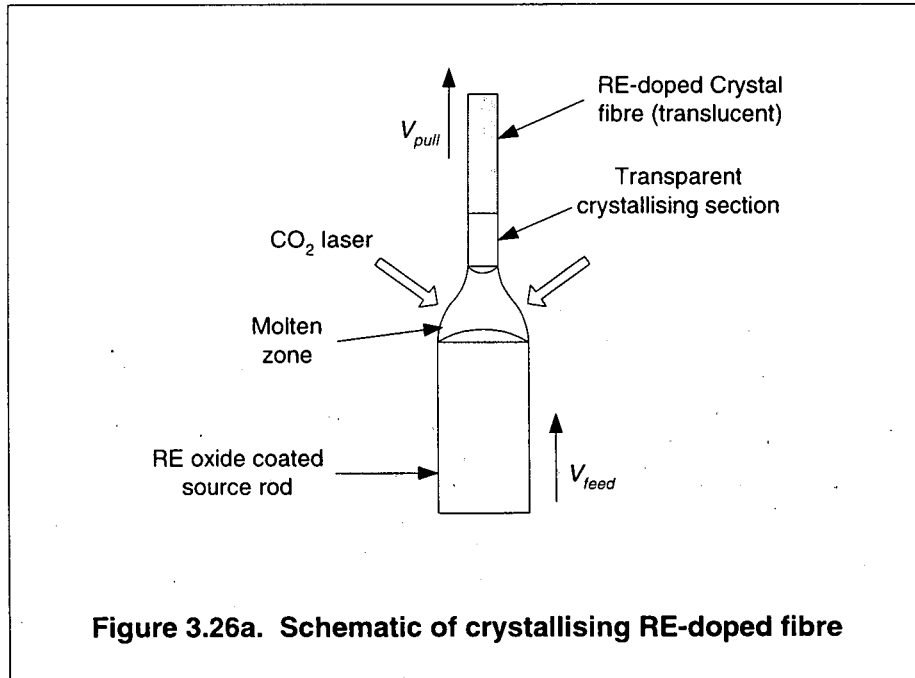
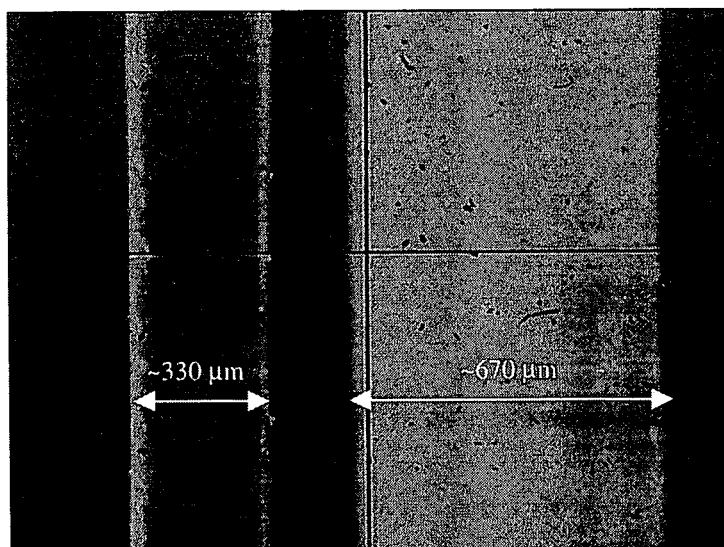
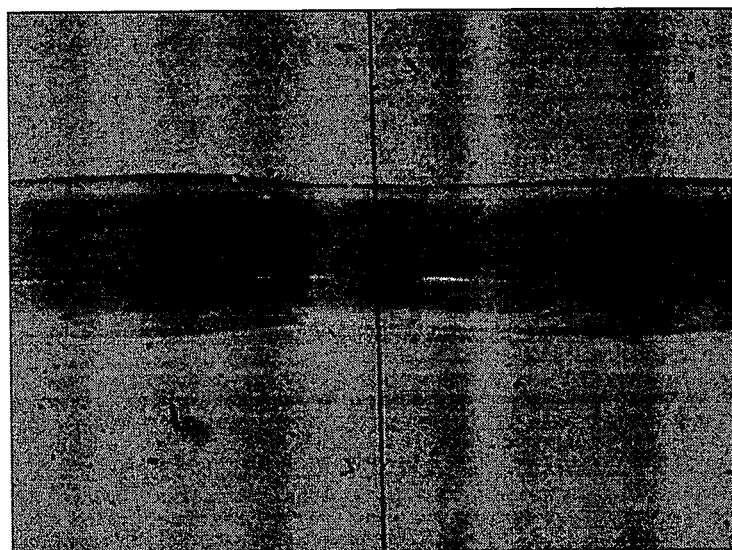


Figure 3.25c. Er<sup>3+</sup> + Yb<sup>3+</sup>:Al<sub>2</sub>O<sub>3</sub> fibre





**Figure 3.27a. Examples of YSZ fibres/rods produced by LHPG**



**Figure 3.27b. Large diameter variation along fibre due to fluctuating laser power**

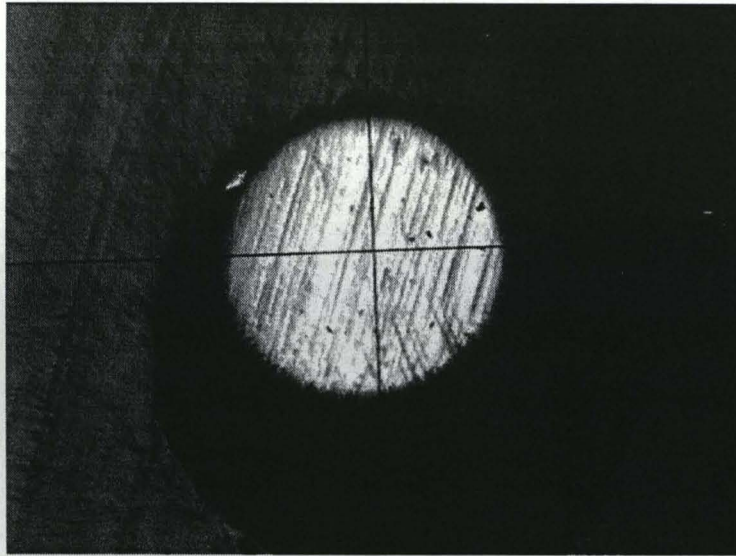


**Figure 3.27c. Cross-sectional view of YSZ fibre/rod**

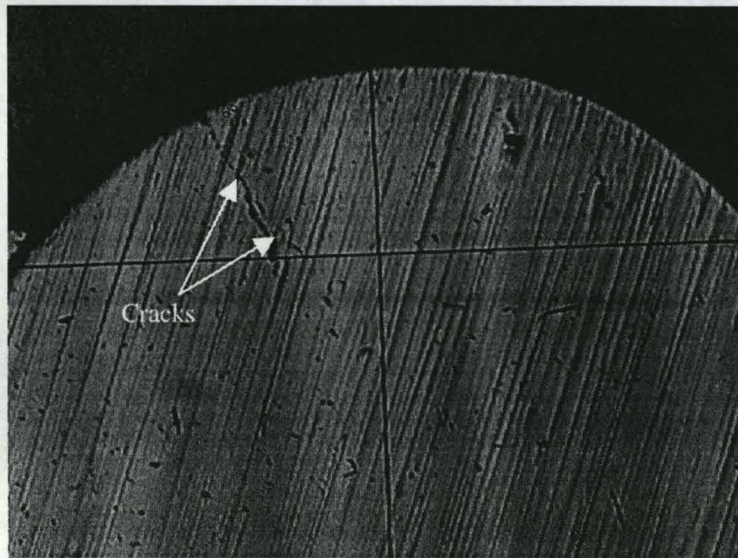


**Figure 3.27d. Defects in YSZ fibre**

### 3.5 References to Chapter 3

- 3.1 A. I. Mlavsky and H. E. LaBelle, *Growth of Continuous Whiskers from the Melt* in: *Whisker Technology*, A. P. Levitt (Ed.), John Wiley & Sons, Inc., New York, 121, 1970
- 3.2 R. S. Feigelson, *Preparation of Single crystal fibers*, Inst. Phys. Conf. Ser., Paper presented at the Int. Conf. Mater. For Non-linear and Electro-optics No. 103: Part I (Cambridge, England), 75, 1989
- 3.3 E. K. Renwick, E. E. Robertson, I. S. Ruddock and R. Illingworth, *Optical transmission properties of single crystal fibres*, Opt. Commun., **123**, 477, 1996
- 3.4 R. S. Feigelson, *Opportunities for Research on Single-Crystal Fibers*, Mater. Sci. Eng., **B1**, 67, 1988
- 3.5 V. A. Tatarchenko, *Capillary Shaping in Crystal Growth from Melts. I. Theory*, J. Cryst. Growth, **37**, 272, 1977
- 3.6 V. A. Tatarchenko, V. S. Uspenski, E. V. Tatarchenko, J. Ph. Nabot, T. Duffar and B. Roux, *Theoretical model of crystal growth shaping process*, J. Cryst. Growth, **180**, 617, 1997
- 3.7 J. J. Fitzgibbon and J. M. Collins, *High volume production of low loss sapphire optical fibers by Saphikon EFG (Edge defined Film-fed Growth) method*, Proc. SPIE, **3262**, 135, 1998
- 3.8 Y. Mimura, Y. Okamura, Y. Komazawa, and C. Ota, *Growth of Fiber Crystals for Infrared Optical Waveguides*, Jpn. J. Appl. Phys., **19**(5), 1269, 1980
- 3.9 D. W. G. Ballentyne and S. M. Al-Shukri, *The Growth of Electrooptic Organic Crystals in Monomode Optical Fibres*, J. Cryst. Growth, **48**, 491, 1980
- 3.10 H. Oguri, H. Yamamura and T. Orito, *Growth of MgO doped LiNbO<sub>3</sub> single crystal fibers by novel drawing down method*, J. Cryst. Growth, **110**, 669, 1991
- 3.11 K. Shimamura, S. Uda, T. Yamada, S. Sakaguchi and T. Fukuda, *Silicon Single Crystal Fiber Growth by Micro Pulling Down Method*, Jpn. J. Appl. Phys., **35**(2), L793, 1996
- 3.12 H. C. Kuhlmann (Ed.), *Thermocapillary Convection in Models of Crystal*

- Growth*, Springer-Verlag, Berlin, 1, 1999
- 3.13 S. Uda, J. Kon, J. Ichikawa, K. Inaba, K. Shimamura and T. Fukuda, *Interface field-modified solute partitioning during Mn: LiNbO<sub>3</sub> crystal fibre growth by micro-pulling down method. I. Axial distribution analysis*, J. Cryst. Growth, **179**, 567, 1997
- 3.14 S. Uda, J. Kon, K. Shimamura, K. Ichikawa, K. Inaba, and T. Fukuda, *Interface field-modified solute partitioning during Mn: LiNbO<sub>3</sub> crystal fibre growth by micro-pulling down method. II. Radial distribution analysis*, J. Cryst. Growth, **182**, 403, 1997
- 3.15 C. W. Lan, S. Uda and T. Fukuda, *Theoretical analysis of the micro-pulling-down process for Ge<sub>x</sub>Si<sub>1-x</sub> fiber crystal growth*, J. Cryst. Growth, **193**, 552, 1998
- 3.16 G. P. Pazzi and P. Fabeni, *BGO Crystalline Fibres*, Opt. Laser Technol., **24**(4), 193, 1992
- 3.17 V. I. Chani, K. Nagata, T. Kawaguchi, M. Imaeda and T. Fukuda, *Segregation and uniformity of K<sub>3</sub>Li<sub>2</sub>(Ta, Nb)<sub>5</sub>O<sub>12</sub> fiber crystals grown by micro-pulling-down method*, J. Cryst. Growth, **194**, 374, 1998
- 3.18 Y. Terada, K. Shimamura and T. Fukuda, *Growth and optical properties of RE doped bulk and fiber single crystals by Czochralski and micro pulling down methods*, J. Alloys and Compounds, **275-277**, 697, 1998
- 3.19 B. M. Epelbaum, A. Yoshikawa, K. Shimamura, T. Fukuda, K. Suzuki and Y. Waku, *Microstructure of Al<sub>2</sub>O<sub>3</sub>/Y<sub>3</sub>Al<sub>5</sub>O<sub>12</sub> eutectic fibers grown by  $\mu$ -PD method*, J. Cryst. Growth, **198/199**, 471, 1999
- 3.20 A. Yoshikawa, B. M. Epelbaum, K. Hasegawa, S. D. Durbin and T. Fukuda, *Microstructures in oxide eutectic fibers grown by a modified micro-pulling-down method*, J. Cryst. Growth, **205**, 305, 1999
- 3.21 V. I. Chani, A. Yoshikawa, H. Machida, T. Satoh and T. Fukuda, *Growth of Tb<sub>3</sub>Ga<sub>5</sub>O<sub>12</sub> fiber and bulk crystals using micro-pulling-down apparatus*, J. Cryst. Growth, **210**, 663, 2000
- 3.22 N. Ohnishi and T. Yao, *A Novel Growth Technique for Single-Crystal Fibers: The Micro-Czochralski ( $\mu$ -CZ) Method*, Jpn. J. Appl. Phys., **28**(2), L278, 1989
- 3.23 A. Kurosaka, M. Aoyagi, H. Tominaga, O. Fukuda and H. Osanai, *Superconducting Bi-Sr-Ca-Cu-O crystalline fibers prepared by the micro-*

- Czochralski method*, Appl. Phys. Lett., **55**(4), 390, 1989
- 3.24 S. T. Mileiko and V. I. Kazmin, *Crystallization of fibers inside a matrix: a new way of fabrication of composites*, J. Mater. Sci., **27**, 2165, 1992
- 3.25 S. T. Mileiko and V. I. Kazmin, *Structure and mechanical properties of oxide fiber reinforced metal matrix composites produced by the internal crystallization method*, Compos. Sci. Technol., **45**, 209, 1992
- 3.26 S. T. Mileiko (Ed.), *Metal and Ceramic based Composites*, Elsevier, Amsterdam, 587, 1997
- 3.27 V. N. Kurlov, V. M. Kiiko, A. A. Kolchin and S. T. Mileiko, *Sapphire fibres grown by a modified internal crystallisation method*, J. Cryst. Growth, **204**, 499, 1999
- 3.28 M. M. Fejer, J. L. Nightingale, G. A. Magel and R. L. Byer, *Laser-Heated Pedestal Growth Apparatus for Single-Crystal Optical Fibers*, Rev. Sci. Instrum., **55**(11), 1791, 1984
- 3.29 M. M. Fejer, *PhD Thesis*, Stanford University, 1986
- 3.30 R. S. Feigelson, W. L. Kway and R. K. Route, *Single-Crystal Fibers by the Laser-Heated Pedestal Growth Method*, Opt. Eng., **24**(6), 1102, 1985
- 3.31 V. Phomsakha, R. S. F. Chang and N. Djeu, *Novel implementation of laser heated pedestal growth for the rapid drawing of sapphire fibres*, Rev. Sci. Instrum., **65**(12), 3860, 1994
- 3.32 S. V. Tsivinskiy, *Factors Governing the Dislocations Density in the Czochralski Method of Growing Crystals*, Fiz. Met. Metalloved., **25**(6), 1013, 1968
- 3.33 T. Inoue and H. Komatsu, *Effects of the Crystal Diameter on the Dislocation Density in KCL Crystals Grown by the Czochralski Method*, Krist. Tech., **14**(12), 1511, 1979
- 3.34 J. H. Sharp, *PhD Thesis*, University of Strathclyde, 1992
- 3.35 D. H. Jundt, M. M. Fejer and R. L. Byer, *Growth and Optical Properties of Single-Crystal Sapphire Fibers*, Proc. SPIE, **1048**, 39, 1989
- 3.36 Z. Lu, Z. Ding, J. Chen, X. Chen, L. Ye and X. Tang, *The stable growth of single-crystal fibres*, Int. J. Optoelectron., **7**(1), 31, 1992
- 3.37 M. J. F. Digonnet, C. J. Gaeta, D. O'Meara and H. J. Shaw, *Clad Nd:YAG Fibers for Laser Applications*, J. Lightwave Technol., **LT-5**(5), 642, 1987
- 3.38 L. M. Thomas, D. M. Andrauskas and H. R. Verdún, *Growth and*

- Characterization of Nickel-Doped Garnets by the Laser-Heated Pedestal Growth Method*, Proc. SPIE, **1104**, 87, 1989
- 3.39 C. R. Black, D. M. Andrauskas, G. F. de la Fuente and H. R. Verdún, *Laser Heated Pedestal Growth of Nd-Doped Oxide Crystals for Diode Pumping*, Proc. SPIE, **1104**, 175, 1989
- 3.40 R. Burlot, M. Ferriol, R. Moncorgé and G. Boulon, *Li<sub>2</sub>O evaporation during the laser heated pedestal growth of LiTaO<sub>3</sub> single-crystal fibers*, Eur. J. Solid State Inorg. Chem., **t.35**(1), 1, 1998
- 3.41 P. N. Moar, S. T. Huntington, J. Katsifolis, L. W. Cahill, A. Roberts and K. A. Nugent, *Fabrication, modeling, and direct evanescent field measurement of tapered optical fiber sensors*, J. Appl. Phys., **85**(7), 3395, 1999
- 3.42 I. K. Ilev and R. W. Waynant, *Uncoated hollow taper as a simple optical funnel for laser delivery*, Rev. Sci. Instrum., **70**(10), 3840, 1999
- 3.43 M. M. Fejer, G. A. Magel and R. L. Byer, *High-speed high-resolution fiber diameter variation measurement system*, Appl. Opt., **24**(15), 2362, 1985
- 3.44 G. A. Magel, D. H. Jundt, M. M. Fejer and R. L. Byer, *Low-loss single crystal sapphire optical fibers*, Proc. SPIE, **618**, 89, 1986
- 3.45 H. K. Lee, *Final Year Project Report*, University of Glasgow, 1998
- 3.46 E. Miller, *Final Year Project Report*, University of Glasgow, 1998
- 3.47 W. Lee, *Final Year Project Report*, University of Glasgow, 1998
- 3.48 B. T. Lim, *Final Year Project Report*, University of Glasgow, 2000
- 3.49 J. L. Nightingale, *PhD Thesis*, Stanford University, 1985
- 3.50 V. Evtuhov and J. K. Neeland, *Pulsed Ruby Lasers in: Lasers Vol. I*, A. K. Levine (Ed.), Edward Arnold, London, 1, 1966
- 3.51 G. N. van den Hoven, E. Snoeks, A. Polman, C. van Dam, J. W. M. van Uffelen and M. K. Smit, *Upconversion in Er-implanted Al<sub>2</sub>O<sub>3</sub> waveguides*, J. Appl. Phys., **79**(3), 1258, 1996
- 3.52 A. Polman, *Erbium implanted thin film photonic materials*, J. Appl. Phys., **82**(1), 1, 1997
- 3.53 R. Serna and C. N. Afonso, *In situ growth of optically active erbium doped Al<sub>2</sub>O<sub>3</sub> thin films by pulsed laser deposition*, Appl. Phys. Lett., **69**(11), 1541, 1996
- 3.54 C. E. Chryssou and C. W. Pitt, *Er<sup>3+</sup>-doped Al<sub>2</sub>O<sub>3</sub> Thin Films by Plasma-Enhanced Chemical Vapor Deposition (PECVD) Exhibiting a 55-nm Optical*

- Bandwidth*, IEEE J. Quant. Electron., **34**(2), 282, 1998
- 3.55 K. A. Ritley and C. P. Flynn, *Growth of b-axis rare earths on sapphire by molecular beam epitaxy*, Appl. Phys. Lett., **72**(2), 170, 1998
- 3.56 Y. Shen, Y. Wang, L. YE and Z. Ding, *Study on the doped crystal fiber high temperature sensor*, Proc. SPIE, **2292**, 421, 1994
- 3.57 Z. Zhang, J. H. Herringer and N. Djeu, *Monolithic crystalline fiber optic temperature sensor*, Rev. Sci. Instrum., **68**(5), 2068, 1997
- 3.58 L. Tong, Y. Wang and Z. Ding, *Growth and characterisrics of Y-ZrO<sub>2</sub> SCF for high-temperature optic sensors*, Proc. SPIE, **2292**, 429, 1994
- 3.59 L. Tong, Y. Shen, L. Ye and Z. Ding, *A zirconia single-crystal fiber-optic sensor for contact measurement of temperatures above 2000 °C*, Meas. Sci. Technol., **10**, 607, 1999

## **Chapter 4 –Fibre Characterisation and Experimental Techniques**

### **4.0 Introduction**

### **4.1 Fibre diameter measurements**

4.1.1 Diameter measurement experiment

4.1.2 Results and Discussion

### **4.2 Loss measurements and scattering losses**

4.2.1 Experiment on loss measurements

4.2.2 Results and Discussion

### **4.3 Coupling of sapphire to silica fibres**

4.3.1 Experiment

4.3.2 Results and Discussion

### **4.4 Absorption spectra measurements**

4.4.1 Experiment

4.4.2 Results and Discussion

### **4.5 Fluorescence spectra measurements**

4.5.1 Experiment

4.5.2 Results and Discussion

### **4.6 Fluorescence lifetime measurements**

4.6.1 Experiment

4.6.2 Results and Discussion

### **4.7 References to Chapter 4**

## Chapter 4 – Fibre Characterisation and Experimental Techniques

### 4.0 Introduction

The crystal fibres produced using the laser heated pedestal growth technique include pure *a*- and *c*-axis sapphire, Cr<sup>3+</sup>-doped sapphire, singly doped Er<sup>3+</sup>:Al<sub>2</sub>O<sub>3</sub>, Er<sup>3+</sup>:Yb<sup>3+</sup>:Al<sub>2</sub>O<sub>3</sub> with equal concentrations of Er<sup>3+</sup> and Yb<sup>3+</sup>, and Yb<sup>3+</sup>:Er<sup>3+</sup>:Al<sub>2</sub>O<sub>3</sub> where the ratio Yb<sup>3+</sup> to Er<sup>3+</sup> is approximately 10:1. For sensing applications, these fibres have to be appropriately characterised to obtain the optimum conditions/parameters with which they can be utilised. Several important properties are therefore considered. In particular, doped fibres are expected to exhibit fluorescence hence, a knowledge of the absorption bands/lines is considered paramount to the successful employment of suitable excitation sources with the “correct” excitation wavelengths. The absorption and fluorescence spectra are thus studied. Further, the fluorescence lifetime decays of the doped fibres are measured since they are generally independent of the excitation intensity fluctuations and are thus advantageous when used in fluorescence-based fibre optic sensing. Pure Al<sub>2</sub>O<sub>3</sub> fibres have been measured for diameter variations, too large of which will render these fibres unsuitable since transmission losses incurred will be too large. In addition, since the crystal fibres grown are typically below 220 mm in length, it has been considered useful to find suitable means of coupling them to longer delivery/collection silica fibres. For this investigation, only pure sapphire fibres are used. Losses due to scattering and absorption are also studied for ruby fibres while the absorption of the rare earth-doped fibres are considered to be too large for any transmission measurements to be made. The various experimental techniques detailed in this work have been selected for simplicity, cost-savings and relatively good accuracy.

### 4.1 Fibre diameter measurements

Diameter variations are an important factor which can ultimately determine the usability of the fibres. Various techniques have been proposed and demonstrated for dynamic and stationary measurement of fibre diameters, many of which involve

scanning a laser beam transversely across the fibre axis [4.1, 4.2, 4.3, 4.4, 4.5, 4.6, 4.7]. The principles which can be employed include forward light scattering [4.2, 4.6], in which the fringe period measured from the resulting interference fringes produced is proportional to the fibre diameter, the shadow pulse method by measuring the time interval in which a shadow is cast onto the detector in the presence of a fibre [4.1, 4.4], and by measuring the natural birefringence of crystals to extract the diameter information [4.7]. Some of these methods can also be adopted for measuring the diameters of as-grown fibres with relative ease. One of the techniques, the shadow count technique [4.1, 4.4], has been investigated in this work (**Chapter 3**) and is currently under further development for future integration into the fibre growth system. For a quick reference of the diameters of fibres already grown, however, a simple method has been used and is described in the following experiment. Measurement of the diameters will thus give an approximation of the diameter uniformity and general geometrical quality of the fibres produced by LHPG.

#### **4.1.1 Diameter measurement experiment**

The diameters of several LHPG sapphire fibres have been measured in order to have an idea of the percentage variation. A schematic of the simple fibre diameter measurement method used is shown in **Figure 4.1**. The system was first calibrated against a known linear scale using the eye-piece (*J. Swift & Son*) and graticule (*GRATICULES LTD*) technique [4.5] in conjunction with an optical microscope. A X20 planar microscope objective has been used throughout all the measurements. The 1 mm linear scale of the graticule was divided into 100 small divisions while the eye-piece worked in a similar fashion to a micrometer head, with 100 divisions per rotation of the spindle. Thus, for calibration purposes, a reference start position was chosen and the readings on both graticule ( $L_1 \mu\text{m}$ ) and eye-piece ( $n_1$  division) were taken. The eye-piece was then rotated through a certain linear translation distance to obtain  $L_2 \mu\text{m}$  at  $n_2$  divisions, resulting in a calibration scale factor, *CSF*, which can be given as

$$CSF = \left( \frac{L_2 - L_1}{n_2 - n_1} \right) \quad (4.1)$$

with a unit of  $\mu\text{m}/\text{division}$ . The fibre diameter can then be accurately determined by multiplying the number of divisions obtained from translating the eye-piece measuring arm from one edge of the fibre to the other edge by the *CSF*. The reading error of the system arising from the slightly out of focus image of the fibre edges was estimated to be  $\pm 5$  divisions.

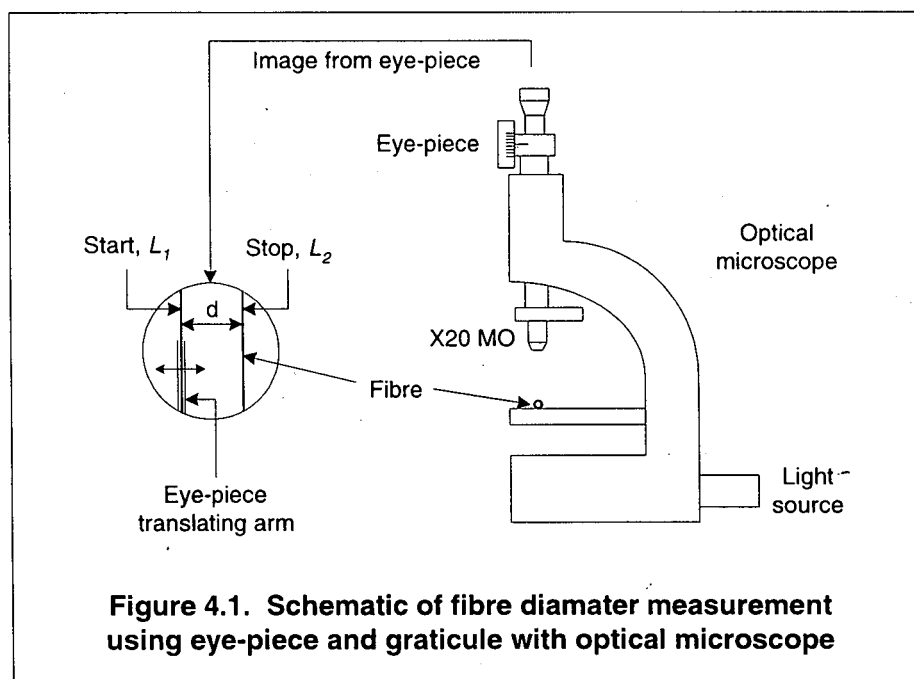


**Figure 4.1. Schematic of fibre diameter measurement using eye-piece and graticule with optical microscope**

### 4.1.2 Results and Discussion

A simple and relatively fast method has been used to measure the diameters of LHPG sapphire fibres in order to have an idea of the percentage variation of the diameter along the fibre length. In most cases, the maximum variations have been found to be  $\sim 2\%$  or less, indicating that good dimensional uniformity can be obtained even when crystal growth was performed under "quasi-closed-loop" conditions without active diameter monitoring and feedback. One example of the diameter variation of a *c*-axis sapphire fibre grown from a  $325\ \mu\text{m}$  source rod has already been shown in **Chapter 3**. With a reading error of  $\pm 5$  divisions from the eye-piece, average experimental errors in the region of  $1 - 2\%$  have been obtained. **Figure 4.2a** illustrates another example of a  $130\ \mu\text{m}$  *c*-axis  $\text{Al}_2\text{O}_3$  fibre, showing a relatively large maximum deviation from the mean diameter. This could be linked to the vibration or perturbation of the rather flexible source rod during growth. **Figure 4.2b** shows diameter measurement of an *a*-axis  $\text{Al}_2\text{O}_3$  fibre. It can be seen from this figure that inaccuracies and errors would inevitably arise due to the inherent non-symmetric cross-section of *a*-axis fibres. **Table 4.1** lists the diameter variations of some measured fibres together with their statistical data. It should also be noted that *c*-axis sapphire fibres of small diameters have rounded hexagonal cross-sections, rather than circular sections. Monitoring of *a*-axis fibres and, to a lesser extent, *c*-axis ones will thus present a certain level of difficulty when active diameter monitoring schemes are employed at a later stage.

Figures 4.2. Diameter variations of c- and a-axis sapphire fibres

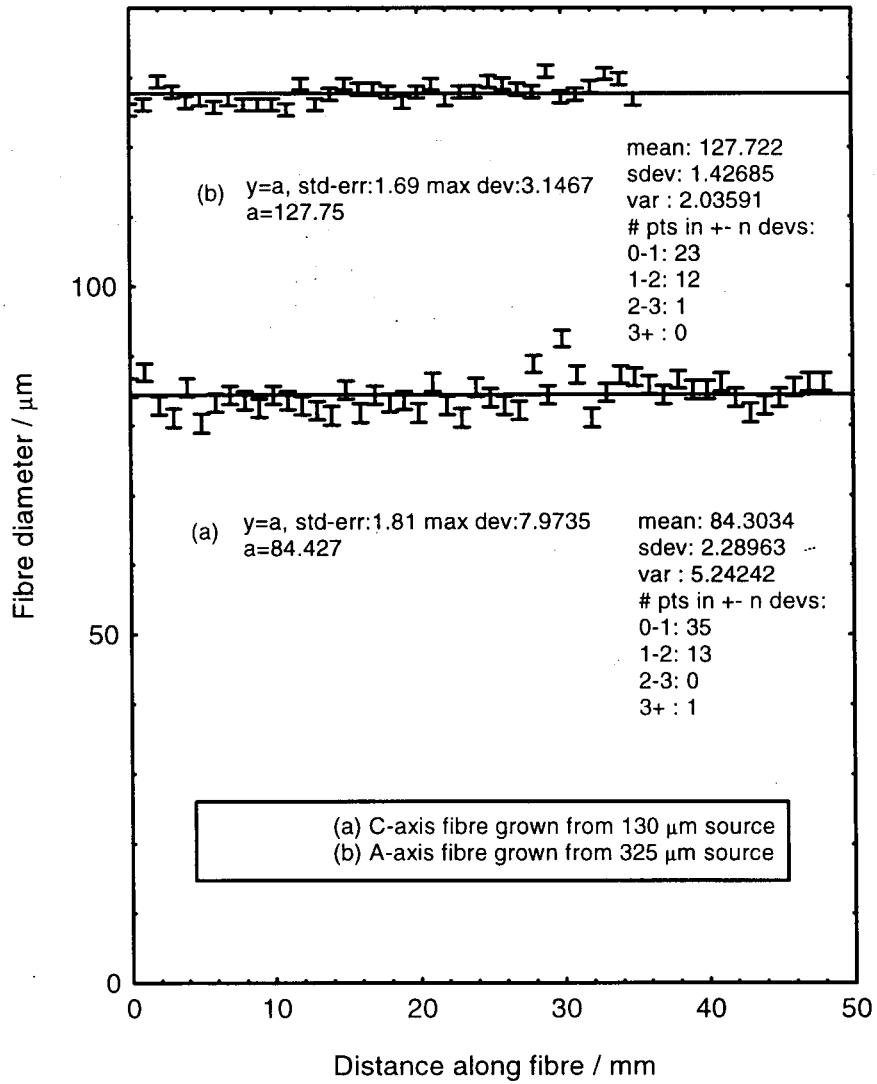


**Table 4.1. Diameter variation of sapphire fibres (*c*- and *a*-axes)**

Fibre type	Source dia. / $\mu\text{m}$	R/r	Measured dia. / $\mu\text{m}$	Std. Dev. / %	Max. Dev. / %
<i>c</i> -axis	130	1.5	84.30	2.72	4.75
<i>a</i> -axis	325	2.5	127.72	1.12	1.82
<i>c</i> -axis (from Chapter 3)	325	2.5	121.35	0.45	2.03

### 4.3 Loss measurements and scattering losses

Since the optical transmission properties of pure sapphire fibres have already been reported, investigations are only carried out for ruby fibres in this work in order to provide an estimate of the losses due to absorption and scattering losses due primarily to the diameter variations. This will also present indirect indications of the  $\text{Cr}^{3+}$  doping concentration level in the as-grown ruby fibres. Three lasers have been used in this investigation, two of whose wavelengths are selected to be strongly absorbed by ruby so that the absorption losses,  $\alpha$ , can be estimated. The third laser has been selected so that it is generally free from absorption by the ruby samples hence, such losses ( $\beta$ ) are assumed to arise from scattering effects due to diameter variations along the fibre. It should be noted that loss measurements at the strongly absorbed wavelengths resulted in total losses ( $\alpha + \beta$ ) from the fibres. By measuring  $\beta$  at the wavelength where absorption is assumed to be negligible, the losses due to absorption,  $\alpha$ , can, in turn, then be inferred.

#### 4.2.1 Experiment on loss measurements

The schematic experimental set-up is shown in **Figure 4.3**. Collimated laser light was focused by a microscope objective (X20 MO) and directed into the entrance port of a 67 mm *Melles Griot* integrating sphere (IS) to obtain the input intensity. Appropriate optical filters corresponding to the respective laser wavelengths have been employed to block any induced fluorescence signal being measured as well as to reduce any erroneous signals due to background noise. Lock-in detection has been used to enhance the signal-to-noise ratio, resulting in stable and relatively noise-free signals arriving at the photodetector where this input intensity was measured and denoted as  $I_{in}$ . A ruby fibre was then positioned in the entrance port in such a way that its end was just protruding into the IS, while light from the laser was coupled into the other end of the sample. The transmitted intensity was then recorded as  $I_{out}$ . Repeated measurements were then taken for each sample and averaged. The two absorption wavelengths selected for this study were obtained from a 500 mW diode-pumped frequency-doubled YAG laser ( $\lambda \sim 532\text{nm}$ ) and a 3 mW laser diode module

at  $\lambda \sim 633$  nm. An absorption-free wavelength at 783 nm was obtained from a 5 mW laser diode module.

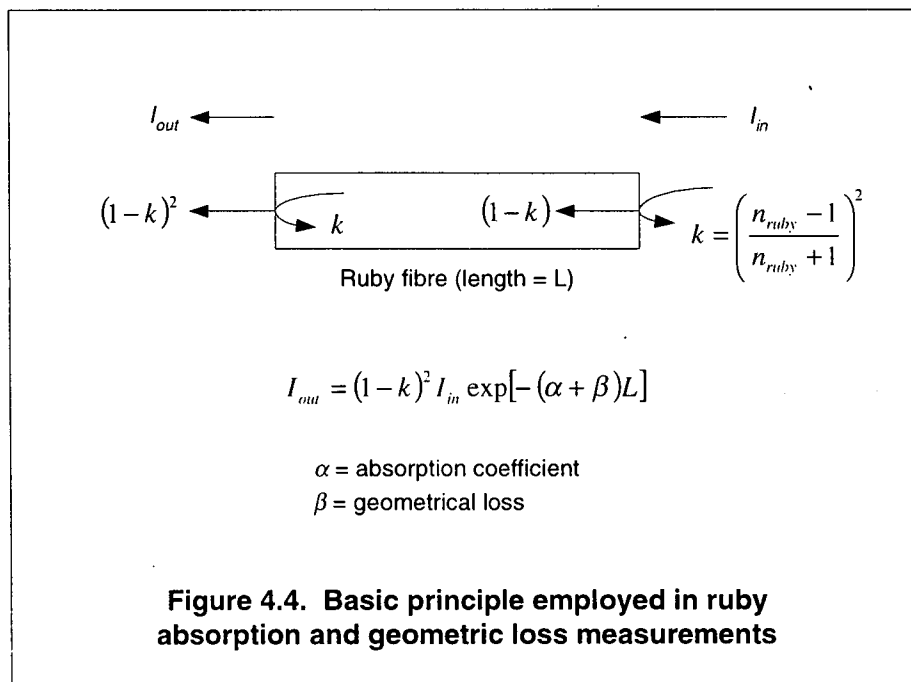
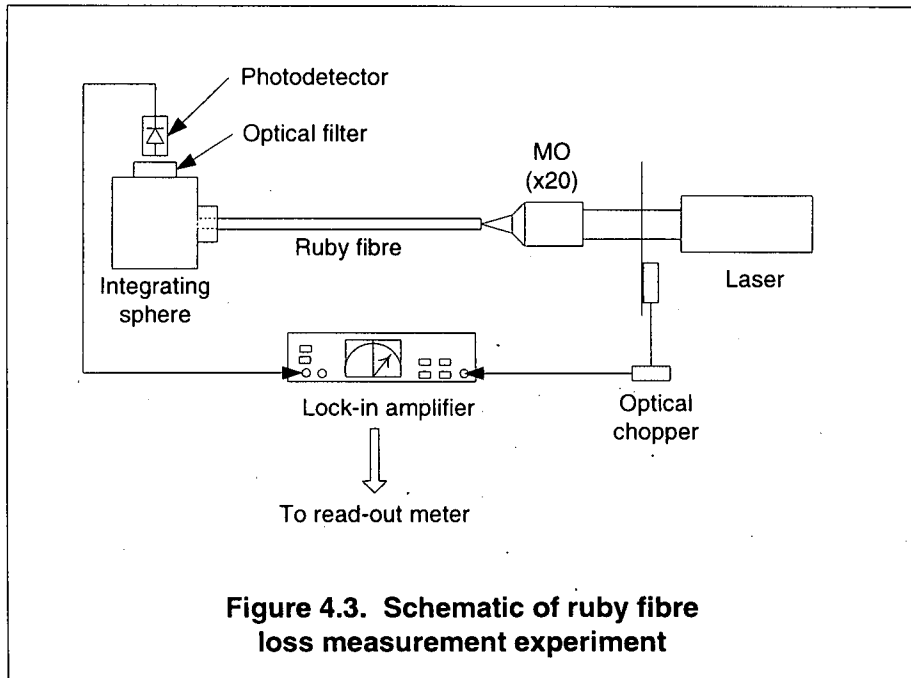
The basic principle behind this measurement technique is illustrated in **Figure 4.4**, in which losses in the fibre due to absorption ( $\alpha$ ) and scattering or geometric losses ( $\beta$ ) can be obtained from the following expression

$$I_{out} = (1 - k)^2 I_{in} \exp[-(\alpha + \beta)L] \quad (4.2)$$

where  $I_{out}$  is the output intensity from the fibre end entering the VS,  $I_{in}$  the beam intensity entering the fibre,  $L$  the length of the fibre. The reflectance at normal incidence,  $k$ , is simply given by

$$k = \left( \frac{n_{ruby} - 1}{n_{ruby} + 1} \right)^2 \quad (4.3)$$

where  $n_{ruby}$  is the refractive index of ruby (taken as 1.76). Note that although ruby is doubly refractive, the ordinary ( $n_o$ ) and extraordinary ( $n_e$ ) refractive indices are identical along the  $c$ -crystallographic axis.



#### 4.2.2 Results and Discussion

Results for two ruby fibres, a diameter 140  $\mu\text{m}$  18 mm long sample (denoted as *Spec11*) and another with a diameter of 87  $\mu\text{m}$  and 25.5 mm in length (*Spec19*), are shown in **Tables 4.2** and **Table 4.3** respectively. *Spec11* has been grown from an approximately 425  $\mu\text{m}$  source rod at a pull rate of 0.5 and diameter reduction ratio of 3. *Spec19*, however, was pulled from a much smaller source rod ( $\sim 130 \mu\text{m}$ ) at a rate of 0.2 mm/min together with a smaller diameter reduction ratio (1.45). A very obvious layer of brownish-green deposit has been observed on the surface of *Spec11*. Loss measurements were first made on this ruby sample without any cleaning. The fibre was later cleaned with hydrochloric (HCl) acid and left to soak in an ultrasonic bath of acid for approximately 24 hours before a second measurement was carried out. Results for both measurements before and after cleaning are presented in **Tables 4.2a** and **4.2b** respectively. No deposits have been found on *Spec19*. The surface appeared to be transparent and unblemished, both from large-scale diameter variation and deposits, hence, no further cleaning with solutions other than acetone was thought to be required. Absorption measurements have been carried out as described above and the corresponding losses are shown in **Table 4.3** for all three laser wavelengths employed (783 nm, 633 nm and 532 nm).

It can be seen from the results for both samples that the largest absorption losses occurred at a wavelength of 532 nm which corresponds almost exactly to one of the absorption peaks of ruby (at  $\sim 550 \text{ nm}$ ) as shown later. At 783 nm, a wavelength which is not known to be highly attenuated by ruby, losses are presumed to be those due to scattering effects only. These are classified as geometrical losses in this work and have been considered to be largely a function of the fibre diameter variations. It is a reasonable assumption since crystalline fibres with small dimensional geometry are found to contain very little grain boundary and dislocation density defects within their structures [4.8]. Most losses in such a case can thus be directly attributed to scattering effects arising from non-uniform or uneven fibre surfaces. At all three wavelengths studied, the measured absorption and geometrical losses have been found to be highest in *Spec11*. Losses for this sample before and after cleaning with HCl acid varied only slightly, as shown in **Tables 4.2a** and **4.2b**, suggesting that the

brownish-green deposits were not merely particles condensing on the fibre surface. On the contrary, the  $\text{Cr}_2\text{O}_3$  particles condensed and deposited on the crystallising ruby fibre may have been oxidised onto or beneath its surface due to the intense heat generated during LHPG. The reason why this layer of deposit has not been observed on the smaller *Spec19* may be due to the slower pull rate used, thus allowing sufficient time for most of the chromium oxide coating layer to be diffused into the melt. The losses obtained in this work, however, can be seen to compare relatively well with those obtained by Jundt *et al.* [4.9] on crystal fibres and loss figures obtained from channel or planar waveguides [4.10].

**Table 4.2a. Absorption loss for *Spec11*  
(without acid cleaning)**

$\lambda / \text{nm}$	$\alpha / \text{cm}^{-1}$	$\beta / \text{dB cm}^{-1}$
783	-	4.81
633	0.21	4.81
532	2.97	4.81

**Table 4.2b. Absorption loss for *Spec11*  
cleaned with acid**

$\lambda / \text{nm}$	$\alpha / \text{cm}^{-1}$	$\beta / \text{dB cm}^{-1}$
783	-	4.57
633	0.13	4.57
532	2.94	4.57

**Table 4.3. Absorption loss for *Spec19*  
without HCl acid cleaning**

$\lambda / \text{nm}$	$\alpha / \text{cm}^{-1}$	$\beta / \text{dB cm}^{-1}$
783	-	1.61
633	0.06	1.61
532	0.6	1.61

### 4.3 Coupling of sapphire to silica fibres

Some consideration has been given to the delivery of excitation light to and collection of signals from the crystalline fibres studied in this work. Some means should be found to enable light to be easily delivered to the sensing probe made of various crystalline materials. Collection of the resulting signals from the crystal fibres, which have been modified by the intended measurand(s) should also be a relatively simple and straightforward process.

Since crystal fibres, such as sapphire and YAG, are generally expensive and cannot be produced in lengths rivalling those of glass-based fibres, one potential way of avoiding high costs is to use a conventional silica fibre to couple to the sensing crystal fibre. A quick and easy way is to simply butt-couple the two and hold them together securely using a sleeve and adhesives as shown in **Figure 4.5a**. The sleeve material, its size and the adhesives to be used have to be carefully selected depending on the type of application. In the case of high temperature sensing beyond 1300 K, the range of materials is severely limited commercially. Another way of joining the two fibres is to fusion splice them together, resulting in a permanent coupling (**Figure 4.5b**). It should be noted that although silica melts at ~1950 K, it can only be practically employed up to ~1300 or 1400 K (near its annealing temperature and within the transition/softening temperature) under short-term exposure to such environments.

#### 4.3.1 Experiment

Investigations into the feasibility of coupling two dissimilar fibres have been carried out on pure sapphire and conventional silica fibres. The properties of these two materials considered most relevant to this study are listed in **Table 4.4**, showing the considerably large dissimilarities between the two. A schematic of the butt-coupling experiment is shown in **Figure 4.6**. Light at 633 nm from a 3 mW laser diode was focused onto one end of a 200  $\mu\text{m}$  *Thorlabs* FVP-200-PF silica fibre. The other end, held by a fibre chuck, has been positioned into the *Melles Griot* integrating sphere in such a way that only the end protruded into the sphere and the intensity was recorded. The sapphire fibre (~35 mm long and 170  $\mu\text{m}$  in diameter) used for this

test was held by a *Melles Griot* x-y-z positioning stage which, in turn was attached to a rotation stage, effectively providing a 4-axis alignment capability. It was then aligned co-linearly with the longitudinal axis of the silica fibre and carefully brought into contact with it. In a similar fashion, the crystal fibre has been positioned inside the sphere such that only the end section protruded into the sphere and the transmitted intensity from this coupling is then measured. The principle behind this experiment is almost identical to that used for measuring fibre losses (**Eq. 3.2** in **Section 4.2**) except that, in this case, there is no loss due to absorption ( $\alpha$ ) since sapphire is transparent from  $\sim 0.24$  to  $4 \mu\text{m}$  [4.9]. All the losses have been assumed to be due only to scattering and coupling losses. However, total losses would be dominated by the fibre coupling and insertion losses (denoted as the total coupling losses for simplicity) due to the mismatch in properties of the two materials while scattering effects could become significant if large diameter variations were present.

Efforts have been made to permanently splice both sapphire and silica fibres together, as illustrated in **Figure 4.5b**, since it would present a more robust coupling. A commercial fusion splicer and the  $\text{CO}_2$  laser have been employed to provide the heat source. However, after numerous attempts, it was found to be almost impossible to splice the two materials together without the joint/interface being mechanically extremely fragile. The sapphire fibres ( $\sim 170 \mu\text{m}$ ) have been selected to match, as closely as possible, the silica fibre diameter ( $\sim 200 \mu\text{m}$ ), but, the large difference in their thermal expansion coefficients and melting points, always resulted in silica fibres being melted first. During arcing (fusion) of the splicing machine, contraction of the silica fibre pulled the glass material at the tip back into a mini-dome while slight damages to the tip of the sapphire fibre was observed. The arcing temperature was always found to be too high for the silica fibre and not sufficient enough to melt the sapphire fibre. A photograph of an end-damaged sapphire fibre is shown in **Figure 4.7**. Concurrently, splicing has also been attempted in the LHPG chamber using a  $\text{CO}_2$  laser. The silica fibre was attached to the feed stage while the sapphire fibre was fixed to the pulling stage. The laser was then used to heat the silica fibre until a rounded tip was formed, supplying just enough power to maintain this shape. The sapphire fibre has to be lowered quickly, at this stage, into the quasi-molten pool of silica to avoid too much heat being transmitted to the top section of

the silica fibre. This would result in "melt-back" of the silica. Once dipped into the silica pool, the viscous glass material was observed to wet the nominally smaller sapphire fibre by surface tension. Once this has been achieved, the laser power was slowly reduced over a period of time at constant intervals ( $\sim 1/2$  hr intervals) until the splice/joint has cooled to the surrounding temperature. This relatively time-consuming procedure has been adopted to prevent overcooling of the newly-formed fusion splice, which would otherwise result in instant fracture of the joint due to the different thermal coefficients of the two materials. A splice fabricated using this technique is shown in **Figure 4.8**. Losses from this type of coupling were estimated by first measuring the transmitted light intensity of the silica fibre and later with the sapphire fibre spliced onto the silica. The light coupling efficiency between the microscope objective and silica fibre is assumed constant before and after splicing. Results of the losses due to both butt-coupling and fusion splicing are shown in **Table 4.5**.

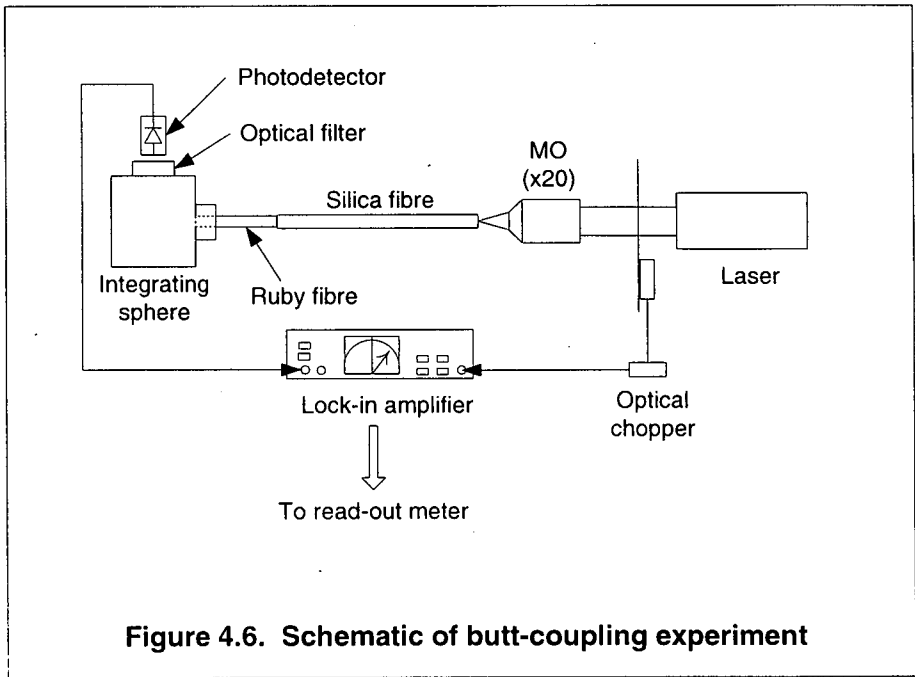
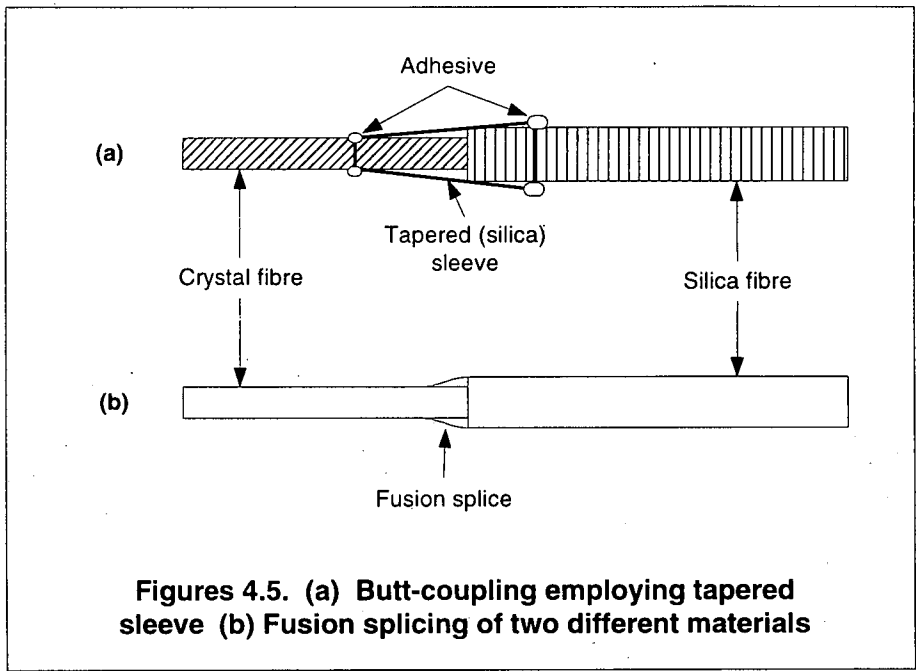


**Table 4.4. Properties of sapphire and silica**

Properties \ Materials	Al <sub>2</sub> O <sub>3</sub>	SiO <sub>2</sub>	Fused SiO <sub>2</sub>
Thermal expansion $\alpha$ (293-1273 K) / K <sup>-1</sup>	5.8 x 10 <sup>-6</sup>	0.5-0.75 x 10 <sup>-6</sup>	0.54 x 10 <sup>-6</sup>
Thermal conductivity at 293 K / Wm <sup>-1</sup> K <sup>-1</sup>	41.9	1.2-1.4	1.46
Specific heat C <sub>v</sub> at 298 K / JK <sup>-1</sup> kg <sup>-1</sup>	753	750	670-740
Melt temperature / K	2323	1950	1950
Refractive index	1.765	1.46	1.46
Upper continuous use temperature / K	2073-2223	<1373	1373
Transmission / $\mu$ m	0.24-4.00	-	0.38-2.5

### 4.3.2 Results and Discussion

Results from the two types of coupling indicate a relatively significant difference between them. For the purpose of comparison, the same set of silica and sapphire fibres used for butt-coupling has been employed in fusion-coupling studies. The losses from fusion splicing sapphire to silica are considerable compared to that from butt-coupling and can be attributed mainly to the mis-match of thermal properties between the two materials. As listed in **Table 4.4**, the melting point of sapphire is  $\sim 2320$  K while silica melts at  $\sim 1950$  K. With a lower thermal conductivity in silica, this implies that much of the heat will not be easily conducted away and at the temperature which has been used during the fusion splicing process, the intense heat will lead to quicker melting of the silica fibre tip. Upon cooling, the different expansion coefficients, densities, conductivity and fundamental dissimilarities of the two materials will inherently lead to the building up of high levels of stress in the critical joint area, which, in turn, may lead to hairline cracks, grain boundary and density defects being formed. It can be seen from **Figure 4.8** that the silica fibre was "wrapped" around the end of the sapphire fibre, resulting in an obvious thickening at the joint. Parts of the internal structure can also be seen containing hairlines originating from the body of the joint and spreading out to the two fibres. These have been interpreted as line cracks which would reduce the integrity of the joint and its adjacent regions. The resulting joint was found to be very fragile and removing both fibres from the growth chamber turned out to be highly delicate. Several splices have been broken during this process. Moreover, the large difference in refractive indices between sapphire and silica will result in much reflection of the propagating light from the sapphire interface. Large optical scattering losses then occur when light is transmitted through this silica/sapphire fibre, particularly at the splice.

In addition to the above disadvantages, the very brittle nature of the joint also serves to dissuade one from using this coupling technique in fibre optic sensing applications. The butt-coupling technique has been adopted throughout this project when coupling between the sensing crystalline probe and conventional silica fibre was required. Using a silica sleeve, the larger silica fibre was first inserted. Next, the sapphire fibre was carefully inserted into the other free end and butted against the silica fibre. To secure the two fibres, adhesives can then be applied to both ends of

the sleeve while at the same time ensuring that the fibres are still butted against each other.

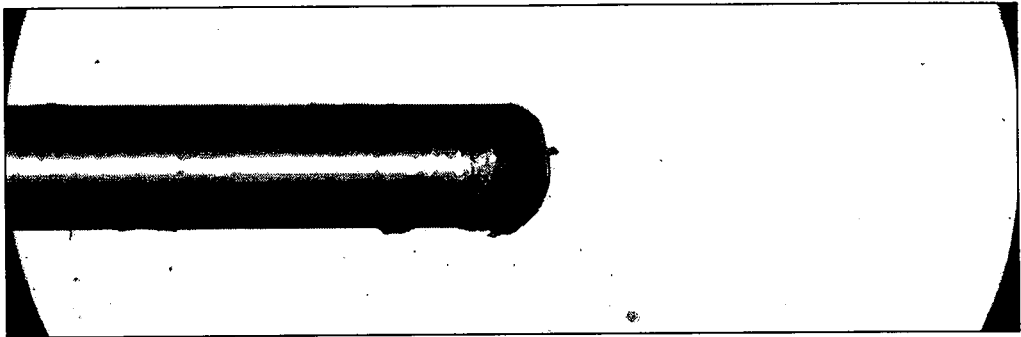


**Figure 4.7. Damage incurred to end of sapphire fibre subjected to fusion splicing**

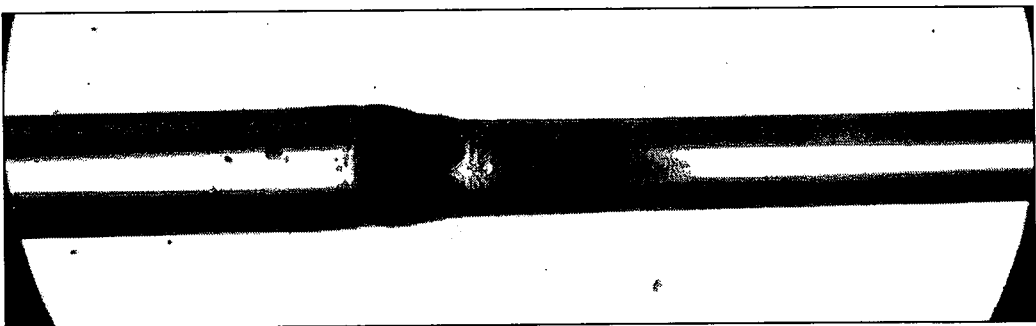


**Figure 4.8. Splicing of sapphire to silica fibres using CO<sub>2</sub> laser**

**Table 4.5. Losses due to coupling between sapphire and silica fibres**

Coupling type	Butt coupling	Fusion splicing (with CO <sub>2</sub> laser)
Fibre length / cm		3.5
Laser wavelength / nm		633
Refractive index		1.76
$I_{in}$	6.80	(6.80)
$I_{out}$	3.18	0.95
Total losses / dB	2.61	7.88
Losses / cm <sup>-1</sup>	0.17	0.52

## 4.4 Absorption spectra measurements

The measurement of absorption bands of the doped crystal fibres, in the visible and IR ranges, enables the determination of appropriate pump wavelengths to be used for inducing fluorescence emission from these fibres. A laser source with an emission wavelength near the peak absorption wavelength of the doped material was most generally selected in order for efficient excitation of the active dopants incorporated in such fibres.

### 4.4.1 Experiment

A schematic of the absorption experiment is shown in **Figure 4.9**. Broadband light from a stabilised *Schott* KLT-1500-T lamp, with wavelengths spanning from below ~400 nm to beyond ~1700 nm, has been used as the probe beam. The output from this source is collimated with a pair of lenses and focused onto one end of the doped fibre with a microscope objective (MO). Light exiting the fibre from the other end is collected by another MO, collimated and then focused onto the entrance slit of a DIGIKRÖM DK480 monochromator (*CVI Laser Corporation*) via a lens selected to closely match the  $f$ -number of the machine. The entrance and exit slit widths of the monochromator are set at 200  $\mu\text{m}$  or less during the experiment while the scan steps used are 0.5 nm per step. For the visible wavelength range, a simple silicon PIN photodetector or a *Hamamatsu* photomultiplier tube (PMT) has been used while detection in the IR range employed a *New Focus, Inc.* M2153 InGaAs photodetector. An optical chopper has also been used in conjunction with a *Sci-Tech* lock-in amplifier to enable a high signal-to-noise ratio for stable and accurate detection of any weak incoming signals. Data acquisition and remote control of the monochromator are performed by a dedicated computer using Labview software.

Certain wavelength regions of the broadband light are absorbed by active dopants when transmitted through the fibre and the absorption spectra can be determined by monitoring the transmitted light throughout the broadband wavelength range. A typical spectrum from the KLT-1500-T lamp is shown in **Figures 4.10a** (visible) and **4.10b** (IR). The reduction in the intensity along certain wavelength range is thus an indication of the absorption lines/bands of the various doped materials. The

transmitted intensity through a doped fibre can then be divided by the reference light intensity, measured when no fibre was present, to obtain the desired absorption spectra (visible and IR).

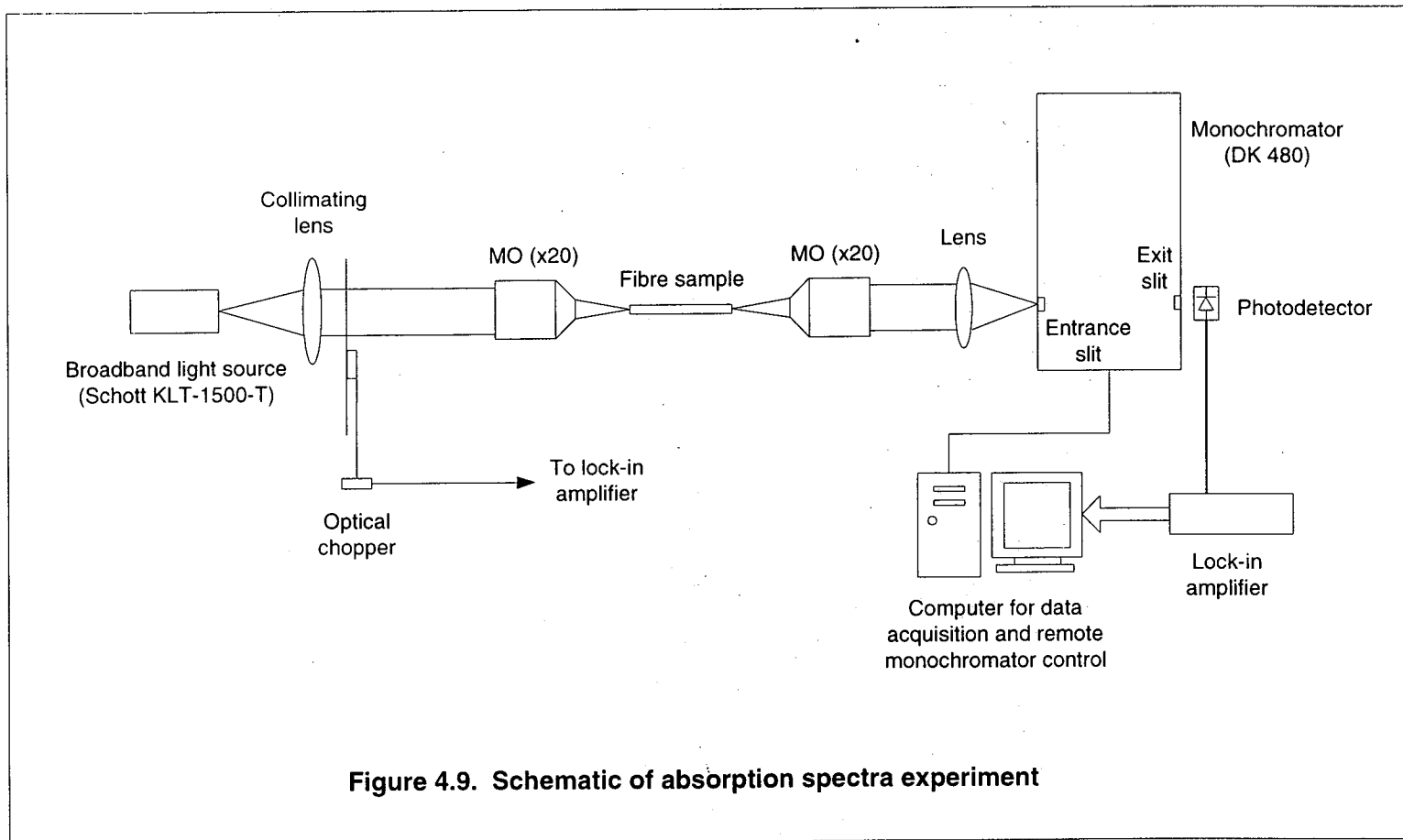


Figure 4.9. Schematic of absorption spectra experiment

Figure 4.10a. Visible spectrum of Schott KLT-1500-T lamp

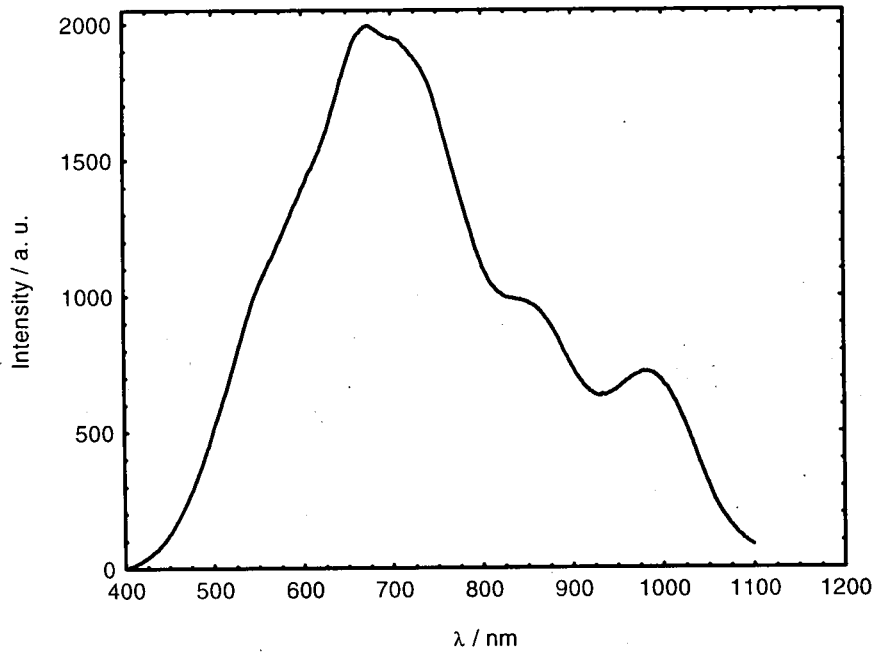
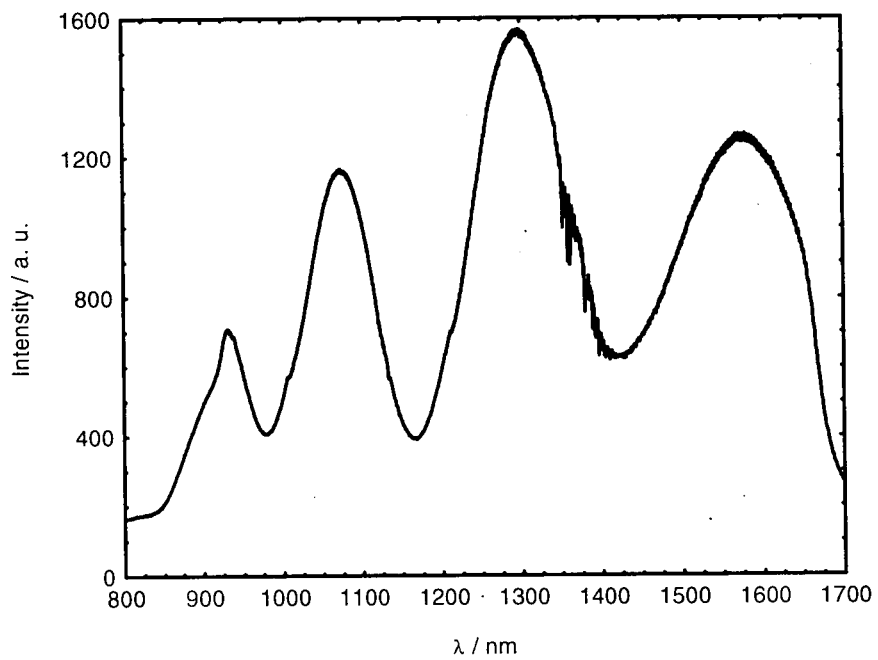


Figure 4.10b. IR spectrum of KLT-1500-T lamp



#### 4.4.2 Results and Discussion

Results have been obtained for all the doped fibres investigated in this study.  $\text{Cr}^{3+}:\text{Al}_2\text{O}_3$  (ruby) fibres have been found to exhibit absorption over a wide spectral range in the visible, while RE-doped sapphire fibres were found to absorb at several narrow spectral bands in the visible and IR regions.

The visible absorption spectrum of ruby fibres is presented in **Figure 4.11**. A very broad absorption range can clearly be seen, spanning from approximately 380 – 700 nm. This corresponds to the strong  $\text{Cr}^{3+}$  interaction with the crystal field and coupling to the crystal lattice of the host material, as is the case for most transition metal ions in general [4.11, 4.12, 4.13, 4.14, 4.15, 4.16]. This spectrum agrees very well with published data [4.17, 4.18]. In addition, two broad peaks with a bandwidth of ~100 nm and centred at ~410 and 550 nm are observed. These absorption characteristics are associated with transitions from the ground state,  $^4\text{A}_2$ , to the broad absorption bands of the  $^4\text{F}_1$  and  $^4\text{F}_2$  energy levels in ruby for the observed 410 and 550 nm peaks respectively [4.19].

For rare-earth ions doped in ionic crystals, the shielding of the  $4f$  electrons by complete  $5s^2$  and  $5p^6$  outer shells leads to weak transitions with the crystal field as well as weak coupling to the phonon energies (crystal lattice) of crystal host, hence, the absorption bands are relatively narrow in both the visible and infrared spectral regions [4.20, 4.21]. In the visible absorption spectrum shown in **Figure 4.12a**, seven narrow absorption peaks can be observed in singly  $\text{Er}^{3+}:\text{Al}_2\text{O}_3$  fibres at 514, 516.1, 521.9 and 540.1 nm in the green, and at 643.8, 649 and 653.1 nm in the red. The two strongest absorption peaks in the green occur at 516.1 and 521.9 nm while the red absorption peaks are seen to be relatively weaker. These absorption peaks are typical of  $\text{Er}^{3+}$ -doped materials and have been seen in both  $\text{Er}^{3+}$ -doped silicate glasses, thin films and crystals (such as YAG, YLF and KYF) [4.22, 4.23, 4.24]. They are associated with transitions from the  $^4\text{I}_{15/2}$  ground state to the  $^2\text{H}_{11/2}$  and  $^4\text{S}_{3/2}$  manifolds (green), and the  $^4\text{F}_{9/2}$  manifold (red) in Er-doped materials. The IR absorption spectrum, shown in **Figure 4.12b**, clearly illustrates several relatively strong narrow absorption bands indicated on the figure while two intense peaks can be seen at 1511 and 1529 nm, these corresponding to the well-known  $\text{Er}^{3+}$  transition

from the ground state to the  $^4I_{13/2}$  manifold [4.22, 4.23]. The 970 nm band is also attributed to the  $^4I_{15/2} \rightarrow ^4I_{11/2}$  transition [4.22, 4.23]. Several unknown narrow absorption bands centred around 1160, 1405, 1418, 1423 and 1460 nm can also be seen concurrently. They are attributed to the presence of tiny amounts of other impurities in the erbium oxide powder used during the dip-coating process. However, the band at ~1160 nm is suspiciously close to the  $Er^{3+}$  excited state absorption (ESA) at 1140 nm [4.22] while the bands in the 1460 nm region are rather similar to those observed in  $Er^{3+}$ :YAG [4.24].

Codoped sapphire fibres, with approximately equal concentrations of  $Er^{3+}$  and  $Yb^{3+}$ , have been observed to exhibit broader absorption lines in the visible in comparison to the singly  $Er^{3+}$ -doped fibres. This is due to the presence of  $Yb^{3+}$  which is known to be a very efficient sensitising ion and can lead to slight relaxation of the selection rule due to the very efficient energy transitions between the co-dopants, hence, resulting in additional absorption lines available for pumping [4.25, 4.26, 4.27, 4.28, 4.29]. As indicated in **Figure 4.13a**, various narrow absorption lines can be observed corresponding to the respective spectral regions. The blue absorption peak (487.5 nm) is due to transition from the ground state to the  $^4F_{7/2}$  manifold in  $Er^{3+}$ , the green peaks (517.7 + 524 and 540.6 nm) are a result of ground state absorption to the  $^2H_{11/2}$  and  $^4S_{3/2}$  manifolds respectively while the red absorption peaks arise from the  $^4I_{15/2} \rightarrow ^4F_{9/2}$  transition. The wide absorption bands in the 850 to ~1000 nm region occur due to co-doping with  $Yb^{3+}$  ions and result from the combination of the  $^4I_{15/2} \rightarrow ^4I_{11/2}$  transition from  $Er^{3+}$  and the  $^2F_{7/2} \rightarrow ^2F_{5/2}$  transition in  $Yb^{3+}$ . The IR absorption spectrum is shown in **Figure 4.13b** with only the relevant regions where absorption bands have been observed, indicating strong absorption bands peaking at ~936 and 958 nm respectively. These bands are relatively wide compared to the visible absorption lines and confirm the combined transitions from both  $Er^{3+}$  and  $Yb^{3+}$ . The broad absorption centred at ~1464 nm can also be seen and has been attributed to impurity contamination during the source preparation process. The peaks at 1511, 1523 and 1526 nm are associated with the  $^4I_{15/2} \rightarrow ^4I_{13/2}$  transition in  $Er^{3+}$  [4.22, 4.23].

For codoped fibres with an  $\text{Yb}^{3+}$  to  $\text{Er}^{3+}$  concentration ratio of approximately 10:1, no infrared absorption bands in the 1500 nm region has been observed. This could be due to the presence of very low amounts of  $\text{Er}^{3+}$  in the fibres, resulting in very weak absorption characteristics in this region which were beyond the limit of detection of the system used. The visible absorption spectrum ranging from 400 – 1000 nm is presented in **Figure 4.14** and indicates a relatively strong absorption band with peaks at 910, 931 and 962 nm. Another weaker but broader band centred at ~800 nm can also be observed and is characteristic of  $\text{Yb}^{3+}$  absorption [4.30] due to the  ${}^2\text{F}_{7/2} \rightarrow {}^2\text{F}_{5/2}$  transition. The three peaks in the 900 nm region can be attributed to a combination of the  $\text{Er}^{3+}$  and  $\text{Yb}^{3+}$  transitions from the ground state to their respective absorption bands at the  ${}^4\text{I}_{11/2}$  and  ${}^2\text{F}_{5/2}$  manifolds [4.22, 4.23, 4.25, 4.30]. In addition, no other absorption lines have been observed in the green and red spectral regions of these fibres in comparison to the equally  $\text{Er}^{3+} + \text{Yb}^{3+}$ -codoped  $\text{Al}_2\text{O}_3$  fibres discussed earlier. This again may be due to the presence of the very small amounts of  $\text{Er}^{3+}$  while at the same time implies that the codopant  $\text{Yb}^{3+}$  ions are very efficient absorbers in the 800 – 1000 nm region.

Figure 4.11. Visible absorption spectrum of ruby fibre and bulk ruby crystal

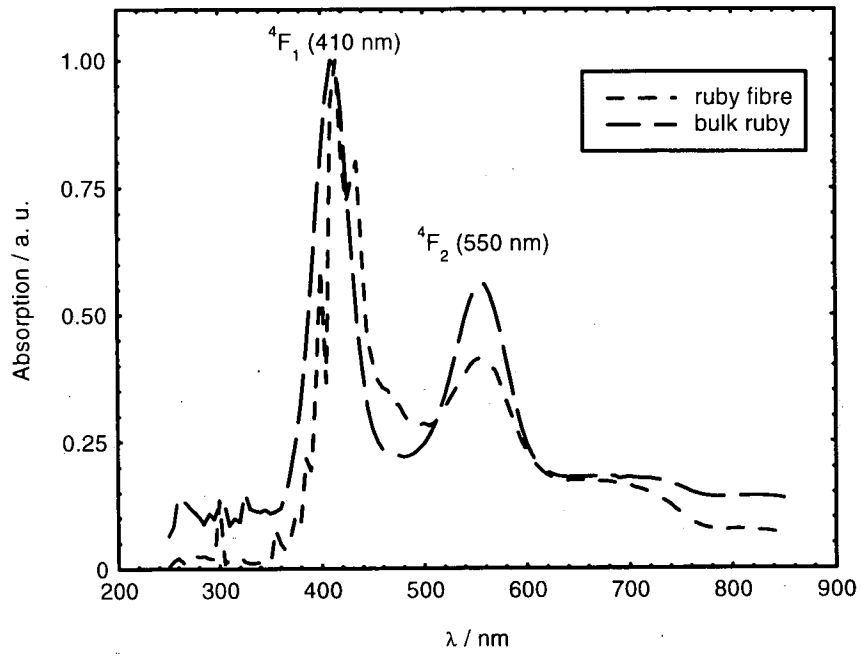


Figure 4.12a. Visible absorption spectrum of  $\text{Er}^{3+}:\text{Al}_2\text{O}_3$  fibre (doped tip)

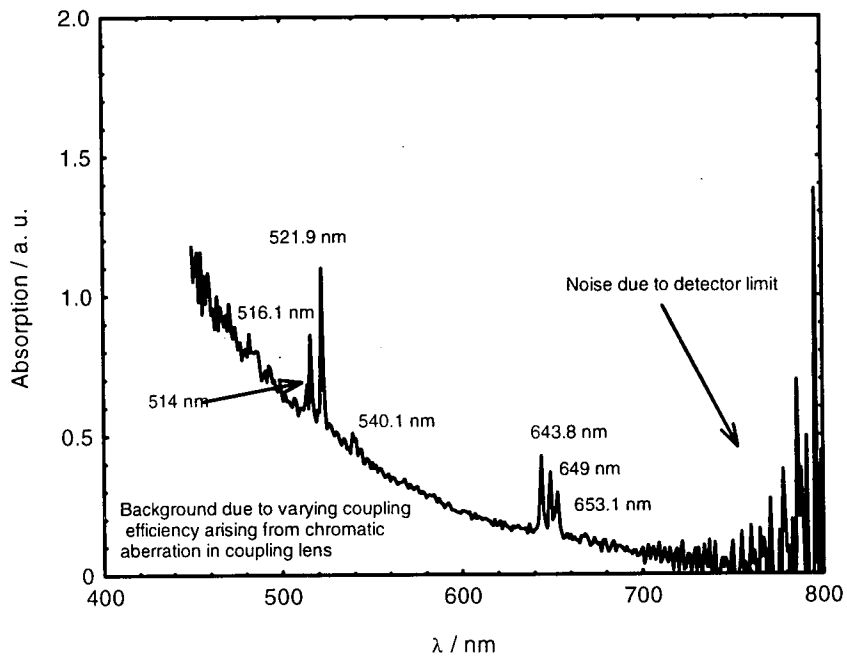


Figure 4.12b. IR absorption spectrum of  $\text{Er}^{3+}:\text{Al}_2\text{O}_3$  fibre (doped tip)

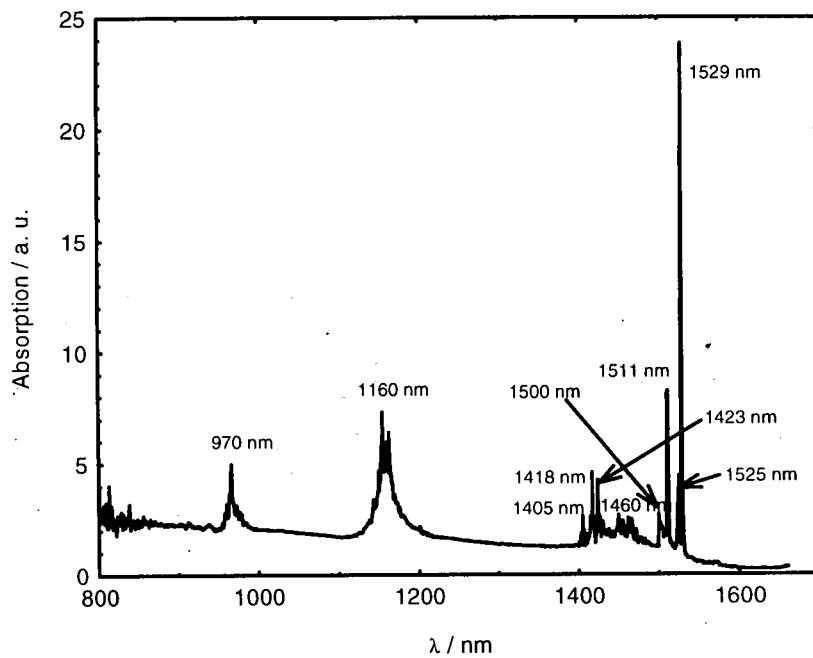


Figure 4.13a. Visible absorption spectrum of  $\text{Yb}^{3+}$ -sensitised  $\text{Er}^{3+}:\text{Al}_2\text{O}_3$  fibre

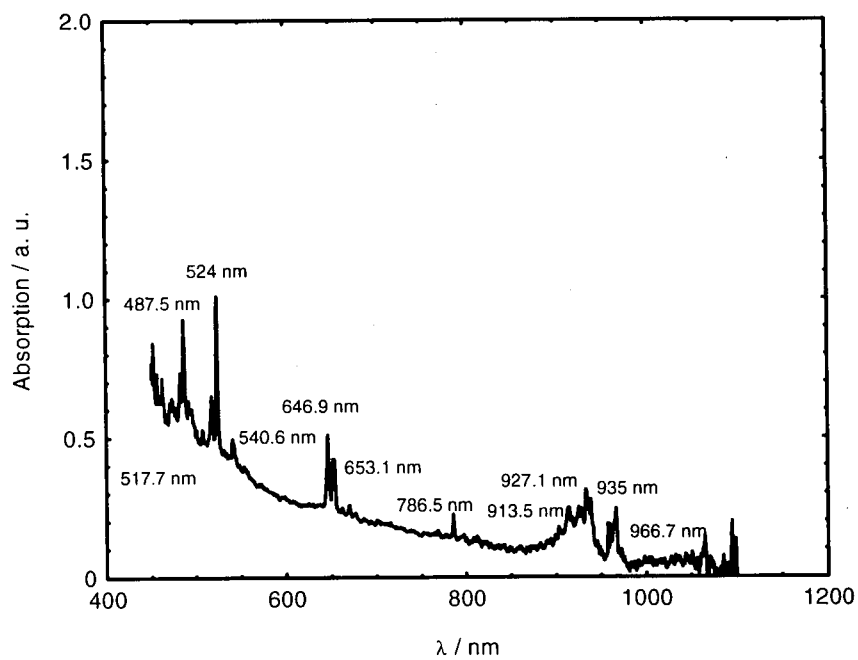


Figure 4.13b. IR absorption spectrum of  $\text{Yb}^{3+}$  sensitised  $\text{Er}^{3+}:\text{Al}_2\text{O}_3$  fibre

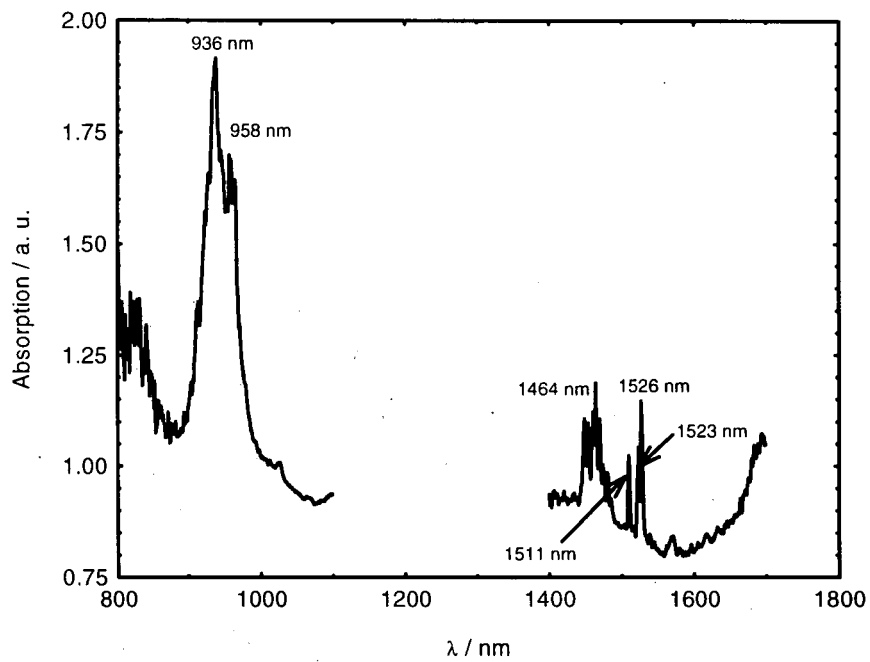
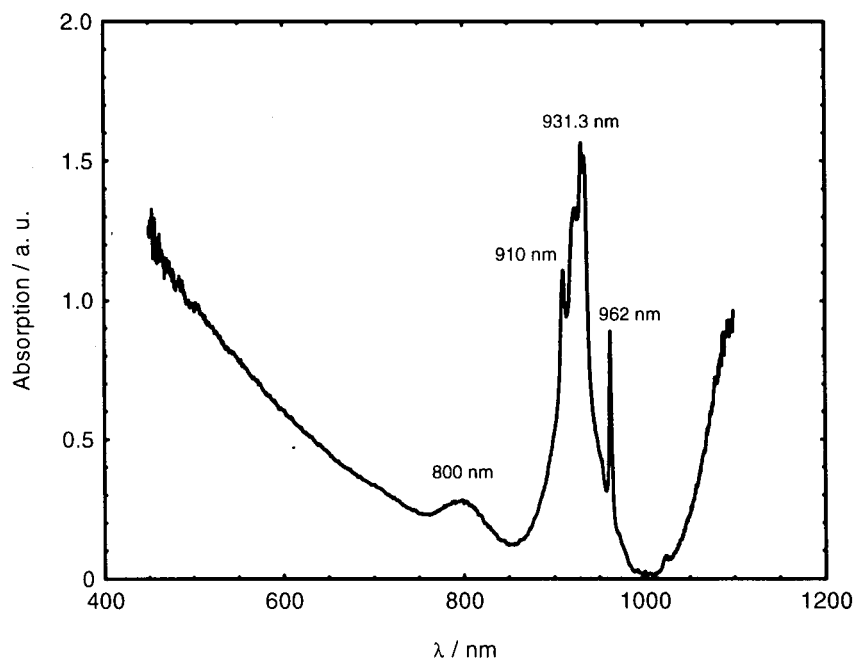


Figure 4.14. Visible absorption spectrum of  $\text{Yb}^{3+}:\text{Er}^{3+}:\text{Al}_2\text{O}_3$  fibre



## 4.5 Fluorescence spectra measurements

Room temperature fluorescence emission measurements have been carried out to confirm the presence of the various active materials which have been incorporated in sapphire fibres by the growth technique employed. Such measurements are also used to determine the fluorescence characteristics from which optimum performance may be realised in sensing applications. Although ruby is easily recognised from its fluorescence emission spectrum due to the sharp R-lines at 692.9 and 694.3 nm [4.19], RE-doped fibres, with emission in the visible and IR spectral regions, are relatively more difficult to characterise. However, the resulting sharp emission lines detected from these fibres confirm their highly crystalline nature. In addition, the high doping levels used led to particularly intense upconversion signals in codoped fibres.

### 4.5.1 Experiment

Fluorescence emissions from the doped fibres in both the visible and IR have been measured using the experimental set-up shown in **Figure 4.15**. Where possible, fluorescence emission was excited by using laser pumping matched to the material absorption bands. **Table 4.6** lists the pump lasers that have been employed for fluorescence excitation in various doped fibres used in this work. As illustrated in **Figure 4.15**, the laser radiation is coupled into the doped fibre through the use of a microscope objective while another objective is used to collect the fluorescence from the fibre end and collimates it through a focusing lens into the monochromator. For ruby fibres, the 514.5 nm line from a *Spectra Physics* Ar<sup>+</sup> ion laser (2010-10S series) has been used to excite the sharp R-lines. Both the Ar<sup>+</sup> ion laser at 488 nm and a laser diode array, with central wavelengths of 960 and 965 nm, have been employed for RE-doped samples. The pump laser beam is modulated by an optical chopper and lock-in detection is used for signal recovery. Signals are then fed into the computer and stored for later processing.

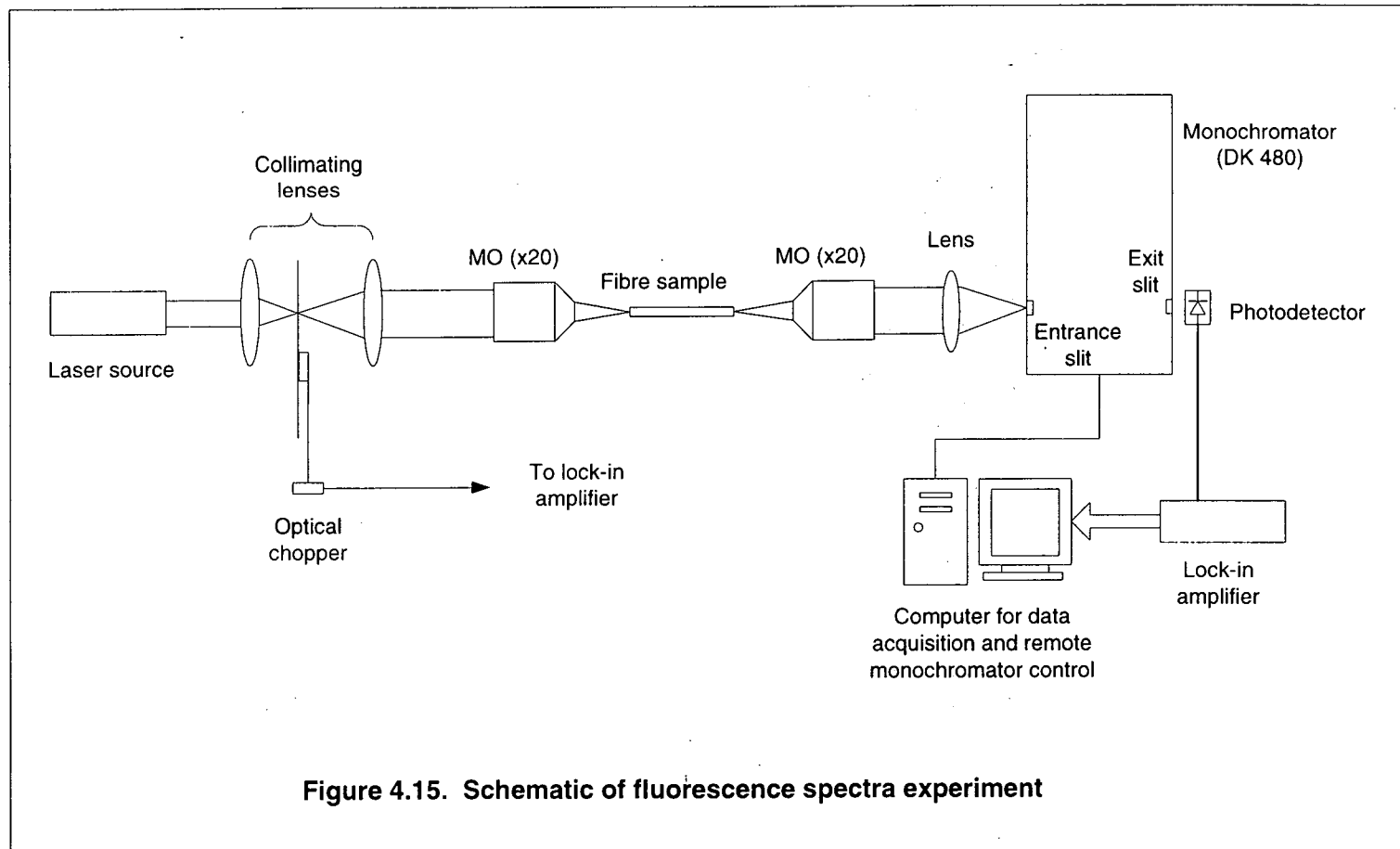


Figure 4.15. Schematic of fluorescence spectra experiment

**Table 4.6. Laser sources employed for fluorescence studies**

Fibre	Laser	Emission $\lambda$ / nm
$\text{Cr}^{3+}:\text{Al}_2\text{O}_3$	Ar <sup>+</sup> ion Frequency-doubled YAG	514.5 532
$\text{Er}^{3+}:\text{Al}_2\text{O}_3$	Ar <sup>+</sup> ion IR laser diode	488 960, 965
$\text{Er}^{3+} + \text{Yb}^{3+}:\text{Al}_2\text{O}_3$	Ar <sup>+</sup> ion IR laser diode	488 960, 965
$\text{Yb}^{3+} + \text{Er}^{3+}:\text{Al}_2\text{O}_3$	IR laser diode	960, 965

## 4.5.2 Results and Discussion

The fluorescence spectra (visible and IR regions) of the various doped fibres have been obtained from by the method described above. In these fibres, direct fluorescence (where the emission wavelength is longer than that of the excitation source) and upconversion (emitted wavelength shorter than the excitation wavelength) have been observed concurrently. The emitted spectrum from ruby fibres is presented in **Figure 4.16**. The two peaks are characteristic of the  $R_1$  and  $R_2$  lines in ruby fluorescence and are found to be centred at 694.3 and 692.9 nm respectively. They agree very well with published data [4.17, 4.19] and are a result of the splitting of the  ${}^2E$  energy level into the  $\bar{E}$  and  $2\bar{A}$  states with an energy gap of  $\sim 29 \text{ cm}^{-1}$  (i.e. with a separation of 1.4 nm between the two R peaks) when  $\text{Cr}^{3+}$  ions are subjected to a trigonally-distorted crystal field in an  $\text{Al}_2\text{O}_3$  host [4.19]. The  $R_1$  line is associated with the transition of the  $\bar{E}$  level to the ground state,  ${}^4A_2$ , while the  $R_2$  line is due to the  $2\bar{A} \rightarrow {}^4A_2$  transition. The full width at half maximum bandwidth of the  $R_1$  and  $R_2$  lines are found to be 0.65 and 0.6 nm respectively.

The visible emission spectrum of singly  $\text{Er}^{3+}:\text{Al}_2\text{O}_3$  fibres is presented in **Figure 4.17a** and shows relatively strong upconversion in the green and red spectral regions. The upconversion line at 525 nm is superimposed onto one of the additional laser lines at the same wavelength. This line is attributed to the  ${}^2H_{11/2} \rightarrow {}^4I_{15/2}$  transition from  $\text{Er}^{3+}$  doped in ionic crystals while the other green lines (at 540, 541.5, 552.5, 554.5 and 559 nm) are results of splitting of the main  ${}^4S_{3/2}$  manifold into several sublevels [4.28]. Transitions to the ground state then give rise to the lines detected. The well-resolved red upconversion lines are also shown on the same figure, with five main peaks at 644.3, 653.1, 660.2, 667.7 and 674.2 nm. These are also due to splitting of the main  ${}^4F_{9/2}$  manifold into sublevels with transition to  ${}^4I_{15/2}$ , the ground state [4.23, 4.28]. It should be noted that the upconversion emission in the green and red are relatively sharp lines with both regions separated by  $\sim 85$  nm. The IR fluorescence spectrum is shown in **Figure 4.17b** with the wavelengths of interest being in the 1500 nm region. The emitted lines (at 1511.5, 1523, 1531.5 and 1547 nm) are associated with the transitions from the split  ${}^4I_{13/2}$  manifold to the  ${}^4I_{15/2}$  ground state for  $\text{Er}^{3+}$  [4.23, 4.24] and have been reported in Er-doped YAG crystals [4.24]. The additional emission bands are assumed to have resulted from

contamination from other impurities although the fluorescence in the 1460 region is rather similar to that observed in Er:YAG [4.24]. In particular, the 1025 nm line could have resulted from the presence of small quantities of Yb<sup>3+</sup> impurities in the source material. Another curious set of emission lines has been observed in the 1600 – 1680 region and corresponds quite well to emission due to ESA from the <sup>4</sup>I<sub>9/2</sub> manifold [4.22]. Although this was not likely to occur if a single excitation wavelength had been used, the very high dopant concentration of ~12 at. % measured using EPMA (electron probe micro-analysis) could have resulted in self-activated excited state transitions. This phenomenon is not clearly understood currently and further studies are required to better understand the material behaviours/characteristics due to self-activated effects.

Similar emission characteristics have been detected from Er<sup>3+</sup>:Yb<sup>3+</sup>:Al<sub>2</sub>O<sub>3</sub> fibres doped with similar concentration levels of co-dopants, the significant differences being the much stronger upconversion intensities in both the green and red; the IR intensity was also found to be relatively stronger in comparison to Er<sup>3+</sup>:Al<sub>2</sub>O<sub>3</sub> with much larger peaks at 1523 and 1531.5 nm. The upconversion and IR fluorescence spectra are presented in **Figures 4.18a** and **4.18b** respectively. Another observation which can be made from the visible spectrum is the merging of the sharp green and red emission lines into a more dense structure. Further, a small peak at ~480 nm can be seen, corresponding to the <sup>4</sup>F<sub>7/2</sub> → <sup>4</sup>I<sub>15/2</sub> transition in Er<sup>3+</sup>. This line is relatively weak compared to the much stronger green and red upconversion. A broad but similarly intense emission in the 800 nm region can also be seen in **Figure 4.18a**. This is due to the transition from the split <sup>2</sup>F<sub>5/2</sub> manifold to the ground state in Yb<sup>3+</sup> [4.30]. From the IR spectrum in **Figure 4.18b**, the 1025 nm line emitted from Yb<sup>3+</sup> is clearly obvious and approximately equal in intensity in comparison to the peak 1531.5 nm emission. Again, additional emission bands have been detected in the 1460, 1570 and 1600 – 1680 regions. These bands have been assumed to be contributions from impurity cross-contamination in the RE powders employed in dip-coating the source rods. However, the effects from any possible “self-activation” of the doped fibres due to very high dopant concentration levels should not be ignored since the emission furthest into the infrared region (1600 – 1680) coincides with the excited state absorption transition from Er<sup>3+</sup> at 1680 nm.

In highly  $\text{Yb}^{3+}:\text{Al}_2\text{O}_3$  fibres codoped with low  $\text{Er}^{3+}$  concentration, both the green and red upconversion intensities were found to have reduced in strength relative to that of the blue peak at  $\sim 480$  nm. In particular, the red upconversion was observed to be approximately 3 times stronger than the green upconversion. However, the visible emission spectrum (shown in **Figure 4.19a**) indicates that the narrow-line structures of both spectral regions can still be clearly resolved. The green lines arise due to emissions from the  ${}^2\text{H}_{11/2} \rightarrow {}^4\text{I}_{15/2}$  and  ${}^4\text{S}_{3/2} \rightarrow {}^4\text{I}_{15/2}$  transitions, resulting in two different green bands with central wavelengths of 532.8 and 544 nm respectively. The red lines have been associated with transitions from the sublevels within the  ${}^4\text{F}_{9/2}$  manifold to the ground state,  ${}^4\text{I}_{15/2}$ . From the IR fluorescence spectrum presented in **Figure 4.19b**, no emission lines in the 1500 nm region due to the  $\text{Er}^{3+}$  transitions ( ${}^4\text{I}_{13/2} \rightarrow {}^4\text{I}_{15/2}$ ) have been detected. This implies that most of the pump photons have been efficiently absorbed by the  $\text{Yb}^{3+}$  ions and channelled into the excitation of the higher energy levels from which upconversion occurs. Another significant observation which can be made is the stronger 996 nm line from  $\text{Yb}^{3+}$  relative to the 1025 nm line from fibres produced with such doping combinations. This could be due to thermal population of the higher lying sublevel from the low lying level as reported by Berthou and Jørgensen [4.31] and Maurice *et al.* [4.32]. These lines stem from the sublevel transitions within the main  ${}^4\text{F}_{5/2}$  manifold of  $\text{Yb}^{3+}$  to the  ${}^4\text{F}_{7/2}$  state.

Figure 4.16. Fluorescence spectrum of ruby fibre

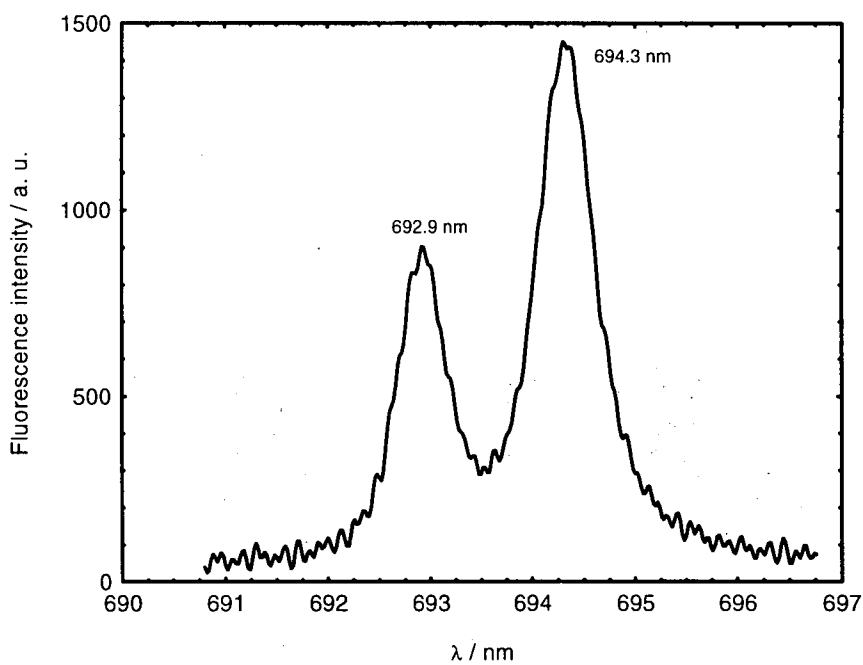


Figure 4.17a. Upconversion spectrum of  $\text{Er}^{3+}:\text{Al}_2\text{O}_3$  fibre (doped tip)

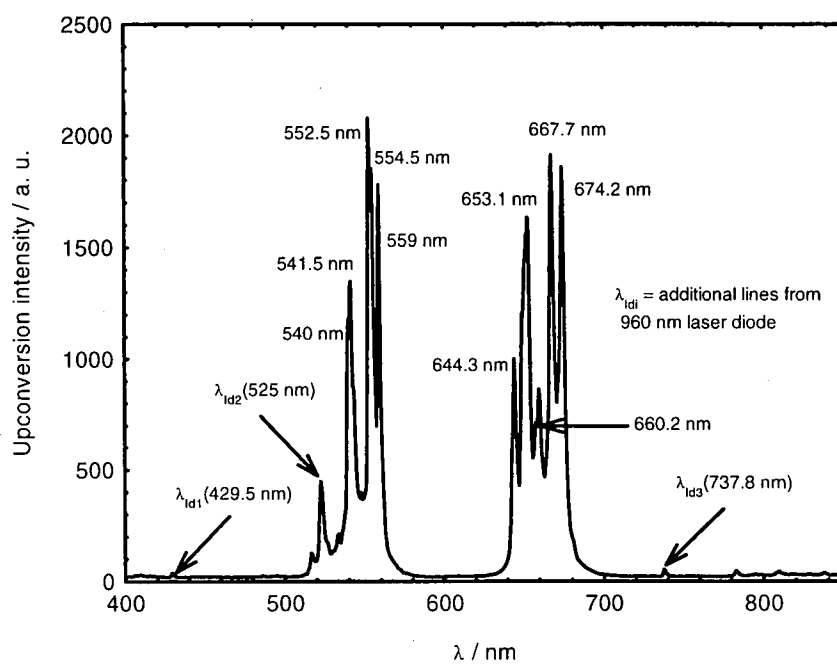


Figure 4.17b. IR fluorescence spectrum of  $\text{Er}^{3+}:\text{Al}_2\text{O}_3$  fibre (doped tip) pumped by laser diode at 960 nm

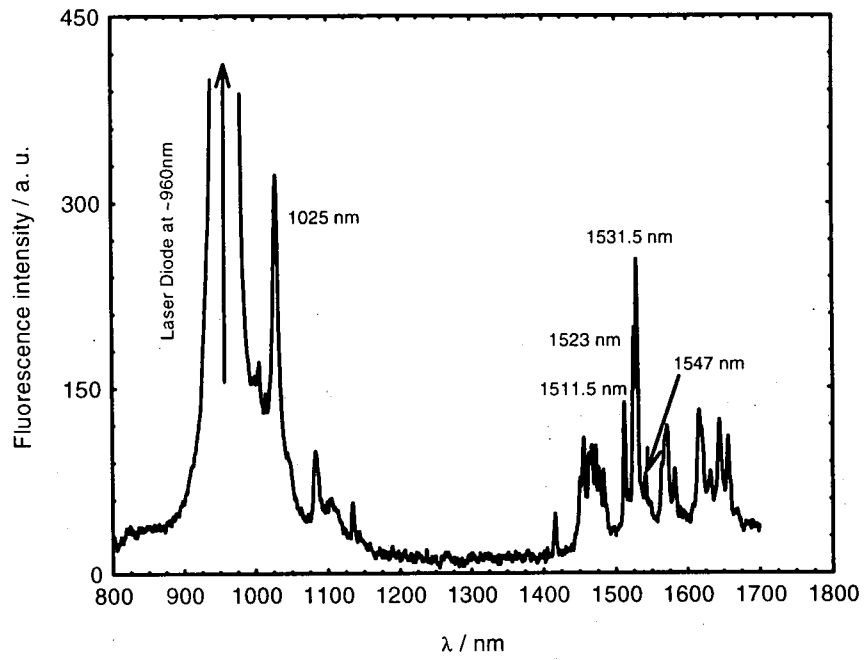


Figure 4.18a. Upconversion spectrum of  $\text{Er}^{3+} + \text{Yb}^{3+}$  codoped  $\text{Al}_2\text{O}_3$  fibre

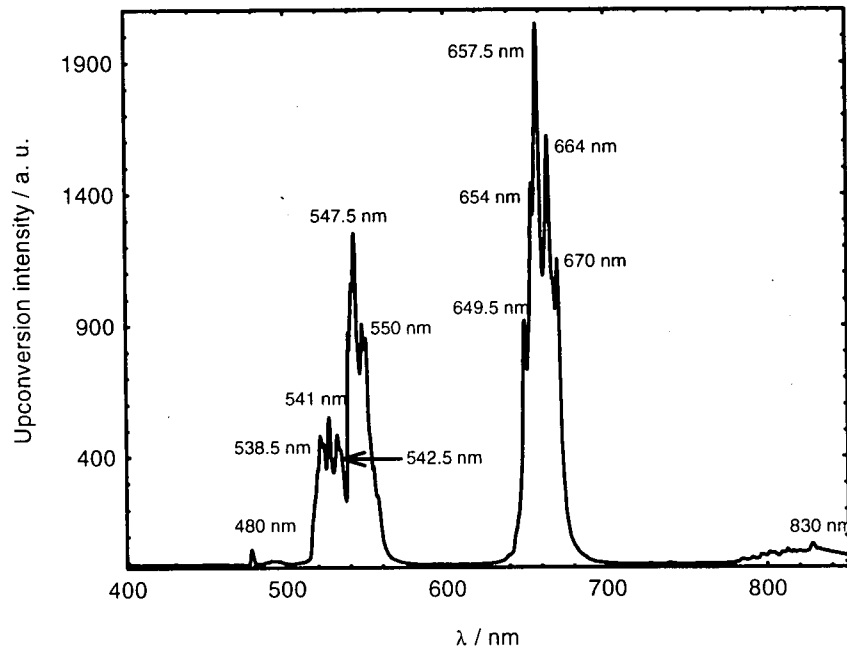


Figure 4.18b. IR fluorescence spectrum of  $\text{Er}^{3+} + \text{Yb}^{3+}$  codoped  $\text{Al}_2\text{O}_3$  fibre

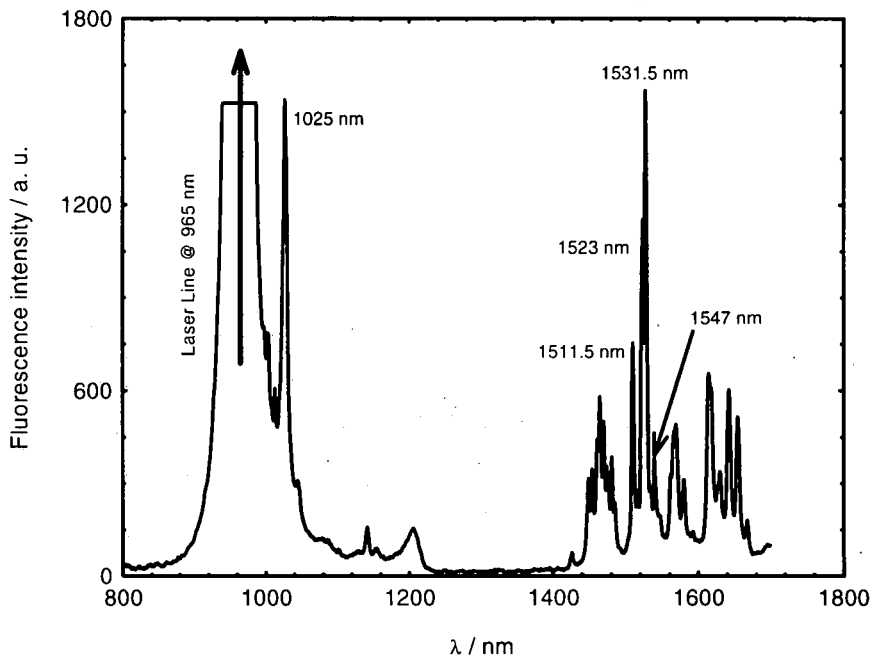


Figure 4.19a. Upconversion spectrum of  $\text{Yb}^{3+}:\text{Er}^{3+}:\text{Al}_2\text{O}_3$  fibre

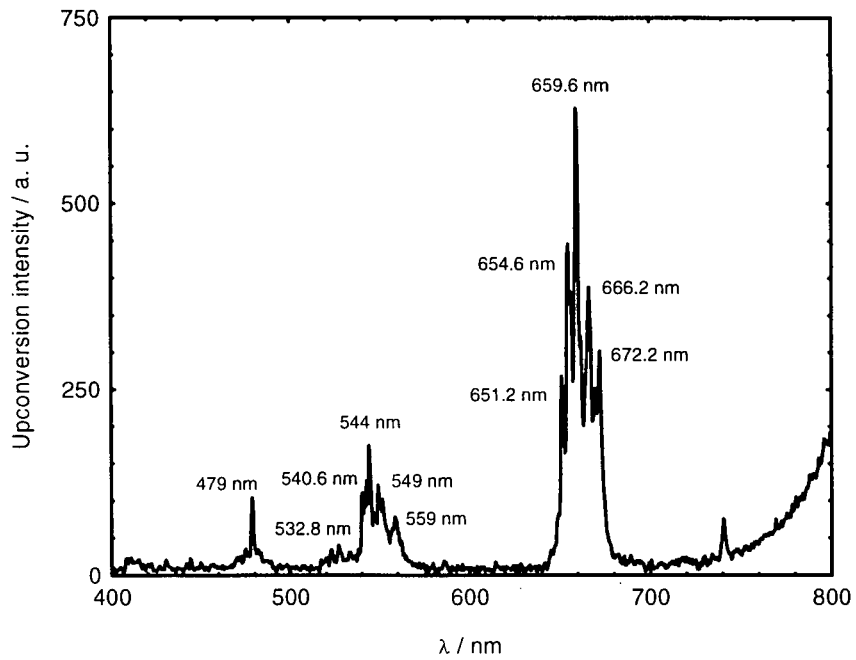
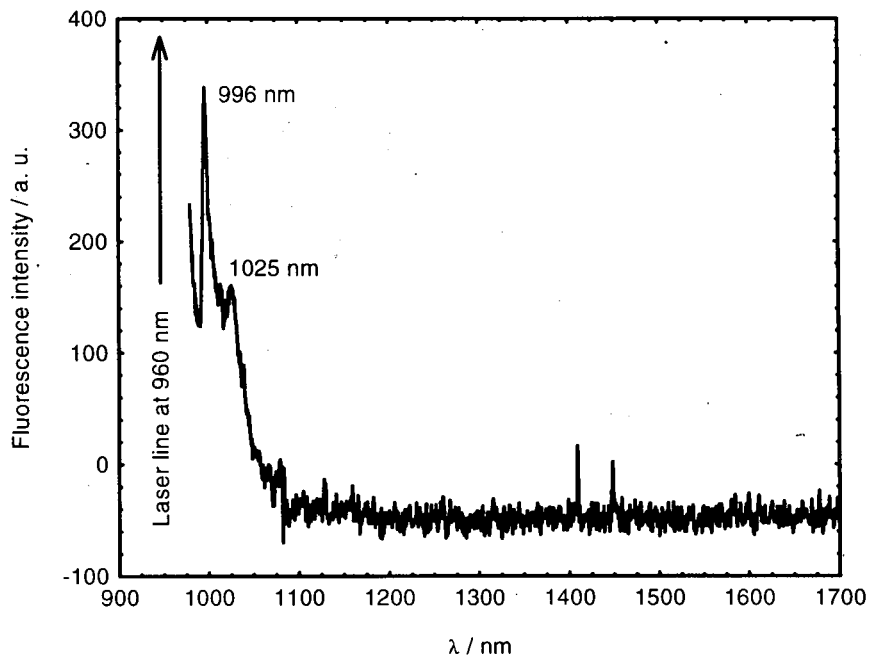


Figure 4.19b. IR fluorescence spectrum of  $\text{Yb}^{3+}:\text{Er}^{3+}:\text{Al}_2\text{O}_3$  fibre



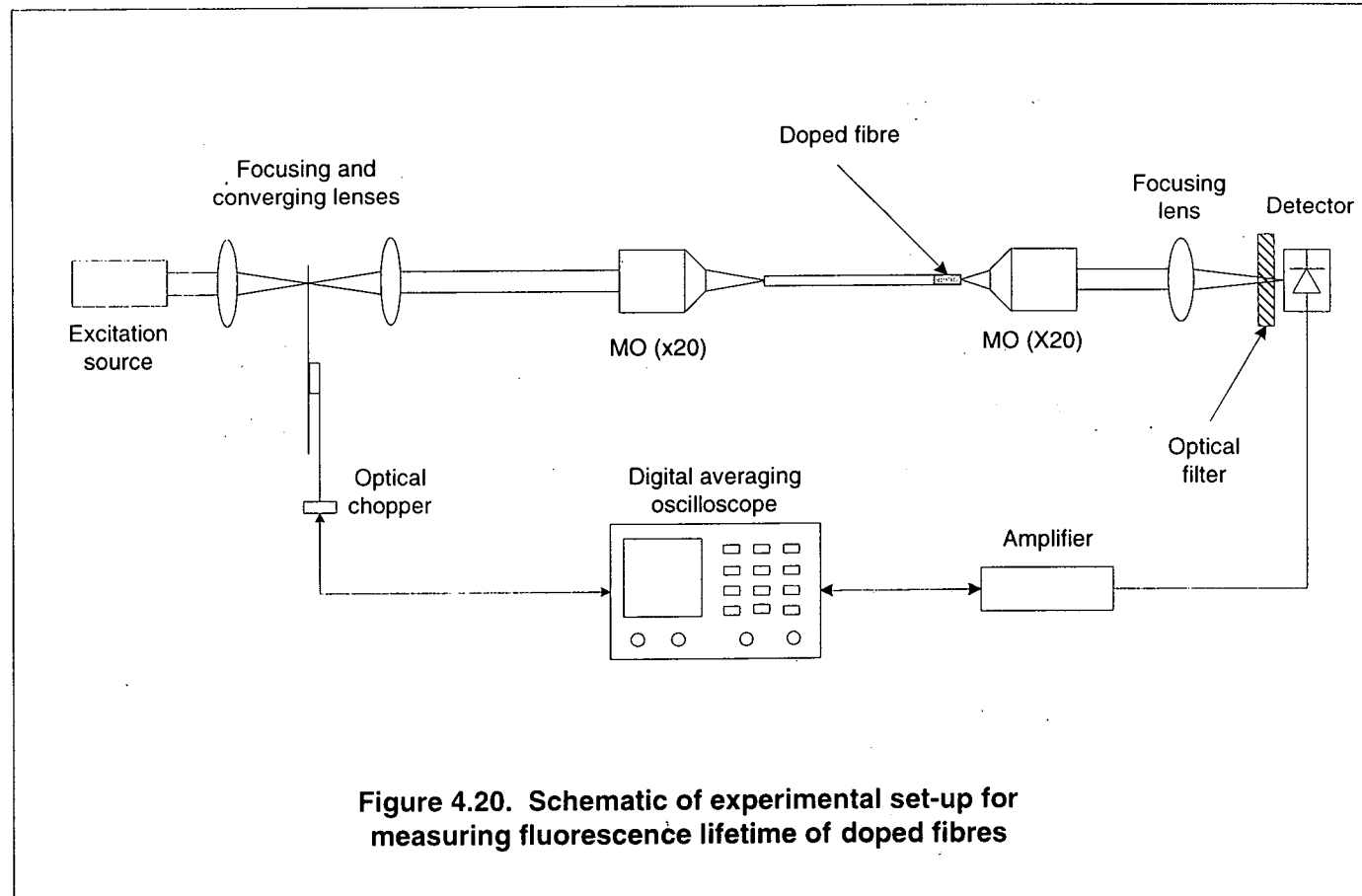
## 4.6 Fluorescence lifetime measurements

The use of the fluorescence lifetime decay from suitably doped fluorescent materials is an advantageous technique in fluorescence-based fibre optic sensing in that the lifetime can be relatively independent of the excitation intensity fluctuations [4.33]. However, the lifetime of any fluorescent materials is dependent on the concentration levels of the dopant(s) used [4.34, 4.35] hence, care must be taken to avoid operating near or above the critical concentration level beyond which the decay behaviour is no longer exponential. It is thus thought attractive to exploit the fluorescence lifetime decay of the doped crystal fibres produced in this work in sensing applications. The following experiment thus sets out to characterise the lifetime behaviour of these transition metal ion and rare-earth ion-doped fibres.

### 4.6.1 Experiment

A schematic of the experimental set-up used for measuring the fluorescence lifetimes of the doped fibres is illustrated in **Figure 4.20**. Lasers have been employed used as excitation sources where possible and are selected to match the absorption bands of the particular material being investigated. The fluorescence lifetime of ruby fibres and the IR lifetime of  $\text{Er}^{3+}:\text{Yb}^{3+}$ -codoped fibres were measured in transmission while the upconversion lifetime of the latter fibres were measured in reflection. For transmission measurements, excitation light was first collimated and injected into the fibre via a microscope objective. The output signal was then collected by another objective and directed onto an appropriate photodetector (avalanche photodiode used for ruby and high speed InGaAs photodetector used for IR lifetime detection) by a focusing lens. An optical filter was placed in front of the photodetector to permit only the fluorescence signal of interest to be detected. The filter used was selected to match the central or peak wavelengths of the fluorescence from ruby and the RE-doped fibres. To measure the upconversion lifetimes in reflection, a monochromator was used with its slits adjusted to provide a reasonable bandpass at the wavelength of interest and a PMT served as the detector. The resulting signal was then amplified and sent to a digital oscilloscope with averaging facilities to be averaged and stored for further processing. An optical chopper enabled pulsed modulation of the

excitation signal and also served as the oscilloscope trigger. The acquired data from all the measurements were then curve fitted to obtain the lifetimes.



## 4.6.2 Results and Discussion

A typical fluorescence lifetime curve from ruby fibres can be seen in **Figure 4.21a**, indicating an exponentially decaying profile. This decay stems from the dominant radiative decay arising from the  ${}^2E \rightarrow {}^4A_2$  transition [4.36]. The curve fitting technique applied resulted in a lifetime decay rate of 3.48 ms, in good agreement with data already published [4.37]. A good fit has also been obtained, as indicated by the confidence of fit,  $r^2$ .

The fitted IR fluorescence lifetime of  $\text{Er}^{3+}:\text{Yb}^{3+}$ -codoped fibres can be seen in **Figure 4.21b**, this radiative decay resulting from the  ${}^4I_{13/2} \rightarrow {}^4I_{15/2}$  transition at room temperature. A very fast decay time,  $\tau$ , has been obtained (see **Figure 4.21b**). It should be noted that due to the highly doped nature of these fibres, most of the pump photons have been channelled into upconversion resulting in relatively weak IR signals being detected. The IR lifetime is thus considered not suitable for the intended temperature sensing applications since rapid non-radiative decay due to thermal quenching will dominate the fluorescence lifetime at elevated temperatures and, consequently, the already weak intensity will decrease to a level beyond the limits of the detection system much more quickly at lower temperatures. The fluorescence lifetime decay of RE erbium-doped materials have been reported to be highly dependent on the doping levels and pump intensities [4.34, 4.38].

An example of the upconversion lifetime decay has been fitted and shown in **Figure 4.21c**. The fitted signal was averaged from the green upconversion intensity at the 547 nm line over a bandpass of ~3 nm which was determined by the slit widths of the monochromator, hence the decay rate can be attributed to the  ${}^4S_{3/2} \rightarrow {}^4I_{15/2}$  transition. A highly non-exponential nature can be seen in the figure, with a slow decay superimposed on a rapidly decaying initial profile. The fitted lifetime is shown in the figure but it can be seen that a bad fit has been obtained using an exponential. This lifetime characteristic clearly involves other complicated transitions and interaction dynamics of the material which are beyond the scope of this present study. The modulated red upconversion intensity was also observed to exhibit similar profile and was thus not fitted.

Figure 4.21a. Fluorescence lifetime decay of ruby fibre at room temperature

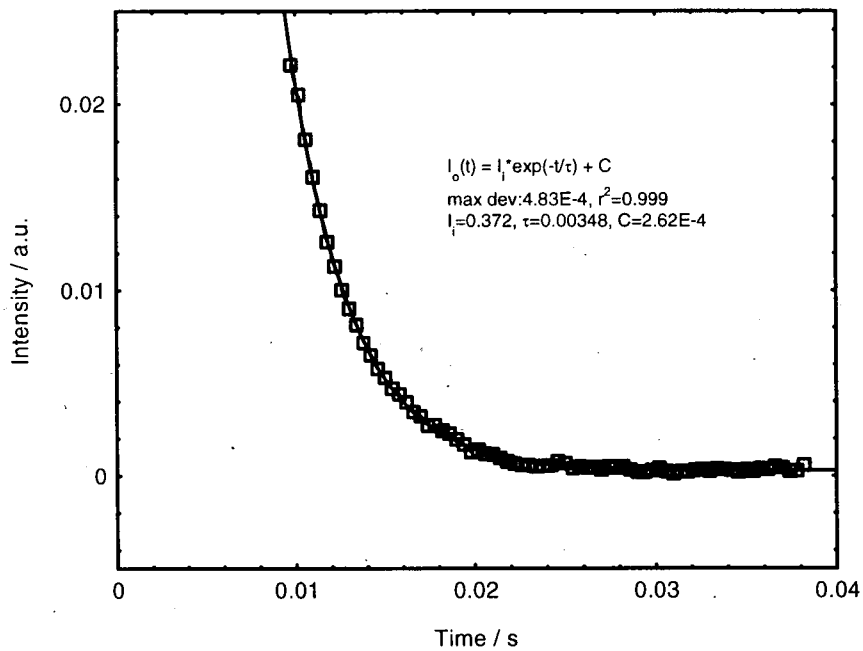


Figure 4.21b. IR fluorescence lifetime decay of  $\text{Er}^{3+}:\text{Yb}^{3+}:\text{Al}_2\text{O}_3$  fibre at room temperature (pump  $\lambda = 965 \text{ nm}$ )

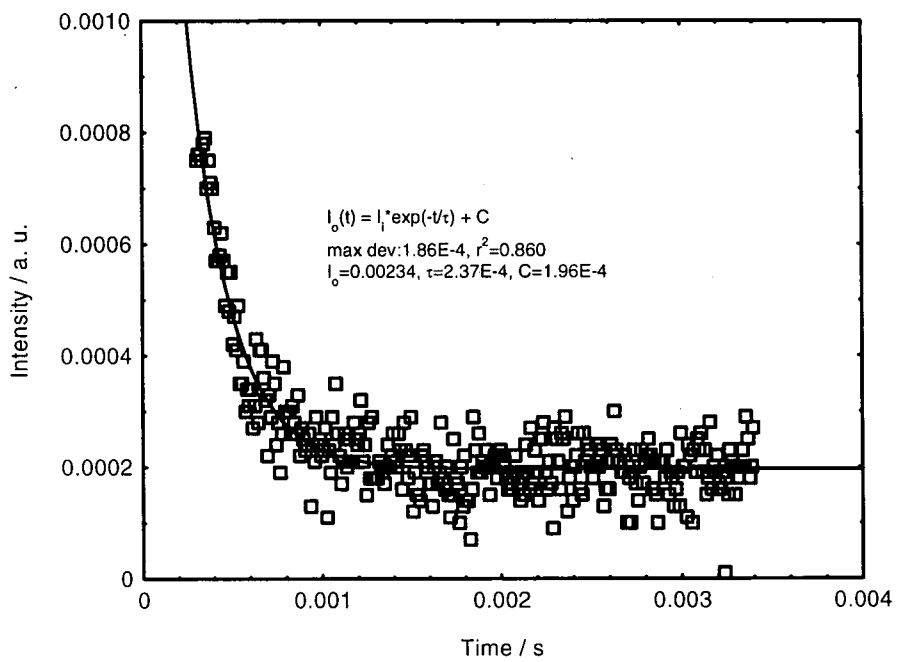
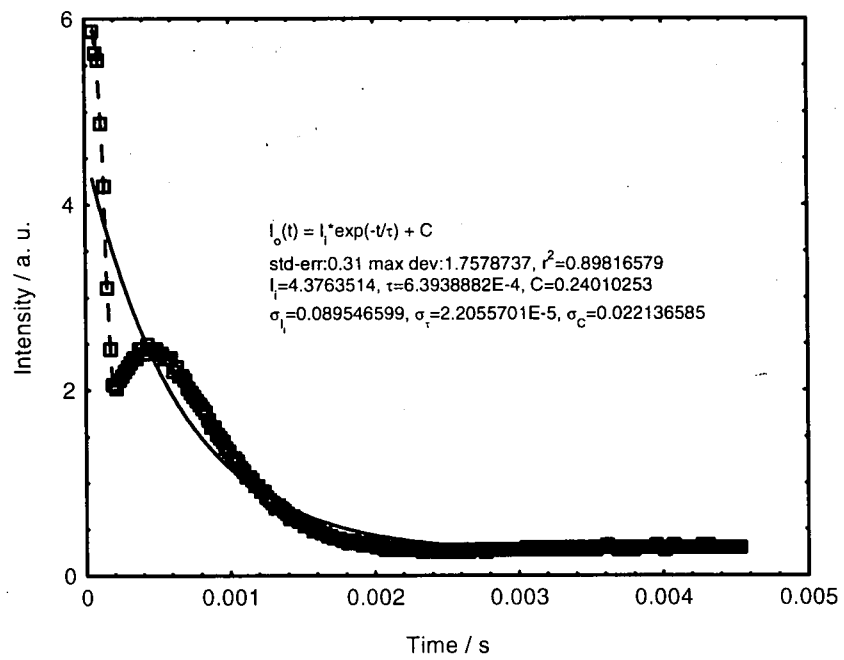


Figure 4.21c. Green upconversion lifetime decay of  $\text{Er}^{3+}:\text{Yb}^{3+}:\text{Al}_2\text{O}_3$  fibre at room temperature (pump  $\lambda = 965 \text{ nm}$ )



## 4.7 References to Chapter 4

- 4.1 L. G. Cohen and P. Glynn, *Dynamic measurement of optical fibre diameter*, Rev. Sci. Instrum., **44**(12), 1749, 1973
- 4.2 D. H. Smithgall, L. S. Watkins and R. E. Frazee Jr., *High-speed noncontact fiber-diameter measurement using forward light scattering*, Appl. Opt., **16**(9), 2395, 1977
- 4.3 P. L. Chu, *Measurements in Optical Fibres*, Proc. IREE Aust., 102, 1979
- 4.4 M. Dobosz, *Measurement of Fiber Diameter Using a Dual Edge Diode Beam of Light*, Opt. Commun., **62**(4), 243, 1987
- 4.5 J. G. N. Baines, A. G. Hallam, K. W. Raine and N. P. Turner, *Fiber Diameter Measurements and Their Calibration*, IEEE J. Lightwave Technol., **8**(9), 1259, 1990
- 4.6 G. E. Smith, *Measurement of Fiber Coating Geometry Using a Transversely Scanning Laser Beam*, Nat. Inst. Standards and Technol., **792**, 175, 1990
- 4.7 A. G. Sinclair, G. McCormick, J. H. Sharp, I. S. Ruddock and R. Illingworth, *Uniaxial crystalline fibres: optical methods for determining their physical characteristics*, Meas. Sci. Technol., **4**, 1501, 1993
- 4.8 S. V. Tsivinskiy, *Factors Governing the Dislocations Density in the Czochralski Method of Growing Crystals*, Fiz. Met. Metalloved., **25**(6), 1013, 1968
- 4.9 D. H. Jundt, M. M. Fejer and R. L. Byer, *Characteristics of single-crystal sapphire fibers for optical power delivery systems*, Appl. Phys. Lett., **55**(21), 2170, 1989
- 4.10 J. H. Sharp, N. A. Gallen and P. D. Townsend, *Optical Waveguide in  $Cr^{3+}:Gd_3Ga_5O_{12}$  Made by Ion Implantation*, J. Modern Opt., **43**(6), 1996
- 4.11 J. Friedel, *Transition Metals. Electronic Structure Of The d-Band. Its Role In The Crystalline and Magnetic Structures* in: *The Physics Of Metals. I. Electrons*, J. M. Ziman (Ed.), Cambridge University Press, Cambridge, 340, 1969
- 4.12 B. Henderson and G. F. Imbusch, (Eds.), *Optical spectroscopy of transition metal ions in solids* in: *Optical Spectroscopy of Inorganic Solids*, Clarendon Press, Oxford, 408, 1989
- 4.13 Y. Tanabe and S. Sugano, *On the Absorption Spectra of Complex ions. I, J.*

- Phys. Soc. Jpn, **9**(5), 753, 1954
- 4.14 Y. Tanabe and S. Sugano, *On the Absorption Spectra of Complex ions. II*, J. Phys. Soc. Jpn, **9**(5), 753, 1954
- 4.15 D. E. Rimmer and D. F. Johnston, *A study of the origin of the trigonal crystal field in ruby. I. Analysis of experimental data*, Proc. Phys. Soc., **89**, 943, 1966
- 4.16 D. E. Rimmer and D. F. Johnston, *A study of the origin of the trigonal crystal field in ruby. II. Theory*, Proc. Phys. Soc., **89**, 953, 1966
- 4.17 T. H. Maiman, *Optical and Microwave-Experiments in Ruby*, Phys. Rev. Lett., **4**(11), 564, 1960
- 4.18 T. H. Maiman, *Optical Maser Action in Ruby*, Brit. Commun. Electron., **7**, 674, 1960
- 4.19 V. Evtuhov and J. K. Neeland, *Pulsed Ruby Lasers in: Lasers Vol. I*, A. K. Levine (Ed.), Edward Arnold, London, 1, 1966
- 4.20 S. Hüffner, *Optical Spectra of Transparent Rare Earth Compounds*, Academic Press, London, 1978
- 4.21 B. Henderson and G. F. Imbusch (Eds.), *Spectroscopy of lanthanide (rare-earth) and actinide ions in: Optical Spectroscopy of Inorganic Solids*, Clarendon Press, Oxford, 387, 1989
- 4.22 W. J. Miniscalco, *Erbium-Doped Glasses for Fiber Amplifiers*, IEEE J. Lightwave Technol., **9**(2), 234, 1991
- 4.23 A. Polman, *Erbium implanted thin film photonic materials*, J. Appl. Phys., **82**(1), 1, 1997
- 4.24 T. Danger, J. Koette, R. Brede, E. Heumann, G. Huber and B. H. T. Chai, *Spectroscopy and green upconversion laser emission of Er<sup>3+</sup>-doped crystals at room temperature*, J. Appl. Phys., **76**(3), 1413, 1994
- 4.25 P. E. -A. Möbert, E. Heumann, G. Huber and B. H. T. Chai, *Green Er<sup>3+</sup>:YLiF<sub>4</sub> upconversion laser at 551 nm with Yb<sup>3+</sup> codoping: a novel pumping scheme*, Opt. Lett., **22**(18), 1412, 1997
- 4.26 M. E. Fermann, D. C. Hanna, D. P. Shepherd, P. J. Suni and J. E. Townsend, *Efficient Operation of An Yb-Sensitised Er Fibre Laser at 1.56 μm*, Electron. Lett., **24**(18), 1135, 1988
- 4.27 F. Di Pasquale and M. Federighi, *Improved Gain Characteristics in High-Concentration Er<sup>3+</sup>/Yb<sup>3+</sup> Codoped Glass Waveguide Amplifiers*, IEEE J.

- Quant. Electron., **30**(9), 2127, 1994
- 4.28 R. Scheps, *Upconversion Laser Processes*, Prog. Quant. Electron., **20**(4), 271, 1996
- 4.29 W. Koechner (Ed.), *Solid-State Laser Engineering (2<sup>nd</sup> Ed.)*, Springer-Verlag, Berlin, 1988
- 4.30 E. Maurice, S. A. Wade, S. F. Collins, G. Monnom and G. W. Baxter, *Self-referenced point temperature sensor based on a fluorescence intensity ratio in Yb<sup>3+</sup>-doped silica fiber*, Appl. Opt., **36**(31), 8264, 1997
- 4.31 H. Berthou and C. K. Jörgensen, *Optical-fiber temperature sensor based on upconversion-excited fluorescence*, Opt. Lett., **15**(19), 1100, 1990
- 4.32 E. Maurice, G. Monnom, B. Dussardier, A. Saïssy, and D. B. Ostrowsky, *Thermalization effects between upper levels of green fluorescence in Er-doped silica fibers*, Opt. Lett., **19**(13), 990, 1994
- 4.33 K. T. V. Grattan and Z. Y. Zhang, *Fiber Optic Fluorescence Thermometry*, K. T. V. Grattan and A. Augousti (Eds.), Chapman and Hall, London, 1995
- 4.34 G. N. van den Hoven, E. Snoeks, A. Polman, J. W. M. van Uffelen, V. S. Oei and M. K. Smit, *Photoluminescence characterization of Er-implanted Al<sub>2</sub>O<sub>3</sub> films*, Appl. Phys. Lett., **62**(24), 3065, 1993
- 4.35 S. P. Jamison and G. F. Imbusch, *Temperature dependence of the luminescence from heavily doped ruby*, J. Lumin., **75**, 143, 1997
- 4.36 W. H. Fonger and C. W. Struck, *Temperature dependences of Cr<sup>3+</sup> radiative and nonradiative transitions in ruby and emerald*, Phys. Rev. B, **11**(9), 3251, 1975
- 4.37 Z. Zhang, K. T. V. Grattan and A. W. Palmer, *Temperature dependences of fluorescence lifetimes in Cr<sup>3+</sup>-doped insulating crystals*, Phys. Rev. B, **48**(11), 7772, 1993
- 4.38 G. N. van den Hoven, E. Snoeks, A. Polman, C. van Dam, J. W. M. van Uffelen and M. K. Smit, *Upconversion in Er-implanted Al<sub>2</sub>O<sub>3</sub> waveguides*, J. Appl. Phys., **79**(3), 1258, 1996

## **Chapter 5 – Ruby-based Crystal Fibre Sensors**

### **5.0 Introduction**

### **5.1 Theory of temperature and deformation influences on the fluorescence characteristics of ruby**

5.1.1 Temperature dependence

5.1.2 Dependence on physical deformations (high pressure and stress)

### **5.2 Absorption and fluorescence spectra of ruby single-crystal fibres**

### **5.3 Temperature sensing experiments**

5.3.1 Fluorescence lifetime decay of single-crystal ruby fibres

5.3.1.1 Experiment

5.3.1.2 Results and Discussion

5.3.2 Wavelength shifts of ruby fibre R-lines with temperature

5.3.2.1 Experiment

5.3.2.2 Results and Discussion

### **5.4 Strain measurement experiments**

5.4.1 Fluorescence lifetime decay of ruby fibres

5.4.1.1 Experiment

5.4.1.2 Results and Discussion

5.4.2 Wavelength shifts of ruby fibre R-lines

5.4.2.1 Experiment

5.4.2.2 Results and Discussion

### **5.5 References to Chapter 5**

## Chapter 5 – Ruby-based Crystal Fibre Sensors

### 5.0 Introduction

Although most commonly considered as a precious gem stone by many, ruby ( $\text{Cr}^{3+}:\text{Al}_2\text{O}_3$ ) is also well-known as the crystalline material used as a laser material. In the first demonstration of successful laser operation by Maiman in 1960, a ruby rod was used to lase in the pulsed mode [5.1]. Ten years later, Burrus and Stone [5.2] were able to produce continuous laser emission from ruby with concentrations of  $\text{Cr}^{3+}$  ions equal to that used by Maiman (0.05 wt.%) and 0.02 wt.%, this time however, the laser material being in single crystal fibre form with diameters of  $\sim 40 \mu\text{m}$ . Since that very first operation of a ruby laser, several studies have been carried out into the fluorescence characteristics of ruby crystals and their dependence on external physical influences, especially that of temperature [5.3, 5.4, 5.5], physical deformations [5.6, 5.7, 5.8, 5.9]. The earliest exploitation of thermally-induced changes in ruby fluorescence characteristics can be attributed to Grattan and colleagues [5.10], who monitored the relative change in intensities of the two ruby R-lines (at 694.3 and 692.7 nm) due to temperature increment. These workers were able to construct a low cost temperature sensor based on the ruby crystal. This was then followed by an investigation of the temperature-dependent ruby fluorescence lifetime decay using an optical fibre delivery/collection system [5.11]. An earlier temperature monitoring scheme based on the temperature-dependence of ruby lifetime decay [5.12] had already demonstrated the potential of using ruby or more generally, fluorescent materials, for fibre optic temperature sensing applications, although in both studies the maximum temperature investigated was below  $200^\circ\text{C}$ . With the introduction of phase-sensitive detection techniques, termed phase-locked detection (PLD), by Zhang *et al.* [5.13], the maximum temperature limit which can be measured can be greatly extended. In this work, the combination of phase-sensitive lock-in detection and feed-back control of the excitation source modulation frequency led to greatly increased signal-to-noise ratio which effectively suppressed the relatively high level of noise associated with the detected decay signal. Recently, the temperature-dependent measurement of the fluorescence decay lifetime of a single crystal ruby fibre (fabricated by the LHPG technique in our laboratory) was

extended to  $\sim 600$  °C (873 K) using the PLD signal detection and processing scheme [5.14].

It should be noted that most of the temperature-dependence studies carried out to date on ruby have involved the use of small ruby crystals, which have been cut from bulk ruby laser rods; the crystal being attached to a conventional silica fibre used for delivering the excitation source while another silica fibre was used for collecting the fluorescence signal either in the transmission [5.11] or reflection mode [5.15]. The use of the transmission probe, while allowing for some cost savings in terms of avoiding certain optical coupling components for separating the emitted fluorescence signal from the excitation source, implies having to route the collection fibre through the measurement area, leading to difficulties and inconvenience in many implementations. In terms of practical applications of a fluorescence-based temperature sensor, the reflection probe, although requiring additional coupling components, would thus be preferred. **Figures 5.1a** and **5.1b** illustrate the transmission and reflection sensing probes respectively.

Until recently, ruby has not been readily available in single crystal fibre form. Early work [5.16] on the use of single-crystal ruby fibres as temperature probes demonstrated the potential of such fibres over other probes using bulk ruby crystals. Curve-fitting of the exponentially decaying fluorescence lifetime at two points in the periodically varying detected signal was mentioned as the principle technique used for measuring the lifetime decay in this work and a poorly-resolved fluorescence emission spectrum was shown. The maximum operating temperature was given as 450 °C (723 K). In a later report [5.17], the authors were able to demonstrate an almost linear relationship between the detected lifetime decay (using again the two-point curve-fitting technique) and the monitored temperature up to  $\sim 450$ °C. The authors also reported the difference in the fluorescence intensity obtained with respect to temperature when two different optical filters were used. However, in both work, the crystallographic orientations of the ruby fibres were not mentioned.

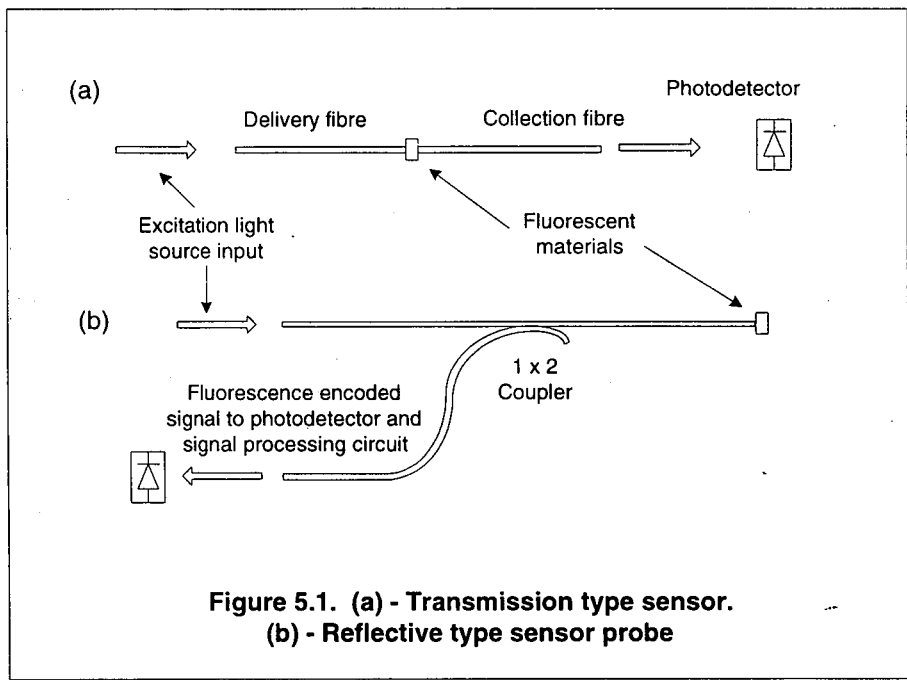


Figure 5.1. (a) - Transmission type sensor.  
 (b) - Reflective type sensor probe

Beside the change in fluorescence decay time when bulk ruby is subjected to elevated temperatures, early work also investigated the temperature-induced shift in the two sharp R-lines characteristic of ruby [5.3, 5.18, 5.19]. Such a sensing configuration has also been studied in this work. The temperature-induced shifts in the  $R_1$  and  $R_2$  ruby lines could have important implications in the detected lifetime decay data measured with the aid of optical narrowband filters and will be discussed in a later part of this chapter relating to the lifetime monitoring temperature sensing scheme.

The sensitivity of the ruby R-lines to other deformations such as compressive stress [5.6; 5.20], pressure [5.7, 5.21, 5.22] and shock-wave compression and tension [5.9, 5.23, 5.24] have also been reported, again involving bulk crystals. Since being found to be sensitive to pressure by Forman *et al.* [5.7], ruby R-line shifts have been used extensively for very high pressure calibration (in the megabar range) in diamond anvil cells under various shock-loading [5.9] conditions. In compression experiments [5.24], the ruby samples were often subjected to shock-waves induced by an impactor or a projectile accelerated towards the target sample at very high velocities. These samples were aligned along either the a- or c-axis crystallographic orientation. The resultant R-line spectra were then captured by time-resolved measurements and the desired stress and/or strain data along the respective a- or c-orientation inferred from the R-line shifts. The shift in the  $R_1$  line has been found to be dependent on the crystal orientation in nonhydrostatic (extremely high pressure, >100 GPa) conditions, while the  $R_2$  shift has been found to be independent of both crystal orientation and the test conditions, i.e., it behaves similarly under both hydrostatic and nonhydrostatic measurements [5.9, 5.22].

Taking into consideration the parameters which can be readily measured by monitoring the changes in the fluorescence characteristics of ruby, this chapter thus sets out to investigate some important physical influences which may or may not be reflected in the resultant fluorescence properties of single crystal ruby fibres which have been fabricated by the LHPG technique. It also tries to address the basic problem of cross-sensitivity in a crystal fibre sensor, or in a more general sense in any optical fibre sensing techniques.

However, in order to have a clearer understanding of these influences on the ruby fluorescence emission such as lifetime decays, etc, a brief explanation relating to the interaction of the  $\text{Cr}^{3+}$  ions with their sapphire host lattice crystal field and phonon energies is given below.

## 5.1 Theory of temperature and deformation influences on the fluorescence characteristics of ruby

### 5.1.1 Temperature dependence

As far back as 1916 [5.25], the effect which temperature has on the absorption and fluorescence characteristics of ruby has been studied. Although the fluorescence lifetime decay of the ruby samples could not be determined with the detection equipment available at that time, the absorption and sharp ruby R-lines were found generally to shift towards the red with increasing temperature. At the time of the publication of the first successful operation of a ruby laser, Maiman [5.26] also reported observations of changes in the ground-state population and optical absorption between two excited states (excited state absorption – ESA) in the ruby crystal being studied. The fluorescence decay rate from the metastable  ${}^2\text{E}$  level of ruby was initially found to be  $\sim 5$  msec (compared to the now accepted values of  $\sim 3 - 3.5$  msec [5.27, 5.5] for ruby fluorescence emission). For stimulated emission in ruby, however, the decay lifetime of the  $\text{R}_1$  line (at 694.3 nm) was observed to decrease to  $\sim 0.6$  msec while the linewidth was also found to narrow quite considerably [5.28]. A simplified schematic energy-level diagram for ruby is shown in **Figure 5.2**.

$\text{Cr}^{3+}$  ions have their  $3d$  outer shells incomplete [5.29] hence, they allow for strong interaction with nearby ions, the host crystal field strength and lattice vibrations. Ruby is formed by incorporating  $\text{Cr}^{3+}$  ions into an  $\text{Al}_2\text{O}_3$  host lattice at sites with a threefold axis of symmetry by substitutionally replacing the  $\text{Al}^{3+}$  ions [5.30]. This site results in the  $\text{Cr}^{3+}$  ion being subjected to a trigonally-distorted octahedral crystal field which splits the  $3d^3$  energy levels of the ion. Due to a combination of a distorted field linked with an even-parity energy term and spin-orbit coupling [5.31], the lowest-lying excited  ${}^2\text{E}$  state splits into the  $\bar{\text{E}}$  and  $2\bar{\text{A}}$  states with an energy gap of

$\sim 29 \text{ cm}^{-1}$ . The resulting sharp R-lines observed in ruby is thus due to the  $\bar{E} \rightarrow {}^4A_2$  transition for the  $R_1$  line (694.3 nm) and the  $2\bar{A} \rightarrow {}^4A_2$  transition for the slightly weaker  $R_2$  line (692.9 nm).

The temperature dependence of the ruby fluorescence decay time may be understood by means of two configurational co-ordinate models with the aid of a simplified Tanabe-Sugano diagram [5.32, 5.33] for ruby.  $\text{Cr}^{3+}$  ions, as mentioned earlier, interact strongly with the crystal field and lattice vibrations in ionic crystal hosts. Changes in temperature, which lead to changes in crystal field strength, phonon densities and energies, can consequently have a strong effect on the decay lifetime of ruby. As can be seen in the simplified Tanabe-Sugano diagram (**Figure 5.3**), which shows the normalised energy of the low-lying states,  $E/B$ , plotted against the normalised crystal field strength,  $D_q/B$ , the energy splitting,  $\Delta E$ , in ruby which has a high crystal field strength ( $D_q/B \sim 2.5$ ) [5.34, 5.35], between the  ${}^4T_2$  and  ${}^2E$  states is positive. As described by Grattan and Zhang [5.32], the relatively short lifetime of the  ${}^4T_2$  state implies that the fluorescence emission from the sharp R-lines is dominated by the longer-lived  ${}^2E$  lowest excited state (i.e.  ${}^2E \rightarrow {}^4A_2$  radiative transition) at low temperature. The transition between the  ${}^2E \rightarrow {}^4A_2$  states thus determines the temperature dependence of the fluorescence lifetime. At 300 K, the fluorescence lifetime is  $\sim 3.5 \text{ ms}$  [5.5]. With the elevation of temperature, some  $\text{Cr}^{3+}$  ions are promoted to the fast decaying  ${}^4T_2$  state from the  ${}^2E$  level. As the temperature is increased further, more and more ions are promoted to this state, depleting the population of the  ${}^2E$  state, hence, phonon terminated and non-radiative transitions from the  ${}^4T_2$  to the  ${}^4A_2$  ground state will begin to dominate. These transitions also lead to wide phonon sidebands forming in addition to the sharp R-lines. This will, in effect, lead to a decrease in the fluorescence lifetime to  $\sim 1 \mu\text{s}$  at  $600 \text{ }^\circ\text{C}$  (873 K) [5.14] as well as a decrease in the fluorescence intensity measured for a single crystal ruby fibre.

The two-level model [5.4, 5.5] can be used to describe the radiative transition of  $\text{Cr}^{3+}$  ions from the  ${}^2E \rightarrow {}^4A_2$  states in a high field crystal at low temperature where non-radiative transitions from the  ${}^4T_2$  state can be assumed to be negligible due to the preferential population and, hence, radiative decay from the  ${}^2E$  state. **Figure 5.4**

shows the two-model diagram. However, at elevated temperatures, non-radiative transitions  ${}^4T_2 \rightarrow {}^4A_2$  dominate and, in this model, the  ${}^2E$  state acts as a storage level for the excited ions into the  ${}^4T_2$  state. This is possible only when the two states are assumed to be in a "quasi-thermodynamic equilibrium" and is verified by the very short relaxation time of  $\sim 7$  ps [5.36] between the two states. An expression of the temperature-dependence of the fluorescence lifetimes, taking into account the degeneracies of the  ${}^4T_2$  and  ${}^2E$  states has also been formulated for this model:

$$\tau = \tau_s \frac{1 + C_d e^{-\Delta E / kT}}{1 + (\tau_s / \tau_i) e^{-\Delta E / kT}} = \tau_s \frac{1 + 3e^{-\Delta E / kT}}{1 + \alpha e^{-\Delta E / kT}} \quad (5.1)$$

where  $\tau$  is the fluorescence lifetime,  $\Delta E$  the energy gap between the  ${}^4T_2$  and  ${}^2E$  states,  $\tau_i$  and  $\tau_s$  the lifetimes of the  ${}^4T_2$  and  ${}^2E$  states respectively,  $k$  the Boltzmann's constant,  $T$  the temperature, and  $C_d$  the ratio of degeneracy of  ${}^4T_2 / {}^2E$ .

With this model, Zhang *et al.* [5.5] were able to obtain a reasonably good fit over the measured lifetime data from 300 to 570 K. From room temperature up to  $\sim 550$  K, there exists a non-monotonic decay of the lifetime, leading to a slight difference between the fitted curve and the measured data. Beyond  $\sim 600$  K, the non-radiative  ${}^4T_2 \rightarrow {}^4A_2$  transition dominates, as demonstrated by the rapid decrease of measured lifetime with increasing temperature, and the fitted curve beyond this temperature is thus no longer accurate.

**Figure 5.5** shows a simplified configurational coordinate model for ruby which has been used to predict the temperature-dependent lifetime change by including effects from both the radiative  ${}^2E \rightarrow {}^4A_2$  and non-radiative  ${}^4T_2 \rightarrow {}^4A_2$  transitions. Again, the  ${}^4T_2$  and  ${}^2E$  states have to be assumed to be in equilibrium "quasi-thermodynamically", hence,

$$\frac{n_i}{n_s} = C_d e^{-\Delta E / kT} \quad (5.2)$$

where  $n_i$  and  $n_s$  are the populations of the  ${}^4T_2$  and  ${}^2E$  states respectively;  $C_d$ ,  $\Delta E$ ,  $k$  and  $T$  are as defined in **Eq. 5.1**. By substituting **Eq. 5.2** into **Eq. 7** in **Ref. [5.5]**, the rate change in the total population of the  ${}^4T_2$  and  ${}^2E$  states can be given by the expression:

$$\frac{dn}{dt} = -\frac{1/\tau_s + (1/\tau_i)e^{-\Delta E/kT} + (1/\tau_q)e^{-(\Delta E_q + \Delta E)/kT}}{1 + 3e^{-\Delta E/kT}} \quad (5.3)$$

where  $\tau_q$  is the non-radiative decay rate (or thermal quenching rate) and  $\Delta E_q$  the thermal quenching energy gap between the  ${}^4T_2$  and  ${}^4A_2$  states; the rest of the variables are defined in **Eq. 5.1**. Integrating **Eq. 5.3**, the fluorescence lifetime,  $\tau$ , can be found:

$$\tau = \tau_s \frac{1 + 3e^{-\Delta E/kT}}{1 + \alpha e^{-\Delta E/kT} + \beta e^{-(\Delta E_q + \Delta E)/kT}} \quad (5.4)$$

where  $\alpha = \tau_s/\tau_i$  and  $\beta = \tau_s/\tau_q$ . This equation was fitted to the lifetime data of ruby from 300 to 800 K and the fitted curve was found to be relatively accurate [5.5], with a deviation of  $\sim 1\%$  over the data range.

However, at temperatures below 300 K in ruby, the authors [5.5], using the two-level model, found a discrepancy of  $\sim 17\%$  between the fitted and theoretical  $\Delta E$  values, from spectroscopic data obtained and suggested that contributions from the splitting of the  ${}^2E$  into the  $\bar{E}$  and  $2\bar{A}$  states as well as that from the induced wide phonon sidebands could affect the temperature dependence of the fluorescence lifetime. The observed increase in lifetime at temperatures below 100 K can then be explained by taking into account the longer radiative decay rate from the  $2\bar{A}$  (692.9 nm) state. It has also been shown by Fonger and Struck [5.4] that the  ${}^2E \rightarrow {}^4A_2$  transition is basically a narrow line at 295 K and the  ${}^4T_2$  population is small. However, thermal repopulation of this level at 663 K dramatically increases the intensity of the  ${}^4T_2$  state relative to that of the  ${}^2E$  state by 30 times. Since the  ${}^4T_2$  is a very rapid non-radiative state which is dominant at elevated temperatures, the ensuing fluorescence lifetime of the ruby crystal is thus drastically reduced. The phonon sidebands of the

transition  ${}^2E \rightarrow {}^4A_2$ , already obvious at liquid nitrogen temperature, couples strongly to the host lattice in an ionic crystal, hence, any thermal perturbation will also lead to a much increased contribution to the lifetime decay of ruby. Hence, the phonon-induced effect and the splitting of the  ${}^2E$  state into  $\bar{E}$  and  $2\bar{A}$  should be accounted for if the overall fluorescence lifetime characteristics are to be better predicted.

By considering the Boltzmann statistics over the 0 – 100 K region, which can be given as

$$I_{R1}/I_{R2} = \alpha_R e^{-\Delta E_R / kT} \quad (5.5)$$

where  $I_{R1}$  and  $I_{R2}$  are the intensities of the  $R_1$  and  $R_2$  lines respectively,  $\Delta E_R$  is the splitting energy between the  $\bar{E}$  and  $2\bar{A}$  states, and  $\alpha_R$  (representing the degeneracies between the two sublevels) = 0.65 [5.5], together with the phonon effects, **Eq. 5.1** may be modified to obtain

$$\tau = \tau \frac{1 + e^{-\Delta E_R / kT} + 6e^{-\Delta E / kT}}{\coth(h\nu_1 / 2kT) + \alpha_R \coth(h\nu_2 / 2kT) e^{-\Delta E_R / kT} + \alpha e^{-\Delta E / kT}} \quad (5.6)$$

where the  $\coth(h\nu_i / 2kT)$  terms are assumed to be the  $R_1$  and  $R_2$  phonon sidebands induced by  $h\nu_1$  and  $h\nu_2$  respectively. The modified equation has been found to fit the measured data more accurately with less deviation (~0.2 times) compared to the original two-level model [5.5].

One can then see that the two models proposed may be used to describe the temperature dependence of ruby fluorescence lifetime more satisfactorily. With appropriate choice of the fit parameters, they can also allow prediction of the temperature-dependent fluorescence lifetime with sufficient accuracy for temperature sensing applications. The models may also be applied to materials with similar crystal field strength.

Another fluorescence characteristic which is affected when subjected to elevated temperature is a spectral shift in the R-lines. Perhaps not very adequate for

temperature sensing due to the small changes involved over a wide range of temperatures, it is seen as important when ruby is used for high pressure and shock-wave measurements. The lineshift with temperature could thus be used as a compensation factor. Several authors have applied empirical and theoretical models in attempts to fit the  $R_1$  and  $R_2$  lines from ruby emission with varying success [5.3, 5.18, 5.19, 5.37, 5.38]. The curve fitting involved in the work mentioned in the references above generally treats the fit parameters within a limited temperature range, with relatively good results and accuracy obtained.

The R-line shift in ruby was studied by Gibson [5.25] while investigating the absorption spectrum of ruby at various temperature points. Small shifts of the R-lines towards the red were also observed. McCumber and Sturge [5.18] later proposed a model based on the effect of Raman scattering two-phonon electronic energy interaction to describe both the lineshift and line broadening for a temperature range from 77 to 400 K. Although their model agreed reasonably well with experimental data within the temperature region investigated, the higher energy regions of the phonon interaction were neglected, and the authors suggested that their model should be valid up to a temperature of  $\sim 700$  K. It was concluded from that study that the effect of temperature was due to the interaction between the acoustic phonons and the electronic energy levels of the impurity  $\text{Cr}^{3+}$  ions. Izatt *et al.* [5.3] also studied the temperature dependence of the R-line shift of ruby by measuring the radius of the Fabry-Pérot fringes produced by emission from a ruby laser. They were able to obtain good agreement with the experimental data and with the model postulated by McCumber and Sturge [5.18] from 66 to 300 K. Although suggestions have been made to better fit the model to experimental data above this temperature (300 K), this would mean changing the parameters of the fit or scaling the actual temperature to coincide with that predicted by the theoretical curve at the particular set of fit parameters. This implies that a different set of parameters would have to be used to fully describe the wide temperature range to be considered. However, it was implicitly suggested that the R-lines, and, hence, the intrinsic shifts with temperature, are strongly dependent on chromium concentration (therefore supporting the phonon-electron interaction theory) and the crystal strain.

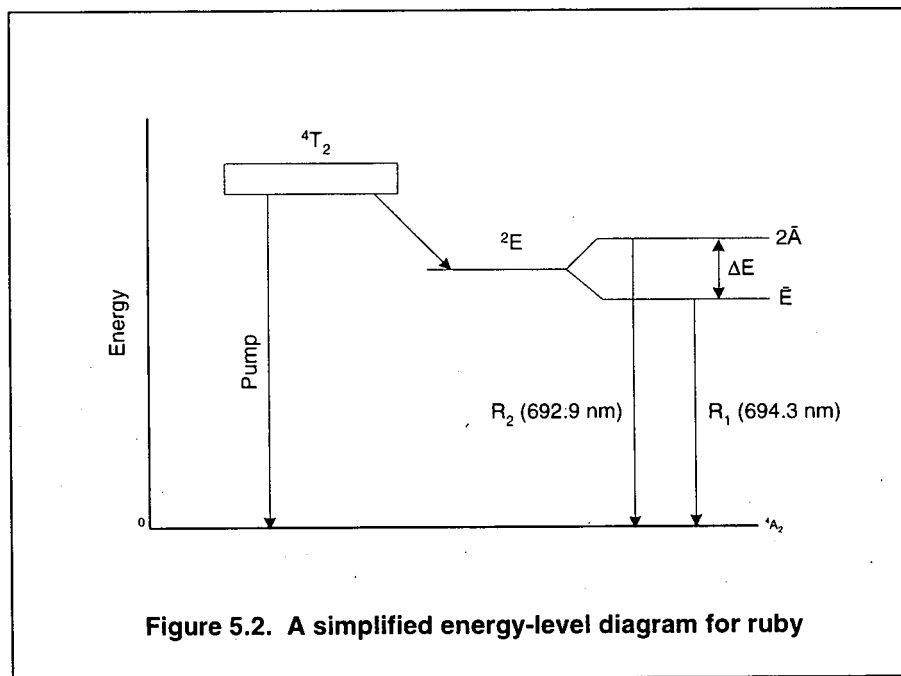


Figure 5.2. A simplified energy-level diagram for ruby

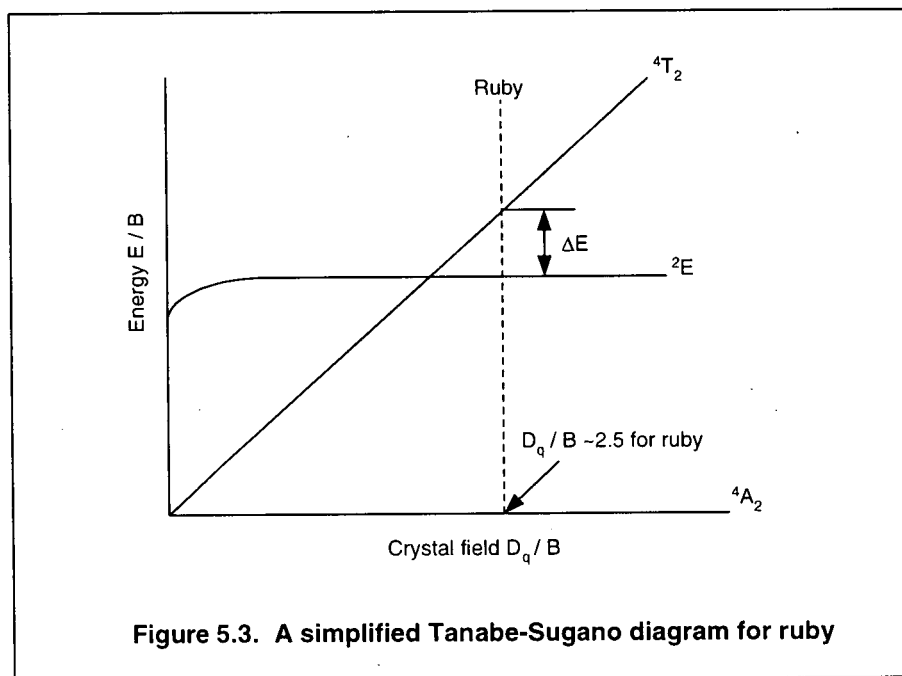
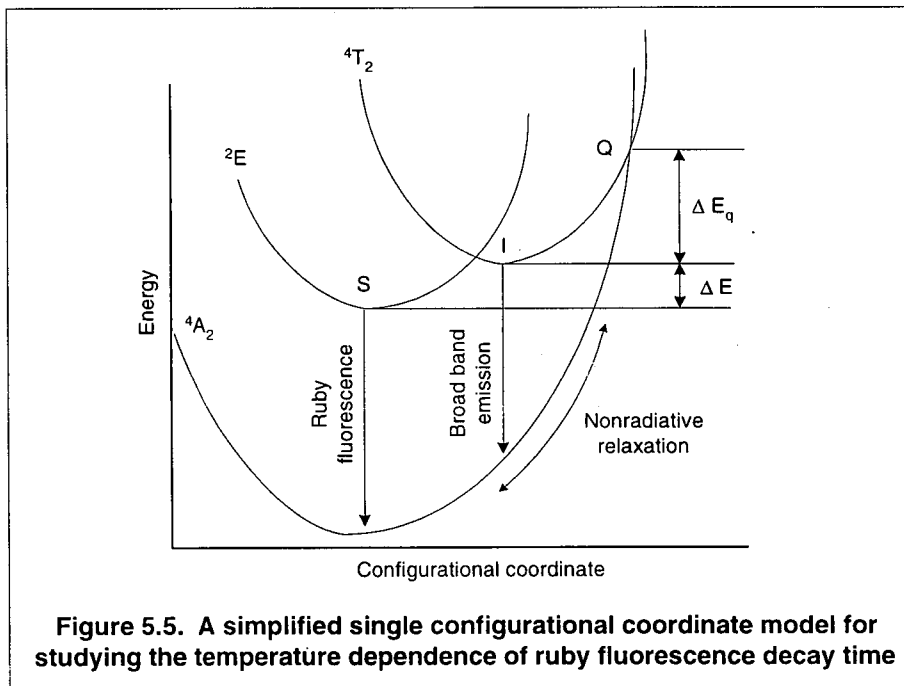
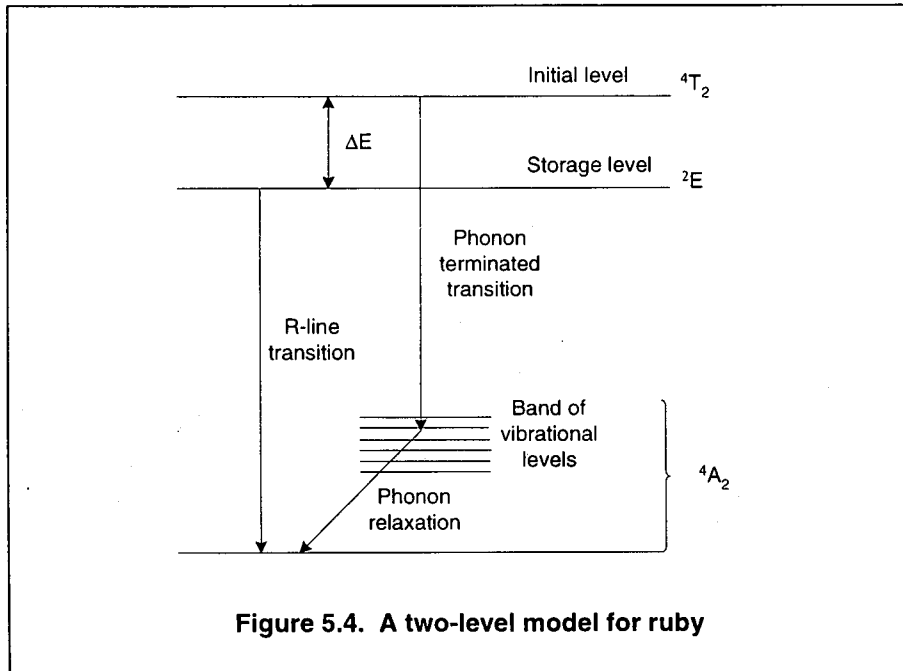


Figure 5.3. A simplified Tanabe-Sugano diagram for ruby



Since the R-line shifts may not vary constantly or uniformly with temperature, it is highly possible that beyond a certain temperature the  $R_1$  and  $R_2$  lines may overlap and it would then be almost impossible to distinguish one from the other, making any measurements a difficult task. One way to overcome this is to use a double-Lorentzian line shape [5.18] to describe the characteristic fluorescence curve of ruby, which was investigated by both Munro *et al.* [5.37] (using a Voigt profile: combination of Gaussian and Lorentzian shapes) and Ragan *et al.* [5.19]. Munro *et al.* [5.37] compared the theoretical fit with the measured lineshift, linewidth and the relative intensities of the two R-lines up to a temperature of 570 K at various hydrostatic pressure levels up to a maximum of  $\sim 14.5$  GPa. Their model fits the data reasonably but the many-parameter equation used would seem rather cumbersome and convergence to the desired results would depend on selecting an appropriate set of starting values. Although a little contradictory in their statement concerning the relationship between chromium concentration and the width of the R-lines, Ragan *et al.* [5.19] provided a very simple cubic model which can be used to correlate the measured data to the theoretical prediction over a wide temperature range from 0 to 600 K with relatively good accuracy. To describe the ruby fluorescence line shape, they used a double Lorentzian which fits very well to the line. Polarisation measurements performed on the  $R_1$  and  $R_2$  intensities showed that the ruby fluorescence is highly polarised perpendicular to the c-axis. The authors [5.19] also found that, since the two R-lines do not shift together exactly, a double-Lorentzian line shape could be useful in overcoming the overlapping of these two lines at high temperatures ( $\sim 450$  K). The interaction between the acoustic phonons and the electronic energy levels caused by incorporation of the impurity  $\text{Cr}^{3+}$  ions was also suggested as one of the mechanisms of R-line shifting. The general cubic equation used by the authors can be given as

$$R_i(T) = \alpha + \beta T + \delta T^2 + \gamma T^3 \quad (5.7)$$

where  $R_i(T)$  represents either the  $R_1$  or  $R_2$  line being studied,  $\alpha$ ,  $\beta$ ,  $\delta$  and  $\gamma$  the fit parameters (constants) and given as  $14423 \text{ cm}^{-1}$ ,  $4.49 \times 10^{-2} \text{ cm}^{-1} \text{ k}^{-1}$ ,  $-4.81 \times 10^{-4} \text{ cm}^{-1} \text{ k}^{-2}$  and  $3.71 \times 10^{-7} \text{ cm}^{-1} \text{ k}^{-3}$  respectively for  $R_1$  and  $14452 \text{ cm}^{-1}$ ,  $3 \times 10^{-2} \text{ cm}^{-1} \text{ k}^{-1}$ ,  $-3.88 \times 10^{-4} \text{ cm}^{-1} \text{ k}^{-2}$  and  $2.55 \times 10^{-7} \text{ cm}^{-1} \text{ k}^{-3}$  respectively for  $R_2$ . The unit for **Eq. 5.7**

is given as  $\text{cm}^{-1}$ . Note that all the above work on the ruby R-line shifts did not take into account the contribution from thermal expansion of the crystal which could be relatively considerable, as pointed out by Ma *et al.* [5.38]. Moreover, in the work of McCumber and Sturge [5.18], Izatt *et al.* [5.3] and Ragan *et al.* [5.19], the phonon-electronic interaction considered was that due solely to acoustic phonons. Interactions with optical phonons were excluded. These contributions have been considered in a recent work [5.38] which provided a relatively more complete analysis of the thermally-induced change in the fluorescence characteristics of ruby.

### 5.1.2 Dependence on physical deformations (high pressure and stress)

Similar to the temperature-dependence, the fluorescence characteristics of ruby can be influenced by stresses applied due to high pressure or shock-wave loading to its *a*- or *c*-crystallographic plane. Ruby's trigonally distorted octahedral crystal field already results in the splitting of the sharp R-line, which occurs when the impurity  $\text{Cr}^{3+}$  ions, incorporated into sapphire, substitutionally replace  $\text{Al}^{3+}$  ions, altering the trigonal crystal field symmetry associated with the  $\text{Al}_2\text{O}_3$  lattice [5.39,5.40]. This results in the splitting of the excited  ${}^2\text{E}$  state into the  $\bar{\text{E}}$  and  $2\bar{\text{A}}$  states which is observed optically as the two R-lines ( $\text{R}_1$  and  $\text{R}_2$  lines). Application of external stresses can lead to a change in the amount of splitting, resulting in shifts in the R-lines or other fluorescence characteristics such as broadening of the linewidths or relative intensity changes in the two R-lines. The trigonal crystal field effect has also been discussed by Macfarlane [5.41] in a paper investigating the influence of stress upon ruby. The two reasons given in that paper for the apparent shift in the ruby fluorescence spectrum are: (1) impurity ions ( $\text{Cr}^{3+}$ ) occupying non-centrosymmetric sites, leading to different shifts in their energy levels, hence the resulting splitting of the sharp line spectrum; (2) application of stress will lower the site symmetry group from  $G_o$  to  $G_s$  and lead to lifting of the electronic degeneracy of the single ion, thus if  $G_s = G_o$  then only a shift will be observed. That study proved inconclusive since there was little information on the motion of non-centrosymmetric site lattices such as that of  $\text{Cr}^{3+}:\text{Al}_2\text{O}_3$  and, hence its effect on the trigonal field parameters ( $v_s$  and  $v_s'$ , the subscript "s" implying stress-induced values) upon application of external stresses. However, Macfarlane [5.41] suggested that the parameters under investigation were comparable to that of another material, MgO, and the trigonal

splittings of  $3d^3$ ,  $3d^7$  and  $3d^8$  electronic systems can be used to predict the behaviour of the electronic energy levels of ruby (a  $3d^3$  system) under compressive stress.

It has been shown that the excited state splitting ( $\Lambda$ ) of the lowest excited  ${}^2E$  state due to stress is dependent on the diagonal trigonal crystal field parameter,  $v$ , which is strongly dependent on the immediate surrounding of the chromium ion,  $Cr^{3+}$  [5.41]. The  $\alpha$ - $Al_2O_3$  host lattice is trigonally symmetric and the  $Cr^{3+}$  ions substituting for the  $Al^{3+}$  ions alters the energy-level structure of the otherwise free  $Cr^{3+}$  ions [5.39]. Thus the unstressed level splittings of the  $Cr^{3+}$  ions in  $Al_2O_3$  due to the trigonal field of the host lattice form the sharp R-lines characteristic of ruby fluorescence emission. The principle contribution, as mentioned earlier, to the splitting of this state is proportional to the on-diagonal trigonal field parameter,  $v$ , hence changes in these splittings due to induced stresses can be interpreted as changes in the corresponding trigonal field parameters. These applied stresses can change the trigonal field but not the symmetry of the host lattice, thus leading to variation of the energy level splittings [5.6]. This variation is therefore reflected as shifts in the R-lines when ruby is subjected to very high isotropic pressure or high compressive stress.

The use of the ruby R-lines as a precision measurement technique for pressure in a diamond anvil cell (DAC) was first reported by Forman *et al.* [5.7]. Employing a piece of ruby crystal with  $\sim 0.05$  wt. %  $Cr^{3+}$  in a DAC, they monitored the shift in the two sharp R-lines up to a maximum pressure of 40 kbar. By least-squares curve fitting, the R-lines were found to shift linearly with the applied pressure, with the  $R_1$  shift being of the order of  $-0.77$   $cm^{-1}/kbar$  and in  $R_2$  approximately  $-0.84$   $cm^{-1}/kbar$ . Notice the difference in the rates of shift between the two R-lines and the high pressures involved in the experiment which was conducted at room-temperature. No line broadening was observed up to  $\sim 40$  kbar but it was suggested that under non-hydrostatic conditions line broadening could occur. Since then the shifts of the ruby R-lines have been used routinely for pressure calibration in DACs [5.21, 5.22, 5.42]. Several studies have been carried out to investigate and attempt to fully characterise the R-line shifts with pressure [5.8, 5.37, 5.43]. Shock-wave loading, where the conditions are generally non-hydrostatic, have also been investigated [5.8, 5.9, 5.23].

The modified Voigt profile (a mixture of the Gaussian and Lorentzian profiles) may be used to better represent the two R-lines of the ruby fluorescence so that at very high hydrostatic and non-hydrostatic pressures, difficulty introduced by these two lines overlapping may be overcome. This could be due to the broadening of the R-lines at very high pressures, leading to a large non-uniform distribution of the pressure and consequently, the difficulty in distinguishing both lines. Stresses due to hydrostatic compression of more than 14 GPa have been measured [5.37]. Some studies have neglected the effect produced by the R<sub>2</sub> line (most likely due to the difficulty in modelling and representing both the R-lines simultaneously) but, later works have taken into consideration both the R-lines [5.8, 5.22, 5.23, 5.24, 5.37], where contributions from the R<sub>1</sub> and R<sub>2</sub> lines have been found to be important with respect to the pressure applied. Munro *et al.* [5.37] fitted a rather involved but relatively accurate model to describe the ruby fluorescence spectrum with many dependent parameters and found that the intensities, relative intensity, peak positions and linewidths of the two R-lines vary with pressure and, of course, with temperature. Their model was able to account for the overlap of the two R-lines, albeit within experimental errors, while there was uncertainty involved in fitting their model to determine the change in linewidths. The linewidths were observed to increase rapidly with temperature but little change was found when under hydrostatic pressure. However, under nonhydrostatic conditions, the linewidths broadened significantly, making ruby a good sensing medium for detecting the onset of nonhydrostatic pressure conditions. Such a condition could be caused by the uneven distribution of the applied pressure on the ruby sample.

Shock-loading was used by Gupta and colleagues [5.23, 5.24, 5.44] to investigate the deformation effects on both the R<sub>1</sub> and R<sub>2</sub> line. Shock-compression tests are useful since they allow effects due to nonhydrostatic loading, crystal orientation and stress gradients to be measured separately [5.22]. The wavelength shifts for both R-lines were found to behave differently for loading along the *a*- and *c*- axes. The shifts of the R<sub>1</sub> line were observed to be dependent on both crystallographic orientation and nonhydrostatic stresses, indicating that the R<sub>1</sub> lineshift was not reliable after the limit of hydrostaticity was breached. On the other hand, R<sub>2</sub> was found to be independent of both parameters, leading one to conclude that it is a more suitable component for pressure measurement in DACs where nonhydrostaticity is frequently encountered.

Hence, the loading direction with respect to the crystallographic orientation of ruby is an important consideration and this could have certain implication when considering uniaxial strain tests on single-crystal ruby fibres.

It must, however, be noted that the high pressure and shock-wave experiments carried out by the various authors have all been under compression loading, none has involved pure uniaxial strain/tensile loading. Under hydrostatic pressure loading, the  $R_1$  and  $R_2$  lines shift equally while under nonhydrostatic loading, shifts in these two lines are unequal, due to the change in the energy level splitting of the  $\bar{E}$  and  $2\bar{A}$  states. Shock-wave tests, being able to separate the parameters to be measured, induce density compression in the ruby sample under investigation and this leads to uniaxial strain being created along the desired axis of the test sample.

## 5.2 Absorption and fluorescence spectra of ruby single-crystal fibres

Although the absorption spectrum of ruby is strongly dependent on the polarisation of light entering the sample [5.30], there is only a relatively small difference between the  $R_1$  and  $R_2$  intensities in its emission spectrum in both parallel and perpendicular orientations. The absorption spectrum of a ruby fibre grown by the LHPG technique, as shown in **Figure 5.6**, closely resembles that reported by He and Clarke [5.45], where light was polarised parallel to the sample's  $c$ -axis. The absorption spectrum of a bulk ruby laser rod is also shown in the figure for comparison. Unpolarised light from a stabilised Tungsten-Halogen lamp was used in these measurements and was transmitted along the  $c$ -axis of both the ruby fibre and rod.

The fluorescence from the same fibre is shown in **Figure 5.7**, together with that from the bulk ruby rod for comparison. A *Spectra Physics 2060-10S*  $\text{Ar}^+$  ion laser was used to excite the fluorescence along the fibre's  $c$ -axis. The experimental set-ups used for both the absorption and fluorescence measurements have already been described in **Chapter 4**.

The main objective of the absorption measurement is to confirm that high quality ruby single-crystal fibres can be grown using source fabrication techniques discussed previously in **Chapter 3** in combination with the laser heated pedestal growth

technique. As shown in **Figure 5.6**, the strong interaction of  $\text{Cr}^{3+}$  ions with the crystal field in sapphire leads to the observed wide absorption spectrum in the fibre, ranging from the UV (~350 nm) to the deep-red (~700 nm). Hence, a wide range of light sources can be used to excite the fibre. The two absorption peaks of ruby are centred at approximately 410 nm and 550 nm. The fluorescence spectrum from the ruby fibre showing the two sharp R-lines typical of ruby was excited using the 514.5 nm line of the  $\text{Ar}^+$  laser. The fluorescence spectrum shown in **Figure 5.7** agrees very well with the published work of He and Clarke [5.45], obtained from a *c*-axis ruby fibre, and that of Shen *et al.* [5.17]. The peak of the  $\text{R}_1$  line is at 694.3 nm while the slightly weaker  $\text{R}_2$  line peaks at 692.9 nm, corresponding to published data.

Figure 5.6. Absorption spectra of ruby SCF and bulk ruby rod

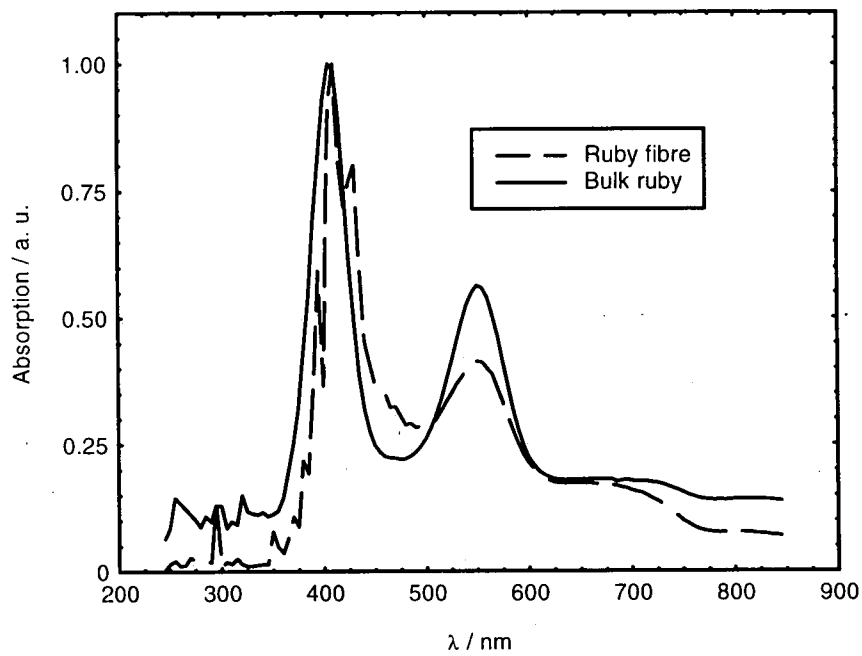
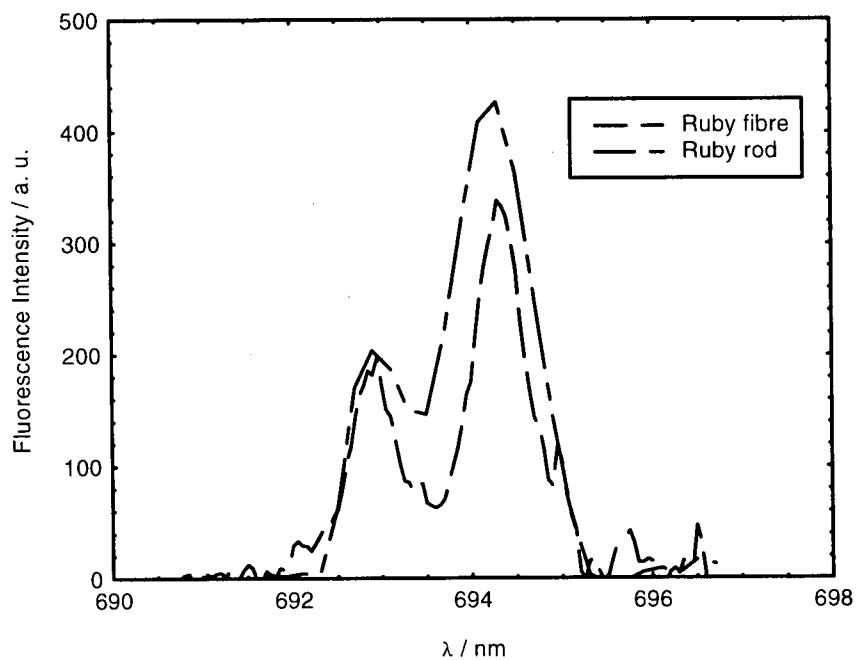


Figure 5.7. Fluorescence spectra of ruby fibre and bulk ruby rod



### 5.3 Temperature sensing experiments

In order to demonstrate the potential use of single crystal ruby fibres as temperature sensing probes, both the fluorescence lifetime decay and wavelength shifts of the two R-lines are measured with respect to temperature. At high temperature ( $\sim 873$  K), the lifetime decay rate of the ruby is expected to be very fast, around the microsecond regions, while the wavelength shifts in the  $R_1$  and  $R_2$  are expected to overlap and to be dominated by emission from the phonon sidebands.

#### 5.3.1 Fluorescence lifetime decay of single-crystal ruby fibres

Many  $\text{Cr}^{3+}$  doped materials, such as ruby, are characterised by strong interaction of the impurity ions with the host crystal and are thus considered as suitable sensing materials for fluorescence-based thermometric applications. In fluorescence-based sensing, the fluorescence decay time is a particularly attractive parameter used as a measurand since such a scheme has the advantage of being independent of excitation intensity. Moreover, the fluorescence lifetime is an intrinsic feature of a particular fluorescent material and should, in principle, be reproducible from material to material. This has important implications for fibre optic sensing in that the sensing probe, made of any particular fluorescent material, is easily replaceable if worn or damaged.

The fluorescence lifetime of ruby can be accurately assumed to decay in an exponential manner. Other competitive processes such as nonradiative decay can also take place, where energy is released as heat or phonons. Nonradiative decay is especially dominant at relatively high temperatures where thermal processes can promote ions from the first to the second excited state ( ${}^2E \rightarrow {}^2T_2$ ). One should also consider the effect on lifetime due to the concentration of the  $\text{Cr}^{3+}$  impurity ions. The fluorescence intensity increases with increasing concentration of the  $\text{Cr}^{3+}$  ions until a critical level is reached, after which higher concentrations lead to a reduction of its fluorescence intensity [5.32]. This effect is known as concentration quenching and in ruby, the fluorescence lifetime is independent of the impurity's concentration up to a critical level of around 0.3 wt. % [5.32]. Higher concentrations also lead to a decrease in the observed fluorescence lifetime. Moreover, it has been reported that

above ~1 wt. % of chromium content, the lifetime decay is no longer a simple exponential [5.46]. Hence, care has to be exercised in selecting a sensing ruby fibre with concentration levels below the critical value, with regards to both concentration quenching and non-exponential decay rate.

### 5.3.1.1 Experiment

The ruby fibres used in this work were found to have an average chromium concentration of 0.1 wt. %, measured using the EMPA (electron micro-probe analysis) technique. The fibre is considered to be sufficiently highly doped, containing approximately twice the chromium concentration level to that of a typical ruby laser material. Fibres were grown using the laser heated pedestal growth technique and found to be of high optical quality. No surface blemishes were observed when inspected with an optical microscope and diameter variations were measured to be of the order of  $\pm 1 - 2$  %. The main sample used in this study had a nominal diameter of  $\sim 167 \mu\text{m}$  and a total length of  $\sim 75$  mm. One end was tapered for better reflection of the fluorescence signal.

The experimental set-up for monitoring the temperature-dependent fluorescence lifetime is illustrated in **Figure 5.8**. A silica fibre, *Thorlabs FVP-200-PF*, with a core diameter of  $200 \mu\text{m}$  was used as a lead-in fibre to transmit the excitation light to the target ruby fibre. The two fibres were simply butt-coupled together through the use of a silica capillary which was tapered to cater for the slight difference in diameters between the two fibres. This is shown by the insert in **Figure 5.8**. They were then held together rigidly by applying some high temperature ceramic adhesive to both ends of the tubing. The reflected fluorescence signal collected by the same silica fibre was routed via a 1 x 2 fibre coupler to a photodetector. The detector used was a *Hamamatsu C5460* avalanche photodiode (APD) with a cut-off frequency of 10 MHz, sufficiently fast for this application. A high speed (10 to 100 MHz) voltage amplifier (*FEMTO*) was used to match signal levels to those required at the input of the 500 MHz *HP* digitising oscilloscope. The excitation beam from the  $\text{Ar}^+$  laser was modulated by an optical chopper which also served as the trigger for the oscilloscope. The gain of the amplifier was set at the minimum of 10 dB and was

maintained throughout the experiment. In order to separate the desired fluorescence signal from the excitation source, an optical narrow bandpass interference filter centred at 694 nm, with a FWHM of  $\pm 2$  nm was employed just in front of the APD. This ensured a relatively "clean" signal from the ruby fibre with no excitation light leakage detected. A microscope objective (X20, NA 0.54) was used to collimate the output from the coupler and a focusing lens ( $f \sim 50$ mm) directed the signal onto the detection circuit.

Before the fluorescence lifetime from the ruby fibre could be monitored with any accuracy and confidence, tests were carried out to characterise the bandwidth of the whole signal detection circuit. The ruby fibre was removed from this test and the square wave, modulated signal from the  $\text{Ar}^+$  laser observed directly. Of particular relevance is the rise and fall time of the detected signal. It should be noted that the optical chopper was placed at the confocal point in the laser beam expander to optimise, as far as possible, the system response. The test signal of the whole system was averaged over 2048 times (11 bit averaging) by the digitising oscilloscope and the data stored on disk. Curve fitting was then applied, assuming that the decay of the system (falling edge of the  $\text{Ar}^+$  laser pulse) was exponential, and  $\tau_{\text{system}}$ , the lifetime was found to be  $\sim 7.4 \mu\text{s}$  (**Figure 5.9**). This thus formed the limit to the lifetime which can be reliably measured in this experiment.

For temperature characterisation, a *CARBOLITE Eurotherm* furnace with a quoted stability of  $\pm 1$  K and a maximum temperature limit of 1473 K served as the heat source. High temperature ceramic wool was used to plug both ends of the heating chamber in order to maintain a more stabilised temperature at the set level. The ruby fibre which was used as the sensing probe, was inserted into the heating chamber of the furnace through one of the ceramic wool plugs and was not allowed to be in contact with the chamber wall. The upper limit of the temperature investigated was  $\sim 973$  K and this, in practice, should have no significant effect on the silica fibre. A type "K" thermocouple was also inserted into the heating chamber to serve as a calibration.

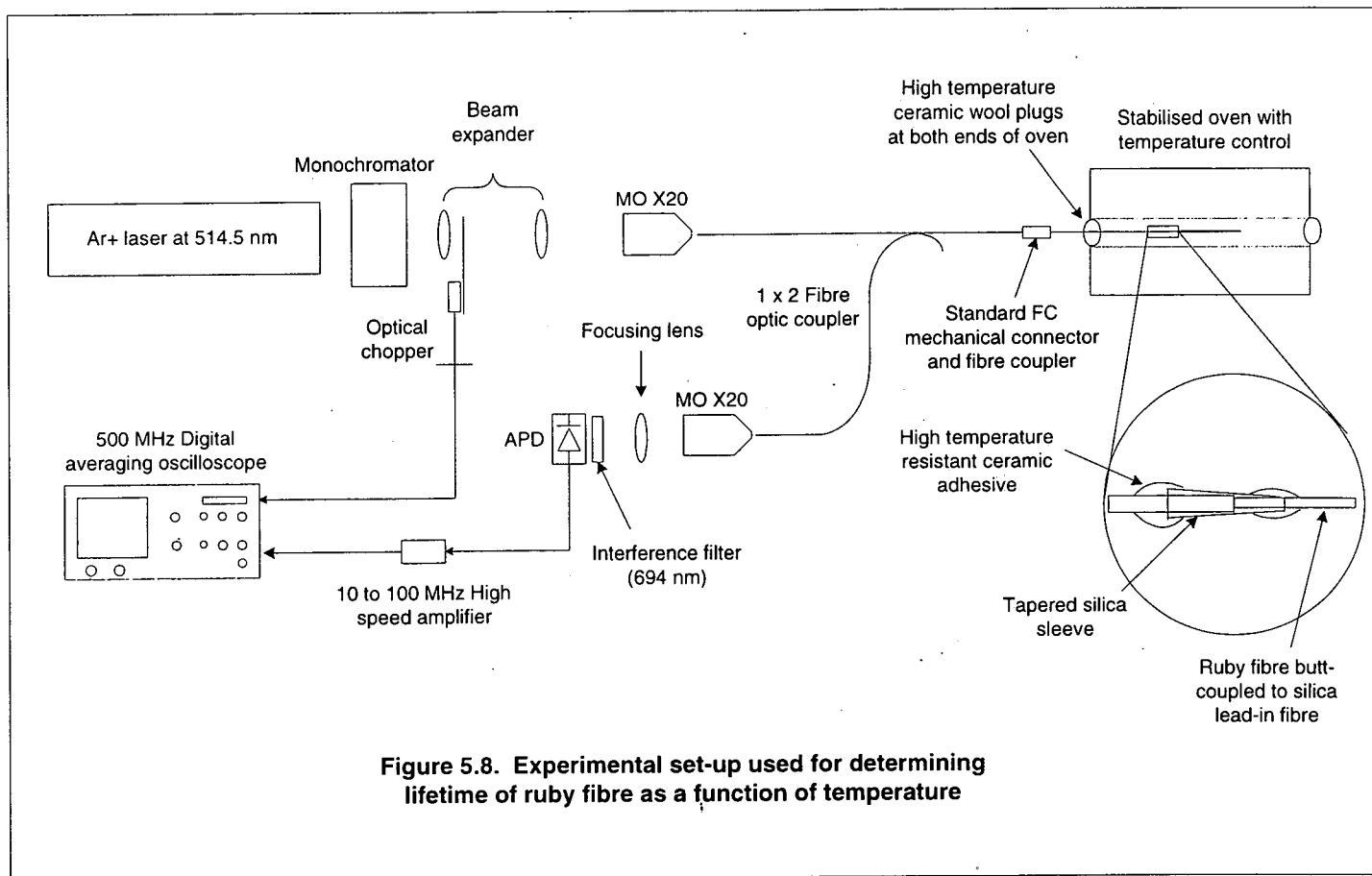
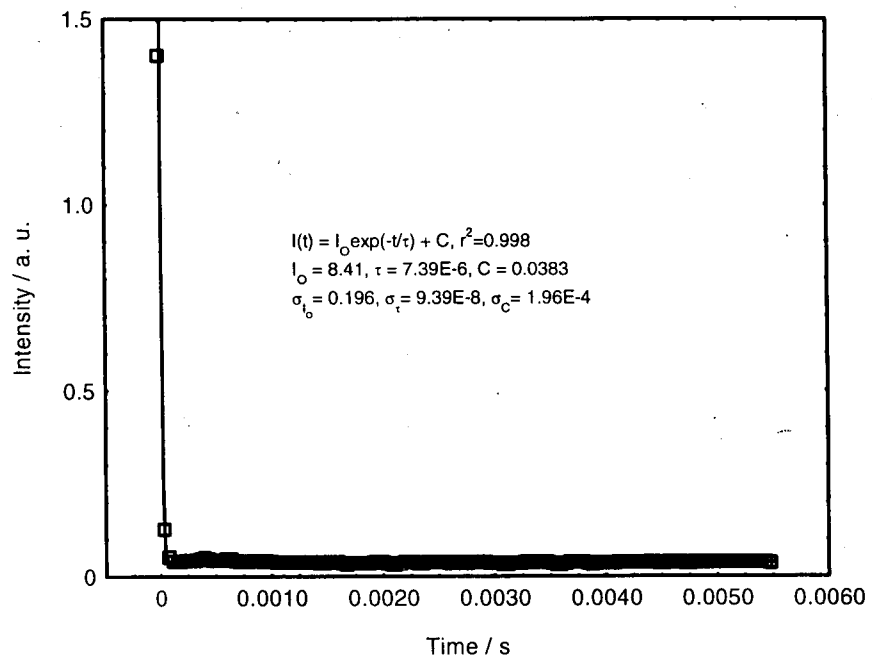


**Figure 5.8. Experimental set-up used for determining lifetime of ruby fibre as a function of temperature**

Figure 5.9. Falling edge of the modulated Ar<sup>+</sup> laser signal at 514.5 nm



### 5.3.1.2 Results and Discussion

The least-squares curve fitting technique was applied to the averaged lifetime data captured by the *HP* digital oscilloscope. The results for each temperature increment were observed to decay in intensity in a single exponential manner. The fluorescence lifetime of the sensor was taken at intervals of 50 K starting at room temperature. The single exponential equation used for fitting all curves is given as

$$I(t) = I_0 e^{(-t/\tau)} + C \quad (5.8)$$

where  $I(t)$  is the intensity of the decaying fluorescence signal at time  $t$ ,  $I_0$  the intensity value at  $t = 0$ ,  $\tau$  the lifetime decay of the fluorescence signal and  $C$  is a constant due to any dc offset in the detected signal.

The fluorescence lifetime of the ruby fibre at 292 K, the room temperature, is shown in **Figure 5.10a** where some of the curve statistics are also displayed. The level of determination of the curve fit,  $r^2$ , indicates the “goodness” or confidence of the curve fitting achieved while the standard deviation of the fitted lifetime is displayed as  $\sigma_\tau$ . The errors (in %) have been calculated using the deviations from the measured data and these limit the resolution of the sensor over the temperature range investigated. Subsequent curve fittings for all monitored temperatures up to 923 K are also plotted in the remainder of **Figures 5.10**. **Table 5.1** is a compilation of all the measured lifetime values and their respective standard deviations against temperature, while **Figure 5.11** plots the ruby fibre fluorescence lifetime as a function of temperature together with the associated errors. **Figure 5.12** shows the lifetime data from a bulk ruby laser rod together with the experimental data for comparison.

One of the the two models (modified two-level model and single configurational coordinate model) proposed by Zhang *et al.* [5.5] has also been studied and shall be discussed below. The single configurational coordinate model as discussed earlier has been used to fit the experimentally obtained lifetime data and the equation (**Eq. 5.4**) is expressed again as

$$\tau = \tau_s \frac{1 + 3e^{-\Delta E / kT}}{1 + \alpha e^{-\Delta E / kT} + \beta e^{-(\Delta E_q + \Delta E)}}$$

where all the parameters to be fitted are as defined in **Eq. 5.4**. The fitted values for  $\Delta E$ ,  $\alpha$ ,  $\beta$  and  $\Delta E_q$  are given in **Table 5.2**. In **Table 5.3**, the experimental and calculated lifetime values using the SCC model are shown for comparison. The fitted curve for temperatures up to 923 K can be seen in **Figure 5.13**. The model fits reasonably well to the data except at high temperatures, where, as we might expect from the low signal intensities at these temperatures, relatively large errors are obtained. An approximation of the sensitivity of the model is also shown in **Figure 5.14**, where the sensitivity curve can be observed to increase to a negative maximum at ~400 K before decreasing again quite rapidly to a minimum at 923 K, the maximum operating temperature.

For the fluorescence lifetime sensor using a single-crystal ruby fibre, it can be seen from **Figures 5.10** that very good fits have been achieved throughout most of the temperature range up to 773 K where the confidence of fit was almost 100 %. At this temperature, the standard deviation of the fitted lifetime decay was seen to remain significantly low at ~0.5  $\mu$ s and the error associated with this deviation was calculated to be 0.32 %, giving a resolution of ~2.4 K. The accuracy of the curve fitting procedure at this temperature and beyond was affected by the low intensity of the decay signal. The maximum deviation of the lifetime limited the resolution of temperature measurements and was also the limit of resolution of the whole sensor system. The maximum deviation was found to be ~4.6 % at 923 K, translating into an approximate error of 43 K or 30 °C. The average resolution for the sensing scheme was calculated to be ~ 2.4 K or 1.6 °C from room temperature (292 K) to 773 K. Below 673 K, a resolution of better than 1 K has been obtained as can be seen in **Table 5.1**. This allowed temperature changes of less than 1 K to be accurately detected. It could thus imply the possibility of high resolution measurement of the fluorescence lifetime as well as the effectiveness and simplicity of the detection/signal processing techniques employed in this sensing scheme. One major disadvantage of such a scheme, however, is the relatively large amount of time spent in capturing the data on the averaging oscilloscope and the curve fitting technique.

The total time required to average the 11 bit data set has been timed to be less than 3 ½ minutes. This was followed by the rather time-consuming least-squares curve fitting procedure. However, good fits with small errors have been obtained.

In addition, the relatively close agreement achieved from the experimental data fitted with the SCC model (Eq. 5.4) also indicated accurate prediction of the fluorescence lifetime characteristics of these single-crystal ruby fibres with theory which has been discussed earlier. This model takes into consideration the rapid non-radiative transition and thermal quenching rates within a relatively large temperature range. Hence, as predicted by the model, relatively long lifetimes (~2 – 3 ms) were measured at low temperatures while beyond 600 K, when non-radiative transition and thermal quenching became dominant, the fluorescence lifetime was found to fall rapidly below 1 ms, resulting in increasing errors being obtained. The relatively large errors encountered have been found to limit the resolution and accuracy obtainable when employing the SCC model as a calibration curve. However, comparison with published data from Zhang *et al.* [5.5] and Grattan and Zhang [5.32] shows that reasonably good agreement has been achieved by using the single configurational coordinate model to fit the lifetime decay values measured in this work. This in turn validated the theory of crystal field strength and phonon-lattice interactions as well as the assumption made on the non-radiative transition or thermal quenching effect from the short-lived  $^4T_2$  state. It can be seen that the lifetime decays monotonically with temperature and no ambiguities of the same lifetime at two or more different temperatures have been observed. At ~673 K, the beginning of a change in the gradient of the lifetime/temperature curve can also be observed. The large discrepancies from 823 K could be due to instability in the data averaging and signal processing schemes employed. Moreover, the flattening of the lifetime between 873 K and 923 K have occurred very near the minimum lifetime limit of the whole sensing system. This resulted in considerable inaccuracies, even though the minimum limit has been determined as ~7.4  $\mu$ s, and have been reflected in the large errors obtained at this two temperatures as calculated in **Table 5.1** (1.98 % and 4.62 % at 873 and 923 K respectively). Another important factor contributing to this disparity in both sets of results is the choice of optical filters used. In this work, a narrow bandpass optical filter having a central wavelength of 694 nm, the ruby peak fluorescence wavelength, with a FWHM bandwidth of  $\pm 2$  nm was used. This

FWHM tolerance, however, isolates the sideband phonon energies associated with ruby emission characteristics which are highly temperature-dependent. The filter used in the compared work [5.14] was a longpass filter with passband from 670 nm upwards. The sensitivity curve of the SCC model used in this work has been plotted in **Figure 5.14**. The amplitude of the sensitivity for the SCC model can be seen to reach a maximum value at ~673 K, followed by a decrease towards the minimum with increasing temperature. The sensitivity of the curve is negative in value due to the drop in the lifetime rate with temperature.

It can thus be seen that, within experimental error, the rate of the fluorescence lifetime decay of ruby fibres with temperature has been accurately measured using an averaging technique provided by a digitising oscilloscope. These fibres are thus considered to be suitable as a fluorescence-based thermometric sensor probe from room temperature to ~923 K although in practical implementation, the signal detection and processing scheme have to be altered to offer a fast and accurate response since the temperature variation may not be static but quasi-static or dynamic. One such signal detection and processing configuration may be that using phase-sensitive feedback lock-in detection reported by Zhang *et al.* [5.13].

Figure 5.10a. Ruby fibre lifetime decay at room temperature (292 K)

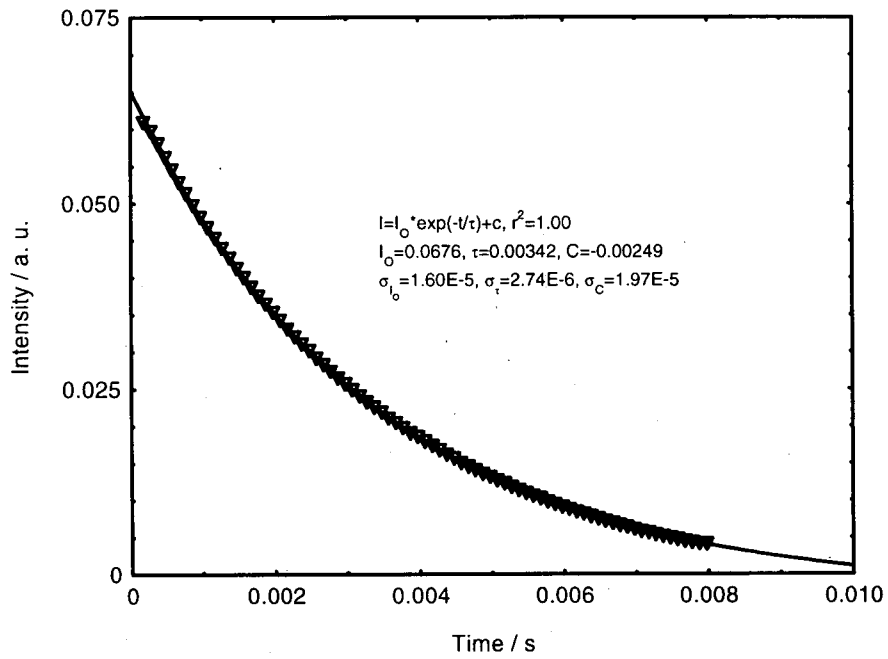


Figure 5.10b. Lifetime decay at 373 K

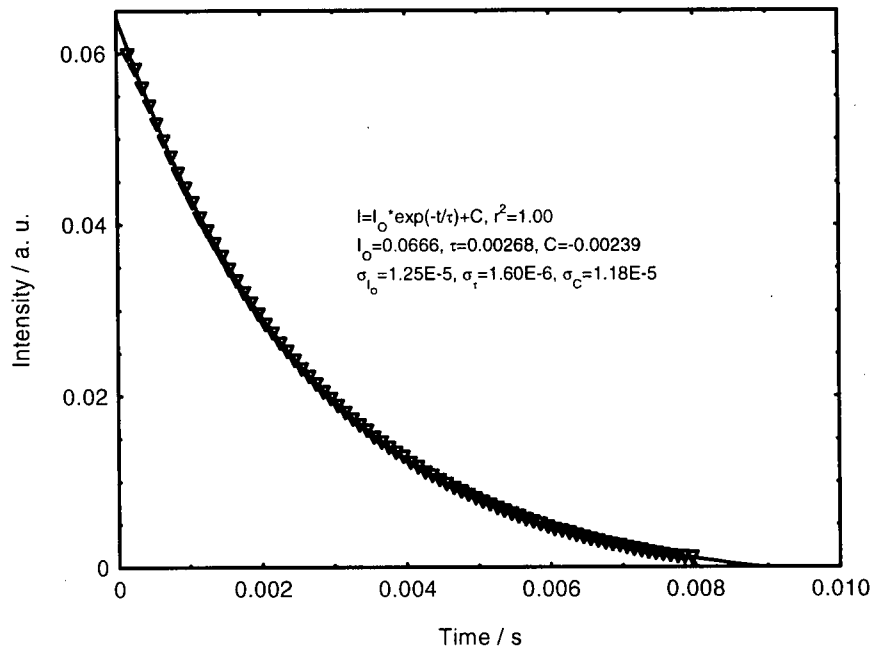


Figure 5.10c. Lifetime decay at 374 K

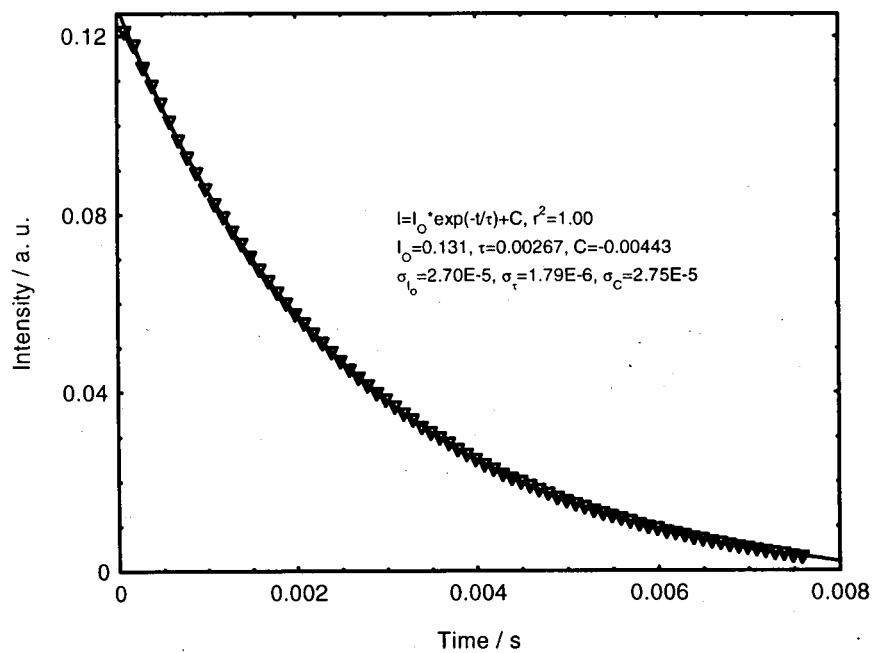


Figure 5.10d. Lifetime decay at 473 K

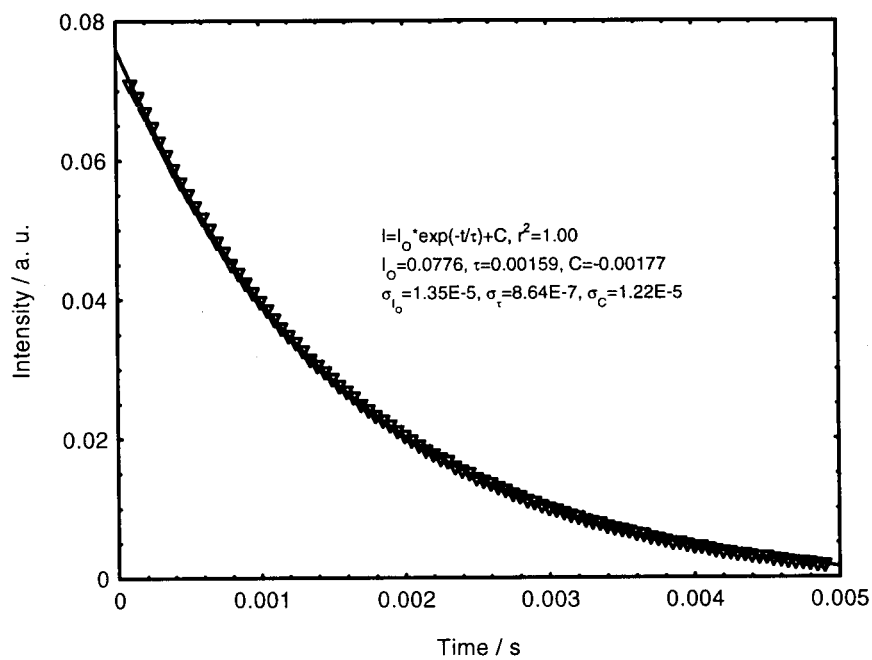


Figure 5.10e. Lifetime decay at 573 K

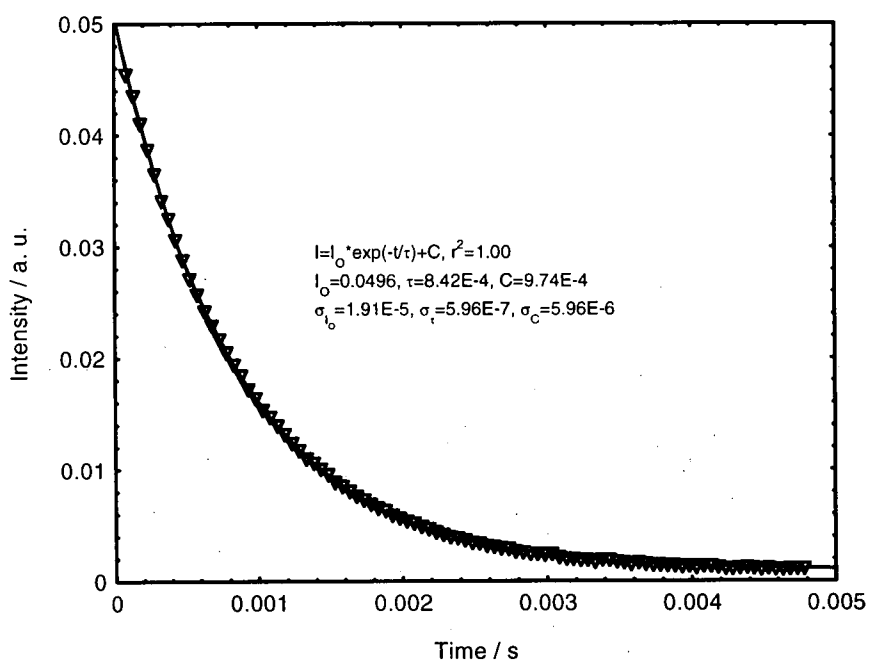


Figure 5.10f. Lifetime decay at 673 K

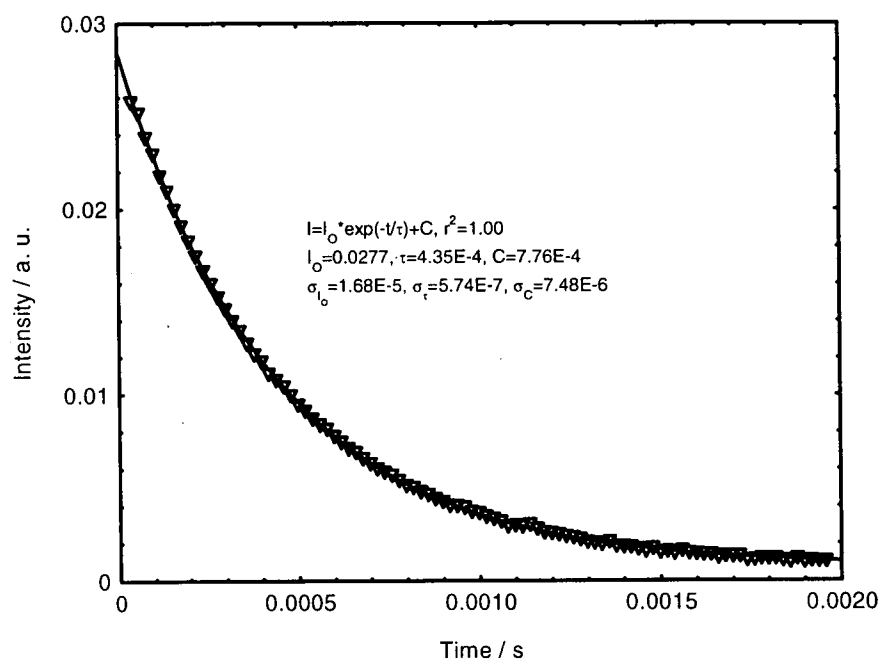


Figure 5.10g. Lifetime decay at 773 K

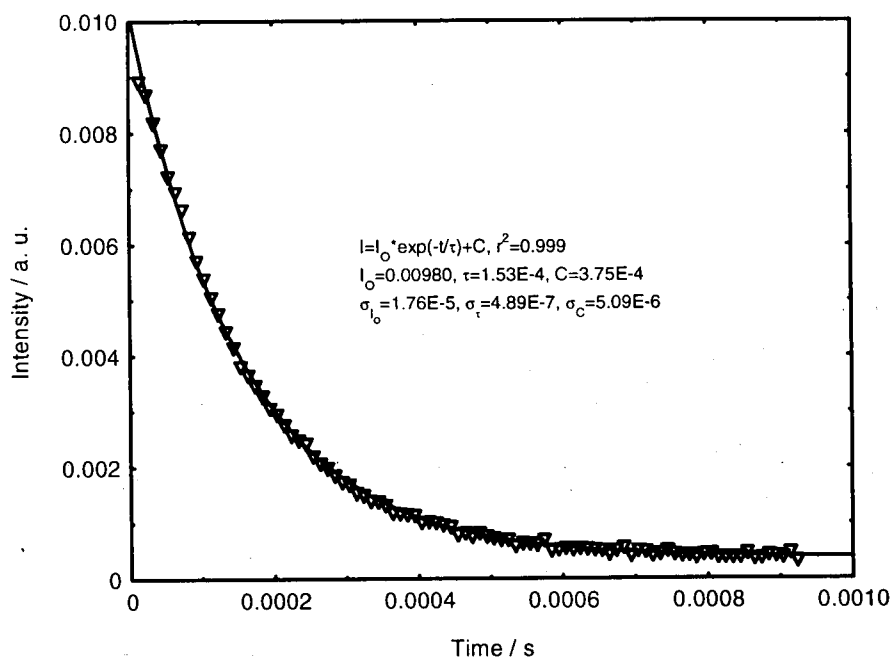


Figure 5.10h. Lifetime decay at 873 K

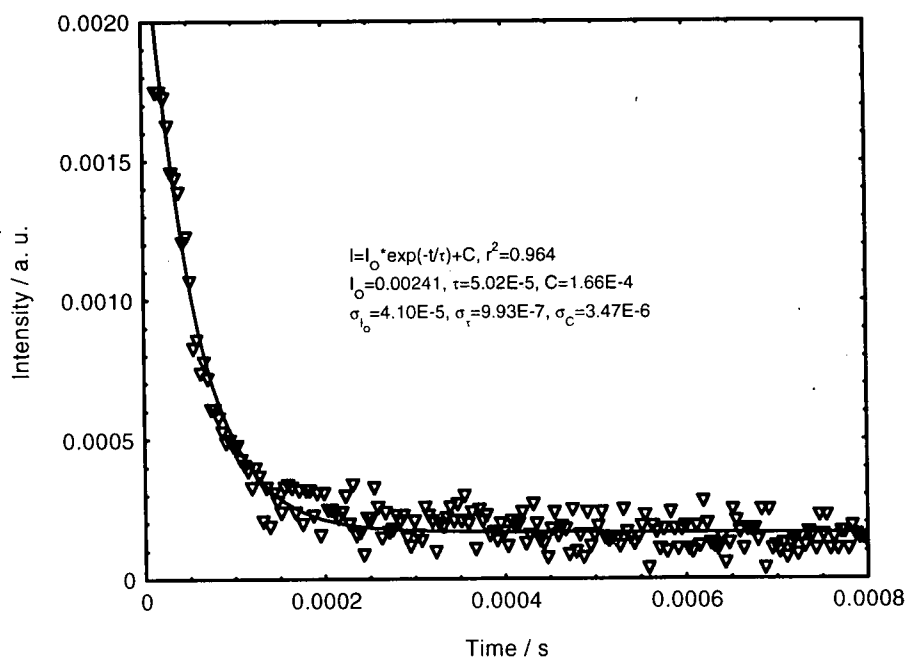


Figure 5.10i. Lifetime decay at 923 K

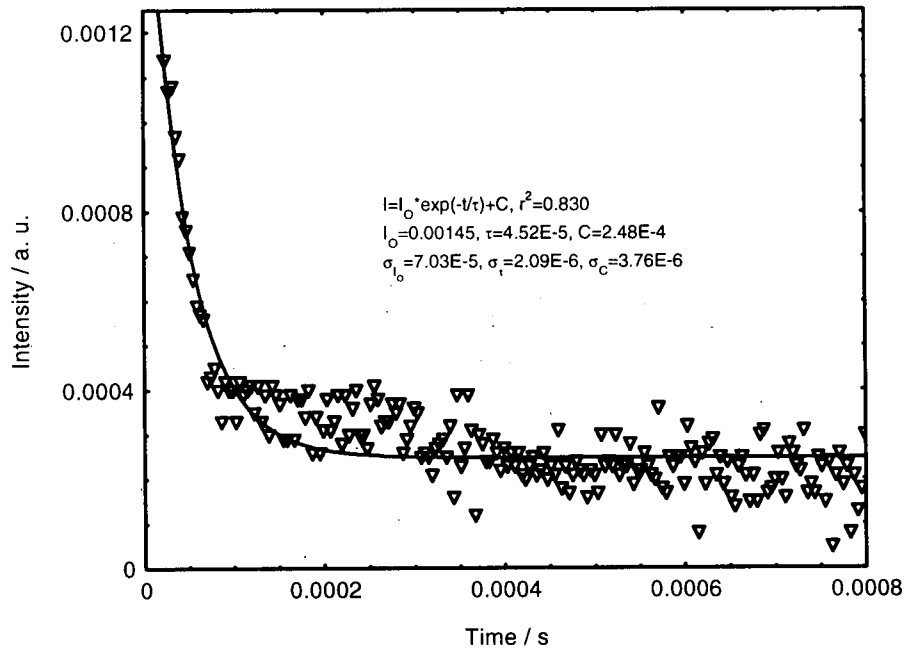


Figure 5.11. Temperature dependence of ruby fibre fluorescence lifetime

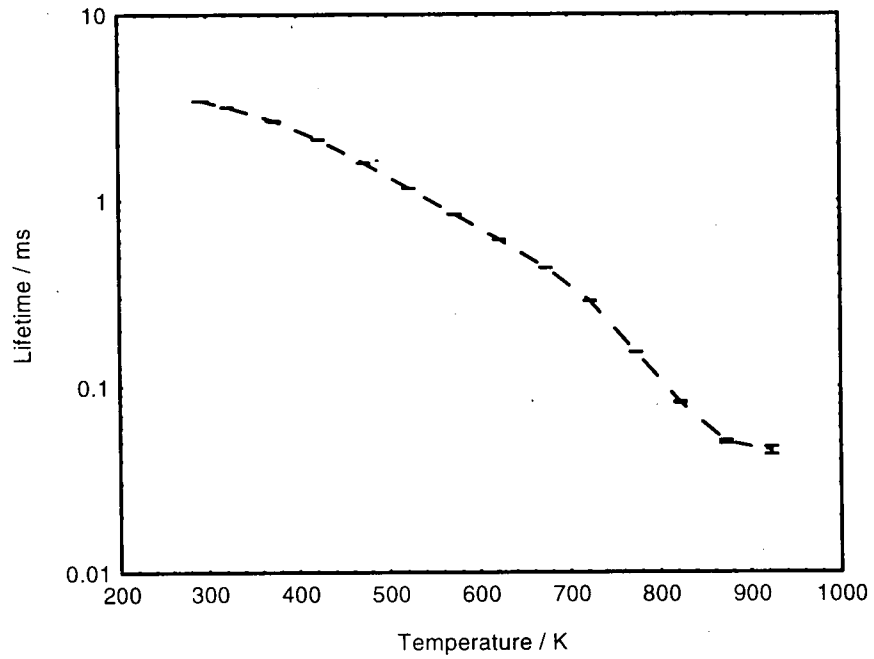


Figure 5.12. Temperature dependence of fluorescence lifetime of ruby fibre and bulk ruby rod

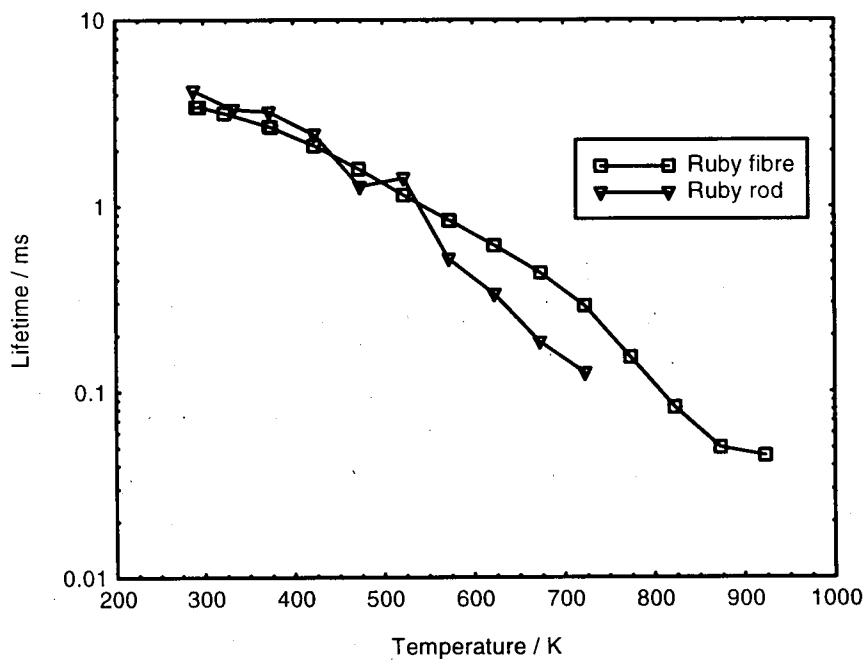


Figure 5.13. Single configurational coordinate model for ruby fibre

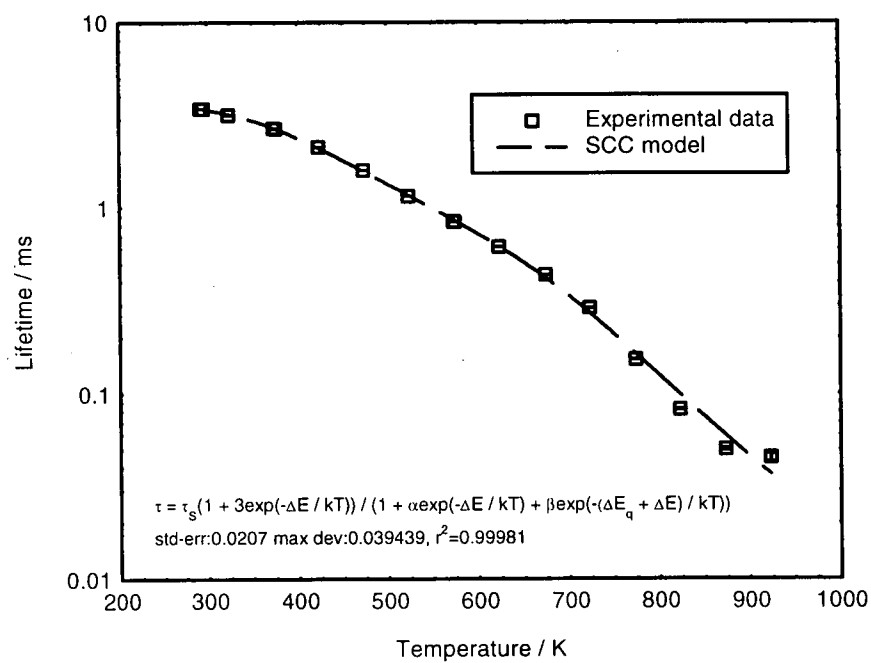
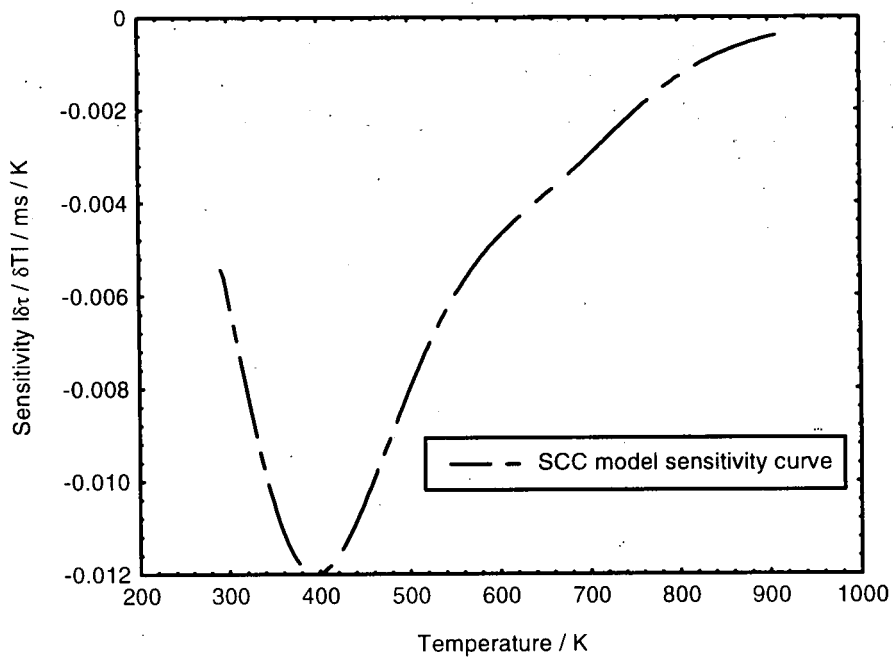


Figure 5.14. Sensitivity curve of SCC model



**Table 5.1. Measured lifetime as a function of temperature.**

Temp. / K	$\tau$ / ms	$\sigma_{\tau}$ / ms	Error / %	$r^2$
292	3.42	$2.74 \times 10^{-3}$	0.08	1
295	3.42	$5.2 \times 10^{-3}$	0.15	1
323	3.16	$2.06 \times 10^{-3}$	0.065	1
373	2.68	$1.6 \times 10^{-3}$	0.06	1
374	2.67	$1.79 \times 10^{-3}$	0.067	1
375	2.66	$1.37 \times 10^{-3}$	0.052	1
423	2.12	$7.81 \times 10^{-4}$	0.037	1
473	1.59	$8.64 \times 10^{-4}$	0.054	1
523	1.16	$7.64 \times 10^{-4}$	0.066	1
573	0.842	$5.96 \times 10^{-4}$	0.071	1
574	0.839	$4.38 \times 10^{-4}$	0.052	1
623	0.615	$5.77 \times 10^{-4}$	0.094	1
673	0.435	$5.74 \times 10^{-4}$	0.132	1
723	0.289	$5.12 \times 10^{-4}$	0.177	1
773	0.153	$4.89 \times 10^{-4}$	0.32	0.999
823	0.0822	$6.3 \times 10^{-4}$	0.766	0.995
873	0.0502	$9.93 \times 10^{-4}$	1.98	0.964
923	0.0452	$2.09 \times 10^{-3}$	4.62	0.83

**Table 5.2. Fitted parameters for SCC model.**

$\tau_s$ / ms	$\Delta E$ / $\text{cm}^{-1}$	$\alpha$	$\beta$	$\Delta E_q$ / $\text{cm}^{-1}$
3.617	1637.4	197.6	$2.818 \times 10^6$	4888.26

**Table 5.3. Comparison of measured and calculated lifetimes using SCC model.**

Temp. / K	Measured $\tau$ / ms	Calculated $\tau$ / ms	Error / %	Std. Dev. / %
292	3.42	3.41	0.246	8.401
295	3.42	3.40	0.728	
323	3.16	3.20	-1.249	
373	2.68	2.69	-0.256	
374	2.67	2.68	-0.194	
375	2.66	2.66	-0.131	
423	2.12	2.09	1.232	
473	1.59	1.57	1.326	
523	1.16	1.16	-0.265	
573	0.842	0.86	-1.827	
574	0.839	0.851	-1.555	
623	0.615	0.617	-0.385	
673	0.435	0.423	2.861	
723	0.289	0.271	6.172	
773	0.153	0.165	-8.058	
823	0.0822	0.0987	-20.048	
873	0.0502	0.05929	-18.12	
923	0.0452	0.03651	19.226	

### 5.3.2 Wavelength shifts of ruby fibre R-lines with temperature

As has been discussed earlier, the lineshifts in the ruby R-lines, although more appropriate in high pressure and shock-loading applications, have been found to vary with temperature in earlier studies [5.25]. The R-line shifts towards the red are relatively small and, hence, are more normally used as a compensation factor in high pressure measurements in DACs than for thermometric applications. At elevated temperatures, the temperature-induced lineshifts are nonuniform and overlapping of the  $R_1$  and  $R_2$  lines have been observed in this work. The stronger  $R_1$  line is still relatively visible while the  $R_2$  line is seen to merge into the main body of the R-line fluorescence beyond  $\sim 873$  K. Although one way to overcome this overlapping phenomenon entails the use of fitting a model to describe the ruby fluorescence lineshape, it has not been used in this work. Instead, the two R-lines have been tracked over the temperature range investigated; when the  $R_2$  line became obscured, the  $R_1$  line was monitored up to a temperature when it too became difficult to resolve. Hence, only the true shifts in the fluorescence lines were investigated, not the model, least of all because when the lines merged, large errors may arise due to uncertainties in the actual movement of the R-lines.

The wavelength shifts of the ruby R-lines have been studied by various authors and have been attributed to: electronic-phonon (both optical and acoustic phonons) energy interactions between the  $\text{Cr}^{3+}$  ions and the host lattice;  $\text{Cr}^{3+}$  concentration in  $\text{Al}_2\text{O}_3$  host crystals; and thermal expansion of the ruby crystal at elevated temperatures [5.3, 5.18, 5.19, 5.37, 5.38, 5.47]. Although it has been reported that the ruby fluorescence is strongly dependent on the polarisation direction of the crystal [5.19], *c*-oriented single-crystal ruby fibres have been used in this investigation. It has been shown in **Figure 5.7** that the emission spectrum of these ruby fibres closely resembled that of **Ref. [5.45]**, confirming that the emission from the fibres employed were polarised along the *c*-axis.

#### 5.3.2.1 Experiment

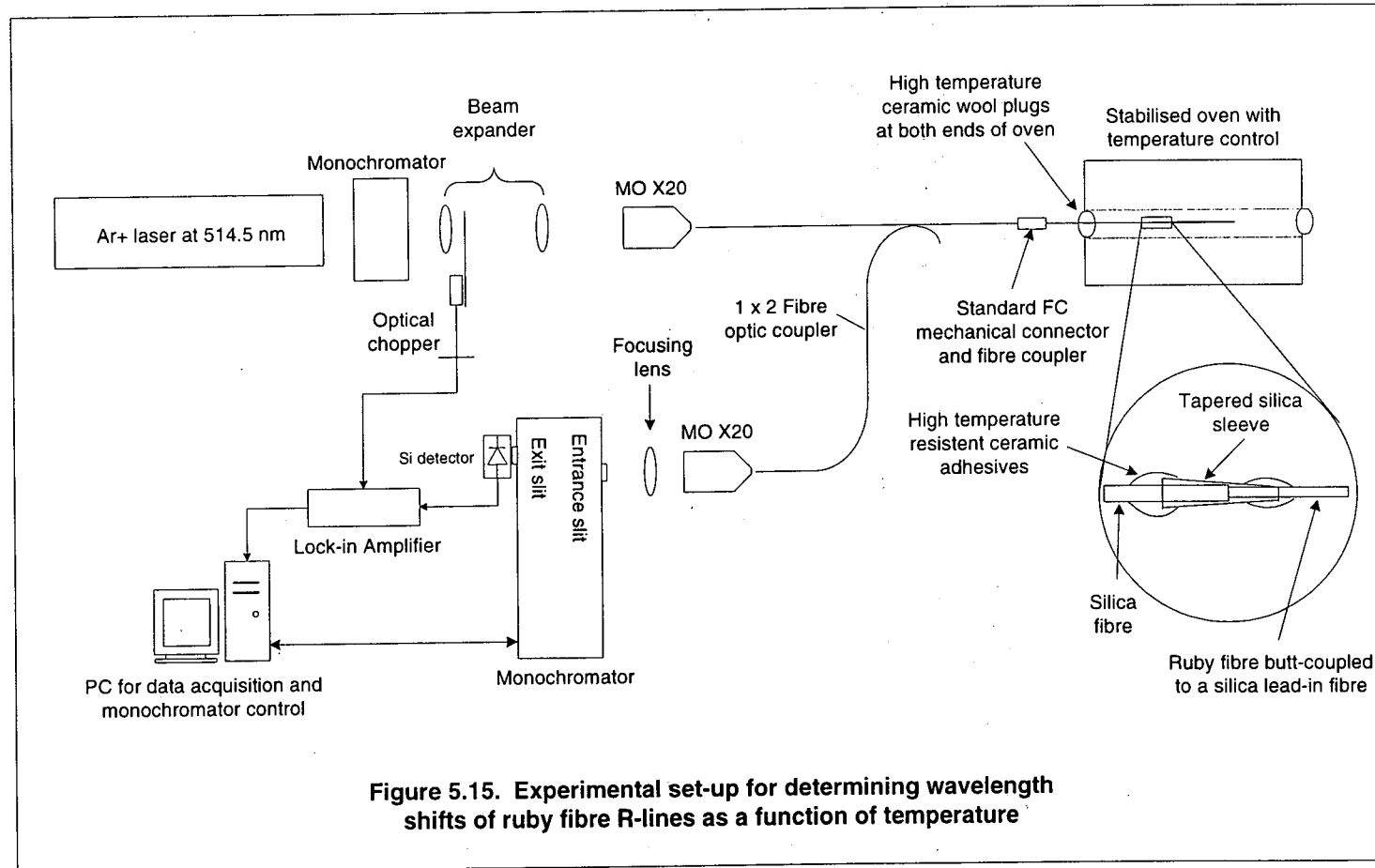
For consistency, the same principal fibre sample used in lifetime measurements experiment was employed here, where the shifts in R-line positions were monitored

with respect to increments in temperature. The experimental set-up was similar to that used for temperature-dependent fluorescence lifetime measurements except that, in this case, the detection system included a monochromator.

A schematic diagram of the experiment is shown in **Figure 5.15**. Fibres were inserted into the *CARBOLITE* tube furnace and not allowed contact the furnace walls. Once again, fibres were butt-coupled to the silica fibre using a silica tubing with a tapering diameter profile along its length and both ends sealed using high temperature adhesives (*Fortafix AL/CS*). Measurements were taken in reflection mode where the fluorescence signal, excited by an  $\text{Ar}^+$  ion laser, was collected from the second port of the 1 x 2 fibre coupler and collimated with a microscope objective (X20). The collimated output from the M.O. was then imaged onto the entrance slit of a ½ metre monochromator using a 40 mm focusing lens, with both entrance and output slit widths set at 100  $\mu\text{m}$ . The monochromator used was a *DIGIKRÖM DK480* from *CVI Laser Corporation* with a focal length of 480 mm, an effective aperture ratio of  $f/7.8$  and a Czerny-Turner configuration. The long focal length provided by the monochromator ensured that stray light was significantly reduced.

The output from the *CVI* monochromator was detected using a conventional Si PIN photodiode connected up to a *Sci-Tech* lock-in amplifier to increase the signal-to-noise ratio of the measurement system. The use of lock-in amplification also enabled a very stable detection of the desired signal when the monochromator was scanned through the required spectral range (690 to 697 nm) in steps of  $\sim 0.02$  nm per scan. The task of controlling (and coordinating) the scanning rate of the monochromator and the data acquisition was performed by a dedicated computer program written in LabView. All measured data were stored in the computer for subsequent analysis.

The experimental repeatability was assessed and was seen to fall within the 0.02 nm specified by the scanning steps, except at very high temperature where the inherent noise from the ruby fluorescence was relatively high.



### 5.3.2.2 Results and Discussion

The fluorescence spectrum of the ruby fibre at room temperature is shown in **Figure 5.16**. Three other fluorescence spectra taken at different temperatures, at 473, 623 and 673 K, are also shown for comparison. It is apparent that the  $R_2$  line, with its relative intensity much reduced but still clearly visible at 673 K, has shifted more towards the red than the  $R_1$  line. This resulted in it becoming difficult to resolve at 773 K or above.

The wavelength shifts of the two R-lines as a function of temperature are plotted in **Figures 5.17a** and **5.17b**. Although no model such as the Lorentzian and Gaussian profile was used to describe the fluorescence spectrum, a sliding data window technique over  $\sim 0.4$  nm was used to smooth the high frequency fluctuations observed throughout the whole spectrum in order to improve peak detection. The error obtained, by comparing measured and smoothed peak values, with this technique is within the 0.03 nm imposed by the resolution of the monochromator, hence, the resulting data may be taken as having an accuracy of this value. Up to  $\sim 500$  K, the shifts in both lines are linear and almost uniform. Beyond this temperature, they can be seen to diverge, with the  $R_2$  line shifting more than the  $R_1$  line. The red shift of the  $R_2$  line is more obvious and increases more significantly from  $\sim 573$  K onwards until the limit of measurement at 823 K, where the line appears to merge or overlap with the main body of the fibre fluorescence. At this temperature, only the  $R_1$  line is still visible, as shown in **Figure 5.18**. The maximum temperature investigated in this work was  $\sim 973$  K, at which point the signal was lost in background noise.

Although both shifts from the R-lines are almost linear, a relatively large increase can be seen at  $\sim 623$  K. The shifts in both R-lines have been re-confirmed in another experiment. Hence, it can be seen that there are two temperature regions where the wavelength shifts are linear for the two lines, separated by a sharp but significant increase from 623 to 673 K (**Figures 5.17**). They represent almost a doubling of the wavelength shifts for both lines.

Calibration curves are thus deemed appropriate to describe the shifts in the two temperature regions for both R-lines. Two sets of cubic calibration curves are used

to predict the wavelength shifts of the ruby fibre, as has been reported by Ragan *et al.* [5.19], for temperatures up to 623 K (350 °C). These are plotted in **Figure 5.19a**. The general cubic expression, given in **Eq. 5.7**, is used here,

$$R_i(T) = \alpha + \beta T + \delta T^2 + \gamma T^3$$

where  $\alpha = 693.74$  nm,  $\beta = 0.0023464$  nm K<sup>-1</sup>,  $\delta = -1.5802 \times 10^{-6}$  nm K<sup>-2</sup> and  $\gamma = 7.6748 \times 10^{-10}$  nm K<sup>-3</sup> for the R<sub>1</sub> line, and 692.29 nm, 0.0027091 nm K<sup>-1</sup>,  $-2.498 \times 10^{-6}$  nm K<sup>-2</sup> and  $1.4853 \times 10^{-9}$  nm K<sup>-3</sup> respectively for R<sub>2</sub>. Neglecting the sharp rise in lineshifts between 623 and 673 K, the same expression can also be used to calibrate the R-lines from 673 K to the maximum temperature (973 K and 823 K respectively for R<sub>1</sub> and R<sub>2</sub>), giving  $\alpha = 694.25$  nm,  $\beta = -3.3161 \times 10^{-4}$  nm K<sup>-1</sup>,  $\delta = 3.7492 \times 10^{-6}$  nm K<sup>-2</sup> and  $\gamma = -1.8444 \times 10^{-9}$  nm K<sup>-3</sup> for R<sub>1</sub>. The fitted curves for this temperature range have been plotted in **Figure 5.19b**. For R<sub>2</sub>, where the largest error occur at the maximum temperature of 823 K, the respective fitted values of  $\alpha$ ,  $\beta$ ,  $\delta$  and  $\gamma$  are 695.33 nm,  $-0.005613$  nm K<sup>-1</sup>,  $3.9402 \times 10^{-6}$  nm K<sup>-2</sup> and  $1.2679 \times 10^{-9}$  nm K<sup>-3</sup>. **Tables 5.4a** and **5.4b** list all the fit parameters for R<sub>1</sub> and R<sub>2</sub> from 291 to 623 K and from 673 to 973 K respectively. The measured and calculated (using **Eq. 5.7**) values of the lineshifts are given in **Tables 5.5a** and **5.5b** where the maximum deviation from the average measured lineshifts at each corresponding temperature has been treated as the error. The wavelength coefficients of R<sub>1</sub> and R<sub>2</sub> have been found by differentiating the equations for the respective temperature ranges and substituting the appropriate temperature data. These are listed in **Tables 5.6**. Since these lines can be approximated as linear, the wavelength coefficients have also been found by obtaining the gradients from different straight lines fitted to the experimental data. These have been listed in **Tables 5.6** and for comparison the average from the cubic fits were taken. **Figures 5.20a** and **5.20b** show the relatively good agreement that have been obtained using the linear fits.

The maximum red shift of the R-lines was found to be ~1.23 nm for the R<sub>1</sub> line. The characteristic R-lines due to energy splitting of the lowest excited ruby state by the various electron-phonon interactions have been found to be slightly sensitive to temperature. Hence, application of increasing thermal energy can lead to further

changes or shifts in the split states which in turn results in the observed wavelength shifts of the R-lines. The temperature-induced shifts in both the R-lines of the *c*-axis ruby fibre have been monitored up to 973 K for the stronger R<sub>1</sub> line and 823 K for the R<sub>2</sub> line. Due to relatively large shifts of the R-lines from 623 K to 673 K, a single continuous fit cannot be used to describe the wavelength coefficient. Hence, the separate temperature regions have been investigated employing two simple calibration curves based on that reported by Ragan *et al.* [5.19]. This doubling of the wavelength shift have not been reported anywhere in published literature, hence, the causes are still unknown. The only parameters which have been changed were the laser power and the sensitivity of the lock-in amplifier used. No observable changes in the position of the R-line have been detected by changing the laser power, while increasing the lock-in amplifier's sensitivity by one setting only increased the intensity detected by a factor of 3. At room temperature, changing these parameters led to no change in the position of the observed spectrum. However, the large increase in the temperature-induced lineshifts could be due to the beginning of a sudden change in gradient in the lifetime measurement experiment at ~673 K which has also been reported elsewhere [5.14]. This can be explained in terms of the domination of the non-radiative decay from the <sup>4</sup>T<sub>2</sub> state due to thermal quenching. Since the fluorescence characteristics of the fibre are highly sensitive to these effects at elevated temperatures, changing any measurement parameters in order to obtain a better detected signal could have a large effect in the energy transitions due to further perturbations of both non-radiative decay and lattice vibrations which, in turn, could have led to the large wavelength shifts measured.

For temperature-dependent lineshifts of the ruby fibre, the region of "ambiguity" between 623 and 673 K has to be discounted until more studies are conducted to investigate this phenomenon but two relatively sensitive regions may be used. The monitored temperature must also be static unless relatively fast and accurate processing schemes can be used in determining the fluorescence spectrum.

Figure 5.16. Shift of ruby fibre R-lines with temperature

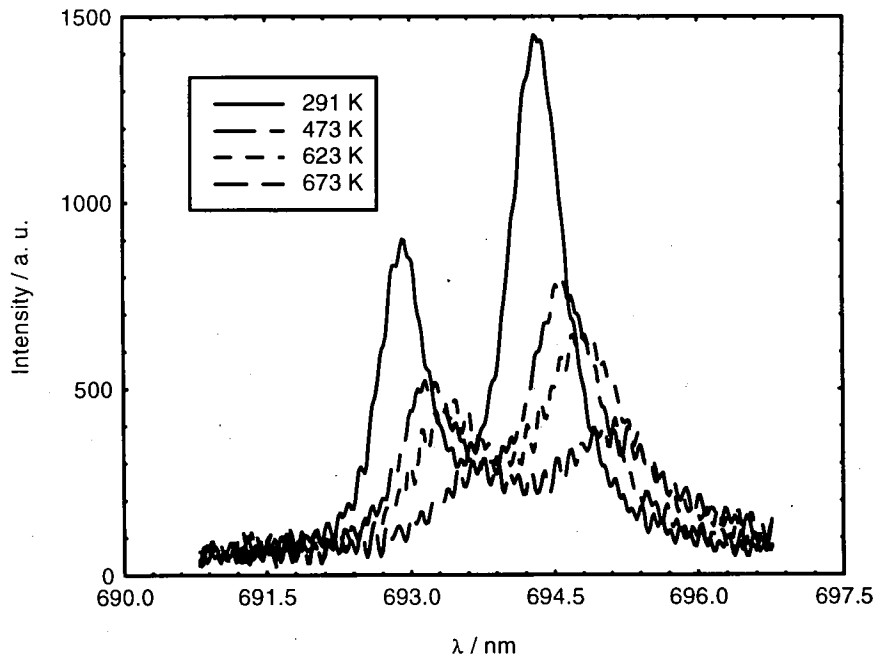


Figure 5.17a. Absolute  $R_1$  and  $R_2$  lineshifts of ruby fibre with temperature

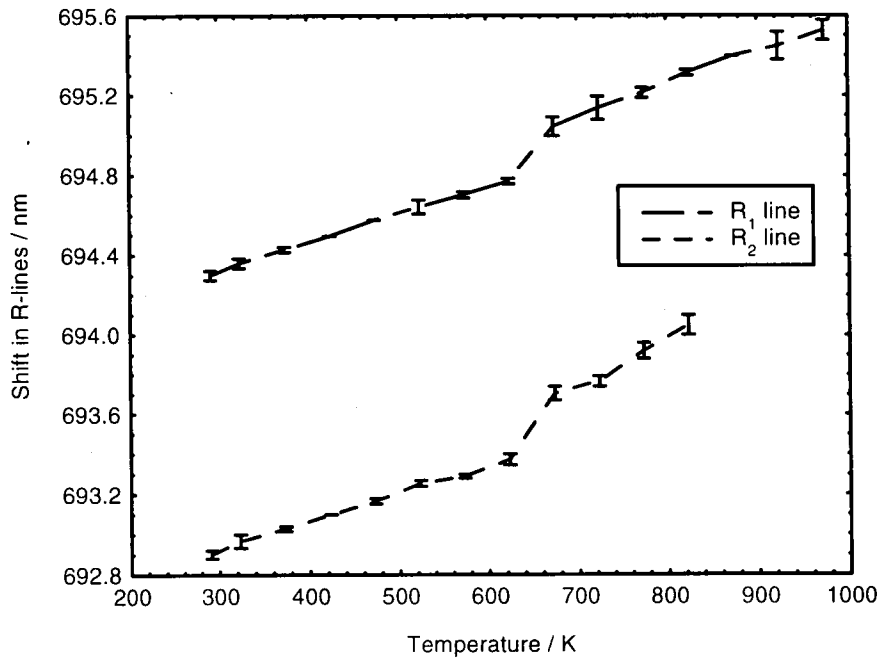


Figure 5.17b. Relative  $R_1$  and  $R_2$  lineshifts of ruby fibre with temperature

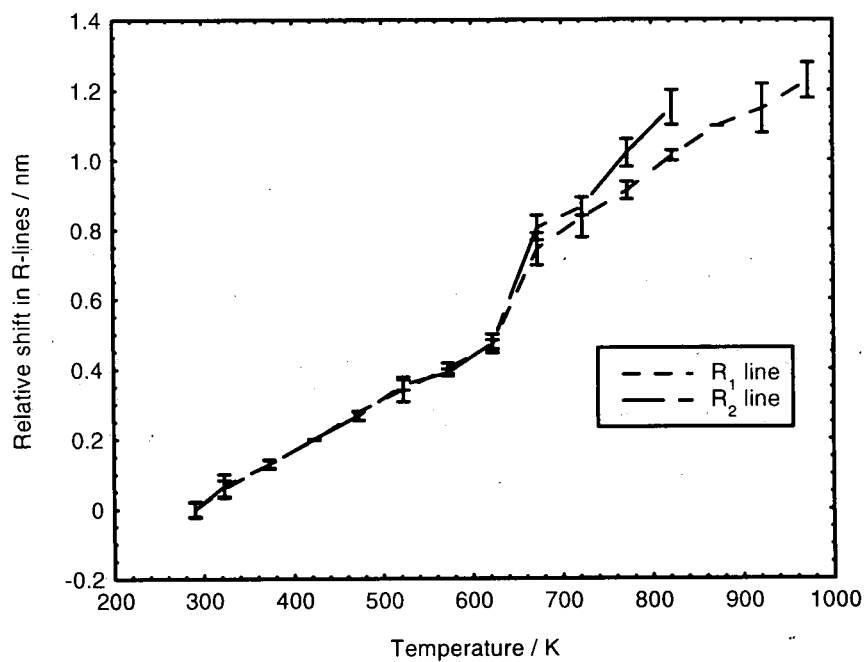


Figure 5.18. Ruby fibre spectrum at 823 K

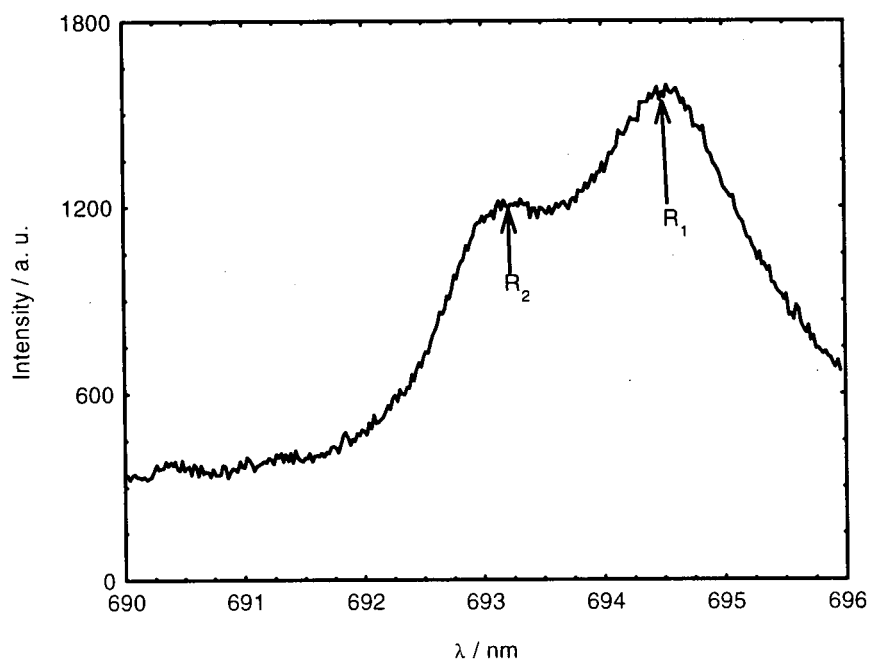


Figure 5.19a. Calibration curves of  $R_1$  and  $R_2$  lines from 291 to 623 K

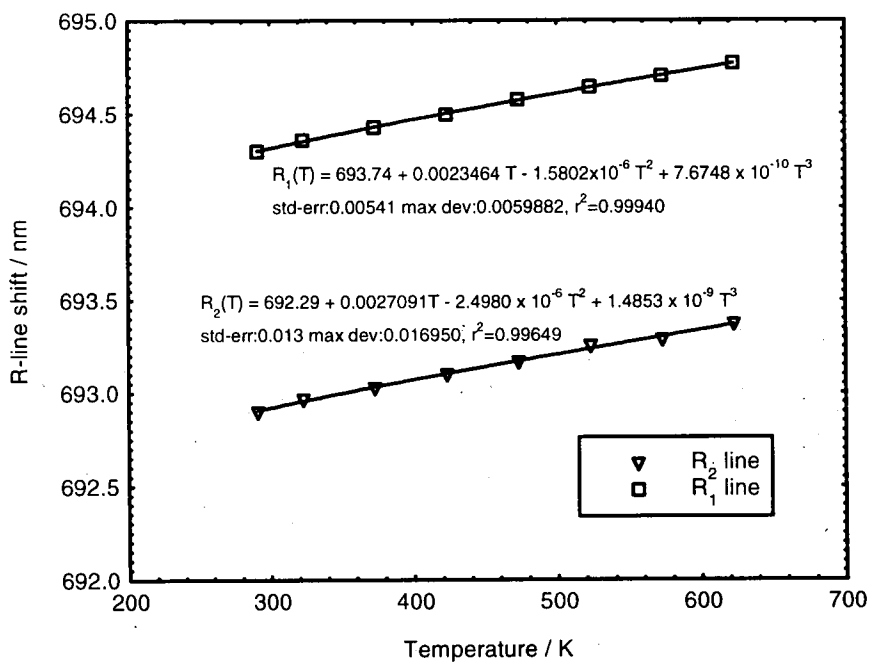


Figure 5.19b. Calibration curves of  $R_1$  and  $R_2$  lines from 673 to 973 K

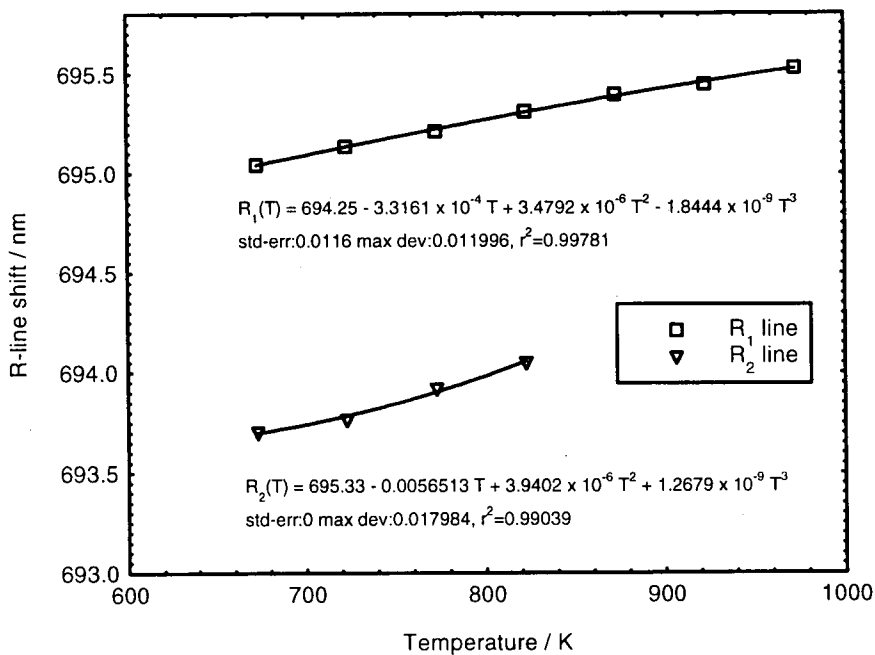


Figure 5.20a. Determination of wavelength coefficient from straight line fit as a function of temperature (291 to 623 K)

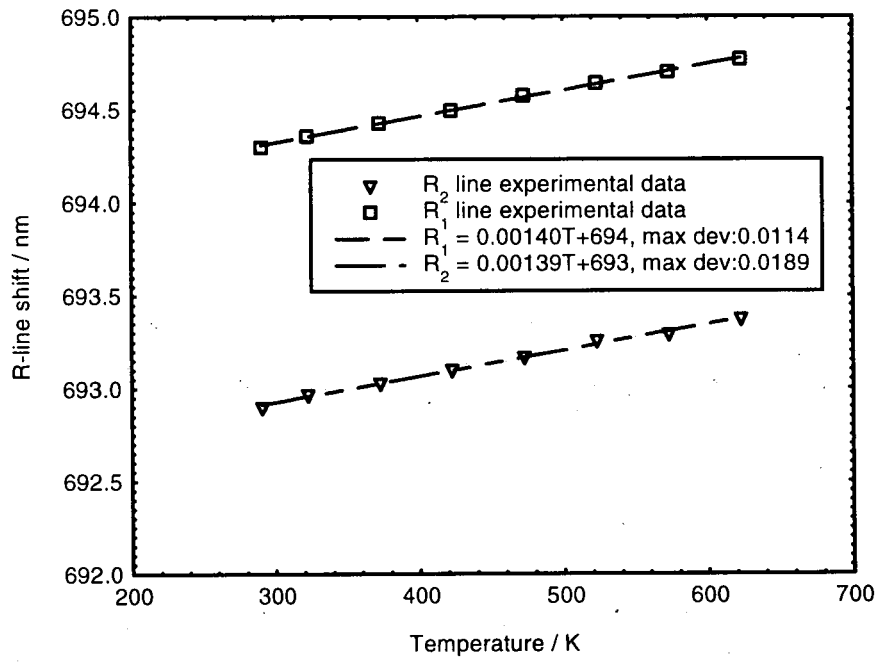
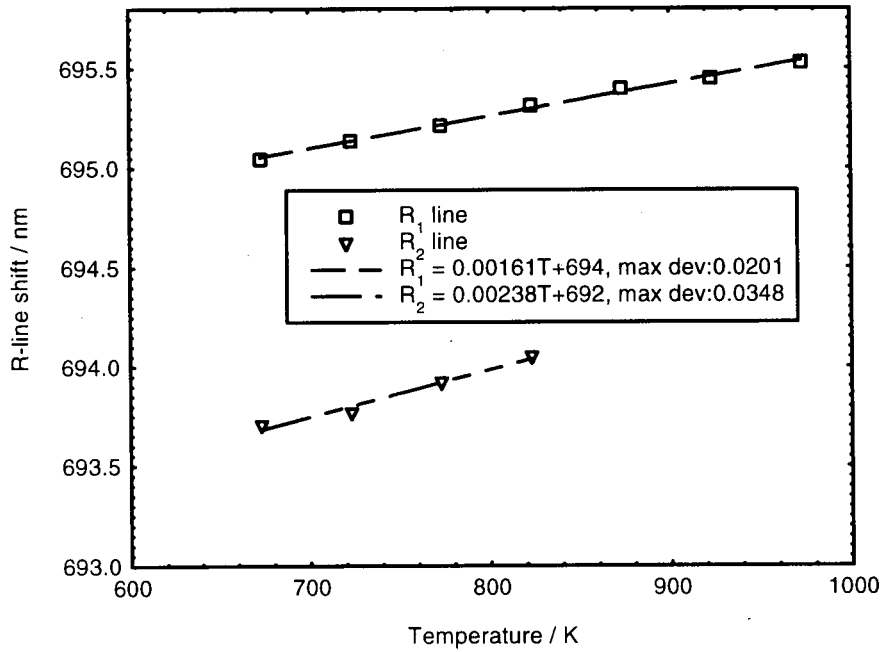


Figure 5.20b. Determination of wavelength coefficient from straight line fit as a function of temperature (673 to 973 K)



**Table 5.4a. Fitted parameters for R<sub>1</sub> and R<sub>2</sub> lineshifts from 291 to 623 K**

R <sub>1</sub> line			
$\alpha$	$\beta$	$\delta$	$\gamma$
/nm	/nm K <sup>-1</sup>	/nm K <sup>-2</sup>	/nm K <sup>-3</sup>
693.74	0.0023464	-1.5802 x 10 <sup>-6</sup>	7.6748 x 10 <sup>-10</sup>
R <sub>2</sub> line			
692.29	0.0027091	-2.498 x 10 <sup>-6</sup>	1.4853 x 10 <sup>-9</sup>

**Table 5.4b. Fitted parameters for R<sub>1</sub> lineshift from 673 to 973 K and for R<sub>2</sub> lineshift from 673 to 823 K**

R <sub>1</sub> line			
$\alpha$	$\beta$	$\delta$	$\gamma$
/nm	/nm K <sup>-1</sup>	/nm K <sup>-2</sup>	/nm K <sup>-3</sup>
694.25	-3.3161 x 10 <sup>-4</sup>	3.4792 x 10 <sup>-6</sup>	-1.8444 x 10 <sup>-9</sup>
R <sub>2</sub> line			
695.33	-0.0056513	3.9402 x 10 <sup>-6</sup>	1.2679 x 10 <sup>-9</sup>

**Table 5.5a. Measured and calculated shifts for R<sub>1</sub> position.**

From 291 to 623 K				
Temp. / K	Measured / nm	Calculated / nm	Error / nm	Std. Dev. / nm
291	694.3	694.3079	0.0079	0.00413
323	694.36	694.3589	-0.0011	
373	694.4287	694.4352	0.00648	
423	694.4967	694.5079	0.01117	
473	694.5767	694.5775	0.00083	
523	694.6417	694.6447	0.00303	
573	694.7017	694.71	0.00835	
623	694.77	694.7741	0.00407	
From 673 to 973 K				
673	695.0434	695.0404	-0.003	0.00821
723	695.1347	695.1319	-0.0028	
773	695.2117	695.2207	0.00898	
823	695.3117	695.3055	-0.0062	
873	695.3967	695.385	-0.0117	
923	695.4467	695.4576	0.01095	
973	695.5267	695.5222	-0.0045	

**Table 5.5b. Measured and calculated shifts for R<sub>2</sub> position.**

From 291 to 623 K				
Temp. / K	Measured / nm	Calculated / nm	Error / nm	Std. Dev. / nm
291	692.9	692.9034	0.00342	0.00981
323	692.9667	692.9545	-0.0122	
373	693.028	693.03	0.00203	
423	693.1	693.1014	0.0014	
473	693.1667	693.1697	0.00301	
523	693.255	693.2361	-0.0189	
573	693.29	693.3016	0.01158	
623	693.3733	693.3674	-0.0059	
From 673 to 823 K				
673	693.705	693.6978	-0.0072	0.01523
723	693.766	693.7829	0.01695	
773	693.92	693.9016	-0.0184	
823	694.05	694.0546	0.00457	

**Table 5.6a. Wavelength coefficients of R<sub>1</sub> line.**

Temp. / K	Cubic equation / nm K <sup>-1</sup>	Average / nm K <sup>-1</sup>	Straight line fit / nm K <sup>-1</sup>
291	0.001622	0.001419	0.0014
323	0.001566		
373	0.001488		
423	0.001422		
473	0.001367		
523	0.001323		
573	0.001291		
623	0.001271		
673	0.001845	0.001592	0.00161
723	0.001807		
773	0.001741		
823	0.001647		
873	0.001526		
923	0.001377		
973	0.0012		

**Table 5.6b. Wavelength coefficients of R<sub>2</sub> line.**

Temp. / K	Cubic equation / nm K <sup>-1</sup>	Average / nm K <sup>-1</sup>	Straight line fit / nm K <sup>-1</sup>
291	0.001633	0.001418	0.00139
323	0.00156		
373	0.001466		
423	0.001393		
473	0.001343		
523	0.001315		
573	0.001309		
623	0.001326		
673	0.001375	0.002383	0.00238
723	0.002035		
773	0.002713		
823	0.003411		

## 5.4 Strain measurement experiments

Bulk ruby crystals have routinely been used as pressure sensors where they are subjected to very high compressive stresses in the megabar or GPa range utilising the diamond anvil cell (DAC). Under such environments, the fluorescence spectrum, or more precisely the sharp R-lines, and fluorescence lifetime have been found to change with increasing pressure. All previous studies on the influence of various deformation on the fluorescence characteristics have involved compression of the crystal density and none has been reported on pure uniaxial extensional straining. In the experiments detailed below, single-crystal ruby fibres were uniaxially strained along the *c*-crystallographic axis and the effect investigated in terms of lifetime and lineshift changes.

### 5.4.1 Fluorescence lifetime decay of ruby fibres

It has been well-accepted that a combination of trigonal crystal field distortion and electron-phonon interactions (EPIs) in ruby gives rise to the splitting of the lowest excited state into the R<sub>1</sub> and R<sub>2</sub> lines [5.39, 5.40, 5.48]. In pressure sensing under very high pressures, further perturbations to the crystal field strength and EPIs have been observed as shifts in the R-lines or changes in the fluorescence lifetime [5.49, 5.50, 5.51]. Under nonhydrostatic conditions, Eggert *et al.* [5.51] have reported on the increase of the ruby radiative lifetime (<sup>2</sup>E → <sup>4</sup>A<sub>2</sub> transition) with pressure up to 130 GPa and attributed this dependence to the distortion of the trigonal crystal field at high pressures. Under pure uniaxial straining, the fluorescence lifetime decay rate would thus be expected to change according to the trigonal field and EPI theory.

#### 5.4.1.1 Experiment

A photograph of the uniaxial straining device is shown in **Figure 5.21**. It consists of a micrometer head, with a resolution of 1 μm, which moves a translation stage relative to a fixed platform. Smooth movement of the stage was ensured by two hardened stainless steel guiding pins which also constrained movement to only one axis. The sensing ruby fibre probe was inserted into two holes drilled through the top section of both the movable and fixed translation stages and a strong adhesive

(*Permabond F241* with hardener number 1) was applied to rigidly secure the fibre co-linearly with the longitudinal axis of the turning micrometer head. The fibre was butt coupled to a silica fibre with the aid of a silica capillary similar to that used for temperature experiments. The silica fibre was in turn attached to a 1 x 2 fibre coupler. Excitation light at 514.5 nm from an Ar<sup>+</sup> laser was launched into one port of the coupler to induce fluorescence from the ruby fibre. The reflected signal was collected via the other port and collimated with a microscope objective (X20, NA 0.54). The reflected signal, containing both the excitation light and the desired fluorescence signal, was, however, found to be too weak to be detected directly using this technique. Hence, the exponentially decaying fluorescence signal was measured using the set-up shown in **Figure 5.22**. A narrow bandpass optical filter like that used in earlier temperature sensing measurements was placed in front of the high speed Si detector to allow only the fluorescence signal through. The data averaging was performed using a 500 MHz *HP* digital oscilloscope over 11 bits. An optical chopper was used to modulate the excitation beam at its focal spot and the resulting signal detected by the oscilloscope was the superpositioning of the fluorescence signal on the square-wave modulated excitation source. The strain-testing device was tightly bolted onto the optical bench so that no erroneous data would be added as a result of any accidental movement of the device when turning the micrometer head. This also ensured that the fibre could be safely stretched without any accidental breakage. The fibre used here had *c*-axis orientation with one section grown as sapphire with the gauge end Cr<sup>3+</sup>-doped. It can be seen in the insert of **Figure 5.22**.

The gauge length of the ruby fibre to be strained was measured as ~12.3 mm and the fibre was uniaxially strained at 5 µm per step up to a maximum extension of 100 µm. Hence the maximum strain applied can be considered to be ~8110 µε. Throughout the experiment, other parameters were kept constant.

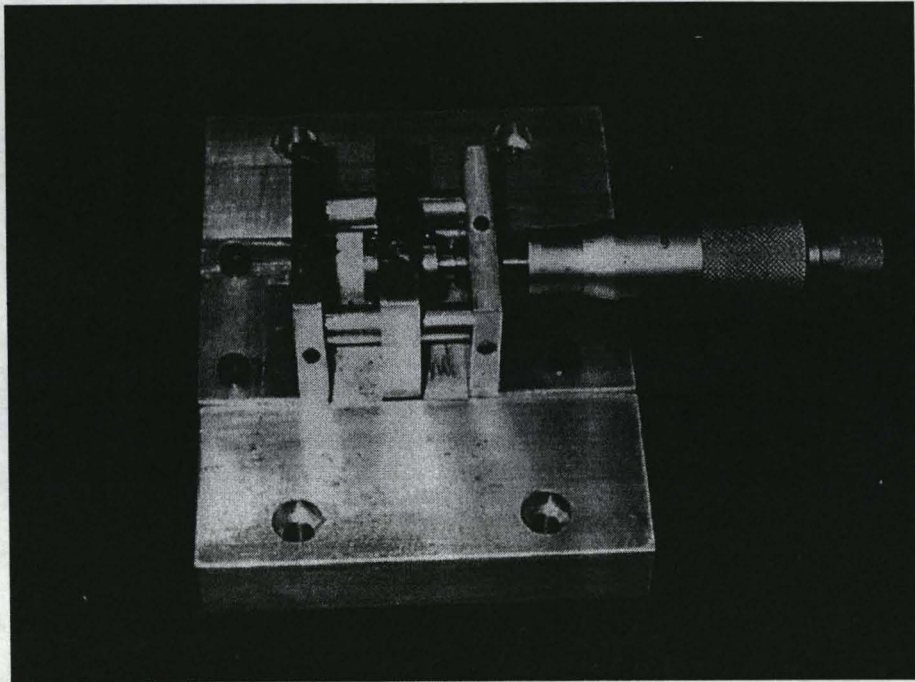


**Figure 5.21.** Photograph of strain testing device used in experiment

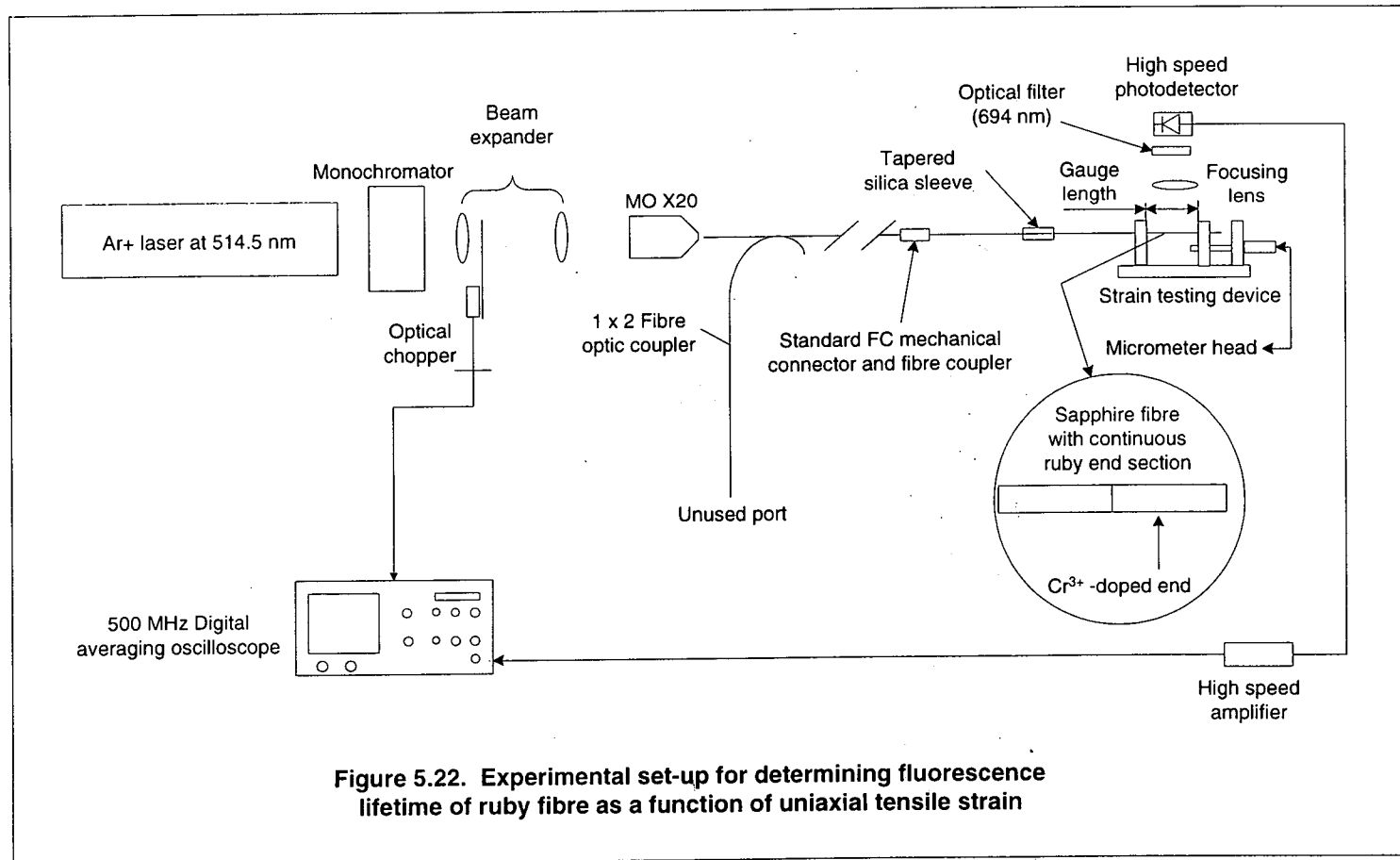


Figure 5.22. Experimental set-up for determining fluorescence lifetime of ruby fibre as a function of uniaxial tensile strain

#### 5.4.1.2 Results and Discussion

The strain applied to the test specimen was calculated as the extension or elongation applied through the micrometer head over its original length. The lifetime decay of the ruby fibre at 0 strain (or  $\delta L = 0 \mu\text{m}$ ) is shown in **Figure 5.23** with a lifetime of 3.43 ms. A good level of determination was obtained through curve fitting, with  $r^2$ , the fitting confidence, better than 0.998 at each strain level. This has been shown in **Figure 5.23** together with statistics on the standard deviation from the fitted values for all parameters. It was thought that the decay rate would be affected by the increase in strain but over the monitored strain levels up to the maximum value of 8110  $\mu\text{m}$ , no observable change has been detected. The lifetime decay fluctuated at  $\sim 3.45$  ms. **Figure 5.24** shows the lifetime at an extension of  $\delta L = 100 \mu\text{m}$  over the gauge length of 12.3 mm (which is  $\sim 8110 \mu\text{m}$ ) where  $\tau$  was fitted to be 3.44 ms. This was found to be effectively the same as  $\tau$  at 0  $\mu\text{m}$ . An initial set of lifetime values with increasing strain was plotted with no apparent change in the decay rate. This led to the suspicion that the fibre had not been strained at all due to the following reasons: the adhesive used to bond the fibre onto the strain testing apparatus had given way and/or the micrometer pin moving the variable translation stage had come loose. However, repetition for the experiment with fresh adhesive produced identical results. Confirmation of the fibre being stressed rather than the adhesive came when at  $\sim 33500 \mu\text{m}$ , the fibre failed.

**Figure 5.25a** plots the lifetime values as a function of the applied strain. The deviation from the curve fitting process was taken as the error of the experiment at each corresponding strain and shown as error bars in the figure. With no change in the lifetime data, it was thus not possible to apply any calibration curves to obtain the strain response. The calculated lifetime values are given in **Table 5.7**. In this experiment, no calculation has been made of the response from the adhesive used, for example the slippage, since the ruby fibre was demonstrated to be relatively independent of uniaxial strains up to fracture. A comparison of the temperature and strain dependence of the fluorescence lifetime decay is shown in **Figure 5.25b**, indicating the relative insensitivity of the lifetime to strains. Hence, the problem of

cross-sensitivity to strain when measuring any temperature dependent lifetime values can be avoided.

A simple and easy-to-use device has been fabricated for the use in strain testing of single crystal ruby fibres with *c*-crystallographic orientation produced by the LHPG technique. Initial ambiguities concerning the slippage of the secured fibres as well as the adhesive used have been overcome by careful loading and coating of both fibres and adhesives, respectively, and allowing appropriate curing times between employment. The experiments conducted have so far indicated that ruby fibres strained uniaxially along its *c*-axis produced no significant dependence whatsoever on its fluorescence lifetime decay and shifts in R-line positions. From the strong fluorescence signals measured, it can be seen that there is strong coupling between the Cr<sup>3+</sup> ions and the host crystal field and lattice but no strong dependence on strain has been observed. Ruby crystals oriented along both the *a*- or *c*-crystallographic axis have been reported to suffer dissimilar changes in their spectrum. However, by tension straining a *c*-oriented ruby fibre, the inter-ionic distance between the Cr<sup>3+</sup> ions and Al<sub>2</sub>O<sub>3</sub> crystal host is forced to increase and the whole fibre structure stretched. The crystal field would be distorted by a certain amount and the EPI would be perturbed, but as seen in strain measurements in this work, the introduction of such a deformation has relatively little effect on both the lifetime decay rate as well as the R-line position shifts. In **Figure 5.25a**, where the fluorescence lifetime from the *c*-axis has been plotted as a function of the applied tensile strain,  $\tau$ , the lifetime can be seen to fluctuate between 3.42 and 3.56 ms. Some studies [5.52, 5.53] have found the strain dependence of glass fibres doped with rare-earth ions to be relatively sensitive and linear. However, the maximum strains which can be applied were relatively low compared to that used in this work. This is due largely to the intrinsically weak physical properties of glass-based fibres. In addition, the cross-sensitivity between strain and another parameter (for example, temperature) would have to be resolved using more complicated signal processing techniques than would have been the case if the sensing probe was sensitive to only one parameter.

Figure 5.23. Ruby fibre lifetime decay at 0 strain ( $\delta L = 0 \mu\text{m}$ )

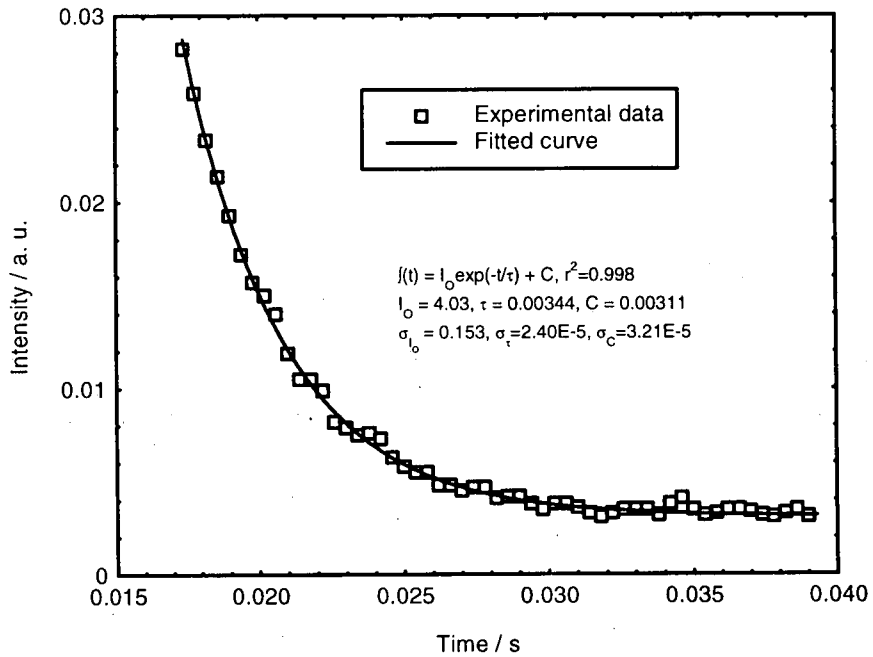


Figure 5.24. Ruby fibre lifetime decay at 8110  $\mu\epsilon$  ( $\delta L = 100 \mu\text{m}$ )

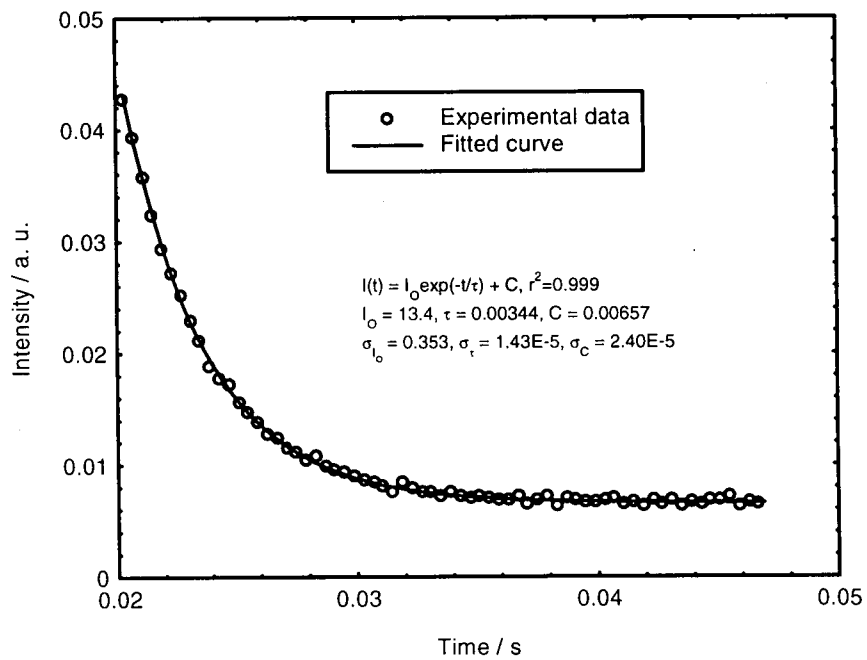


Figure 5.25a. Fluorescence lifetime decay of ruby fibre as a function of uniaxial strain

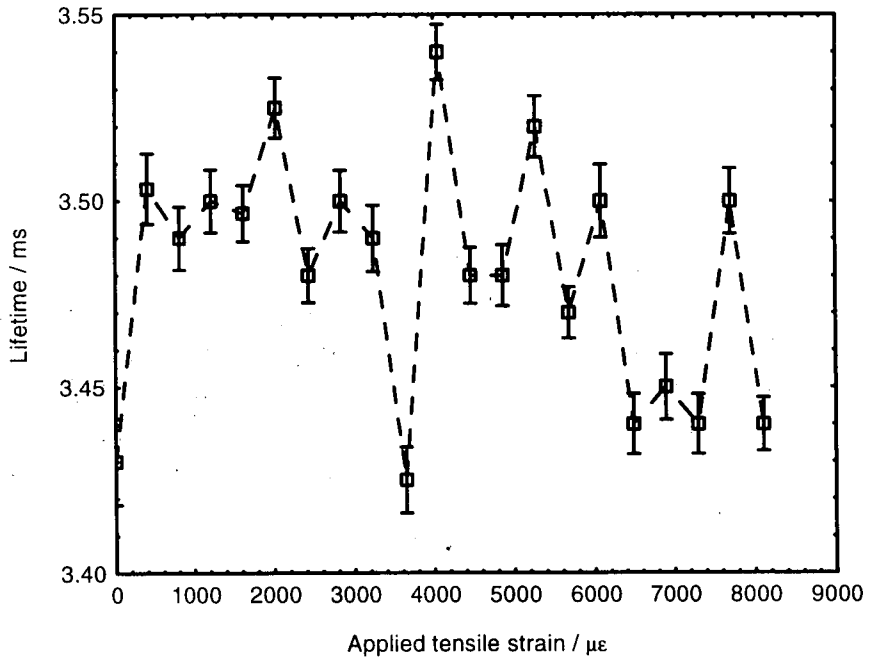
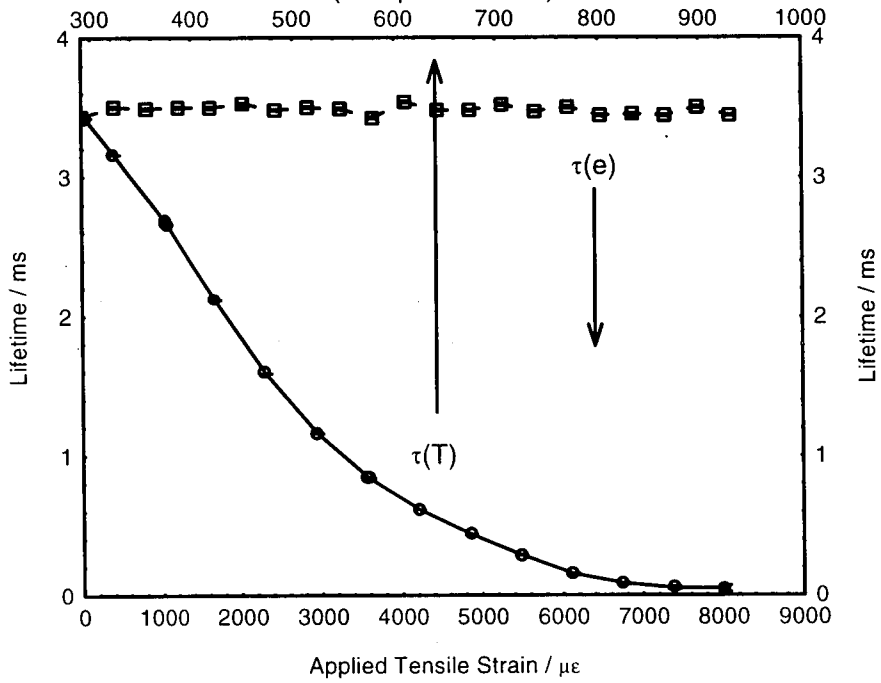


Figure 5.25b. Comparison of strain and temperature dependence of ruby fibre fluorescence lifetime (Temperature / K)



**Table 5.7. Lifetime decay of ruby fibre as a function of applied strain (Gauge length = 12.3 mm).**

Strain / $\mu\epsilon$	Measured $\tau$ / ms	Error / ms
0	3.43	$2.32 \times 10^{-2}$
405.52	3.503	$1.9 \times 10^{-2}$
811.03	3.49	$1.69 \times 10^{-2}$
1216.55	3.5	$1.70 \times 10^{-2}$
1622.06	3.497	$1.52 \times 10^{-2}$
2027.58	3.525	$1.60 \times 10^{-2}$
2433.09	3.48	$1.45 \times 10^{-2}$
2838.61	3.5	$1.66 \times 10^{-2}$
3244.12	3.49	$1.78 \times 10^{-2}$
3649.64	3.425	$1.76 \times 10^{-2}$
4055.15	3.54	$1.48 \times 10^{-2}$
4460.67	3.48	$1.50 \times 10^{-2}$
4866.18	3.48	$1.65 \times 10^{-2}$
5271.70	3.52	$1.64 \times 10^{-2}$
5677.21	3.47	$1.37 \times 10^{-2}$
6082.73	3.5	$1.96 \times 10^{-2}$
6488.24	3.44	$1.62 \times 10^{-2}$
6893.76	3.45	$1.77 \times 10^{-2}$
7299.27	3.44	$1.61 \times 10^{-2}$
7704.79	3.5	$1.77 \times 10^{-2}$
8110.30	3.44	$1.43 \times 10^{-2}$

## 5.4.2 Wavelength shifts of ruby fibre R-lines

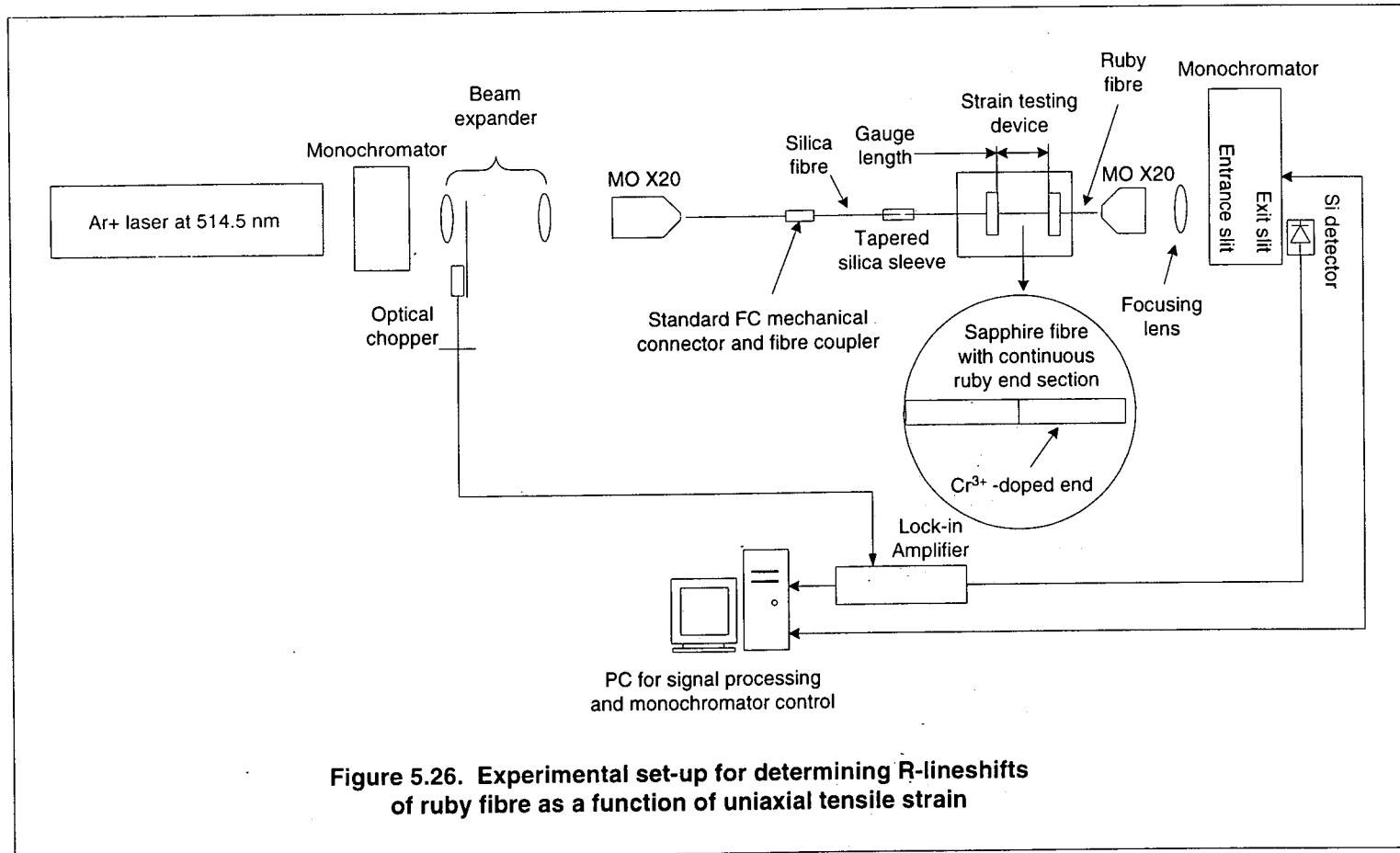
The wavelength shifts of the R-lines of ruby fibres due to application of longitudinal strains have been investigated here. In order to monitor any significant changes in the positions of both lines, one of the fibre sample has been tested to destruction. While previous studies on the effects of deformation on the fluorescence characteristics have generally involved the ruby samples being subjected to very high compression and the resulting strain states measured as compressive strains, the strain applied in this work is defined as the change or elongation in the original length ( $\delta L/L$ ,  $\delta L$  and  $L$  being the elongation and original gauge length respectively) when the sample is subjected to tension [5.54].

### 5.4.2.1 Experiment

As shown in **Figure 5.21**, the strain testing device was used in determining the wavelength shift in both the  $R_1$  and  $R_2$  lines of the same ruby fibre employed in measuring strain-induced lifetime decay rates earlier (**Section 5.4.1.1**). The only notable change is in the use of a monochromator to detect the shift in the R-lines.

The pump source was provided by an  $\text{Ar}^+$  ion laser with the laser power kept constant throughout the duration of the experiment. Excitation light was delivered to the ruby fibre via a 1 x 2 coupler to the silica fibre which in turn was coupled to the target ruby fibre. The reflected light collected was collimated and subsequently focused onto the entrance slit of the monochromator. This signal was again found to be too weak and the transmission technique illustrated in **Figure 5.26** was adopted. Using lock-in techniques and computer control, the R-line shifts were monitored from 0 strain to a maximum of 33500  $\mu\epsilon$ , beyond which further tensioning of the translation stage resulted in the breakage of the ruby fibre. The elongation prior to fibre failure was estimated to be  $\sim 240 \mu\text{m}$ . The gauge length used in this lineshift work was subsequently reduced to  $\sim 6 \text{ mm}$  hence, the breaking strain of the ruby fibre can be estimated to be approximately 40000  $\mu\epsilon$ . A scan step of 0.05 nm was used, thus giving a measurement resolution of  $\pm 0.05 \text{ nm}$ . As previously, digital smoothing

was provided by the software used to analyse the fluorescence data over a 0.4 nm sliding average to localise the curve peaks.



### 5.4.2.2 Results and Discussion

The spectrum of each fibre was averaged over a minimum of 6 scans at each applied strain. Deviation from the average of the scans was then taken as the error associated with the measurement. At 0 strain, the R-lines have been measured as 694.3 nm and 692.9 nm respectively. The relative wavelength shifts of the two R-lines of the fibre with uniaxial strain were monitored and are plotted in **Figure 5.27a**. Over the range of applied strain investigated, it can be seen that there was no significant change between the lineshifts for both the R<sub>1</sub> and R<sub>2</sub> lines. The lineshifts with strain remained almost a horizontal line, indicating a very low strain coefficient. For a straight line plotted through the experimental data, a coefficient of  $\sim -3.62 \times 10^{-6}$  nm /  $\mu\epsilon$  can be obtained for the R<sub>1</sub> line while for the R<sub>2</sub> line, it is  $\sim -3.64 \times 10^{-6}$  nm /  $\mu\epsilon$ . This can be seen in **Figure 5.27b** where the straight lines are reasonably good fits albeit with low levels of determination ( $r^2$ ) for both R-lines.

The positions of the R-lines at 0 strain and at the maximum of 33 500  $\mu\epsilon$  are compared in **Figure 5.28**. No significant strain-dependence can be observed. **Table 5.8** lists all the measured R-lineshifts at each corresponding applied strain. During the course of this experiment, no loosening of the fibre from the adhesive nor slippage of the adhesive itself occurred due to the relatively high uniaxial tensile strain applied. The typical shear strength of the adhesive when fully cured has been given as 35 MPa and the shear modulus has been quoted by "*Permabond Adhesives Ltd.*" as 0.14 GPa. The maximum permissible strain which can be applied before any degradation of the *F241* adhesive was thus calculated to be  $\sim 250\,000$   $\mu\epsilon$ . It has been assumed that the ruby single-crystal fibre suffered brittle fracture at an elongation of 240  $\mu\text{m}$ . Over a gauge length of  $\sim 6$  mm, the strain may be calculated as  $\sim 40\,100$   $\mu\epsilon$ . In uniaxial tension, the maximum strain at the point of fracture of the fibre is at least 5 times less than that of the adhesive used. It can thus be safely assumed that the fibre broke due mainly to the physical extension suffered by application of tension.

As had been treated in the earlier temperature-induced wavelength shift experiment, the ruby fibre R-lineshifts were found to have relatively low sensitivities (low

wavelength coefficients for both R-lines) to temperature. Under tensile straining, the wavelength shifts would likely be even smaller, considering that strain-induced lifetime decay rates have been found not to be sensitive to tension. The negative gradients of the fitted lines in **Figure 5.27b** indicated a minute shift towards the blue spectral region. Unlike the red shifts observed when subjected to increasing temperature, straining of the ruby fibre actually shifts the R-line peaks towards the higher energy regions. Along the *a*-crystallographic axis of the ruby fibre, however, there could be larger effects on the fluorescence characteristics upon application of uniaxial tensile strains. An investigation into *a*-axis strained ruby fibres could, perhaps, lead to more meaningful interpretation of the effects of strains. An attempt in using *c*-axis ruby fibres in measuring stress has been reported by Ma *et al.* [5.55], although in that work, the target was embedded into matrices made of  $\gamma$  - TiAl. The push-out technique employed by the authors, however, resulted only in compressive stresses being incurred within the embedded fibre structures.

Clearly, from the experiments carried out to date, *c*-axis ruby fibres have been found to be strongly dependent on temperature yet no significant variation in the fluorescence characteristics has been observed upon tensile strain loading. With a high melting point crystal host, sudden excursion of temperature beyond the detectable limits of the fluorescence characteristics could be easily tolerated without any physical damage to the fibre integrity. It could thus be a useful tool as temperature sensing probes in very harsh environments where conventional glass fibres cannot be employed. Moreover, it fulfils one of the major considerations in any practical sensor: sensitivity only to the parameter being measured.

Figure 5.27a. Relative shift in R-lines as a function of uniaxial strain

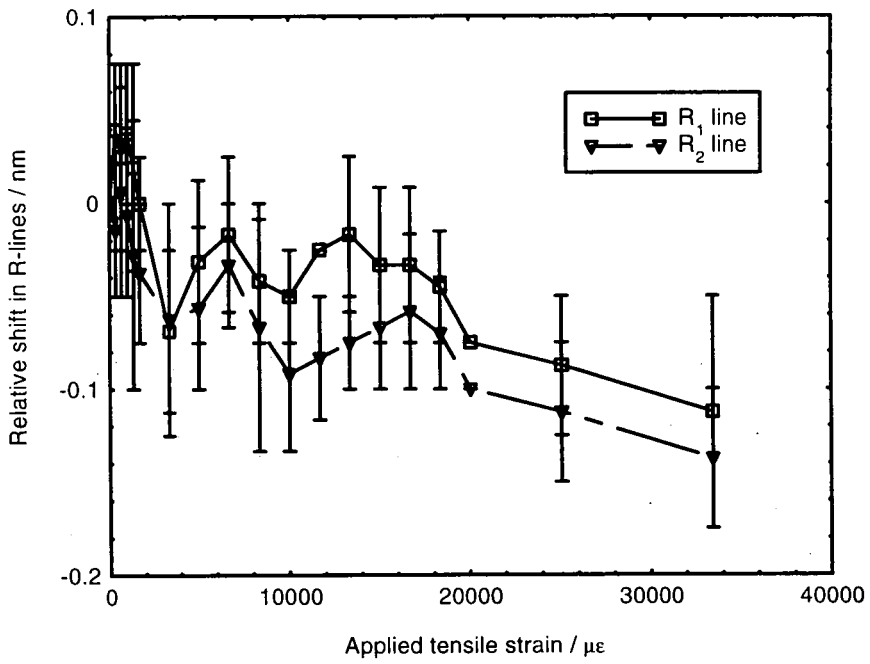


Figure 5.27b. Wavelength shift in R-lines as a function of uniaxial strain

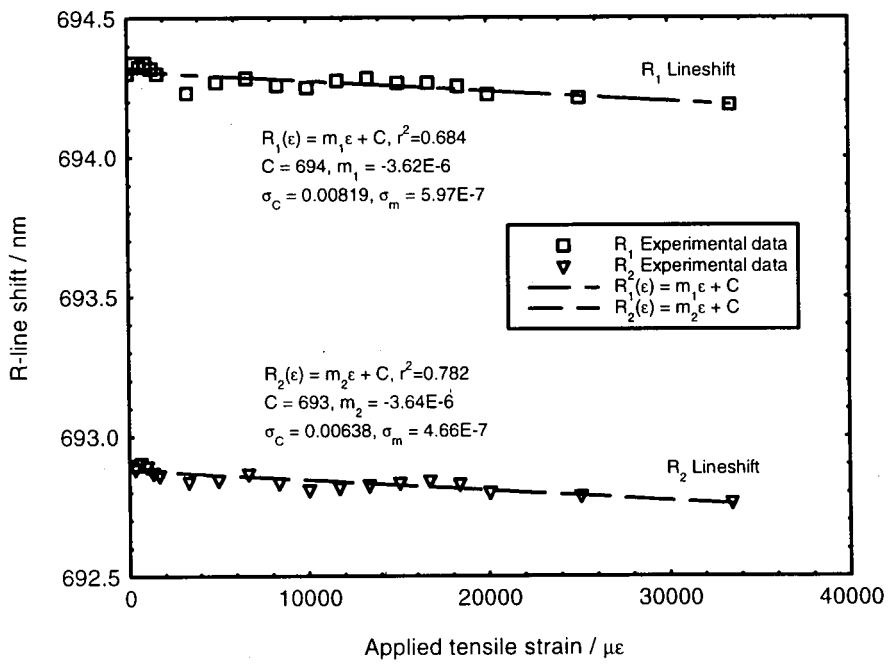
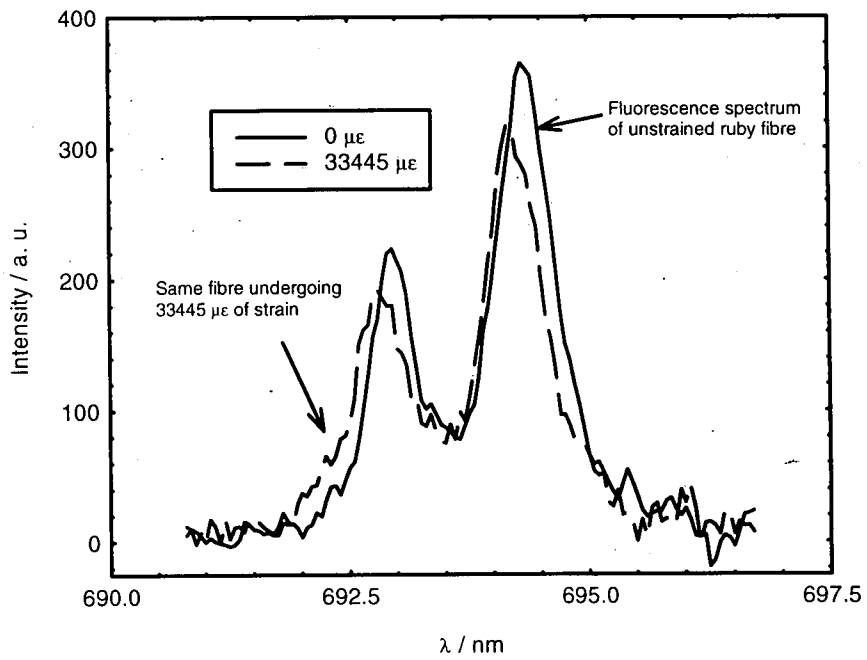


Figure 5.28. Unstrained and highly-strained ruby fibre fluorescence spectra



**Table 5.8. Relative positions of R-lines with applied strain (Gauge length ~6 mm).**

Strain / $\mu\epsilon$	Avg. $R_1$ / nm	Max. Err. / nm	Avg. $R_2$ / nm	Max. Err. / nm
0	0	0.025	0	0
334.45	0.0393	0.0357	-0.0143	0.0357
668.90	0.025	0.05	0.0063	0.0563
1003.344	0.0375	0.0375	-0.0062	0.0438
1337.79	0.0194	0.0556	-0.0278	0.0722
1672.24	0	0.025	-0.0375	0.0375
3344.48	-0.0687	0.0438	-0.0625	0.0625
5016.72	-0.0312	0.04375	-0.0562	0.0438
6688.96	-0.0167	0.0417	-0.0333	0.0333
8361.20	-0.0417	0.0333	-0.0667	0.0667
10033.44	-0.05	0.025	-0.0917	0.0417
11705.69	-0.025	0	-0.0833	0.0333
13377.93	-0.0167	0.0417	-0.075	0.025
15050.17	-0.0333	0.0417	-0.0667	0.0333
16722.41	-0.0333	0.0417	-0.0583	0.0417
18394.65	-0.045	0.03	-0.07	0.03
20066.89	-0.075	0	-0.1	0
25083.61	-0.0875	0.0375	-0.113	0.0375
33444.82	-0.113	0.0625	-0.1375	0.0375

## 5.5 References to Chapter 5

- 5.1 T. H. Maiman, *Stimulated Optical Radiation in Ruby*, Nature, **187**, 493, 1960
- 5.2 C. A. Burrus and J. Stone, *Room-temperature continuous operation of a ruby fiber laser*, J. Appl. Phys., **49**(6), 3118, 1978
- 5.3 J. R. Izatt, R. C. Mitchell and H. A. Daw, *Thermal Dependence of Ruby Laser Emission*, J. Appl. Phys., **37**(4), 1558, 1966
- 5.4 W. H. Fonger and C. W. Struck, *Temperature dependences of  $Cr^{3+}$  radiative and nonradiative transitions in ruby and emerald*, Phys. Rev. B, **11**(9), 3251, 1975
- 5.5 Z. Zhang, K. T. V. Grattan and A. W. Palmer, *Temperature dependences of fluorescence lifetimes in  $Cr^{3+}$ -doped insulating crystals*, Phys. Rev. B, **48**(11), 7772, 1993
- 5.6 E. Feher and M. D. Sturge, *Effect of Stress on the Trigonal Splittings of  $d^3$  Ions in Sapphire ( $\alpha-Al_2O_3$ )*, Phys. Rev., **172**(2), 244, 1968
- 5.7 R. A. Forman G. J. Piermarini, J. D. Barnett and S. Block, *Pressure Measurement Made by the Utilization of Ruby Sharp-Line-Luminescence*, Science, **176**, 284, 1972
- 5.8 S. M. Sharma and Y. M. Gupta, *Theoretical analysis of R-line shifts of ruby subjected to different deformation conditions*, Phys. Rev. B, **43**(1), 879, 1991
- 5.9 X. A. Shen and Y. M. Gupta, *Effect of crystal orientation on ruby R-line shifts under shock compression and tension*, Phys. Rev. B, **48**(5), 2929, 1993
- 5.10 K. T. V. Grattan, R. K. Selli and A. W. Palmer, *Ruby fluorescence wavelength division fiber-optic temperature sensor*, Rev. Sci. Instrum., **58**(7), 1231, 1987
- 5.11 K. T. V. Grattan, R. K. Selli and A. W. Palmer, *Ruby decay-time fluorescence thermometer in a fiber-optic configuration*, Rev. Sci. Instrum., **59**(8), 1328, 1988
- 5.12 R. R. Sholes and J. G. Small, *Fluorescent decay thermometer with biological applications*, Rev. Sci. Instrum., **51**(7), 882, 1980
- 5.13 Z. Zhang, K. T. V. Grattan and A. W. Palmer, *A novel signal processing scheme for a fluorescence based fiber-optic temperature sensor*, Rev. Sci. Instrum., **62**(7), 1735, 1991
- 5.14 J. H. Sharp, H. C. Seat, Z. Y. Zhang and K. T. V. Grattan, *Single-Crystal*

- Ruby Fibres for Fluorescence-Based Temperature Sensing*, Paper presented at Sensors and their Applications X (Cardiff, Wales), 219, 1999
- 5.15 Y. L. Hu, Z. Y. Zhang, K. T. V. Grattan, A. W. Palmer and B. T. Meggitt, *Ruby-based decay-time thermometry: effect of probe size on extended measurement range (77-800 K)*, Sensors and Actuators A, **63**, 85, 1997
- 5.16 Y. Shen and R. Xu, *Development of a compact sapphire fiber thermometer probe using fluorescent decay*, Proc. SPIE, **2895**, 144, 1996
- 5.17 Y. Shen, Y. Wang, L. Tong and L. Ye, *Novel sapphire fiber thermometer using fluorescent decay*, Sensors and Actuators A, **71**, 70, 1998
- 5.18 D. E. McCumber and M. D. Sturge, *Linewidth and Temperature Shift of the R Lines in Ruby*, J. Appl. Phys., **34**(6), 1682, 1963
- 5.19 D. D. Ragan, R. Gustavsen and D. Schiferl, *Calibration of the ruby  $R_1$  and  $R_2$  fluorescence shifts as a function of temperature from 0 to 600 K*, J. Appl. Phys., **72**(12), 5539, 1992
- 5.20 Q. Ma and D. R. Clarke, *Stress Measurement in Single-Crystal and Polycrystalline Ceramics Using Their Optical Fluorescence*, J. Am. Ceram. Soc., **76**(6), 1433, 1993
- 5.21 G. J. Piermarini, S. Block, J. D. Barnett and R. A. Forman, *Calibration of the pressure dependence of the  $R_1$  ruby fluorescence line to 195 kbar*, J. Appl. Phys., **46**(6), 2774, 1975
- 5.22 Y. M. Gupta and X. A. Shen, *Potential use of the ruby  $R_2$  line shift for static high-pressure calibration*, Appl. Phys. Lett., **58**(6), 583, 1991
- 5.23 P. D. Horn and Y. M. Gupta, *Luminescence R-line spectrum of ruby crystals shocked to 125 kbar along the crystal c axis*, Phys. Rev. B, **39**(2), 973, 1989
- 5.24 J. K. Hyun, S. M. Sharma and Y. M. Gupta, *Ruby R-line shifts for shock compression along  $(1\bar{1}02)$* , J. Appl. Phys., **84**(4), 1947, 1998
- 5.25 K. S. Gibson, *The Effect Of Temperature Upon The Absorption Spectrum Of A Synthetic Ruby*, Phys. Rev., **8**, 38, 1916
- 5.26 T. H. Maiman, *Optical And Microwave-Optical Experiments In Ruby*, Phys. Rev. Lett., **4**(11), 564, 1960
- 5.27 M. J. Martin (Ed.), *CRC Handbook of Laser Science and Technology*, Vol I, CRC Press Inc., Florida, 119, 1982
- 5.28 T. H. Maiman, *Optical Maser Action in Ruby*, Brit. Commun. Electron., **7**, 674, 1960

- 5.29 J. Friedel, *Transition Metals. Electronic Structure Of The d-Band. Its Role In The Crystalline And Magnetic Structures* in: *The Physics Of Metals. 1. Electrons*, J. M. Ziman (Ed.), Cambridge University Press, Cambridge, 340, 1969
- 5.30 V. Evtuhov and J. K. Neeland, *Pulsed Ruby Lasers* in: *Lasers*, Vol. 1, A. K. Levine (Ed.), Edward Arnold Ltd., London, 1, 1966
- 5.31 B. Henderson and G. F. Imbusch (Eds.), *Optical spectroscopy of transition metal ions in solids* in: *Optical Spectroscopy of Inorganic Solids*, Clarendon Press, Oxford, 408, 1989
- 5.32 K. T. V. Grattan and Z. Y. Zhang, *Temperature Dependences of Cr<sup>3+</sup> Fluorescence Lifetimes* in: *Fiber Optic Fluorescence Thermometry*, K. T. V. Grattan and A. Augousti (Eds.), Chapman and Hall, Suffolk, 35, 1995
- 5.33 S. Sugano, Y. Tanabe and H. Kamimura (Eds.), *Multiplets of transition metal-ions in crystals*, Academic Press, New York, 107, 1970
- 5.34 Y. Tanabe and S. Sugano, *On the Absorption Spectra of Complex Ions. I*, J. Phys. Soc. Jpn, **9**(5), 753, 1954
- 5.35 Y. Tanabe and S. Sugano, *On the Absorption Spectra of Complex Ions. II*, J. Phys. Soc. Jpn, **9**(5), 766, 1954
- 5.36 S. K. Gayen, W. B. Wang, V. Petricevic, R. Dorsinville and R. R. Alfano, *Picosecond excite-and-probe absorption measurement of the <sup>4</sup>T<sub>2</sub> state nonradiative lifetime in ruby*, Appl. Phys. Lett., **47**, 455, 1985
- 5.37 R. G. Munro, G. J. Piermarini, S. Block and W. B. Holzapfel, *Model line-shape analysis for the ruby R lines used for pressure measurement*, J. Appl. Phys., **57**(2), 185, 1985
- 5.38 D. Ma, Y. Liu, N. Ma and J. Chen, *Theoretical calculations of thermal shifts and thermal broadenings of sharp lines and zero-field splitting for ruby. Part I. Thermal shifts of R<sub>1</sub> and R<sub>2</sub> lines*, J. Phys. Chem. Solids, **61**, 799, 2000
- 5.39 D. E. Rimmer and D. F. Johnston, *A study of the origin of the trigonal crystal field in ruby. I. Analysis of experimental data*, Proc. Phys. Soc., **89**, 943, 1966
- 5.40 D. E. Rimmer and D. F. Johnston, *A study of the origin of the trigonal crystal field in ruby. II. Theory*, Proc. Phys. Soc., **89**, 953, 1966
- 5.41 R. M. Macfarlane, *Stress-Induced Trigonal Crystal-Field Parameters in Some Oxide Lattices*, Phys. Rev., **158**(2), 252, 1967

- 5.42 W. L. Vos and J. A. Schouten, *On the temperature correction to the ruby pressure scale*, J. Appl. Phys., **69**(9), 6744, 1991
- 5.43 S. M. Sharma and Y. M. Gupta, *Oscillator strength of ruby  $R_1$  line under high pressure*, Appl. Phys. Lett., **54**(1), 84, 1989
- 5.44 M. D. Knudson and Y. M. Gupta, *Feasibility of stimulated emission to measure R-line shifts in shock compressed ruby*, J. Appl. Phys., **85**(9), 6425, 1999
- 5.45 J. He and D. R. Clarke, *Polarization Dependence of the  $Cr^{3+}$  R-Line Fluorescence from Sapphire and Its Application to Crystal Orientation and Piezospectroscopic Measurement*, J. Am. Ceram. Soc., **80**(1), 69, 1997
- 5.46 S. P. Jamison and G. F. Imbusch, *Temperature dependence of the luminescence from heavily doped ruby*, J. Lumin., **75**, 143, 1997
- 5.47 W. C. Zheng and S. Y. Wu, *Theoretical studies of the temperature dependence of zero-field splitting of  $Cr^{3+}$  centers in ruby*, Phys. Rev. B, **54**(2), 1117, 1996
- 5.48 S. Sugano and M. Peter, *Effect of Configuration Mixing and Covalency on the Energy Spectrum of Ruby*, Phys. Rev., **12**(2), 381, 1961
- 5.49 L. D. Merkle, I. L. Spain and R. C. Powell, *Effects of pressure on the spectra and lifetimes of  $Nd_xY_{1-x}P_5O_{14}$  and ruby*, J. Phys. C, **14**, 2027, 1981
- 5.50 Y. Sato-Sorensen, J. Appl. Phys., *Measurements of the lifetime of the ruby  $R_1$  line under high pressure*, **60**(8), 2985, 1986
- 5.51 J. H. Eggert, K. A. Goettel and I. F. Silvera, *Ruby at high pressure. II. Fluorescence lifetime of the R line to 130 Gpa*, Phys. Rev. B, **40**(8), 5733, 1989
- 5.52 T. Sun, Z. Y. Zhang, K. T. V. Grattan and A. W. Palmer, *Intrinsic doped fluorescence decay-time based measurements – strain and temperature characteristics for sensor purposes*, Rev. Sci. Instrum., **69**(12), 4186, 1998
- 5.53 A. Arnaud, D. I. Forsyth, T. Sun, Z. Y. Zhang and K. T. V. Grattan, *Strain and temperature effects in erbium-doped fibre for decay-time based sensing*, Rev. Sci. Instrum., **71**(1), 104, 2000
- 5.54 A. P. Boresi, R. J. Schmidt and O. M. Sidebottom (Eds.), *Advanced Mechanics of Materials (5<sup>th</sup> Ed.)*, John Wiley & Sons Inc., New York, 3, 1993
- 5.55 Q. Ma, L. C. Liang, D. R. Clarke and J. W. Hutchinson, *Mechanics of*

*the Push-Out Process from In Situ Measurement of the Stress Distribution  
along Embedded Sapphire Fibers, Acta. Metall. Mater., 42(10), 3299, 1994*

## Chapter 6 – Rare Earth-based Crystal Fibre Sensors

### 6.0 Introduction

### 6.1 Rare earth $\text{Er}^{3+}$ and $\text{Yb}^{3+}$ ions in $\text{Al}_2\text{O}_3$ and upconversion processes

### 6.2 Temperature sensing based on $\text{Er}^{3+}$ , equally $\text{Er}^{3+} + \text{Yb}^{3+}$ -codoped and high $\text{Yb}^{3+} + \text{low Er}^{3+}$ -codoped $\text{Al}_2\text{O}_3$ fibres

#### 6.2.1 Temperature sensing with $\text{Er}^{3+}:\text{Al}_2\text{O}_3$ fibres

6.2.1.1 FIRs of green upconversion and IR emission for temperature sensing

6.2.1.2 Experiments

6.2.1.3 Results and Discussion

#### 6.2.2 Temperature sensing with equally $\text{Er}^{3+} + \text{Yb}^{3+}$ -codoped $\text{Al}_2\text{O}_3$ fibres

6.2.2.1 Temperature dependence of green and red upconversion FIRs

6.2.2.2 Experiments on green and red FIRs

6.2.2.3 Results and Discussion

6.2.2.4 Temperature sensing based on upconversion intensity of equally codoped  $\text{Er}^{3+} + \text{Yb}^{3+}:\text{Al}_2\text{O}_3$  fibres

6.2.2.5 Experiment on intensity-based temperature sensor

6.2.2.6 Results and Discussion

6.2.2.7 Temperature dependence of the green and red upconversion decay lifetimes

6.2.2.8 Lifetime experiment

6.2.2.9 Results and Discussion

#### 6.2.3 Temperature sensing with high $\text{Yb}^{3+} + \text{low Er}^{3+}:\text{Al}_2\text{O}_3$ fibres

6.2.3.1 Temperature dependence of IR FIR of highly  $\text{Yb}^{3+}$ : lowly  $\text{Er}^{3+}$ -codoped  $\text{Al}_2\text{O}_3$  fibres

6.2.3.2 Experiment on temperature dependence of high  $\text{Yb}^{3+}$ : low  $\text{Er}^{3+}:\text{Al}_2\text{O}_3$  fibres

6.2.3.3 Results and Discussion

6.2.3.4 Temperature dependence of the FIRs of upconversion emission in the green and red from high  $\text{Yb}^{3+}$ : low  $\text{Er}^{3+}$ -codoped  $\text{Al}_2\text{O}_3$  fibres

6.2.3.5 Experiment on temperature dependence of green and red upconversion FIRs from high  $\text{Yb}^{3+}$ : low  $\text{Er}^{3+}:\text{Al}_2\text{O}_3$  fibres

6.2.3.6 Results and Discussion

### 6.3 References to Chapter 6

## Chapter 6 – Rare Earth-based Crystal Fibre Sensors

### 6.0 Introduction

Initial applications for rare earth (RE) doped fibres have been in the field of optical telecommunications and, concurrently, in visible and IR solid state lasers [6.1, 6.2, 6.3, 6.4]. In addition, rapid development in fibre optic telecommunications in the past two decades have resulted in increased demands for low-loss devices in the form of active fibres, such as fibre amplifiers and lasers. The main advantages of such devices are the unique features of low-loss and tight beam confinement offered by a fibre geometry, as well as the high optical energy densities available and signal amplification. As one of the most commercially successful and important RE ions, trivalent  $\text{Er}^{3+}$  doped in ionic crystal and glass hosts are particularly of great interest in optical telecommunications due to their intra-4f emission in the wavelength region of 1.53 to 1.54  $\mu\text{m}$  [6.5, 6.6], corresponding to the standard low-loss communications wavelength of silica at 1.55  $\mu\text{m}$ . The earliest reported signal amplification process from a RE-doped material in fibre form has been aptly demonstrated by Koester and Snitzer [6.7] in a fibre laser using  $\text{Nd}^{3+}$ -doped glasses, this ion being chosen for the long lifetime of the metastable state and the “immunity” to concentration quenching. Further research has yielded advancement in RE-doped end-pumped fibre lasers [6.8, 6.9], the fabrication of low-loss rare earth-doped fibres [6.10] which finally cumulated in the demonstration of the first erbium-doped fibre amplifiers at the optical telecommunications wavelength of 1.54  $\mu\text{m}$  [6.11]. In a relatively short period of time, erbium-doped fibre amplifiers (EDFAs) have become one of the most significant advances in fibre optic telecommunications technology due to the high gain/amplification of signals at 1.5  $\mu\text{m}$  provided by the excitation of trivalent  $\text{Er}^{3+}$  ions when pumped with a suitable laser source (although optical gain has been demonstrated over the entire  $\text{Er}^{3+}$  emission spectrum [6.12]). Besides the high gain which can be achieved and low pump power requirements, EDFAs also exhibit high saturation power, low noise and low inter-channel cross-talk [6.2]. These devices have reshaped the future of optical communications, replacing the generally bulky and costly optoelectronic/electro-optic pre-amplifiers and repeaters commonly employed for signal regeneration in long haul fibre optic telecommunications

systems and networks with an all-fibre low loss solution. The attractive characteristics exhibited by EDFAs have, in principle, been attributed to the long lifetime of the metastable excited state, permitting high population inversions to be obtained under modest pump powers, with gain values of 20 dB or more readily attainable over the entire emission spectrum [6.12]. While almost all studies on EDFAs have been carried out using silica-based fibres, the amount of  $\text{Er}^{3+}$  which can be incorporated into these fibres is limited by the RE solubility in silica, thereby limiting the concentration to very small quantity per unit length of silica fibre [6.12]. This implies that in order to achieve the desired gain values, a relatively long length of doped fibre may have to be used. In recent years, novel device development in integrated optoelectronics have resulted in thin, film planar waveguides playing an important role in integrating a number of key optical components on a single chip [6.13]. This can be achieved through the use of various fabrication technologies such as ion beam implantation [6.14], pulsed laser deposition [6.15], plasma-enhanced chemical vapor deposition [6.16], molecular beam epitaxy [6.17] and sol-gel techniques [6.18, 6.19].  $\text{Er}^{3+}$ -doped planar waveguides are, in particular, attractive due to its emission wavelength which coincides with that of optical communications at  $\sim 1.5 \mu\text{m}$  and has thus generated great research interests. Moreover, waveguides fabricated through the various techniques permit relatively easy control of the desired concentration level of the active  $\text{Er}^{3+}$  species to be doped onto planar substrates which can be based on a combination of various host materials [6.5, 6.13, 6.16] and can also be easily incorporated into current integrated opto-electronic devices. However, samples fabricated by the use of high-energy ion beams typically result in the requirement of thermal annealing to repair the damages often imparted to the waveguides. In addition, with current advance in micro-machining, waveguide designs can be greatly improved and allow a number of devices to be fabricated on a single chip. Together with amplifiers, miniature splitters, couplers and wavelength division multiplexers have been fabricated on a planar substrate/chip and may enable many optical functions to be carried out efficiently with low loss and cost/space savings.

In an equally significant development, the narrow absorption and, in particular, emission lines in the visible and IR spectrum of RE ions when doped in various glass and crystal hosts have been vigorously studied for potential applications as solid state

laser materials [6.20, 6.21, 6.22, 6.23, 6.24]. These materials may be efficiently pumped by high power IR laser sources which are widely available at reasonable costs. The unique features of transitions from the  $4f$  electronic configuration in RE ions not only lead to IR emission/fluorescence from the first excited state but can also result in simultaneous emissions from states at higher energy levels. Visible emissions from RE-doped crystals generally consist of sharp lines grouped in several wavelength regions [6.25]. The fluorescence from  $\text{Er}^{3+}$ - and  $\text{Nd}^{3+}$ -doped YAG crystals, at  $2.94\ \mu\text{m}$  and  $1.06\ \mu\text{m}$  respectively, are by far the most well-known solid state lasers using RE-doped materials. High-powered  $\text{Nd}^{3+}$ :YAG lasers have been commonly used for a wide range of laser materials processing applications including welding and drilling of high strength steels [6.26], and bacterial sterilisation [6.27, 6.28] while the  $2.94\ \mu\text{m}$  radiation from  $\text{Er}^{3+}$ :YAG lasers is now commonly used in medical applications [6.29, 6.30]. In addition, the possibility of upconverted emission in the visible (blue, green, and red) from various rare earth-doped crystals implies the constantly widening opportunities in developing compact solid state laser devices. Over the last two decades several upconversion lasers employing RE ions in crystals have been established. They include  $\text{Er}^{3+}$ ,  $\text{Nd}^{3+}$ ,  $\text{Ho}^{3+}$ ,  $\text{Tm}^{3+}$ ,  $\text{Pr}^{3+}$  ions which have been incorporated into various crystal hosts [6.22, 6.31, 6.32, 6.33, 6.34, 6.35] and are listed in **Table 6.1** together with their emission wavelengths and energy level transitions. Particularly interesting are those with emissions in the blue where there are potential commercial applications in improved capacity data storage, CD inscription and holographic displays. In some cases, co-doping with another ion such as  $\text{Yb}^{3+}$  may result in improved absorption and emission characteristics, often followed by higher output powers, improved gain and efficient energy transfer [6.36, 6.37]. The  $\text{Yb}^{3+}$  ion, in this case, is thus known as the sensitiser or donor ion. The potential for development in this class of laser materials is extensive due to the numerous possible combinations of RE ions with host crystals/glasses. In addition, rare earth-doped fibre lasers have also become available and compatibility with existing optical telecommunications networks will lead to improved efficiencies and a widening of the application areas such as into the field of fibre optic sensing [6.38, 6.39, 6.40]. Research and development on rare earth devices such as amplifiers and lasers are also continuously driven by the rapid progress in optical telecommunications.

**Table 6.1. Some upconversion laser crystals (Note: TPA denotes two-photon absorption, CET denotes cooperative energy transfer and PA denotes photon avalanche upconversion)**

Material	$\lambda$ / nm	Transition	Mechanism	Pump / nm	Ref.
Ho:Ba(Y, Yb)F <sub>8</sub>	551.5	<sup>5</sup> S <sub>2</sub> → <sup>5</sup> I <sub>8</sub>	CET	IR flashlamp	6.34
Er:BaY <sub>2</sub> F <sub>8</sub>	551.7	<sup>5</sup> S <sub>2</sub> → <sup>5</sup> I <sub>8</sub>	CET	790, 970	6.34
	470.3	<sup>2</sup> P <sub>3/2</sub> → <sup>4</sup> I <sub>13/2</sub>	CET	790, 970	
Tm:Ba(Y, Yb)F <sub>8</sub>	455	<sup>1</sup> D <sub>2</sub> → <sup>3</sup> H <sub>6</sub>	CET	960	6.34
	510	<sup>1</sup> D <sub>2</sub> → <sup>3</sup> H <sub>5</sub>	CET	960	
Er:KYF <sub>4</sub>	561	<sup>2</sup> H <sub>9/2</sub> → <sup>4</sup> I <sub>13/2</sub>	TPA	812	6.34
Nd:LaF <sub>3</sub>	380.1	<sup>4</sup> D <sub>3/2</sub> → <sup>4</sup> I <sub>11/2</sub>	TPA	788 + 591	6.34
Er:LiYF <sub>4</sub>	551	<sup>4</sup> S <sub>3/2</sub> → <sup>4</sup> I <sub>15/2</sub>	TPA	810 + 970	6.32
Er:Lu <sub>3</sub> Al <sub>5</sub> O <sub>12</sub>	561	<sup>4</sup> S <sub>3/2</sub> → <sup>4</sup> I <sub>15/2</sub>	TPA	810 + 970	6.32
Pr:LaCl <sub>3</sub>	635	<sup>3</sup> P <sub>0</sub> → <sup>3</sup> F <sub>2</sub>	TPA	1010 + 835	6.22
Pr:LaCl <sub>3</sub>	644	<sup>3</sup> P <sub>0</sub> → <sup>3</sup> F <sub>2</sub>	PA	677	6.22
Nd:LaF <sub>3</sub>	380	<sup>4</sup> D <sub>3/2</sub> → <sup>4</sup> I <sub>11/2</sub>	TPA	1060 + 590	6.22
Er:YAlO <sub>3</sub>	549.6	<sup>4</sup> S <sub>3/2</sub> → <sup>4</sup> I <sub>15/2</sub>	TPA	792 + 840	6.34
Er:YAlO <sub>3</sub>	549.8	<sup>4</sup> S <sub>3/2</sub> → <sup>4</sup> I <sub>15/2</sub>	CET	806.9	6.22
Er:YAlO <sub>3</sub>			PA	800	
Er:YLiF <sub>4</sub>	560.6	<sup>2</sup> H <sub>9/2</sub> → <sup>4</sup> I <sub>13/2</sub>	CET	967	6.34
Er:YLiF <sub>4</sub>	551.1	<sup>4</sup> S <sub>3/2</sub> → <sup>4</sup> I <sub>15/2</sub>	CET	797, 969	6.34
Er:YLiF <sub>4</sub>	469.7	<sup>2</sup> P <sub>3/2</sub> → <sup>4</sup> I <sub>13/2</sub>	CET	1500	6.34
Nd:YLiF <sub>4</sub>	413	<sup>2</sup> P <sub>3/2</sub> → <sup>4</sup> I <sub>11/2</sub>	PA	603.6	6.34
Tm:YAG	486.2	<sup>1</sup> G <sub>4</sub> → <sup>3</sup> H <sub>6</sub>	TPA	785 + 638	6.34
Tm:YLiF <sub>4</sub>	453	<sup>1</sup> D <sub>2</sub> → <sup>3</sup> F <sub>4</sub>	TPA	781 + 648	6.34
Tm:YLiF <sub>4</sub>	483	<sup>1</sup> G <sub>4</sub> → <sup>3</sup> H <sub>6</sub>	PA	648	6.34
Tm:YLiF <sub>4</sub>	450.2	<sup>1</sup> D <sub>2</sub> → <sup>3</sup> F <sub>4</sub>	TPA	784 + 648	6.34
Yb, Er:YLiF <sub>4</sub>	551	<sup>4</sup> S <sub>3/2</sub> → <sup>4</sup> I <sub>15/2</sub>	CET	959	6.35

As with other sensor devices, temperature, strain, stress and pressure remain the most important physical parameters which are sensed both in the laboratories and in many industrial processes. Since RE-doped materials can exhibit different fluorescence characteristics as a function of the various external influences, numerous sensing schemes may be realised over a relatively wide and diverse range of measurands. Early fibre optic thermometric sensing schemes based on rare earth-doped materials employed  $\text{Nd}^{3+}$ -doped crystals and glasses with relatively long fluorescence lifetimes in the IR wavelength regions. Even at elevated temperatures the decay times could be easily detected without the need for sophisticated, expensive timing/electronic circuits and signal processing [6.41, 6.42, 6.43]. In those studies, the Nd-doped glasses have been found to be suitable only for temperature measurements up to approximately 700 K, beyond which permanent damage to the glass materials occurred [6.42, 6.43]. As has been discussed in **Chapter 5**, ruby fibres may be used for temperature sensing up to ~920 K before the signal-to-noise ratio becomes too low for accurate measurement of the temperature-dependent fluorescence lifetime. This can be attributed to the effects of thermal quenching of the fluorescence process at elevated temperatures which, in turn, leads to a significant reduction in the fluorescence intensity. Fibre optic sensors which can enable measurements beyond this temperature can find important applications in many process industries, combustion engine health monitoring, aerospace industry and in many chemical processes [6.44]. In this respect, it is thus obvious that sensors based on  $\text{Cr}^{3+}$ -doped materials may not be suitable for this operation and are limited to the lower or mid-temperature range below 1000 K. Although  $\text{Nd}^{3+}$ :YAG, used as a sensing crystal in a fibre optic thermometric sensor, has been investigated for its temperature-dependent fluorescence lifetime decay at its emission line of 1.064  $\mu\text{m}$  for temperatures up to approximately 1200 K [6.42], it has been found to exhibit non-monotonic response throughout the investigated temperature range. Its fluorescence lifetime has been found to increase initially with temperature up to a peak at ~1000 K before decreasing rapidly again with increasing temperature. Temperature sensing operation is thereby limited to beyond 1000 K and up to ~1200 K. More studies on  $\text{Nd}^{3+}$ -doped crystals ( $\text{Nd}^{3+}$ :YAG) have found that the fluorescence lifetime decay as a function of temperature do not corroborate each other [6.42, 6.45, 6.46]. This material, thus, might not be appropriate as a standard temperature sensor when replacement of the sensor head is required, unless calibration is performed on all the

doped crystals prior to actual employment. The results, however, strongly suggest that different dopant concentration levels have been used by the various authors, leading to discrepancies between their temperature calibration curves. This is a reasonable suggestion since the dopant concentration levels in various materials, such as  $\text{Cr}^{3+}:\text{Al}_2\text{O}_3$  [6.47],  $\text{Er}^{3+}$ -doped silica [6.48] and  $\text{Nd}^{3+}:\text{YVO}_4$  [6.49], are known to influence the resulting fluorescence lifetimes of the transitions from the excited to ground states. In addition to using fluorescence lifetime decay as an indication of temperature variation, the fluorescence intensity ratio technique has also been applied to monitor the relative change in two typical peaks from the fluorescence spectrum of  $\text{Nd}^{3+}$ -doped silica fibres, where reasonable sensitivity to temperature has been obtained [6.50]. While the importance of temperature sensing employing  $\text{Nd}^{3+}$ -doped crystals or glasses has been stressed by the large amount of published work, the strain characteristics of  $\text{Nd}^{3+}:\text{SiO}_2$  fibres have also been studied by Sun *et al.* [6.51] for potential temperature-strain sensing applications. However, it has been found that the lifetime variation due to strains is very small and largely dominated by variation due to temperature-dependence.

More promising RE-based fibre optic sensors have been those employing  $\text{Er}^{3+}$  ions in various host fibres [6.48, 6.52, 6.53, 6.54, 6.55] due to its emission wavelength in the 1530 nm region, which coincides with the operational wavelength of  $\sim 1540$  nm in fibre optic communications systems, especially those utilising EDFAs. It would be very advantageous, technologically and economically, if a single fibre optic link could be made to perform the dual function of transmitting/receiving optical communications signals and sensing the desired parameters which could adversely affect the former primary function. Lifetime decay from the  $1.53 \mu\text{m}$  emission line of  $\text{Er}^{3+}$ -doped silica fibres, which is relatively independent of pump intensity, has been investigated for high temperature sensing applications up to  $\sim 1200$  K [6.48, 6.52]. The erbium concentration levels were found to influence the lifetime decay of the  $1.5 \mu\text{m}$  emission line, excited by a 980 nm laser diode, with a faster decay rate at higher  $\text{Er}^{3+}$  concentration levels [6.48]. Moreover, at a high Er ion concentration (4370 ppm used in that work [6.48, 6.52]), the fluorescence decay was found to be non-single exponential while fibres with lower concentration levels of erbium ions (200 ppm and 960 ppm) had single exponential decay characteristics. All the fibres exhibited a marked increase in sensitivity as the temperature was increased beyond

~970 K (of ~5 times, compared to that <670 K). Annealing at a relatively high temperature (~1200 K) was required to achieve stable decay rates throughout the investigated temperature range. The long lifetime after annealing (from 8-10 ms) also permitted fast and uncomplicated detection of the 1.5  $\mu\text{m}$  signal using currently available electronics/detectors at high temperatures and this would consequently reduce the errors incurred due to weak signals at such temperatures. In many fibre optic sensing systems, as in all other sensors, cross-sensitivity between two or more parameters is generally undesirable and can be a limiting factor in the range of the sensor due to the difficulty in differentiating the effect of one parameter from the other(s). Both temperature and strain effects have been investigated to evaluate the different contributions from the two effects, which may then enable separate measurements of the individual parameter or simultaneous monitoring of the two together [6.53]. By studying fibre samples with different dopant concentrations over a temperature range of ~290 to 420 K, the relative strain-dependent lifetime coefficients in the  $\text{Er}^{3+}$ -doped fibres ( $\sim 10$  to  $12 \times 10^{-7} / \mu\epsilon$ ) were found to be higher than that found in  $\text{Nd}^{3+}$ -doped fibres ( $14 \times 10^{-7} / \mu\epsilon$ ). However, the temperature-dependent lifetime decay has been found to dominate the small strain effects by approximately  $10^3$  times.  $\text{Er}^{3+}$ -doped materials have several narrow absorption bands in both the visible and IR regions, and can thus be excited by using various sources with emission wavelengths corresponding to the appropriate absorption peaks. Using the 1480 nm excitation of an  $\text{Er}^{3+}$ -doped fibre to monitor the fluorescence intensity ratio of the 1530 and 1552 nm lines as a function of temperature, Ko *et al.* [6.54] were able to demonstrate distributed sensing capabilities from  $\text{Er}^{3+}$ -doped fibres over a measurement length of 100 m. The authors thus demonstrated the temperature sensing potential of erbium-doped fibres with varying degrees of success. Incorporated into a high melting crystal, the temperature sensing range of the erbium-doped material may be extended up to ~1500 K or even near the melting point of the crystal hosts, as has been demonstrated by Henry *et al.* [6.55] using YAG as the crystal host. The sensing probe was constructed in such a way that only a short end section of the YAG crystalline fibre was doped with  $\text{Er}^{3+}$  ions, making it the active tip from which fluorescence signals could be detected in a reflective mode. The emission at 1.6  $\mu\text{m}$  from this material has been attributed to the transition from  $^4I_{13/2}$  to the ground ( $^4I_{15/2}$ ) state and the device was employed for thermometric

applications by dipping into a molten pool of aluminium.  $\text{Er}^{3+}$  concentration levels used by the authors [6.55] were kept relatively low (5 at.% and 3 at.%) in order to avoid the competing upconversion processes characteristic of rare earth-based systems. The two probes were also found to exhibit identical exponential temperature-dependent lifetime decay when the pump power was kept below a critical level.

The  $\text{Yb}^{3+}$  ion is commonly known as a "sensitiser" ion [6.56, 6.57] and has been normally employed as a co-dopant for  $\text{Er}^{3+}$ -doped materials to enable improved absorption and emission properties of such systems [6.37]. As a single dopant in silica, the transition from  ${}^2\text{F}_{5/2}$  to  ${}^2\text{F}_{7/2}$ , with its 3 level splittings, gives rise to fluorescence emission at ~1030 nm, 980 nm and a weaker line at ~910 nm, although it is tunable from ~0.95 to 1.1  $\mu\text{m}$  [6.58, 6.59].  $\text{Yb}^{3+}$  ions, essentially a two-level system, have been employed as the active co-dopant in erbium-doped fibre amplifiers and lasers [6.36, 6.39], and in  $\text{Yb}^{3+}$ :YAG laser crystals emitting at ~1030 nm [6.20, 6.21, 6.57]. Despite its considerable importance as a laser material and sensitiser,  $\text{Yb}^{3+}$  ions have only recently been studied for potential sensing applications. The fluorescence intensity ratio (FIR) technique was employed by Maurice *et al.* [6.58] to investigate the temperature dependence of the closely-spaced 1030 and 976 nm lines from the  ${}^2\text{F}_{7/2}$  to  ${}^2\text{F}_{5/2}$  transition of  $\text{Yb}^{3+}$  ions doped in silica fibres. Using a single pump source at 810 nm, the fluorescence intensities of the two thermally-coupled lines, which occur due to Stark level splitting of the  ${}^2\text{F}_{7/2}$  manifold, were induced and monitored as a ratio against temperature variations up to ~900 K. Errors of less than 1.4 °C have been reported by the authors [6.58] over the range of temperature investigated together with an average deviation of ~0.6 °C. Additional studies have been carried out recently into potential fibre optic sensors based on the  $\text{Yb}^{3+}$ -doped fibres with varying concentration levels [6.60, 6.61, 6.62]. The PLD (phase-lock detection) scheme, with its rapid response and accuracy, was utilised to monitor the fluorescence lifetime decay from the unique two-level transition of the  $\text{Yb}^{3+}$  ions at its peak wavelength of 976 nm. Again, the  $\text{Yb}^{3+}$  concentration levels were found to affect the detected lifetime, with the most highly-doped sample exhibiting the most significant difference in its lifetime compared to two other samples which have considerably lower  $\text{Yb}^{3+}$  concentrations [6.60].

Annealing by heat treating the  $\text{Yb}^{3+}$ -doped fibres at approximately 970 K was also required in order to obtain a stable fluorescence lifetime over extended periods of time for the samples studied. As in both neodymium and erbium studies, the possibility of simultaneous strain and temperature sensing in ytterbium-doped fibres has been investigated [6.61], the results of which indicated a small strain-dependent sensitivity to the much more dominating temperature-induced lifetime variation. This observation was further re-enforced in FIR studies on the simultaneous strain and temperature measurements from the fluorescence intensities of ytterbium-doped silica fibres [6.62]. Further investigations of ytterbium-based fluorescence thermometry have also led to divalent  $\text{Yb}^{2+}$  ions being incorporated into fluoride-based fluorescent dyes and employed for sensing of rotating elements in the cryogenic (20 – 120 K) range [6.63].

Due to the numerous possibilities of doping a wide range of rare earth ions in several materials, notably silica, other rare earth-based fibre optic fluorescence sensors have been reported. They include  $\text{Tm}^{3+}$ -silica fibres which have been studied up to a temperature of 1370 K [6.64] while still higher temperatures (~1600 K) can be reached by using  $\text{Tm}^{3+}$ :YAG crystals [6.65]. Both these studies have exploited the temperature-dependent fluorescence lifetime decay from the first excited state of the  $\text{Tm}^{3+}$  energy levels.  $\text{Pr}^{3+}$  ions are also interesting since one of its main emission band is centred around the “second” low-loss optical communications window of 1.3  $\mu\text{m}$  due to the  $^1\text{G}_4 \rightarrow ^3\text{H}_5$  transition [6.59]. The fluorescence lifetime of  $\text{Pr}^{3+}$ -doped ZBLAN fibres has been calibrated across a relatively low temperature range up to 770 K and interestingly, the lifetime decay was found to increase steadily with temperature [6.66]. This has been attributed to the thermalisation effect of the higher energy levels of the  $\text{Pr}^{3+}$  transitions at elevated temperatures and has been explained by considering a three-level model as put forward by the authors [6.66]. Other potential sensor materials based on rare earths include  $\text{Pr}^{3+}$ :YAG [6.67] and  $\text{Sm}^{2+}$  ions doped in various hosts [6.68] where temperature dependence of their fluorescence lifetimes have been reported.

In addition to RE-based sensors utilising the IR fluorescence characteristics as a measure of the desired physical parameter(s), another class of sensors also exists, based on the upconverted emission of erbium and erbium + ytterbium co-doped in

glass fibres [6.69, 6.70, 6.71]. Upconversion in erbium-doped systems results in emissions in the blue, green, red and deep red spectral regions [6.13, 6.22, 6.33, 6.72], with  $\text{Yb}^{3+}$  ions serving as a sensitizer to enable efficient absorption of the pump energy, which can then be transferred to the acceptor  $\text{Er}^{3+}$  ions efficiently [6.37]. Also, much stronger upconversion emission can be obtained, as observed in this work. Although there is difficulty in monitoring the lifetime decay of upconversion processes since they are inherently non-exponential, several authors have used the narrow green emitted lines as a basis for temperature sensing, employing two particular lines from the green spectrum in a ratiometric technique [6.69, 6.70, 6.71]. Excited state absorption and/or cooperative upconversion results in different energy levels being excited by the two transitions within the green spectrum which are separated by a small energy gap. The temperature-dependent intensity ratio of these two thermally coupled upconversion transitions can then be used as a measure of temperature variations [6.69, 6.70]. Depending on the host materials used, temperature sensing with upconversion materials may be employed for different temperature ranges.

Both IR fluorescence and visible upconversion have been observed in the rare earth-based crystal fibres fabricated by the LHPG technique in this work. In particular, the temperature dependence of both the IR and visible emissions from such fibres has been found to exhibit interesting characteristics. While a detailed study of the spectroscopy of rare earth-doped materials is beyond the scope of this work, a brief discussion of the most important and relevant processes/transitions in rare earth ions ( $\text{Er}^{3+}$ ,  $\text{Yb}^{3+}$  and  $\text{Er}^{3+} + \text{Yb}^{3+}$  ions) investigated in this work shall be undertaken in the following section. It should also be noted that this is the first reported work, to the knowledge of the author, on the melt growth of RE-doped  $\text{Al}_2\text{O}_3$  fibres by the laser heated pedestal growth technique.

### **6.1 Rare earth $\text{Er}^{3+}$ and $\text{Yb}^{3+}$ ions in $\text{Al}_2\text{O}_3$ and upconversion processes**

Rare earth-doped materials are characterised by their intra-4f transitions [6.25]. The two outer electronic shells are filled shells and almost all transitions from RE materials initiate from within the 4f shells which are incomplete, and are in turn "shielded" from any strong interaction with the surrounding environment. This

protective shield is afforded by the outer  $5s^2$  and  $5p^6$  shells and consequently, the weak interaction with crystalline fields when doped in ionic crystals lead to the unique sharp and narrow lines in the absorption and emission spectra. Moreover, due to the shielding, the emission wavelengths remain relatively constant when RE ions such as  $\text{Er}^{3+}$  are doped in various materials. In  $\text{Er}^{3+}$ -doped crystals, this intra- $4f$  transition results in emission around the 1530 to 1550 nm region, coincident with the optical communications wavelength of 1.54  $\mu\text{m}$ . Hence,  $\text{Er}^{3+}$  has become one of the most intensely studied of the rare-earth ions. Some information on the properties of  $\text{Er}^{3+}$  and  $\text{Yb}^{3+}$  ions, the RE ions used in this work, are presented in **Table 6.2** [6.20, 6.25], which shows only the outer relevant electronic configurations.

Although free  $\text{Er}^{3+}$  ions do not allow transitions around 1.5  $\mu\text{m}$  or in the visible spectrum since such transitions are parity-forbidden [6.25, 6.72], doping these ions into solid hosts induces weak coupling of the electronic states of opposite parity to the  $4f$  electrons. This is because the interaction with the crystal field can introduce and mix other states of different parity into the  $4f$  states, leading to partial relaxation of the selection rule [6.25]. Transitions are then allowed and are known as  $4f - 4f$  interactions [6.25]. The radiative lifetime of the 1.5  $\mu\text{m}$  emission arising from the transition of the first excited state is relatively long [6.12, 6.13, 6.25, 6.72], typically in the millisecond region, thus implying that population inversion between this state and the ground state can be achieved at a relatively low pump power. Furthermore, in addition to transitions leading to lines in the IR and the visible,  $\text{Er}^{3+}$  and  $\text{Er}^{3+} + \text{Yb}^{3+}$  ions doped in ionic crystals also give rise to additional lines which cannot be completely accounted for by the crystal field splitting due to the static  $4f - 4f$  transitions. These additional lines may, however, be attributed to the coupling of the phonons from the dynamic crystal field with the  $4f$  electrons [6.25]. This electron-phonon interaction also determines the lifetimes of the relevant excited states, with radiative decays which are not strongly affected by or dependent on temperature, implying that non-radiative decay by optical phonons are the main reason for the temperature dependence of the lifetime of transitions from RE-doped crystals. The non-radiative decay occurs by emission of a large number of phonons (multi-phonon) which bridge the energy gap from one crystal field splitting level to another [6.25]. Hence, due to the screening of the  $4f$  electrons by the two outer shells, and

consequently the weak interaction between these electrons and the crystal lattice, a relatively weaker dependence of the multi-phonon non-radiative decay on temperature could be expected when using RE-doped materials for thermometric applications. This implies that suitable RE-based crystals may be used for probing higher temperatures when compared to transition metal-ion-doped materials, such as the ruby fibres discussed in **Chapter 5**, where strong interaction is observed between the outer electrons and the crystal field of the host crystal.

Rare earth ions can also exchange energy among themselves since the interactions between the ions can be sufficiently large such that excitation radiation is transferred from one ion to another, particularly in crystal hosts doped with two or more types of RE ions [6.25, 6.72]. In this exchange, one type of ion can be excited by a suitable pump source with a relatively narrow bandwidth while another emits the radiation. Although the levels involved in resonant energy transfer are generally similar, energy transfer between ions of different energy levels can also occur, with the energy mismatch being compensated for by phonon interactions where phonons are either absorbed or emitted to achieve energy conservation.

The energy level diagram of  $\text{Er}^{3+}$  is shown in **Figure 6.1a** and can be used to explain the transitions and interactions discussed earlier. In  $\text{Yb}^{3+}$ , only a two-level energy system exists with resulting emission in the 1000 nm region due to the  $^2\text{F}_{5/2} \rightarrow ^2\text{F}_{7/2}$  transition, as shown in **Figure 6.1b**. In  $\text{Er}^{3+}$ , the  $^4\text{I}_{13/2}$  state is the first metastable excited state for the transition of the 1530 nm line. Any process or interaction which depopulates the  $\text{Er}^{3+}$  ion from this state, other than radiative decay with 1530 nm emission, thus reduces the efficiency of the fluorescence as well as its intensity. One form of energy transfer is the migration of ions from the first excited state to the ground state. As can be seen in **Figure 6.1a**, non-radiative multi-phonon relaxation of the  $^4\text{I}_{13/2} \rightarrow ^4\text{I}_{15/2}$  transition is a possible process which can deplete the excited  $\text{Er}^{3+}$  population due to the interaction between the excited electrons and the dynamic crystal lattice. This process is characterised by fast non-radiative decay to the ground state since only a relatively small number of electron-phonon couplings are required to bridge the energy gap between the two levels (excited and ground states) when the energy of the coupling phonon increases [6.12]. Hence, at relatively low temperatures ( $<273$  K), the lifetime of the excited state transition is largely

determined by radiative decay while at higher temperatures, the fluorescence lifetime is dominated by non-radiative decay due to multi-phonon emission which, at elevated temperatures, will result in thermal quenching of the transitions. In co-doped systems involving both  $\text{Er}^{3+}$  and  $\text{Yb}^{3+}$  ions, similar thermal behaviour can be expected although such systems generally utilise the “sensitiser” ions,  $\text{Yb}^{3+}$ , as donors which can absorb radiation at the resonant pump wavelength (in this case, ~960 to 965 nm, as already illustrated in **Chapter 3**) and subsequently transfer most of this energy efficiently to the acceptor  $\text{Er}^{3+}$  ions. The co-doped system is shown in **Figure 6.1c**.

Another process, which can lead to the depopulation of the excited state, results when the excited ions absorb more pump energy/photons and are excited or promoted to a still higher energy level, from which decay to either the  $^4\text{I}_{13/2}$  state or other lower state(s) will occur non-radiatively or radiatively at an unwanted wavelength. This excited state absorption (ESA) process is possible due to the relatively long fluorescence lifetime of the first excited state where transitions from this level to the ground results in the IR emission at ~1.5  $\mu\text{m}$ . In optical telecommunications and amplification applications this type of process is considered as detrimental since it reduces the number density of excited ions and thus limits the population inversion at the metastable state. Another mechanism is upconversion in which transitions from the excited ions, when promoted to higher energy levels, give rise to emission in the visible spectrum (the so-called “unwanted” wavelength). Upconversion is generally a very efficient process and is dependent on either or both the concentration levels of the RE ions as well as the pump power and wavelength [6.22]. Such processes result in the emission of higher energy radiation with shorter wavelength in the visible spectrum. Hence, very efficient lasers in the visible can be fabricated from RE-doped crystalline or glass materials.  $\text{Er}^{3+}$  and  $\text{Yb}^{3+}$ -sensitised  $\text{Er}^{3+}$ -doped materials (both crystals and glasses) have been reported to emit upconverted radiation in the blue, green and red spectral regions [6.22, 6.33, 6.73, 6.74, 6.75].

**Table 6.2. Some basic properties of RE erbium and ytterbium elements**

Atomic no.	Element	Trivalent electronic configuration	Ground state	Ionic radius / nm	Electrons in 4f shell
68	Erbium	$4f^{11}5s^25p^6$	$^4I_{15/2}$	0.096	11
70	Ytterbium	$4f^{13}5s^25p^6$	$^2F_{7/2}$	0.094	13

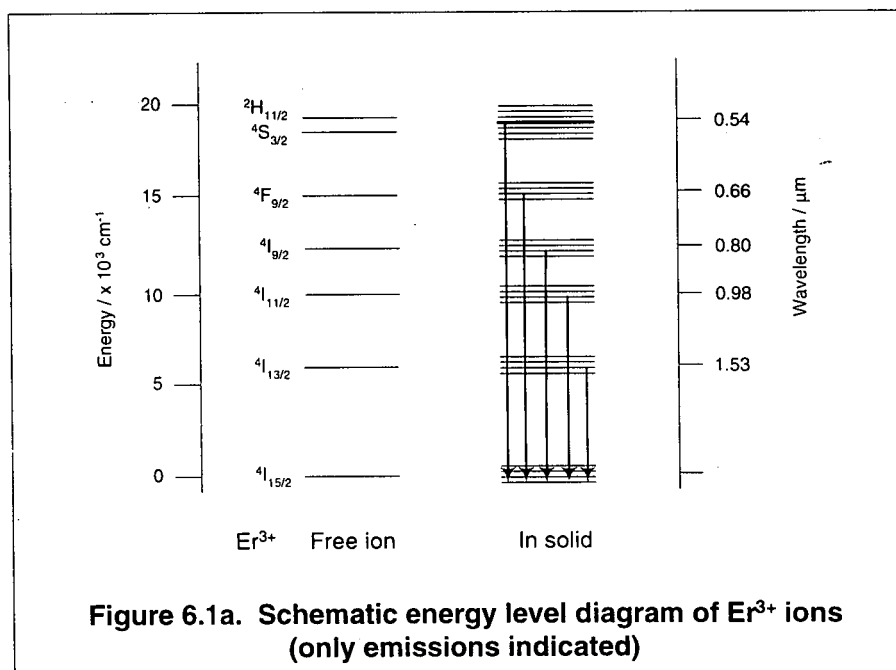


**Figure 6.1a. Schematic energy level diagram of  $Er^{3+}$  ions (only emissions indicated)**

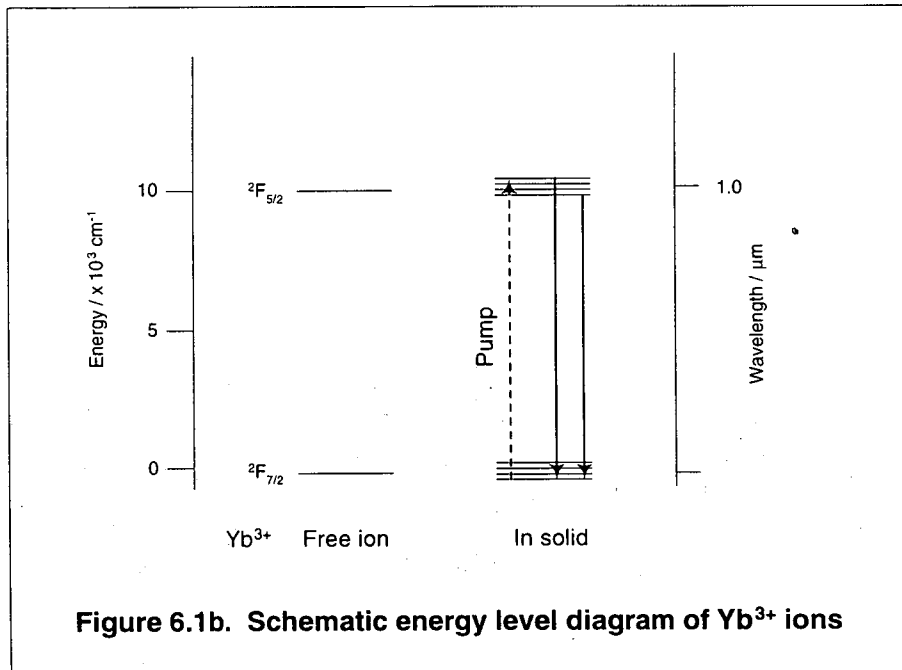


Figure 6.1b. Schematic energy level diagram of  $\text{Yb}^{3+}$  ions

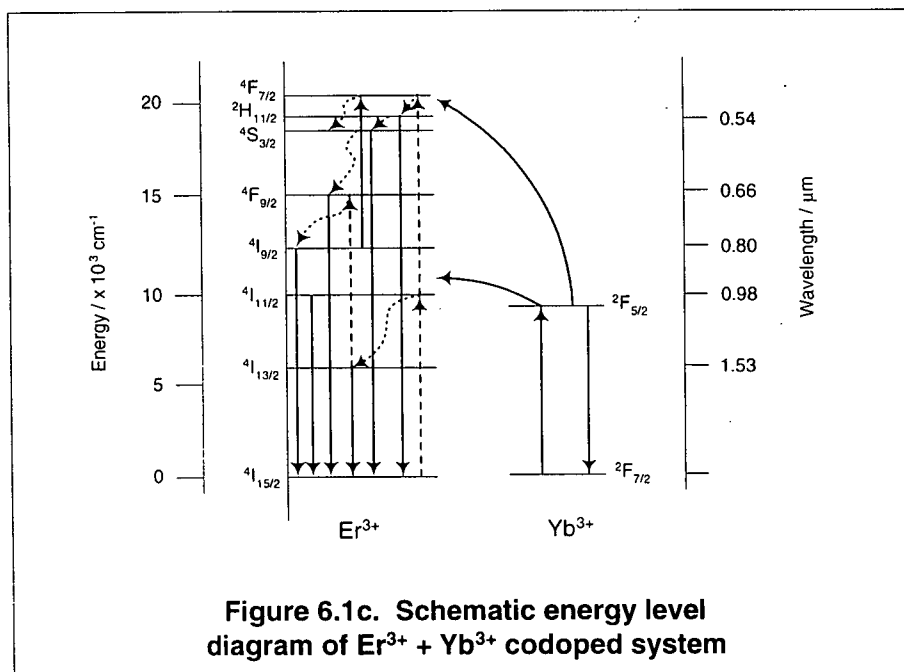


Figure 6.1c. Schematic energy level diagram of  $\text{Er}^{3+} + \text{Yb}^{3+}$  codoped system

In singly  $\text{Er}^{3+}$ -doped materials, the most common upconversion mechanism is ESA or two-photon absorption where an excited ion absorbs another photon from the pump source and is elevated to the  $^4\text{F}_{9/2}$  state from which visible emission occurs in the red (~650 to 660 nm). Upconversion from the  $^4\text{S}_{3/2}$  level leads to transition in the green (~545 to 550 nm). The 520 nm emission observed originates from the  $^2\text{H}_{11/2}$  level [6.12, 6.72, 6.22]. See **Figures 6.1a** and **6.1c**. However, if the concentration level of erbium is very high, the distance between the  $\text{Er}^{3+}$  ions ( $r$ ) is small and two types of transitions can occur. Interactions between neighbouring excited  $\text{Er}^{3+}$  ions can take place in which the strength of interaction is dependent on the separation between two ions as  $1/r^6$  [6.72]. The resulting effect is the reduction in the number of excited ions at a given excitation power, leading to energy migration where the excited ion transfers its energy to another ion in the ground state. This also leads to loss of photon energy whose lifetime can be described as a non-radiative decay when both excited ions finally decay to the ground. Concentration quenching of this nature does not permit gain or amplification of the optical signal but, in fact, leads to reduction of the excited state population with energy dissipated mostly as thermal energy [6.22, 6.72]. Another concentration quenching effect can also occur and is manifested in the form of cooperative upconversion. In such a scheme, two neighbouring  $\text{Er}^{3+}$  ions, both in the first excited state,  $^4\text{I}_{13/2}$ , interact with the resulting effect that one ion is promoted further to a higher energy level,  $^4\text{I}_{9/2}$ , while the second ion relaxes to the ground state ( $^4\text{I}_{15/2}$ ). Subsequent absorption of more pump photons can result in upconversion to the  $^4\text{F}_{9/2}$ ,  $^4\text{S}_{3/2}$  or  $^2\text{H}_{9/2}$  levels with emissions in the red (~660 nm), green (~545-550 nm) and blue (~410 nm) respectively. The green line also seen at ~520 nm can be considered as the effect resulting from the crystal field Stark-splitting of the  $^4\text{S}_{3/2}$  manifold [6.25]. With ytterbium ion sensitiser, co-doped  $\text{Er}^{3+} + \text{Yb}^{3+}$  systems can result in improved upconversion processes due to the efficient energy transfer provided by the co-dopant,  $\text{Yb}^{3+}$  [6.22, 6.75]. In co-doped systems, upconversion is almost invariably a cooperative energy transfer process due to the role played by the sensitiser or donor ion. However, depending on the dopant concentration levels as well as the pump wavelength employed, co-doping can also result in improved gain characteristics at the primary emission wavelength of 1530 nm [6.37, 6.76].

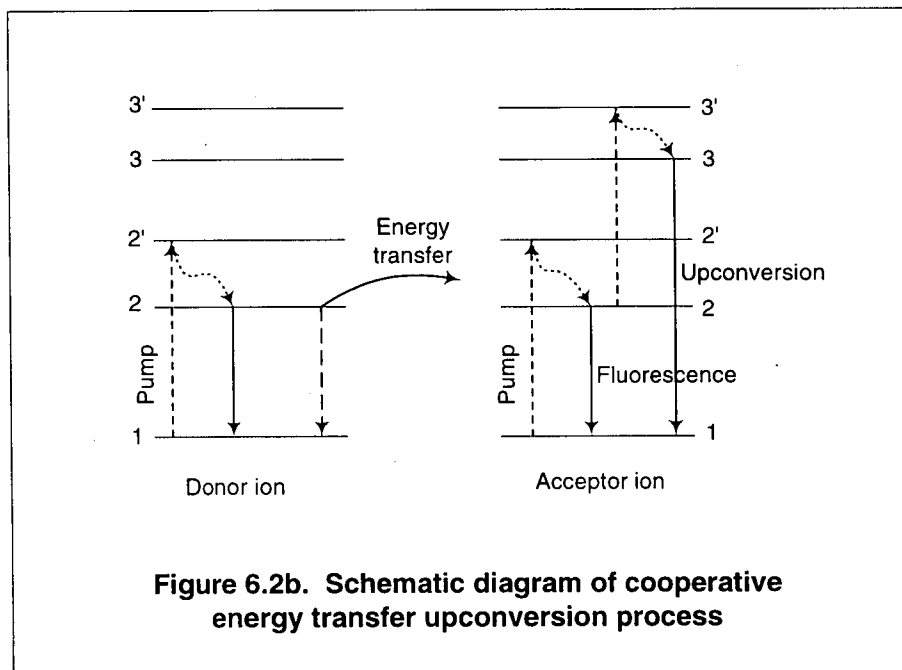
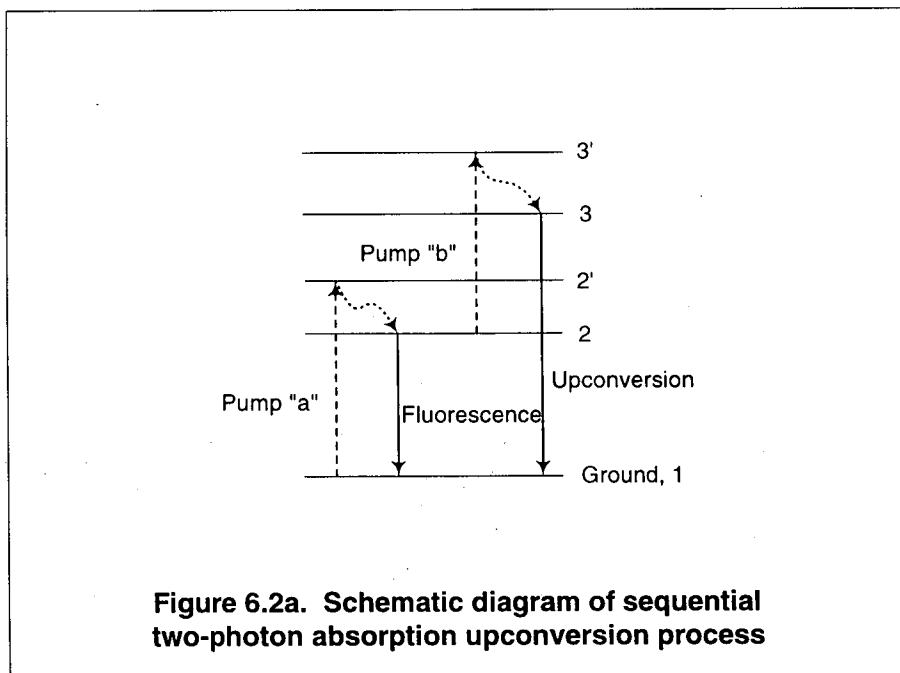
There is great interest in upconversion processes since very efficient and compact solid state lasers in the visible can be achieved by IR pumping of RE-doped materials. Although initial applications for (IR) upconversion materials were intended for detection of IR radiation or display of IR images [6.77, 6.78], the most attractive applications are found in the realisation of upconversion lasers emitting in the visible spectrum while offering simple construction and efficient energy transfer as compared to other non-linear techniques of converting IR radiation into the visible (such as frequency-doubling, second harmonic generation, etc.). Upconversion results in the population of an excited state having an energy level which is higher than both that of the first excited state and the pump photon, with emission wavelengths typically shorter than that of the pump source as well. There are generally three mechanisms of upconversion known and all involve the absorption of photons and subsequent energy transfer processes to generate radiation in the visible spectrum [6.22]. These are illustrated in **Figures 6.2** using a modified three-level model for simplicity.

In two-photon absorption upconversion the pump photons are absorbed sequentially and require a metastable state between the ground and the emitting states. It is from this state, acting as an energy store, that further photon absorption occurs, promoting the excited ion into a still higher energy level. As schematically shown in **Figure 6.2a**, the ion initially in the ground state is excited by absorption of pump photon, "a", to level 2 following rapid non-radiative multi-phonon decay from level 2'. Radiative decay from this metastable state is possible with resulting emission for  $\text{Er}^{3+}$ , in the 1.5  $\mu\text{m}$  region. Non-radiative multi-phonon decay to the ground state is also possible but the large energy gap between this state and the ground, compared to the phonon energy, prevents this from occurring [6.22]. The absorption of another pump photon, "b", promotes the excited ion to level 3' before the radiative decay from 2 to the ground state can occur. Rapid relaxation populates level 3', from which the transition to level 1 (ground) produces the upconverted emission in the visible spectrum. This process is known as excited state absorption or sequential two-photon upconversion since the ion from one excited state is promoted to a higher energy level by absorption of another pump photon and generally requires two pump wavelengths.

Upconversion involving the absorption of pump photons by two distinct RE ions can also occur in which the two neighbouring ions absorb a pump photon of the same energy to populate the metastable state. In such a process, only one pump wavelength is required. The absorption of this pump photon enables the two ions to be promoted to an excited state, from which, by the cooperative energy transfer mechanism, one ion is further excited into a higher energy level while the second ion decays/relaxes to the ground. Cooperative upconversion is illustrated schematically in **Figure 6.2b**. Since it is a process generally associated with the excitation and energy transfer of two distinct ions,  $\text{Yb}^{3+}$  ions are particularly suitable as the donor ions, hence, the name "sensitisers". Ytterbium ions thus serve as the donor in co-doped systems with absorption in the 1  $\mu\text{m}$  region. The main absorption peak has been found to be in the region of 950 to 970 nm in this work. However, in singly doped ( $\text{Er}^{3+}$ , for example) systems, relatively large doping concentration levels and high pump intensities are required for efficient cooperative upconversion processes [6.22, 6.33, 6.72]. As shown in **Figure 6.2b**, pump photons are absorbed by neighbouring donor-acceptor ion pairs in the ground state, promoting both ions to the excited metastable level 2. The excited ions can relax radiatively (or non-radiatively) to the ground state or be promoted by cooperative energy transfer (from the donor ions) to the next higher energy state, level 3 following rapid decay from level 3'. The energy gaps between the  $2 \rightarrow 1$  and  $2 \rightarrow 3'$  transitions are generally not identical and the energy excess/deficit must be compensated for in some ways by the crystal lattice of the host in a phonon-assisted energy transfer process [6.22, 6.72]. Thus, for efficient cooperative upconversion, the donor-acceptor ion pairs must be closely situated to each other, where the interaction strength depends on the factor  $1/r^6$ , where  $r$  is the separation between the ion pair. This also implies that a high concentration level would increase the upconversion efficiency, with a donor-acceptor ion pair density distribution set up within the crystal host as a consequence. The subsequent effect of such a density gradient is the non-exponential fluorescence decay from the upconverted emission of the visible spectrum ( $3 \rightarrow 1$  transition) due to the existence of different ion pair separations in the host material [6.22]. If, however, there is rapid migration of the excitation energy among the ion pairs, an

effectively even distribution of the ion pair energy gradient can occur, resulting in exponential fluorescence decay for the upconversion process.

The final upconversion mechanism is a relatively complicated process in which excitation is initiated by absorption of the pump photon from an excited ion [6.22, 6.33]. In photon avalanche, as shown in **Figure 6.2c**, non-resonant absorption of the pump photon is accredited as the main reason for producing an initial excited population in the metastable state, level 2. A photon which matches or is resonant with the energy gap of the  $2 \rightarrow 3'$  transition promotes a ground state ion to the excited metastable level 2. This could also occur as a result of thermal excitation of the metastable state [6.22]. In singly doped systems, both donors and acceptors are of the same species. Thus a donor ion in the metastable state 2 is excited into the emitting level 3 after absorption of a pump photon. Cross relaxation of the donor ion then results in the excited ion decaying to the metastable level while at the same time promoting the ground state ion into the metastable level as shown in **Figure 6.2c**, on the right. Therefore, under suitable pumping conditions, this process can lead to rapid multiplication of populations in the metastable state, resulting in an avalanche of excited ions in that state. A two-photon absorption process can also occur in photon avalanche upconversion at low pump intensities although the latter mechanism differs from the former in that an initial non-resonant pumping is observed. At high pump intensities or above the avalanche threshold, however, cross relaxation between the upper emitting and ground ions dominates the population of the metastable level.



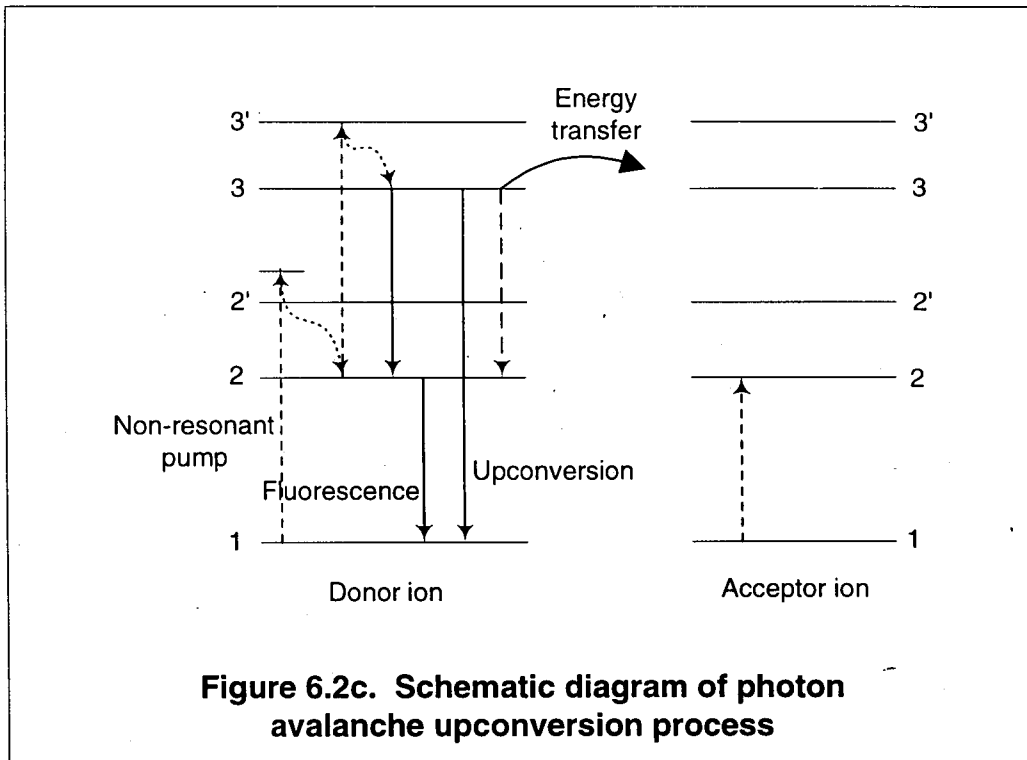


**Figure 6.2c. Schematic diagram of photon avalanche upconversion process**

## 6.2 Temperature sensing based on $\text{Er}^{3+}$ , equally $\text{Er}^{3+} + \text{Yb}^{3+}$ -codoped and high $\text{Yb}^{3+}$ + low $\text{Er}^{3+}$ -codoped $\text{Al}_2\text{O}_3$ fibres

As discussed in the previous section, the radiative decays involved in fluorescence and upconversion processes are not necessarily temperature-dependent partly due to the shielding provided to the  $4f$  electrons by the  $5s^2$  and  $5p^6$  outer electronic shells. However, the non-radiative decay due to multi-phonon transitions, in part due to the high dopant concentration levels utilised in this work, can lead to a certain level of temperature dependence or thermal quenching. This temperature dependence has been investigated in the current work up to the maximum operating temperature of the equipment employed.

Three types of rare earth-doped crystal probes based on sapphire fibres as the host material, with diameters in the  $130\ \mu\text{m}$  range (compatible with most multi-mode fibres), have been fabricated and investigated for their temperature dependences. The fabrication of RE-doped  $\text{Al}_2\text{O}_3$  fibres by any melt growth methods has not been reported in the literature and this work presents the first attempts at growing such fibres for high temperature sensing applications employing emission in both the visible and IR spectra. The bulk of the results are based on visible emission lines. One important reason for this is the high dopant concentration incorporated into the sapphire fibres. As has already been discussed, the interaction strength for the  $4f-4f$  transitions varies with the separation between two excited ions as  $1/r^6$ , which in turn is highly dependent on the concentration levels of the RE ions. Such high levels of ion concentration is considered to be the main factor which has led to very efficient cooperative energy transfer while depleting the population of the first excited state for transition in the IR region. Although it has not been possible to conduct an SEM (scanning electron microprobe) or EMPA (electron microprobe analysis) study on a variety of RE-doped fibres for a systematic estimate of the maximum dopant concentration levels which can be achieved, one sapphire fibre singly doped at one end with  $\text{Er}^{3+}$  ions has been probed with the EMPA, revealing concentration levels averaging  $\sim 12$  at. %. **Figure 6.3** presents an end view of the doped sample where the brighter regions are areas of high Er concentration compared to the slightly darker regions. The dark portion in the middle is actually a hollow in the surface of the sample and occurred as a result of the melting technique used which led to

contraction on this part of the sample upon cooling. The top section of the fibre has been polished down to a flatness of 1  $\mu\text{m}$ . EMPA scans were conducted using facilities located within the Department of Geology. The Er concentration levels at the various localised points are also indicated in **Figure 6.3**.

Although initial attempts in producing RE-doped  $\text{Al}_2\text{O}_3$  fibres by the LHPG technique employing small diameter source rods were problematic, subsequent growths using larger diameter source rods resulted in sapphire fibres doped with  $\text{Er}^{3+}$ ,  $\text{Er}^{3+} + \text{Yb}^{3+}$ -codoped (approximately equal  $\text{Er}^{3+}$  and  $\text{Yb}^{3+}$  contents) and high  $\text{Yb}^{3+} + \text{low Er}^{3+}$ -codoped ions. The most significant disadvantage of using singly erbium-doped fibres was found to be the lack of convenient, broad absorption bands where inexpensive pump sources at suitable wavelengths are readily available. Moreover,  $\text{Er}^{3+}$ -doped systems are also susceptible to strong excited state absorption which further restrict the pump wavelengths that can be used [6.72-6.76]. Hence, one of the main motivations for codoping with  $\text{Yb}^{3+}$  ions is the wide absorption band available from approximately 900 to 1000 nm, as shown in **Figure 6.4**. Subsequent energy transfer processes from the donor  $\text{Yb}^{3+}$  ions can result in very efficient excitation of the  $\text{Er}^{3+}$  ions, leading to improved fluorescence characteristics.

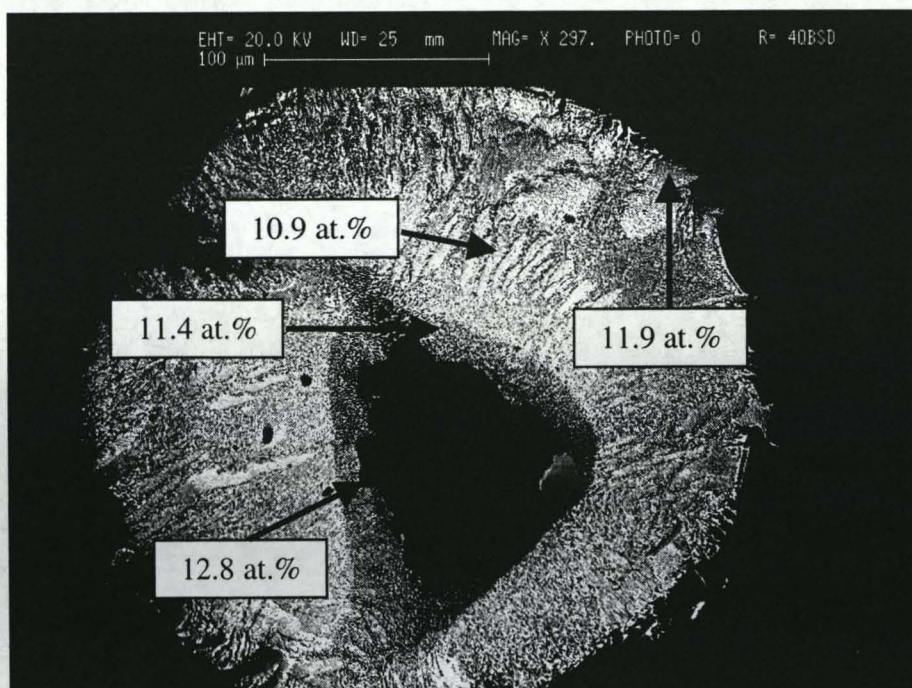
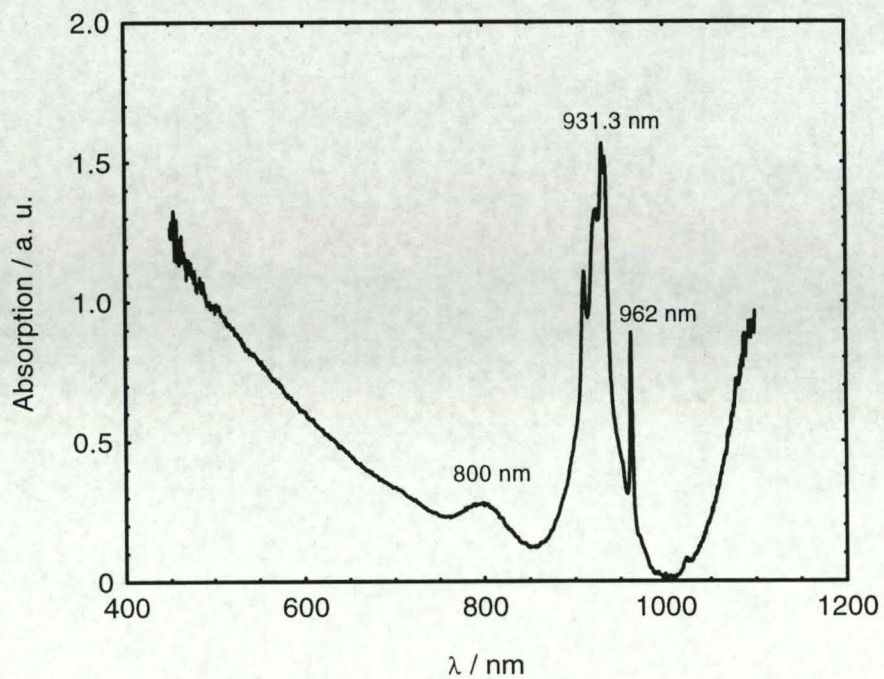


**Figure 6.3. SEM image of Er<sup>3+</sup>-doped tip in Al<sub>2</sub>O<sub>3</sub> (Arrows indicate points where discrete scans have been made with estimated Er concentration levels)**

**Figure 6.4. Visible absorption spectrum of Yb<sup>3+</sup>:Er<sup>3+</sup>:Al<sub>2</sub>O<sub>3</sub> fibre**



## 6.2.1 Temperature sensing with Er<sup>3+</sup>:Al<sub>2</sub>O<sub>3</sub> fibres

The temperature dependence of both the IR fluorescence and visible emission from two samples of Er<sup>3+</sup>:Al<sub>2</sub>O<sub>3</sub> fibres is investigated. Although the high Er<sup>3+</sup> concentration levels incorporated into the sapphire host fibres have resulted in fluorescence lifetimes which are too rapid (<200 μs) to be fully exploited over a wide temperature range, spectral emission in the IR and visible regions can still be measured under lock-in detection. Er<sup>3+</sup> ions when doped into crystal hosts have been found to produce sharp emissions in several spectral regions. Cooperative upconversion processes have resulted in visible emission in both the green and red spectral regions, but the upconversion intensities have been found to be quite weak. They have been investigated for potential thermometric applications up to a temperature of ~500 K. Relatively stronger lines have been observed in the IR, from ~1500 to 1550 nm and have been used for temperature investigation based on the ratio between these lines. The maximum temperature monitored using the IR fluorescence intensity ratios (FIRs) was ~720 K.

### 6.2.1.1 FIRs of green upconversion and IR emission for temperature sensing

The centre wavelengths of the four IR lines used are respectively 1511.5, 1523.0, 1531.5 and 1547.0 nm. They are shown in **Figure 6.5**. The visible emission studied is between 540 and 550 nm, with five lines investigated, again in a ratiometric technique. Only results for the green emission is reported for reasons which will be discussed later. The sharp lines (**Figure 6.6**) observed within such a relatively narrow spectral bandwidth reinforced the conclusion that the sapphire fibres were single-crystals rather than polycrystalline in nature. Otherwise, as is the case in glasses (amorphous), the emission would be very broad and these lines would have been poorly resolved. The five lines employed are 540, 541.5, 552.5, 554.5 and 559 nm. Even though the 520 nm line has been observed here and exploited in the work of Maurice *et al.* [6.69], it has not been used in this study due to the almost coincidental additional line emitted by the pump source used, which has been observed at ~525 nm. Using the 520 nm emission as one of the primary ratiometric lines would thus lead to difficulty in separating the signal from the laser emission and possibly give inaccurate values.

Figure 6.5. IR fluorescence lines used in FIR temperature measurements ( $\text{Er}^{3+}:\text{Al}_2\text{O}_3$  fibre)

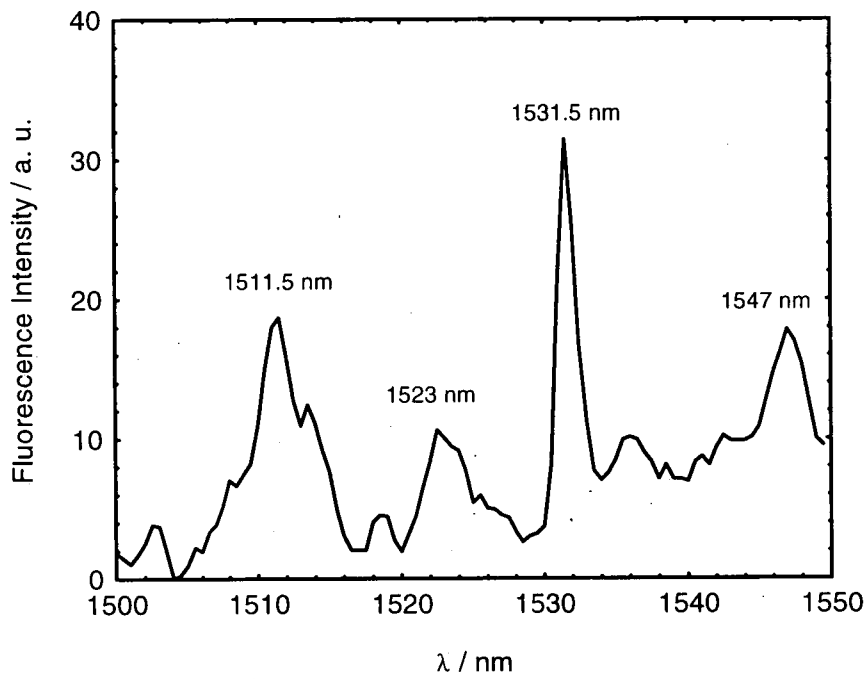
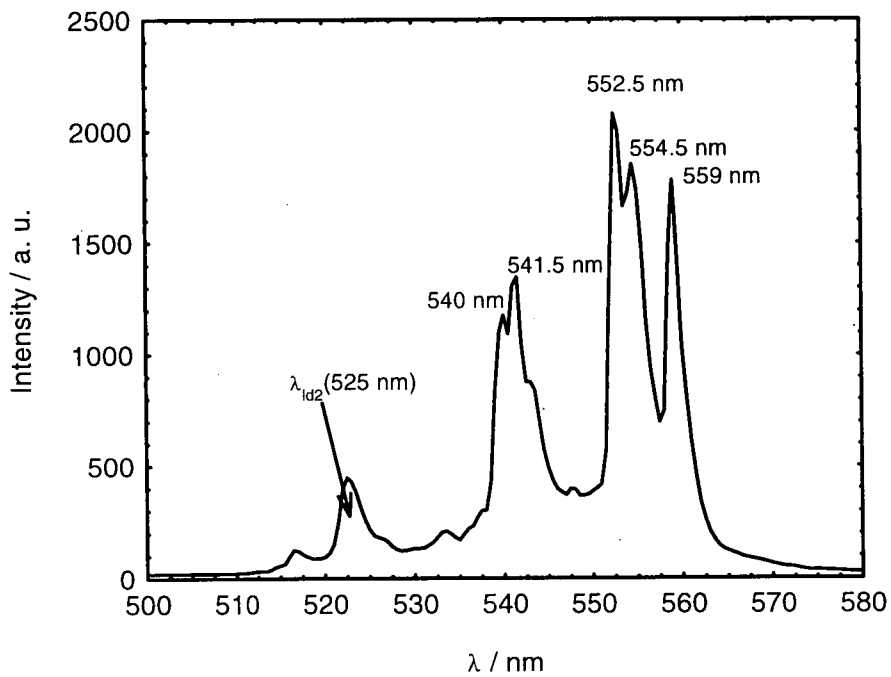


Figure 6.6. Green upconversion spectrum of  $\text{Er}^{3+}:\text{Al}_2\text{O}_3$  fibre (doped tip)



### 6.2.1.2 Experiments

The temperature dependence of the emission spectra of these erbium-doped sapphire fibres have been studied. Two configurations were examined: one in which fibres were doped with a high concentration of  $\text{Er}^{3+}$  ions (~12 wt. %) only at the tip while the other where fibre sections of ~20 mm in length were doped. Due to the weak upconversion in singly doped Er fibres, it was not possible to detect any reasonable amount of visible emission from fibres using reflection-based measurements, hence a simple technique has been arrived at in order that the emission lines could be measured. Fibres doped only at their tips were approximately 40 mm in length and a schematic of the experimental set-up is shown in **Figure 6.7**. The temperature dependent measurements have been obtained in transmission. A hollow cylindrical ring approximately 20 mm in length was fabricated from a *Duratec 750* machinable high temperature ceramic rod and employed to surround the fibre end to maintain a relatively stable thermal environment. The fibre was in turn attached to a K-type thermocouple to verify the temperature at which the fibre tip has been subjected to. Excitation of the active tip was achieved by pump light from a 960 nm laser diode (*LACRYS*) which was transmitted to the sapphire fibre via a multimode silica fibre butt-coupled with the aid of a silica sleeve. Both fibres were held securely by application of high temperature ceramic adhesive at both ends of the sleeve. A 50 mm focal length lens was used to collect and collimate light emitted from the fibre tip onto another 50 mm lens which focused the desired green emission into the monochromator. Lock-in detection, in conjunction with a *Hamamatsu R928* PMT, have been employed to provide sensitive and accurate signal recovery, with the data being sent to a computer acquisition and storage system for later processing.

For acquisition of the IR signals (1500 – 1550 nm), the other fibre configuration was used. Doped sections were estimated to be approximately 20 mm long and fibres were used in reflection measurements as shown in **Figure 6.8**. The approximate length of these fibre was approximately 150 mm thus, the active probe, which has been doped with erbium could be inserted relatively deep into the stabilised *CARBOLITE* tube furnace. As in the ruby fibre studies, high temperature ceramic wool has been used to plug both ends of the furnace with the main aim of reducing heat loss at high temperatures and providing a stable thermal environment. In

addition, a K-type thermocouple has also been inserted into the furnace tube to monitor any significant variation of the actual temperature from the furnace set point. Collimated light from the IR laser diode (960 nm) was launched into the end of the fibre via a X20 microscope objective. The reflected IR signal from the fibre was then directed into the monochromator as illustrated and detected by lock-in techniques. The monochromator was scanned from ~1500 to 1550 nm, where the IR fluorescence lines to be measured could be expected. The detection of the IR signal was achieved with a high-gain InGaAs photodetector at the exit slit, the values of which were converted by an A-D card and sent to a dedicated computer for storage and later analysis.

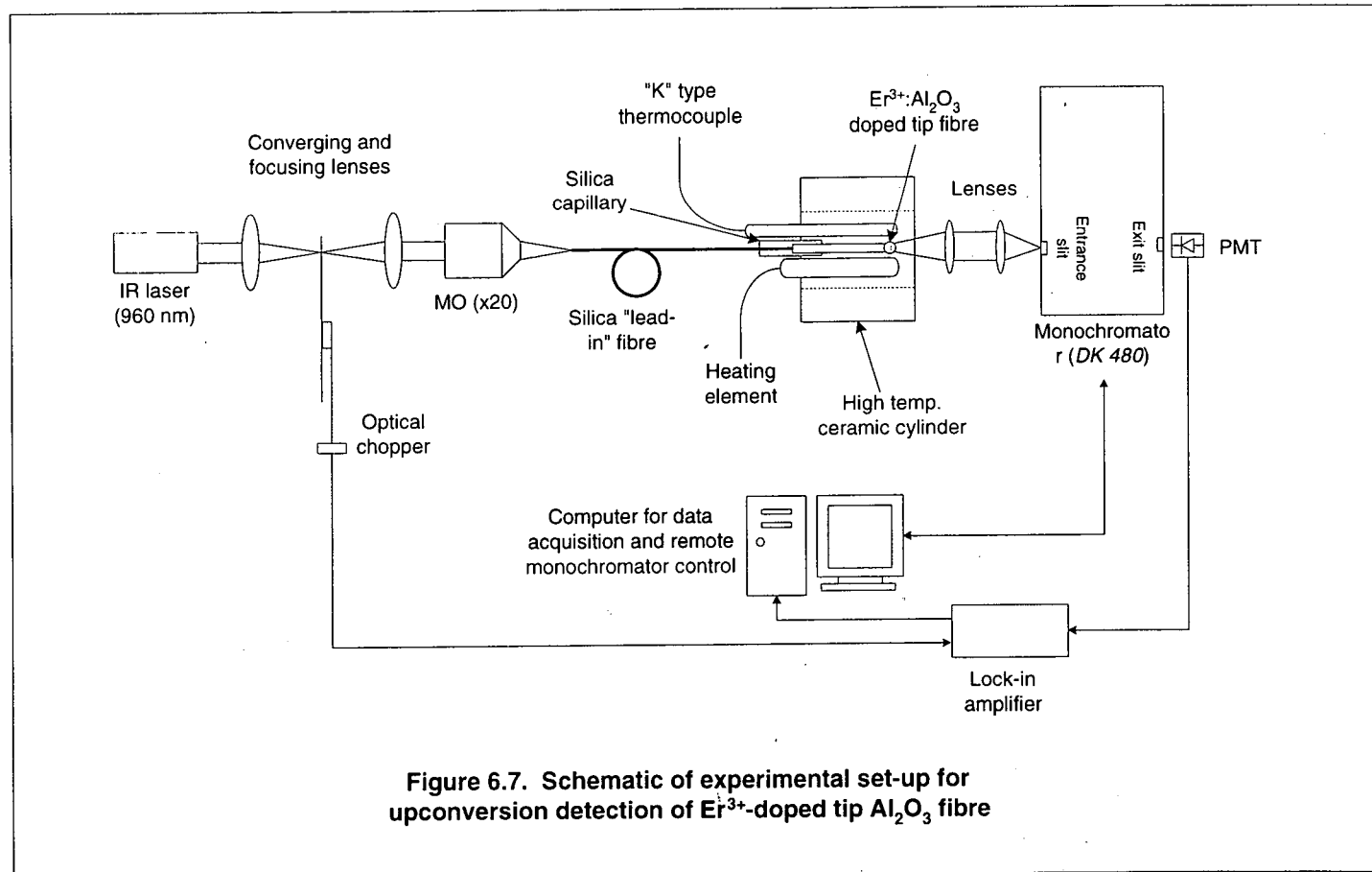
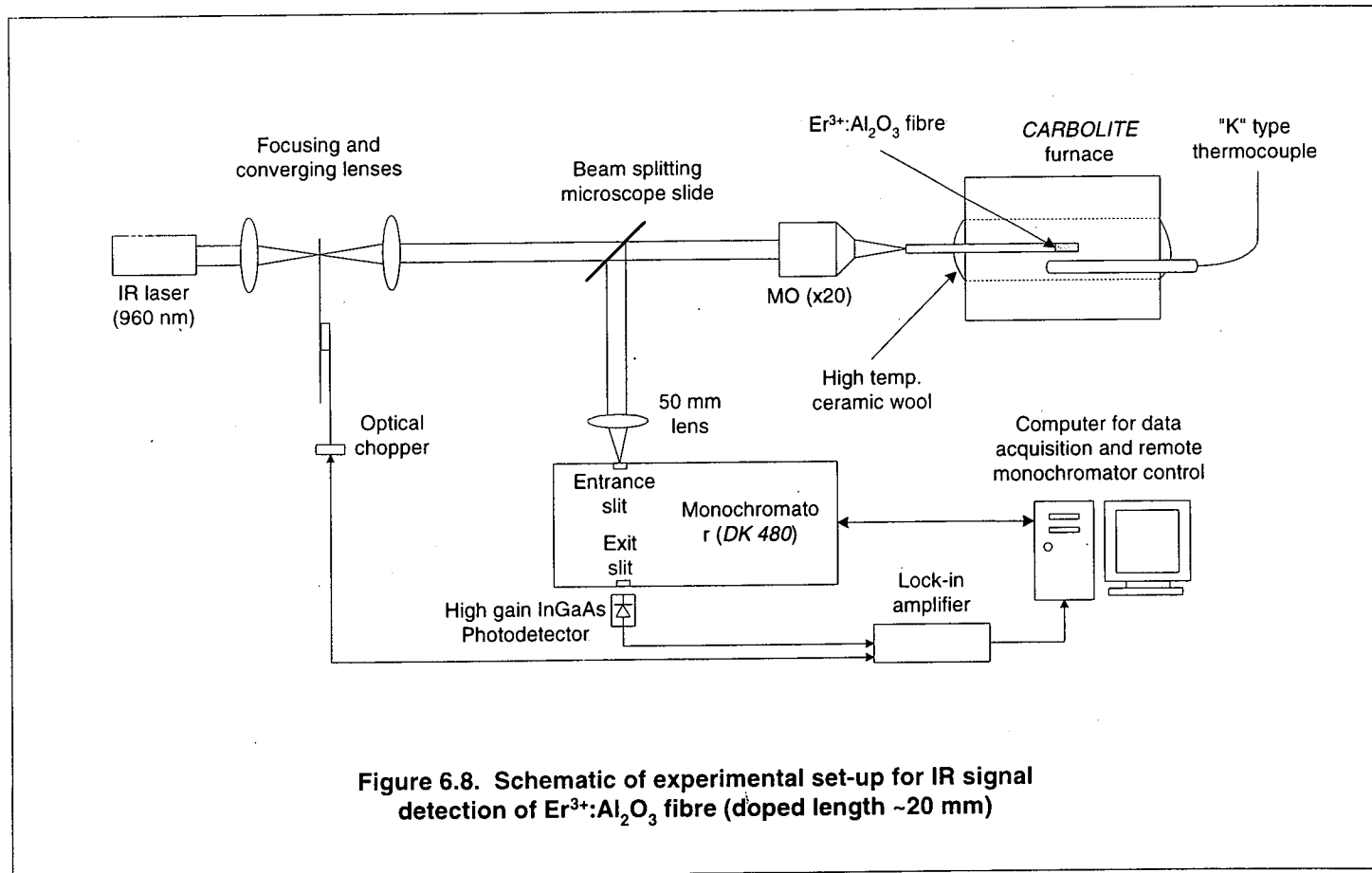


Figure 6.7. Schematic of experimental set-up for upconversion detection of  $\text{Er}^{3+}$ -doped tip  $\text{Al}_2\text{O}_3$  fibre



**Figure 6.8. Schematic of experimental set-up for IR signal detection of Er<sup>3+</sup>:Al<sub>2</sub>O<sub>3</sub> fibre (doped length ~20 mm)**

### 6.2.1.3 Results and Discussion

The five lines from the green fluorescence emission have been monitored from room temperature up to ~500 K. Although the  $\text{Er}^{3+}$ -doped silica fibres which have been employed up to 1000 K [7.79] were excited by a pump source which was resonant with one of its absorption peaks, the low temperature measured in this work has been limited by the weak signal due to poor overlap between the pump wavelength used and the absorption peak of  $\text{Er}^{3+}:\text{Al}_2\text{O}_3$ . If better matching was obtained by using a suitable pump source, stronger signals would result and higher temperatures could then be measured. Thus, beyond ~500 K, the signals were found to be too weak and the background noise levels dominated the emission spectrum. The intensity of these five lines have been used in a ratiometric method and resulted in an array of 10 curves, each representing an intensity ratio of two of these lines as a function of temperature. The way in which the ratios have been employed are presented in **Table 6.3**, where  $FIR_{g12}$  represents the intensity ratio of the 540 and 542.5 nm lines, and so on. The temperature dependences of the ten intensity ratios are shown in **Figures 6.9** with  $FIR_{g12}$  to  $FIR_{g15}$  plotted in **6.9a**,  $FIR_{g23}$  to  $FIR_{g25}$  in **6.9b** and  $FIR_{g34}$  to  $FIR_{g45}$  in **6.9c**. A majority of the FIRs can be seen to exhibit a non-monotonic characteristic as a function of increasing temperature. Based on the widest temperature range available, only 2 lines from these ten have been selected for potential thermometric applications and they have been re-plotted in **Figures 6.10a** and **6.10b**. They were  $FIR_{g12}$  and  $FIR_{g15}$ , the fluorescence intensity ratios between the 540 and 541.5 nm lines, and the 540 and 559 nm lines respectively. The denotation  $FIR_{IRij}$  is used for the ratios from the IR lines.

The results of the 6 fluorescence intensity ratios from the IR emission lines are presented in **Figures 6.11a** and **6.11b**, indicating  $FIR_{IR12}$  to  $FIR_{IR14}$  and  $FIR_{IR23}$  to  $FIR_{IR34}$  respectively while **Table 6.3** also illustrates how the 6 ratios have been arrived at:  $FIR_{IR12}$  denoting the ratio of intensities of 1511.5 nm over 1523 nm, etc. The six intensity ratios for the IR lines are plotted as a function of temperature in **Figures 6.11**. Again, non-monotonic characteristics are exhibited by all the curves from room temperature onwards. Further, only  $FIR_{IR24}$  and  $FIR_{IR34}$  show an increase with temperature while the other curves exhibit a generally decreasing profile as temperature is increased. The maximum temperature investigated utilising the IR

emissions was up to ~720 K beyond which signals became weak and were dominated by noise. The decreasing ratios of two curves have been selected for potential temperature sensing from 373 K up to ~723 K. Below 373 K, however, non-monotonic decay would render any temperature measurements ambiguous over the entire temperature range. The two selected intensity ratios,  $FIR_{IR12}$  and  $FIR_{IR13}$ , are re-plotted in **Figures 6.12a** and **6.12b** respectively.

The crystalline  $Al_2O_3$  host has provided an ionic crystal field from which interactions between the crystal lattice (phonons) and the  $Er^{3+}$  dopant ions (electrons), as well as a high dopant concentration level have led to narrow-line emissions in the visible and IR spectral regions, with slightly broader bandwidths at four IR spectral lines. In particular, the Stark-splitting [6.13, 6.25] of the  $^4S_{3/2}$  manifold can lead to the formation of several other levels within this manifold with very narrow energy gaps. This has been observed in the current work from the detected green upconverted emission produced from  $Er^{3+}$ -doped sapphire fibres. The primary transition manifold is  $^4S_{3/2}$ , hence the five constituent levels are denoted as  $^4S_{3/2(a)}$ ,  $^4S_{3/2(b)}$ ,  $^4S_{3/2(c)}$ ,  $^4S_{3/2(d)}$  and  $^4S_{3/2(b)}$ , corresponding to 540, 541.5, 552.5, 554.5 and 559 nm respectively. Transitions from these levels to the ground,  $^4I_{15/2}$ , therefore result in the green upconverted emission which has been detected. The two FIRs were selected based on the widest temperature range possible and least errors incurred, resulting thus in  $FIR_{g12}$  and  $FIR_{g15}$  being the most suitable. In addition, the other 8 curves exhibited non-monotonic decreases in their FIRs over a wider temperature region as seen in **Figures 6.9**. The intensity of the 540 nm line is less temperature dependent than both the 541.5 and 559 nm lines, as evident from the steady increase in the ratios  $FIR_{g12}$  and  $FIR_{g15}$  with temperature as shown in **Figures 6.10a** and **6.10b**. It could also imply that the increasing temperature provided thermal energy to excite ions from the lower energy levels at 541.5 and 559 nm to the higher energy level at 540 nm. Estimation of the errors from the measured data resulted in a maximum error margin of ~9 % for  $FIR_{g12}$  and 11.5 % for  $FIR_{g15}$ , corresponding to ~44 K and ~52 K respectively. These large errors obtained can be attributed to the relatively weak upconversion signal emitted from the doped tip of the fibres which were very small in size (measuring less than 0.3 mm in diameter). The thermalisation effect or thermally-assisted energy transfer from the  $^4S_{3/2}$  state (~540 nm) to the adjacent  $^2H_{11/2}$  (520 nm) state has been reported as the main reason for the increase in the

intensity of the 520 nm line when temperature was increased [6.80, 6.79]. This phenomenon has been exploited [6.80, 6.79] in the search for potential erbium-doped temperature sensors which can be self-referencing. The originally weaker  ${}^2\text{H}_{11/2}$  transition (to the  ${}^4\text{I}_{15/2}$  ground state) at 520 nm at room temperature steadily gained in strength (intensity) with increasing temperature while the 540 nm line produced by the  ${}^4\text{S}_{3/2} \rightarrow {}^4\text{I}_{15/2}$  transition decreased in intensity. This intrinsic property of the erbium-doped fibres, in effect, makes such devices relatively independent of the pump power fluctuations and, at the same time, self-referenced sensors employing such fluorescence/upconversion-based devices can be realised. However, the 520 nm upconversion has not been employed here since the 960 nm pump source was found to emit three additional lines in the visible. The emission from the laser in the visible up to  $\sim 850$  nm has been measured and is shown in **Figure 6.13**. It has been found that when the pump radiation was transmitted through the fibre, the intensities of these lines were reduced to a much lower level, although they could still be observed, as in **Figure 6.6**. In silica, fluorescence from the  ${}^2\text{H}_{11/2}$  (520 nm) level has been accounted for [6.79] as the consequence of the population of this level by excitation from the lower  ${}^4\text{S}_{3/2}$  (540 nm) state due to thermal coupling effects between these closely-spaced states. In  $\text{Al}_2\text{O}_3$  [6.72], however, this has been attributed to second order cooperative upconversion excitation between the  $\text{Er}^{3+}$  ions in the  ${}^4\text{I}_{11/2}$  state (980 nm). The pump wavelength used in this work ( $\sim 960$  nm) has been found to be relatively resonant with the  ${}^4\text{I}_{11/2}$  level since the  ${}^4\text{I}_{11/2}$  manifold can have several levels due to splitting. In addition, as has been shown in **Chapter 4**, this pump wavelength coincides with absorption peak around the 960 nm region. However, a poor spectral overlap between the pump and absorption peaks explains the low energy transfer efficiency in singly  $\text{Er}^{3+}$  doped sapphire fibres and the resulting low upconversion intensity. The low intensity is likely to be also due to the small volume of the doped tips fabricated.

The excited  ${}^4\text{I}_{11/2}$  population can decay non-radiatively through multi-phonon relaxation to the  ${}^4\text{I}_{13/2}$  level, from which emission in the 1530 nm region can occur. Alternatively, with high erbium concentration together with relatively high pump intensities of resonant wavelength with the absorption peaks, there can be further excitation to populate the  ${}^2\text{H}_{11/2}$  (520 nm) and  ${}^4\text{S}_{3/2}$  (540 nm) states, which then results in emission in the green. This could help to explain the relatively weaker

upconversion intensities measured compared to the IR intensity in singly Er<sup>3+</sup>-doped sapphire fibres pumped at ~960 nm. Moreover, it has also been observed that within the <sup>2</sup>H<sub>11/2</sub> and <sup>4</sup>S<sub>3/2</sub> main manifolds, sublevels due to Stark splitting can exist, leading to emission in the green ranging from 518 to 543 nm in Er<sup>3+</sup>:YAlO<sub>3</sub> [6.22, 6.33], although in Al<sub>2</sub>O<sub>3</sub> the emission has been observed to have slightly shifted to the 525 → 559 nm green spectral region. Between the two primary manifolds, the temperature dependence of the relative populations may be expressed as a decaying exponential function from the ratio, *R*, of the 520 to 540 nm lines in the form of

$$R = C \exp(-\Delta E/kT) \quad (6.1)$$

where  $\Delta E$  is the energy gap between the two manifolds,  $k$  the Boltzmann constant,  $T$  the temperature in Kelvin and  $C$  a constant which depends on the degeneracies of the two levels as well as the detector sensitivities [6.80, 6.79]. The sublevels within the <sup>4</sup>S<sub>3/2</sub> and <sup>2</sup>H<sub>11/2</sub> states due to Stark-splitting have not been observed before in Er<sup>3+</sup>:Al<sub>2</sub>O<sub>3</sub> (crystals and fibres) and hence, little is known about its inter-manifold interaction or energy transfer. However, these interactions are thought to follow an exponential function with respect to temperature and exhibit the thermalisation effect reported [6.80, 6.79], hence, the above equation (Eq. 6.1) has been applied in attempts to fit the temperature-dependence to the respective ratios, *FIR<sub>g12</sub>* and *FIR<sub>g15</sub>*, and the fitted results are shown in **Figures 6.10a** and **6.10b**. **Table 6.4** lists the fitted values for the intensity ratios – these are significantly different from those of published data for silica fibres [6.80] although one must bear in mind that the phonon energies and spectra of these materials are also very different. The energy gap,  $\Delta E$ , of *FIR<sub>g12</sub>* is approximately three times that of the theoretical value as indicated in **Table 6.4**, although the fitted  $\Delta E$  (629.03 cm<sup>-1</sup>) of *FIR<sub>g15</sub>* is very close to that given in theory (629.43 cm<sup>-1</sup>). In addition, the maximum temperature studied here was only up to 500 K while in Er<sup>3+</sup>-doped silica fibres, temperatures up to 1000 K have been achieved using upconversion [6.79]. However, it can be seen from **Figures 6.10a** and **6.10b** that both fitted curves follow the experimentally obtained data quite closely although large errors will be induced if the fit equation was to be used for temperature calibration. It should also be noted that the large errors measured have occurred because of the weak signals detected and that with improved or stronger

fluorescence from the doped fibre, a better approximation using **Eq. 6.1** can be expected. More significantly, perhaps, the material used in this work is different from those used by Maurice *et al.* [6.69, 6.79] and Berthou and Jørgensen [6.80]. Hence, very different excitation dynamics and energy transfer characteristics may be involved, where the considerably different phonon energies between  $\text{Al}_2\text{O}_3$  and silica contribute to the discrepancies in the fitted values using **Eq. 6.1**. Modification of this model (**Eq. 6.1**) might then be required to accurately fit the temperature-dependent data obtained for  $\text{Al}_2\text{O}_3$  host crystals. Nevertheless, a close exponential profile of the temperature-dependent fluorescence intensity ratios can be seen.

The two selected FIRs in the IR emission,  $FIR_{IR12}$  and  $FIR_{IR13}$ , have been obtained from sapphire fibres with sections of ~20 mm doped with  $\text{Er}^{3+}$  ions. This was done to increase the interaction volume between the pump and doped fibre. The dependence on temperature of  $FIR_{IR12}$  and  $FIR_{IR13}$  are re-plotted in **Figures 6.12a** and **6.12b**. Unlike doping  $\text{Er}^{3+}$  (and in general, all RE ions) in glass, which tends to result in broad linewidths, sharp lines are produced from the emission of  $\text{Er}^{3+}$  ions doped into ionic crystals [6.25]. The FIRs of the two sets of IR lines from the  $\text{Er}^{3+}:\text{Al}_2\text{O}_3$  fibre used in this work can thus be sufficiently well resolved for potential temperature sensor studies. The fitted curves according to the model governed by **Eq. 6.1** are also presented in **Figures 6.12a** and **6.12b** where reasonable agreement with experimental data has been obtained. However, the experimentally determined data contained large errors of 5.8 % and ~12 % for  $FIR_{IR12}$  and  $FIR_{IR13}$  respectively. It should also be noted here that the IR signals emitted from these fibre samples, although stronger than the emission from the end-doped fibres, are still relatively weak compared to the signal intensities from  $\text{Er}^{3+} + \text{Yb}^{3+}$ -codoped fibres to be discussed in the following section. As can be seen from **Figures 6.12**, both ratios are found to decrease with increasing temperature in an almost exponential manner. Large errors are incurred obviously by fitting the model, **Eq. 6.1**, to the experimentally obtained data (**Figures 6.12a** and **6.12b**) but all evidence from the profiles of the curve-fitting procedures of the IR fluorescence intensity ratios also suggests a thermalisation (or also known as thermal population effect) energy transfer process among the various sublevels of the  $^4I_{13/2}$  manifold. This thermal population can occur due to both the weak coupling between the active ions and crystal lattice as well as the small energy gaps separating the sublevels. The fitted

values of  $\Delta E$  and  $C$  are given in **Table 6.5**. In the infrared, the fitted  $\Delta E$  values for both intensity ratios are also very different from and are approximately 11 and 4 times the theoretical values for  $FIR_{IR12}$  and  $FIR_{IR13}$  respectively.

**Table 6.3. Denotation of green and infrared fluorescence intensity ratio (FIR) of singly Er<sup>3+</sup>-doped Al<sub>2</sub>O<sub>3</sub> fibre.**

Denotation (visible)	Intensity ratio (I <sub>λ1</sub> / I <sub>λ2</sub> )	Denotation (infrared)	Intensity ratio (I <sub>λ1</sub> / I <sub>λ2</sub> )
FIR <sub>g12</sub>	I <sub>540nm</sub> / I <sub>541.5nm</sub>	FIR <sub>IR12</sub>	I <sub>1511.5nm</sub> / I <sub>1523nm</sub>
FIR <sub>g13</sub>	I <sub>540nm</sub> / I <sub>552.5nm</sub>	FIR <sub>IR13</sub>	I <sub>1511.5nm</sub> / I <sub>1531.5nm</sub>
FIR <sub>g14</sub>	I <sub>540nm</sub> / I <sub>554.5nm</sub>	FIR <sub>IR14</sub>	I <sub>1511.5nm</sub> / I <sub>1547nm</sub>
FIR <sub>g15</sub>	I <sub>540nm</sub> / I <sub>559nm</sub>	FIR <sub>IR23</sub>	I <sub>1523nm</sub> / I <sub>1531.5nm</sub>
FIR <sub>g23</sub>	I <sub>541.5nm</sub> / I <sub>552.5nm</sub>	FIR <sub>IR24</sub>	I <sub>1523nm</sub> / I <sub>1547nm</sub>
FIR <sub>g24</sub>	I <sub>541.5nm</sub> / I <sub>554.5nm</sub>	FIR <sub>IR34</sub>	I <sub>1531.5nm</sub> / I <sub>1547nm</sub>
FIR <sub>g25</sub>	I <sub>541.5nm</sub> / I <sub>559nm</sub>		
FIR <sub>g34</sub>	I <sub>552.5nm</sub> / I <sub>554.5nm</sub>		
FIR <sub>g35</sub>	I <sub>552.5nm</sub> / I <sub>559nm</sub>		
FIR <sub>g45</sub>	I <sub>554.5nm</sub> / I <sub>559nm</sub>		

**Table 6.4. Fit parameters of visible FIRs using thermal population model, Eq. 6.1 (Er<sup>3+</sup>:Al<sub>2</sub>O<sub>3</sub> fibre)**

Parameters	FIR <sub>g12</sub>		FIR <sub>g15</sub>	
	Theoretical	Fitted	Theoretical	Fitted
C	-	17.28	-	6.27
ΔE / cm <sup>-1</sup>	51.30	151.54	629.43	629.03

**Table 6.5. Fit parameters of infrared FIRs using thermal population model, Eq. 6.1 (Er<sup>3+</sup>:Al<sub>2</sub>O<sub>3</sub> fibre)**

Parameters	FIR <sub>IR12</sub>		FIR <sub>IR13</sub>	
	Theoretical	Fitted	Theoretical	Fitted
C	-	-1.17	-	-1.84
ΔE / cm <sup>-1</sup>	49.96	568.02	86.40	359.94

Figure 6.9a. Green intensity ratios,  $FIR_{g12} - FIR_{g15}$ , as a function of temperature ( $Er^{3+}$ -doped tip  $Al_2O_3$  fibre)

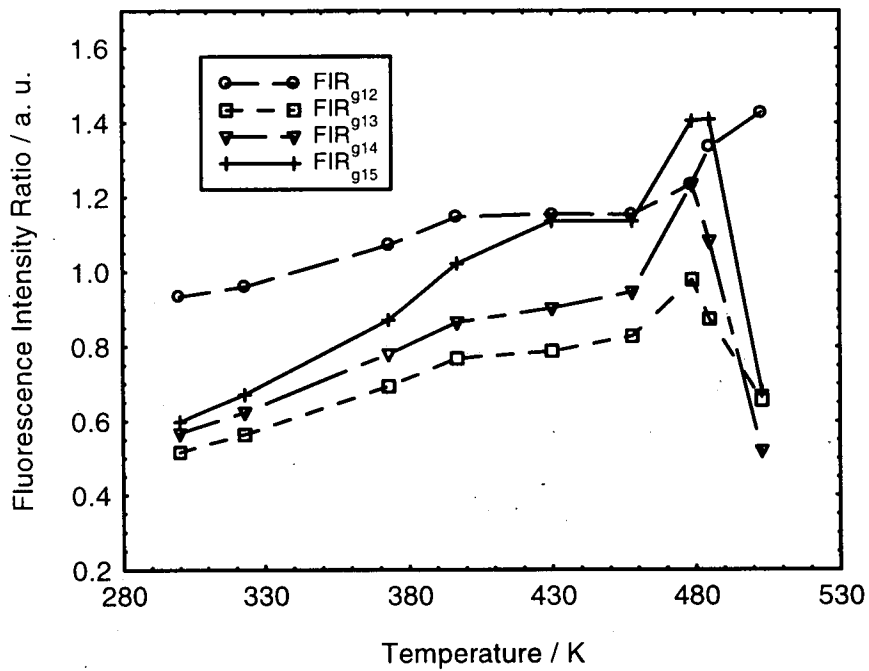


Figure 6.9b. Green intensity ratios,  $FIR_{g23} - FIR_{g25}$ , as a function of temperature ( $Er^{3+}$ -doped tip  $Al_2O_3$  fibre)

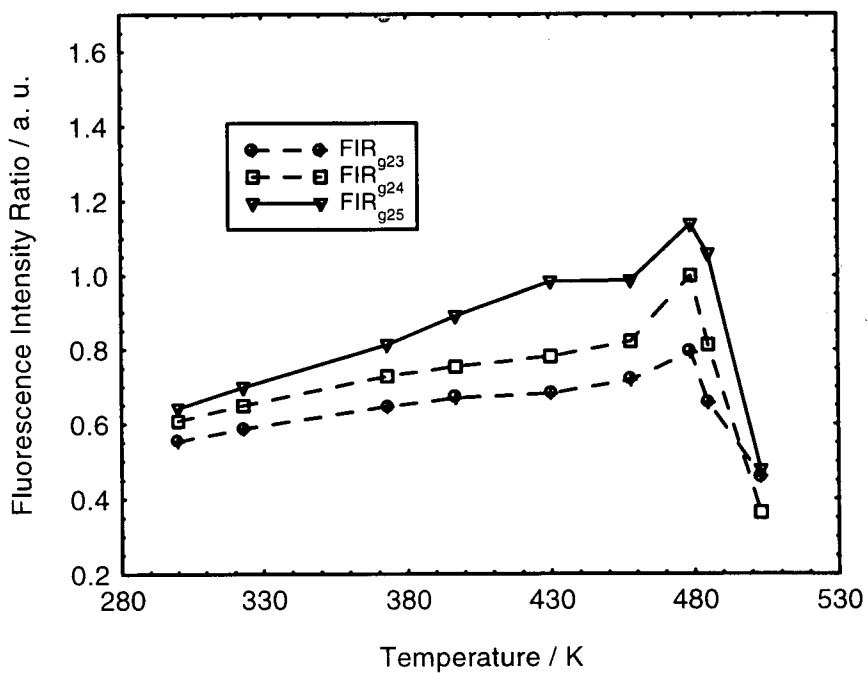


Figure 6.9c. Green intensity ratios,  $\text{FIR}_{g34} - \text{FIR}_{g45}$ , as a function of temperature ( $\text{Er}^{3+}$ -doped tip  $\text{Al}_2\text{O}_3$  fibre)

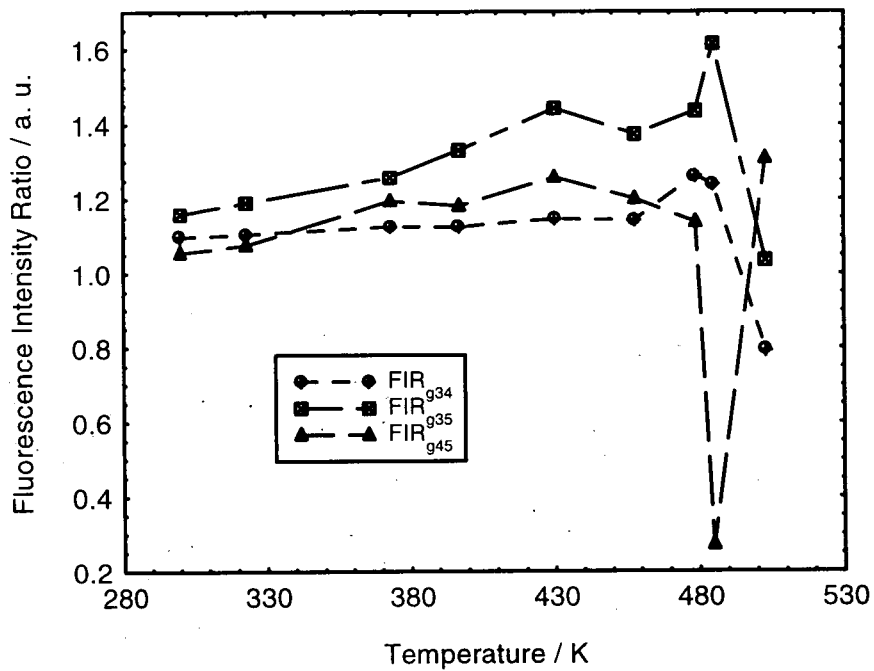


Figure 6.10a. Modeling of green  $\text{FIR}_{g12}$  ( $I_{540\text{nm}}/I_{541.5\text{nm}}$ ) using Eq. 6.1 ( $\text{Er}^{3+}$ -doped tip  $\text{Al}_2\text{O}_3$  fibre)

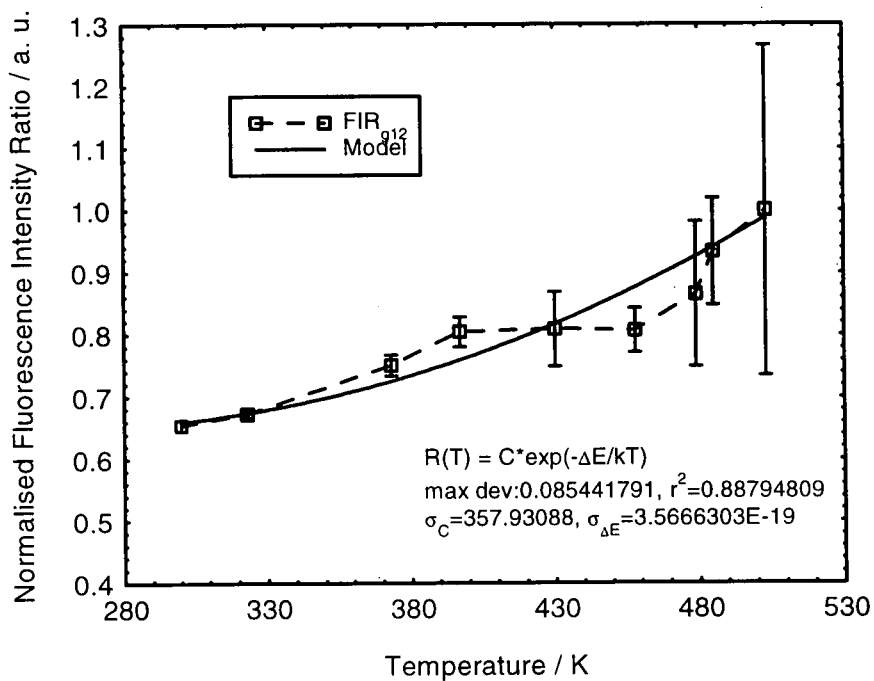


Figure 6.10b. Modeling of green FIR<sub>g15</sub> ( $I_{540\text{nm}}/I_{559\text{nm}}$ ) using Eq. 6.1 ( $\text{Er}^{3+}$ -doped tip  $\text{Al}_2\text{O}_3$  fibre)

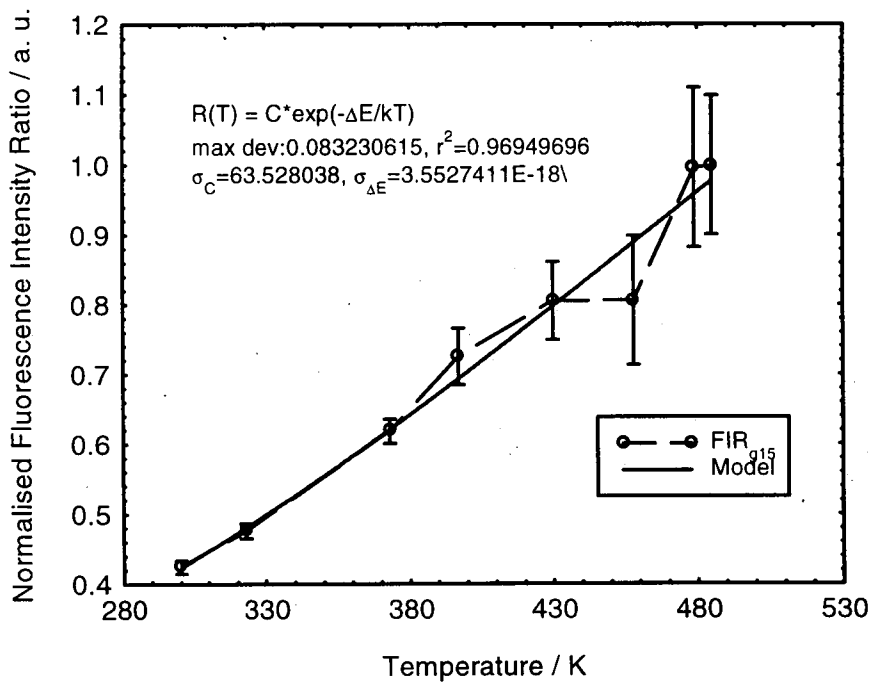


Figure 6.11a. Infrared FIR<sub>IR12</sub> - FIR<sub>IR14</sub> as a function of temperature ( $\text{Er}^{3+}:\text{Al}_2\text{O}_3$  fibre)

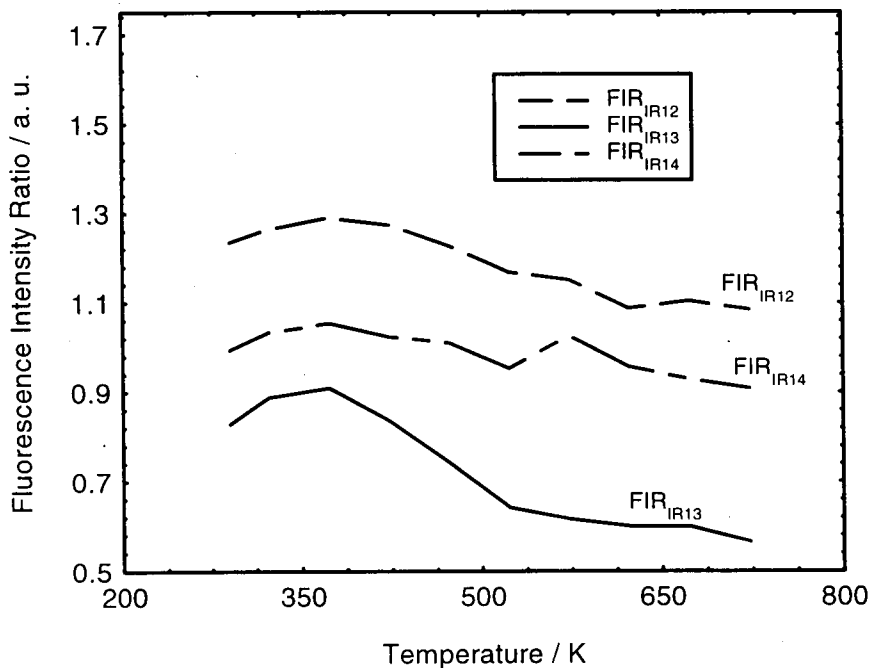


Figure 6.11b. Infrared  $FIR_{IR23} - FIR_{IR34}$  as a function of temperature ( $Er^{3+}:Al_2O_3$  fibre)

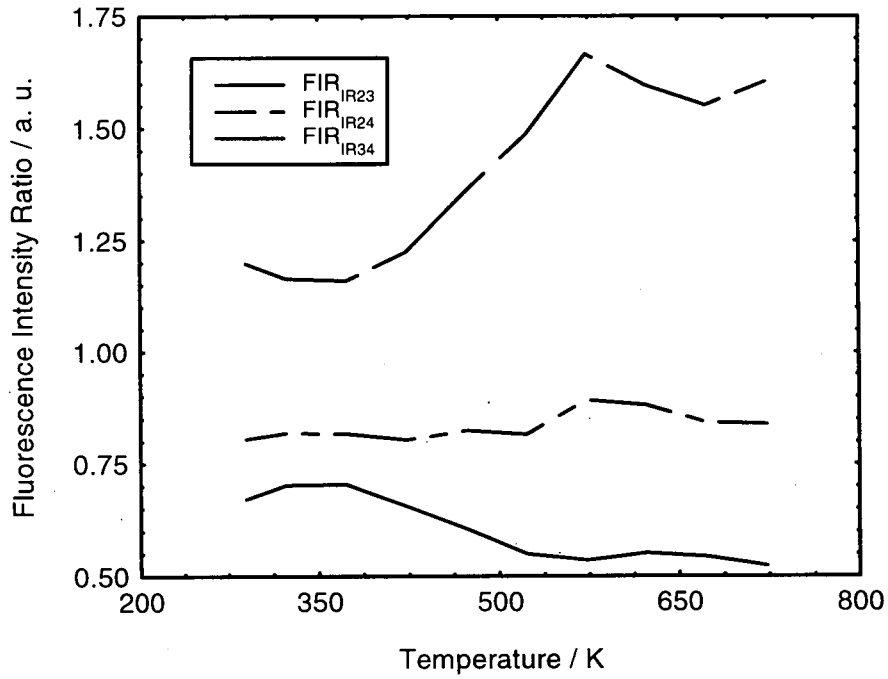


Figure 6.12a. Modelling of infrared  $FIR_{IR12}$  ( $I_{1511.5nm}/I_{1523nm}$ ) using Eq. 6.1 ( $Er^{3+}:Al_2O_3$  fibre)

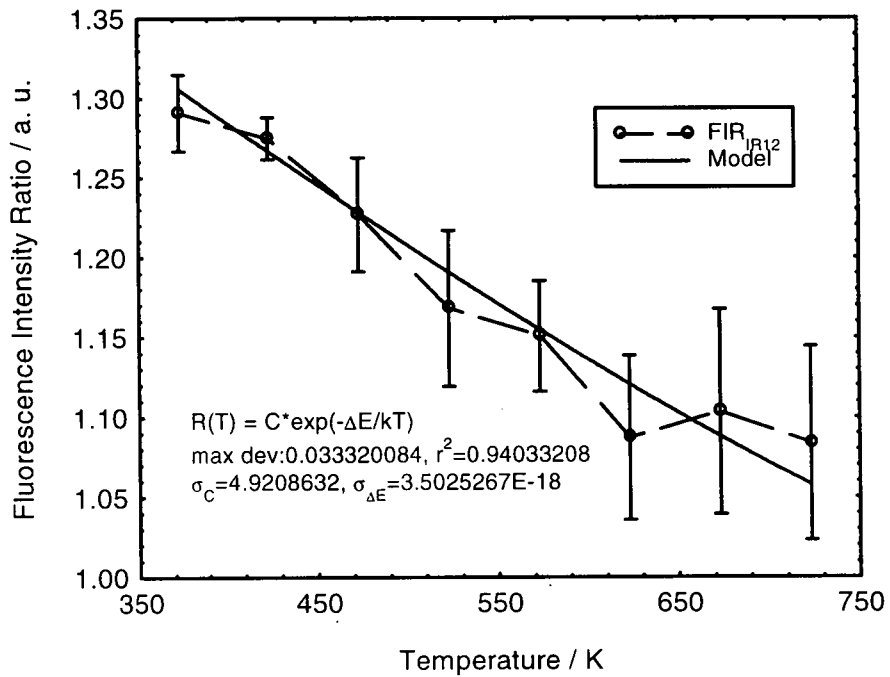


Figure 6.12b. Modeling of infrared FIR<sub>IR13</sub> ( $I_{1511.5\text{nm}}/I_{1547\text{nm}}$ ) using Eq. 6.1 ( $\text{Er}^{3+}\text{Al}_2\text{O}_3$  fibre)

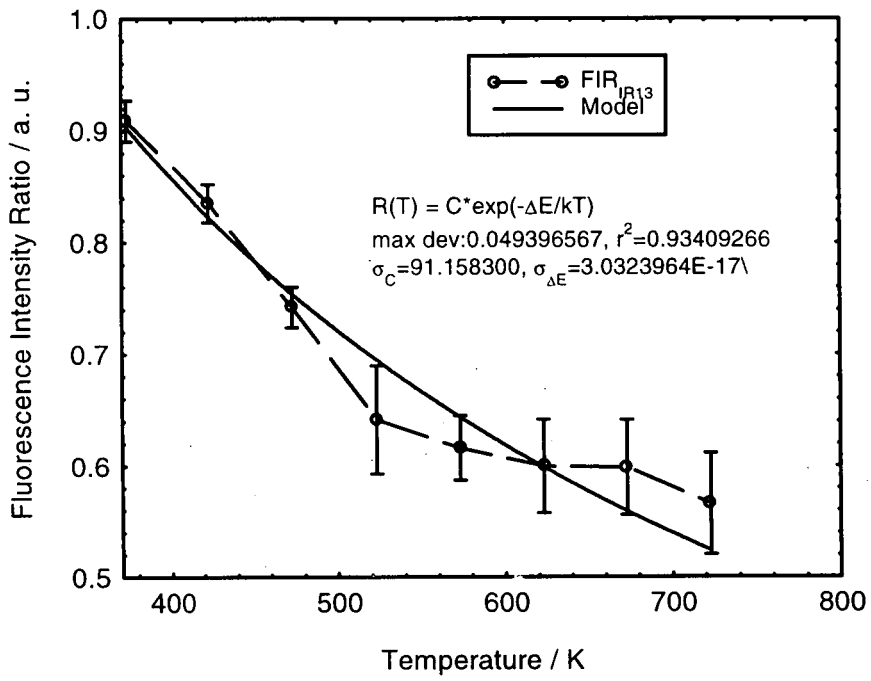
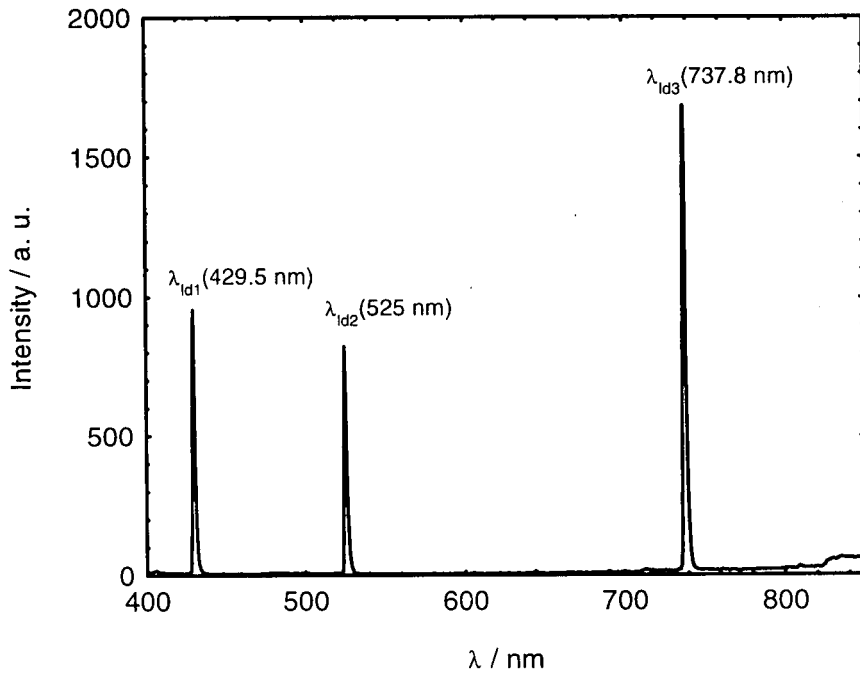


Figure 6.13. Additional visible lines of laser diode at 960 nm



### 6.2.2 Temperature sensing with equally $\text{Er}^{3+}$ + $\text{Yb}^{3+}$ -codoped $\text{Al}_2\text{O}_3$ fibres

Codoping with  $\text{Yb}^{3+}$  sensitizer ions provides a broad absorption band in the region of 800 – 1000 nm for excitation of the  $\text{Er}^{3+}$  ions, relaxing the need for accurate matching of pump wavelength [6.22]. This ultimately results in a stronger fluorescence intensity from the  $\text{Er}^{3+}$  as has been observed, while the high dopant concentration incorporated into the  $\text{Al}_2\text{O}_3$  host ensured that most of the pump photons went into upconversion excitation of the  $^4\text{F}_{9/2}$  and  $^4\text{S}_{3/2}$  populations. Upconversion from these levels to the ground state then led to emission in the red and green spectral regions. At elevated temperatures, where there is an abundance in the supply of thermal energy, rapid non-radiative multi-phonon decay will thus occur, resulting in a temperature-dependence of the narrow emitted lines from these spectral regions. The ratio of the intensities from both the green and red fluorescence can therefore be expected to be dependent on temperature and exploited in fibre optic thermometry. IR emission in the 1530 nm region was found to be relatively weak in these fibres and has not been investigated since most of the pump energy was channelled into excitation of the higher lying energy manifolds from which the intense visible emission was detected.

Due to the strong upconversion intensities in the green and red, it has been possible to perform temperature-dependence investigations in both bands using three different techniques. The green and red upconverted emissions both resulted in five distinct, sharp lines and the fluorescence intensity ratios (FIRs) of these lines have been monitored up to ~1220 K for the green (538 – 550 nm) and for the red (649 - 670 nm). Opening the monochromator slits to allow a relatively broad bandpass, the intensities of both the green and red upconversion have also been monitored up to ~1320 K and ~1420 K for the green and red respectively. In addition, lifetime decays of both green and red bands as a function of temperature have also been pursued, albeit to a lower temperature range of ~1000 K.

### 6.2.2.1 Temperature dependence of green and red upconversion FIRs

Green and red upconversions have been measured in  $\text{Er}^{3+} + \text{Yb}^{3+}$ -codoped  $\text{Al}_2\text{O}_3$  fibres and emission from these regions was observed to exhibit narrow-linewidth structures from within the same manifold in the respective spectral regions. In the green, sublevels within the  $^4\text{S}_{3/2}$  level have resulted in several sharp lines at 538.5, 541, 542.5, 547.5 and 550 nm. In the red upconversion, the lines have been observed at 649.5, 654, 657.5, 664 and 670 nm, and have been considered to originate from the  $^4\text{F}_{9/2}$  state where Stark-splitting has resulted in several sublevels within that manifold [6.22, 6.33]. The five green lines have been plotted in **Figure 6.14** while **Figure 6.15** shows the well-resolved structures from the red upconversion. The effect of thermal population of the various sublevels has also been assumed to dominate the fluorescence intensity ratios between these sharp-line emissions. Previous reports employing  $\text{Er}^{3+} + \text{Yb}^{3+}$ -codoped systems have involved multi-component glasses [6.70, 6.81] and silica [6.69] as host materials, thereby restricting the maximum temperature which can be probed to well below 1000 K. In this work, the high melting point of the crystalline  $\text{Al}_2\text{O}_3$  host fibres has been exploited to attempt temperature measurements up to 1200 K and investigate the suitability of these RE-doped sapphire fibres for high temperature sensing applications.

Figure 6.14. Narrow-line structures of green upconversion emission ( $\text{Er}^{3+}:\text{Yb}^{3+}:\text{Al}_2\text{O}_3$  fibre)

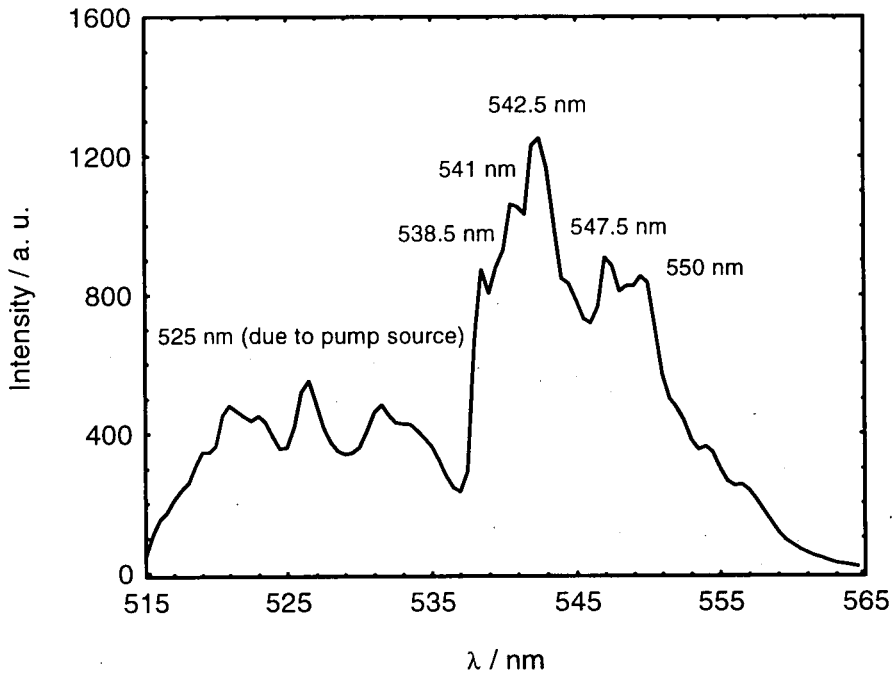
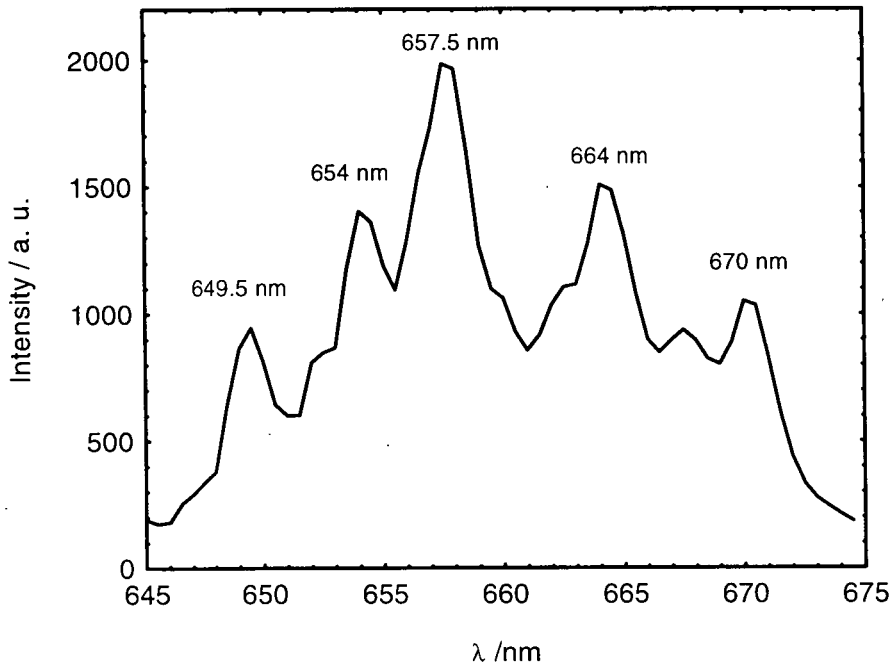


Figure 6.15. Narrow-line structures of red upconversion ( $\text{Er}^{3+}:\text{Yb}^{3+}:\text{Al}_2\text{O}_3$  fibre)



### 6.2.2.2 Experiments on green and red FIRs

Compared to singly  $\text{Er}^{3+}$ -doped  $\text{Al}_2\text{O}_3$  fibres which have been used in earlier experiments, the incorporation of sensitising  $\text{Yb}^{3+}$  ions has resulted in strong upconversion signals both in the green and red, enabling one of the codoped fibres to be employed in a reflective mode for the following temperature studies. **Figure 6.16** shows a schematic of the experimental set-up used in the FIR measurements.

$\text{Er}^{3+}:\text{Yb}^{3+}:\text{Al}_2\text{O}_3$  fibres were doped at one section of  $\sim 20$  mm with the active RE ions of approximately equal concentrations. The pump wavelength used was obtained from a 960 nm *LACRYS* laser diode array which was focused to a point and collimated via a set of condensing and collimating lenses to enable more efficient pulse modulation with an opto-mechanical chopper for lock-in detection. The collimated light was then directed into the aperture of a microscope objective (X20 MO) which focused it onto the end of the fibre. Upconversion from the far doped end of these fibres was collected via the same MO and guided into the monochromator by a thin beam splitter. The length of the fibres employed was approximately 90 mm with fibres inserted into the heating chamber of a *CARBOLITE* (model *MTF 12/25/250*) tube furnace in such a way that the whole of the doped sections were completely inside the furnace. Only a short length of the pure sapphire section, long enough to be secured to a three-axis translation stage, was protruding. High temperature ceramic wool was introduced at both ends of the tube furnace to prevent excess heat loss and maintain a stable thermal environment. A *Hamamatsu R928* photomultiplier tube (PMT) was used to detect the upconversion signals dispersed through the monochromator, in conjunction with sensitive and stable lock-in techniques. A chopper positioned at the focused spot just after the condensing lens provided a means of pulse-modulating the pump source. Data acquisition was carried out by a dedicated computer which also, via a Labview programme, controlled the monochromator via an *RS232* link and synchronisation of the signal detection process. Data were then saved for subsequent processing and analysis.

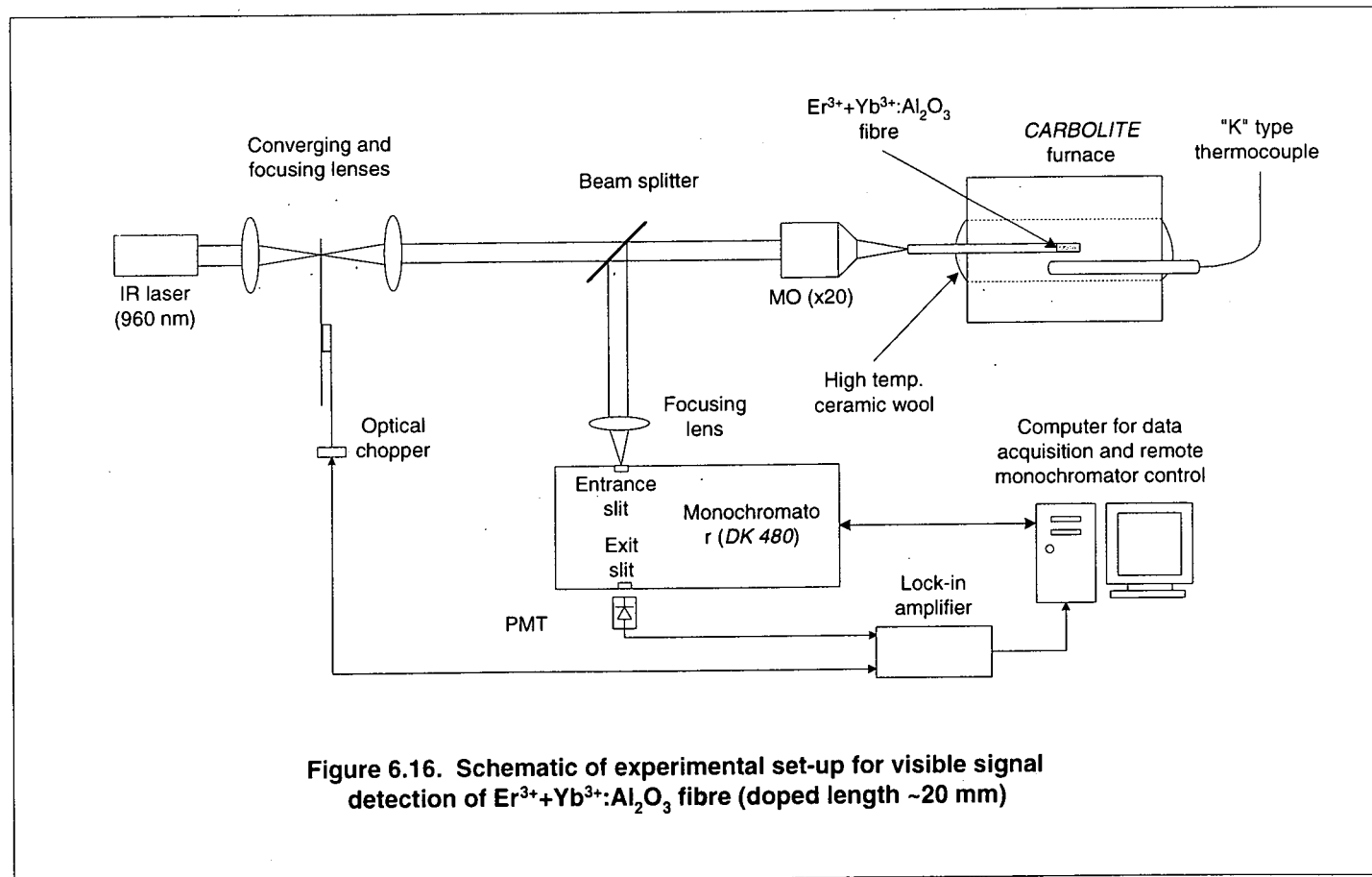


Figure 6.16. Schematic of experimental set-up for visible signal detection of  $\text{Er}^{3+}+\text{Yb}^{3+}:\text{Al}_2\text{O}_3$  fibre (doped length ~20 mm)

### 6.2.2.3 Results and Discussion

Both the FIRs of the green and red upconversion lines have been monitored up to ~1220 K, beyond which the respective signals were found to be very weak. **Table 6.6** indicates how the fluorescence intensity ratios of the 538 – 550 nm (green) and 649 – 670 nm (red) upconversion lines have been arrived at. Similar to the ratiometric technique used for  $\text{Er}^{3+}:\text{Al}_2\text{O}_3$  fibres earlier,  $\text{FIR}_{g12}$  is the intensity ratio of the 538.5 to 541 nm lines while  $\text{FIR}_{g45}$  is the ratio of the 547.5 to 550 nm intensities, and so on. For the red emission, the subscript “r” is used to describe the intensity ratio of the five lines, other nomenclature remaining unchanged, i. e.  $\text{FIR}_{r12}$  represents the 649.5 nm to 654 nm intensity ratio, etc.

The five lines which have been employed from both emissions give rise to an array of 10 fluorescence intensity ratios in each of the respective spectra, resulting in  $\text{FIR}_{g12}$  to  $\text{FIR}_{g45}$  for the green upconversion and from  $\text{FIR}_{r12}$  to  $\text{FIR}_{r45}$  in the red upconversion. The 10 FIRs of the green and red upconversion are plotted in **Figures 6.17a** ( $\text{FIR}_{g12} - \text{FIR}_{g15}$ ), **6.17b** ( $\text{FIR}_{g23} - \text{FIR}_{g25}$ ) and **6.17c** ( $\text{FIR}_{g34} - \text{FIR}_{g45}$ ), and **Figures 6.18a** ( $\text{FIR}_{r12} - \text{FIR}_{r15}$ ), **6.18b** ( $\text{FIR}_{r23} - \text{FIR}_{r25}$ ) and **6.18c** ( $\text{FIR}_{r34} - \text{FIR}_{r45}$ ) respectively, as a function of temperature, with a majority of the ratios exhibiting an increase with increasing temperature. Of these, two from each spectrum ( $\text{FIR}_{g25}$  and  $\text{FIR}_{g35}$  from the green upconversion,  $\text{FIR}_{r25}$  and  $\text{FIR}_{r35}$  from the red) have been selected for potential temperature sensing due to the wider dynamic range available as compared to the rest of the FIRs over similar temperature ranges. It is also expected that the selected lines can offer a larger change in their temperature-dependent ratios, as evident from the steeper slopes shown in **Figures 6.17** and **6.18**. Attempts have been made to determine the origin of temperature dependence of the intensity ratios from the sublevels within the same manifold described by the thermal population model given in **Eq. 6.1**. These are shown in **Figure 6.19a** for  $\text{FIR}_{g25}$  and  $\text{FIR}_{g35}$  of the green emission ( $^4\text{S}_{3/2}$  or  $^2\text{H}_{11/2} \rightarrow ^4\text{I}_{15/2}$  transition) and in **Figure 6.19b** for the red intensity ratios,  $\text{FIR}_{r25}$  and  $\text{FIR}_{r35}$ , due to the  $^4\text{F}_{9/2} \rightarrow ^4\text{I}_{15/2}$  transition. The fitted parameters are listed in **Table 6.7** for the green ( $\text{FIR}_{g25}$  and  $\text{FIR}_{g35}$ ) and in **Table 6.8** for the two red FIRs.

It can be seen that the majority of the FIRs measured have shown an increase in ratio with an increase in temperature, consistent with thermal population of the higher levels from below, while only a handful of the intensity ratios were found to decrease with increasing temperature. Moreover, FIRs which decrease with temperature can be seen to exhibit relatively small changes compared to those exhibiting an apparent increase in ratio values with increasing temperature. This would suggest relatively poor phonon coupling between these levels. In effect, due to the stronger fluorescence signals detected from the highly codoped fibre, it has been possible to monitor a wider temperature range (from room temperature up to  $\sim 1223$  K) than was practical with previous results based on singly  $\text{Er}^{3+}$ -doped sapphire fibres. From the green upconversion emission,  $FIR_{g25}$  and  $FIR_{35}$  are shown (**Figures 6.17b** and **6.17c**) to exhibit larger temperature dependences than the other FIRs over the same temperature range and are thus investigated further for their suitability in temperature sensing. Similarly, the two most prominent red FIRs selected for further temperature dependence studies are  $FIR_{r25}$  and  $FIR_{r35}$ . The uncertainty obtained from the measured intensity ratio data has been found to be relatively large, particularly at very high temperatures, with the maximum being  $\sim 48$  % for  $FIR_{g25}$  and  $FIR_{g35}$  at 1223 K. On the other hand, the maximum errors for the red FIRs have been found to be 7 % or less throughout the entire temperature range (291 – 1223 K). This is likely to be due to the much stronger signal in the red compared to the green upconversion.

Further attempts to better describe this thermalisation (or thermal population) effect on particular sublevels within the same transition manifold or between the levels of different manifolds have been based on the model expressed by **Eq. 6.1**. The fitted curves can be seen in **Figure 6.19a** for the green ratios and in **Figure 6.19b** for the red FIRs, with the usual fit parameters listed in **Tables 6.7** and **6.8** respectively. From the curve fitting procedure, it can be noticed that despite there not being an exact fit for all FIRs, the general exponential profile has been exhibited by all lines concerned. In particular, the fitted value of the energy gap for the green upconversion ratio between the 541 nm and 550 nm lines, and between the 542.5 nm and 550 nm lines are radically different from that of  $\sim 700$   $\text{cm}^{-1}$  already published [6.70]. Although a different material has been used as the host in that work (chalcogenide glass), this suggests that other factors such as second or even third

order excitation within the same manifold/level may have been the cause of this discrepancy.

**Table 6.6. Denotation of green and red fluorescence intensity ratio (FIR) of  $\text{Er}^{3+}:\text{Yb}^{3+}$ -codoped  $\text{Al}_2\text{O}_3$  fibre.**

Denotation (visible)	Intensity ratio ( $I_{\lambda_1} / I_{\lambda_2}$ )	Denotation (infrared)	Intensity ratio ( $I_{\lambda_1} / I_{\lambda_2}$ )
FIR <sub>g12</sub>	$I_{538.5\text{nm}} / I_{541\text{nm}}$	FIR <sub>r12</sub>	$I_{649.5\text{nm}} / I_{654\text{nm}}$
FIR <sub>g13</sub>	$I_{538.5\text{nm}} / I_{542.5\text{nm}}$	FIR <sub>r13</sub>	$I_{649.5\text{nm}} / I_{657.5\text{nm}}$
FIR <sub>g14</sub>	$I_{538.5\text{nm}} / I_{547.5\text{nm}}$	FIR <sub>r14</sub>	$I_{649.5\text{nm}} / I_{664\text{nm}}$
FIR <sub>g15</sub>	$I_{538.5\text{nm}} / I_{550\text{nm}}$	FIR <sub>r15</sub>	$I_{649.5\text{nm}} / I_{670\text{nm}}$
FIR <sub>g23</sub>	$I_{541\text{nm}} / I_{542.55\text{nm}}$	FIR <sub>r23</sub>	$I_{654\text{nm}} / I_{657.5\text{nm}}$
FIR <sub>g24</sub>	$I_{541\text{nm}} / I_{547.5\text{nm}}$	FIR <sub>r24</sub>	$I_{654\text{nm}} / I_{664\text{nm}}$
FIR <sub>g25</sub>	$I_{541\text{nm}} / I_{550\text{nm}}$	FIR <sub>r25</sub>	$I_{654\text{nm}} / I_{670\text{nm}}$
FIR <sub>g34</sub>	$I_{542.5\text{nm}} / I_{547.5\text{nm}}$	FIR <sub>r34</sub>	$I_{657.5\text{nm}} / I_{664\text{nm}}$
FIR <sub>g35</sub>	$I_{542.5\text{nm}} / I_{550\text{nm}}$	FIR <sub>r35</sub>	$I_{657.5\text{nm}} / I_{670\text{nm}}$
FIR <sub>g45</sub>	$I_{547.5\text{nm}} / I_{550\text{nm}}$	FIR <sub>r45</sub>	$I_{664\text{nm}} / I_{670\text{nm}}$

Figure 6.17a. FIRs ( $\text{FIR}_{g_{12}} - \text{FIR}_{g_{15}}$ ) of green upconversion as a function of temperature ( $\text{Er}^{3+}:\text{Yb}^{3+}:\text{Al}_2\text{O}_3$  fibre)

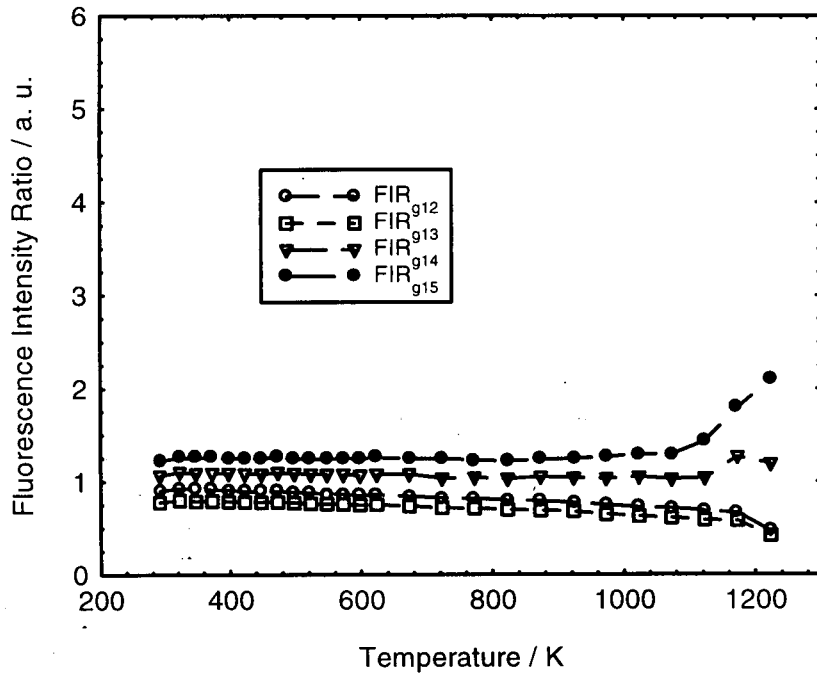


Figure 6.17b. FIRs ( $\text{FIR}_{g_{23}} - \text{FIR}_{g_{25}}$ ) of green upconversion as a function of temperature ( $\text{Er}^{3+}:\text{Yb}^{3+}:\text{Al}_2\text{O}_3$  fibre)

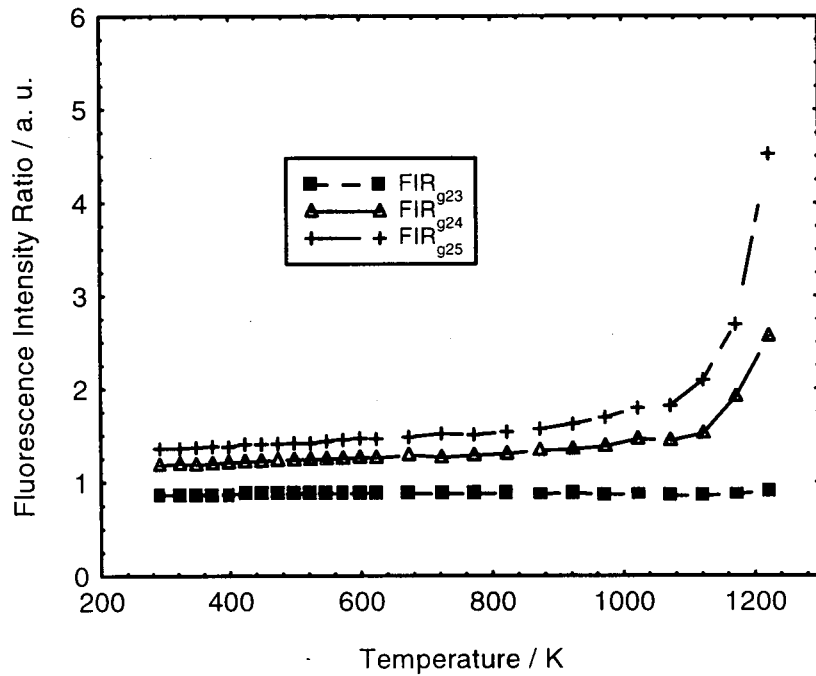


Figure 6.17c. FIRs ( $\text{FIR}_{g34} - \text{FIR}_{g45}$ ) of green upconversion as a function of temperature ( $\text{Er}^{3+}:\text{Yb}^{3+}:\text{Al}_2\text{O}_3$  fibre)

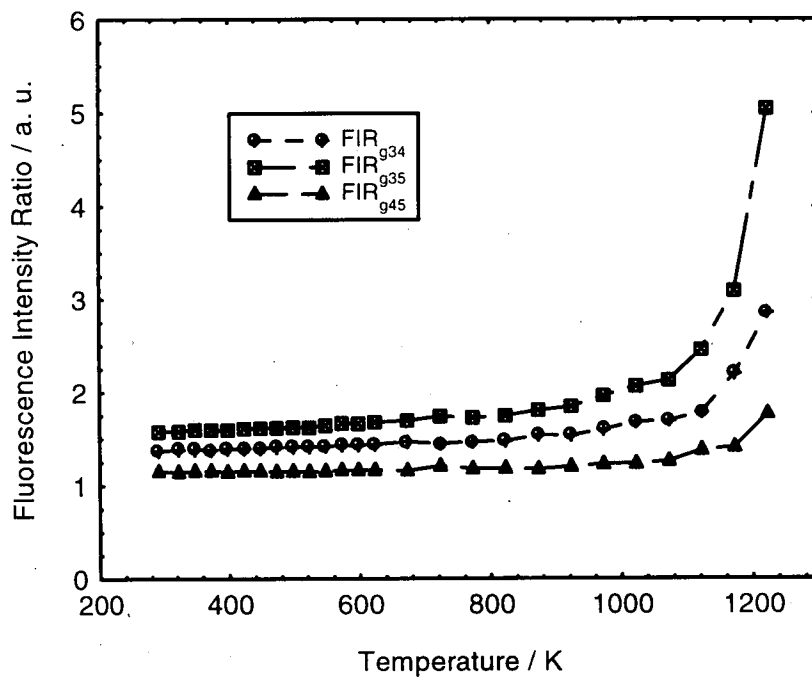


Figure 6.18a. FIRs ( $\text{FIR}_{r12} - \text{FIR}_{r15}$ ) of red upconversion as a function of temperature ( $\text{Er}^{3+}:\text{Yb}^{3+}:\text{Al}_2\text{O}_3$  fibre)

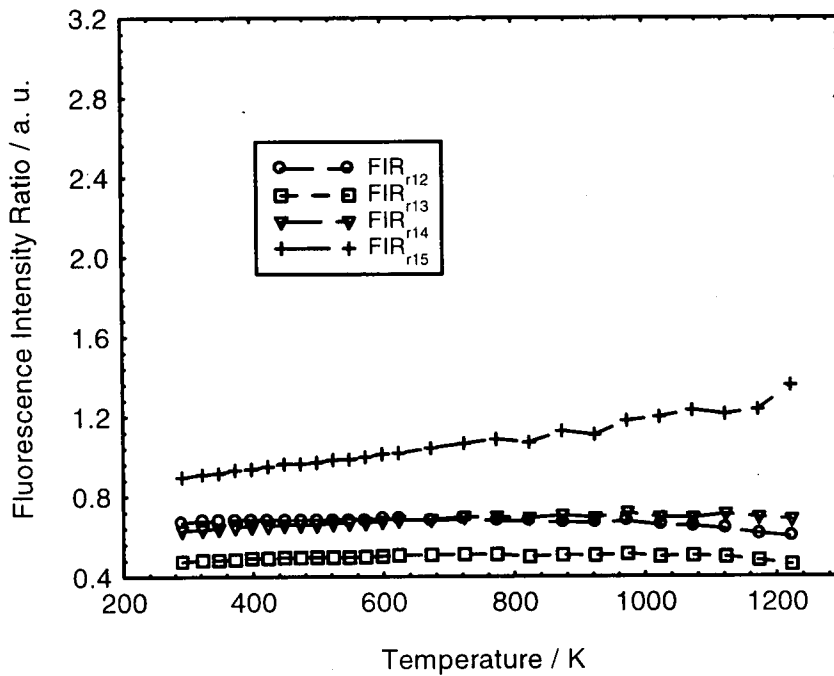


Figure 6.18b. FIRs ( $\text{FIR}_{r23} - \text{FIR}_{r25}$ ) of red upconversion as a function of temperature ( $\text{Er}^{3+}:\text{Yb}^{3+}:\text{Al}_2\text{O}_3$  fibre)

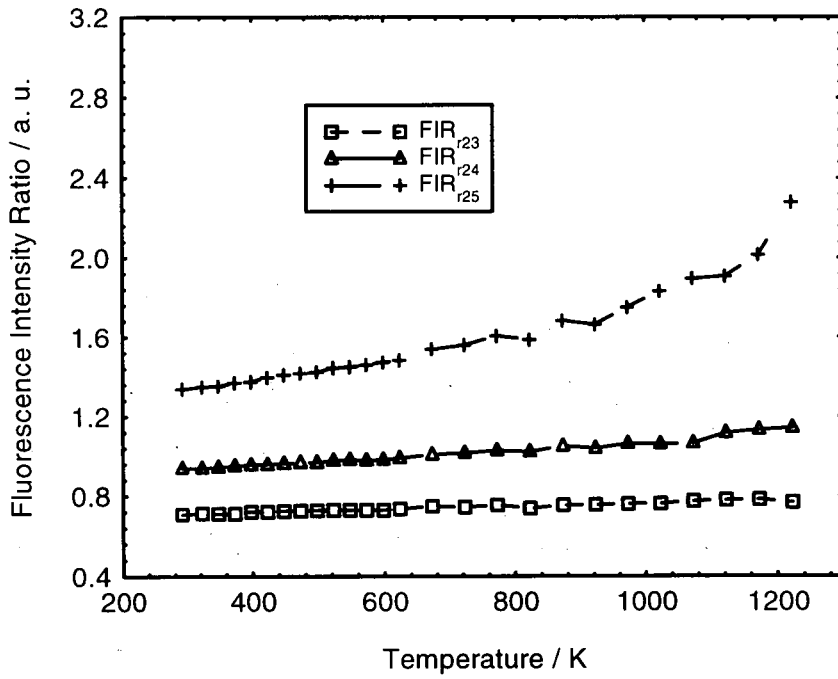


Figure 6.18c. FIRs ( $\text{FIR}_{r34} - \text{FIR}_{r45}$ ) of red upconversion as a function of temperature ( $\text{Er}^{3+}:\text{Yb}^{3+}:\text{Al}_2\text{O}_3$  fibre)

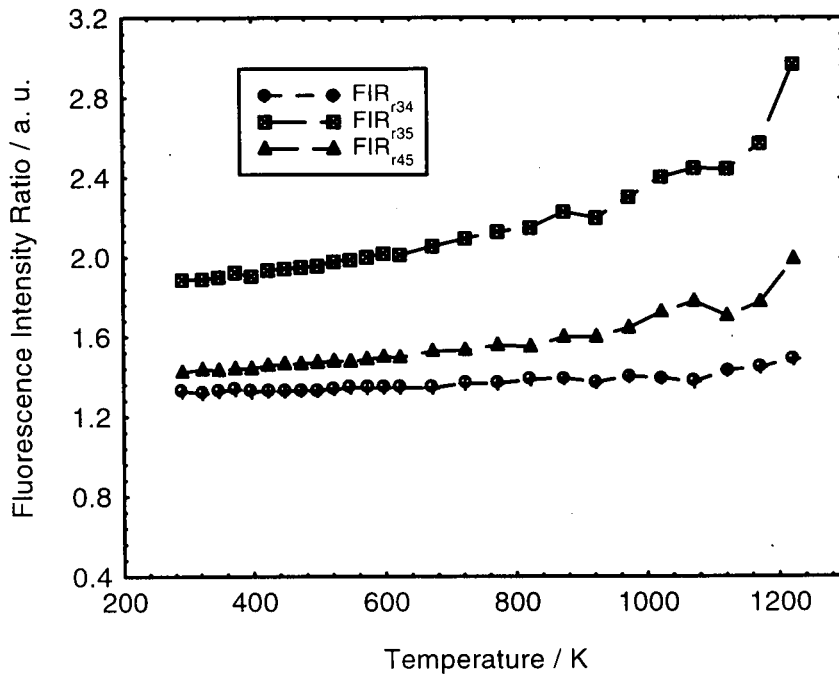


Figure 6.19a. Thermal model of green FIR<sub>g25</sub> ( $I_{541\text{nm}}/I_{550\text{nm}}$ ) and FIR<sub>g35</sub> ( $I_{542.5\text{nm}}/I_{550\text{nm}}$ ) based on Eq. 6.1 ( $\text{Er}^{3+}:\text{Yb}^{3+}:\text{Al}_2\text{O}_3$  fibre)

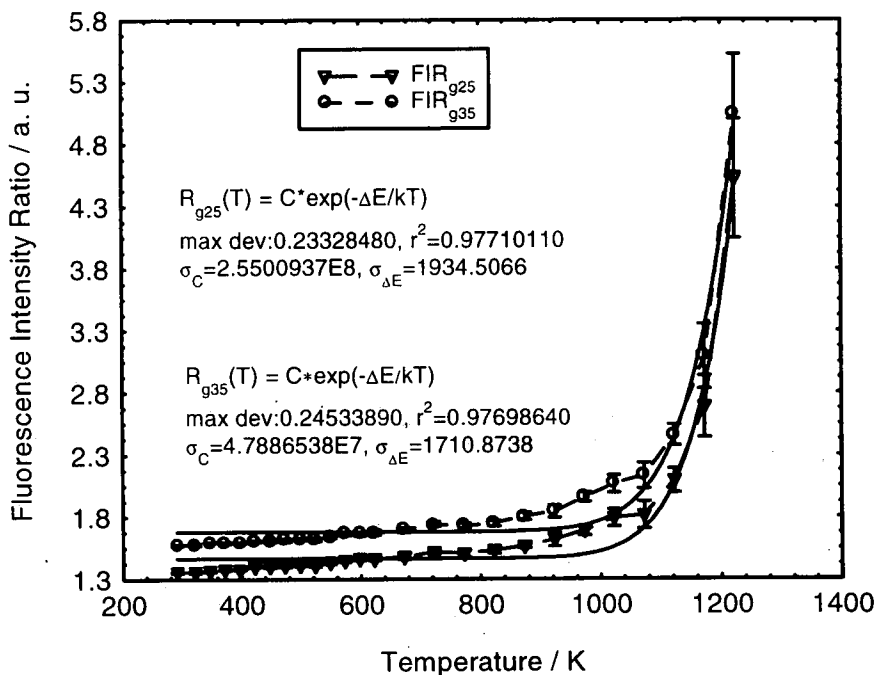
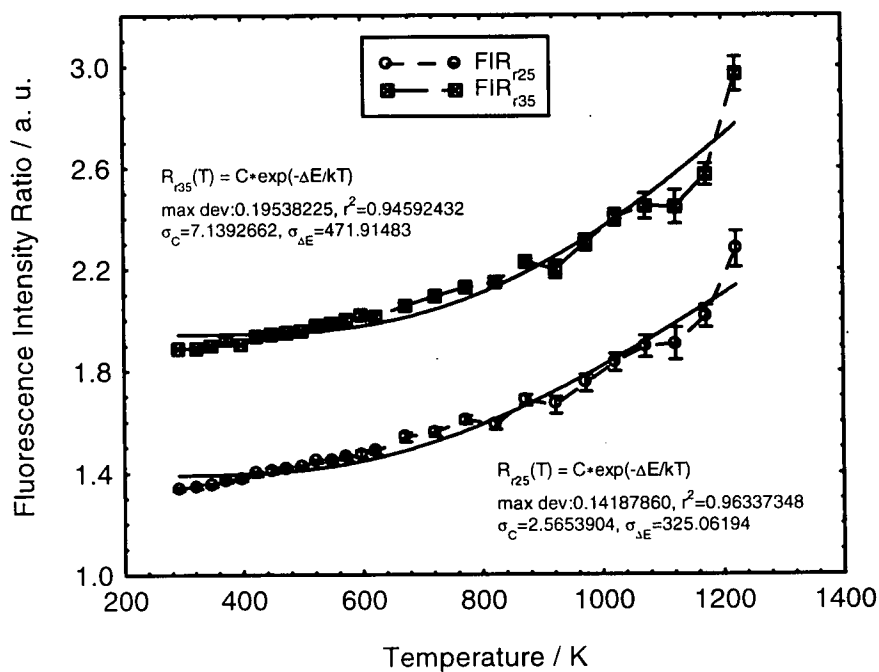


Figure 6.19b. Thermal model of red FIR<sub>r25</sub> ( $I_{654\text{nm}}/I_{670\text{nm}}$ ) and FIR<sub>r35</sub> ( $I_{657.5\text{nm}}/I_{670\text{nm}}$ ) based on Eq. 6.1 ( $\text{Er}^{3+}:\text{Yb}^{3+}:\text{Al}_2\text{O}_3$  fibre)



**Table 6.7. Fit parameters of green FIRs using thermal population model, Eq. 6.1 (Er<sup>3+</sup>:Yb<sup>3+</sup>-codoped Al<sub>2</sub>O<sub>3</sub> fibre)**

Parameters	FIR <sub>g25</sub>		FIR <sub>g35</sub>	
	Theoretical	Fitted	Theoretical	Fitted
<i>C</i>	-	1.47	-	1.68
$\Delta E / \text{cm}^{-1}$	302.47	15172.25	25.14	13772.73

**Table 6.8. Fit parameters of red FIRs using thermal population model, Eq. 6.1 (Er<sup>3+</sup>:Yb<sup>3+</sup>-codoped Al<sub>2</sub>O<sub>3</sub> fibre)**

Parameters	FIR <sub>r25</sub>		FIR <sub>r35</sub>	
	Theoretical	Fitted	Theoretical	Fitted
<i>C</i>	-	1.39	-	1.94
$\Delta E / \text{cm}^{-1}$	365.15	2132.61	283.75	2593.94

#### 6.2.2.4 Temperature sensing based on upconversion intensity of equally codoped $\text{Er}^{3+} + \text{Yb}^{3+}:\text{Al}_2\text{O}_3$ fibres

The simplicity of intensity-based fibre optic sensors is one of the main reasons for their commercial success although one main drawback of such a sensor has been the need to monitor and eliminate any variations in the source power. The strong upconversion emission from the green and red spectral regions of the codoped fibre has been exploited as a potential intensity-based temperature sensor. One of the easiest ways to correct for any power fluctuation, and hence upconversion intensity fluctuation, is to monitor both the emission intensities and the pump laser intensity simultaneously, the ratio of which can then be used to correlate to the variation in temperature. An additional photodetector was thus required for the monitoring of the laser power. However, the availability of fast and stable photodetectors at relatively low cost in the visible spectrum can allow this task to be simplified both in practical and economic terms.

Both the green and red upconversions have been investigated, where emission intensity from the excited level  $^4\text{S}_{3/2}$  (or  $^2\text{H}_{11/2}$ ) to the ground state  $^4\text{I}_{15/2}$ , resulting in a bright green fluorescence, and the  $^4\text{F}_{9/2} \rightarrow ^4\text{I}_{15/2}$  transition, resulting in red fluorescence, have been monitored simultaneously as a function of temperature up to 1323 K and 1423 K respectively. It has also been assumed that the green and red upconversion intensities exhibit an exponentially decaying behaviour with increase in temperature according to the following expression

$$I(T) = I_i \exp(-\Delta E / kT) \quad (6.2)$$

where  $I(T)$  is the intensity of the green or red upconversion at temperature  $T$ ,  $I_i$  the original intensity at an initial temperature,  $\Delta E$  is the energy gap between the respective upconversion and ground energy levels,  $k$  the Boltzmann's constant and  $T$  the temperature measured. This is similar to **Eq. 6.1** although the integrated intensity over a passband of  $\sim 3$  nm from the excited level to the ground state is measured instead. The model is thus a reasonable assumption as shown later by the close fit of this equation to the experimentally obtained data.

### 6.2.2.5 Experiment on intensity-based temperature sensor

The upconversion intensities due to the  ${}^4S_{3/2}$  (or  ${}^2H_{11/2}$ )  $\rightarrow$   ${}^4I_{15/2}$  (green) and  ${}^4F_{9/2} \rightarrow$   ${}^4I_{15/2}$  (red) transitions have been measured and normalised to the laser power over a relatively wide temperature range (294  $\rightarrow$  1323 and 1423 K, in the green and red respectively). With the aid of the monochromator, the same spectral bandwidths for both upconversion intensities can be employed by adjustment of the slit widths which act as a narrowband optical filter.

**Figure 6.20** shows a schematic of the experimental set-up of the intensity measurement method. A laser diode array with an emission wavelength in the region of 960 nm has been used as the appropriate excitation source for the  $\text{Er}^{3+} + \text{Yb}^{3+}:\text{Al}_2\text{O}_3$  fibre. The beam was first focused to a point before diverging again onto another lens to be collimated and directed into a microscope objective (X20 MO). The MO has been used to focus the 960 nm radiation into the end of the fibres. The far end of the fibres consisting of a doped section  $\sim 20$  mm long, was positioned as deeply as possible into the heating chamber of a stabilised tube furnace. The backscattered or reflected upconversion signal generated from the doped fibre, via the MO, was reflected by a beam splitter onto a 50 mm focusing lens which then focused the upconversion and pump signals onto the slits of the monochromator. The beam splitter also diverted a fraction of the pump power onto a photodetector to enable the pump intensity to be measured. To enable a reasonably large amount of both the green and red upconversion intensities to be detected, the wavelengths of the peak intensities of each spectrum were determined (542 nm for the green and 657.5 nm for the red). The widths of the entrance and exit slits of the monochromator were then widened to  $\sim 2000$   $\mu\text{m}$  to set a bandpass of  $\sim 3$  nm for both emissions.

A PMT was used to detect the green and red intensities in conjunction with a lock-in amplifier, the pump signal was mechanically modulated by a chopper, so that a highly stable yet sensitive output voltage signal could be achieved. Once the intensity reading at room temperature has been obtained, the temperature of the oven was varied from 323 K up to a maximum of 1323 K for the green upconversion. The

maximum temperature investigated using the red upconversion intensity was ~1423 K. For both emissions, very strong output signals could be measured up to relatively high temperatures. Towards the maximum temperature for the respective monitored spectrum, noise became noticeably more severe. The pump intensity was also monitored and found to be stable throughout the entire experiment.

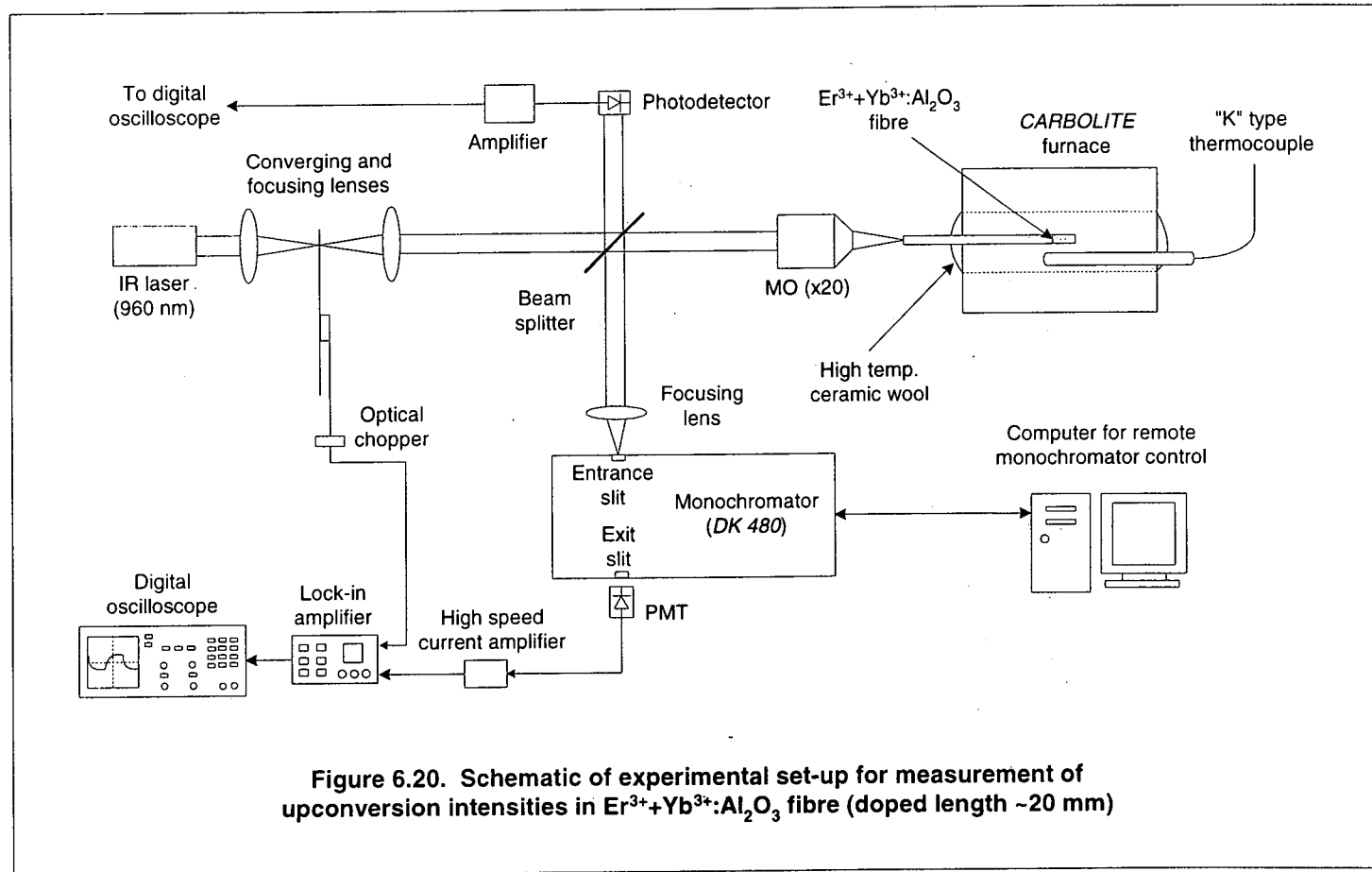


Figure 6.20. Schematic of experimental set-up for measurement of upconversion intensities in  $\text{Er}^{3+}+\text{Yb}^{3+}:\text{Al}_2\text{O}_3$  fibre (doped length ~20 mm)

### 6.2.2.6 Results and Discussion

The output intensities from the green and red upconversion emissions were monitored and averaged. The narrow bandpass of the monochromator permitted a clear signal at the target wavelength range to be accurately detected as well as excluded the possibility of detecting the otherwise erroneous intensity from the additional line emitted by the pump laser (at ~525 nm).

The measured intensities, normalised to the monitored laser power, are shown in **Figure 6.21a** for the green emission up to 1323 K and in **Figure 6.21b** for the red up to 1423 K. The two figures also show the associated errors plotted as a percentage of the normalised values with the largest errors obtained towards the maximum temperature points. Due to the stronger upconversion intensity in the red compared to the green, it has been possible to study the emission up to a higher temperature of 1423 K. As with the previous studies discussed in earlier sections, an accurate calibration curve which is fast and simple to use is desirable so that the measured data can be of practical use. Through the use of **Eq. 6.2**, such a curve has been fitted to both the normalised green and red intensities, and can be seen in **Figures 6.21a** and **6.21b** together with the experimental data respectively. It is also seen that relatively good fits have been obtained. **Table 6.9a** compares the difference between the measured and fitted data for the  ${}^4S_{3/2} \rightarrow {}^4I_{15/2}$  (green) transition while the difference in the red emission due to the  ${}^4F_{9/2} \rightarrow {}^4I_{15/2}$  transition can be found in **Table 6.9b**. An estimate of the sensitivity of the two upconversion intensities has been obtained by differentiating **Eq. 6.2** for each of the normalised data concerned. The sensitivity curves are plotted in **Figure 6.21c**, showing a maximum at the point when the slopes of the intensity-temperature curve for both emissions (**Figures 6.21a** and **6.21b**) are steepest. It was also considered that the ratio of the red to the green intensities could be of some value as a temperature-dependent sensing parameter. This ratio is shown in **Figure 6.22**.

It can be seen in **Figure 6.21a** that the green decreases steadily as the temperature is increased. This curve “flattens” out towards the higher temperatures and very large errors can be seen at 1323 and 1273 K. This is in part due to the drastically weakened emission intensity at elevated temperatures detected by the PMT, thus

contributing to fluctuations in the output signal which is then dominated by noise. Nevertheless, it can be seen (**Figure 6.21a**) that the decay profile of the green upconversion intensity with temperature is almost an exponential, as shown by the adjacent fitted curve using **Eq. 6.2**. The comparison of the measured and fitted data, shown in **Table 6.9a**, reveals that a reasonably good fit has been achieved. However, large percentage errors have been encountered due to the ever diminishing intensity as temperature was raised, with a maximum error of more than 90 % at 1223 K. The red intensity has also been found to exhibit an exponentially decaying dependence on temperature (**Figure 6.21b**). The fitted curve using **Eq. 6.2** can also be seen to fit the measured data reasonably well, with a rather general agreement between the measured and fitted values (**Table 6.9b**). The maximum error in the red is more than 600 % at 1323 K. This could be attributed to the fact that the green emission is a second-order upconversion process. The excited population at the  $^4S_{3/2}$  state is a result of direct excitation from the  $^4F_{9/2}$  state, hence at elevated temperatures, the depletion of the  $^4F_{9/2}$  population due to non-radiative multi-phonon decay would take precedent over that from the higher excited state, leading to further reduction in the probability of transition between the two levels. This would ultimately lead to a much depleted excited state population in the higher  $^4S_{3/2}$  level and, due to the existence of several sublevel transitions within that manifold, result in a decay from this level with a lifetime which might not be exponential [6.12, 6.22, 6.72, 6.76]. Hence, the assumption that the reduction in observed intensity in both upconversion processes was attributed to contribution from non-radiative multi-phonon relaxation to the ground state can be found to be reasonable. The strong upconversion in both the green and red spectral regions can be related to the main dynamics of the energy transfer processes between the first excited state and the  $^4F_{9/2}$  level, and the second-order upconversion population of the even higher energy levels,  $^2H_{11/2}$  and  $^4S_{3/2}$ , as discussed by various authors [6.22, 6.69, 6.70, 6.71, 6.79, 6.80]. In addition, the existence of the various sublevels within a primary manifold has been considered to be due to the effect of Stark splitting due to electronic interaction with the crystal lattice and the RE ions. The idea of a thermalisation effect resulting in thermal population of the  $^2H_{11/2}$  level from the slightly lower energy level  $^4S_{3/2}$  has also been suggested as the main mechanism for the relative change in intensities of the inter-manifold sublevels. The resulting peaks of the sublevels can thus be seen to undergo thermally-assisted energy transfer among

themselves as the temperature is raised and providing a means to track these changes can lead to potential thermometric applications.

The intensity ratio of the red to green upconversion, shown in **Figure 6.22**, in contrast, was not found to be very practical for sensing purposes as demonstrated by a non-monotonic profile in which there is a large reduction in ratio at 1273 K. This is probably due to the large percentage errors present when taking the ratio of both intensities. However, an increase in the ratio can be seen with increasing temperature, implying that the green upconversion transition is more temperature dependent while the red transition is relatively more stable at elevated temperatures. Also, if the already large percentage errors (towards the high temperature end) from the respective upconversion intensities measured could be reduced, a monotonic relationship in this ratio could probably be realised.

Figure 6.21a. Green upconversion intensity as a function of temperature ( $\text{Er}^{3+}:\text{Yb}^{3+}:\text{Al}_2\text{O}_3$  fibre)

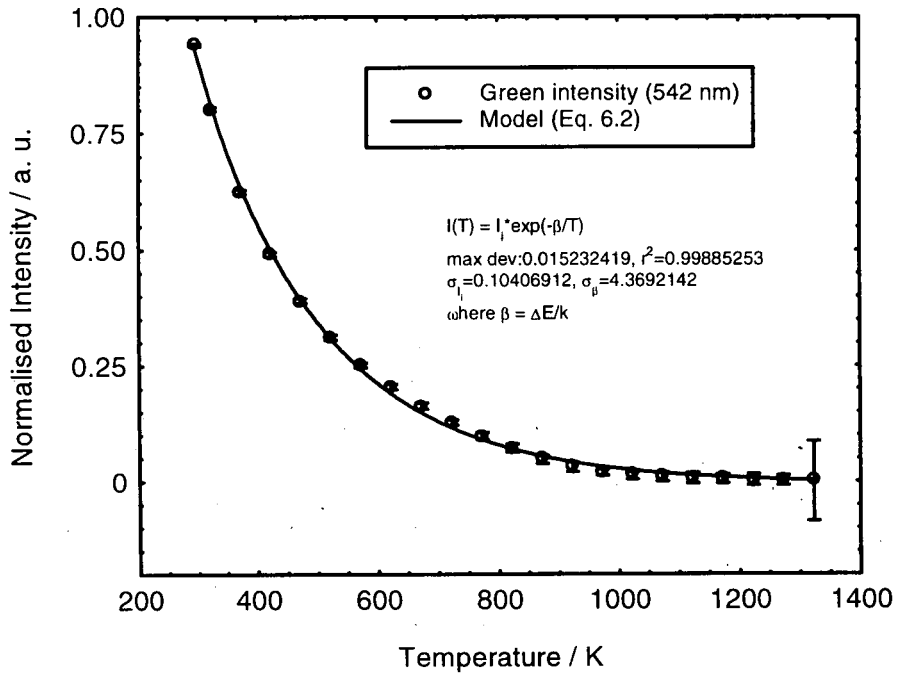
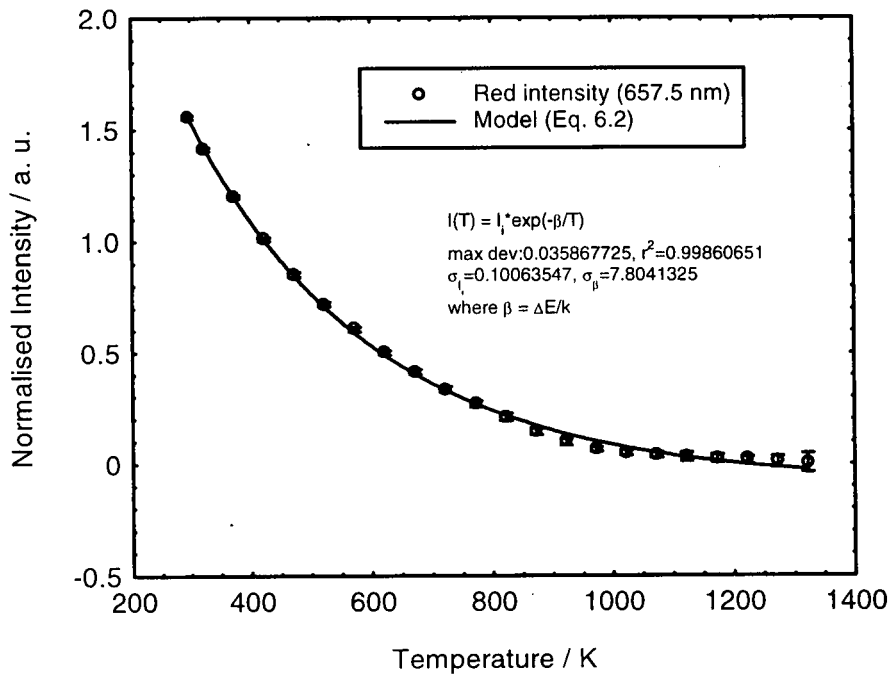


Figure 6.21b. Red upconversion intensity as a function of temperature ( $\text{Er}^{3+}:\text{Yb}^{3+}:\text{Al}_2\text{O}_3$  fibre)



**Table 6.9a. Comparison of experimental and exponentially-fitted data in green upconversion intensity changes with temperature (Er<sup>3+</sup>:Yb<sup>3+</sup>:Al<sub>2</sub>O<sub>3</sub> fibre)**

Temp / K	Normalised intensity values	Fitted values using Eq. 6.2	Error / %
295	0.939733	0.930003	-1.04
323	0.801903	0.812394	1.31
373	0.625142	0.637984	2.05
423	0.490979	0.500827	2.01
473	0.389967	0.392967	0.77
523	0.311147	0.308145	-0.96
573	0.250760	0.241441	-3.72
623	0.204190	0.188985	-7.45
673	0.162966	0.147734	-9.35
723	0.126939	0.115293	-9.17
773	0.098109	0.089782	-8.49
823	0.071687	0.069720	-2.74
873	0.047626	0.053943	13.26
923	0.030898	0.041536	34.43
973	0.018939	0.031779	67.79
1023	0.012796	0.024106	88.39
1073	0.009435	0.018072	91.54
1123	0.007070	0.013327	88.49
1173	0.005036	0.009596	90.55
1223	0.003333	0.006661	99.84
1273	0.002129	0.004354	104.48
1323	0.000780	0.002539	225.17

**Table 6.9b. Comparison of experimental and exponentially-fitted data in red upconversion intensity changes with temperature (Er<sup>3+</sup>:Yb<sup>3+</sup>:Al<sub>2</sub>O<sub>3</sub> fibre)**

Temp / K	Normalised intensity values	Fitted values using Eq. 6.2	Error / %
295	1.555697	1.564177	0.55
323	1.412111	1.42187	0.69
373	1.200295	1.197578	-0.23
423	1.010749	1.006644	-0.41
473	0.851904	0.844107	-0.92
523	0.718775	0.705743	-1.81
573	0.605050	0.587957	-2.82
623	0.499664	0.487689	-2.40
673	0.413093	0.402334	-2.60
723	0.334178	0.329673	-1.35
773	0.267827	0.267818	-0.003
823	0.207990	0.215163	3.45
873	0.143031	0.170339	19.09
923	0.096359	0.132181	37.18
973	0.063831	0.099699	56.19
1023	0.048189	0.072047	49.51
1073	0.038738	0.048508	25.22
1123	0.030091	0.02847	-5.39
1173	0.022634	0.011412	-49.58
1223	0.015917	-0.00311	-119.54
1273	0.008297	-0.01547	-286.46
1323	0.004407	-0.02599	-689.88

Figure 6.21c. Sensitivity curves of red and green upconversion intensity as a function of temperature ( $\text{Er}^{3+}:\text{Yb}^{3+}:\text{Al}_2\text{O}_3$  fibre)

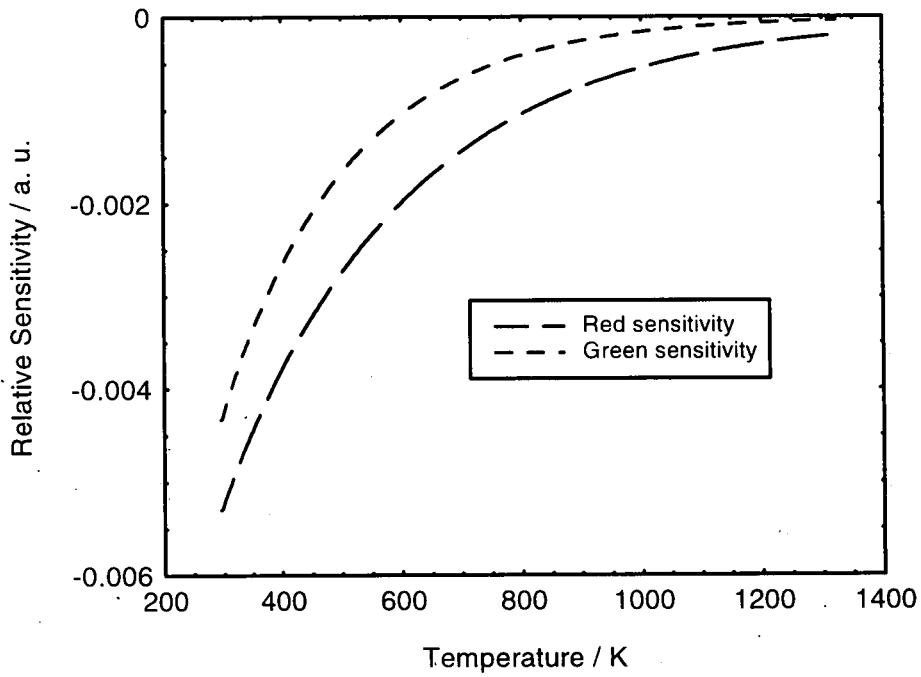
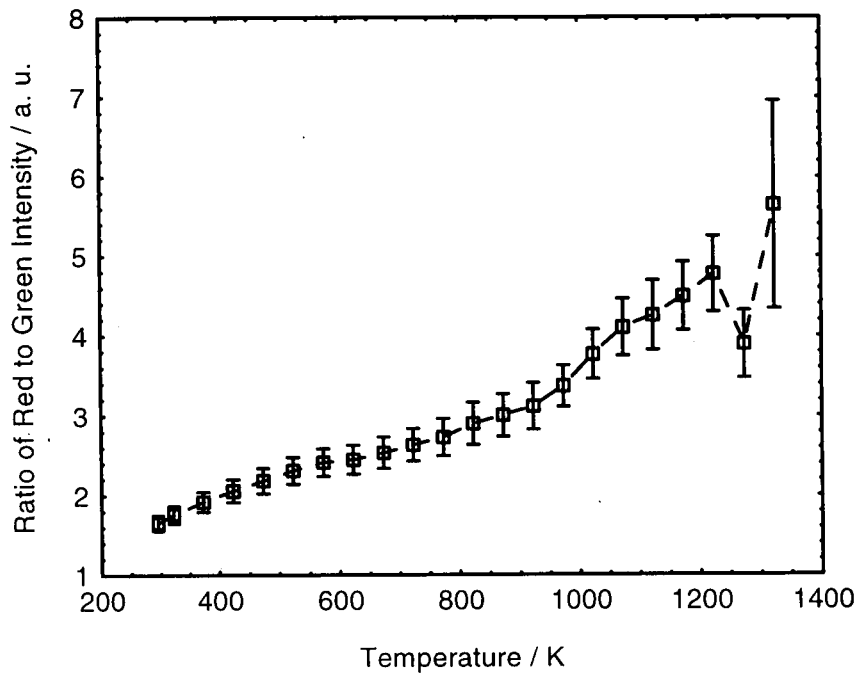


Figure 6.22. Intensity ratio of red to green upconversion as a function of temperature ( $\text{Er}^{3+}:\text{Yb}^{3+}:\text{Al}_2\text{O}_3$  fibre)



### 6.2.2.7 Temperature dependence of the green and red upconversion decay lifetimes

The temperature-dependences of the decay lifetimes of both the green and red upconversion emissions are investigated in this work for their suitability in thermometric applications. Plotted in **Figures 6.23a** and **6.23b** are the decay lifetimes of both the green and red upconversion at 323 K. A slower decay back to the ground state can be seen (see inserts) to be superimposed onto an initial rapid decay. No earlier data has been reported on this "uncharacteristic" behaviour of the upconversion lifetime decay of any RE-doped materials. However, it has already been seen in an earlier experiment that the primary manifolds, namely the  $^4S_{3/2}$ ,  $^2H_{11/2}$  and  $^4F_{9/2}$  states, consist of several Stark-split sublevels which resulted in sharp emission lines separated by very narrow energy gaps. Employing the fluorescence intensity ratio method, these lines were also seen to exhibit a dependence on temperature, with relative changes occurring between their peak intensities. The inter-manifold energy transfer dynamics among these sharp lines between the respective spectral emissions have been already been considered [6.71, 6.79, 6.80] to be due to a thermally-assisted excitation process between the green  $^4S_{3/2}$  and  $^2H_{11/2}$  states, with the higher level,  $^2H_{11/2}$ , being populated as a result. The competing processes between the  $^4S_{3/2} \rightarrow ^4I_{15/2}$  and  $^2H_{11/2} \rightarrow ^4I_{15/2}$  transitions thus lead to relative changes in their respective intensities with temperature. Such thermally-assisted population processes are also suggested to be the main mechanisms determining the lifetime decay characteristics of the green and red (within the  $^4F_{9/2}$  manifold of the  $^4F_{9/2} \rightarrow ^5I_{15/2}$  transition) upconversion, where competing lower sublevels are thought to lead to a very rapid decay as portrayed by the figures. Repopulation of the higher energy sublevels from the lower levels may then be reflected in the formation of another lifetime profile, followed by subsequent decay to the ground state.

Although the very fast initial lifetime decay attributed to the first stage transition process involving the various sublevels may not be monitored rapidly enough or have a sufficiently wide range over the temperatures to be investigated, attempts have been made in this work to relate the slower decay encompassed by the relatively weaker second decay lifetime to changes in the temperature to which the

codoped fibre has been subjected. In addition, due to the very high dopant concentration levels of both the  $\text{Er}^{3+}$  and  $\text{Yb}^{3+}$  ions, the lifetime decay was not expected to behave in an exponential manner.

#### 6.2.2.8 Lifetime experiment

A schematic of the experimental set-up can be seen in **Figure 6.24**. It is relatively similar to earlier experiments on measuring the intensities and FIRs of the codoped fibre. An IR laser diode at 960 nm was employed as the pump source. Focusing and collimation of the beam was done using a set of lenses as shown in the figure. The doped end-section of the sapphire fibre was pumped by the 960 nm radiation via a X20 MO which focused the collimated beam into the end of the fibre. Backscattered upconversion emission in the green and red was then reflected and guided by a thin beam splitter into the entrance slit. The photodetector employed was a *R928 Hamamatsu* PMT attached to the exit slit of the monochromator. Both the entrance and exit slitwidths have been set to  $\sim 2000 \mu\text{m}$  wide, in effect, acting as a narrowband filter. The output signal from the PMT was connected to a high-speed current amplifier to provide a  $50 \Omega$ -terminated input to the 500 MHz *HP* digitising oscilloscope where 11 bit averaging of the signal resulted in a lifetime decay profile being acquired. The data for each temperature point investigated were then saved onto a floppy disc and transferred to a computer for analysis.

Figure 6.23a. Lifetime decay of green upconversion at 323 K ( $\text{Er}^{3+}:\text{Yb}^{3+}:\text{Al}_2\text{O}_3$  fibre)

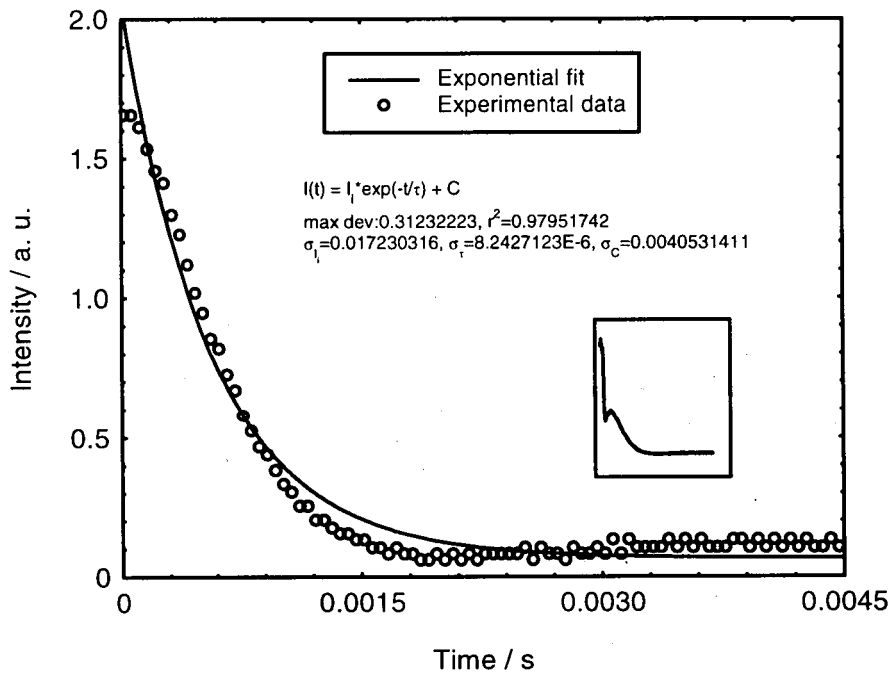
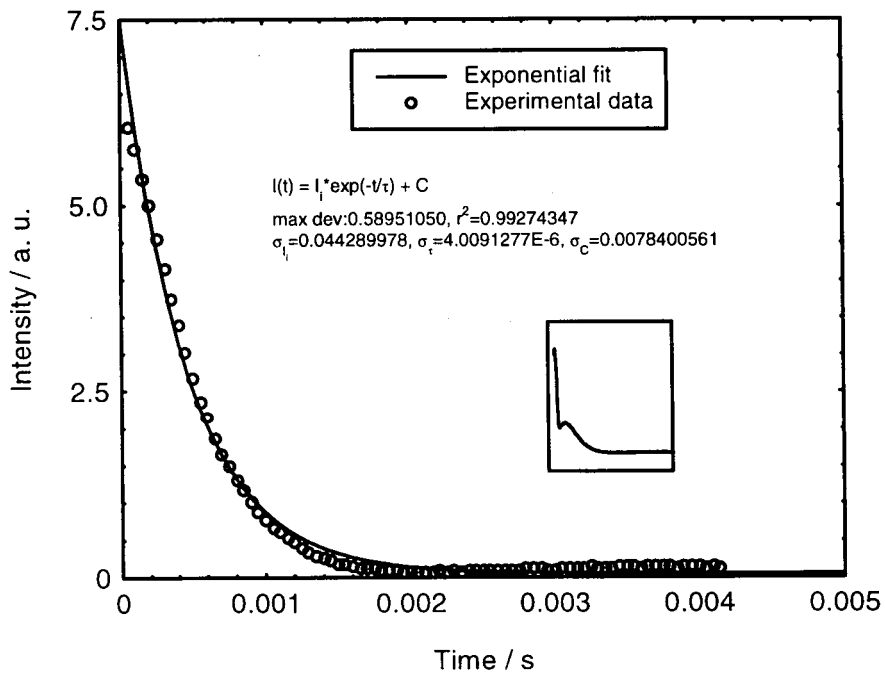
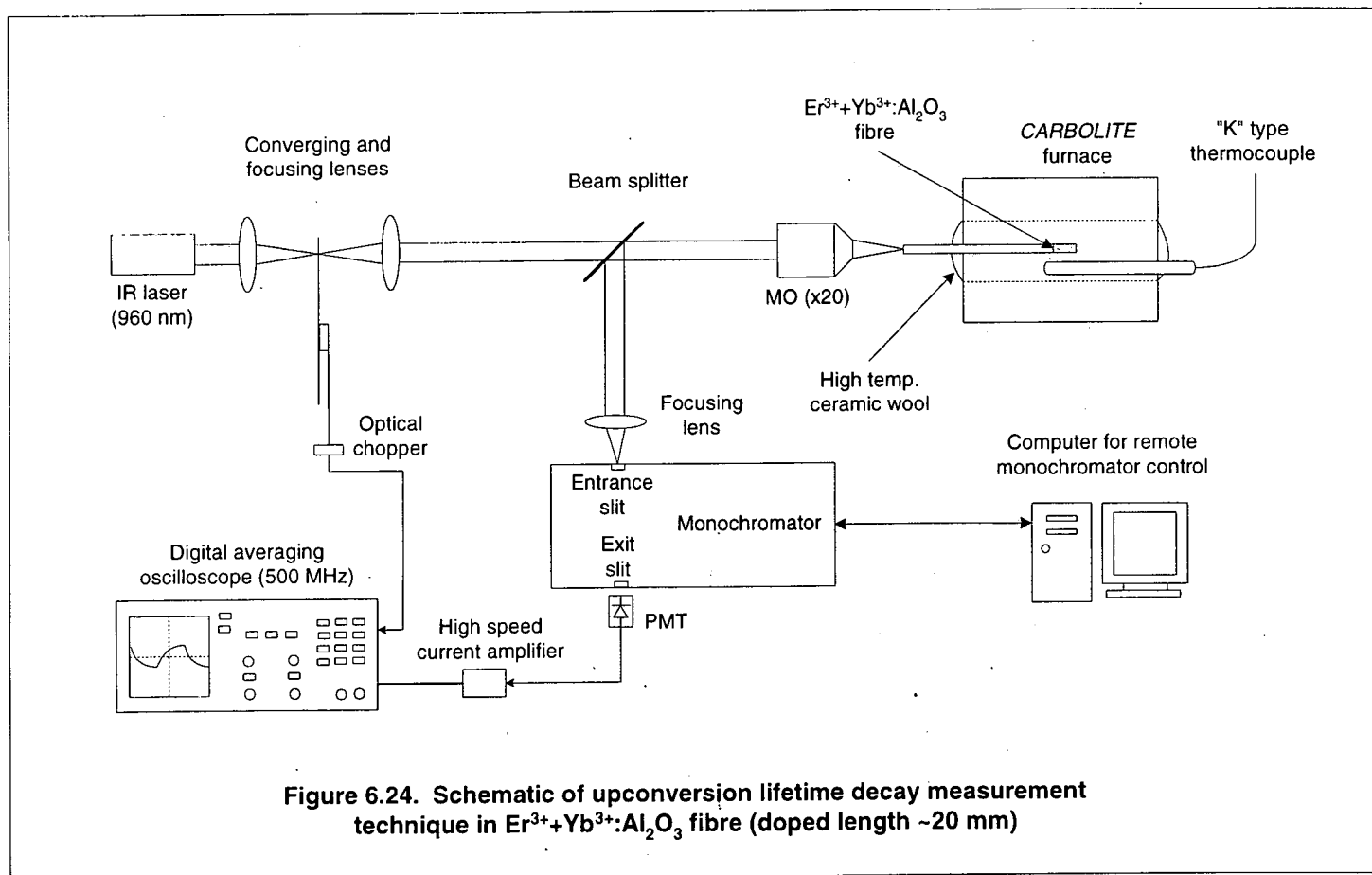


Figure 6.23b. Lifetime decay of red upconversion at 323 K ( $\text{Er}^{3+}:\text{Yb}^{3+}:\text{Al}_2\text{O}_3$  fibre)





### 6.2.2.9 Results and Discussion

The dependence on temperature of the upconversion decay lifetimes for the green and red emissions has been investigated as a potential temperature sensing mechanism as described in the previous section. The acquired data from the averaging oscilloscope has been processed using an *Easyplot* software package for curve fitting and some statistical analysis. The decay lifetimes have been assumed to be of an exponential nature and an exponential fit applied to all lifetime data. However, the actual decay from both the green and red emissions was found to be rather non-exponential. **Figure 6.25** shows the result of the exponential curve-fitting applied to obtain the temperature dependence of the green upconversion decay lifetime up to  $\sim 973$  K. The standard deviations from the curve-fitting procedure have been shown as a percentage error of the detected lifetime and are relatively large. The maximum error was found to be  $\sim 3\%$  at 973 K, corresponding to a resolution of  $\sim 29.5$  K at that temperature. In **Figure 6.26**, the temperature dependence of the red upconversion lifetime has been determined from fitting an exponential to the acquired data at each temperature point. The maximum temperature studied in the red was  $\sim 1123$  K, which was also the temperature at which the maximum error,  $\sim 5.78\%$ , was obtained. This corresponded to a practical resolution of 64.9 K. The two results from curve fitting procedures, one for green upconversion lifetimes and the other for the red lifetimes, are listed in **Tables 6.10** and **6.11** respectively.

It is obvious from **Figures 6.25** and **6.26** that the upconversion lifetimes in the green and red spectral emissions are clearly not suitable for employment as a potential temperature-dependent parameter. The green upconversion lifetimes have been found to fluctuate throughout almost the temperature range investigated and while relatively large errors have been associated with each temperature point, the lifetime dependence on temperature did not exhibit any monotonic characteristics. The only significant temperature region in which the lifetimes seem to exhibit any positive sensing potential was found to be between 523 and 823 K, where the green upconversion lifetimes were seen to increase steadily from 523 K to 823 K (**Figure 6.25**). Beyond 823 K, it was found to decrease sharply again with increasing temperature. The irregular nature of the lifetimes makes it very difficult to correlate

them to temperatures, and in particular, the non-exponential nature of the upconversion lifetime decay results in complicated models or functions which may have to be used in order to fully describe the obtained lifetime data. The lifetimes of the red upconversion shown in **Figure 6.26** can also be seen to vary markedly over the entire temperature range. The segment over which the lifetimes are seen to exhibit any potential monotonous characteristics can be found between 723 K and 1123 K, although not all the lifetimes exhibit an increase with increasing temperature. This is due in large part to the non-exponential lifetime decay from the red emission and perhaps, to a more important extent, to the complicated dynamics behind the transitions between the green and red upconversion processes. The red spectrum may be known as a first-order upconversion process while the green emission can be attributed as a second-order mechanism which continuously depletes the excited state population from the  $^4F_{9/2}$  level [6.72]. The prediction of the emission from the first excited state resulting in 1.53  $\mu\text{m}$  emission as well as the green and red upconversion transitions based on models thus gets more complicated and non-exponential. In particular, the concentration levels of the constituent dopant materials also contribute significantly to such behaviours.

It is thus seen that the lifetimes from both the green and red upconversion processes cannot be employed for temperature sensing purposes. Other ways would have to be found to exploit the strong visible emissions from  $\text{Er}^{3+} + \text{Yb}^{3+}$ -codoped  $\text{Al}_2\text{O}_3$  fibres in order to employ them in temperature sensing applications. Earlier work carried out have focused on the relative changes in the emission peaks of the sublevels within the green and red manifolds. In addition, the intensities of both upconversion emissions have been found to exhibit a smooth monotonous decrease in magnitude with increasing temperature. These investigations are thus justified as the lifetimes have been found to be clearly impractical for such an application.

Figure 6.25. Temperature dependence of green upconversion lifetime decay ( $\text{Er}^{3+}:\text{Yb}^{3+}:\text{Al}_2\text{O}_3$  fibre)

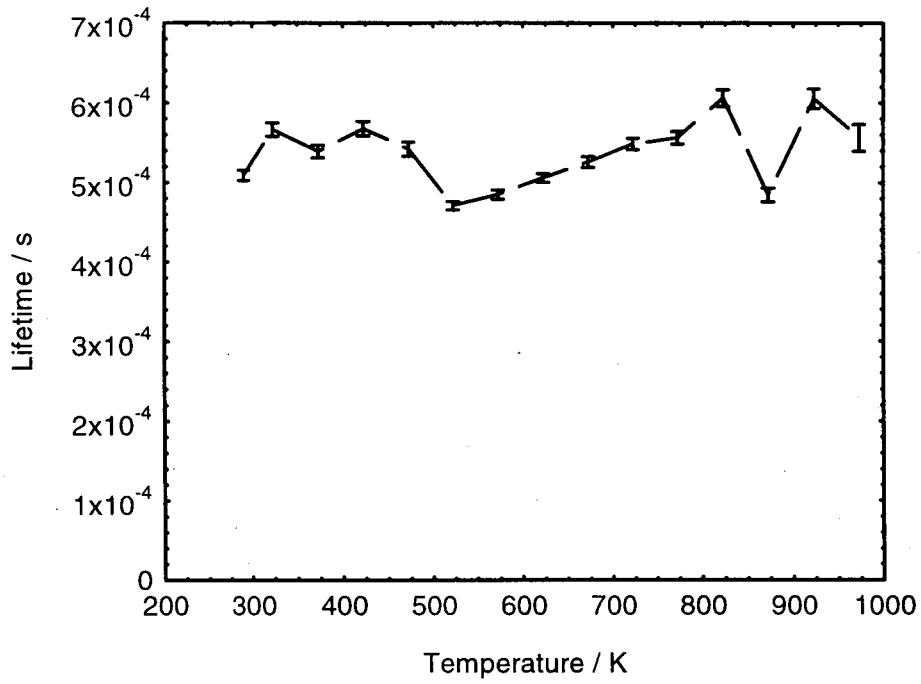
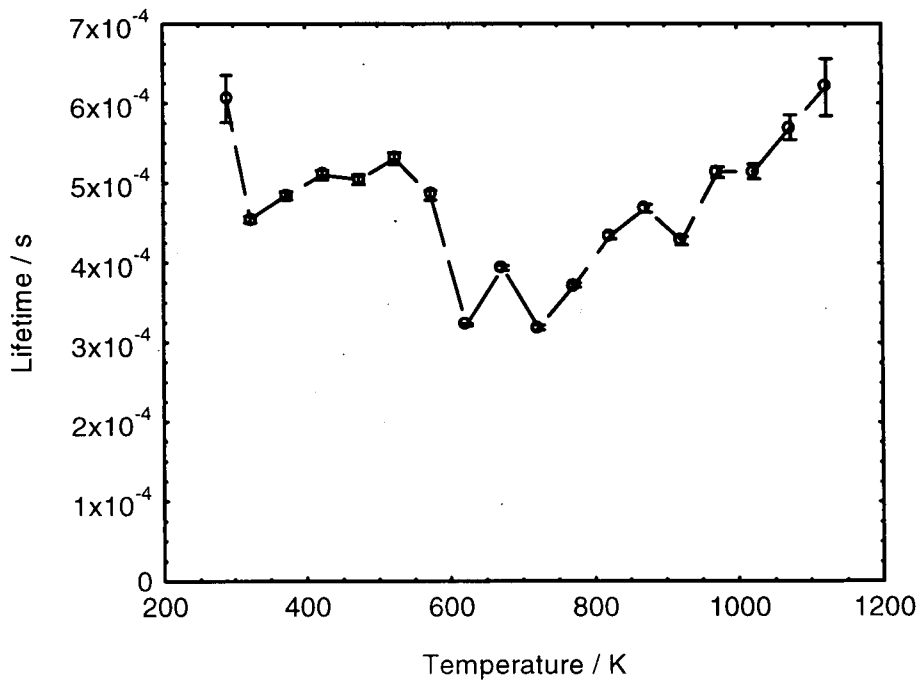


Figure 6.26. Temperature dependence of red upconversion lifetime decay ( $\text{Er}^{3+}:\text{Yb}^{3+}:\text{Al}_2\text{O}_3$  fibre)



**Table 6.10. Lifetime decay of green upconversion in Er<sup>3+</sup>:Yb<sup>3+</sup>:Al<sub>2</sub>O<sub>3</sub> fibre (r<sup>2</sup> denotes the level of fitting confidence)**

Temp / K	Upconversion lifetime / s	Error / %	Accuracy / K	r <sup>2</sup>
295	5.09055E-04	1.26	3.64	0.986
323	5.66290E-04	1.46	4.70	0.979
373	5.39121E-04	1.43	5.34	0.981
423	5.67241E-04	1.57	6.63	0.977
473	5.41982E-04	1.65	7.80	0.976
523	4.70860E-04	1.15	6.03	0.987
573	4.85109E-04	1.21	6.94	0.985
623	5.05817E-04	1.04	6.45	0.989
673	5.25591E-04	1.30	8.73	0.983
723	5.47834E-04	1.29	9.35	0.983
773	5.55784E-04	1.41	10.92	0.98
823	6.05846E-04	1.73	14.26	0.97
873	4.84409E-04	1.73	15.12	0.97
923	6.05480E-04	1.99	18.34	0.965
973	5.56654E-04	3.03	29.49	0.916

**Table 6.11. Lifetime decay of red upconversion in Er<sup>3+</sup>:Yb<sup>3+</sup>:Al<sub>2</sub>O<sub>3</sub> fibre (r<sup>2</sup> denotes the level of fitting confidence)**

Temp / K	Upconversion lifetime / s	Error / %	Accuracy / K	r <sup>2</sup>
295	6.05523E-04	4.92	14.28	0.848
323	4.54122E-04	0.88	2.85	0.993
373	4.83862E-04	1.02	3.79	0.990
423	5.09525E-04	1.15	4.87	0.988
473	5.03843E-04	1.18	5.60	0.987
523	5.30110E-04	1.37	7.18	0.983
573	4.84543E-04	1.25	7.15	0.986
623	3.22107E-04	0.45	2.82	0.998
673	3.93558E-04	0.81	5.46	0.993
723	3.18844E-04	0.91	6.55	0.992
773	3.71832E-04	0.76	5.85	0.995
823	4.34276E-04	1.04	8.58	0.990
873	4.67913E-04	1.04	9.10	0.990
923	4.27436E-04	1.18	10.86	0.986
973	5.13364E-04	1.32	12.83	0.983
1023	5.14156E-04	1.82	18.59	0.970
1073	5.69486E-04	2.75	29.46	0.940
1123	6.20031E-04	5.78	64.94	0.767

### 6.2.3 Temperature sensing with high Yb<sup>3+</sup> + low Er<sup>3+</sup>:Al<sub>2</sub>O<sub>3</sub> fibres

In this section, RE-codoped Al<sub>2</sub>O<sub>3</sub> fibres with very high Yb<sup>3+</sup> and low Er<sup>3+</sup> concentrations (in an approximately 10:1 ratio) have been employed. This was done to obtain the additional IR signals from Yb<sup>3+</sup> in the 1000 nm region for fluorescence intensity ratio measurements as well as potential lifetime detection. Fibre optic sensing schemes employing Yb<sup>3+</sup>-doped glasses have been recently reported by several authors [6.58, 6.60, 6.61, 6.62, 6.63]. While most of the RE ions may be trivalent in nature, schemes based on divalent ytterbium have been in doped bulk fluoride-based crystals and employed for temperature sensing in the cryogenic range between 60 and 130 K [6.63]. The active material employed by the authors [6.63] was a sol-gel coated dye of an active Yb<sup>2+</sup>:CaF<sub>2</sub> layer onto a rotating disc from which the temperature-dependent fluorescence lifetime could then be measured. Like many fluorescence-based sensing schemes, the measurement of the fluorescence decay lifetime of the active materials remains a useful tool to correlate with its dependence on temperature (or other physical parameters). A large body of work on RE-doped fibre optic sensing schemes have been undertaken by researchers to investigate suitable materials for the various requirements in temperature and strain sensing. The interesting emission wavelength of Yb<sup>3+</sup>-doped materials, in the 980 – 1200 nm region, as well as the all-important role of efficient energy transfer sensitiser ions have generated great interest especially in fibre optic telecommunications for these active dopants. In addition, co-doping with Yb<sup>3+</sup> also enables systems such as those doped with Er<sup>3+</sup> to exhibit a broader absorption band. This is highly advantageous since a broad range of pump wavelengths, in the 800 – 1000 nm range where inexpensive high-powered IR laser diodes are commercially available, can then be employed as excitation sources.

The fluorescence decay lifetimes of Yb<sup>3+</sup>-doped silica glass fibres have been employed as temperature and strain sensors [6.60, 6.61, 6.62]. Although temperatures in the 1000 K region can be accurately measured, heat treatment or “thermal annealing” is needed to be carried out in order to ensure stabilised and repeatable lifetime measurements over long periods of time [6.60]. In addition, an earlier temperature sensing scheme has been proposed based on the ratio of the

fluorescence intensities of two emissions at ~976 and 1030 nm, the main fluorescence emission peaks of materials doped with Yb<sup>3+</sup> [6.58].

### 6.2.3.1 Temperature dependence of IR FIR of highly Yb<sup>3+</sup>: lowly Er<sup>3+</sup>-codoped Al<sub>2</sub>O<sub>3</sub> fibres

The fluorescence intensity ratio remains a useful technique in the area of fibre optic sensing in that, suitably selected fluorescent materials, with sufficiently strong emission bands/peaks in a particular spectral region can be employed as indications of the changing parameter to be measured. In particular, fluorescence and/or upconversion from transitions with closely-spaced energy gaps are attractive since the excitation of the manifolds are inextricably linked to the effect of thermal population effects [6.80, 6.79] with an increase in the temperature providing sufficient thermal energy-assisted promotion of the excited ions from one level to another. Hence, by taking the ratio of the intensities of the specific transitions, and accounting for the intrinsic properties of the doped materials, sensing schemes based on this fluorescence intensity ratio can be considered as a "self-referenced" technique without having to stringently monitor the pump power fluctuation. A point temperature sensor has been demonstrated by Maurice *et al.* [6.58] employing such a technique, exploiting the IR fluorescence spectrum from the ytterbium-doped fibre. The sensor probe was fabricated from a silica fibre doped with Yb<sup>3+</sup> ions and a laser pump source at 810 nm has been employed to excite emissions from the energy sublevels of the <sup>2</sup>F<sub>5/2</sub> manifold. The IR fluorescence results in peaks at 910, 976 and 1030 nm, the latter two of which have been used in a FIR technique as a measure of temperature. The ratio of the intensities from the two transitions to the ground state, <sup>2</sup>F<sub>5/2</sub>(a) at 1030 nm and <sup>2</sup>F<sub>5/2</sub>(b) at 976 nm, due to thermal population or coupling between the two sublevels can thus be described using a model given by the expression

$$R = \frac{\sigma^b}{\sigma^a} \exp(-\Delta E / kT) \quad (6.3)$$

where  $R$  is the fluorescence intensity ratio,  $\sigma^a$  and  $\sigma^b$  are the emission cross sections of the <sup>2</sup>F<sub>5/2</sub>(a) and <sup>2</sup>F<sub>5/2</sub>(b) sublevels respectively,  $\Delta E$  the energy gap between these

two sublevels,  $k$  the Boltzmann's constant and  $T$  the temperature in K. This is an identical equation to the one used in earlier work on upconversion fluorescence intensity ratios of  $\text{Er}^{3+}:\text{Al}_2\text{O}_3$  and codoped  $\text{Er}^{3+} + \text{Yb}^{3+}:\text{Al}_2\text{O}_3$  fibres. Such a scheme has also been investigated in this work where the sensing probe employed was a  $\text{Yb}^{3+}:\text{Er}^{3+}:\text{Al}_2\text{O}_3$  fibre with observed emissions at 996 and 1025 nm when pumped at ~965 nm. Coupled to the high melting point of the sapphire host fibre, a "self-referenced" temperature sensor based on the FIR of ytterbium-doped sapphire fibre can be achieved, with the experiment being described below.

### **6.2.3.2 Experiment on temperature dependence of infrared FIR of high $\text{Yb}^{3+}$ : low $\text{Er}^{3+}:\text{Al}_2\text{O}_3$ fibres**

A schematic of the experimental set-up is shown in **Figure 6.27**. The high  $\text{Yb}^{3+}$ : low  $\text{Er}^{3+}:\text{Al}_2\text{O}_3$  fibre was held securely inside a tube furnace in such a way that the doped section, approximately 20 mm in length, was positioned as deeply as possible inside the heating chamber of the furnace. Excitation of the doped fibre was provided by an IR laser diode array operating at a centre wavelength of 965 nm. The potential temperature sensing probe was configured in a reflective mode as shown in the figure. An optical filter centred near the laser emission wavelength was placed immediately after the chopper, near the minimum focal spot in order to reduce the laser background "noise" from the actual measured signal. This excitation light was then focused into the sapphire end of the fibre. The backscattered/reflected signal was then directed onto the entrance slit of the monochromator and detected by a sensitive InGaAs photodetector. Lock-in techniques have been employed for sensitive and stable signal acquisition while a computer was used to store the required information as well as to control the function of the monochromator.

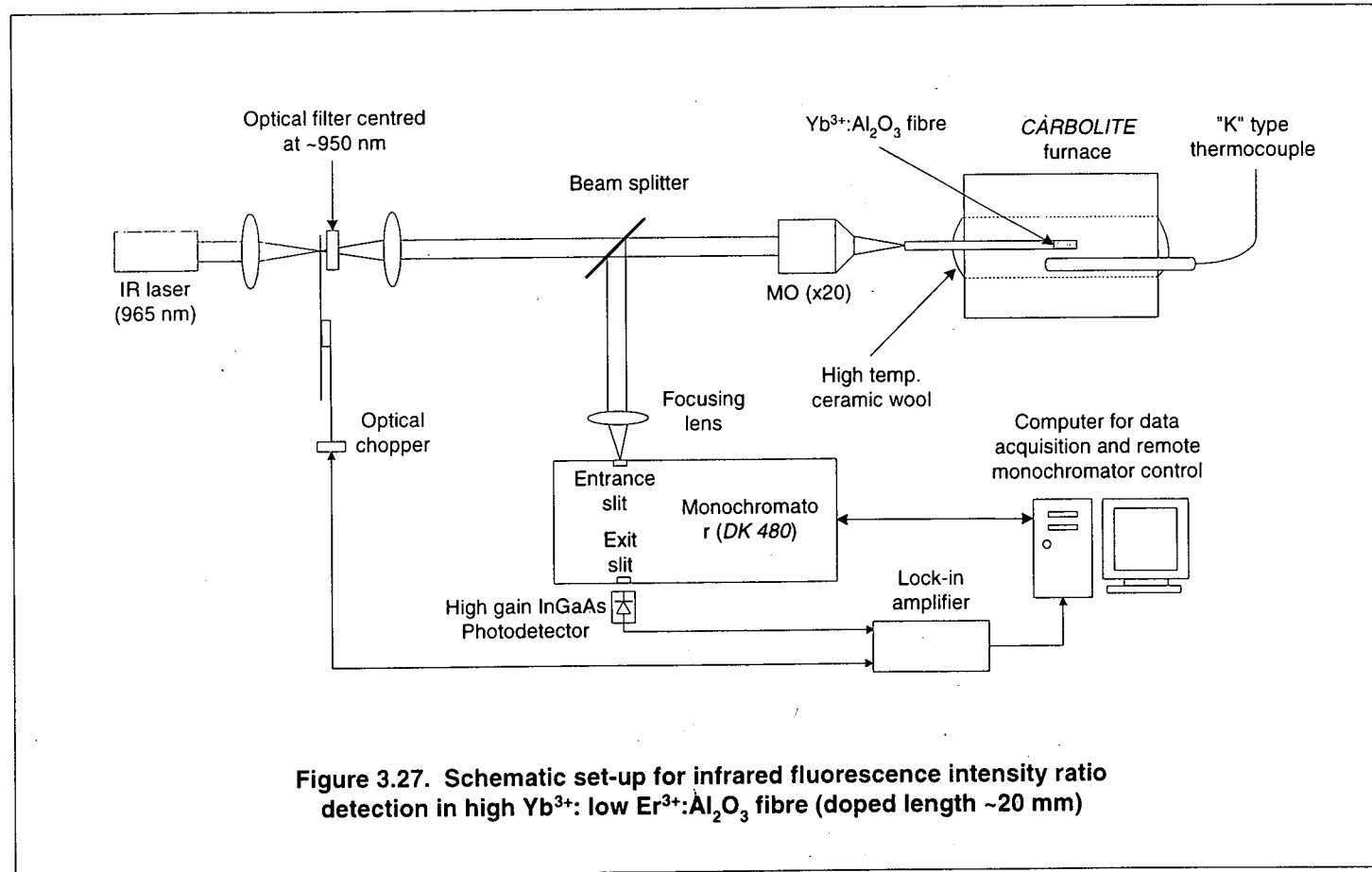


Figure 3.27. Schematic set-up for infrared fluorescence intensity ratio detection in high Yb<sup>3+</sup>: low Er<sup>3+</sup>:Al<sub>2</sub>O<sub>3</sub> fibre (doped length ~20 mm)

### 6.2.3.3 Results and Discussion

The intensity ratio of the fluorescence emission at 1025 and 996 nm ( $I_{1025\text{nm}}/I_{996\text{nm}}$ , where  $I$  is the intensity) from the  $\text{Yb}^{3+}:\text{Er}^{3+}:\text{Al}_2\text{O}_3$  fibre has been detected as described by the experiment shown in **Figure 6.27** for temperatures ranging from 292 to 723 K. The measured FIR in the infrared region can be seen in **Figure 6.28**, where an increasing exponential profile of the curve with temperature is relatively obvious. In addition, the steadily increasing FIR with temperature up to 723 K is found to be monotonic. The error on the measured data has also been found to be reasonably small throughout the entire temperature range, with a maximum of  $\sim 1.05\%$  at 723 K. Hence, a relatively good accuracy can be achieved. The thermal population model governed by **Eq. 6.3** (albeit for another material) has been tested on the data obtained in this work and the curve fitted with this model is shown together with the experimental data in **Figure 6.28** while the relevant fitted parameters are given in **Table 6.12**.

The results of the temperature-dependence of the infrared fluorescence intensity ratio of the 1025 to 996 nm lines presented in **Figure 6.28** are an indication of the suitability of utilising  $\text{Yb}^{3+}:\text{Er}^{3+}:\text{Al}_2\text{O}_3$  fibres for temperature monitoring. The experimental data are found to be repeatable as well as reliable, while the change in the fluorescence intensity ratio can also be seen to be monotonic. The room temperature intensity peak of the 996 nm line dominates the 1025 nm intensity. By increasing the temperature, the latter intensity has been observed to increase a little until this intensity reached a peak value at  $\sim 473$  K before it started to stabilise again. This can be seen in **Figure 6.29** which shows the fluorescence traces at three temperatures: 292, 373 and 473 K. The results obtained here are quite dissimilar from published temperature sensing work on  $\text{Yb}^{3+}$ -doped silica fibres [6.58], where the peak intensities of the 976 and 1030 nm lines behaved in a reverse manner. The intensity of the  ${}^2\text{F}_{5/2}(\text{a}) \rightarrow {}^2\text{F}_{7/2}$  transition, resulting in fluorescence at a wavelength of 1030 nm, was found to decrease gradually with increasing temperature. On the other hand, however, the intensity at 976 nm (in that work) due to the next-higher sublevel  ${}^2\text{F}_{5/2}(\text{b}) \rightarrow {}^2\text{F}_{7/2}$  transition was thermally excited/populated by the lower-energy sublevel,  ${}^2\text{F}_{5/2}(\text{a})$ , and found to be relatively stable, after a small increase. It should be noted that the two emission wavelengths in that work [6.58] were at 976

and 1030 nm while the two fluorescence peaks from the highly ytterbium-codoped  $\text{Er}^{3+}$  sapphire fibres employed in this work have been observed at 996 and 1025 nm. This apparent relative shift in both wavelengths could be due to the different phonon energies intrinsic to the two different host materials used, the electronic-phonon interaction dynamics between the RE  $\text{Yb}^{3+}$  ions and the hosts as well as the different excitation wavelengths employed. In addition, the change in fluorescence intensities of the two wavelengths from the  $\text{Yb}^{3+}:\text{Er}^{3+}:\text{Al}_2\text{O}_3$  fibre was such that the longer wavelength intensity increased slightly before decreasing again and stabilising at or after 473 K while the 996 nm fluorescence intensity was found to steadily decrease.

In order to better understand the energy transfer process from the Stark-split excited states in  $\text{Yb}^{3+}$  to the ground state, with resulting fluorescence emissions at 996 and 1025 nm, a model such as that given by **Eq. 6.3**, may be used to describe the relative change in the peak intensities of the two emission lines in a ratiometric technique. By monitoring this ratio as changes in temperature are effected, a good estimate of the behaviours of the two lines (in the form of a ratio of their peak intensities), from the point of the thermal excitation of population levels of the higher state from the lower energy state, can thus be obtained. In singly  $\text{Yb}^{3+}$ -doped hosts, only two effective population levels exist,  $^2\text{F}_{5/2}$  the excited level and  $^2\text{F}_{7/2}$  the ground state, although it is known that multiple sublevels can occur due to Stark-splitting of the crystal lattice. Interactions such as these thus result in the formation of several other closely-spaced energy sublevels within a single manifold and, in turn, can lead to fluorescence emissions characterised by narrow sharp lines separated by very small wavelength bands. Fluorescence at 910, 976 and 1030 nm have been reported by Maurice *et al.* [6.58] who employed the intensity ratio of the 1030 to 976 nm emissions for thermometric applications involving a  $\text{Yb}^{3+}$ -doped silica fibre as the sensor probe, obtaining a sensitivity of 1.1 % / °C as a result. In this work, the energy gap, the theoretical  $\Delta E$ , between the 996 and 1025 nm fluorescence emissions is given by  $284.1 \text{ cm}^{-1}$ . However, the use of **Eq. 6.3** yielded a fitted  $\Delta E$  value of  $443.5 \text{ cm}^{-1}$  which agrees to within a factor of  $\sim 1.5$  times that of the theoretical value. This is a reasonable expectation since the simplified model governed by **Eq. 6.3** only considers an extremely simplified model of the physical processes with an energy gap difference between the Stark-split sublevels of a singly doped system. This

upconversion process has been attributed to the presence of a small quantity of active  $\text{Er}^{3+}$  ions and can lead to complex de-population routes for the first excited state in the codoped system in which non-exponential decay of the IR fluorescence can occur dependent on dopant concentration level and pump intensity [6.22, 6.72]. Thus, the loss of the excited population, which leads to fluorescence at 996 ( ${}^2\text{F}_{5/2}(\text{b}) \rightarrow {}^2\text{F}_{7/2}$  transition) and 1025 ( ${}^2\text{F}_{5/2}(\text{1}) \rightarrow {}^2\text{F}_{7/2}$  transition) nm, to the still higher energy states required for upconversion to occur via the  $\text{Er}^{3+}$  ion may need to be taken into account. Nevertheless, a curve based on the model given by **Eq. 6.3** can be achieved and the fitted data are listed in **Table 6.13**. The equation can also be differentiated and an estimation of the sensitivity expressed below as a measure of the sensitivity,  $S$ , of the sensing probe

$$S = \frac{1}{R} \frac{dR}{dT} = \frac{\Delta E}{kT^2} \quad (6.4)$$

where  $R$  is the fluorescence intensity ratio between the two energy sublevels as given in **Eq. 6.3**,  $\Delta E$  the energy gap between them ( $\sim 284.1 \text{ cm}^{-1}$ , in this work) and  $k$  the Boltzmann's constant ( $1.38 \times 10^{-23} \text{ J/K}$ ). This would yield a sensitivity of  $\sim 0.5 \% / \text{K}$  at room temperature, 292 K. The FIR curve in **Figure 6.28** is based on the ratio  $I_{1025\text{nm}}/I_{996\text{nm}}$  where  $I$  here represents the peak fluorescence intensity at the respective wavelengths. A very good agreement can be observed where a maximum error of  $\sim 1.35 \%$  has been obtained between the measured and fitted ratio.

Although, it should in practice be possible to measure the emission intensities at both wavelengths to a much higher temperature level, the main difficulty encountered in this experiment on the infrared FIR was the relatively wide laser emission wavelength band. The IR laser used had a central wavelength of 965 nm and was found to be near the fluorescence wavelengths of the doped fibre at 996 and 1025 nm. At high amplification, provided by the lock-in techniques employed, the laser background signal was also detected upon which the desired fluorescence from the  $\text{Yb}^{3+} + \text{Er}^{3+}$ -codoped sapphire fibre was superimposed. Hence, the maximum temperature investigated has been limited to  $\sim 723 \text{ K}$  beyond which the background signal due to the excitation pump laser dominated the 996 and 1025 nm fluorescence.

Figure 6.28. Modelling the temperature dependence of infrared FIR ( $I_{1025\text{nm}} / I_{996\text{nm}}$ ) of  $\text{Yb}^{3+}:\text{Er}^{3+}:\text{Al}_2\text{O}_3$  fibre using Eq. 6.3

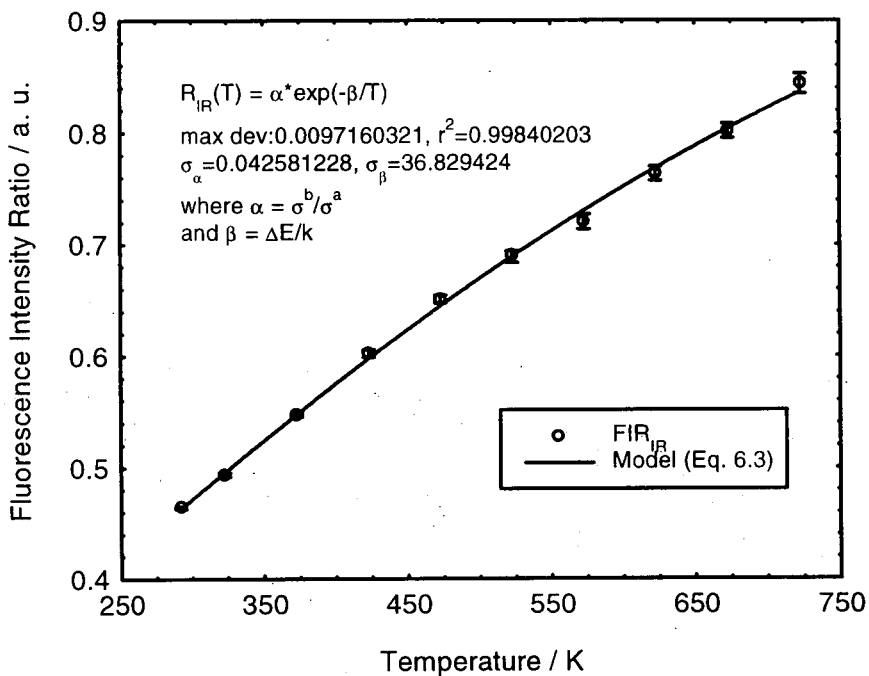
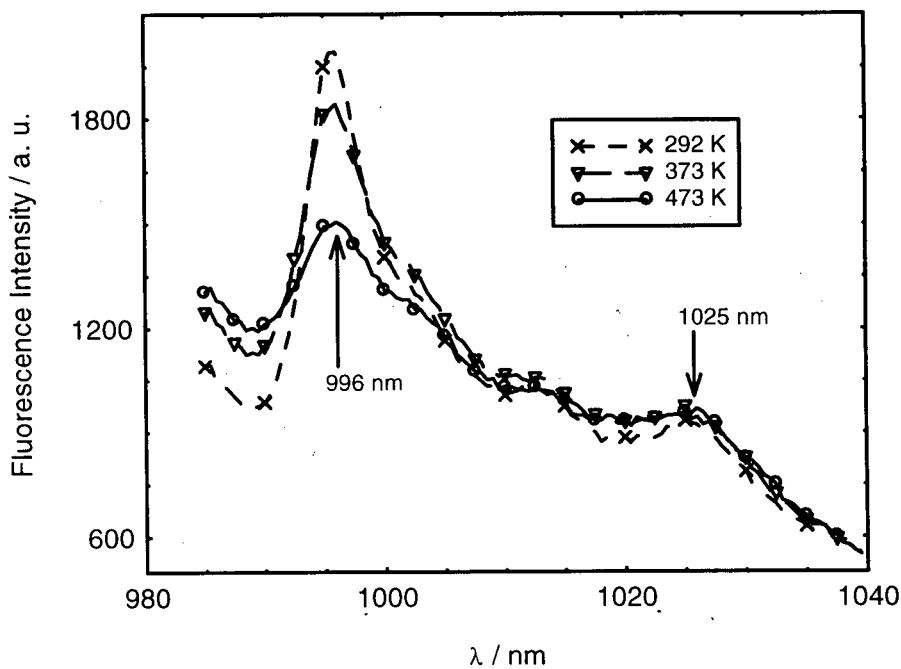


Figure 6.29. Temperature dependence of IR fluorescence at 292, 373 and 473 K



**Table 6.12. Fit parameters of IR FIRs based on Eq. 6.3 (high Yb<sup>3+</sup>: low Er<sup>3+</sup>:Al<sub>2</sub>O<sub>3</sub> fibre)**

Parameters	FIR <sub>g15</sub>	
	Theoretical	Fitted
<i>C</i>	-	1.24
$\Delta E / \text{cm}^{-1}$	284.06	443.48

**Table 6.13. Comparison of measured and fitted infrared FIRs based on Eq. 6.3 (high Yb<sup>3+</sup>: low Er<sup>3+</sup>:Al<sub>2</sub>O<sub>3</sub> fibre)**

Temp / K	Normalised FIR <sub>IR</sub> values	Fitted FIR	Error / %
292	0.464240	0.463276	-0.21
323	0.493627	0.495717	0.42
373	0.546949	0.547726	0.14
423	0.602223	0.597843	-0.73
473	0.651181	0.645182	-0.92
523	0.688927	0.689404	0.07
573	0.720751	0.730467	1.35
623	0.763601	0.768486	0.64
673	0.801582	0.803650	0.26
723	0.843779	0.836176	-0.90

#### 6.2.3.4 Temperature dependence of the FIRs of upconversion emission in the green and red from high Yb<sup>3+</sup>: low Er<sup>3+</sup>-codoped Al<sub>2</sub>O<sub>3</sub> fibres

With the doping technique adopted to produce high concentration Yb<sup>3+</sup> sapphire fibres codoped with low quantities of Er<sup>3+</sup> in a 10:1 concentration ratio, strong IR signals due to the Yb<sup>3+</sup> emission have been realised. These have been found to be dominated by the laser background particularly at elevated temperatures and was one of the main reasons for not measuring the lifetime decay from the 1000 nm fluorescence due to Yb<sup>3+</sup>. No other absorption peaks have been detected in the visible absorption spectrum of these fibres (**Chapter 4**) except in the main absorption bands centred at around 800 and 950 nm due to Yb<sup>3+</sup>. However, the introduction of an IR pump source at 965 nm was found to induce relative strong visible emission which could be observed visually. With the monochromator, both green and red upconversions were detected. These are reminiscent of active Er<sup>3+</sup> transitions from the higher excited states, <sup>4</sup>S<sub>3/2</sub> (or <sup>2</sup>H<sub>11/2</sub>) and <sup>4</sup>F<sub>9/2</sub> to the ground state, <sup>4</sup>I<sub>15/2</sub>. In addition, a scan of the absorption spectra (visible and IR) revealed no presence of Er<sup>3+</sup> ions, which would otherwise have resulted in narrow absorption peaks in the blue (~480 nm), green (~515 nm), red (~650 nm) and in the infrared (~1500 nm). The IR fluorescence spectrum also revealed no emission at the typical 1.53 μm wavelength region. It is well-known that Yb<sup>3+</sup> ions are highly efficient sensitizers [6.37] for Er<sup>3+</sup>-doped materials thus, only a minute amount of the latter ions would have enabled the visible transitions in the green and red to occur. These characteristics observed thus confirm the low Er<sup>3+</sup> concentration levels in the doped fibres, implying that most, if not all, of the pump energy has been efficiently channelled into the excitation of the higher energy levels (from which green and red upconversion has been detected) while at the same time depleting the excited population of the first excited state to the effect that no emission in the 1.5 μm region occurred. Further, the use of high Yb<sup>3+</sup> concentration levels has enabled emission characteristic of these ions to be measured, as demonstrated earlier, which was also the main objective of producing fibres doped in this manner. Experiments were, nevertheless, carried to study the temperature-dependence of the FIRs of the various narrow lines within the respective green and red upconversion spectra.

### 6.2.3.5 Experiment on temperature dependence of green and red upconversion FIRs from high Yb<sup>3+</sup>: low Er<sup>3+</sup>: Al<sub>2</sub>O<sub>3</sub> fibres

The schematic experimental set-up used for the detection of green and red FIRs was very similar to that shown in **Figure 6.27** while the sensing probe employed was a highly Yb<sup>3+</sup>-codoped sapphire fibre, with scant traces of Er<sup>3+</sup> ions. Excitation light from an IR laser at an emission wavelength of 965 nm has been used to pump the fibre where its far-end-section has been doped with Yb<sup>3+</sup> ions. The backscattered upconversion was then detected by a PMT attached to the exit slit of the monochromator. As with all earlier experiments concerning the detection of intensities, lock-in detection techniques have been employed in order to provide stable, sensitive and accurate measurements. The chopper has been used to modulate the pump source into square pulses while a computer was employed, both for data acquisition and to control the monochromator. The detected data were then processed accordingly. The sensing fibre has been placed inside the stabilised oven in such a way that the doped section, approximately 20 mm long, was completely inserted into the heating chamber. Only a short sapphire section, sufficiently long to be secured by the three-axis translation stage, was allowed to protrude from one end of the oven. In addition, high temperature ceramic wool has been used to plug both ends of the tube furnace to prevent heat excessive loss to the surrounding as well as to maintain a stable thermal environment within the furnace. This can be seen in **Figure 6.27**. Moreover, in comparison with the Er<sup>3+</sup> + Yb<sup>3+</sup>-codoped Al<sub>2</sub>O<sub>3</sub> fibres studied earlier, the upconversion intensities of the Yb<sup>3+</sup>:Er<sup>3+</sup>:Al<sub>2</sub>O<sub>3</sub> fibre have been found to be much weaker.

### 6.2.3.6 Results and Discussion.

The narrow inter-manifold green and red upconversion intensities have been fully exploited and investigated for potential sensing purposes. In the green upconversion fluorescence intensity ratios, two lines have been selected from different manifolds, namely the <sup>2</sup>H<sub>1/2</sub> and <sup>4</sup>S<sub>3/2</sub> states. Although several sublevels do exist within the two main manifolds, the main emission lines from the two levels, having the largest relative intensity peaks within their respective level, have been found to be at a wavelength of 532.8 and 544 nm respectively. These were then used in a

fluorescence intensity ratio (FIR) technique as a function of temperature as shown in **Figure 6.30**, since no additional lines in this region from the pump source used were detected (an optical filter has been employed to permit only 965 nm emission from the pump source). A relatively smooth monotonic reduction in the FIR (ratio of intensities of 532.8 to 544 nm lines) can be seen. From the  ${}^4F_{9/2}$  manifold, where transition to the ground state results in upconversion in the red spectral region, five lines with clearly separated peaks can be seen. The five lines, at 651.2, 654.6, 659.6, 666.2 and 672.2 nm, originate due to Stark splitting of the  ${}^4F_{9/2}$  manifold which results in several sublevels, each of which undergoes transition to the ground state. Using the intensity ratios of these lines, an array of 10 FIRs have been obtained and are shown in **Figures 6.31**.  $FIR_{r12} - FIR_{r15}$  are presented in **Figure 6.31a**,  $FIR_{r23} - FIR_{r25}$  in **Figure 6.31b** and  $FIR_{r34} - FIR_{r45}$  are shown in **Figure 6.31c**. All the FIRs exhibited a non-monotonic decaying nature with increasing temperature while most can be seen to be relatively independent of temperature (i.e. not highly sensitive). However, two curves have been selected as potential possibilities in a sensing application, albeit up to a maximum temperature of only 773 K. The two curves are based on the intensity ratios of the 654.6 to 672.2 nm lines ( $FIR_{r25}$ ) and 659.6 to 672.2 nm lines ( $FIR_{r35}$ ). They have been re-plotted in **Figure 6.32**. In addition, the theoretical model (**Eq. 6.1**), which has been discussed earlier, based on the thermal population of the higher energy level by the next lower level has been investigated for both the green and red upconversion. The resulting fitted curves based on the model are also plotted in **Figures 6.30** (for the green FIR) and **6.32** (for the red FIRs). The constants fitted by using the model, **Eq. 6.1**, to the experimental data are also listed in **Tables 6.14** and **6.15** for the green and red upconversion emissions respectively.

The green intensity ratio, as provided by the 532.8 to 544 nm lines (shown in **Figure 6.30**) has been pursued up to a temperature of 873 K. It gives a relatively clear indication of the suitability of using the intensities generated from the  ${}^2H_{11/2}$  and  ${}^4S_{3/2}$  excited states in a ratiometric way as a means of temperature measurements. A very large error margin has been encountered at the maximum temperature and this was attributed to the very weak backscattered green signals from the doped fibre. Nevertheless, a relatively good agreement with the thermalisation effect, up to 773

K, predicted by the model using **Eq. 6.1** has been obtained, as evident in **Figure 6.30**.

The emissions from the red upconversion process due to the  ${}^4F_{9/2} \rightarrow {}^4I_{15/2}$  transition and the inter-manifold interaction among the sublevels led to a more complicated mechanism which has proved difficult to describe using the model (**Eq. 6.1**). However, it can be observed that a somewhat exponential profile has been followed (**Figure 6.32**), indicating that, perhaps, a slight modification to **Eq. 6.1** might be required in order to correctly predict the behaviour of those lines when subjected to increasing temperature. The major limitation posed by the red emissions consists of a non-monotonic decay profile of the selected FIRs (in fact, all FIRs exhibited this non-monotonous characteristic) when subjected to increasing temperature, hence the change in FIRs has been restricted to a maximum temperature limit of 773 K.

Figure 6.30. Modelling the green FIR<sub>g15</sub> ( $I_{532.8nm}/I_{544nm}$ ) of Yb<sup>3+</sup>:Er<sup>3+</sup>:Al<sub>2</sub>O<sub>3</sub> fibre as a function of temperature

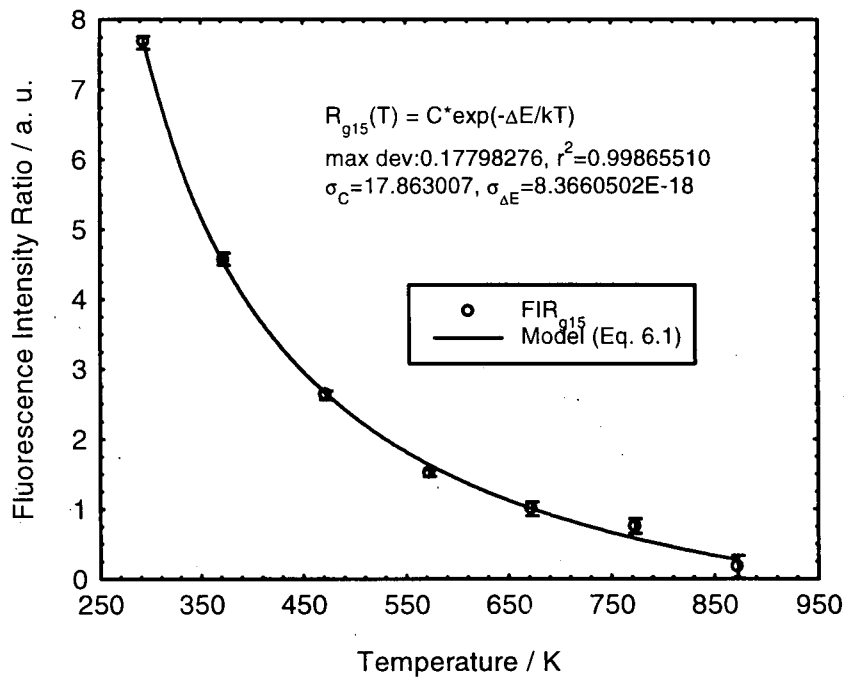


Figure 6.31a. Red FIRs of Yb<sup>3+</sup>:Er<sup>3+</sup>:Al<sub>2</sub>O<sub>3</sub> fibre as a function of temperature (FIR<sub>r12</sub> - FIR<sub>r15</sub>)

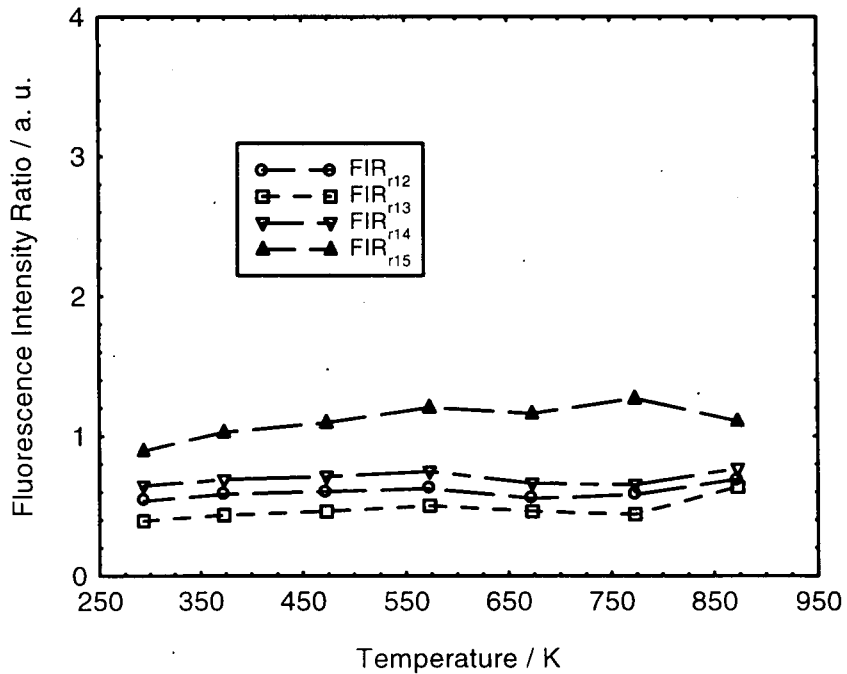


Figure 6.31b. Red FIRs of  $\text{Yb}^{3+}:\text{Er}^{3+}:\text{Al}_2\text{O}_3$  fibre as a function of temperature ( $\text{FIR}_{r23} - \text{FIR}_{r25}$ )

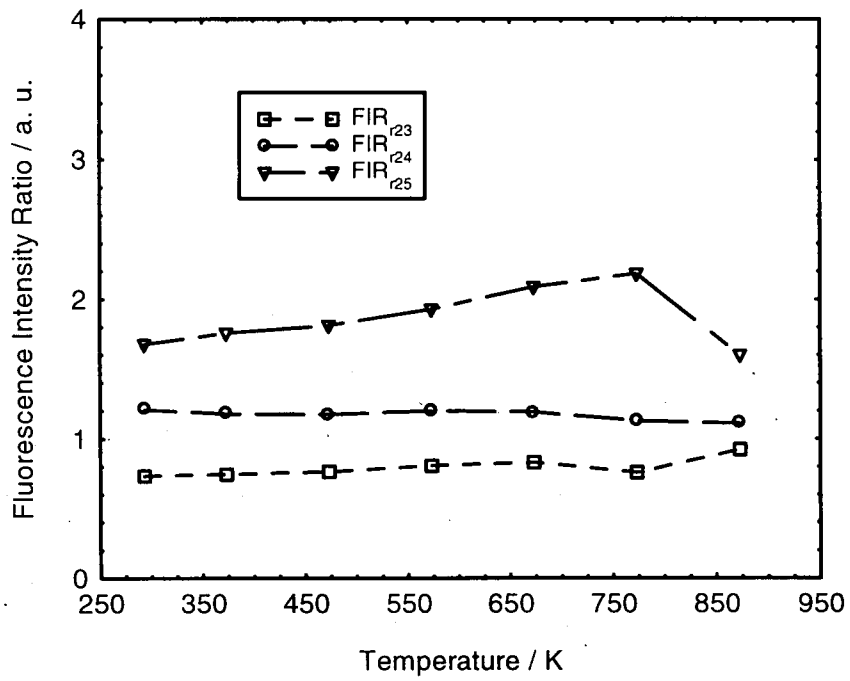


Figure 6.31c. Red FIRs of  $\text{Yb}^{3+}:\text{Er}^{3+}:\text{Al}_2\text{O}_3$  fibre as a function of temperature ( $\text{FIR}_{r34} - \text{FIR}_{r45}$ )

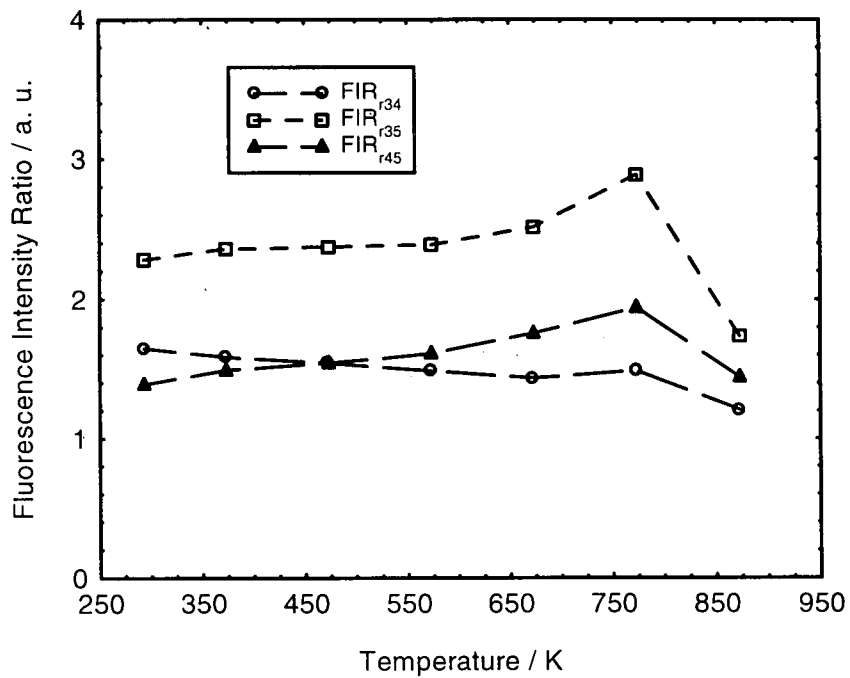
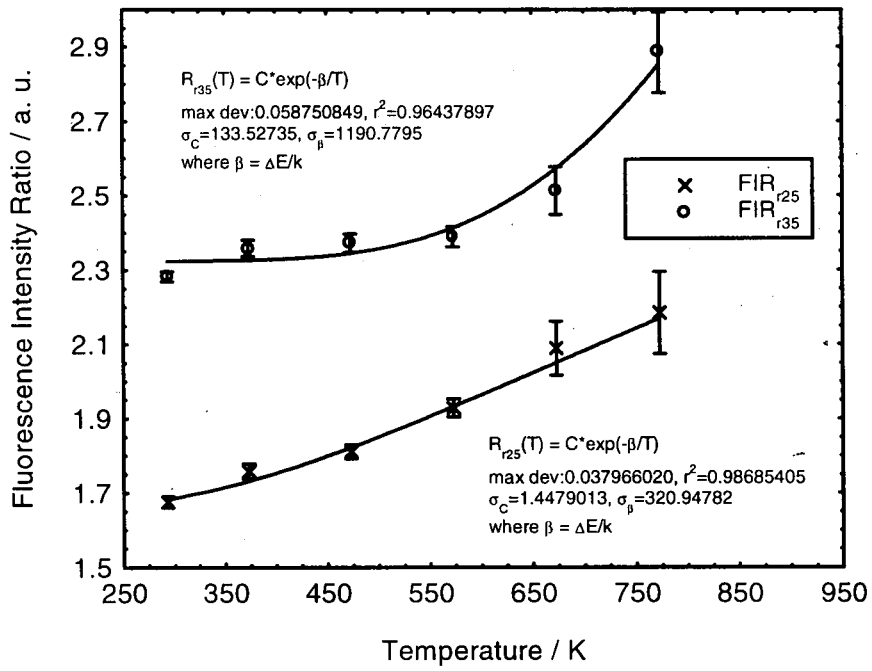


Figure 6.32. Modelling the red FIR<sub>r25</sub> ( $I_{654.6\text{nm}}/I_{672.2\text{nm}}$ ) and FIR<sub>r35</sub> ( $I_{659.6\text{nm}}/I_{672.2\text{nm}}$ ) of Yb<sup>3+</sup>:Er<sup>3+</sup>:Al<sub>2</sub>O<sub>3</sub> fibre as a function of temperature



**Table 6.14. Fit parameters of green FIRs using thermal population model, Eq. 6.1 (high Yb<sup>3+</sup>: low Er<sup>3+</sup>:Al<sub>2</sub>O<sub>3</sub> fibre)**

Parameters	FIR <sub>g15</sub>	
	Theoretical	Fitted
<i>C</i>	-	3.15
$\Delta E / \text{cm}^{-1}$	386.42	3566.86

**Table 6.15. Fit parameters of red FIRs using thermal population model, Eq. 6.1 (high Yb<sup>3+</sup>: low Er<sup>3+</sup>:Al<sub>2</sub>O<sub>3</sub> fibre)**

Parameters	FIR <sub>r25</sub>		FIR <sub>r35</sub>	
	Theoretical	Fitted	Theoretical	Fitted
<i>C</i>	-	3.01	-	88.74
$\Delta E / \text{cm}^{-1}$	399.98	947.49	284.18	2746.12

### 6.3 References to Chapter 6

- 6.1 W. Koechner (Ed.), *Solid-State Laser Engineering* (2<sup>nd</sup> Ed.), Springer-Verlag, Berlin, 1988
- 6.2 M. J. F. Digonnet (Ed.), *Rare Earth Doped Fiber Lasers and Amplifiers*, Marcel Dekker, New York, 1993
- 6.3 F. Gan, *Laser Materials*, World Scientific, Singapore, 1995
- 6.4 R. C. Powell, *Physics of Solid-State Laser Materials*, AIP Press/Springer-Verlag, New York, 1998
- 6.5 G. N. van den Hoven, E. Snoeks, A. Polman, J. W. M. van Uffelen, V. S. Oei and M. K. Smit, *Photoluminescence characterization of Er-implanted Al<sub>2</sub>O<sub>3</sub> films*, Appl. Phys. Lett., 62(24), 3065, 1993
- 6.6 R. Serna, M. Jiménez de Castro, J. A. Chaos, C. N. Afonso and I. Vickridge, *The role of Er<sup>3+</sup>-Er<sup>3+</sup> separation on the luminescence of Er-doped Al<sub>2</sub>O<sub>3</sub> films prepared by pulsed laser deposition*, Appl. Phys. Lett., 75(26), 4073, 1999
- 6.7 C. J. Koester and E. Snitzer, *Amplification in a fiber laser*, Appl. Opt., 3, 1182, 1964
- 6.8 J. Stone and C. A. Burrus, *Neodymium-doped silica lasers in end-pumped fiber geometry*, Appl. Phys. Lett., 23(7), 388, 1973
- 6.9 R. J. Mears, L. Reekie, S. B. Poole and D. N. Payne, *Neodymium-doped silica single-mode fibre laser*, Electron. Lett., 21, 738, 1985
- 6.10 S. B. Poole, D. N. Payne and M. E. Fermann, *Fabrication of low-loss optical fibres containing rare-earth ions*, Electron. Lett., 21, 737, 1985
- 6.11 R. J. Mears, L. Reekie, I. M. Jauncey and D. N. Payne, *Low-noise erbium-doped fibre amplifier operating at 1.54 μm*, Electron. Lett., 23, 1026, 1987
- 6.12 W. J. Miniscalco, *Erbium-Doped Glasses for Fiber Amplifiers at 1500 nm*, IEEE J. Lightwave Technol., 9(2), 234, 1991
- 6.13 A. Polman, *Erbium implanted thin film photonic materials*, J. Appl. Phys., 82(1), 1, 1997
- 6.14 G. N. van den Hoven, A. Polman, E. Alves, M. F. da Silva, A. A. Melo and J. C. Soares, *Lattice site and photoluminescence of erbium implanted in α-Al<sub>2</sub>O<sub>3</sub>*, J. Mater. Res., 12(5), 1401, 1997
- 6.15 R. Serna and C. N. Afonso, *In situ growth of optically active erbium doped Al<sub>2</sub>O<sub>3</sub> thin films by pulsed laser deposition*, Appl. Phys. Lett., 69(11), 1541,

1996

- 6.16 C. E. Chryssou and C. W. Pitt, *Er<sup>3+</sup>-Doped Al<sub>2</sub>O<sub>3</sub> Thin Films by Plasma-Enhanced Chemical Vapor Deposition (PECVD) Exhibiting a 55-nm Optical Bandwidth*, IEEE J. Quant. Electron., **34**(2), 282, 1998
- 6.17 K. A. Ritley and C. P. Flynn, *Growth of b-axis rare earths on sapphire by molecular beam epitaxy*, Appl. Phys. Lett., **72**(2), 170, 1998
- 6.18 A. Bahtat, M. Bouazaoui, M. Bahtat, C. Garapon, B. Jacquier and J. Mugnier, *Upconversion fluorescence spectroscopy in Er<sup>3+</sup>:TiO<sub>2</sub> planar waveguides prepared by a sol-gel process*, J. Non-Cryst. Solids, **202**, 16, 1996
- 6.19 X. Orignac, D. Barbier, X. M. Du, R. M. Almeida, O. McCarthy and E. Yeatman, *Sol-gel silica/titania-on-silica Er/Yb-doped waveguides for optical amplification at 1.5 μm*, Opt. Mater., **12**, 1, 1999
- 6.20 W. Koechner (Ed.), *Properties of Solid-State Laser Materials* in: *Solid State Laser Engineering* (2<sup>nd</sup> Ed.), Springer-Verlag, Berlin, 28, 1988
- 6.21 F. Gan, *Rare Earth Ions Doped Laser Crystals* in: *Laser Materials*, World Scientific, Singapore, 209, 1995
- 6.22 R. Scheps, *Upconversion Laser Processes*, Prog. Quant. Electron., **20**(4), 271, 1996
- 6.23 F. Auzel, *Towards composite solid state laser materials*, J. Alloys and Compounds, **275-277**, 692, 1998
- 6.24 G. Huber, E. Heumann, T. Sandrock and K. Petermann, *Up-conversion processes in laser crystals*, J. Lumin., **72-74**, 1, 1997
- 6.25 S. Hüfner, *Optical Spectra of Transparent Rare Earth Compounds*, Academic Press, London, 1, 1978
- 6.26 E. E. S. Ng, *PhD Thesis*, University of Glasgow, 1999
- 6.27 A. C. B. Yeo, *PhD Thesis*, University of Glasgow, 1999
- 6.28 G. N. Armstrong, *PhD Thesis*, University of Glasgow, 2000
- 6.29 D. W. Chen, C. L. Fincher, T. S. Rose, F. L. Vernon and R. A. Fields, *Diode-pumped I-W continuous-wave Er:YAG 3-μm laser*, Opt. Lett., **24**(6), 385, 1999
- 6.30 C. C. Neubaur and G. Stevens Jr., *Erbium:YAG laser cataract removal: Role of fiber-optic delivery system*, J. Cataract Refract. Surg., **25**, 514, 1999
- 6.31 B. P. Scott, F. Zhao, R. S. F. Chang and N. Djeu, *Upconversion-pumped blue laser in Tm:YAG*, Opt. Lett., **18**(2), 113, 1993

- 6.32 T. Danger, J. Koetke, R. Brede, E. Heumann, G. Huber and B. H. T. Chai, *Spectroscopy and green upconversion laser emission in Er<sup>3+</sup>-doped crystals at room temperature*, J. Appl. Phys., **76**(3), 1413, 1994
- 6.33 R. Scheps, *Er<sup>3+</sup>:YAlO<sub>3</sub> Upconversion Laser*, IEEE J. Quant. Electron., **30**(12), 2914, 1994
- 6.34 R. M. Macfarlane, *Blue-green solid state upconversion lasers*, Journal de Physique IV, **C4**, C4-289, 1994
- 6.35 P. E. -A. Möbert, E. Heumann, G. Huber and B. H. T. Chai, *Green Er<sup>3+</sup>:YLiF<sub>4</sub> upconversion laser at 551 nm with Yb<sup>3+</sup> codoping: a novel pumping scheme*, Opt. Lett., **22**(18), 1412, 1997
- 6.36 M. E. Fermann, D. C. Hanna, D. P. Shepherd, P. J. Suni and J. E. Townsend, *Efficient Operation of An Yb-Sensitised Er Fibre Laser at 1.56 μm*, Electron. Lett., **24**(18), 1135, 1988
- 6.37 F. Di Pasquale and M. Federighi, *Improved Gain Characteristics in High-Concentration Er<sup>3+</sup>/Yb<sup>3+</sup> Codoped Glass Waveguide Amplifiers*, IEEE J. Quant. Electron., **30**(9), 2127, 1994
- 6.38 K. Hsu, C. M. Miller, J. T. Kringlebotn, E. M. Taylor, J. Townsend and D. N. Payne, *Single-mode tunable erbium:ytterbium fiber Fabry-Perot microlaser*, Opt. Lett., **19**(12), 886, 1994
- 6.39 M. J. F. Digonnet and E. Snitzer, *Nd<sup>3+</sup> and Er<sup>3+</sup>-Doped Silica Fiber Lasers in: Rare Earth Doped Fiber Lasers and Amplifiers*, M. J. F. Digonnet (Ed.), Marcel Dekker, New York, 237, 1993
- 6.40 P. R. Morkel, *Narrow Line Width and Tunable Fiber Lasers in: Rare Earth Doped Fiber Lasers and Amplifiers*, M. J. F. Digonnet (Ed.), Marcel Dekker, New York, 281, 1993
- 6.41 K. T. V. Grattan and A. W. Palmer, *Infrared fluorescence "decay-time" temperature sensor*, Rev. Sci. Instrum., **56**(9), 1784, 1985
- 6.42 K. T. V. Grattan, J. D. Manwell, S. M. L. Sim and C. A. Willson, *Lifetime Investigation of Fluorescence from Neodymium:Yttrium Aluminium Garnet at Elevated Temperatures*, Opt., Commun., **62**(2), 104, 1987
- 6.43 K. T. V. Grattan, A. W. Palmer and C. A. Willson, *A miniaturised microcomputer-based neodymium 'decay-time' temperature sensor*, J. Phys. E: Sci. Instrum., **20**, 1201, 1987
- 6.44 K. T. V. Grattan, *The use of fibre optic techniques for temperature*

- measurements*, Measurement and Control, **20**, 32, 1987
- 6.45 J. R. Thornton, W. D. Fountain, G. W. Flint and T. G. Crow, *Properties of Neodymium Laser Materials*, Appl. Opt., **8**(6), 1087, 1969
- 6.46 P. F. Liao and H. P. Weber, *Fluorescence quenching of the  $^4F_{3/2}$  state in Nd-doped yttrium aluminium garnet (YAG) by multiphonon relaxation*, J. Appl. Phys., **45**(7), 2931, 1974
- 6.47 S. P. Jamison and G. F. Imbusch, *Temperature dependence of the luminescence from heavily doped ruby*, J. Lumin., **75**, 143, 1997
- 6.48 Z. Y. Zhang, K. T. V. Grattan, A. W. Palmer, B. T. Meggitt and T. Sun, *Fluorescence decay-time characteristics of erbium-doped optical fiber at elevated temperatures*, Rev. Sci. Instrum., **68**(7), 2764, 1997
- 6.49 J. G. Sliney Jr., K. M. Leung, M. Brinbaum and A. W. Tucker, *Lifetimes of the  $^4F_{3/2}$  state in Nd:YVO<sub>4</sub>*, J. Appl. Phys., **50**(5), 3778, 1979
- 6.50 S. A. Wade, J. C. Muscat, S. F. Collins and G. W. Baxter, *Nd<sup>3+</sup>-doped optical fiber temperature sensor using the fluorescence intensity ratio technique*, Rev. Sci. Instrum., **70**(11), 4279, 1999
- 6.51 T. Sun, Z. Y. Zhang, K. T. V. Grattan and A. W. Palmer, *Intrinsic doped fluorescence decay-time based measurements – strain and temperature characteristics for sensor purposes*, Rev. Sci. Instrum., **69**(12), 4186, 1998
- 6.52 Z. Y. Zhang, K. T. V. Grattan, A. W. Palmer, B. T. Meggitt and T. Sun, *Characterization of erbium-doped intrinsic optical fiber sensor probes at high temperatures*, Rev. Sci. Instrum., **69**(8), 2924, 1998
- 6.53 A. Arnaud, D. I. Forsyth, T. Sun, Z. Y. Zhang and K. T. V. Grattan, *Strain and temperature effects on erbium-doped fiber for decay-time based sensing*, Rev. Sci. Instrum., **71**(1), 104, 2000
- 6.54 P. K. Y. Ko, M. S. Demokan and H. Tam, *Distributed Temperature Sensing with Erbium-Doped Fiber Amplifiers*, IEEE J. Lightwave Technol., **14**(10), 2236, 1996
- 6.55 D. M. Henry, J. H. Herringer and N. Djeu, *Response of 1.6  $\mu\text{m}$  Er:Y<sub>3</sub>Al<sub>5</sub>O<sub>12</sub> fiber-optic temperature sensor up to 1520 K*, Appl. Phys. Lett., **74**(23), 3447, 1999
- 6.56 W. Koechner (Ed.), *Introduction in: Solid-State Laser Engineering* (2<sup>nd</sup> Ed.), Springer-Verlag, Berlin, 1, 1988
- 6.57 R. C. Powell, *Rare-Earth-Ion Laser Materials in: Physics of Solid-State*

- Laser Materials*, AIP Press/Springer-Verlag, New York, 339, 1998
- 6.58 E. Maurice, S. A. Wade, S. F. Collins, G. Monnom and G. W. Baxter, *Self-referenced point temperature sensor based on a fluorescence intensity ratio in Yb<sup>3+</sup>-doped silica fiber*, *Appl. Opt.*, **36**(31), 8264, 1997
- 6.59 F. Gan, *Laser Glass Fibers in: Laser Materials*, World Scientific, Singapore, 326, 1995
- 6.60 T. Sun, Z. Y. Zhang, K. T. V. Grattan and A. W. Palmer, *Ytterbium-based fluorescence decay time fiber optic temperature sensor systems*, *Rev. Sci. Instrum.*, **69**(12), 4179, 1998
- 6.61 T. Sun, Z. Y. Zhang, K. T. V. Grattan and A. W. Palmer, *Intrinsic strain and temperature characteristics of Yb-doped silica-based optical fibers*, *Rev. Sci. Instrum.*, **70**(2), 1447, 1999
- 6.62 S. A. Wade, G. W. Baxter, S. F. Collins, K. T. V. Grattan and T. Sun, *Simultaneous strain-temperature measurement using fluorescence from Yb-doped silica fiber*, *Rev. Sci. Instrum.*, **71**(6), 2267, 2000
- 6.63 F. Bresson and R. Devilles, *Fluorescence temperature sensing on rotating samples in the cryogenic range*, *Rev. Sci. Instrum.*, **70**(7), 3046, 1999
- 6.64 Z. Y. Zhang, K. T. V. Grattan, A. W. Palmer and B. T. Meggitt, *Thulium-doped intrinsic fiber optic sensor for high temperature measurements (>1100 °C)*, *Rev. Sci. Instrum.*, **69**(9), 3210, 1998
- 6.65 Z. Y. Zhang, K. T. V. Grattan, A. W. Palmer and B. T. Meggitt, *Thulium-doped fiber optic decay-time temperature sensors: Characterization of high temperature performance*, *Rev. Sci. Instrum.*, **71**(4), 1614, 2000
- 6.66 T. Sun, Z. Y. Zhang, K. T. V. Grattan, A. W. Palmer and S. F. Collins, *Temperature dependence of the fluorescence lifetime in Pr<sup>3+</sup>:ZBLAN glass for fiber optic thermometry*, *Rev. Sci. Instrum.*, **68**(9), 3447, 1997
- 6.67 X. Wu, W. M. Dennis and W. M. Yen, *Temperature dependence of cross-relaxation processes in Pr<sup>3+</sup>-doped yttrium aluminum garnet*, *Phys. Rev. B*, **50**(10), 6589, 1994
- 6.68 H. Song, T. Hayakawa and M. Nogami, *Comparison of temperature dependence of the fluorescence of Sm<sup>2+</sup>-ion doped in different hosts*, *J. Lumin.*, **81**, 153, 1999
- 6.69 E. Maurice, G. Monnom, D. B. Ostrowsky and G. W. Baxter, *High Dynamic Range Temperature Point Sensor Using Green Fluorescence Intensity Ratio*

- in Erbium-Doped Silica Fiber*, IEEE J. Lightwave Technol., **13**(7), 1349, 1995
- 6.70 P. V. dos Santos, M. T. de Araujo, A. S. Gouveia-Neto, J. A. Medeiros and A. S. B. Sombra, *Optical temperature sensing using upconversion fluorescence emission in Er<sup>3+</sup>/Yb<sup>3+</sup>-codoped chalcogenide glass*, Appl. Phys. Lett., **73**(5)578, 1998
- 6.71 P. V. dos Santos, M. T. de Araujo, A. S. Gouveia-Neto, J. A. Medeiros and A. S. B. Sombra, *Optical Thermometry Through Infrared Excited Upconversion Fluorescence Emission in Er<sup>3+</sup> and Er<sup>3+</sup>-Yb<sup>3+</sup>-codoped Chalcogenide Glasses*, IEEE J. Quant. Electron., **32**(2), 395, 1999
- 6.72 G. N. van den Hoven, E. Snoeks, A. Polman, C. vanDam, J. W. M. van Uffelen and M. K. Smit, *Upconversion in Er-implanted Al<sub>2</sub>O<sub>3</sub> waveguides*, J. Appl. Phys., **79**(3), 1258, 1996
- 6.73 B. Herreros, G. Lifante, F. Cussó, P. D. Townsend and P. J. Chandler, *Green up-conversion emission in Er<sup>3+</sup>-doped LiNbO<sub>3</sub> ion-implanted planar waveguides*, J. Lumin., **72-74**, 198, 1997
- 6.74 X. Zhang, J. Yuan, X. Liu, J. P. Jouart and G. Mary, *Red laser induced upconversion luminescence in Er-doped calcium aluminium germanate garnet*, J. Appl. Phys., **82**(8), 3987, 1997
- 6.75 Y. Mita, K. Hirama, N. Ando, H. Yamamoto and S. Shionoya, *Luminescence processes in Tm<sup>3+</sup>- and Er<sup>3+</sup>-ion-activated, Yb<sup>3+</sup>-ion-sensitized infrared upconversion devices*, J. Appl. Phys., **74**(7), 4703, 1993
- 6.76 C. E. Chrissy, C. W. Pitt, P. J. Chandler and D. E. Hole, *Photoluminescence characterisation of Er<sup>3+</sup>/Yb<sup>3+</sup> co-implanted alumina (Al<sub>2</sub>O<sub>3</sub>) thin films and sapphire crystals*, IEEE Proc.-Optoelectron., **145**(6), 325, 1998
- 6.77 L. Esterowitz, A. Schnitzler, J. Noonan and J. Bahler, *Rare Earth Infrared Quantum Counter*, Appl. Opt., **7**(10), 2053, 1968
- 6.78 G. C. Bhar and S. Das, *A system review of infrared upconversion*, Ind. J. Pure & Appl. Phys., **33**, 169, 1995
- 6.79 E. Maurice, G. Monnom, B. Dussardier, A. Saïssy and D. B. Ostrowsky, *Thermalization effects between upper levels of green fluorescence in Er-doped silica fibers*, Opt. Lett., **19**(13), 990, 1994
- 6.80 H. Berthou and C. K. Jörgensen, *Optical-fiber temperature sensor based on upconversion-excited fluorescence*, Opt. Lett., **15**(19), 1990

- 6.81 K. W. Quoi, R. A. Lieberman, L. G. Cohen, D. S. Shenk and J. R. Simpson,  
*Rare-Earth Doped Optical Fibers for Temperature Sensing*, IEEE J.  
Lightwave Technol., **10**(6), 847, 1992

## **Chapter 7 – Sapphire Fibre-based Polarimetric Sensors**

### **7.0 Introduction**

### **7.1 Fundamental principles of polarimetry-based sensing**

### **7.2 Polarimetric sensing with sapphire fibres**

### **7.3 Temperature sensing experiments**

7.3.1 Temperature sensing with *c*-axis sapphire fibres

7.3.2 Results and Discussion

7.3.3 Temperature sensing with *a*-axis sapphire fibres

7.3.4 Results and Discussion

### **7.4 3-point bending of sapphire fibres**

7.4.1 3-point bending of *c*-axis sapphire fibres

7.4.2 Results and Discussion

7.4.3 3-point bending of *a*-axis sapphire fibres

7.4.4 Results and Discussion

### **7.5 References to Chapter 7**

## Chapter 7 – Sapphire Fibre-based Polarimetric Sensors

### 7.0 Introduction

One of the most important parameters which can be used to describe the propagation of light in any birefringent media is its state of polarisation (SOP) where the electric field associated with an electromagnetic wave may be split into two constituent vectors which are orthogonal to each other as well as to the direction of propagation in a medium. This in turn leads to a difference in the propagation constants of the two vectors, resulting directly in a difference in the propagating velocities of the orthogonal modes and is also known as birefringence. Such a principle can, thus, form one of the many ways in which optical fibres or materials can be exploited for sensing applications. Sensed parameters such as temperature, pressure, stress, strain, force, current, voltage and magnetic field can be encoded as changes in intensity, wavelength or phase, or a combination of all three in a sensing scheme [7.1, 7.2, 7.3]. Most fibre optic polarimetric sensing work to date has been research-based and carried out in the laboratory, and some prominent fibre sensors based on the polarimetric or birefringent properties of both optical fibres and materials are briefly described in the following.

Measurements of current and voltage have increasingly critical implications in the power utilities industry where high electrical powers coupled with large electromagnetic field environments are employed. Conventional monitoring techniques which are typically used for current/voltage sensing may not be operable in such harsh electromagnetic environments while optical techniques can be viewed as an attractive alternative since the desired current and/or voltage parameter can be measured with relative ease, accuracy and reliability with minimal interference from the large surrounding electric and magnetic fields. The variations in the SOP and birefringence of light, such as phase retardation (or retardance), refractive index changes, electro- and magneto-optical effects, have been exploited, particularly, over the last decade or more in fibre optic sensing applications for measurements of current, magnetic field and voltage [7.4, 7.5, 7.6, 7.7, 7.8, 7.9, 7.10]. The Faraday effect is usually employed for magnetic field and, hence, current sensing in which the

magneto-optic effect, induced by a magnetic field on a linearly polarised propagating light beam inside an optical fibre or material, causes the polarisation of the light to be rotated in one preferred direction [7.4, 7.7, 7.8]. An important parameter of the induced rotation of the polarised light is the Verdet constant which determines the strength of the rotation and is intrinsic to the particular sensing material used. Integration of the magnetic field along a closed loop is dependent on the current passing through a conductor [7.8] where the rate of rotation of the electric field vector is determined by the product of the Verdet constant and the magnetic field strength [7.4, 7.7]. Magnetic field and current measurements through the Faraday effect require the sensing fibre to be coiled around a conductor. Although this can introduce additional unwanted birefringence into the current measurement system, various means can be devised to minimise or eliminate the extraneous complications which may result. Therefore, in such a sensing technique, application of a current through a conductor induces a magnetic field to circulate around the sensing fibre coil resulting, in turn, in the rotation of the linearly polarised input lightwave propagating through this fibre. This rotation, which can be attributed to the Faraday effect found in various diamagnetic, paramagnetic and ferrimagnetic materials [7.9] such as Ga:YIG (gallium-doped yttrium iron garnet), ZnSe and BSO ( $\text{Bi}_{12}\text{SiO}_{20}$ ) crystals [7.7, 7.8], can be detected through the use of a combination of polarisers, quarter-wave plates, half-wave plates and/or analysers. The Faraday effect is not the only mechanism which can be used for detection of magnetic fields and/or currents. Other methods such as magnetostrictive and Lorentz force sensors [7.11] involve the fibre undergoing a physical change in length due to the presence of a current carrying conductor or coil, thereby resulting in the change in the state of polarisation of the lightwave at the output of the fibre. However, the sensing principle based on the Faraday effect which induces a rotation of the linear polarisation of the input light in the presence of an electric current can serve as a simple and effective magnetic field/current sensor. Large currents up to 1200 A with good signal-to-noise ratio have been measured using the Faraday effect sensor [7.6] while a good linear relationship between the detector output and the measured magnetic field has been demonstrated by Mitsui *et al.* [7.7] for magnetic fields up to 1000 Oe employing the same principle.

In voltage sensors utilising fibre optic techniques, either the Kerr or Pockels effect may be employed as the sensing mechanism [7.7, 7.10] in that the birefringence induced in the sensing element due to an electric field causes the two orthogonally polarised components of the input lightwave to propagate along the medium at two different velocities. The birefringence due to the Kerr effect is proportional to the square of the transverse electric field while that due to the Pockels effect is linearly or directly proportional to the electric field [7.7, 7.11, 7.12]. Hence, by measuring the degree of elliptical polarisation due to the difference in the two component velocities propagating through the sensing fibre, the corresponding dependence on the voltage or electric field applied to cause this change in the polarisation state can be determined. By applying an electric field across a BSO crystal exhibiting the Pockels effect, relatively high voltages up to 500 V have been measured with good accuracy and linearity by Mitsui *et al.* [7.7]. The second order Kerr effect, which is relatively weaker than the Pockels effect, has also been exploited in voltage measurements up to 400 V with reasonable success [7.10] where the sensing element used was a low birefringence fibre positioned in-between two conductor plates through which a voltage was applied.

The polarimetric properties of both low and high birefringence optical fibres have also been adapted for fibre optic sensing applications where other physical parameters can be measured. The polarisation state of light within an optical fibre can be modified by applying a disturbance such as a force, load or weight transversely to the axis of propagation. Such a simple principle has been exploited in polarimetric weight sensors [7.13], pressure transducers [7.14] and in potential smart structure sensing applications [7.15, 7.16, 7.17] where the fundamental sensing mechanism is based on the polarimetric conditions of the lightwave. The sensing fibres in most cases have been embedded in either composite or metallic host materials where the designated low or high birefringence fibre can then be perturbed by an external influence to produce a change in its birefringence. Since the ultimate parameter measured by a photodetector is an intensity change, the required information due to the physical influence which has been encoded in such a quantity can then be extracted from the overall photodetector output via simple and appropriate expressions.

Another important area of application which can exploit the birefringent properties associated with fibre optic polarimetric sensors is in the monitoring of critical strain/stress levels to which civil structures have been subjected [7.18, 7.19]. While both quasi-static and dynamic strain measurements are possible, the ongoing progress and development of large arrays of strain sensors capable of being multiplexed onto a fibre optic link for civil engineering and, in particular, smart structure applications offer great potential benefits for fibre optic sensing. Fibre optic strain sensing based on polarimetry share the same fundamental principle as most other polarimetric sensors mentioned earlier. The sensor can be embedded in a variety of host materials (materials with isotropic and homogeneous characteristics are generally preferred) and strains applied either transversely [7.18] or longitudinally [7.19] with respect to the sensing probe axis. The desired strain values can then be extracted from the sensor output intensities as changes in birefringence, phase or ellipticity. In addition, since conventional glass fibre materials can withstand only relatively low strains, the selection of appropriate fibre materials can, in effect, extend the sensing range to permit extreme strain levels to be monitored.

Temperature, as an important physical parameter which plays a major role in many practical applications such as the process, chemical and manufacturing industries, has been intensely investigated since the advent of fibre optic sensing and various schemes, through numerous optical sensing techniques, have been devised in attempts to measure this parameter with high accuracy. Fibre optic polarimetry is a suitable technique since birefringent fibres are known to be sensitive to temperature [7.20, 7.21]. The stress-induced birefringence which is built into optical fibres during the drawing process implies that a difference in thermal expansion coefficient exists between the stressed sections and the cladding/core [7.21]. Thus, upon cooling, a lateral stress is created within the fibre and this results in the fibre becoming birefringent. Further, both the refractive index and physical length of the glass fibres are temperature-dependent. Polarimetric temperature sensors employing both birefringent fibres and polarising bulk optics have, therefore, been proposed and demonstrated by various authors [7.22, 7.23, 7.24, 7.25]. However, the maximum temperatures which have been studied in most of these sensors were below 150 °C (or 423 K) and this could be attributed to the relatively low melting point (generally <723 K) of the glass materials used in fabricating the birefringent fibres and optics.

As in all fibre optic sensors, polarimetric sensors are no exception and suffer from cross-sensitivities between two or more parameters which are to be measured since additional birefringence can be introduced through various means such as bending, stress, strain and surrounding temperature variation. In the case of temperature sensing, where the birefringent fibre is known to be highly sensitive to both temperature and strain [7.26], cross-sensitivities between these parameters can render the sensor ineffective with respect to the desired measurand(s) and compensating schemes have to be applied to reduce or eliminate these effects. One of the simplest way to overcome cross-sensitivity effects is to simultaneously measure both parameters (temperature and strain) as reported by Haderler *et al.* [7.27] while another slightly more complicated technique involves monitoring two output signals (using two photodetectors) simultaneously from the same measurand [7.22] which can then be differentiated one against the other to eliminate any perturbation effects to produce a sensor which is dependent only on the desired physical influence. In order to extend the temperature range to beyond 1300 K, other suitable materials which can withstand such thermally hostile environments have to be employed. Sapphire is a suitable candidate since it has a very high melting point (2323 K) and is mechanically stable up to 2073 – 2173 K, hence, it can be used in fibre optic sensing applications where the temperature excursions beyond 1800 K are common, such as temperature monitoring in internal combustion engines and turbo-jet engines. Polarimetric temperature sensors based on sapphire have been demonstrated for measurements with a relatively large range from 298 K up to 1773 K [7.28, 7.29]. By exploiting the anisotropy and temperature-dependent length change of the sapphire rods in a birefringence-balanced configuration, the relative intensity of the sensor output has been tracked up to 2173 K and a reasonable sensitivity of 5 K has been achieved. However, in the work reported by Wang *et al.* [7.28], two sapphire rods each of which was 3.23 mm in diameter were arranged end to end with each other such that slow axis of the first rod was aligned with the fast axis of the second resulting in a birefringence-balanced sensing probe. Accurate alignment of the two rods would thus be an important factor in the success of the sensor and this type of arrangement would be even more critical when much smaller fibres (<300  $\mu\text{m}$ ) were used.

## 7.1 Fundamental principles of polarimetry-based sensing

One of the main effects of birefringence in an optical fibre is that the electric field of a lightwave propagating in the fibre is horizontally and vertically-resolved into orthogonally polarised vectors which travel at slightly different velocities. Although the state of polarisation of the light can have an adverse influence on the whole system in interferometric sensors where the phase of the optical wave propagating in the fibre has to be measured, the SOP can be utilised in a number of ways which can provide benefits to fibre optic sensing applications based on polarimetry or the change in birefringence of the light/fibre properties. The typical single-mode fibre can thus be considered as a dual-mode fibre in practice since real fibres contain a certain degree of non-circularity in their cores. The splitting of the fundamental linearly polarised state of light will result in two orthogonally polarised states and travel at different velocities governed by the birefringence,  $b$ , which can be expressed as [7.12]

$$\beta_x - \beta_y = \Delta\beta = bk_0 \quad (7.1)$$

where  $\beta_x$  and  $\beta_y$  are the effective propagation vectors in the  $x$  and  $y$  polarisation directions respectively and  $k_0$  is the propagation number of the wave with wavelength,  $\lambda_0$ , in vacuum given by [7.30]

$$k_0 = \frac{2\pi}{\lambda_0} \quad (7.2)$$

There are several ways in which birefringence can be introduced into an optical fibre or an optical material. Theoretically, the fundamental  $HE_{11}$  mode in a single-mode fibre is linearly polarised such that light launched into and its propagation through a perfectly constructed, i.e. circularly symmetric, fibre will be maintained in its original polarised form [7.12, 7.31]. In practice, however, this is not possible and a certain degree of birefringence is thus inevitably effected in the fibre due to the imperfect circular geometry and asymmetric stress distributions which are built up upon cooling after the fibre drawing process. The mechanical loading or conditions

of the set-up of the fibre are also reasons for the occurrence of birefringence. Tension winding of fibres into coils, multi-layer windings which can give rise to cross-overs between the fibre sections and clamping of the fibre can also result in stress states being built up within the fibre and converted into birefringence. As mentioned above, the Pockels, Kerr and Faraday effects can influence the SOP of a lightwave propagating in a fibre and can be exploited as fibre optic electric and magnetic field sensing mechanisms [7.32]. Another source of birefringence, instead of producing linear birefringence, can lead to the rotation of the state of polarised light within a fibre. Mechanisms which cause circular birefringence include twist stress and magnetic fields [7.12]. In addition, birefringence can also be related to the change in refractive indices induced in an optical fibre when light travelling along the fibre is linearly polarised due to stress-induced birefringence formed within the fibre during fabrication and is known as the photoelastic effect [7.12, 7.33]. The forms of birefringence mentioned above are sensitive to various external perturbations effected by one or more physical parameters such as stress, strain, temperature, force and pressure and are thus appropriate as transduction mechanisms in fibre optic polarimetry-based sensing applications. However, as is usually the case in most practical situations, both linear and circular birefringence can be found to exist together in a fibre and can be treated using the Jones and/or Mueller analyses.

A simple and common method of defining a state of polarisation is the use of the four-component Stokes vector representation and are expressed as [7.32, 7.33]

$$s_0 = A_x^2 + A_y^2 \quad (7.3)$$

$$s_1 = A_x^2 - A_y^2 \quad (7.4)$$

$$s_2 = 2A_x A_y \cos \delta \quad (7.5)$$

$$s_3 = 2A_x A_y \sin \delta \quad (7.6)$$

where  $A_x$  and  $A_y$  are the intensities of the orthogonally polarised components in the  $x$  and  $y$  directions respective and  $\delta$  the retardation in radians of the  $y$ -component with respect to the  $x$ -component. Experimentally, it can be relatively simple to determine

the four Stokes components through the use of appropriate combination of a linear polariser, a quarter-wave plate and a photodetector sensitive to the wavelength investigated. In general, a quarter-wave plate leads to the conversion of a linearly polarised lightwave into circular polarisation. It is noted, however, that since it is beyond the scope of this work to give a complete treatment of the analyses involved in describing the subject of polarisation, only the relevant expressions are given.

The first of the Stokes component,  $s_0$ , represents the total intensity of the lightwave given as [7.32, 7.33]

$$s_0^2 = s_1^2 + s_2^2 + s_3^2 \quad (7.7)$$

$s_1$  indicates the intensity difference between the horizontal ( $x$ ) and vertical ( $y$ ) orthogonal polarisation components.  $s_2$  represents the intensity difference between the  $\pi/4$  and  $3\pi/4$  polarisation components while  $s_3$  is the difference in intensity between the right and left circular components. Another method to describe the polarisation state of a lightwave is through the use of a Poincaré sphere in which any one possible state can be mapped to the surface of the sphere. However, this technique is quite tedious to employ when a large number of optical elements is involved. Both the Jones and Mueller calculus are two of the analytical techniques which can be more suitably exploited to describe a polarisation state and its transformation through the use of relatively straightforward matrices [7.32, 7.33]. The state of polarisation in the Jones calculus is represented by a two-component complex matrix in the form [7.33]

$$\hat{a} = \begin{bmatrix} A_x e^{i\delta_x} \\ A_y e^{i\delta_y} \end{bmatrix} \quad (7.8)$$

where  $A_x$  and  $A_y$  are the intensities of the orthogonal  $x$  and  $y$  polarisation components,  $\delta_x$  and  $\delta_y$  the phases of the  $x$  and  $y$  waves respectively. The optical elements, such as polarisers, wave-plates and retarders which are involved in the Jones analysis are represented by  $2 \times 2$  with complex components. The polarisation state in the Mueller

calculus, on the other hand, can be represented by the four-component Stokes vector,  $\hat{S}$ , given as [7.33]

$$\hat{S} = \begin{bmatrix} A_x^2 + A_y^2 \\ A_x^2 - A_y^2 \\ 2A_x A_y \cos \delta \\ 2A_x A_y \sin \delta \end{bmatrix} \quad (7.9)$$

where all the parameters have already been defined in **Eqs. 7.3 – 7.6**. In order for the optical elements to be incorporated into the Mueller analysis, they are represented by 4 x 4 matrices in which all the associated quantities are real, as opposed to the Jones calculus formalism. Both methods, however, can be employed in an identical manner in the way that the desired lightwave output state,  $\hat{I}_o$ , after passing through the various optical components in its propagation path, can be obtained by multiplying the respective matrices representing the optical components sequentially in the form given by [7.33]

$$\hat{I}_o = M_f M_{f-1} \dots M_2 M_1 \hat{I}_i \quad (7.10)$$

where  $\hat{I}_i$  is the input polarisation state and the subscripts after the matrix elements,  $M$ , denote the order in which the lightwave encounters the optical elements. Analysing the transformation of the state of polarisation of a lightwave through a series of optical components by using the Jones or Mueller technique can thus be relatively simple and straightforward.

Another polarimetric mechanism which can be employed in sensing applications is the change in refractive index of certain materials due to the direct application of stress and/or strain [7.32, 7.33, 7.34]. These types of materials are also known as photoelastic materials and can obviously be employed for strain, weight, force, pressure and stress (or any external which can create stress/strain states in the fibre) monitoring. Application of one of the external perturbations which results in the creation of stress or strain in the photoelastic material in a direction generally

perpendicular to the axis of propagation of the lightwave will thus lead to a retardation,  $\delta$ , of the light given as [7.33]

$$\delta = \frac{2\pi C_{\sigma} t}{\lambda} \sigma_i + \frac{2\pi C_{\epsilon} t}{\lambda} \epsilon_i \quad (7.11)$$

where  $C_{\sigma}$  and  $C_{\epsilon}$  denote the stress-optic and strain-optic coefficients respectively,  $t$  the optical path length through the photoelastic material,  $\sigma_i$  the applied stress in a direction  $i$ ,  $\epsilon_i$  the applied strain in direction  $i$  and  $\lambda$  the wavelength of the input lightwave.

## 7.2 Polarimetric sensing with sapphire fibres

Besides having good physical properties such as high melting point, high strength and good mechanical stability at high temperatures, sapphire is also a uniaxial anisotropic crystalline material exhibiting double refraction (in effect, making it naturally birefringent). Unlike isotropic materials such as glasses and amorphous solids, in which the velocity of light travelling in the medium is the same in all directions and for all polarisations, the intrinsic optical properties of anisotropic materials depend on the direction of light propagation in the medium. Thus, in all but one direction through sapphire, double refraction occurs in which the input lightwave is split into its two orthogonal components and propagates at two different velocities through the crystal. The component of light for which there is no change in velocity with direction (i.e. having constant refractive index) is known as the ordinary ray (refractive index,  $n_o$ ) while that which undergoes velocity change depending on the direction of travel within the crystal is known as the extraordinary ray (with refractive index,  $n_e$ ). In addition, the polarisation plane of the ordinary ray is perpendicular to a principal crystallographic section containing the direction of the optic axis while the extraordinary component is in parallel with the optic axis [7.35, 7.36]. The one direction through which there is no double refraction is the optic axis and the two components thus travel at the same velocity along this axis. In crystals or materials in which only one such axis (optic axis) exists, the material is referred to as uniaxial.

Therefore, when unpolarised (or polarised) light is transmitted in sapphire along the optic axis, the crystal behaves isotropically and the state of polarisation of the input lightwave remains unchanged while propagating through the crystal. The  $c$ -axis in sapphire is thus a principal crystallographic plane/section which is parallel to the optic axis. In any other axis such as the  $a$  or  $b$  axis, double refraction occurs and while the ordinary ray ( $o$ -ray) remains constant, the velocity of the extraordinary ray ( $e$ -ray) depends on the direction of travel in the crystal. In sapphire the velocity of the ordinary ray is always slower than that of the extraordinary ray [7.37], hence, sapphire is known as a negative uniaxial crystal [7.35, 7.36]. As both the change in refractive indices between the  $o$ - and  $e$ -rays and the change in the physical length of sapphire are dependent on temperature, a polarimetric high temperature sensor based on this material can be realised by determining the resulting retardation of the output polarisation state from a linearly polarised input lightwave. Further, the respective intensities of the orthogonally polarised components after transmission through the sapphire material (sapphire fibre in this case) can also be analysed for its temperature dependence. In addition, other perturbations such as bending and strain can also introduce variation in birefringence into a sapphire system through similar mechanisms which have been mentioned previously. A polarimetric bend/strain sensor can thus be realised by investigation of the bend/strain dependence of sapphire.

### 7.3 Temperature sensing experiments

The anisotropy and high melting point of sapphire are exploited for potential polarimetry-based high temperature sensing applications. Both  $c$ - and  $a$ -axis fibres have been investigated in which the four-component Stokes vector ( $s_0 - s_3$ ) as well as the direct intensities of the orthogonal components of the output lightwave were measured using dedicated detectors. By measuring the Stokes components, the resulting retardation,  $\delta(T)$ , of the lightwave in propagating through the sapphire fibres as a function of temperature can be obtained from dividing Eq. 7.6 by Eq. 7.5 to give

$$\delta(T) = \tan^{-1} \left( \frac{s_3}{s_2} \right) \quad (7.12)$$

Also, the direct measurement of the intensities of the orthogonally polarised components of the output lightwave can be used to indicate the temperature-dependent state of polarisation [7.17] in travelling through the two types of fibres (*a*- and *c*-axis). This has been done using the difference-over-sum technique which has the added benefit of reducing or eliminating any light source intensity fluctuation. The resulting ratio,  $R(T)$ , from this technique can be written in the form

$$R(T) = \frac{I_{\rightarrow} - I_{\uparrow}}{I_{\rightarrow} + I_{\uparrow}} \quad (7.13)$$

where  $I_{\rightarrow}$  represents the measured intensity of the horizontally polarised component and  $I_{\uparrow}$  the intensity of the vertical component.

### 7.3.1 Temperature sensing with *c*-axis sapphire fibres

Although the ordinary and extraordinary rays in *c*-oriented sapphire fibres have the same propagating velocities (i.e.  $n_o = n_e$ ) through the material, application of heat to one end of the fibre may induce variations in the refractive indices and will cause changes in the physical length of the heated section through thermal expansion which can then result in changes in the detected quantities given by **Eqs. 7.12** and **7.13**. These have been investigated in the following experiments.

The schematic diagram for the temperature-dependent phase retardation (**Eq. 7.12**) measurement system employing *c*-axis sapphire fibres is shown in **Figure 7.1**. The optic axis in this case is also the longitudinal fibre axis and this is perpendicular to the rounded hexagonal *c*-crystallographic plane/section of the sapphire fibre. A 10 mW *Mitsubishi Corp* IR laser diode (central wavelength at 1310 nm) driven by a *Laser2000* general purpose laser diode driver was employed as the light source. Light launched from the laser diode was collimated by a microscope objective (X20 MO) and linearly polarised in the horizontal direction after passing through a linear

polariser. The horizontally polarised 1310 nm light was then focused onto one end of a *c*-oriented sapphire fibre with the aid of another microscope objective (X10 MO). The sapphire fibre used was approximately 653 mm long with a nominal diameter of 425  $\mu\text{m}$  and fine-polished to 1  $\mu\text{m}$  at both ends. A stabilised *CARBOLITE* tube furnace, approximately 300 mm in length, has been positioned as shown in **Figure 7.1** so that the output light could be measured from the other end of the fibre. High-temperature ceramic wool has been used as plugs to cover both ends of the tube furnace to maintain a stable thermal environment within the furnace chamber as well as to reduce radiation emitted by the furnace material at high temperatures ( $>1073$  K). Both ends of the fibre were also supported on two *New Focus 9122* fibre holders, with the input end locked so that the fibre could not be moved accidentally. Another X10 MO served to collimate the output light intensity onto the detector surface of a *Thorlabs Inc. PA430* polarimeter with a sensitive wavelength range from 1100 to 1700 nm. The polarimeter can be set to acquire the desired number of averages or samples and has been configured to measure the normalised Stokes parameters as defined by **Eqs. 7.3 – 7.6** from which the associated retardation value can be obtained from **Eq. 7.12**. The maximum temperature investigated was 1373 K, beyond which the signal was lost in the background thermal emission from the fibre as indicated by the polarimeter while the temperature increment was 50 K up to the maximum. The number of data averages taken per temperature point was 100 and stored inside a computer for further processing to obtain the desired retardation values.

To measure the direct intensities of the orthogonal components from the same *c*-oriented sapphire fibre, the experimental set-up as shown by the schematic diagram in **Figure 7.2** has been used. Green laser light with a central wavelength of 532 nm from a *Laser2000* frequency-doubled Nd:YAG laser was polarised by a linear polariser with its axis in the horizontal position and launched into one end of the sapphire fibre via a X10 MO. The relatively long length of the fibre used enabled the furnace to be positioned approximately mid-way between the fibre and another X10 MO was used to collimate the output light. A non-polarising beam splitter was then employed to equally split the on-coming collimated beam onto two identical *Hamamatsu C5460* avalanche photodiodes (APDs). In addition, two linear polarisers with their polarisation axes orthogonally aligned (one horizontal and the second

vertical) have been placed directly in front of the APDs, resulting in two intensities,  $I_{\rightarrow}$  and  $I_{\uparrow}$  respectively being measured/monitored. The maximum temperature studied was 1473 K, which was also the maximum limit of the furnace, with each temperature increment of 100 K.

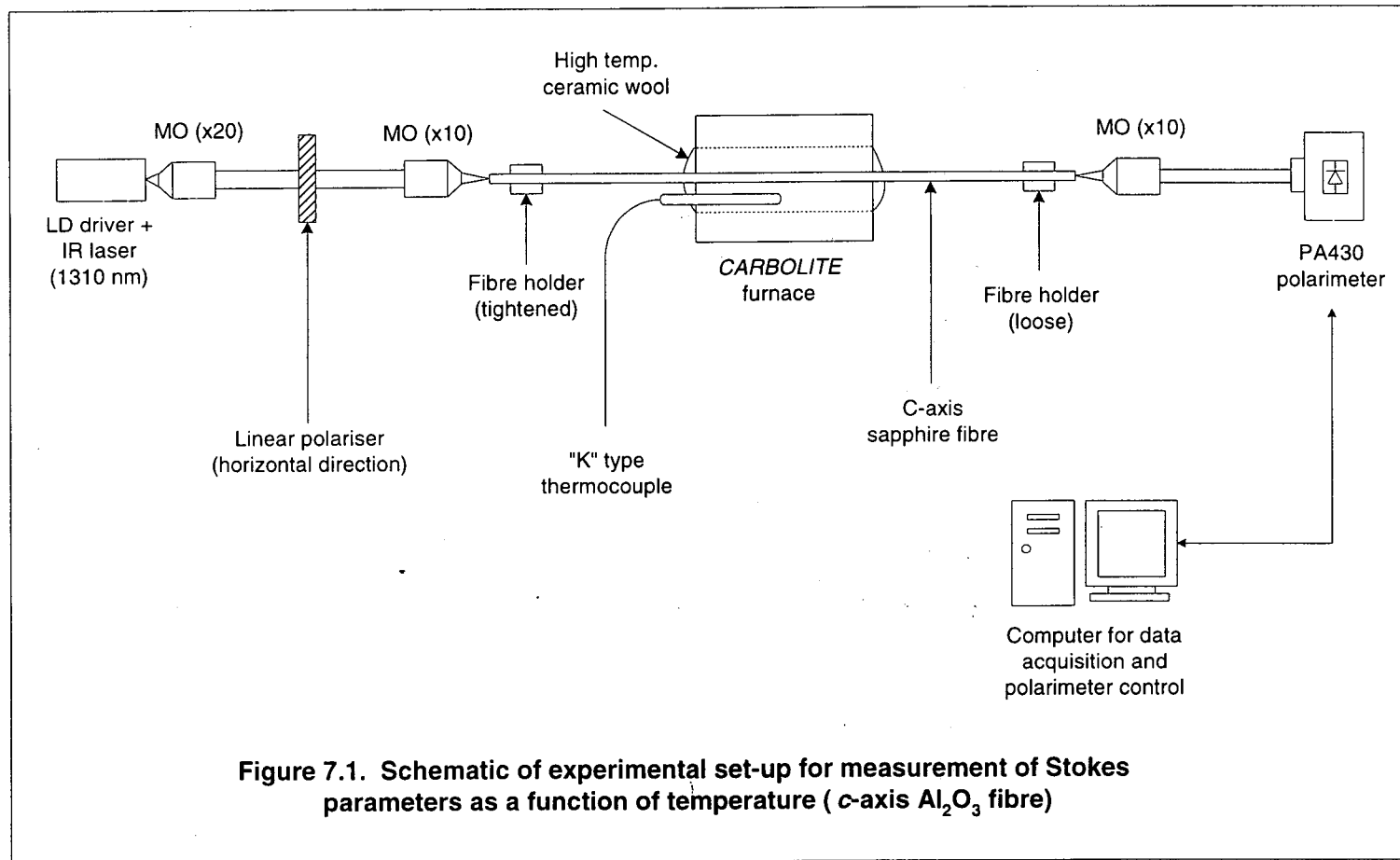
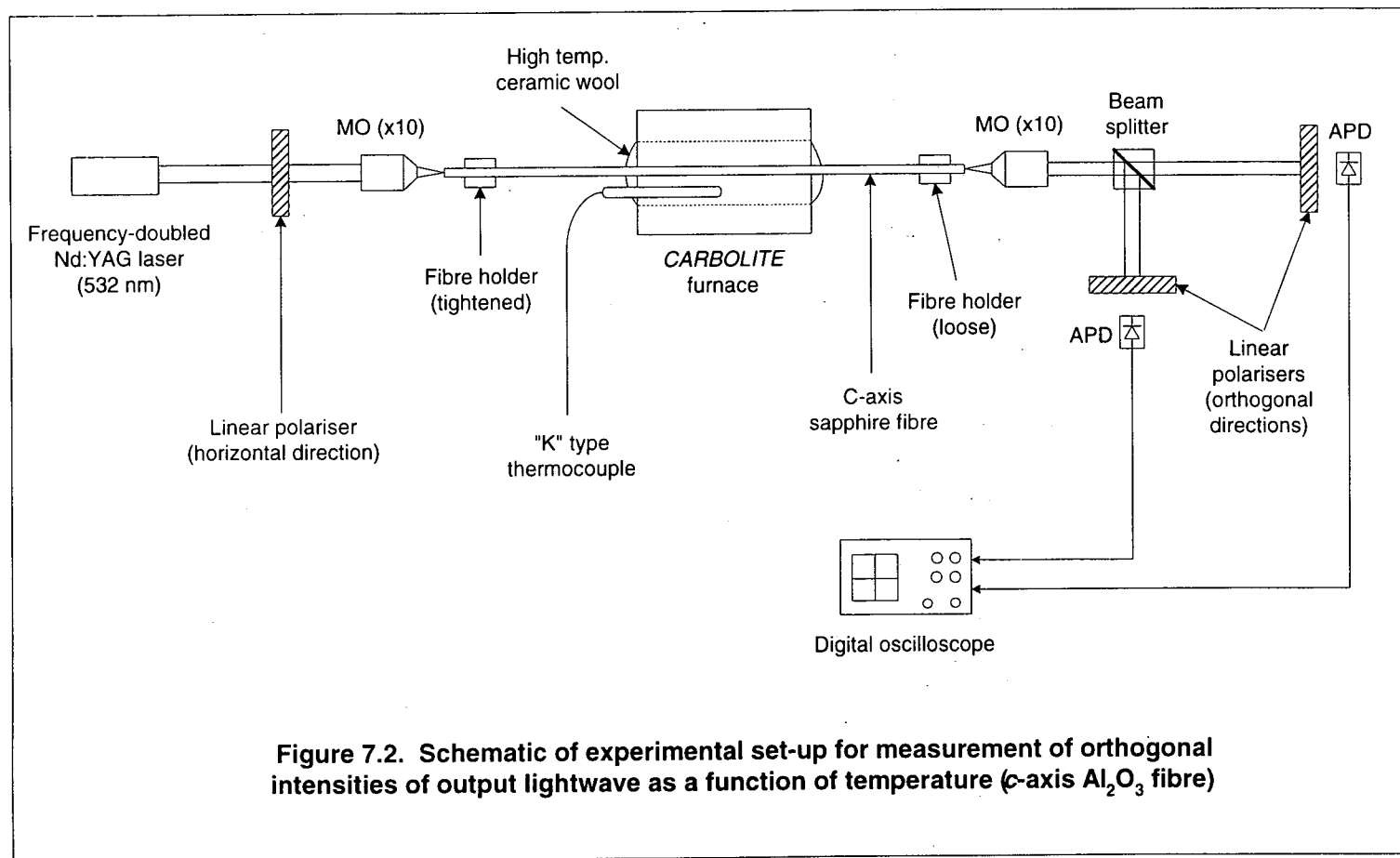


Figure 7.1. Schematic of experimental set-up for measurement of Stokes parameters as a function of temperature (*c*-axis  $\text{Al}_2\text{O}_3$  fibre)



### 7.3.2 Results and Discussion

The normalised Stokes parameters have been measured using the *Thorlabs PA430* polarimeter and the associated retardation for the *c*-axis sapphire obtained via **Eq. 7.12**. In this way, the retardation values corresponding to the various temperatures up to 1373 K have been obtained and are plotted in **Figure 7.3**. As shown in the figure, there is generally no meaningful correlation between the change in retardation and temperature throughout the entire temperature range investigated for the *c*-axis sapphire fibre. The retardation can be seen to fluctuate irregularly between 0.15 and  $-0.25$  rad about a centre retardation at approximately  $-0.05$  rad. It is, thus, rather obvious that this parameter is not a suitable indication of temperature and this technique employing a polarimeter to obtain the retardation indirectly by measuring the four-component Stokes vector cannot be readily exploited for temperature sensing applications. More generally and importantly, it shows that there is no significant change in the retardation of the components of light when subjected to high temperatures while propagating within the fibre. This also indicates that both the ordinary and extraordinary refractive indices remained relatively constant. Another important consideration is the fact that the fibres used were not clad, hence, the polarised input signal propagating along the fibre could have been scrambled, making measurements difficult.

The measured intensities of the orthogonal components of the output light have been monitored by two APDs in accordance to **Figure 7.2**. By employing a difference-over-sum technique, a ratio,  $R(T)$ , of the lightwave orthogonal intensities, or more generally, the state of polarisation of the light since this is also a measurement of the relative phase or velocities of the orthogonal components [7.17], has been obtained as a function of temperature. The results of  $R(T)$  have been plotted in **Figure 7.4** up to a maximum temperature of 1473 K in steps of 100 K. Again, this ratio has been found to be relatively independent of temperature, indicating that, in general, *c*-axis sapphire fibres are unsuitable as polarimetric temperature sensing elements. This also indicates that the lightwave travelling along the fibre remains relatively unchanged when subjected to a wide range of temperatures. The values of  $R(T)$  can be observed to be generally constant, close to a value of 1, implying that the state of the detected output light remained linearly polarised while travelling through the

sapphire fibre. Therefore, the state of linear polarisation (horizontal direction) as enforced by the input polariser can be assumed to remain constant in a  $c$ -axis sapphire fibre. The retardation,  $\delta(T)$  and difference-over-sum ratio,  $R(T)$ , are given in **Tables 7.1a** and **7.1b** respectively, together with the associated errors which have been found to be relatively large. The large errors can be attributed to the fluctuating components as a direct result of scrambling of the lightwave within the fibre.

As has been described in the above experiments and indicated in **Figures 7.1** and **7.2**, the outputs from both lasers have been horizontally polarised by the linear polariser with its fast axis aligned along the horizontal position. This implies that since  $n_o$  and  $n_e$  in the  $c$ -axis sapphire fibres remain unchanged, the polarisation state of light propagating in the fibre remains constant. At the output to the detectors (polarimeter and APDs), the magnitude of the vertical component (or intensity) detected would have been zero or close to zero while the horizontal intensity was at a maximum value. The fact that  $R(T)$  was found to be approximately constant ( $\sim 1$ ) indicates that the state of polarisation is being scrambled as the light propagates along the fibre. This arises due to the highly multi-mode nature of the fibre with many possible skew rays able to propagate. Previous workers using sapphire mini-rods [7.28, 7.29] were able to ensure a collimated beam passed cleanly through the samples with no total internal reflections from the rod walls. This polarisation scrambling was therefore not observed in this case.

Figure 7.3. Retardation of  $c$ -axis  $\text{Al}_2\text{O}_3$  fibre as a function of temperature

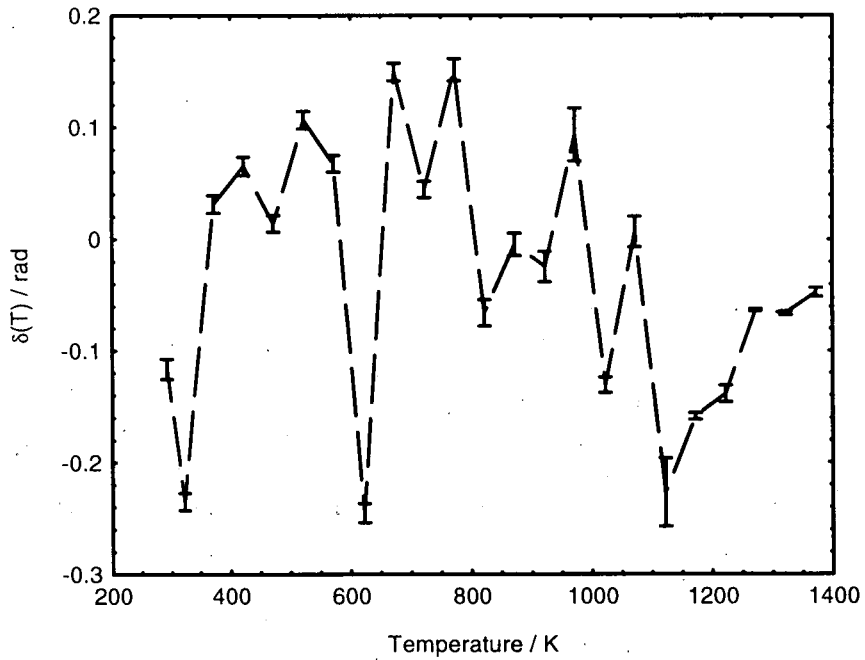
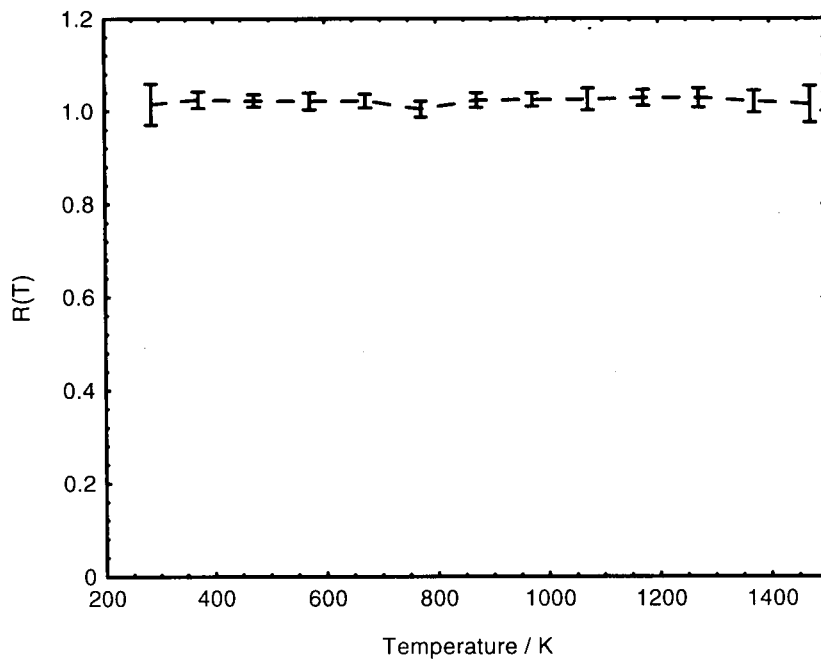


Figure 7.4. Ratio of orthogonally polarised components of light from  $c$ -axis  $\text{Al}_2\text{O}_3$  fibre as a function of temperature



**Table 7.1a. Retardation of *c*-axis sapphire fibre as a function of temperature**

Temp / K	$\delta(T)$ / rad	Error / %
292	-0.116286	15.37
323	-0.235110	6.63
373	0.031462	48.90
423	0.065565	24.87
473	0.013989	106.70
523	0.106553	14.60
573	0.067559	21.68
623	-0.245209	7.09
673	0.149286	10.64
723	0.044737	32.83
773	0.151123	12.94
823	-0.065662	36.27
873	-0.004533	440.35
923	-0.024372	112.45
973	0.093418	50.51
1023	-0.130579	10.74
1073	0.006943	395.73
1123	-0.226746	27.10
1173	-0.158715	3.74
1223	-0.138314	10.76
1273	-0.063333	3.64
1323	-0.066195	5.18
1373	-0.047533	17.16

**Table 7.1b. Difference-over-sum ratio,  $R(T)$ , of *c*-axis sapphire fibre as a function of temperature**

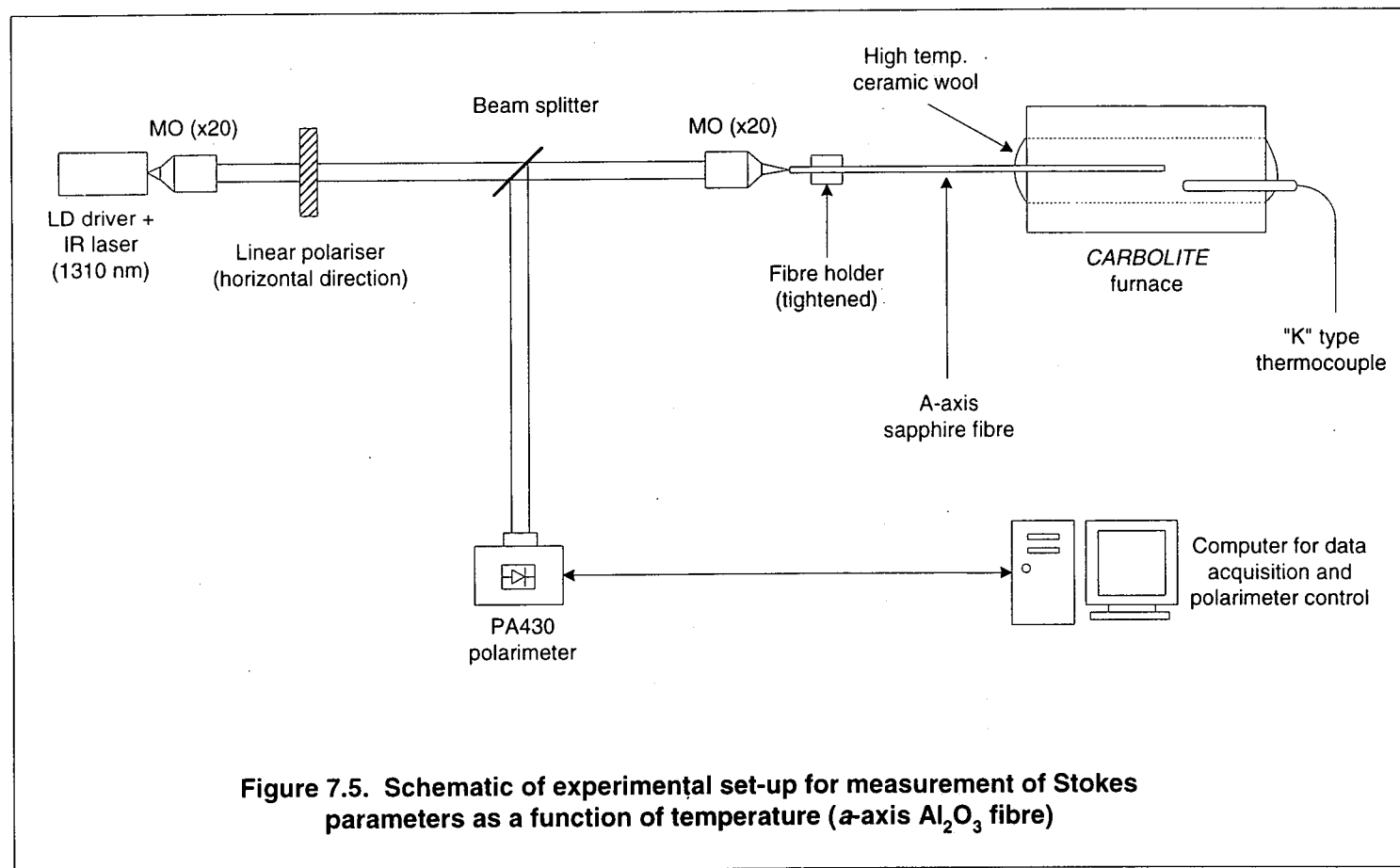
Temp / K	$R(T)$	Error / %
285	1.014801	8.72
373	1.024121	3.51
473	1.022400	2.60
573	1.021016	3.57
673	1.021939	2.86
773	1.004186	3.37
873	1.023516	3.12
973	1.024253	2.74
1073	1.025272	4.69
1173	1.028609	3.39
1273	1.028504	3.98
1373	1.020887	4.63
1473	1.015031	7.74

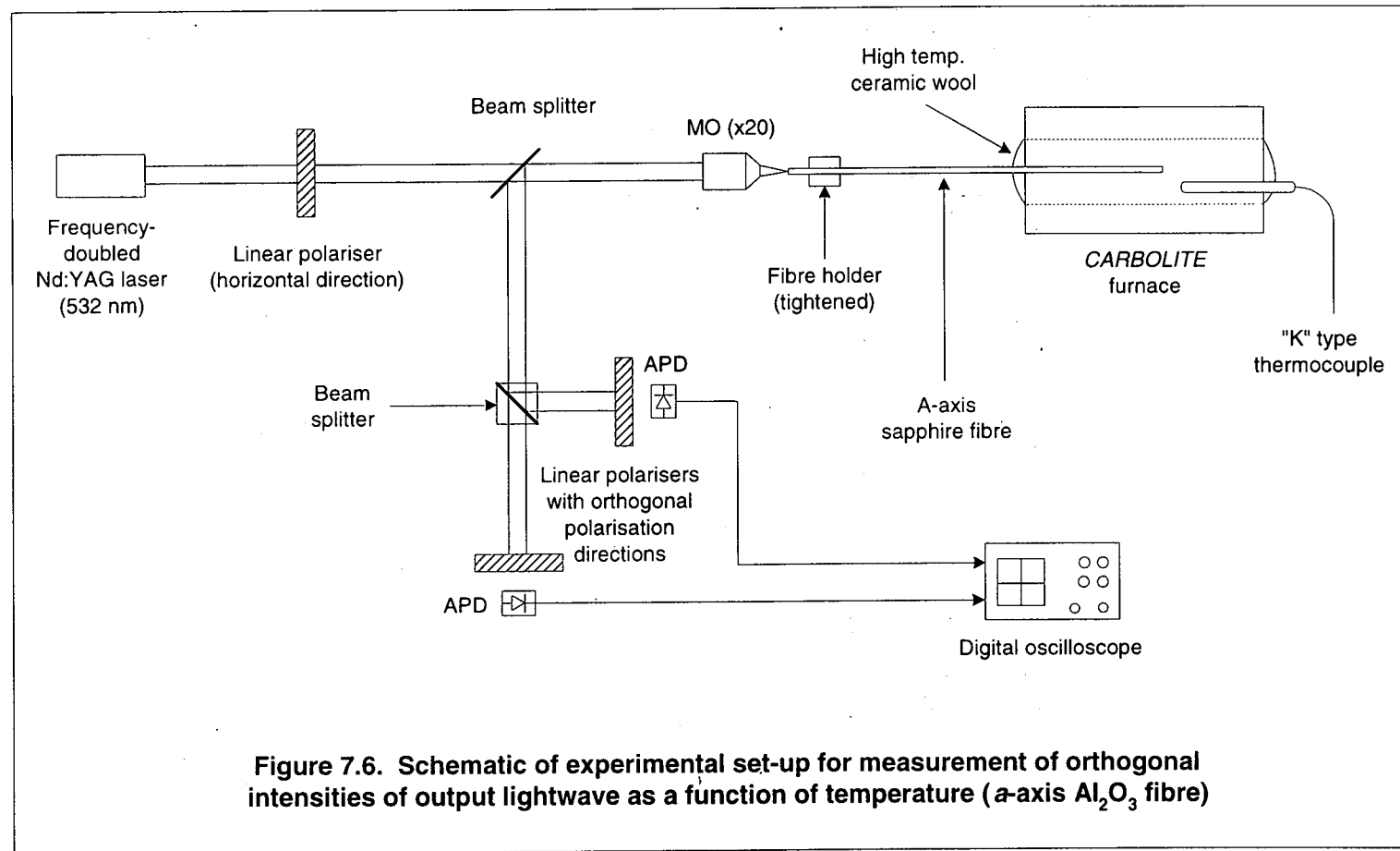
### 7.3.3 Temperature sensing with *a*-axis sapphire fibres

For the measurement of the retardation due to an *a*-axis sapphire fibre, a schematic diagram of the temperature sensing experiment is shown in **Figure 7.5**. 1310 nm light from an infrared laser diode was linearly polarised in the horizontal direction after being collimated through a X20 microscope objective. Another X20 MO has been used to focus the polarised radiation onto one end of an *a*-oriented sapphire fibre which was ~200 mm in length with a nominal diameter of ~130  $\mu\text{m}$ . The fibre was not of sufficient length to be inserted through the entire furnace chamber to enable the output light to be measured from the other end. Hence, a reflective scheme has been employed in which approximately 100 mm of the sapphire fibre were positioned inside the furnace. High temperature ceramic wool was also used in this experiment to plug the two ends of the tube furnace for preventing excessive heat loss and reducing undesired radiation from the furnace at high temperatures. The reflected light from the far end of the fibre which has been located inside the furnace was collimated by the second X20 MO and guided into the PA430 polarimeter by a beam splitter as shown in the figure. The relative changes in the four Stokes parameters with respect to the values at room temperature were then measured by the polarimeter and the data stored inside a computer. The Stokes parameters have been monitored at each temperature increment of 100 K from room temperature up to a maximum temperature of 1473 K. An arbitrary direction of polarisation has been decided for the fibre, hence, the horizontally polarised input light was launched into the fibre end at a random angle with respect to the elongated *a*-crystallographic section/plane. This was seen to be a reasonable choice since it has been decided to measure only the relative retardation of light at elevated temperatures from that at room temperature. An average of the Stokes parameters was recorded by the polarimeter at each temperature increment and stored for further processing to obtain the desired retardation values.

**Figure 7.6** shows a schematic diagram of the experiment used to monitor the two orthogonal output intensities after travelling through the sapphire fibre which has been subjected to heating provided by the *CARBOLITE* furnace. Light at a wavelength of 532 nm from a frequency-doubled Nd:YAG laser was polarised in the horizontal direction and launched into the *a*-axis fibre by a X20 MO. The reflected

radiation was then collimated by the same MO. A beam splitter was used to direct the collimated light onto two avalanche photodiodes via another non-polarising beam splitter as shown in the figure. Two linear polarisers with orthogonal polarisation axes were placed directly in front of the APDs so that one was used to measure the vertical output component while the other measured the horizontal output intensity from the sapphire fibre. The orthogonal intensities were displayed on a *Tektronix* digital oscilloscope capable of averaging functions and recorded.





### 7.3.4 Results and discussion

The calculated retardation values,  $\delta(T)$ , of the  $a$ -axis sapphire fibre can be obtained from the third and fourth ( $s_2$  and  $s_3$ ) Stokes parameters according to Eq. 7.12. The resulting retardation has been plotted in Figure 7.7 as a function of temperature over a relatively wide range from room temperature up to 1473 K. It can be seen that there is an obvious dependence of the calculated retardation on temperature. The retardation profile resembles a section of a sinusoid, increasing rapidly from 673 K, after an initial decrease from room temperature, to a peak of  $-0.0228$  rad at 1073 K. This was followed by a small reduction in retardation as the temperature was further increased and was observed to remain relatively constant beyond 1273 K. The minimum retardation of approximately  $-0.0459$  rad was observed at 373 K. The largest temperature sensitivity of the  $a$ -axis sapphire fibre can be inferred from the steep gradient between 673 and 1073 K, indicating a possibly useful temperature-dependent retardation curve within this range.

The ratio,  $R(T)$ , obtained from the difference-over-sum technique of both the orthogonal intensities measured using two APDs over the same temperature range as the above experiment is presented in Figure 7.8. From the work of Murukeshan *et al.* [7.17], a ratio of  $\pm 1$  can be taken to indicate a linearly polarised output with respect to the input polarisation state while a value of 0 indicates circular polarisation. Using this technique, a small temperature dependence of  $R(T)$  has also been observed.  $R(T)$  was found to increase from 0.645 at room temperature (291 K) to a maximum value of 0.759 at 1273 K. A slight decrease has been observed in the  $R(T)$  values between 773 and 973 K. This could very well be due to very small temperature-induced bending/expansion of the fibre section which was positioned horizontally (parallel to the longitudinal furnace axis) inside the furnace at elevated temperatures. In addition, the sensitivity could be reduced due to the polarisation scrambling again. However, it can be seen that the  $R(T)$  values over the entire temperature range remained between 0.6 and 0.8 radians, indicating that the lightwave which has been elliptically polarised at room temperature was subjected to further changes in its polarisation state as temperature was increased. The maximum ratio at 1273 K was seen to be closest to the circular polarisation state for an  $a$ -axis sapphire fibre. Although relatively large errors have been incurred, the general

profile of the  $R(T)$  curve is seen to be temperature dependent. However, other ways should be found to increase the sensitive range of the  $R(T)$  values for practical sensing applications employing such fibres. One way to do this is to change the orientation of the fibre axis to the input SOP to  $45^\circ$  [7.28, 7.33]. Both the retardation and difference-over-sum values for the  $a$ -axis sapphire fibre are listed in **Tables 7.2a** and **7.2b** respectively.

It is noted that the angle the horizontally polarised input lightwave made with respect to the  $a$ -crystallographic plane of the sapphire fibre has been arbitrarily selected and not at  $\pi/4$  rad (or  $45^\circ$ ) as has been reported by several authors [7.28, 7.29]. One of the main reasons for this was the difficulty encountered in the alignment of the fibre plane to the polarisation vibration direction of the input light due to the relatively small diameter ( $\sim 130\mu\text{m}$ ) of the fibre used. It is also noted that materials employed in previous polarisation work by some authors [7.28, 7.29] were, in fact, sapphire rods with diameters larger than 3 mm. Hence, the question of alignment difficulty need not be raised. Indeed, if the vibration direction of the input polarised light and the fast axis ( $a$ -plane) of the fibre has been accurately aligned at  $45^\circ$  to each other, maximum sensitivity from the fibre can be expected [7.28, 7.32, 7.33]. However, this is also the second important reason for the decision to select an arbitrary angle between the vibration direction of the polarised light and the fibre  $a$ -axis. It was thought to be useful for temperature sensing applications in a practical situation to obtain both the retardation,  $\delta(T)$ , and  $R(T)$  responses to temperature without having the need for exact alignment of the associated quantities.

Figure 7.7. Retardation of  $a$ -axis  $\text{Al}_2\text{O}_3$  fibre as a function of temperature

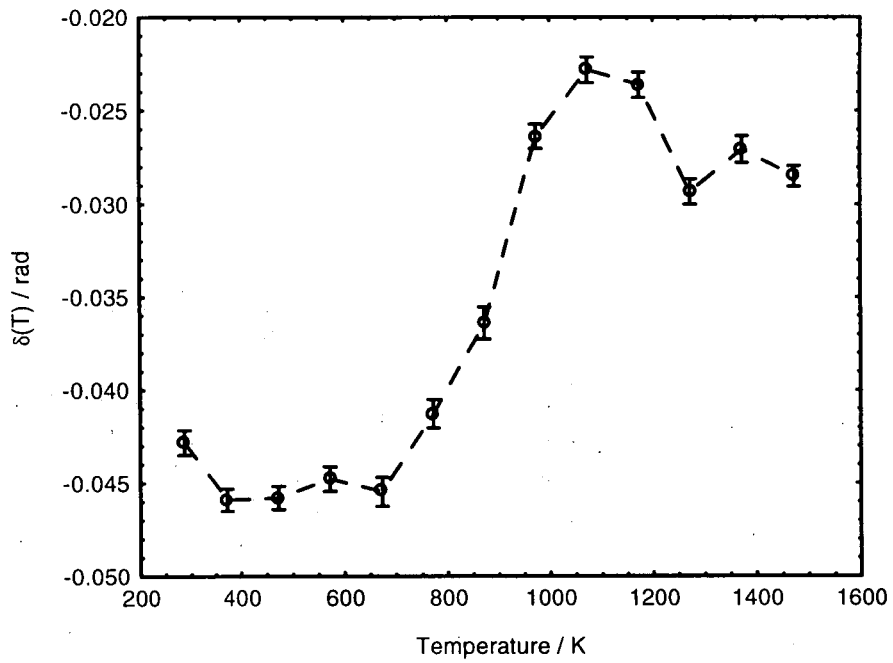
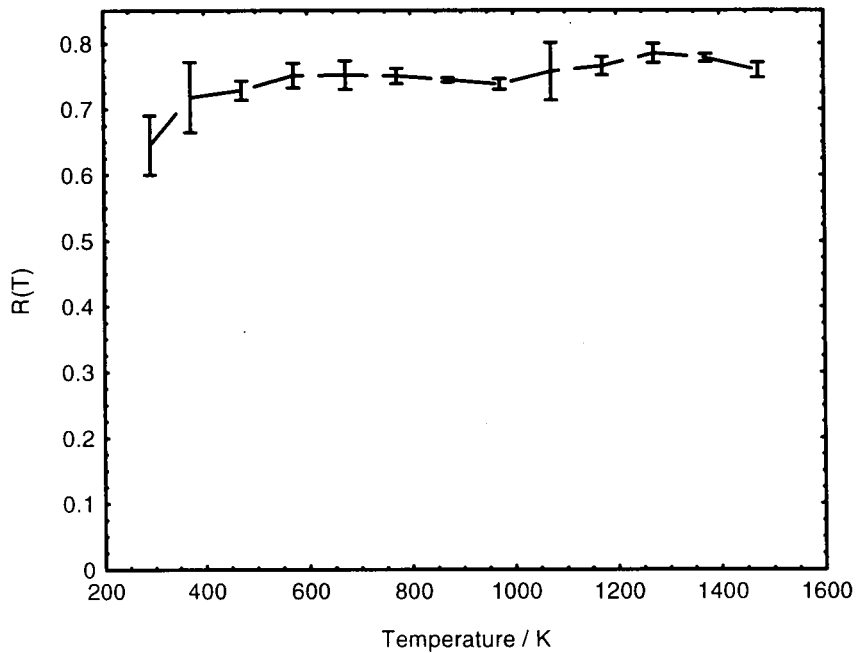


Figure 7.8. Ratio of orthogonally polarised components of light from  $a$ -axis  $\text{Al}_2\text{O}_3$  fibre as a function of temperature



**Table 7.2a. Retardation of  $a$ -axis sapphire fibre as a function of temperature**

Temp / K	$\delta(T)$ / rad	Error / %
287	-0.0428275	3.08
373	-0.0459008	2.60
473	-0.0457820	2.75
573	-0.0447646	2.94
673	-0.0454552	3.42
773	-0.0412807	3.70
873	-0.0364029	4.73
973	-0.0263869	4.96
1073	-0.0228294	5.98
1173	-0.0236199	5.73
1273	-0.0293432	4.65
1373	-0.0270766	5.28
1473	-0.0285049	3.79

**Table 7.2b. Difference-over-sum ratio,  $R(T)$ , of  $a$ -axis sapphire fibre as a function of temperature**

Temp / K	$R(T)$	Error / %
291	0.645416	13.98
373	0.717868	14.97
473	0.728713	4.06
573	0.751130	5.04
673	0.751842	5.81
773	0.750322	3.10
873	0.744096	0.80
973	0.737799	2.15
1073	0.757109	11.55
1173	0.765267	3.71
1273	0.784770	3.79
1373	0.777515	1.54
1473	0.759121	2.98

#### 7.4 3-point bending of sapphire fibres

One of the major applications of fibre optic sensors has been in monitoring the deformations exerted by external influences such as temperature, strain, stress, bending and other parameters on civil structures. Knowledge of the stress/strain levels to which structures have been subjected is an important economic and security/safety factor which can permit preventive maintenance and reduce or eliminate the risk of critical (and sometimes fatal) failures. Another major application in civil engineering is the progress towards smart structure/material sensing [7.38] in which the monitored parameter(s) can, in turn, be used as a feedback to allow automatic corrective measures to be taken or, if a critical level is reached, to terminate any related functions and issue an alarm. Most of these applications have employed glass-based fibres as sensing elements. However, extra care has to be taken when mounting or embedding glass fibres in structures which may undergo very large deformations due to the relatively weak mechanical properties of glass fibres. In cases where high sensitivities are required, the glass fibre may have to be stripped of its protective coating. This will further weaken the strength of such fibres and may render the glass fibres unsuitable for many general sensing applications. Both single-mode and high birefringence glass fibres have been studied for potential smart structure sensing based on polarimetry [7.17] and have been found to be highly sensitive to breakage during the curing process while being embedded in a host material as well as to impact loading during testing. Due to the good physical properties and high strength at elevated temperatures, sapphire fibres may be employed as suitable candidates/alternatives in many structural and smart material sensing applications. In addition, sapphire fibres are generally unclad and suitable means could, perhaps, be found to make them highly sensitive to the parameter(s) of interest.

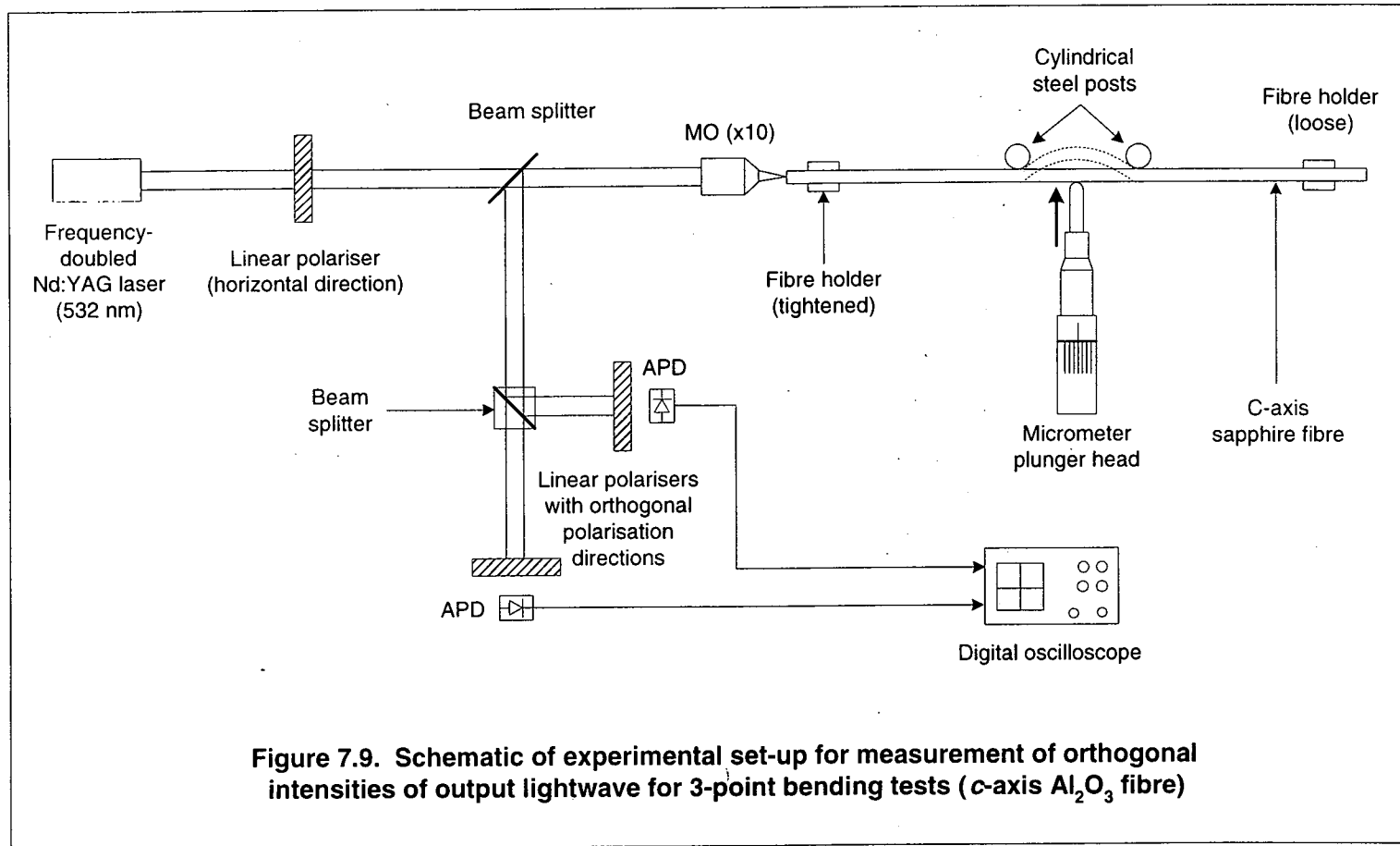
C-oriented sapphire fibres allow propagation of a lightwave along its optic axis without any or with very little variation in its SOP since both the ordinary and extraordinary refractive indices ( $n_o$  and  $n_e$ ) are identical along this optic axis. This also implies that the orthogonal components of input light travel at the same velocity, hence, no retardation or phase difference should be expected. However, while undergoing deformation such as bending, linear birefringence may be induced due to

asymmetric stress distribution within the fibre as well as slight changes to the fibre geometry. The variation of the velocity/phase change of the orthogonal components of an input lightwave due to the application of a load in the form of a 3-point bend has been investigated for *c*-oriented sapphire fibres. The *a*-axis sapphire fibre, on the other hand, exhibits double refraction in which the ordinary and extraordinary light components travel at two different velocities. Bending the fibre may thus result in the introduction of additional birefringence and these fibres were also studied in 3-point bend tests with various bend depths/radii in the following work.

#### 7.4.1 3-point bending of *c*-axis sapphire fibres

A schematic diagram of the experimental set-up for directly measuring the orthogonal components of the output light is shown in **Figure 7.9**. The measurement of the two components allowed the associated intensities to be monitored simultaneously from which the ratio,  $R_{bend}$ , governed by **Eq. 7.13**, was calculated. Green laser light at 532 nm was linearly polarised in the horizontal direction and launched into one end of the same *c*-axis fibre via a X10 MO. Light-reflected from the far end was collimated and directed via a beam splitter to the two APDs in front of which linear polarisers, with orthogonal polarisations aligned in the horizontal and vertical directions, have been located as shown in the figure. The detector outputs were finally sent to a digital oscilloscope so that readouts could be obtained. The input end of the ~650 mm long *c*-axis fibre (diameter ~425  $\mu\text{m}$ ) was secured to prevent any accidental movement while the other far end was supported loosely in a fibre holder. A set of two cylindrical steel rods was inserted vertically into a solid aluminium metal block and positioned at approximately the mid-point of the fibre. The distance between the centres of the rods (gauge length) was measured to be 50 mm. A micrometer plunger head (1 $\mu\text{m}$  resolution) was then securely attached midway between the two rods and the entire assembly was employed as a 3-point bending fixture, as shown in **Figure 7.9**. The whole system has been set up as a reflective scheme in which the reflected lightwave from the far end of the fibre was guided to the two avalanche photodiodes via a set of beam splitters after being re-collimated by the X10 MO as indicated in the figure. Two polarisers with orthogonally aligned polarisation axes were then placed directly in front of the APDs. Both 1 mm and 2 mm bending tests have been carried out with constant bend

increments of 0.1 mm. An average of 30 readings was taken at each increment for both tests.



## 7.4.2 Results and Discussion

The results of the 1 and 2 mm bend tests of the *c*-axis fibre are plotted in **Figures 7.10a** and **7.10b** respectively. The respective difference-over-sum ratios,  $R_{bend}$ , have been calculated using **Eq.7.13** from the recorded orthogonal intensities of the output lightwave. The 1 mm bending to which the sapphire fibre has been subjected has resulted in a relatively unchanged  $R_{bend}$ , implying that the state of polarisation of the input light has remained relatively constant throughout the test. A slight decrease in the ratio can be seen at a bending depth of 0.2 mm. The error associated with this measurement was quite large and the probable reason for this “dip” could be due to the fibre slipping slightly out of contact with the micrometer head as it was being turned. The effects from polarisation scrambling of the lightwave could also be a major contributing factor. However, the general profile of the  $R_{bend}$  curve was found to be relatively constant about a value of 0.7 over the entire 1 mm of bending applied. The errors of the remaining points were also relatively small compared to that at a bend depth of 0.2 mm, as indicated in **Figure 7.10a**. The resulting  $R_{bend}$  values for the 1 mm bend test are listed in **Table 7.3a**.

The 2 mm bend test of the sapphire fibre resulted in an almost identical  $R_{bend}$  profile for approximately the first half of bending up to 0.7 mm. Due to the relatively large errors obtained for this bending range, it could be reasonable to state that there has been no change observed in the ratio. The difference-over-sum ratio obtained for this bending depth was found to be 0.728, which was also the peak  $R_{bend}$  of the 2 mm bend test. Beyond 0.7 mm, a relatively small but linear decrease of  $R_{bend}$  to ~0.689 can be seen in **Figure 7.10b** over the next 1.3 mm of bending. The errors for this range were also found to be relatively small compared to those before 0.7 mm. In general, the ratios calculated with the difference-over-sum technique are seen to be relatively constant over the entire 2 mm range about an average  $R_{bend}$  of 0.7. This implies that there has been no significant changes detected in the intensities of the orthogonal components travelling within the fibre which has been subjected to bending. **Table 7.3b** gives the  $R_{bend}$  values for the 2 mm bend test on the *c*-axis sapphire fibres.

From the results of the tests performed, it has been found that *c*-axis sapphire fibres were insensitive to bending. Although other sensing mechanisms/schemes can be used in conjunction with such fibres to measure deformations such as stress, strain and bending, etc., polarimetry, by monitoring the phase retardation or birefringence of the sapphire fibre, is clearly not a very suitable technique as applied to *c*-axis fibres. **Figure 7.10a** shows a rather constant  $R_{bend}$  profile over a 1 mm bending test while in **Figure 7.10b**, the bending depth has been increased to 2 mm and similar results have been obtained. A small negative slope can be seen beyond 0.7 mm of bending and this could be used to show the relative low dependence of the state of polarisation or birefringence (of *c*-oriented sapphire fibres) on bending. In addition, the values of the ratio,  $R_{bend}$ , for both 1 and 2 mm bending have been obtained at approximately 0.7 and, if the principle employed by *Murukeshan et al.* [7.17] is to be taken into account, this could imply that the linearly polarised input lightwave in the horizontal direction was converted into a slightly elliptical polarisation state, close to the linear state of polarisation, upon propagating through the *c*-axis fibre. However, it was more likely the case that the linearly polarised input light has been scrambled when travelling within the fibre, leading to an “apparent” elliptical polarisation, since sapphire fibres are generally unclad. The application of bending served to increase the polarisation scrambling effect. This could thus be a more likely cause for the  $R_{bend}$  values which have been calculated even though in *c*-oriented sapphire fibres, the ordinary and extraordinary refractive indices are the same (meaning the orthogonal component velocities of light should be identical), implying that the state of polarisation of light, linearly polarised or unpolarised, should remain unchanged.

Figure 7.10a. Calculated difference-over-sum ratio for 1 mm bending (*c*-axis Al<sub>2</sub>O<sub>3</sub> fibre)

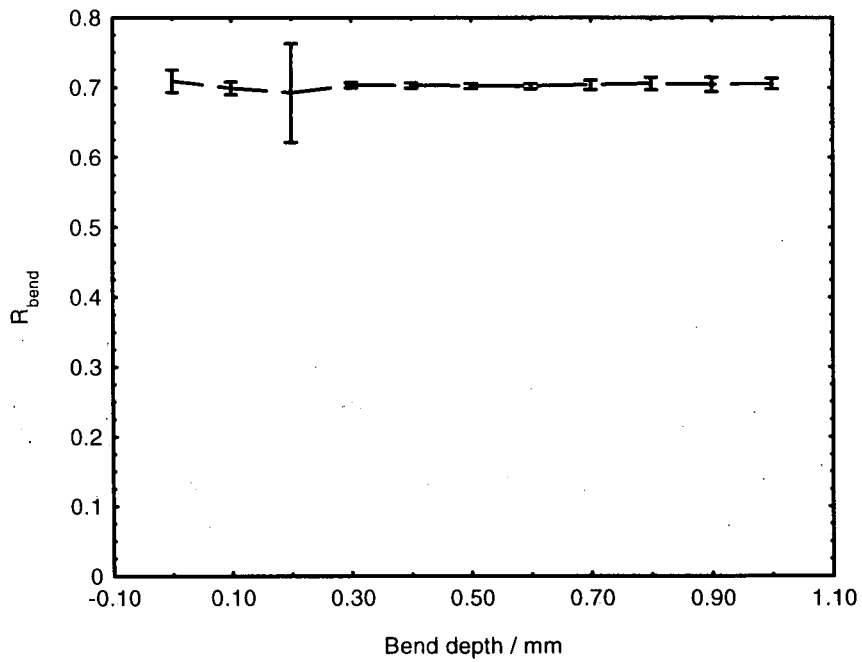
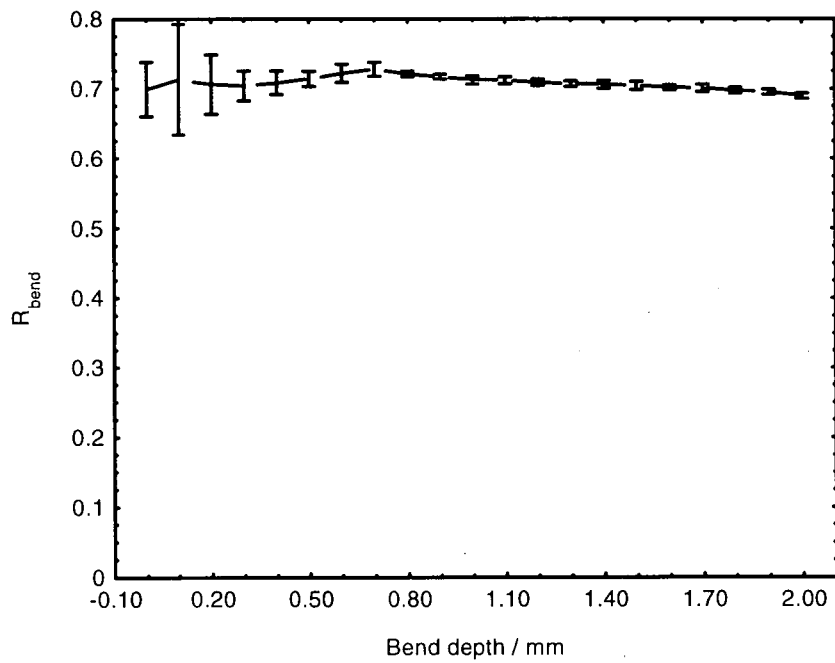


Figure 7.10b. Calculated difference-over-sum ratio for 2 mm bending (*c*-axis Al<sub>2</sub>O<sub>3</sub> fibre)



**Table 7.3a. Results of 1 mm 3-point bend test of *c*-axis sapphire fibre**

Bend depth / mm	$R_{bend}$	Error / %
0	0.708945	4.49
0.1	0.698830	2.71
0.2	0.692234	20.47
0.3	0.703299	1.07
0.4	0.702918	1.12
0.5	0.702250	0.99
0.6	0.701898	1.06
0.7	0.703762	1.88
0.8	0.705546	2.49
0.9	0.704151	2.94
1.0	0.705408	2.09

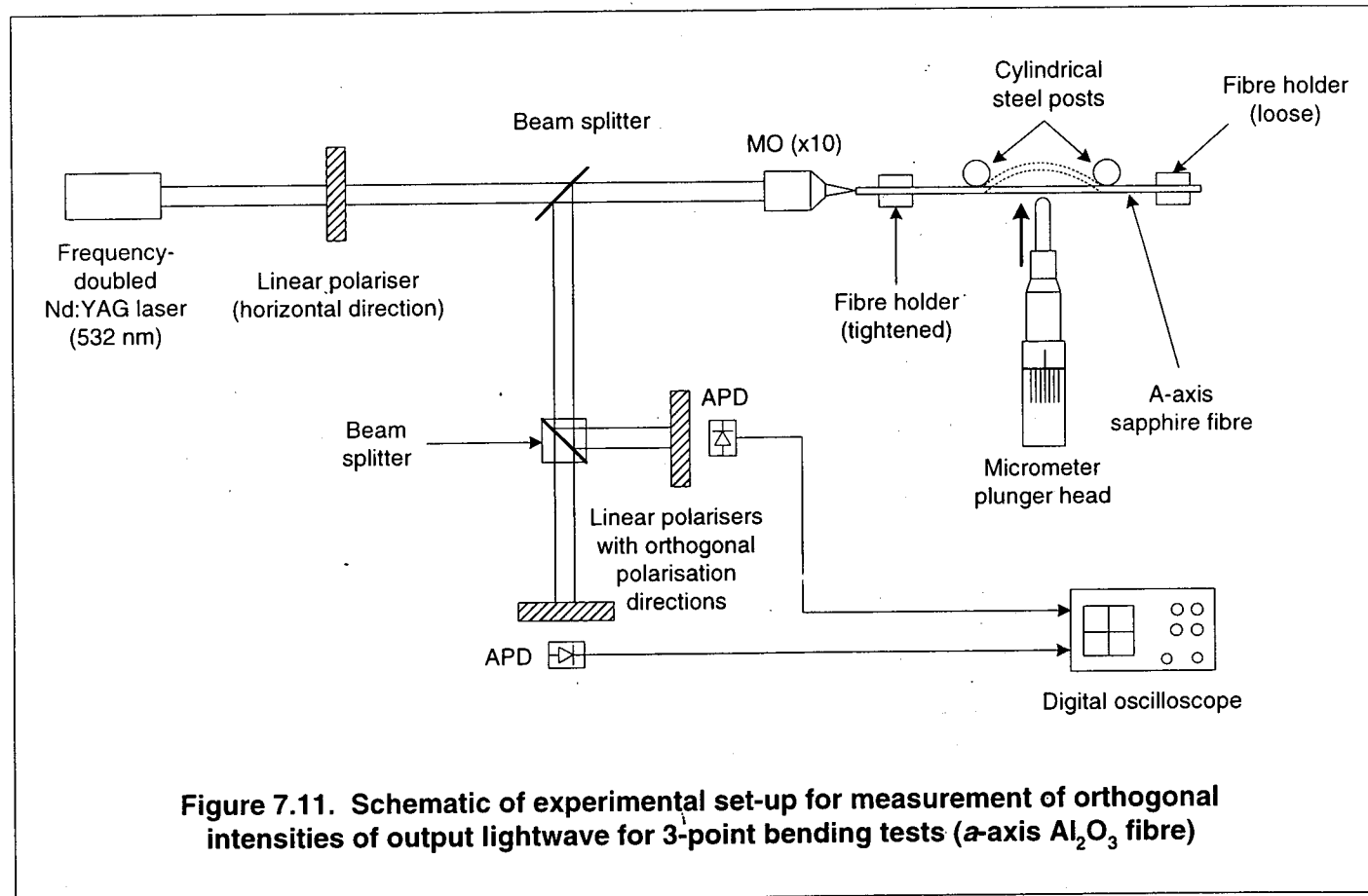
**Table 7.3b. Results of 2 mm 3-point bend test of *c*-axis sapphire fibre**

Bend depth / mm	$R_{bend}$	Error / %
0	0.698928	11.16
0.1	0.712946	22.26
0.2	0.705964	12.02
0.3	0.703929	6.07
0.4	0.708302	4.77
0.5	0.713765	3.06
0.6	0.721990	3.56
0.7	0.727727	2.77
0.8	0.720609	1.15
0.9	0.716753	0.99
1.0	0.712194	1.63
1.1	0.711615	1.39
1.2	0.708454	1.37
1.3	0.706700	1.17
1.4	0.705659	1.59
1.5	0.704006	1.65
1.6	0.701083	0.99
1.7	0.700508	1.45
1.8	0.697308	1.24
1.9	0.695159	1.07
2.0	0.689476	1.15

### 7.4.3 3-point bending of *a*-axis sapphire fibres

The *a*-axis sapphire fibres used in the bending tests were of nominal diameters of 130  $\mu\text{m}$  and were  $\sim 200$  mm in length. The test fibres have been set up in a reflective configuration as shown in the schematic diagram in **Figure 7.11**. 532 nm light from a frequency-doubled Nd:YAG laser was linearly polarised after transmission through a linear polariser with its polarisation direction horizontally aligned and focused onto one end of the sapphire fibre. The same 3-point bending fixture used in bending tests for *c*-axis fibres has been adopted in this experiment and was positioned approximately along the middle of the fibre as shown. The far end of the *a*-axis fibre was held loosely with a fibre holder and light was allowed to be reflected from this end face which has been polished to 1  $\mu\text{m}$  in a lapping machine. After collimation through a X20 microscopic objective, the output lightwave from the fibre was then reflected off a beam splitter and directed towards the detection circuit, consisting of two APDs, two linear polarisers with orthogonal polarisation directions and a digital oscilloscope. As shown in **Figure 7.11**, the polarisers placed before the APDs allowed the orthogonal components of the lightwave to be measured/recorded so that the difference-over-sum ratio of the orthogonal intensities could be calculated using **Eq. 7.13**.

Three bend tests have been conducted, with bend depths of 0.5, 1, and 2 mm. Depth increments of 0.5 and 2 mm tests were 0.05 and 0.1 mm respectively while the fibre in the 1 mm bend test was actually bent through 1.4 mm. The initial depth increment was 0.05 mm up to a bending of 0.4 mm after which it was increased to 0.1 mm for the next 1 mm of bending. A micrometer plunger head with a resolution of 1  $\mu\text{m}$  has been employed for the bending purpose and was initially adjusted so that it only just made contact with the surface of the test fibres.



#### 7.4.4 Results and Discussion

The calculated difference-over-sum ratios for the 1 mm bending test have been plotted in **Figure 7.12a** and the results are listed in **Table 7.4a**. The ratio was found to increase steadily from the initial no bending state ( $R_{bend} = 0.704$ ) to a value of 0.771 at a bend depth of 0.4 mm where the increment was a constant 0.05 mm for this bending range (0 – 0.4 mm). Beyond this depth, a larger depth increment (0.1 mm) has been used and this led to a further increase in the ratio which could still be seen up to a peak of 0.780 at 1.2 mm of bending. However, the increase within this range is of a smaller magnitude than the initial increase, hence, it is less obvious. The ratios were then found to “flatten out” after this peak and remained relatively constant up to the maximum bending depth of 1.4 mm. The maximum change in  $R_{bend}$  has been found to be 0.076 (minimum value  $\sim 0.704$  and maximum  $R_{bend} \sim 0.780$ ) for the entire range of the 1.4 mm bending for this 1 mm bend test. The results of the *a*-axis fibre bend test compares rather favourably against those from the earlier *c*-axis fibre bending tests. Although the errors associated with this experiment were relatively large, there is a clear dependence of the birefringence or the state of polarisation of *a*-axis sapphire fibres on the physical bending effect. In addition, since sapphire is birefringent or doubly refractive, this set of results (**Figure 7.12a**) also implies the variation of an elliptical state of polarisation towards the more linearly polarised state given by a ratio of 1, since the  $R_{bend}$  values were found to be above 0.7 throughout the entire test range.

The 2 mm bend test can be seen to result in a  $R_{bend}$  profile which was almost entirely different from that for the 1 mm bending. The plotted difference-over-sum ratios in **Figure 7.12b** for the *a*-axis sapphire fibre due to 2 mm of bending can be seen to be relatively constant over the entire bending range. Relatively large errors were incurred throughout the range and the  $R_{bend}$  curve was found to exhibit hardly any significant variation right from the initial zero bending state where the  $R_{bend}$  value was calculated to be 0.950. However, upon careful observation of the figure, the profile was found to be relatively linear with only a very small change of 0.013 between the maximum and minimum values of  $R_{bend}$ . The maximum  $R_{bend}$  was calculated to be 0.962 at a bend depth of 1.7 mm while the minimum value was 0.949 at 0.1 mm of bending. Each increment in the bend depth as exerted by the

micrometer plunger head was 0.1 mm, however, due to the relatively small diameter of the  $a$ -axis fibres employed for the bending experiments, slippage of the fibre surface from the tip of the micrometer head could have occurred. This would be the most probable reason for the results which have been obtained since any slippage would result in no actual bending force being imparted to the fibre. The lightwave travelling within the fibre would thus not be subjected to further birefringence from the anisotropic sapphire fibre apart from the original source of double refraction. The values of the ratio,  $R_{bend}$ , for this 2 mm bend test were also found to be close to 1, suggesting a rather highly linear state of polarisation of the orthogonal output components. Further, all the sapphire fibres used were unclad samples which could readily have scrambled the linear SOP (horizontal direction) of the input lightwave. A value close to one, however, implies that the intensity of the vertical component must be very weak, which would then reinforce the principle of a preferential scrambling of the vertical component by the  $a$ -axis fibre which, in turn, could be due to the angle between the input vibration direction and the  $a$ -crystallographic plane of the fibre. For the discrepancies between the 1 mm and 2 mm bending tests to occur, this must mean that the fibre, which was supposed to be secured in the fibre holder, had been rotated accidentally. The results from the 2 mm bend test are listed in **Table 7.4b**.

The calculated  $R_{bend}$  values for the 0.5 mm bend test have been plotted in **Figure 7.12c** and the bend increment was 0.05 mm over the test range. The fibre holder securing the input end of the  $a$ -axis sapphire fibre was tightened to prevent further movement of the fibre. However, the calculated ratio values of the orthogonal light components using **Eq. 7.13** were observed exhibit a rather linear behaviour which can be seen in the figure. The maximum and minimum  $R_{bend}$  values were found to be 0.615 and 0.588 at bending depths of 0.40 and 0 mm respectively, giving a useful  $R_{bend}$  range of approximately 0.027 over the 0.5 mm bending range. It can also be seen that there is an obvious dependence of the difference-over-sum ratio,  $R_{bend}$ , on bending even though the bending range studied was relatively narrow (0.5 mm). In terms of the state of polarisation of the propagating components within the fibre, it can be seen to be similar to that for the 1 mm bend test. From the mean value of  $\sim 0.6$ , the linearly polarised input lightwave can be said to have been converted to a somewhat elliptical polarisation state. By bending the fibre, this elliptical SOP was

then forced closer to a linear polarisation state, as indicated by the almost linear increase of the  $R_{bend}$  value to the peak at a bend depth of 0.4 mm. The results of the 0.5 mm bend test are also given in **Table 7.4c**.

For the purpose of comparison, the three results from the corresponding bend tests have been normalised to their initial no-bending values and plotted in **Figure 7.12d**. There are clearly two distinct sets of behaviour from the  $a$ -axis fibres when subjected to bending tests with varying bend depths. The approximate linear increase of  $R_{bend}$  over the 0.5 mm bend test was found to be quite similar to that exhibited by the fibre for 1 mm bending. This could be used to confirm the general behaviour of the  $a$ -axis sapphire fibre to bending stress when linearly polarised light was forced to be split into its orthogonal components with slightly different propagating velocities by the sapphire fibres. The similarity of the 0.5 and 1 mm bend tests also leads to the implication that the 2 mm test had been conducted with serious but not unexpected errors arising from the bending fixture (such as fibre slippage), the use of unclad fibres and, perhaps more importantly, the choice of the angle between the polarisation vibration direction and the crystallographic plane of the crystal fibre.

Figure 7.12a. Calculated difference-over-sum ratio for 1.4 mm bending (*a*-axis Al<sub>2</sub>O<sub>3</sub> fibre)

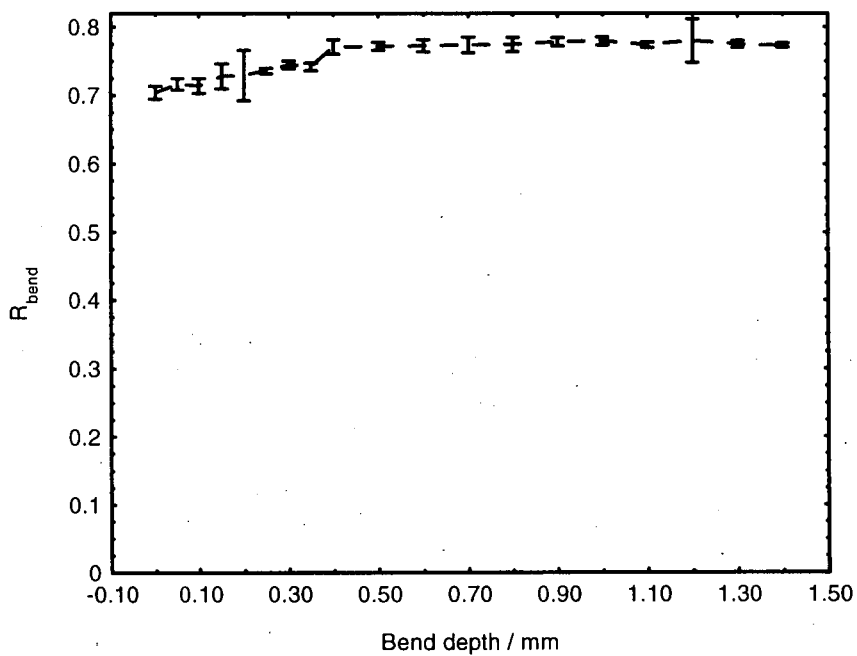


Figure 7.12b. Calculated difference-over-sum ratio for 2 mm bending (*a*-axis Al<sub>2</sub>O<sub>3</sub> fibre)

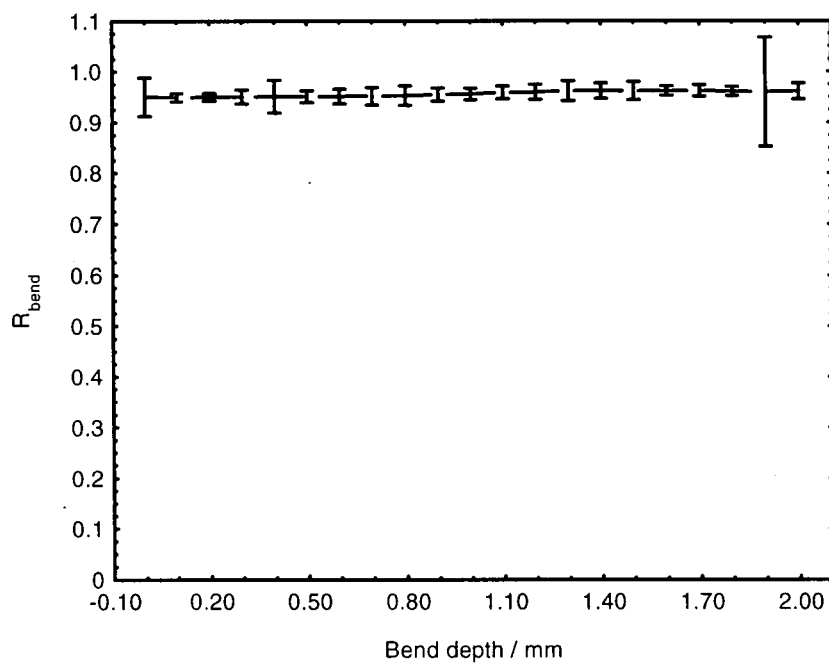


Figure 7.12c. Calculated difference-over-sum ratio for 0.5 mm bending (*a*-axis Al<sub>2</sub>O<sub>3</sub> fibre)

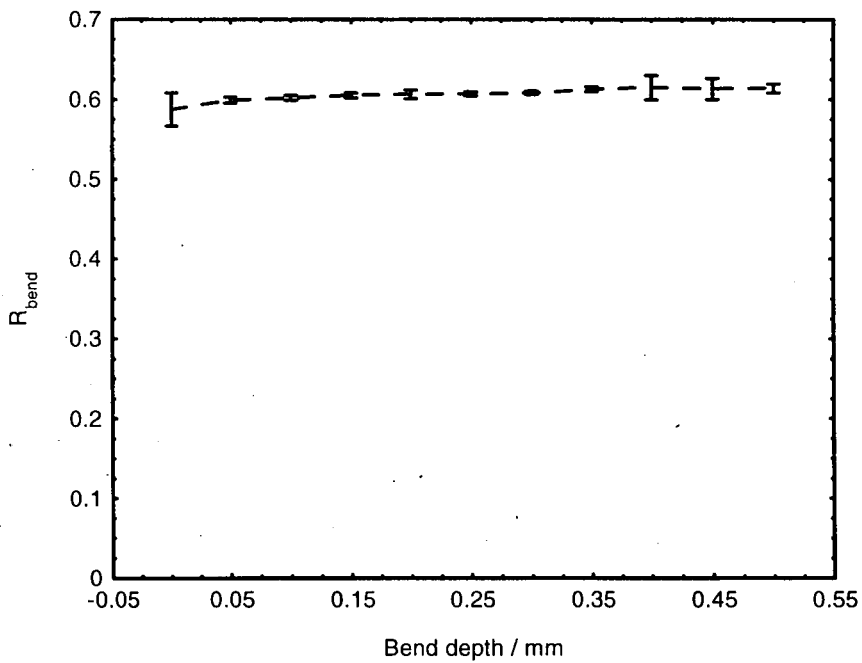
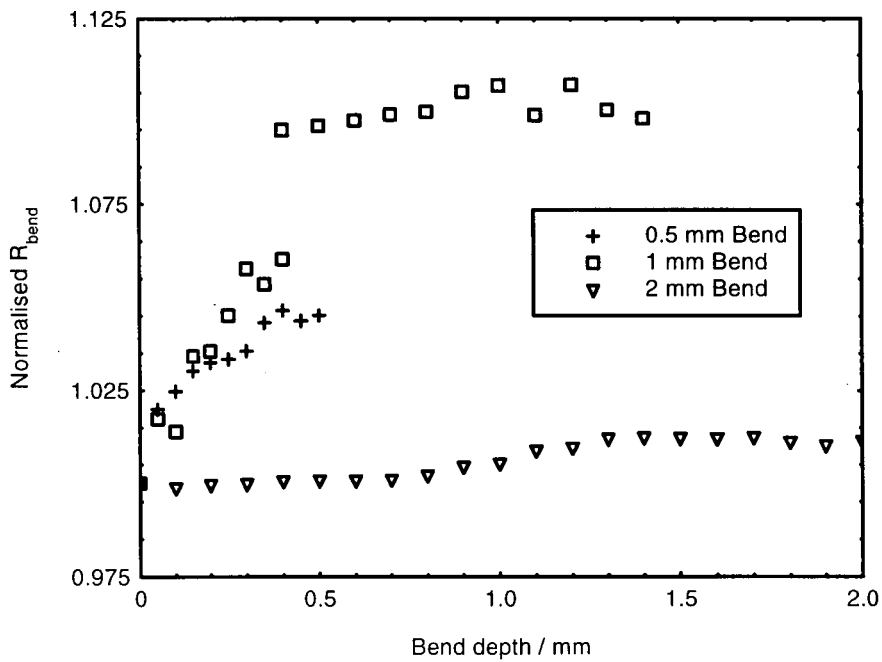


Figure 7.12d. Comparison of  $R_{\text{bend}}$  values for 0.5, 1 and 2 mm bending tests



**Table 7.4a. Results of 1 mm 3-point bend test of *a*-axis sapphire fibre**

Bend depth / mm	$R_{bend}$	Error / %
0	0.704110	2.67
0.05	0.716316	2.40
0.10	0.713940	3.01
0.15	0.728188	5.02
0.20	0.729144	10.08
0.25	0.735898	1.16
0.30	0.744712	1.57
0.35	0.741851	1.50
0.40	0.770929	2.71
0.50	0.771746	1.49
0.60	0.772760	2.27
0.70	0.773905	2.99
0.80	0.774419	2.67
0.90	0.778200	1.54
1.00	0.779438	1.48
1.10	0.773781	1.02
1.20	0.779521	8.15
1.30	0.774799	1.28
1.40	0.773133	0.80

**Table 7.4b. Results of 2 mm 3-point bend test of *a*-axis sapphire fibre**

Bend depth / mm	$R_{bend}$	Error / %
0	0.950186	7.93
0.1	0.948957	1.69
0.2	0.949725	1.55
0.3	0.950050	2.86
0.4	0.950764	6.77
0.5	0.950937	2.47
0.6	0.950980	3.02
0.7	0.951084	3.61
0.8	0.952242	4.05
0.9	0.954397	2.68
1.0	0.955306	2.37
1.1	0.958586	2.61
1.2	0.959387	3.06
1.3	0.961647	4.01
1.4	0.961943	3.18
1.5	0.961772	3.69
1.6	0.961731	1.94
1.7	0.962080	2.39
1.8	0.960849	1.79
1.9	0.959935	22.40
2.0	0.961106	3.27

**Table 7.4c. Results of  
0.5 mm 3-point bend test  
of *a*-axis sapphire fibre**

Bend depth / mm	$R_{bend}$	Error / %
0	0.587534	7.07
0.05	0.599234	1.29
0.10	0.602082	1.01
0.15	0.605269	1.00
0.20	0.606572	1.77
0.25	0.607140	0.78
0.30	0.608468	0.78
0.35	0.612923	1.00
0.40	0.614843	4.91
0.45	0.613231	4.26
0.50	0.614069	1.81

## 7.5 References to Chapter 7

- 7.1 J. Dakin and B. Culshaw (Eds.), *Optical Fiber Sensors Vol I: Principles and Components*, Artech House, Boston, 1988
- 7.2 E. Udd (Ed.), *Fiber Optic Sensors: An Introduction for Engineers and Scientists*, John Wiley and Sons, Inc., New York, 1991
- 7.3 D. A. Krohn (Ed.), *Fiber Optic Sensors: Fundamentals and Applications*, Instrum. Soc. Am., Research Triangle Park, 1992
- 7.4 A. Papp and H. Harms, *Magneto-optical current transformer. 1: Principles*, *Appl. Opt.*, **19**(22), 3729, 1980
- 7.5 H. Aulich, W. Beck, N. Douklias, H. Harms, A. Papp and H. Schneider, *Magneto-optical current transformer. 2: Components*, *Appl. Opt.*, **19**(22), 3735, 1980
- 7.6 H. Harms and A. Papp, *Magneto-optical current transformer. 3: Measurements*, *Appl. Opt.*, **19**(22), 3741, 1980
- 7.7 T. Mitsui, K. Hosoe, H. Usami and S. Miyamoto, *Development of Fiber-Optic Voltage Sensors and Magnetic-Field Sensors*, *IEEE Trans. Power Del.*, **PWRD-2**(1), 87, 1987
- 7.8 Y. N. Ning, Z. P. Wang, A. W. Palmer, K. T. V. Grattan and D. A. Jackson, *Recent progress in optical current sensing techniques*, *Rev. Sci. Instrum.*, **66**(5), 3097, 1995
- 7.9 R. B. Wagreich and C. C. Davis, *Performance Enhancement of a Fiber-Optic Magnetic Field Sensor Incorporating an Extrinsic Fabry-Perot Interferometer*, *Proc. SPIE*, **2895**, 11, 1996
- 7.10 Z. Wang, Y. Liao, S. Lai, H. Zhao and X. Chen, *A novel method for simultaneous measurement of current and voltage using one low-birefringence fiber*, *Opt. Laser Technol.*, **30**, 257, 1998
- 7.11 F. Bucholtz, *Fiber Optic Magnetic Sensors* in: *Fiber Optic Sensors: An Introduction for Engineers and Scientists*, E. Udd (Ed.), John Wiley and Sons, New York, 369, 1991
- 7.12 V. Handerek, *Foundations of optical fiber technology* in: *Optical Fiber Sensor Technology*, K. T. V. Grattan and B. T. Meggitt (Eds.), Chapman and Hall, London, 11, 1995

- 7.13 G. Liu and S. L. Chuang, *Polarimetric optical fiber weight sensor*, *Sensors and Actuators A*, **69**, 143, 1998
- 7.14 N. Fürstenau, M. Schmidt, W. J. Bock and W. Urbanczyk, *Dynamic pressure sensing with a fiber-optic polarimetric pressure transducer with two-wavelength passive quadrature readout*, *Appl. Opt.*, **37**(4), 663, 1998
- 7.15 T. Kosaka, N. Takeda and M. Hara, *Development of miniature load sensors for smart materials and structure by using birefringent fibers*, *Proc. SPIE*, **3670**, 16, 1999
- 7.16 V. M. Murukeshan, P. Y. Chan, L. S. Ong and A. Asundi, *Towards Realization of a Smart Polarimetric Sensor*, *Proc. SPIE*, **3670**, 54, 1999
- 7.17 V. M. Murukeshan, P. Y. Chan, L. S. Ong and A. Asundi, *Effects of different parameters on the performance of a fiber polarimetric sensor for smart structure applications*, *Sensors and Actuators A*, **80**, 249, 2000
- 7.18 B. G. Grossmann and L. T. Huang, *Fiber optic sensor array for multi-dimensional strain measurement*, *Smart Mater. Struct.*, **7**, 159, 1998
- 7.19 M. Schmidt, N. Fürstenau, W. Bock and W. Urbanczyk, *Fiber-optic polarimetric strain sensor with three-wavelength digital phase demodulation*, *Opt. Lett.*, **25**(18), 1334, 2000
- 7.20 W. Eickhoff, *Temperature sensing by mode-mode interference in birefringent optical fibers*, *Opt. Lett.*, **6**(4), 204, 1981
- 7.21 K. S. Chiang, *Temperature sensitivity of coated stress-induced birefringent optical fibers*, *Opt. Eng.*, **36**(4), 999, 1997
- 7.22 J. Xin, Q. Feng, T. Lin, Y. Wang, Z. Zhuang and Y. Liao, *Study on a Novel Compensation Configuration of Polarization-Modulated Fiber-Optic Temperature Sensor*, *Proc. SPIE*, **3201**, 181, 1997
- 7.23 E. De la Rosa, L. A. Zenteno, A. N. Starodumov and D. Monzon, *All-fiber absolute temperature sensor using an unbalanced high-birefringence Sagnac loop*, *Opt. Lett.*, **22**(7), 483, 1997
- 7.24 W. Urbanczyk and W. J. Bock, *Influence of dispersion on sensitivity of highly birefringent fibers to temperature and hydrostatic pressure*, *Appl. Opt.*, **37**(15), 3176, 1998
- 7.25 R. Cortés, A. V. Khomenko, A. N. Starodumov, N. Arzate and L. A. Zenteno, *Interferometric fiber-optic temperature sensor with spiral polarization couplers*, *Opt. Commun.*, **154**, 268, 1998

- 7.26 J. Ma and W. Tang, *Second-order sensitivity effects on optical fiber polarimetric temperature sensor and strain sensor*, *Appl. Opt.*, **36**(34), 9010, 1997
- 7.27 O. Hadeler, E. Rønnekleiv, M. Ibsen and R. I. Laming, *Polarimetric distributed feedback laser sensor for simultaneous strain and temperature measurements*, *Appl. Opt.*, **38**(10), 1953, 1999
- 7.28 A. Wang, G. Z. Wang, K. A. Murphy and R. O. Claus, *Birefringence-balanced polarimetric optical fiber sensor for high-temperature measurements*, *Opt. Lett.*, **17**(19), 1391, 1991
- 7.29 A. Wang, G. Z. Wang, G. Gollapudi, R. G. May, K. A. Murphy and R. O. Claus, *Advances in sapphire optical fiber sensors*, *Proc. SPIE*, **1798**, 56, 1992
- 7.30 F. A. Jenkins and H. E. White, *Vibrations and Waves in: Fundamentals of Optics (4<sup>th</sup> Ed.)*, McGraw-Hill, Singapore, 215, 1981
- 7.31 W. A. Gambling and S. B. Poole, *Optical Fibers for Sensors in: Optical Fiber Sensors Vol I: Principles and Components*, J. Dakin and B. Culshaw (Ed.), Artech House, Boston, 249, 1988
- 7.32 A. J. Rogers, *Essential Optics in: Optical Fiber Sensors Vol I: Principles and Components*, J. Dakin and B. Culshaw (Ed.), Artech House, Boston, 25, 1988
- 7.33 W. B. Spillman Jr., *Multimode Polarization Sensors in: Fiber Optic Sensors: An Introduction for Engineers and Scientists*, E. Udd (Ed.), John Wiley and Sons, New York, 181, 1991
- 7.34 D. A. Krohn, *Phase-Modulated Sensors in: Fiber Optic Sensors: Fundamentals and Applications (2<sup>nd</sup> Ed.)*, Instrum. Soc. Am., Research Triangle Park, 49, 1992
- 7.35 P. Gay, *Light Waves in Isotropic and Anisotropic Media in: An Introduction to Crystal Optics*, Longman, London, 18, 1967
- 7.36 F. A. Jenkins and H. E. White, *Double Refraction in: Fundamentals of Optics (4<sup>th</sup> Ed.)*, McGraw-Hill, Singapore, 544, 1981
- 7.37 S. Singh, *Nonlinear Optical Properties in: CRC Handbook of Laser Science and Technology Vol III. Optical Materials: Part I*, M. J. Weber (Ed.), CRC Press, Boca Raton (Florida), 3, 1986
- 7.38 E. Udd (Ed.), *Fiber Optic Smart Structures*, John Wiley and Sons, New York, 1995

## **Chapter 8 – Conclusions and Future Work**

**8.0 Conclusions**

**8.1 Future Work**

## Chapter 8 – Conclusions and Future Work

### 8.0 Conclusions

The main objectives involved in this project have been the growth, characterisation and study of single-crystal fibres which exhibit suitable characteristics for employment as fibre optic sensors. Various types of crystal fibres have been grown for these studies. Most of these fibres have been based on  $\text{Al}_2\text{O}_3$  as the host material since sapphire offers attractive advantages such as high strength, optical transparency from  $\sim 0.3$  to  $4 \mu\text{m}$ , high melting point ( $\sim 2323 \text{ K}$ ) as well as good mechanical stability at elevated temperatures. Sapphire fibres can also be grown easily, in addition. Thus, crystal fibres of pure  $\text{Al}_2\text{O}_3$ ,  $\text{Cr}^{3+}$ -doped, singly  $\text{Er}^{3+}$ -doped,  $\text{Er}^{3+} + \text{Yb}^{3+}$ -codoped (of approximately equal erbium and ytterbium contents),  $\text{Yb}^{3+} + \text{Er}^{3+}$ -codoped (high ytterbium and low erbium contents)  $\text{Al}_2\text{O}_3$  together with YSZ (yttria-stabilised zirconia) have been grown using the laser heated pedestal growth method. Source materials used were sapphire fibres, single-crystal and polycrystalline, with diameters from  $130 - 425 \mu\text{m}$ .

The laser heated pedestal growth method was selected as the crystal fibre growth apparatus over several other methods most of which require crucibles (to contain the melt), were more expensive, time consuming and inflexible. In addition, it also provides clean heating, little or no contamination of the growing fibre, fast fibre growth compared to other methods, large temperature gradients so that fast growth and high turnover can be realised, and very high melting temperatures can be achieved, the maximum temperature being limited only by the laser power available. Design and construction of the LHPG station were then initiated. Computer control was employed over hardware control due to the speed, power and simplicity available with a modern and fast computer. Computer control has been utilised to integrate several controls or growth parameters such as pull and feed rates, laser power, x-y positioning, into one programme using Delphi. It also has the added advantage of allowing feedback monitoring of the growing fibre diameter and automatic adjustments/corrections of the related growth parameters. The integration of this monitoring scheme shall be carried out at a later stage. The pull and feed velocities generated by two DC motors were found to be relatively constant while the

laser power has been found to be relatively stable at the power range used for growing crystal fibres. The use of linear slides as the pull and feed translation systems limits the maximum length of fibres that can be grown. It was also found that towards the end of travel of both slides, large frictions were generated, thus limiting the pull fibre to a maximum length of ~220 mm. Fibre optic sensor probes are generally a fraction of the length of fibres used for optical communications, hence, typical lengths of crystal fibres grown in this work are in the range of 20 – 220 mm and have been found to be sufficiently long for the various sensing schemes investigated.

Pure sapphire fibres, in particular, have been observed to grow very easily as *c*- and *a*-axis fibres with rounded hexagonal and rectangular cross-sections respectively. *C*-axis growth can readily be initiated by an appropriate *c*-axis seed crystal, a small polycrystalline seed fibre or even a thin tungsten wire. 130  $\mu\text{m}$  polycrystalline sapphire fibres have been used as seed crystals in this work for the growth of all *c*-axis fibres by the LHPG method. Nominal diameters were measured using the filar-eyepiece technique in conjunction with a microscope and found to be between 87 and 170  $\mu\text{m}$ . *C*-axis is the preferential growth axis, hence, sapphire fibres in this crystallographic orientation were grown with no difficulties and/or complications. To initiate *a*-axis fibre growth, an appropriately selected *a*-axis seed crystal has been employed and fibres grown were in the range of 100 – 220 mm with a nominal diameter of 130  $\mu\text{m}$ . An examination of the fibre geometry revealed that good quality fibres have been produced. Typical deviations of less than 2 % from the mean diameter have been measured for *c*-axis fibres. Since the cross-section of *c*-axis sapphire fibres resembled a rounded hexagon in shape (rather than circular), measurements of the fibre diameters is not straightforward. However, the small diameter deviations obtained can be taken to imply that *c*-axis fibres have been grown with good diameter uniformity. *A*-axis fibres were relatively more difficult and complicated to measure consistently since the cross-section was rather elongated in shape (more rectangular with the shorter ends rounded). Again the small diameter deviations (~2 %) were measured.

Doped fibres were fabricated by dip-coating the  $\text{Al}_2\text{O}_3$  source material into suspensions of appropriate dopant oxides. Ruby fibres ( $\text{Cr}^{3+}:\text{Al}_2\text{O}_3$ ) were found to grow almost as easily as pure  $\text{Al}_2\text{O}_3$  fibres. Brownish-green deposits have been observed on the surfaces of several as-grown fibres and the formation of such deposits depended on the pull rates used during fibre growth. They contributed to relatively large transmission losses of these fibres through absorption and scattering. Slower pull rates (0.2 - 0.5 mm/min) allowed these deposits to be burnt off quite completely, leaving no visible traces on the as-grown ruby fibres. Faster pull rates, on the other hand, resulted in the deposits mentioned being observed on some of the ruby fibres grown (at rates above 0.5 mm/min). Soaking fibres with deposits in hot HCl acid baths over 24 hrs did not remove much of the deposits, as indicated by only a slight reduction of the losses (absorption and scattering) measured. This also suggested that the brownish-green deposits observed could have diffused beneath the surface of the affected fibres due to the intense heating involved, making them almost impossible to clean or remove.

Rare-earth-doped  $\text{Al}_2\text{O}_3$  fibres have never been reported prior to this work and initial attempts to grow them were problematic. The main reasons found were the rather "violent" melting behaviour of rare-earth oxide materials coated on the source fibres when subjected to intense heating and the flexibility of the small diameter (130  $\mu\text{m}$ ) source fibres employed. This resulted in the frequent breaking-off of the melt interface between the source and growing fibres, a problem which was particularly accentuated when both the source and seed fibres were found to have moved out of alignment true to their respective verticals in the heating zone. Since it was not possible to incorporate RE ions along the length of the fibres using small diameter source fibres, it was decided to dope the tip of several 130  $\mu\text{m}$  as-grown sapphire fibres and characterise their emission properties. Beside the expected infrared emission in the wavelength region of 1500 - 1550 nm for  $\text{Er}^{3+}$ -doped tip fibres, upconversion was also observed in the green and red spectral regions. An EPMA (electron probe micro-analysis) scan of this tip revealed very high erbium concentration of ~11 - 12 at.% at several discrete points. Upconversion in the two regions have also been found in the emission characteristics of both the equally  $\text{Er}^{3+}$  +  $\text{Yb}^{3+}$ -codoped and high  $\text{Yb}^{3+}$  + low  $\text{Er}^{3+}$ -codoped tips. Further attempts were then initiated to grow fibres doped with RE ions along their length using more rigid 325

and 425  $\mu\text{m}$  sapphire fibres as source rods. RE-doped fibres were found to grow with relative ease by the change to bigger diameter source rods. Fibres which have been grown included those doped throughout their entire lengths and those with short sections ( $\sim 20$  mm) suitably doped. The sharp, narrow lines emitted from the IR (1500 – 1550 nm), green (520 – 560 nm) and red (650 – 670 nm) upconversion regions in singly  $\text{Er}^{3+}$ -,  $\text{Er}^{3+} + \text{Yb}^{3+}$ -codoped and high  $\text{Yb}^{3+} +$  low  $\text{Er}^{3+}$ -codoped sapphire fibres indicated the highly crystalline nature of these RE-doped fibres when compared to the broad emissions from RE-doped glass fibres.

Many attempts have been made to grow good quality YSZ crystal fibres from polycrystalline source rods approximately 1 mm in diameter but were mostly unsuccessful. Although several YSZ fibres have been grown, very large and periodic diameter variations have been observed in the as-grown fibres rendering them unsuitable for sensing applications since optical losses were estimated to be too large. Fibres re-grown from the first-growth YSZ fibres ( $\sim 667$   $\mu\text{m}$  in diameter) were also observed to exhibit such geometrical faults. In addition, cracks have also been observed along the fibre lengths and cross-sections. The reasons for this difficulty could be due to insufficient heating power from the laser, the large source rod used and the very high melting point of the material. The maximum power output available from the  $\text{CO}_2$  laser employed as the heat source was approximately 30 W and the stability of  $\pm 2$  % as quoted by the manufacturer was only achievable for up to 95 % of the power cycle. Hence, at the limit of 30 W, the laser power was observed to oscillate and was one of the principle causes for the periodic diameter variations produced in YSZ fibres since the molten zone would also be forced to oscillate (expand and contract). In addition to that, it was judged that there was insufficient heating power generated by the  $\text{CO}_2$  laser to efficiently and completely melt the end of the 1 mm source rod whose melting point was at least 3000 K. The cracks which appeared in the YSZ fibres were attributed to the very large thermal gradients involved during growth by the LHPG method due to the fact that the  $\text{CO}_2$  laser heating beam has been focused to a relatively small spot.

Since the maximum length of fibres which can be produced was limited to 220 mm, delivery of any light source beyond this length in a practical field trial would not be

possible to achieve. It was thus thought to be useful to find a way to connect the sapphire-based sensing probes to a less expensive material more readily available. Both butt coupling and fusion splicing of pure sapphire fibres to commercially available silica fibres was attempted, with the former technique found to be easier and more practical. It has not been possible to fusion splice sapphire fibres to silica fibres due to the rather different material properties such as melting point and thermal expansion coefficients. Several attempts have resulted in sapphire being spliced into silica fibres, however, the interface was very brittle and fragile, and broke off very easily. In addition, under microscopic observation, numerous cracks were also observed to be present in the joint, leading to very large scattering losses.

Temperature has been and is still is one of the major concerns in numerous industrial processes, engineering applications and research, hence, it formed the principle parameter investigated in this work. Most of the fibres grown have been sapphire doped with various active materials and fluorescence was thus expected. Temperature dependent characteristics of the fluorescence from all doped fibres and the state of polarisation in pure sapphire fibres were thus studied. Strong fluorescence signals were obtained from the sharp ruby R-line emission at 694.3 and 692.9 nm at room temperature with a relatively long fluorescence decay time of ~3.5 ms. The lifetime was then characterised for its temperature dependence up to 923 K and the lifetime decay profile as a function of temperature has been found to agree reasonably well with theory governed by a model. At high temperatures (>823 K), the fluorescence intensity was observed to reduce quite dramatically and the resulting lifetime measurement was found to have relatively large errors. At 650 K, lifetime was less than 50  $\mu$ s while the fluorescence signal was found to be too weak and error margins during fitting too large for any more meaningful data to be acquired and higher temperatures to be pursued. The variation of the fluorescence lineshifts, on the other hand, could still be monitored with the aid of lock-in detection up to a slightly higher temperature of 973 K. Strain dependence of both the fluorescence lifetime decay and lineshifts in ruby fibres have also been investigated. However, this parameter was found to have only an extremely weak effect on the two fluorescence characteristics. One ruby fibre has been strain-tested to destruction to demonstrate this insensitivity. Since cross-sensitivity between two parameters, especially between temperature and strain/stress, is a major problem and can

adversely affect the efficiency and accuracy of any sensor systems, expensive and complicated processing techniques generally have to be used in order to separate the two (or more) sensitivities. However, this problem could be reduced or even avoided by employing ruby fibres as temperature sensing elements. More importantly, this study on ruby fibres could also be used to suggest that *c*-axis doped sapphire fibres were effectively independent of strain, an important but beneficial implication when other doped sapphire fibres were utilised in temperature sensing applications.

Temperature dependence studies on RE-doped sapphire fibres have mostly been concentrated on the measurements of relative intensities of the sharp emitted lines in the IR and visible upconversion (green and red) regions. In singly  $\text{Er}^{3+}$ -doped  $\text{Al}_2\text{O}_3$  fibres, both the IR and upconversion intensities were found to be relatively weak. This was attributed to the poor spectral overlap between the narrow absorption bands of the erbium ions and the 960 nm pump source employed. Hence, the inefficient excitation was manifest in the form of relatively weak emission intensities. In addition, upconversion is a competing process and tends to remove the excited population from the first excited state where the IR emission originates, further reducing the IR fluorescence intensity. The green upconversion intensity was monitored up to a maximum temperature of 500 K before the signal was too weak and erroneous to be detected. Hence, it was decided not to pursue further temperature studies on the red upconversion intensity since lines emitted in this region were only slightly stronger and any significantly higher temperatures would not be attained. The IR signals were found to be relatively stronger and have been monitored up to 720 K. The fluorescence intensity ratio (*FIR*) of the 1511.5/1523 nm and 1511.5/1531.5 nm lines were selected based on the widest temperature range possible and least errors incurred, while the *FIRs* of the remaining six lines have been found to be non-monotonic over the temperature range studied.

In  $\text{Er}^{3+} + \text{Yb}^{3+}$ -codoped samples containing approximately equal concentration of each dopant species, very intense upconversion emission in the green and red has been observed due to efficient energy transfer afforded by the sensitising  $\text{Yb}^{3+}$  ions. This suggests that most of the pump energy has been channelled into excitation of the higher energy levels, hence, the IR *FIRs* were not studied since they would generally be too weak for any high temperature measurements. Both the green and

red upconversion emission lines have been monitored to a temperature of 1220 K beyond which the respective signals were found to be very weak. Again two *FIRs* from each spectral region ( $FIR_{g25}$  and  $FIR_{g35}$  in the green,  $FIR_{r25}$  and  $FIR_{r35}$  in the red) have been found to be suitable for temperature sensing providing the widest dynamic range. Based on the model described by "Berthou and Jørgensen", a general exponential profile was exhibited by these *FIRs*, indicating reasonable agreement with theory. The small discrepancy would suggest the involvement of other factors such as second or third order transitions within the respective energy manifolds. The red upconversion intensity was also found to be strong relative to the green, thus smaller errors have been obtained. Both the green and red emission intensities, resulting from the  ${}^4S_{3/2} \rightarrow {}^4I_{15/2}$  (green upconversion) and  ${}^4F_{9/2} \rightarrow {}^4I_{15/2}$  (red upconversion) transitions, were also monitored simultaneously up to 1323 and 1423 K respectively. By opening the monochromator slit widths to their maximum, a bandwidth of ~3 nm was used over which the green and red intensities were measured as a function of temperature. For an intensity-based sensing scheme such as this, the pump power was also monitored to reduce or eliminate any power fluctuation. In addition, calibration curves provided by a simple model gave relatively good agreement with theory. The unique advantage of being relatively independent of pump intensity fluctuations offered by monitoring the lifetime decay of both upconversion spectra have also been investigated. However, it was found that the upconversion lifetimes were generally non-exponential in nature and difficult to estimate with reliability.

The temperature sensing schemes using the two earlier RE-doped fibres permitted measurements of mainly the upconversion signals to be achieved. However, it was also desirable to obtain the IR fluorescence from the  $Yb^{3+}$  lines in the 1000 nm region. This was done by doping the sapphire host fibres with very high  $Yb^{3+}$  concentration with respect to the  $Er^{3+}$  contents (in an approximately 10:1 wt. ratio) to produce high  $Yb^{3+}$  + low  $Er^{3+}$ : $Al_2O_3$  fibres. Emission measurements revealed upconversion characteristics (in the green and red) similar to those exhibited by equally  $Er^{3+}$  +  $Yb^{3+}$ -codoped  $Al_2O_3$  fibres reported earlier as well as IR fluorescence with peaks at 996 and 1025 nm, the latter two being a direct emission from the excited ytterbium ions ( ${}^2F_{5/2} \rightarrow {}^2F_{7/2}$  transition). The upconversion detected again demonstrated the high-energy transfer efficiencies of  $Yb^{3+}$  since, in this case, only

very small quantities of  $\text{Er}^{3+}$  ions were incorporated. The respective intensities were, however, found to be quite weak. The visible *FIRs* were then monitored as a function of temperature up to 773 K, a relatively low temperature compared to equally codoped fibres. The IR *FIR* due to the 996 and 1025 nm lines could only be monitored up to an even lower temperature of 723 K. Although the two IR fluorescence were found to be relatively stronger than the upconversion intensities, they were overlapped by the tail of the pump emission. This then resulted in the IR signals being superimposed onto the pump intensity and at the higher temperature range ( $>723$  K), the IR lines were found to fall below the background laser signal. However, good agreement of the IR *FIR* characteristics was obtained through the use of a theoretical model and this IR study also indicated the suitability of utilising high  $\text{Yb}^{3+}$  + low  $\text{Er}^{3+}$ -codoped sapphire fibres for temperature monitoring.

Polarimetric sensing schemes employing *c*- and *a*-axis sapphire fibres have been investigated for temperature and bending dependence characteristics. The main principles adopted for this type of sensing required the calculation of the retardation of the polarisation state experienced by linearly polarised light propagating in the fibres from the detected four-component Stokes parameter (using a polarimeter) as well as the measurement of the intensities of orthogonal light components using a difference-over-sum technique. When the fibres are subjected to external perturbations, any variations in the two properties can then be detected. Sapphire is doubly refractive, hence light launched into these fibres at suitable crystallographic orientation directions will be forced to undergo birefringence, resulting in two slightly different propagating velocities governed by  $n_o$  and  $n_e$ , the ordinary and extraordinary refractive indices. In *c*-oriented fibres where the *c*-axis coincides with the crystal optic axis, both  $n_o$  and  $n_e$  are identical. Any propagating lightwave will thus travel without any change in its associated component velocities and no birefringence *should* be exhibited. Thus, it was anticipated that by subjecting *c*-axis sapphire fibres to temperature and bending, additional birefringence would be induced due to asymmetric stress distributions and slight deformation of the fibre geometry. However, it was found that *c*-axis fibres were relatively insensitive to both temperature and bending. *A*-axis fibres, on the other hand, are naturally birefringent, hence, the resulting SOPs of the input linearly polarised lightwaves were found to be slightly elliptically polarised. Introduction of temperature

variations thus resulted in a useful retardation range between 673 and 1073 K, while the difference-over-sum ratio (or SOP of the propagating lightwave) was found to increase generally with increasing temperature up to 1473 K. For the 0.5, 1 and 2 mm bending tests conducted, the ratio obtained from the difference-over-sum formulation was observed to increase as the bend depth was increased, however, the dynamic range for all three bending test were relatively small. Obviously, unless some ways can be found to increase the dynamic range of the bend dependence, these fibres (*a*-axis sapphire) are not particularly suitable for bend deformation monitoring although it is still possible to correlate any polarimetric parameter variations to temperature.

### **8.1 Future Work**

One of the major problems encountered in this project was the lateral (*x-y*) movement of both seed and source fibres out of true vertical alignment to each other and to the laser focal axis in the LHPG station during fibre growth. This often resulted in fibres having large diameter variations if proper actions were not taken to correct the lateral alignment at an early stage. It would thus be highly advantageous to incorporate a fibre diameter monitoring system into the growth loop so that automatic corrections would be performed by the computer. Such a system would also enable close-loop feedback adjustments of the pull/feed velocities and laser power, if properly integrated, which would, in turn, lead to higher quality fibres with fewer as well as smaller diameter variations than can be produced by an open-loop growth. This would be very useful in conjunction with modifying the current growth station into a continuous belt drive system which would allow "unlimited" lengths of fibre to be produced. It would also permit the current problems of large friction forces towards the ends of the slides and the resulting vibration to be reduced/eliminated.

Although a procedure has been established to ensure equal coating layers of dopant materials on source fibres, uniform dopant distribution along the longitudinally fibre axis cannot be guaranteed. A technique to enable this to be realised would be highly desirable since fibres grown can then be doped more uniformly and better characterised. It would also permit fibres with the desired dopant concentration

level(s) to be produced more repeatably. In addition, other less expensive source materials should be found instead of single-crystal ones, so that savings can be realised on one type of source to enable other types of crystals to be studied.

The maximum output power from the current CO<sub>2</sub> laser employed as the heat source was sufficient for melting source materials with temperatures similar to that of the largest sapphire source fibre used. However, it was found to be insufficient when very high melting point materials, such as YSZ or even yttria fibres, are to be grown. Moreover, most of these polycrystalline or sintered rods can only be purchased in diameters of 1 mm or more currently due to difficulty in grinding them down to smaller sizes. Hence, it would certainly be beneficial if a higher power CO<sub>2</sub> laser of ~100 W output power could be employed to grow a relatively large range of high melting refractory oxides for sensing studies.

It is worth mentioning again that current fibre growth techniques do not permit crystal fibres such as sapphire to be coated with a cladding layer. This is due mainly to the unavailability of suitable cladding materials with matching refractive indices and compatible physical properties (melting points, thermal expansions, strength modulus, etc.). Hence, sapphire fibres are grown generally unclad and large transmission losses are a result of this. The favourable properties of sapphire fibres both as sensing elements and delivery fibre systems, if they can be clad and grown in lengths comparable to glass fibres used in optical telecommunications, would be greatly enhanced. One suggestion for cladding sapphire fibres would be to use other higher melting point materials such as molybdenum and yttrium oxides as coating layers on the sapphire fibre surface and heating them in the growth chamber to enable them to be diffused into the fibre surface. Translating the coated fibre similar to the manner in which crystal fibres were pulled would result in a thin outer layer of cladding material along the entire length of the fibre. Ruby fibres can also be "re-grown" by heating them so that Cr<sup>3+</sup> diffuse out from the core of the sapphire fibre, forming an outer ruby cladding layer. Using this technique, the coating materials to be used should be chosen carefully to approximately match the properties and refractive index of sapphire.

For relating the experimental results of the temperature dependence of the infrared fluorescence and, in particular, upconversion emission of RE-doped sapphire fibres to theory, a in-depth study is required to better understand the complicated dynamics and transition energies in highly doped samples. This could, perhaps, then lead to better and more general models which can, in turn, be used to describe the actual experimental data. Further, the possibility of "self-activated" RE-doped fibres should be explored. This could have important implications in the field of novel laser materials science and physics.

Finally, implementation of the crystal fibres characterised for various sensing parameters would be the next major step in this research. Field trials could be held to test the practical suitability of employing such fibres in a real application. This could be done easily if calibration curves of the appropriate crystal fibres for the related parameter of interest were obtained beforehand. Instead of the sometimes complicated models predicted by theory, simple polynomials of the  $n^{\text{th}}$  level can be fitted to the experimental data on a "look-up" graph in which the vertical (or y) axis is the physical parameter to be measured while the x-axis is the detected changes in light intensities, lineshifts, lifetime decays and fluorescence intensity ratios, etc.

**APPENDIX A**

**List of single-crystal fibres grown by the LHPG method**

Material	Common Name	Melting Point (°C)	Orientation	Application
<b>Oxides</b>				
[1]Al <sub>2</sub> O <sub>3</sub>	Sapphire	2045	a, c	Beam Delivery
[1]Cr <sup>3+</sup> :Al <sub>2</sub> O <sub>3</sub>	Ruby	2045	c	Laser
[1]Ti <sup>3+</sup> :Al <sub>2</sub> O <sub>3</sub>	Ti:Sapphire	2045	c	Laser
[1]BaB <sub>2</sub> O <sub>4</sub>	BBO	1095		NLO
[2]Nd:BaLaGa <sub>3</sub> O <sub>7</sub>		1650		Laser
[3]Ba(Mg <sub>1/3</sub> Ta <sub>2/3</sub> )O <sub>3</sub>	BMT	2900 - 3100	[112]	Superconducting
[4]Nd <sup>3+</sup> :Ba <sub>2</sub> NaNb <sub>5</sub> O <sub>15</sub>	BNN	1456		NLO
[5]Ba <sub>0.9</sub> Sr <sub>0.1</sub> TiO <sub>3</sub>	BST	1600 - 2080	[110]	Ferroelectric
[1]BaTiO <sub>3</sub>	Barium Titanate	1618	c (Hex phase)	Ferroelectric
[1]BaTiO <sub>3</sub>	Barium Titanate	1618	c (Cubic phase)	Ferroelectric
[6]Bi <sub>12</sub> SiO <sub>20</sub>	BSO	895	[011], [001]	Photorefractive
[6]Bi <sub>12</sub> TiO <sub>20</sub>	BTO	883	[011], [001]	Photorefractive
[7]Eu <sup>2+</sup> , Nd <sup>3+</sup> :CaAl <sub>2</sub> O <sub>4</sub>	CAO-EN	1610		Opt. Prop.
[2]Nd:CaGaAl <sub>3</sub> O <sub>7</sub>				Laser
[2]Nd:CaGdGa <sub>3</sub> O <sub>7</sub>		1610		Laser
[2]Nd:CaLaAl <sub>3</sub> O <sub>7</sub>				Laser
[2]Nd:CaMgZrGGG				Laser
[2]Nd:CaYAl <sub>3</sub> O <sub>7</sub>		1880		Laser
[2]Nd:CaZrGGG				Laser
[8]CaMoO <sub>4</sub>				Laser
[1]CaSc <sub>2</sub> O <sub>4</sub>		2200	a, b, c	Model
[1]Nd:CaSc <sub>2</sub> O <sub>4</sub>		2200	c	Laser
[9]CaTiO <sub>3</sub>			[010]	Opt. prop.
[8]CaWO <sub>4</sub>				Laser
[8]Ti <sup>3+</sup> :Ga <sub>2</sub> O <sub>3</sub>				
[10]Ni, Zr:Gd <sub>3</sub> Ga <sub>5</sub> O <sub>12</sub>	Ni, Zr:GGG	1900	[111]	Laser
[1]Gd <sub>2</sub> (MoO <sub>4</sub> ) <sub>3</sub>		1157	[110]	Ferroelastic
[11]Er <sup>3+</sup> :Gd <sub>2</sub> O <sub>3</sub>		2350	C2/m	Laser
[12]Nd <sup>3+</sup> :Gd <sub>2</sub> O <sub>3</sub>		2350	C2/m	Laser
[2]Nd:7Gd <sub>2</sub> O <sub>3</sub> -9SiO <sub>2</sub>		2040		Laser
[13]Gd <sub>3</sub> Sc <sub>2</sub> Al <sub>3</sub> O <sub>12</sub>	GSAG	1900		Laser
[10]Ni, Zr:Gd <sub>3</sub> Sc <sub>2</sub> Al <sub>3</sub> O <sub>12</sub>	Ni, Zr:GSAG	1900	[111]	Laser
[13]Cr:Gd <sub>3</sub> Sc <sub>2</sub> Al <sub>3</sub> O <sub>12</sub>	Cr:GSAG	1900		Laser
[13]Cr:Gd <sub>3</sub> Sc <sub>2</sub> Ga <sub>3</sub> O <sub>12</sub>	Cr:GSGG	1900		Laser
[14]K <sub>3</sub> Li <sub>2-x</sub> Nb <sub>5+x</sub> O <sub>15+2x</sub>	KLN		a	NLO
[14]Nd:K <sub>3</sub> Li <sub>2-x</sub> Nb <sub>5+x</sub> O <sub>15+2x</sub>	Nd:KLN		a	NLO, Laser
[15]KTa <sub>1-x</sub> Nb <sub>x</sub> O <sub>3</sub>	KTN	<1357	[100]	Photorefractive
[8]LaAlO <sub>3</sub>				Laser
[8]LaGaGeO <sub>7</sub>				Laser
[8]La <sub>3</sub> Ga <sub>5</sub> SiO <sub>14</sub>				Laser
[2]Nd:7La <sub>2</sub> O <sub>3</sub> -9SiO <sub>2</sub>		2040		Laser
[8]Ni <sup>2+</sup> :LiGa <sub>5</sub> O <sub>8</sub>				Laser
[1]Li <sub>2</sub> GeO <sub>3</sub>		1170	a, c	Raman
[16]L <sub>2</sub> O-3B <sub>2</sub> O <sub>3</sub>	LBO	834		NLO

[1]LiNbO <sub>3</sub>	Lithium Niobate	1260	a, c	NLO, SAW
[17]MgO :LiNbO <sub>3</sub>		1260	a, c	NLO, Laser
[1]Nd <sup>3+</sup> :LiNbO <sub>3</sub>		1260	c	Laser
[1]LiTaO <sub>3</sub>	Lithium Tantalate	1650	[110]	SAW
[18]Nd :LiYF <sub>4</sub>	Nd :YLF	825	a	Laser
[18]Tm :LiYF <sub>4</sub>	Tm :YLF	825	a	Laser
[1]Cr :Lu <sub>2</sub> O <sub>3</sub>		2400	c, [110]	Laser
[1]Ti :MgAl <sub>2</sub> O <sub>4</sub>		2105		Laser
[8]Cr <sup>3+</sup> :MgAl <sub>2</sub> O <sub>4</sub>		2105		Laser
[19]Ni <sup>2+</sup> :MgAl <sub>2</sub> O <sub>4</sub>	Spinel	2105		Laser, Opt. Amp.
[20]Cr :Mg <sub>2</sub> SiO <sub>4</sub>	Cr :Forsterite	1890		Laser
[2]Nd :MgZrGGG				Laser
[8]Er <sup>3+</sup> , Nd <sup>3+</sup> , Er <sup>3+</sup> -Yb <sup>3+</sup> :NaLa(WO <sub>4</sub> ) <sub>2</sub>				Laser
[8]Er <sup>3+</sup> , Er <sup>3+</sup> -Yb <sup>3+</sup> :NaY(WO <sub>4</sub> ) <sub>2</sub>				Laser
[1]Nb <sub>2</sub> O <sub>5</sub>		1495		Opt. Prop.
[1]Nd <sub>2</sub> SiO <sub>5</sub>		1980		Laser
[8]PbMoO <sub>4</sub>				Laser
[1]Cr :Sc <sub>2</sub> O <sub>3</sub>		2400	c, [110]	Laser
[8]Er <sup>3+</sup> , Ti <sup>3+</sup> :Sc <sub>2</sub> O <sub>3</sub>		2400		Laser
[1]ScTaO <sub>4</sub>		2300	a	Ferroelectric
[1]ScNbO <sub>4</sub>		2100		Ferroelectric
[21]Er <sup>3+</sup> :Sc <sub>2</sub> O <sub>3</sub> :LiNbO <sub>3</sub>				Laser, Opt. Amp.
[22]Nd <sup>3+</sup> :Sc <sub>2</sub> O <sub>3</sub> :LiNbO <sub>3</sub>				NLO
[7]Eu <sup>2+</sup> , Du <sup>3+</sup> :SrAl <sub>2</sub> O <sub>4</sub>	SAO-ED	1960	α-phase	Opt. Prop.
[1]SrBaNb <sub>2</sub> O <sub>6</sub>	SBN	1700	a, c	Photorefractive
[23]Ce :Sr <sub>0.6</sub> Ba <sub>0.4</sub> Nb <sub>2</sub> O <sub>6</sub>	Ce :SBN60	1700	a	Photorefractive
[24]Ce :Sr <sub>0.61</sub> Ba <sub>0.39</sub> Nb <sub>2</sub> O <sub>6</sub>	Ce :SBN61	1700	c	Photorefractive
[1]SrBaTi <sub>2</sub> O <sub>6</sub>		1500	a, c	Ferroelectric
[2]Nd :SrGaAl <sub>3</sub> O <sub>7</sub>		1350		Laser
[2]Nd :SrGdGa <sub>3</sub> O <sub>7</sub>		1600		Laser
[25]SrHfO <sub>3</sub>	SHO	2500	[1-11]	Material Study
[26]Sr <sub>2</sub> RuO <sub>4</sub>			[001]	Superconducting
[1]SrSc <sub>2</sub> O <sub>4</sub>		2200		Model
[1]SrTiO <sub>3</sub>	Strontium Titanate	1860		Superconducting
[27] SrVO <sub>3</sub>	Strontium vanade		[100]	Opt. prop.
[1]Ti :YAIO <sub>3</sub>	Ti :YAP	1875		Laser
[1]Y <sub>3</sub> Al <sub>5</sub> O <sub>12</sub>	YAG	1940	[111], [100]	Laser
[28]Ca, Cr :Y <sub>3</sub> Al <sub>5</sub> O <sub>12</sub>	Ca, Cr :YAG	1940	[110], [111], [211]	Laser
[13]Er :Y <sub>3</sub> Al <sub>5</sub> O <sub>12</sub>	Er :YAG	1940		Laser
[13]Ho :Y <sub>3</sub> Al <sub>5</sub> O <sub>12</sub>	Ho :YAG	2940		
[1]Nd :Y <sub>3</sub> Al <sub>5</sub> O <sub>12</sub>	Nd :YAG	1940	[111], [100]	Laser
[8]Ti <sup>3+</sup> :Y <sub>3</sub> Al <sub>5</sub> O <sub>12</sub>	Ti :YAG	1940		Laser
[13]Tm :Y <sub>3</sub> Al <sub>5</sub> O <sub>12</sub>	Tm :YAG	1940	[111]	Laser
[1]YFe <sub>5</sub> O <sub>12</sub>	YIG	1555	[110]	Isolator
[1]Cr :Y <sub>2</sub> O <sub>3</sub>		2400	c, [110]	Laser
[1]Eu :Y <sub>2</sub> O <sub>3</sub>		2410	c	Laser
[8]Er <sup>3+</sup> , Ho <sup>3+</sup> , Nd <sup>3+</sup> :Y <sub>2</sub> O <sub>3</sub>		>2400		Laser

[29]Tb <sup>3+</sup> , Tm <sup>3+</sup> , Yb <sup>3+</sup> :Y <sub>2</sub> O <sub>3</sub>		2450		Laser
[13]Cr:Y <sub>3</sub> Sc <sub>2</sub> Al <sub>3</sub> O <sub>12</sub>	Cr:YSAG	1900	[111]	Laser
[8]Er <sup>3+</sup> :YScO <sub>3</sub>		>2400		Laser
[30]YVO <sub>4</sub>	Yttrium orthovanadate		a	Laser
[31]Y <sub>2</sub> O <sub>3</sub> -ZrO <sub>2</sub>	YSZ	2700		Thermometry
[32]ZnLiNbO <sub>4</sub>	ZLN			NLO
<b>Fluorides</b>				
[1]BaF <sub>2</sub>	Barium Fluoride	1280	[100]	IR Guiding
[1]CaF <sub>2</sub>	Calcium Fluoride	1360	[111]	IR Guiding
[8]RbMnF <sub>3</sub>				Laser
<b>Eutectics</b>				
[1]LiF-NaF		676		Eutectics
[1]Li <sub>2</sub> O-GeO <sub>2</sub>		1106		Eutectics
[1]NaF-NaCl		640		Eutectics
[1]PbF <sub>2</sub> -Al <sub>2</sub> F <sub>3</sub>		565		
[33]MgTiO <sub>3</sub> -CaTiO <sub>3</sub>		1650- 1720		Microwave
<b>Semiconductors &amp; Metallics</b>				
[1]B <sub>9</sub> C		2400		Thermoelectric
[34]Bi <sub>2</sub> Sr <sub>2</sub> CaCu <sub>2</sub> O <sub>8</sub>		900		Superconducting
[34]Bi <sub>1.8</sub> Sr <sub>1.8</sub> Ca <sub>1.2</sub> Cu <sub>2.2</sub> O <sub>8</sub>		900		Superconducting
[1]Co		1495		Magnetics
[1]Fe		1539		Magnetics
[1]Fe-Co		1500		Magnetics
[1]Ge		960		IR Guiding
[1]LaB <sub>6</sub>		2716		Cathode Filament
[1]Nb		2468		Superconducting
[1]Si		1420	[111]	Model

## References

- [1] R. S. Feigelson, *Mater. Sci. Eng.*, **B1**, 67, 1988
- [2] L. R. Black, D. M. Andrauskas, G. F. de la Fuente and H. R. Verdún, *Proc. SPIE* **1104**, 175, 1989
- [3] R. Guo, A. S. Bhalla and L. E. Cross, *J. Appl. Phys.*, **75** (9), 4704, 1994
- [4] M. Ferriol, G. Foulon, A. Brennier and G. Boulon, *J. Mater. Sci.*, **33**, 1227, 1998
- [5] D. Garcia, R. Guo and A. S. Bhalla, *Mater. Lett.*, **42**, 136, 2000
- [6] V. V. Prokofiev, J. P. Andreetta, C. J. de Lima, M. R. B. Andreetta, A. C. Hernandez, J. F. Carvalho, A. A. Kamshilin and T. Jääskeläinen, *J. Cryst. Growth*, **137**, 528, 1994
- [7] W. Jia, H. Yuan, L. Lu, H. Liu and W. M. Yen, *J. Cryst. Growth*, **200**, 179, 1999
- [8] B. M. Tissue, L. Lu, L. Ma, W. Jia, M. L. Norton and W. M. Yen, *J. Cryst. Growth*, **109**, 323, 1991
- [9] Y. Jiang, R. Guo and A. S. Bhalla, *J. Electroceram.*, **2:3**, 199, 1998
- [10] L. M. Thomas, D. M. Andrauskas and H. R. Verdún, *Proc. SPIE* **1104**, 87, 1989
- [11] A. Brennier, *Chem. Phys. Lett.*, **290**, 329, 1998
- [12] A. Brennier and G. Boulon, *J. Luminesc.*, **82**, 285, 1999
- [13] R. S. F. Chang, S. Sengupta, G. J. Dixon, L. B. Shaw and N. Djeu, *Proc. SPIE* **1104**, 244, 1989
- [14] M. Ferriol, G. Foulon, A. Brenier, M. T. Cohen-Adad, G. Boulon, *J. Cryst. Growth*, **173**, 226, 1997
- [15] T. Imai, S. Yagi, Y. Sugiyama and I. Hatakeyama, *J. Cryst. Growth*, **147**, 350, 1995
- [16] Y. Ji, S. Zhao, Y. Huo, H. Zhang, M. Li and C. Huang, *J. Cryst. Growth*, **112**, 283, 1991
- [17] M. Ferriol, A. Dakki, M. T. Cohen-Adad, G. Foulon, A. Brenier and G. Boulon, *J. Cryst. Growth*, **178**, 529, 1997
- [18] L. B. Shaw and R. S. F. Chang, *J. Cryst. Growth*, **112**, 731, 1991

- [19] L. H. Wang, M. H. Hon, L. F. Scheemeyer, G. A. Thomas and W. L. Wilson, *Mater. Res. Bull.*, **33**(12), 1793, 1998
- [20] W. Jia, L. Lu, B. M. Tissue and W. M. Yen, *J. Cryst. Growth*, **109**, 329, 1991
- [21] R. Burlot, R. Moncorgé and G. Boulon, *J. Lumin.*, **72-74**, 135, 1997
- [22] R. Burlot, R. Moncorgé and G. Boulon, *J. Lumin.*, **72-74**, 812, 1997
- [23] Y. Sugiyama, I. Hatakeyama and I. Yokohama, *J. Cryst. Growth*, **134**, 255, 1993
- [24] J. K. Yamamoto, S. A. Markgraf and A. S. Bhalia, *J. Cryst. Growth*, **123**, 423, 1992
- [25] M. R. B. Andreetta, A. C. Hernandez, S. L. Cuffini, J. A. Guevara and Y. P. Mascarenhas, *J. Cryst. Growth*, **200**, 621, 1999
- [26] D. Reyes Ardila, M. R. B. Andreetta, S. L. Cuffini, A. C. Hernandez, J. P. Andreetta and Y. P. Mascarenhas, *J. Cryst. Growth*, **177**, 52, 1997
- [27] D. Reyes Ardila, J. P. Andreetta and H. C. Basso, *J. Cryst. Growth*, **211**, 313, 2000
- [28] S. Ishibashi, K. Naganuma and I. Yokohama, *J. Cryst. Growth*, **183**, 614, 1998
- [29] C. Goutaudier, F. S. Ermeneux, M. T. Cohen-Adad and R. Moncorge, *J. Cryst. Growth*, **210**, 694, 2000
- [30] C. H. Huang, J. C. Chen and C. Hu, *J. Cryst. Growth*, **211**, 237, 2000
- [31] L. Tong, *J. Cryst. Growth*, **217**, 281, 2000
- [32] M. Ferriol, Y. Terada, T. Fukuda and G. Boulon, *J. Cryst. Growth*, **197**, 221, 1999
- [33] Y. Jiang, R. Guo and A. S. Bhalla, *J. Phys. Chem. Solids*, **59**(5), 611, 1998
- [34] R. S. Feigelson, D. Gazit, D. K. Fork and T. H. Geballe, *Sci.*, **240**, 1642, 1988

**APPENDIX B**

**LHPG control software**

```

unit PIUnit1;
  {$X+}

  interface

    uses
      Windows, Messages, SysUtils, Classes, Graphics, Controls, Forms,
      Dialogs,
      StdCtrls, Global, ComCtrls, ExtCtrls, Buttons, OleCtrls,
      chartfx3, Driver;

    {const
      a = 2;}

    type
      TForm1 = class(TForm)
        GroupBox1: TGroupBox;
        EXIT: TButton;
        INITIALISE_MOTORS: TButton;
        Panel1: TPanel;
        Label1: TLabel;
        PullRate: TEdit;
        Label2: TLabel;
        DiaRatio: TEdit;
        Panel2: TPanel;
        GO: TButton;
        STOP: TButton;
        Label9: TLabel;
        Label8: TLabel;
        Panel5: TPanel;
        Label11: TLabel;
        FibreGrown: TEdit;
        Label12: TLabel;
        Timer1: TTimer;
        OpenDialog1: TOpenDialog;
        GroupBox3: TGroupBox;
        Pull_Vel: TEdit;
        Feed_Vel: TEdit;
        ShowGraph: TButton;
        Label6: TLabel;
        Label7: TLabel;
        GroupBox4: TGroupBox;
        Label13: TLabel;
        Label14: TLabel;
        Label15: TLabel;
        GroupBox5: TGroupBox;
        Label16: TLabel;
        Label17: TLabel;
        GroupBox6: TGroupBox;
        GroupBox7: TGroupBox;
        BottomStageUp: TBitBtn;
        BottomStageDown: TBitBtn;
        BottomStageLeft: TBitBtn;
        BottomStageRight: TBitBtn;
        BottomStageNW: TBitBtn;
        BottomStageNE: TBitBtn;
        BottomStageSW: TBitBtn;
      end;
  end;

```

```

BottomStageSE: TBitBtn;
  BitBtn1: TBitBtn;
  GroupBox8: TGroupBox;
  BottomEdit: TEdit;
BottomScroll: TScrollBar;
  GroupBox9: TGroupBox;
  TopEdit: TEdit;
TopScroll: TScrollBar;
  TopStageUp: TBitBtn;
  TopStageDown: TBitBtn;
  TopStageLeft: TBitBtn;
  TopStageRight: TBitBtn;
  TopStageNW: TBitBtn;
  TopStageNE: TBitBtn;
  TopStageSW: TBitBtn;
  TopStageSE: TBitBtn;
  BitBtn2: TBitBtn;
  GroupBox2: TGroupBox;
  Timer2: TTimer;
GroupBox11: TGroupBox;
  BREAKSTART: TButton;
  BREAKSTOP: TButton;
GroupBox12: TGroupBox;
POSITIONSTART: TButton;
POS_PULL_STOP: TBitBtn;
POS_FEED_STOP: TBitBtn;
  Label18: TLabel;
  Label19: TLabel;
  Timer3: TTimer;
GroupBox10: TGroupBox;
GroupBox13: TGroupBox;
  InLineLength: TEdit;
  EndTaper: TEdit;
  InLineStart: TButton;
  EndStart: TButton;
  FeedUpBitBtn: TBitBtn;
FeedDownBitBtn: TBitBtn;
  Label4: TLabel;
  PullUpBitBtn: TBitBtn;
  PullDownBitBtn: TBitBtn;
  Label5: TLabel;
  Label3: TLabel;
  FeedRate: TEdit;
  Label10: TLabel;
InLineDiaChange: TEdit;
  InLineStop: TButton;
  Label20: TLabel;
  Label21: TLabel;
  Label22: TLabel;
  EndStop: TButton;
GroupBox14: TGroupBox;
GroupBox15: TGroupBox;
  Edit1: TEdit;
ScrollBar1: TScrollBar;
  Button1: TButton;
  Edit2: TEdit;
  Edit3: TEdit;

```

```

        Button2: TButton;
        Edit7: TEdit;
        Edit4: TEdit;
        Edit5: TEdit;
        d: TLabel;
        Label23: TLabel;
        Label24: TLabel;
        Button3: TButton;
        Timer4: TTimer;
        Button4: TButton;
        Edit6: TEdit;
        Label25: TLabel;
        Edit8: TEdit;
        Label26: TLabel;
        Button5: TButton;
    procedure FormCreate(Sender: TObject);
    procedure EXITClick(Sender: TObject);
    procedure GOClick(Sender: TObject);
    procedure STOPClick(Sender: TObject);
    procedure INITIALISE_MOTORSClick(Sender: TObject);
procedure FeedUpBitBtnMouseDown(Sender: TObject; Button: TMouseButton;
    Shift: TShiftState; X, Y: Integer);
    procedure FeedUpBitBtnMouseUp(Sender: TObject; Button: TMouseButton;
    Shift: TShiftState; X, Y: Integer);
    procedure FeedDownBitBtnMouseDown(Sender: TObject;
    Button: TMouseButton; Shift: TShiftState; X, Y: Integer);
procedure FeedDownBitBtnMouseUp(Sender: TObject; Button: TMouseButton;
    Shift: TShiftState; X, Y: Integer);
procedure PullUpBitBtnMouseDown(Sender: TObject; Button: TMouseButton;
    Shift: TShiftState; X, Y: Integer);
    procedure PullUpBitBtnMouseUp(Sender: TObject; Button: TMouseButton;
    Shift: TShiftState; X, Y: Integer);
    procedure PullDownBitBtnMouseDown(Sender: TObject;
    Button: TMouseButton; Shift: TShiftState; X, Y: Integer);
procedure PullDownBitBtnMouseUp(Sender: TObject; Button: TMouseButton;
    Shift: TShiftState; X, Y: Integer);
    procedure PullRateClick(Sender: TObject);
    procedure PullRateExit(Sender: TObject);
    procedure DiaRatioClick(Sender: TObject);
    procedure DiaRatioExit(Sender: TObject);
    procedure PullRateChange(Sender: TObject);
    procedure Timer1Timer(Sender: TObject);
    procedure ShowGraphClick(Sender: TObject);
    procedure BottomScrollChange(Sender: TObject);
procedure BottomStageUpMouseDown(Sender: TObject; Button: TMouseButton;
    Shift: TShiftState; X, Y: Integer);
    procedure BottomStageUpMouseUp(Sender: TObject; Button: TMouseButton;
    Shift: TShiftState; X, Y: Integer);
    procedure BottomStageDownMouseDown(Sender: TObject;
    Button: TMouseButton; Shift: TShiftState; X, Y: Integer);
procedure BottomStageDownMouseUp(Sender: TObject; Button: TMouseButton;
    Shift: TShiftState; X, Y: Integer);
    procedure BottomStageLeftMouseDown(Sender: TObject;
    Button: TMouseButton; Shift: TShiftState; X, Y: Integer);
procedure BottomStageLeftMouseUp(Sender: TObject; Button: TMouseButton;
    Shift: TShiftState; X, Y: Integer);
    procedure BottomStageRightMouseDown(Sender: TObject;

```

```

    Button: TMouseButton; Shift: TShiftState; X, Y: Integer);
    procedure BottomStageRightMouseUp(Sender: TObject;
    Button: TMouseButton; Shift: TShiftState; X, Y: Integer);
procedure BottomStageNEMouseDown(Sender: TObject; Button: TMouseButton;
    Shift: TShiftState; X, Y: Integer);
    procedure BottomStageNEMouseUp(Sender: TObject; Button: TMouseButton;
    Shift: TShiftState; X, Y: Integer);
procedure BottomStageNWMouseDown(Sender: TObject; Button: TMouseButton;
    Shift: TShiftState; X, Y: Integer);
    procedure BottomStageNWMouseUp(Sender: TObject; Button: TMouseButton;
    Shift: TShiftState; X, Y: Integer);
procedure BottomStageSWMouseDown(Sender: TObject; Button: TMouseButton;
    Shift: TShiftState; X, Y: Integer);
    procedure BottomStageSWMouseUp(Sender: TObject; Button: TMouseButton;
    Shift: TShiftState; X, Y: Integer);
procedure BottomStageSEMouseDown(Sender: TObject; Button: TMouseButton;
    Shift: TShiftState; X, Y: Integer);
    procedure BottomStageSEMouseUp(Sender: TObject; Button: TMouseButton;
    Shift: TShiftState; X, Y: Integer);
    procedure TopStageUpMouseDown(Sender: TObject; Button: TMouseButton;
    Shift: TShiftState; X, Y: Integer);
    procedure TopStageUpMouseUp(Sender: TObject; Button: TMouseButton;
    Shift: TShiftState; X, Y: Integer);
procedure TopStageDownMouseDown(Sender: TObject; Button: TMouseButton;
    Shift: TShiftState; X, Y: Integer);
    procedure TopStageDownMouseUp(Sender: TObject; Button: TMouseButton;
    Shift: TShiftState; X, Y: Integer);
procedure TopStageLeftMouseDown(Sender: TObject; Button: TMouseButton;
    Shift: TShiftState; X, Y: Integer);
    procedure TopStageLeftMouseUp(Sender: TObject; Button: TMouseButton;
    Shift: TShiftState; X, Y: Integer);
procedure TopStageRightMouseDown(Sender: TObject; Button: TMouseButton;
    Shift: TShiftState; X, Y: Integer);
    procedure TopStageRightMouseUp(Sender: TObject; Button: TMouseButton;
    Shift: TShiftState; X, Y: Integer);
    procedure TopStageNWMouseDown(Sender: TObject; Button: TMouseButton;
    Shift: TShiftState; X, Y: Integer);
    procedure TopStageNWMouseUp(Sender: TObject; Button: TMouseButton;
    Shift: TShiftState; X, Y: Integer);
procedure TopStageNEMouseDown(Sender: TObject; Button: TMouseButton;
    Shift: TShiftState; X, Y: Integer);
    procedure TopStageNEMouseUp(Sender: TObject; Button: TMouseButton;
    Shift: TShiftState; X, Y: Integer);
procedure TopStageSWMouseDown(Sender: TObject; Button: TMouseButton;
    Shift: TShiftState; X, Y: Integer);
    procedure TopStageSWMouseUp(Sender: TObject; Button: TMouseButton;
    Shift: TShiftState; X, Y: Integer);
procedure TopStageSEMouseDown(Sender: TObject; Button: TMouseButton;
    Shift: TShiftState; X, Y: Integer);
    procedure TopStageSEMouseUp(Sender: TObject; Button: TMouseButton;
    Shift: TShiftState; X, Y: Integer);
    procedure TopScrollChange(Sender: TObject);
    procedure GroupBox2Click(Sender: TObject);
    procedure Timer2Timer(Sender: TObject);
    procedure BREAKSTARTClick(Sender: TObject);
    procedure BREAKSTOPClick(Sender: TObject);
    procedure POSITIONSTARTClick(Sender: TObject);

```

```

procedure POS_PULL_STOPClick(Sender: TObject);
procedure POS_FEED_STOPClick(Sender: TObject);
    procedure Timer3Timer(Sender: TObject);
    procedure DiaRatioChange(Sender: TObject);
    procedure FeedRateChange(Sender: TObject);
    procedure EndStartClick(Sender: TObject);
procedure PullUpBitBtnKeyPress(Sender: TObject; var Key: Char);
    procedure PullUpBitBtnKeyUp(Sender: TObject; var Key: Word;
        Shift: TShiftState);
procedure PullDownBitBtnKeyPress(Sender: TObject; var Key: Char);
    procedure PullDownBitBtnKeyUp(Sender: TObject; var Key: Word;
        Shift: TShiftState);
procedure FeedUpBitBtnKeyPress(Sender: TObject; var Key: Char);
    procedure FeedUpBitBtnKeyUp(Sender: TObject; var Key: Word;
        Shift: TShiftState);
procedure FeedDownBitBtnKeyPress(Sender: TObject; var Key: Char);
    procedure FeedDownBitBtnKeyUp(Sender: TObject; var Key: Word;
        Shift: TShiftState);
    procedure InLineStartClick(Sender: TObject);
    procedure InLineStopClick(Sender: TObject);
    procedure EndStopClick(Sender: TObject);
    procedure Button1Click(Sender: TObject);
    procedure Button2Click(Sender: TObject);
    procedure ScrollBar1Change(Sender: TObject);
    procedure Button3Click(Sender: TObject);
    procedure Button4Click(Sender: TObject);
    procedure Button5Click(Sender: TObject);
        private
            { Private declarations }
            (Vel_Array : array [1..40] of real;
            public
                { Public declarations }
                {Following entries for PI Card}
                FileHandle1      : Integer;
                FileHandle2      : Integer;
                Last_Pull_Position : longint;
                Last_Feed_Position : longint;
                Last_Velocity     : real;
                No_Points         : integer;
                Pnt_Cntr          : integer;
                Point_Now         : integer;
                Page_No           : integer;
                Pull_Vel_Array    : array [1..20] of real;
                Feed_Vel_Array    : array [1..20] of real;
                F                  : TextFile;
                Record_No, K      : Longint;
                Time_Counter      : double;

                {For fibre positioning using keyboard}
                PullMotor_Up      : boolean;
                PullMotor_Down    : boolean;
                FeedMotor_Up      : boolean;
                FeedMotor_Down    : boolean;

                {In_Line Taper}
                Taper_Op          : boolean;
                Relative_Pull_Position : longint;

```

```

    {Following entries for DA Card}
    tempNum          : smallint;
{lpAOVoltageOut      : PT_AOVoltageOut;}
    ii              : integer;
    In_Single_BottomStage : single;
    Out_Single_BottomStage : single;
    In_Single_TopStage   : single;
    Out_Single_TopStage  : single;
    RefSrc             : short;
{LaserOutput         : single;}
    status          : integer;
    P               : integer;

    end;
    var
        Form1: TForm1;

    implementation

        uses PIUnit2;

        {$R *.DFM}
        {$I PItest1.pas}

        const
            n_pull = 4742.716048;
            n_feed = 37941.728384;
{n_pull              := (2*29.6419753*80);
n_feed              := (4*29.6419753*320);}

            Pull_Const_1 = -1317.421134;
{Pull_Const_1 := 4742.716048*1000/3600}

            Pull_Const_2 = -4742716.048;
{Pull_Const_2 := 4742.716048*1000}

        function      ValFn(S:string) : Real;
        var
            code : integer;
            L     : Real;
        begin
            Val(S, L, code);
            ValFn := L;
        end;

        function      StrFn(L: Real) : string;
        var
            S : string;
        begin
            Str(L: 6: 5,S);
            StrFn := S;
        end;

    procedure TForm1.FormCreate(Sender: TObject);
        var
            Response : integer;
        {Following entries for DA Card}
        MaxEntries, OutEntries : Smallint;
        i, j                   : Integer;

```

```

tempStr          : String;
bRun             : boolean;
Chan            : short;
(status         : integer;
begin
{Following entries for PI DC-Controller}
    c842_open;
    Set_BaseAddress($210);
    Board_Installed;
    Axis_Installed;
    InitBoard($9);
    autodetect;

    If autodetect <0 then
        begin
Response := Application.MessageBox('Limit switch hit!', 'ERROR', MB_OK);
        end;

        InitAxis(1);
        InitAxis(2);

        {StrPCopy(Cmd_Str_Pntr, '1ASN'#00');
        translate(Cmd_Str_Pntr, Rep_Str_Pntr);}

        {StrPCopy(Cmd_Str_Pntr, '1SAN'#00');
        translate(Cmd_Str_Pntr, Rep_Str_Pntr);}

Point_Now :=0;      {Initialising counters for Timer}
                    No_Points :=1;
                    Page_No :=1;
                    Pnt_Cntr :=0;

                    {Following entries for DA Card}
                    MaxEntries := 9;
                    bRun := False;

ErrCde := DRV_DeviceGetList(DeviceList[0], MaxEntries, OutEntries);
        If (ErrCde<>0) then
            begin
                DRV_GetErrorMessage(ErrCde, pszErrMsg);
                Response := Application.MessageBox(pszErrMsg, 'Error!', MB_OK);
            end;

ErrCde := DRV_DeviceGetNumOfList(MaxEntries);
        For i:= 0 to (MaxEntries-1) do
            begin
                tempStr := '';
                For j := 0 to MaxDevNameLen do
                    begin
                        tempStr := tempStr + DeviceList[i].szDeviceName[j];
                    end;
                {Edit1.Text :=tempStr;} {Must Change to show device connected}
            end;

ErrCde := DRV_DeviceOpen(dwDeviceNum, DeviceHandle);
        if (ErrCde<>0) then
            begin

```

```

        DRV_GetErrorMessage(ErrCde, pszErrMsg);
Response := Application.MessageBox(pszErrMsg, 'Error!', MB_OK);
        end
        else
            {ptDevGetFeatures.buffer := nil;}
            ptDevGetFeatures.buffer := @lpDevFeatures;
ErrCde := DRV_DeviceGetFeatures(DeviceHandle,
                                ptDevGetFeatures);

tempNum := lpDevFeatures.usMaxAOCh1;
tempNum := lpDevFeatures.usMaxDOCh1;
        {For chan := 0 to 3 do
            begin
                ptAOConfig.chan := chan;
                ptAOConfig.RefSrc := 0;
                ptAOConfig.MaxValue := 10.0;
                ptAOConfig.MinValue := -10.0;
                ErrCde := DRV_AOConfig(DeviceHandle, ptAOConfig);
                end;

                For chan := 4 to 5 do
                    begin
                        ptAOConfig.chan := chan;
                        ptAOConfig.RefSrc := 0;
                        ptAOConfig.MaxValue := 5.0;
                        ptAOConfig.MinValue := 0.0;
                        ErrCde := DRV_AOConfig(DeviceHandle, ptAOConfig);
                    end;}

{ErrCde := DRV_AOVoltageOut(DeviceHandle, lpAOVoltageOut); }

        end;

procedure TForm1.EXITClick(Sender: TObject);
    var
        ptDevGetFeatures : PT_DeviceGetFeatures;
        i, j : integer;
    begin
        c842_close;
        close;
        {Clearing Digital In/Out}
        For i := 0 to 7 do
            begin
                ptDioWriteBit.port := 1;
                ptDioWriteBit.bit := i;
                ptDioWriteBit.state := 0;
                ErrCde := DRV_DioWriteBit(DeviceHandle, ptDioWriteBit);
                end;

            {Clearing Analogue In/Out}
            For j := 0 to 3 do
                begin
                    ptAOVoltageOut.chan := j;
                    ptAOVoltageOut.OutputValue := 0.00;
                    ErrCde := DRV_AOVoltageOut(DeviceHandle, ptAOVoltageOut);
                end;

```

```

        ptAOVoltageOut.chan          := 4;
        ptAOVoltageOut.OutputValue := -9.94;

ErrCde := DRV_AOVoltageOut(DeviceHandle,ptAOVoltageOut);

        {Close DA Card driver and exit}
        bRun          := True;
        ptDevGetFeatures.buffer:= nil;
        if bRun then
            DRV_DeviceClose(DeviceHandle);
            close;
        end;

        procedure TForm1.GOClick(Sender: TObject);
        var Vpull_whole, Vfeed_whole      : longint;
            Vpull_str, Vfeed_str          : string;
            Vpull_real, Real_Feed, Vfeed_real : real;
            f, b, c,i                     : Integer;

            begin
                Last_Pull_Position := 0;
                Last_Feed_Position := 0;

                FeedRate.Text      :=
                StrFn(ValFn(PullRate.Text)/Sqr(ValFn(DiaRatio.Text)));

                {Calculating Pull Rate with 80:1 gearbox ==> Channel 1}
                Vpull_real := (StrToFloat(PullRate.Text)*(n_pull*1000/60));
                Vpull_whole := Trunc(Vpull_real);
                Vpull_str   := '1SV' + IntToStr(Vpull_whole) + #00;

                {Calculating Feed Rate with 320:1 gearbox ==> Channel 2}
                Real_Feed := (ValFn(PullRate.Text)/Sqr(ValFn(DiaRatio.Text)));
                Vfeed_real := (Real_Feed*(n_feed*1000/60));
                Vfeed_whole := Trunc(Vfeed_real);
                Vfeed_str   := '2SV' + IntToStr(Vfeed_whole) + #00;

                StrPCopy(Cmd_Str_Pntr, '1DH'#00'');
                translate(Cmd_Str_Pntr, Rep_Str_Pntr);

                StrPCopy(Cmd_Str_Pntr, '2DH'#00'');
                translate(Cmd_Str_Pntr, Rep_Str_Pntr);

                StrPCopy(Cmd_Str_Pntr, '1SA-50'#00'');
                translate(Cmd_Str_Pntr, Rep_Str_Pntr);

                StrPCopy(Cmd_Str_Pntr, '2SA135'#00'');
                translate(Cmd_Str_Pntr, Rep_Str_Pntr);

                StrPCopy(Cmd_Str_Pntr, Vpull_str);          {Pull Velocity -> Chan 1}
                translate(Cmd_Str_Pntr, Rep_Str_Pntr);

                StrPCopy(Cmd_Str_Pntr, Vfeed_str);          {Feed Velocity -> Chan 2}
                translate(Cmd_Str_Pntr, Rep_Str_Pntr);
            end;

```

```

                {Pull Displacement}
{StrPCopy(Cmd_Str_Pntr, '1MR-1043397531'#00'');} {-ve movement = UP}
{translate(Cmd_Str_Pntr,Rep_Str_Pntr);}           {+ve movement = DOWN}

```

```

                {Feed Displacement - Il faut : 1073600000}
{StrPCopy(Cmd_Str_Pntr, '2MR1073600000'#00'');} {-ve movement = DOWN}
{translate(Cmd_Str_Pntr,Rep_Str_Pntr);}           {+ve movement = UP}

```

```

GO.Enabled           := FALSE;
STOP.Enabled         := TRUE;
FeedUpBitBtn.Enabled := FALSE;
FeedDownBitBtn.Enabled := FALSE;
PullUpBitBtn.Enabled := FALSE;
PullDownBitBtn.Enabled := FALSE;

```

```

Timer1.Enabled      := TRUE;
Timer2.Enabled      := TRUE;
Label13.Caption     := 'Start Time   : ' + TimeToStr(Time);

```

```
end;
```

```
procedure TForm1.STOPClick(Sender: TObject);
```

```
begin
```

```
FileClose(FileHandle1);
FileClose(FileHandle2);
```

```
StrPCopy(Cmd_Str_Pntr, 'CLP'#00'');
translate(Cmd_Str_Pntr,Rep_Str_Pntr);
```

```
StrPCopy(Cmd_Str_Pntr, 'AB'#00'');
translate(Cmd_Str_Pntr,Rep_Str_Pntr);
```

```
FibreGrown.Text     := FloatToStr(get_pos(1)*(-
1)/(2*29.6419753*80*1000));
```

```
GO.Enabled           := FALSE;
STOP.Enabled         := FALSE;
PullRate.Enabled     := FALSE;
DiaRatio.Enabled     := FALSE;
FeedUpBitBtn.Enabled := TRUE;
FeedDownBitBtn.Enabled := TRUE;
PullUpBitBtn.Enabled := TRUE;
PullDownBitBtn.Enabled := TRUE;
Timer1.Enabled       := FALSE;
Timer2.Enabled       := FALSE;

```

```
Point_Now           :=0;
No_Points           :=1;
{Page_No           :=1 ;}
```

```
Pnt_Cntr           :=0; { resets pointer counter }
Label14.Caption     := 'Stop Time   : ' + TimeToStr(Time);
```

```
end;
```

```
procedure TForm1.INITIALISE_MOTORSClick(Sender: TObject);
```

```
{var
```

```

        MyFileStream:TFileStream;
        Buff:array [1..20] of char;
        begin
            PullMotor_UP      := False;
            PullMotor_Down    := False;
            FeedMotor_Up      := False;
            FeedMotor_Down    := False;
            Record_No         := 0;
            Time_Counter      := 0;

            {Taper_Op          := FALSE;}

            { open the First ascii storage Data file}
OpenDialog1.Filter := 'Text files (*.txt)|*.TXT';
            OpenDialog1.execute;

            FileHandle1:=FileCreate(OpenDialog1.FileName);

            { open the Second ascii Data storage file}
OpenDialog1.Filter := 'Text files (*.txt)|*.TXT';
            OpenDialog1.execute;

            FileHandle2:=FileCreate(OpenDialog1.FileName);

            {Initialising PI motors}
            StrPCopy(Cmd_Str_Pntr, 'CLP'#00'');
            translate(Cmd_Str_Pntr,Rep_Str_Pntr);

            StrPCopy(Cmd_Str_Pntr, 'CLR'#00'');
            translate(Cmd_Str_Pntr,Rep_Str_Pntr);

            StrPCopy(Cmd_Str_Pntr, 'SST4'#00'');
            translate(Cmd_Str_Pntr,Rep_Str_Pntr);

            {StrPCopy(Cmd_Str_Pntr, 'ASN'#00'');
            translate(Cmd_Str_Pntr,Rep_Str_Pntr);}

            {StrPCopy(Cmd_Str_Pntr, 'SAN'#00'');
            translate(Cmd_Str_Pntr,Rep_Str_Pntr);}

            StrPCopy(Cmd_Str_Pntr, 'SFP'#00'');
            translate(Cmd_Str_Pntr,Rep_Str_Pntr);

            StrPCopy(Cmd_Str_Pntr, '1DP70'#00'');
            translate(Cmd_Str_Pntr,Rep_Str_Pntr);

            StrPCopy(Cmd_Str_Pntr, '2DP45'#00'');
            translate(Cmd_Str_Pntr,Rep_Str_Pntr);

            StrPCopy(Cmd_Str_Pntr, 'DI8'#00'');
            translate(Cmd_Str_Pntr,Rep_Str_Pntr);

            StrPCopy(Cmd_Str_Pntr, 'DD5'#00'');
            translate(Cmd_Str_Pntr,Rep_Str_Pntr);

            StrPCopy(Cmd_Str_Pntr, 'DL1500'#00'');

```

```

translate(Cmd_Str_Pntr,Rep_Str_Pntr);

StrPCopy(Cmd_Str_Pntr, '1SPV'#00');
translate(Cmd_Str_Pntr, Rep_Str_Pntr);

StrPCopy(Cmd_Str_Pntr, '2SPV'#00');
translate(Cmd_Str_Pntr, Rep_Str_Pntr);

FibreGrown.Text := '0.0';
GO.Enabled := TRUE;
PullRate.Enabled := TRUE;
DiaRatio.Enabled := TRUE;
(STOP.Enabled := TRUE;);
FeedUpBitBtn.Enabled := TRUE;
FeedDownBitBtn.Enabled := TRUE;
PullUpBitBtn.Enabled := TRUE;
PullDownBitBtn.Enabled := TRUE;
GroupBox2.ShowHint := FALSE;

InLineStart.Enabled := TRUE;
InLineStop.Enabled := TRUE;

EndStart.Enabled := TRUE;
EndStop.Enabled := TRUE;

Label13.Caption := 'Start Time';
Label14.Caption := 'Stop Time';
Label15.Caption := 'Current Time';
end;

procedure TForm1.FeedUpBitBtnMouseDown(Sender: TObject;
Button: TMouseButton; Shift: TShiftState; X, Y: Integer);
begin
StrPCopy(Cmd_Str_Pntr, '2DH'#00');
translate(Cmd_Str_Pntr, Rep_Str_Pntr);

StrPCopy(Cmd_Str_Pntr, '2SST4'#00');
translate(Cmd_Str_Pntr,Rep_Str_Pntr);

StrPCopy(Cmd_Str_Pntr, '2SA135'#00');
translate(Cmd_Str_Pntr,Rep_Str_Pntr);

StrPCopy(Cmd_Str_Pntr, '2SV128000'#00'); {158000}
translate(Cmd_Str_Pntr,Rep_Str_Pntr);

(StrPCopy(Cmd_Str_Pntr, '2MR1000000000'#00');
translate(Cmd_Str_Pntr,Rep_Str_Pntr);)

end;

procedure TForm1.FeedUpBitBtnMouseUp(Sender: TObject; Button:
TMouseButton;
Shift: TShiftState; X, Y: Integer);
begin
StrPCopy(Cmd_Str_Pntr, '2CLP'#00');
translate(Cmd_Str_Pntr,Rep_Str_Pntr);

```

```

        StrPCopy(Cmd_Str_Pntr, '2AB'#00');
        translate(Cmd_Str_Pntr,Rep_Str_Pntr);

        end;

procedure TForm1.FeedDownBitBtnMouseDown(Sender: TObject;
Button: TMouseButton; Shift: TShiftState; X, Y: Integer);
begin
    StrPCopy(Cmd_Str_Pntr, '2SST4'#00');
    translate(Cmd_Str_Pntr,Rep_Str_Pntr);

    StrPCopy(Cmd_Str_Pntr, '2SA-135'#00');
    translate(Cmd_Str_Pntr,Rep_Str_Pntr);

    StrPCopy(Cmd_Str_Pntr, '2SV128000'#00');    {158000}
    translate(Cmd_Str_Pntr,Rep_Str_Pntr);

    {StrPCopy(Cmd_Str_Pntr, '2MR-1000000000'#00');
    translate(Cmd_Str_Pntr,Rep_Str_Pntr);}

    end;

procedure TForm1.FeedDownBitBtnMouseUp(Sender: TObject;
Button: TMouseButton; Shift: TShiftState; X, Y: Integer);
begin
    StrPCopy(Cmd_Str_Pntr, '2CLP'#00');
    translate(Cmd_Str_Pntr,Rep_Str_Pntr);

    StrPCopy(Cmd_Str_Pntr, '2AB'#00');
    translate(Cmd_Str_Pntr,Rep_Str_Pntr);

    end;

procedure TForm1.PullUpBitBtnMouseDown(Sender: TObject;
Button: TMouseButton; Shift: TShiftState; X, Y: Integer);
begin
    StrPCopy(Cmd_Str_Pntr, '1DH'#00');
    translate(Cmd_Str_Pntr, Rep_Str_Pntr);

    StrPCopy(Cmd_Str_Pntr, '1SST4'#00');
    translate(Cmd_Str_Pntr,Rep_Str_Pntr);

    StrPCopy(Cmd_Str_Pntr, '1SA-135'#00');
    translate(Cmd_Str_Pntr,Rep_Str_Pntr);

    StrPCopy(Cmd_Str_Pntr, '1SV120000'#00');
    translate(Cmd_Str_Pntr,Rep_Str_Pntr);

    {StrPCopy(Cmd_Str_Pntr, '1MR-1000000000'#00');
    translate(Cmd_Str_Pntr,Rep_Str_Pntr);}

    end;

procedure TForm1.PullUpBitBtnMouseUp(Sender: TObject; Button:
TMouseButton;
Shift: TShiftState; X, Y: Integer);
begin

```

```

        StrPCopy(Cmd_Str_Pntr, '1CLP'#00'');
        translate(Cmd_Str_Pntr,Rep_Str_Pntr);

        StrPCopy(Cmd_Str_Pntr, '1AB'#00'');
        translate(Cmd_Str_Pntr,Rep_Str_Pntr);

        end;

procedure TForm1.PullDownBitBtnMouseDown(Sender: TObject;
Button: TMouseButton; Shift: TShiftState; X, Y: Integer);
begin
    StrPCopy(Cmd_Str_Pntr, '1SST4'#00'');
    translate(Cmd_Str_Pntr,Rep_Str_Pntr);

    StrPCopy(Cmd_Str_Pntr, '1SA135'#00'');
    translate(Cmd_Str_Pntr,Rep_Str_Pntr);

    StrPCopy(Cmd_Str_Pntr, '1SV120000'#00'');
    translate(Cmd_Str_Pntr,Rep_Str_Pntr);

    StrPCopy(Cmd_Str_Pntr, '1MR1000000000'#00'');
    translate(Cmd_Str_Pntr,Rep_Str_Pntr);

    end;

procedure TForm1.PullDownBitBtnMouseUp(Sender: TObject;
Button: TMouseButton; Shift: TShiftState; X, Y: Integer);
begin
    StrPCopy(Cmd_Str_Pntr, '1CLP'#00'');
    translate(Cmd_Str_Pntr,Rep_Str_Pntr);

    StrPCopy(Cmd_Str_Pntr, '1AB'#00'');
    translate(Cmd_Str_Pntr,Rep_Str_Pntr);

    end;

procedure TForm1.PullRateClick(Sender: TObject);
begin
    FeedRate.Text :=
StrFn(ValFn(PullRate.Text)/Sqr(ValFn(DiaRatio.Text)));

    end;

procedure TForm1.PullRateExit(Sender: TObject);
begin
    FeedRate.Text :=
StrFn(ValFn(PullRate.Text)/Sqr(ValFn(DiaRatio.Text)));

    end;

procedure TForm1.DiaRatioClick(Sender: TObject);
begin
    FeedRate.Text :=
StrFn(ValFn(PullRate.Text)/Sqr(ValFn(DiaRatio.Text)));

    end;

```

```

        procedure TForm1.DiaRatioExit(Sender: TObject);
            begin
                FeedRate.Text :=
                StrFn(ValFn(PullRate.Text)/Sqr(ValFn(DiaRatio.Text)));

                end;

        procedure TForm1.PullRateChange(Sender: TObject);
            begin
                If PullRate.Text>'2.0' then
                    begin
                        Application.MessageBox('Max Pull Velocity Exceeded','WARNING', MB_OK);
                        PullRate.Text := '2.0';
                    end;
                end;

        procedure TForm1.Timer1Timer(Sender: TObject);
var
        Delta_Pull_Position, Delta_Feed_Position : longint;
        Pull_Position, Feed_Position           : longint;
        Delta_Time                             : real;
        Pull_Velocity, Feed_Velocity          : double;
        Pntr_Buff1                             : PChar;
Buff1
        Pntr_Buff2                             : PChar;
Buff2
        Current_Interval                       : integer;
        I, No_Series, j, k                     : Integer;
        No_Txed1, No_Txed2                     : Integer;
        ntype                                  : Smallint;
        {Stop_Click                             : boolean;}
        Gb_Pull, Gb_Feed                       : double;

            begin

                Gb_Pull := 80*2000*29.642; {19753;}
                Gb_Feed := 320*2000*29.642; {19753;}

                Pntr_Buff1 := @Buff1;
                Pntr_Buff2 := @Buff2;
Delta_Time := 1.0; { take readings every 1.0 sec }
                Pull_Position := get_pos(1);
                Feed_Position := get_pos(2);
                Delta_Pull_Position := Pull_Position - Last_Pull_Position;
                Delta_Feed_Position := Feed_Position - Last_Feed_Position;

                { change velocity to mm/min or rad/s }
                Pull_Velocity := Delta_Pull_Position/(Delta_Time);
                {Pull_Velocity := Pull_Velocity/(2*29.6*80*1000/60);}
                {*2*pi/Gb_Pull;}
                Pull_Vel.Text := StrFn(Pull_Velocity*(-1));

                Feed_Velocity := Delta_Feed_Position/(Delta_Time);
                {Feed_Velocity := Feed_Velocity/(4*29.6*320*1000/60);}
                {*2*pi/Gb_Feed;}
                Feed_Vel.Text := StrFn(Feed_Velocity);

                { increment the Record No}

```

```

    { put the record Number into file }
    { clear the buffer }
    {for j := 0 to 14 do
    begin
        Buff1[j] := #00;
        Buff1[13] := #0A;
        end;
        Buff1[13] := #0D;
        Buff1[14] := #0A;

        Record_No := Record_No+1;
        StrPcopy(Pntr_Buff1, IntToStr(Record_No));
        No_Txed1:=FileWrite(FileHandle1, Buff1, sizeof(Buff1));}

    {Timer --> taking readings every 0.5 sec}
    {Time_Counter := Time_Counter + 0.5;
    for k := 0 to 14 do
    begin
        Buff2[k] := #00;
        Buff2[13] := #0A;
        end;
        Buff2[13] := #0D;
        Buff2[14] := #0A;

        StrPcopy(Pntr_Buff2, FloatToStr(Time_Counter));
        No_Txed2:=FileWrite(FileHandle2, Buff2, sizeof(Buff2));}

    { put the Pull velocity into file }
    { clear the buffer }
    for j:=0 to 14 do
    begin
        Buff1[j] := #00;
        Buff1[13] := #0A;    {Linefeed}
        end;

        Buff1[13] := #0D;    {Carriage return}

    {storing Vpull into FileHandle1 - which is a text file}
    StrPcopy(Pntr_Buff1, StrFn(Pull_Velocity*(-1)));
    No_Txed1:=FileWrite(FileHandle1, Buff1, sizeof(Buff1));

    { put the Feed velocity into file }
    { clear the buffer }
    for k:=0 to 14 do
    begin
        Buff2[k] := #00;
        Buff2[13] := #0A;
        end;

        Buff2[13] := #0D;

    {storing Vfeed into FileHandle2 - also a text file}
    StrPcopy(Pntr_Buff2, StrFn(Feed_Velocity));
    No_Txed2 := FileWrite(FileHandle2, Buff2, sizeof(Buff2));

    {Pull_Vel.Text      := StrFn(Pull_Velocity);
    Feed_Vel.Text      := StrFn(Feed_Velocity);}

```



```

        Form2Graph.Chartfx1.ThisSerie := 1;
Form2Graph.Chartfx1.ThisValue := Feed_Vel_Array[I];{I*2;}
        end;
        end;

Label15.Caption := 'Current time : ' + TimeToStr(Time);
        If (Point_Now > 19) then
            begin
                Point_Now :=0;
                No_Points :=1;
                {Page_No := Page_No +1;}
            end;

            { now dump Data to file }

        Form2Graph.Chartfx1.CloseData(ntype);
            end;

        procedure TForm1.ShowGraphClick(Sender: TObject);
            begin
                Form2Graph.Show;
            end;

        procedure TForm1.BottomScrollChange(Sender: TObject);
            var
                VRange      : Longint;
                VOffset      : Longint;
                VolRange     : Single;

            begin
                {VOffset := BottomScroll.Max-BottomScroll.Position;
                VRange := BottomScroll.Max-BottomScroll.Min;
                VolRange := ptAOConfig.MaxValue-ptAOConfig.MinValue;
                BottomEdit.Text := FloatToStrF((VOffset / VRange * VolRange +
                ptAOConfig.MinValue), ffFixed, 5, 2);
                BottomEdit.Text:= FloatToStrF(((BottomScroll.Position-500)/100.0),
                ffFixed, 5, 2);}

                BottomEdit.Text:= FloatToStr(BottomScroll.Position/100.0);

            end;

        procedure TForm1.BottomStageUpMouseDown(Sender: TObject;
        Button: TMouseButton; Shift: TShiftState; X, Y: Integer);

            begin

                In_Single_BottomStage := StrToFloat(BottomEdit.Text);
                ptAOVoltageOut.chan := 1;
                ptAOVoltageOut.OutputValue := In_Single_BottomStage;

                ErrCde := DRV_AOVoltageOut(DeviceHandle,ptAOVoltageOut);

            end;

        procedure TForm1.BottomStageUpMouseUp(Sender: TObject;

```

```

Button: TMouseButton; Shift: TShiftState; X, Y: Integer);
    begin
        In_Single_BottomStage      := 0.00;
        ptAOVoltageOut.chan        := 1;
        ptAOVoltageOut.OutputValue := In_Single_BottomStage;

    ErrCde := DRV_AOVoltageOut(DeviceHandle, ptAOVoltageOut);

    end;

procedure TForm1.BottomStageDownMouseDown(Sender: TObject;
Button: TMouseButton; Shift: TShiftState; X, Y: Integer);
    begin
    In_Single_BottomStage      := StrToFloat(BottomEdit.Text);
        ptAOVoltageOut.chan    := 1;
        ptAOVoltageOut.OutputValue := -In_Single_BottomStage;

    ErrCde := DRV_AOVoltageOut(DeviceHandle, ptAOVoltageOut);

    end;

procedure TForm1.BottomStageDownMouseUp(Sender: TObject;
Button: TMouseButton; Shift: TShiftState; X, Y: Integer);
    begin
        In_Single_BottomStage      := 0.00;
        ptAOVoltageOut.chan        := 1;
        ptAOVoltageOut.OutputValue := In_Single_BottomStage;

    ErrCde := DRV_AOVoltageOut(DeviceHandle, ptAOVoltageOut);

    end;

procedure TForm1.BottomStageLeftMouseDown(Sender: TObject;
Button: TMouseButton; Shift: TShiftState; X, Y: Integer);
    begin
    In_Single_BottomStage      := StrToFloat(BottomEdit.Text);
        ptAOVoltageOut.chan    := 0;
        ptAOVoltageOut.OutputValue := -In_Single_BottomStage;

    ErrCde := DRV_AOVoltageOut(DeviceHandle, ptAOVoltageOut);

    end;

procedure TForm1.BottomStageLeftMouseUp(Sender: TObject;
Button: TMouseButton; Shift: TShiftState; X, Y: Integer);
    begin
        In_Single_BottomStage      := 0.00;
        ptAOVoltageOut.chan        := 0;
        ptAOVoltageOut.OutputValue := In_Single_BottomStage;

    ErrCde := DRV_AOVoltageOut(DeviceHandle, ptAOVoltageOut);

    end;

procedure TForm1.BottomStageRightMouseDown(Sender: TObject;
Button: TMouseButton; Shift: TShiftState; X, Y: Integer);
    begin
    In_Single_BottomStage      := StrToFloat(BottomEdit.Text);

```

```

        ptAOVoltageOut.chan          := 0;
        ptAOVoltageOut.OutputValue := In_Single_BottomStage;
ErrCde := DRV_AOVoltageOut(DeviceHandle, ptAOVoltageOut);

        end;

procedure TForm1.BottomStageRightMouseUp(Sender: TObject;
Button: TMouseButton; Shift: TShiftState; X, Y: Integer);
begin
        In_Single_BottomStage      := 0.00;
        ptAOVoltageOut.chan        := 0;
        ptAOVoltageOut.OutputValue := In_Single_BottomStage;
ErrCde := DRV_AOVoltageOut(DeviceHandle, ptAOVoltageOut);

        end;

procedure TForm1.BottomStageNEMouseDown(Sender: TObject;
Button: TMouseButton; Shift: TShiftState; X, Y: Integer);
begin
In_Single_BottomStage      := StrToFloat(BottomEdit.Text);

        ptAOVoltageOut.chan          := 0;
        ptAOVoltageOut.OutputValue := In_Single_BottomStage;
ErrCde := DRV_AOVoltageOut(DeviceHandle, ptAOVoltageOut);

        ptAOVoltageOut.chan          := 1;
        ptAOVoltageOut.OutputValue := In_Single_BottomStage;
ErrCde := DRV_AOVoltageOut(DeviceHandle, ptAOVoltageOut);

        end;

procedure TForm1.BottomStageNEMouseUp(Sender: TObject;
Button: TMouseButton; Shift: TShiftState; X, Y: Integer);
begin
        In_Single_BottomStage      := 0.00;

        ptAOVoltageOut.chan          := 0;
        ptAOVoltageOut.OutputValue := In_Single_BottomStage;
ErrCde := DRV_AOVoltageOut(DeviceHandle, ptAOVoltageOut);

        ptAOVoltageOut.chan          := 1;
        ptAOVoltageOut.OutputValue := In_Single_BottomStage;
ErrCde := DRV_AOVoltageOut(DeviceHandle, ptAOVoltageOut);

        end;

procedure TForm1.BottomStageNWMouseDown(Sender: TObject;
Button: TMouseButton; Shift: TShiftState; X, Y: Integer);
begin
In_Single_BottomStage      := StrToFloat(BottomEdit.Text);

        ptAOVoltageOut.chan          := 0;
        ptAOVoltageOut.OutputValue := -In_Single_BottomStage;
ErrCde := DRV_AOVoltageOut(DeviceHandle, ptAOVoltageOut);

```

```

        ptAOVoltageOut.chan          := 1;
        ptAOVoltageOut.OutputValue := In_Single_BottomStage;
        ErrCde := DRV_AOVoltageOut(DeviceHandle, ptAOVoltageOut);

        end;

        procedure TForm1.BottomStageNWMouseUp(Sender: TObject;
        Button: TMouseButton; Shift: TShiftState; X, Y: Integer);
        begin
            In_Single_BottomStage      := 0.00;

            ptAOVoltageOut.chan        := 0;
            ptAOVoltageOut.OutputValue := In_Single_BottomStage;
            ErrCde := DRV_AOVoltageOut(DeviceHandle, ptAOVoltageOut);

            ptAOVoltageOut.chan        := 1;
            ptAOVoltageOut.OutputValue := In_Single_BottomStage;
            ErrCde := DRV_AOVoltageOut(DeviceHandle, ptAOVoltageOut);

            end;

        procedure TForm1.BottomStageSWMouseDown(Sender: TObject;
        Button: TMouseButton; Shift: TShiftState; X, Y: Integer);
        begin
            In_Single_BottomStage      := StrToFloat(BottomEdit.Text);

            ptAOVoltageOut.chan        := 0;
            ptAOVoltageOut.OutputValue := -In_Single_BottomStage;
            ErrCde := DRV_AOVoltageOut(DeviceHandle, ptAOVoltageOut);

            ptAOVoltageOut.chan        := 1;
            ptAOVoltageOut.OutputValue := -In_Single_BottomStage;
            ErrCde := DRV_AOVoltageOut(DeviceHandle, ptAOVoltageOut);

            end;

        procedure TForm1.BottomStageSWMouseUp(Sender: TObject;
        Button: TMouseButton; Shift: TShiftState; X, Y: Integer);
        begin
            In_Single_BottomStage      := 0.00;

            ptAOVoltageOut.chan        := 0;
            ptAOVoltageOut.OutputValue := In_Single_BottomStage;
            ErrCde := DRV_AOVoltageOut(DeviceHandle, ptAOVoltageOut);

            ptAOVoltageOut.chan        := 1;
            ptAOVoltageOut.OutputValue := In_Single_BottomStage;
            ErrCde := DRV_AOVoltageOut(DeviceHandle, ptAOVoltageOut);

            end;

        procedure TForm1.BottomStageSEMouseDown(Sender: TObject;
        Button: TMouseButton; Shift: TShiftState; X, Y: Integer);
        begin
            In_Single_BottomStage      := StrToFloat(BottomEdit.Text);

            ptAOVoltageOut.chan        := 0;

```

```

    ptAOVoltageOut.OutputValue := In_Single_BottomStage;
    ErrCde := DRV_AOVoltageOut(DeviceHandle, ptAOVoltageOut);

        ptAOVoltageOut.chan      := 1;
    ptAOVoltageOut.OutputValue := -In_Single_BottomStage;
    ErrCde := DRV_AOVoltageOut(DeviceHandle, ptAOVoltageOut);

        end;

    procedure TForm1.BottomStageSEMouseUp(Sender: TObject;
    Button: TMouseButton; Shift: TShiftState; X, Y: Integer);
        begin
            In_Single_BottomStage      := 0.00;

                ptAOVoltageOut.chan      := 0;
            ptAOVoltageOut.OutputValue := In_Single_BottomStage;
            ErrCde := DRV_AOVoltageOut(DeviceHandle, ptAOVoltageOut);

                ptAOVoltageOut.chan      := 1;
            ptAOVoltageOut.OutputValue := In_Single_BottomStage;
            ErrCde := DRV_AOVoltageOut(DeviceHandle, ptAOVoltageOut);

        end;

    {Following entries for Top Stage XY movement}
    procedure TForm1.TopStageUpMouseDown(Sender: TObject; Button:
    TMouseButton;
        Shift: TShiftState; X, Y: Integer);
        begin
            In_Single_TopStage      := StrToFloat(TopEdit.Text);
                ptAOVoltageOut.chan      := 3;
            ptAOVoltageOut.OutputValue := In_Single_TopStage;

            ErrCde := DRV_AOVoltageOut(DeviceHandle, ptAOVoltageOut);

        end;

    procedure TForm1.TopStageUpMouseUp(Sender: TObject; Button:
    TMouseButton;
        Shift: TShiftState; X, Y: Integer);
        begin
            In_Single_TopStage      := 0.00;
                ptAOVoltageOut.chan      := 3;
            ptAOVoltageOut.OutputValue := In_Single_TopStage;

            ErrCde := DRV_AOVoltageOut(DeviceHandle, ptAOVoltageOut);

        end;

    procedure TForm1.TopStageDownMouseDown(Sender: TObject;
    Button: TMouseButton; Shift: TShiftState; X, Y: Integer);
        begin
            In_Single_TopStage      := StrToFloat(TopEdit.Text);
                ptAOVoltageOut.chan      := 3;
            ptAOVoltageOut.OutputValue := -In_Single_TopStage;

            ErrCde := DRV_AOVoltageOut(DeviceHandle, ptAOVoltageOut);

```

```

end;

procedure TForm1.TopStageDownMouseUp(Sender: TObject; Button:
    TMouseButton;
    Shift: TShiftState; X, Y: Integer);
begin
    In_Single_TopStage      := 0.00;
    ptAOVoltageOut.chan    := 3;
    ptAOVoltageOut.OutputValue := In_Single_TopStage;

    ErrCde := DRV_AOVoltageOut(DeviceHandle, ptAOVoltageOut);

end;

procedure TForm1.TopStageLeftMouseDown(Sender: TObject;
    Button: TMouseButton; Shift: TShiftState; X, Y: Integer);
begin
    In_Single_TopStage      := StrToFloat(TopEdit.Text);
    ptAOVoltageOut.chan    := 2;
    ptAOVoltageOut.OutputValue := -In_Single_TopStage;

    ErrCde := DRV_AOVoltageOut(DeviceHandle, ptAOVoltageOut);

end;

procedure TForm1.TopStageLeftMouseUp(Sender: TObject; Button:
    TMouseButton;
    Shift: TShiftState; X, Y: Integer);
begin
    In_Single_TopStage      := 0.00;
    ptAOVoltageOut.chan    := 2;
    ptAOVoltageOut.OutputValue := In_Single_TopStage;

    ErrCde := DRV_AOVoltageOut(DeviceHandle, ptAOVoltageOut);

end;

procedure TForm1.TopStageRightMouseDown(Sender: TObject;
    Button: TMouseButton; Shift: TShiftState; X, Y: Integer);
begin
    In_Single_TopStage      := StrToFloat(TopEdit.Text);
    ptAOVoltageOut.chan    := 2;
    ptAOVoltageOut.OutputValue := In_Single_TopStage;

    ErrCde := DRV_AOVoltageOut(DeviceHandle, ptAOVoltageOut);

end;

procedure TForm1.TopStageRightMouseUp(Sender: TObject;
    Button: TMouseButton; Shift: TShiftState; X, Y: Integer);
begin
    In_Single_TopStage      := 0.00;
    ptAOVoltageOut.chan    := 2;
    ptAOVoltageOut.OutputValue := In_Single_TopStage;

    ErrCde := DRV_AOVoltageOut(DeviceHandle, ptAOVoltageOut);

```

```

end;

procedure TForm1.TopStageNWMouseDown(Sender: TObject; Button:
    TMouseButton;
    Shift: TShiftState; X, Y: Integer);
begin
    In_Single_TopStage      := StrToFloat(TopEdit.Text);

    ptAOVoltageOut.chan     := 2;
    ptAOVoltageOut.OutputValue := -In_Single_TopStage;
    ErrCde := DRV_AOVoltageOut(DeviceHandle, ptAOVoltageOut);

    ptAOVoltageOut.chan     := 3;
    ptAOVoltageOut.OutputValue := In_Single_TopStage;
    ErrCde := DRV_AOVoltageOut(DeviceHandle, ptAOVoltageOut);

end;

procedure TForm1.TopStageNWMouseUp(Sender: TObject; Button:
    TMouseButton;
    Shift: TShiftState; X, Y: Integer);
begin
    In_Single_TopStage      := 0.00;

    ptAOVoltageOut.chan     := 2;
    ptAOVoltageOut.OutputValue := In_Single_TopStage;
    ErrCde := DRV_AOVoltageOut(DeviceHandle, ptAOVoltageOut);

    ptAOVoltageOut.chan     := 3;
    ptAOVoltageOut.OutputValue := In_Single_TopStage;
    ErrCde := DRV_AOVoltageOut(DeviceHandle, ptAOVoltageOut);

end;

procedure TForm1.TopStageNEMouseDown(Sender: TObject; Button:
    TMouseButton;
    Shift: TShiftState; X, Y: Integer);
begin
    In_Single_TopStage      := StrToFloat(TopEdit.Text);

    ptAOVoltageOut.chan     := 2;
    ptAOVoltageOut.OutputValue := In_Single_TopStage;
    ErrCde := DRV_AOVoltageOut(DeviceHandle, ptAOVoltageOut);

    ptAOVoltageOut.chan     := 3;
    ptAOVoltageOut.OutputValue := In_Single_TopStage;
    ErrCde := DRV_AOVoltageOut(DeviceHandle, ptAOVoltageOut);

end;

procedure TForm1.TopStageNEMouseUp(Sender: TObject; Button:
    TMouseButton;
    Shift: TShiftState; X, Y: Integer);
begin
    In_Single_TopStage      := 0.00;

```

```

        ptAOVoltageOut.chan          := 2;
        ptAOVoltageOut.OutputValue := In_Single_TopStage;
        ErrCde := DRV_AOVoltageOut(DeviceHandle, ptAOVoltageOut);

        ptAOVoltageOut.chan          := 3;
        ptAOVoltageOut.OutputValue := In_Single_TopStage;
        ErrCde := DRV_AOVoltageOut(DeviceHandle, ptAOVoltageOut);

        end;

procedure TForm1.TopStageSWMouseDown(Sender: TObject; Button:
        TMouseButton;
        Shift: TShiftState; X, Y: Integer);
        begin
        In_Single_TopStage          := StrToFloat(TopEdit.Text);

        ptAOVoltageOut.chan          := 2;
        ptAOVoltageOut.OutputValue := -In_Single_TopStage;
        ErrCde := DRV_AOVoltageOut(DeviceHandle, ptAOVoltageOut);

        ptAOVoltageOut.chan          := 3;
        ptAOVoltageOut.OutputValue := -In_Single_TopStage;
        ErrCde := DRV_AOVoltageOut(DeviceHandle, ptAOVoltageOut);

        end;

procedure TForm1.TopStageSWMouseUp(Sender: TObject; Button:
        TMouseButton;
        Shift: TShiftState; X, Y: Integer);
        begin
        In_Single_TopStage          := 0.00;

        ptAOVoltageOut.chan          := 2;
        ptAOVoltageOut.OutputValue := In_Single_TopStage;
        ErrCde := DRV_AOVoltageOut(DeviceHandle, ptAOVoltageOut);

        ptAOVoltageOut.chan          := 3;
        ptAOVoltageOut.OutputValue := In_Single_TopStage;
        ErrCde := DRV_AOVoltageOut(DeviceHandle, ptAOVoltageOut);

        end;

procedure TForm1.TopStageSEMouseDown(Sender: TObject; Button:
        TMouseButton;
        Shift: TShiftState; X, Y: Integer);
        begin
        In_Single_TopStage          := StrToFloat(TopEdit.Text);

        ptAOVoltageOut.chan          := 2;
        ptAOVoltageOut.OutputValue := In_Single_TopStage;
        ErrCde := DRV_AOVoltageOut(DeviceHandle, ptAOVoltageOut);

        ptAOVoltageOut.chan          := 3;
        ptAOVoltageOut.OutputValue := -In_Single_TopStage;
        ErrCde := DRV_AOVoltageOut(DeviceHandle, ptAOVoltageOut);

```

```

end;

procedure TForm1.TopStageSEMouseUp(Sender: TObject; Button:
    TMouseButton;
    Shift: TShiftState; X, Y: Integer);
begin
    In_Single_TopStage      := 0.00;

    ptAOVoltageOut.chan     := 2;
    ptAOVoltageOut.OutputValue := In_Single_TopStage;
    ErrCde := DRV_AOVoltageOut(DeviceHandle, ptAOVoltageOut);

    ptAOVoltageOut.chan     := 3;
    ptAOVoltageOut.OutputValue := In_Single_TopStage;
    ErrCde := DRV_AOVoltageOut(DeviceHandle, ptAOVoltageOut);

end;

procedure TForm1.TopScrollChange(Sender: TObject);
begin
TopEdit.Text:= FloatToStr(TopScroll.Position/100.0);
end;

procedure TForm1.GroupBox2Click(Sender: TObject);
begin
    {StrPCopy(Cmd_Str_Pntr, 'SST4'#00');
    translate(Cmd_Str_Pntr,Rep_Str_Pntr);

    StrPCopy(Cmd_Str_Pntr, 'CLP'#00');
    translate(Cmd_Str_Pntr,Rep_Str_Pntr);

    StrPCopy(Cmd_Str_Pntr, 'CLR'#00');
    translate(Cmd_Str_Pntr,Rep_Str_Pntr);

    StrPCopy(Cmd_Str_Pntr, 'ASN'#00');
    translate(Cmd_Str_Pntr,Rep_Str_Pntr);

    StrPCopy(Cmd_Str_Pntr, 'SAN'#00');
    translate(Cmd_Str_Pntr,Rep_Str_Pntr);

    StrPCopy(Cmd_Str_Pntr, 'SFP'#00');
    translate(Cmd_Str_Pntr,Rep_Str_Pntr);

    StrPCopy(Cmd_Str_Pntr, 'DP150'#00');
    translate(Cmd_Str_Pntr,Rep_Str_Pntr);

    StrPCopy(Cmd_Str_Pntr, 'DI10'#00');
    translate(Cmd_Str_Pntr,Rep_Str_Pntr);

    StrPCopy(Cmd_Str_Pntr, 'DD10'#00');
    translate(Cmd_Str_Pntr,Rep_Str_Pntr);

    StrPCopy(Cmd_Str_Pntr, 'DL2000'#00');
    translate(Cmd_Str_Pntr,Rep_Str_Pntr);}

end;

```

```

procedure TForm1.Timer2Timer(Sender: TObject);
var
  a
    : integer;
begin
  {Forcing Feed Motor to exceed limit in upward movement}
  get_pos(2);
  Chan2_Counter:=get_pos(2);
  Edit7.Text := IntToStr(Chan2_Counter);

  If (Chan2_Counter >= 1073400000) then   (616300000)
  begin
    StrPCopy(Cmd_Str_Pntr, '2DH'#00'');
    translate(Cmd_Str_Pntr,Rep_Str_Pntr);

    For a := 0 to 1 do
    begin
      {I1 faut : 1073600000}
      StrPCopy(Cmd_Str_Pntr, '2MR1073600000'#00''); {-ve movement = DOWN}
      translate(Cmd_Str_Pntr,Rep_Str_Pntr);           {+ve movement = UP}

    end;

    end;

    {StrPCopy(Cmd_Str_Pntr, '2CLP'#00'');
    translate(Cmd_Str_Pntr,Rep_Str_Pntr);

    StrPCopy(Cmd_Str_Pntr, '2AB'#00'');
    translate(Cmd_Str_Pntr,Rep_Str_Pntr);}

    end;

procedure TForm1.BREAKSTARTClick(Sender: TObject);
begin
  StrPCopy(Cmd_Str_Pntr, 'CLP'#00'');
  translate(Cmd_Str_Pntr,Rep_Str_Pntr);

  StrPCopy(Cmd_Str_Pntr, 'CLR'#00'');
  translate(Cmd_Str_Pntr,Rep_Str_Pntr);

  StrPCopy(Cmd_Str_Pntr, 'SST4'#00'');
  translate(Cmd_Str_Pntr,Rep_Str_Pntr);

  StrPCopy(Cmd_Str_Pntr, 'SFP'#00'');
  translate(Cmd_Str_Pntr,Rep_Str_Pntr);

  StrPCopy(Cmd_Str_Pntr, '1DP150'#00'');
  translate(Cmd_Str_Pntr,Rep_Str_Pntr);

  StrPCopy(Cmd_Str_Pntr, '2DP100'#00'');
  translate(Cmd_Str_Pntr,Rep_Str_Pntr);

  StrPCopy(Cmd_Str_Pntr, 'DI10'#00'');
  translate(Cmd_Str_Pntr,Rep_Str_Pntr);

  StrPCopy(Cmd_Str_Pntr, 'DD10'#00'');
  translate(Cmd_Str_Pntr,Rep_Str_Pntr);

  StrPCopy(Cmd_Str_Pntr, 'DL2000'#00'');

```

```

translate(Cmd_Str_Pntr, Rep_Str_Pntr);

StrPCopy(Cmd_Str_Pntr, 'DH'#00');
translate(Cmd_Str_Pntr, Rep_Str_Pntr);

StrPCopy(Cmd_Str_Pntr, '1SA-250'#00');
translate(Cmd_Str_Pntr, Rep_Str_Pntr);

StrPCopy(Cmd_Str_Pntr, '2SA-250'#00');
translate(Cmd_Str_Pntr, Rep_Str_Pntr);

StrPCopy(Cmd_Str_Pntr, '1SV95000'#00');
translate(Cmd_Str_Pntr, Rep_Str_Pntr);

StrPCopy(Cmd_Str_Pntr, '2SV128000'#00');
translate(Cmd_Str_Pntr, Rep_Str_Pntr);

(Pull Motor - Up 30 mm)
{StrPCopy(Cmd_Str_Pntr, '1MR-142281481'#00');} {-ve movement = UP}
{translate(Cmd_Str_Pntr, Rep_Str_Pntr);} {+ve movement = DOWN}

(Feed Motor - Down 15 mm)
{StrPCopy(Cmd_Str_Pntr, '2MR-569125926'#00');} {-ve movement = DOWN}
{translate(Cmd_Str_Pntr, Rep_Str_Pntr);} {+ve movement = UP}

end;

procedure TForm1.BREAKSTOPClick(Sender: TObject);
begin
StrPCopy(Cmd_Str_Pntr, 'CLP'#00');
translate(Cmd_Str_Pntr, Rep_Str_Pntr);

StrPCopy(Cmd_Str_Pntr, 'AB'#00');
translate(Cmd_Str_Pntr, Rep_Str_Pntr);

end;

procedure TForm1.POSITIONSTARTClick(Sender: TObject);
begin
StrPCopy(Cmd_Str_Pntr, 'CLP'#00');
translate(Cmd_Str_Pntr, Rep_Str_Pntr);

StrPCopy(Cmd_Str_Pntr, 'CLR'#00');
translate(Cmd_Str_Pntr, Rep_Str_Pntr);

StrPCopy(Cmd_Str_Pntr, 'SST4'#00');
translate(Cmd_Str_Pntr, Rep_Str_Pntr);

{StrPCopy(Cmd_Str_Pntr, '2ASN'#00');
translate(Cmd_Str_Pntr, Rep_Str_Pntr);}

StrPCopy(Cmd_Str_Pntr, 'SFP'#00');
translate(Cmd_Str_Pntr, Rep_Str_Pntr);

StrPCopy(Cmd_Str_Pntr, '1DP75'#00');
translate(Cmd_Str_Pntr, Rep_Str_Pntr);

```

```

StrPCopy(Cmd_Str_Pntr, '2DP80'#00');
translate(Cmd_Str_Pntr,Rep_Str_Pntr);

StrPCopy(Cmd_Str_Pntr, 'DI5'#00');
translate(Cmd_Str_Pntr,Rep_Str_Pntr);

StrPCopy(Cmd_Str_Pntr, 'DD10'#00');
translate(Cmd_Str_Pntr,Rep_Str_Pntr);

StrPCopy(Cmd_Str_Pntr, 'DL2000'#00');
translate(Cmd_Str_Pntr,Rep_Str_Pntr);

StrPCopy(Cmd_Str_Pntr, 'DH'#00');
translate(Cmd_Str_Pntr, Rep_Str_Pntr);

StrPCopy(Cmd_Str_Pntr, 'SA350'#00');
translate(Cmd_Str_Pntr, Rep_Str_Pntr);

StrPCopy(Cmd_Str_Pntr, '1SV100000'#00');
translate(Cmd_Str_Pntr, Rep_Str_Pntr);

StrPCopy(Cmd_Str_Pntr, '2SV128000'#00');
translate(Cmd_Str_Pntr, Rep_Str_Pntr);

(Pull Displacement - 1043397531)
StrPCopy(Cmd_Str_Pntr, '1MR47430000'#00');      {-ve movement = UP}
translate(Cmd_Str_Pntr, Rep_Str_Pntr);          {+ve movement = DOWN}

(Feed Displacement - 1043397531)
StrPCopy(Cmd_Str_Pntr, '2MR-1073741800'#00');  {-ve movement = DOWN}
translate(Cmd_Str_Pntr, Rep_Str_Pntr);          {+ve movement = UP}

{StrPCopy(Cmd_Str_Pntr, '2MR-707377777'#00');
translate(Cmd_Str_Pntr, Rep_Str_Pntr);}

Timer3.Enabled      := FALSE;  {TRUE;}

end;

procedure TForm1.POS_PULL_STOPClick(Sender: TObject);
begin
StrPCopy(Cmd_Str_Pntr, '1CLP'#00');
translate(Cmd_Str_Pntr,Rep_Str_Pntr);

StrPCopy(Cmd_Str_Pntr, '1AB'#00');
translate(Cmd_Str_Pntr,Rep_Str_Pntr);

end;

procedure TForm1.POS_FEED_STOPClick(Sender: TObject);
begin
StrPCopy(Cmd_Str_Pntr, '2CLP'#00');
translate(Cmd_Str_Pntr,Rep_Str_Pntr);

StrPCopy(Cmd_Str_Pntr, '2AB'#00');
translate(Cmd_Str_Pntr,Rep_Str_Pntr);

```

```

Timer3.Enabled           := FALSE;

                                end;

procedure TForm1.Timer3Timer(Sender: TObject);
var   b : integer;
begin
{Forcing Feed Motor to exceed limit in downward movement}
    get_pos(2);
    Chan2_Counter1:=get_pos(2);
    Edit7.Text := IntToStr(Chan2_Counter1);

    If (Chan2_Counter1<=-1073400000) then
        begin
            For b:=0 to 1 do
                begin
                    StrPCopy(Cmd_Str_Pntr, '2DH'#00'');
                    translate(Cmd_Str_Pntr,Rep_Str_Pntr);

StrPCopy(Cmd_Str_Pntr, '2MR-1073600000'#00'');  {-ve movement = DOWN}
    translate(Cmd_Str_Pntr,Rep_Str_Pntr);      {+ve movement = UP}
                end;
                {StrPCopy(Cmd_Str_Pntr, '2AB'#00'');
                translate(Cmd_Str_Pntr,Rep_Str_Pntr);

                StrPCopy(Cmd_Str_Pntr, '2CLP'#00'');
                translate(Cmd_Str_Pntr,Rep_Str_Pntr);}

            end;

                                end;

                                end;

procedure TForm1.DiaRatioChange(Sender: TObject);
begin
    {If DiaRatio.Text<'2' then
    begin
Application.MessageBox('Max Feed Velocity Exceeded','WARNING', MB_OK);
        DiaRatio.Text := '2';
    end;}
end;

procedure TForm1.FeedRateChange(Sender: TObject);
begin
    If ((PullRate.Text= '2.0') and (DiaRatio.Text< '2.82')) then
        begin
Application.MessageBox('Max Feed Velocity Exceeded','WARNING', MB_OK);
            DiaRatio.Text := StrFn(Sqrt(ValFn(PullRate.Text)/0.25));
            FeedRate.Text :=
                StrFn(ValFn(PullRate.Text)/Sqr(ValFn(DiaRatio.Text)));
        end
    else if ((PullRate.Text< '2.0') and (FeedRate.Text> '0.26')) then
        begin
Application.MessageBox('Max Feed Velocity Exceeded','WARNING', MB_OK);
            FeedRate.Text := '0.25';
        end;
end;

```

```

        DiaRatio.Text :=
StrFn(sqrt(ValFn(PullRate.Text)/ValFn(FeedRate.Text)));
        end;
        end;

        procedure TForm1.EndStartClick(Sender: TObject);
                var
                        Vpull_str_ETaper    : string;
                        Vend_real, V2       : real;
                        Vend_whole          : longint;
                        Vend_str            : string;

                begin
{Calculating Pull Rate with 80:1 gearbox ==> Channel 1}
                {For End Taper of Length L}
                        V2 := ValFn(PullRate.Text);
                        Vend_real := V2/Sqr(1-(30/100));

                        Vend_whole := Trunc(Vend_real*(n_pull*1000/60));
                        Vend_str := '1SV' + IntToStr(Vend_whole) + #00;

                {Calculating Acceleration required}
                {where Vel_Grad = Acceleration}
                {EndTaper_Length := ValFn(EndTaperChange.Text);}
                        Vel_Grad := Pull_Const_1*(Sqr(Vtaper_real)-
                                Sqr(V1))/(2*Taper_Length);
                        Acc_whole := Trunc(Vel_Grad);
                        Acc_Taper := '1SA' + IntToStr(Acc_whole) + #00;}

                {Calculating Distance required}
                {Dist_whole := Trunc(Pull_Const_2*Taper_Length);}
                        Dist_Taper := '1MR' + IntToStr(Dist_whole) + #00;}

                        StrPCopy(Cmd_Str_Pntr, '2CLP'#00'');
                        translate(Cmd_Str_Pntr, Rep_Str_Pntr);

                        StrPCopy(Cmd_Str_Pntr, '2AB'#00'');
                        translate(Cmd_Str_Pntr, Rep_Str_Pntr);

                        {StrPCopy(Cmd_Str_Pntr, '1CLP'#00'');
                        translate(Cmd_Str_Pntr, Rep_Str_Pntr);}

                        {StrPCopy(Cmd_Str_Pntr, '1DH'#00'');
                        translate(Cmd_Str_Pntr, Rep_Str_Pntr);}

                        {StrPCopy(Cmd_Str_Pntr, Acc_Taper);
                        translate(Cmd_Str_Pntr, Rep_Str_Pntr);}

{StrPCopy(Cmd_Str_Pntr, Vtaper_str);} {Pull Velocity -> Chan 1}
                {translate(Cmd_Str_Pntr, Rep_Str_Pntr);}

                {Pull Displacement}
                {StrPCopy(Cmd_Str_Pntr, Dist_Taper);} {-ve movement = UP}
                {translate(Cmd_Str_Pntr, Rep_Str_Pntr);} {+ve movement = DOWN}

                {StrPCopy(Cmd_Str_Pntr, '1UP'#00'');
                translate(Cmd_Str_Pntr, Rep_Str_Pntr);}

```

```

end;

procedure TForm1.PullUpBitBtnKeyPress(Sender: TObject; var Key: Char);
begin
    if (PullMotor_Up = False) then
        begin
            { move for ever }
            StrPCopy(Cmd_Str_Pntr, '1DH'#00'');
            translate(Cmd_Str_Pntr, Rep_Str_Pntr);

            StrPCopy(Cmd_Str_Pntr, '1SST4'#00'');
            translate(Cmd_Str_Pntr, Rep_Str_Pntr);

            StrPCopy(Cmd_Str_Pntr, '1SA-135'#00'');
            translate(Cmd_Str_Pntr, Rep_Str_Pntr);

            StrPCopy(Cmd_Str_Pntr, '1SV120000'#00'');
            translate(Cmd_Str_Pntr, Rep_Str_Pntr);

            {StrPCopy(Cmd_Str_Pntr, '1MR-1000000000'#00'');}  {-ve ==> UP}
            {translate(Cmd_Str_Pntr, Rep_Str_Pntr);}          {+ve ==> DOWN}

            PullMotor_Up := TRUE;
            end;

        end;
end;

```

```

procedure TForm1.PullUpBitBtnKeyUp(Sender: TObject; var Key: Word;
    Shift: TShiftState);
begin
    if (PullMotor_Up = TRUE) then
        begin
            { stop the continuous motor running }
            StrPCopy(Cmd_Str_Pntr, '1CLP'#00'');
            translate(Cmd_Str_Pntr, Rep_Str_Pntr);

            StrPCopy(Cmd_Str_Pntr, '1AB'#00'');
            translate(Cmd_Str_Pntr, Rep_Str_Pntr);

            PullMotor_Up := False;
            end;
        end;
end;

```

```

procedure TForm1.PullDownBitBtnKeyPress(Sender: TObject; var Key:
    Char);
begin
    if (PullMotor_Down = False) then
        begin
            StrPCopy(Cmd_Str_Pntr, '1DH'#00'');
            translate(Cmd_Str_Pntr, Rep_Str_Pntr);

            StrPCopy(Cmd_Str_Pntr, '1SST4'#00'');
            translate(Cmd_Str_Pntr, Rep_Str_Pntr);

            StrPCopy(Cmd_Str_Pntr, '1SA135'#00'');

```

```

        translate(Cmd_Str_Pntr, Rep_Str_Pntr);

        StrPCopy(Cmd_Str_Pntr, '1SV120000'#00'');
        translate(Cmd_Str_Pntr, Rep_Str_Pntr);

        {StrPCopy(Cmd_Str_Pntr, '1MR1000000000'#00'');}  {-ve ==> UP}
        {translate(Cmd_Str_Pntr, Rep_Str_Pntr);}          {+ve ==> DOWN}

        PullMotor_Down := TRUE;
        end;

        end;

procedure TForm1.PullDownBitBtnKeyUp(Sender: TObject; var Key: Word;
    Shift: TShiftState);
begin
    if (PullMotor_Down = TRUE) then
        begin
            StrPCopy(Cmd_Str_Pntr, '1CLP'#00'');
            translate(Cmd_Str_Pntr, Rep_Str_Pntr);

            StrPCopy(Cmd_Str_Pntr, '1AB'#00'');
            translate(Cmd_Str_Pntr, Rep_Str_Pntr);

            PullMotor_Down := False;
            end;
        end;

procedure TForm1.FeedUpBitBtnKeyPress(Sender: TObject; var Key: Char);
begin
    if (FeedMotor_Up = False) then
        begin
            { move for ever }
            StrPCopy(Cmd_Str_Pntr, '2DH'#00'');
            translate(Cmd_Str_Pntr, Rep_Str_Pntr);

            StrPCopy(Cmd_Str_Pntr, '2SST4'#00'');
            translate(Cmd_Str_Pntr, Rep_Str_Pntr);

            StrPCopy(Cmd_Str_Pntr, '2SA135'#00'');
            translate(Cmd_Str_Pntr, Rep_Str_Pntr);

            StrPCopy(Cmd_Str_Pntr, '2SV120000'#00'');
            translate(Cmd_Str_Pntr, Rep_Str_Pntr);

            {StrPCopy(Cmd_Str_Pntr, '2MR1000000000'#00'');}  {-ve ==> DOWN}
            {translate(Cmd_Str_Pntr, Rep_Str_Pntr);}          {+ve ==> UP}

            FeedMotor_Up := TRUE;
            end;

        end;

procedure TForm1.FeedUpBitBtnKeyUp(Sender: TObject; var Key: Word;
    Shift: TShiftState);
begin
    if (FeedMotor_Up = TRUE) then

```

```

begin
  { stop the continuous motor running }
  StrPCopy(Cmd_Str_Pntr, '2CLP'#00'');
  translate(Cmd_Str_Pntr,Rep_Str_Pntr);

  StrPCopy(Cmd_Str_Pntr, '2AB'#00'');
  translate(Cmd_Str_Pntr,Rep_Str_Pntr);

  FeedMotor_Up := False;
  end;
end;

procedure TForm1.FeedDownBitBtnKeyPress(Sender: TObject; var Key:
  Char);
begin
  if (FeedMotor_Down = False) then
    begin
      StrPCopy(Cmd_Str_Pntr, '2DH'#00'');
      translate(Cmd_Str_Pntr, Rep_Str_Pntr);

      StrPCopy(Cmd_Str_Pntr, '2SST4'#00'');
      translate(Cmd_Str_Pntr,Rep_Str_Pntr);

      StrPCopy(Cmd_Str_Pntr, '2SA-135'#00'');
      translate(Cmd_Str_Pntr,Rep_Str_Pntr);

      StrPCopy(Cmd_Str_Pntr, '2SV120000'#00'');
      translate(Cmd_Str_Pntr,Rep_Str_Pntr);

      {StrPCopy(Cmd_Str_Pntr, '2MR-1000000000'#00'');}  {-ve ==> UP}
      {translate(Cmd_Str_Pntr,Rep_Str_Pntr);}          {+ve ==> DOWN}

      FeedMotor_Down := TRUE;
      end;
    end;

procedure TForm1.FeedDownBitBtnKeyUp(Sender: TObject; var Key: Word;
  Shift: TShiftState);
begin
  if (FeedMotor_Down = TRUE) then
    begin
      StrPCopy(Cmd_Str_Pntr, '2CLP'#00'');
      translate(Cmd_Str_Pntr,Rep_Str_Pntr);

      StrPCopy(Cmd_Str_Pntr, '2AB'#00'');
      translate(Cmd_Str_Pntr,Rep_Str_Pntr);

      FeedMotor_Down := False;
      end;
    end;

procedure TForm1.InLineStyleClick(Sender: TObject);
var
  Per_Dia_Change      : real;
  Vtaper_real, V1     : real;

```

```

    Taper_Length, Vel_Grad    : real;
    Vtaper_whole, Acc_whole   : longint;
    Dist_whole                : longint;
    Vtaper_str                : string;
    Acc_Taper, Dist_Taper    : string;
    Pull_Pos_1                : longint;
    Init_Pull_Pos             : longint;
    i                          : integer;

begin
    {Taper_Op      := TRUE;}

{Calculating Pull Rate with 80:1 gearbox ==> Channel 1}
    {For In-Line Taper of Length L}
    Per_Dia_Change := ValFn(InLineDiaChange.Text);
    V1              := ValFn(PullRate.Text);
    Vtaper_real    := V1/Sqr(1-(Per_Dia_Change/100));

    Vtaper_whole   := Trunc(Vtaper_real*(n_pull*1000/60));
    Vtaper_str     := '1SV' + IntToStr(Vtaper_whole) + #00;

    {Calculating Acceleration required}
    {where Vel_Grad = Acceleration}
    Taper_Length := ValFn(InLineLength.Text);
    Vel_Grad     := Pull_Const_1*(Sqr(Vtaper_real)-
    Sqr(V1))/(2*Taper_Length);
    Acc_whole    := Trunc(Vel_Grad);
    Acc_Taper   := '1SA' + IntToStr(Acc_whole) + #00;

    {Calculating Distance required}
    Dist_whole   := Trunc(Pull_Const_2*Taper_Length);
    Dist_Taper   := '1MR' + IntToStr(Dist_whole) + #00;

    {StrPCopy(Cmd_Str_Pntr, '1CLP'#00'');
    translate(Cmd_Str_Pntr, Rep_Str_Pntr);}

    {StrPCopy(Cmd_Str_Pntr, '1DH'#00'');
    translate(Cmd_Str_Pntr, Rep_Str_Pntr);}

    StrPCopy(Cmd_Str_Pntr, Acc_Taper);
    translate(Cmd_Str_Pntr, Rep_Str_Pntr);

StrPCopy(Cmd_Str_Pntr, Vtaper_str);      {Pull Velocity -> Chan 1}
    translate(Cmd_Str_Pntr, Rep_Str_Pntr);

    {Pull Displacement}
    {StrPCopy(Cmd_Str_Pntr, Dist_Taper);}      {-ve movement = UP}
    {translate(Cmd_Str_Pntr, Rep_Str_Pntr);}    {+ve movement = DOWN}

    StrPCopy(Cmd_Str_Pntr, '1UP'#00'');
    translate(Cmd_Str_Pntr, Rep_Str_Pntr);

    Init_Pull_Pos := 0;
    Init_Pull_Pos := get_pos(1);

    {Taper_Op := FALSE;}
end;

```

```

procedure TForm1.InLineStopClick(Sender: TObject);
begin
    FileClose(FileHandle1);
    FileClose(FileHandle2);

    StrPCopy(Cmd_Str_Pntr, '1CLP'#00'');
    translate(Cmd_Str_Pntr,Rep_Str_Pntr);

    StrPCopy(Cmd_Str_Pntr, '1AB'#00'');
    translate(Cmd_Str_Pntr,Rep_Str_Pntr);

    StrPCopy(Cmd_Str_Pntr, '2CLP'#00'');
    translate(Cmd_Str_Pntr,Rep_Str_Pntr);

    StrPCopy(Cmd_Str_Pntr, '2AB'#00'');
    translate(Cmd_Str_Pntr,Rep_Str_Pntr);

end;

procedure TForm1.EndStopClick(Sender: TObject);
begin
    FileClose(FileHandle1);
    FileClose(FileHandle2);

    StrPCopy(Cmd_Str_Pntr, '1CLP'#00'');
    translate(Cmd_Str_Pntr,Rep_Str_Pntr);

    StrPCopy(Cmd_Str_Pntr, '1AB'#00'');
    translate(Cmd_Str_Pntr,Rep_Str_Pntr);

    StrPCopy(Cmd_Str_Pntr, '2CLP'#00'');
    translate(Cmd_Str_Pntr,Rep_Str_Pntr);

    StrPCopy(Cmd_Str_Pntr, '2AB'#00'');
    translate(Cmd_Str_Pntr,Rep_Str_Pntr);

end;

procedure TForm1.Button1Click(Sender: TObject);
var
    i, j    : integer;
begin
    For i := 0 to 7 do
        begin
            ptDioWriteBit.port    := 1;
            ptDioWriteBit.bit     := i;
            ptDioWriteBit.state   := 0;
            ErrCde := DRV_DioWriteBit(DeviceHandle,ptDioWriteBit);
        end;

            ptDioWriteBit.port    := 1;
            ptDioWriteBit.bit     := 7;
            ptDioWriteBit.state   := 1;
            ErrCde := DRV_DioWriteBit(DeviceHandle,ptDioWriteBit);
end;

```

```

    {ptDioGetCurrentDOBit.state:= @lpDioGetCurrentDOBit}
      (For j:= 6 to 7 do
        begin
          (ptDioGetCurrentDOBit.port      := 1;
           ptDioGetCurrentDOBit.bit      := 6;
           ErrCde := DRV_DioGetCurrentDOBit(DeviceHandle, ptDioGetCurrentDOBit);}
        {end;}
      {Edit2.Text      := ptDioGetCurrentDOBit.state;}
      end;

    procedure TForm1.Button2Click(Sender: TObject);
      var
        i : integer;
        bits: integer;
      begin
        For i := 0 to 7 do
          begin
            ptDioWriteBit.port      := 1;
            ptDioWriteBit.bit      := i;
            ptDioWriteBit.state    := 0;
            ErrCde := DRV_DioWriteBit(DeviceHandle, ptDioWriteBit);
          end;
        end;

    procedure TForm1.ScrollBar1Change(Sender: TObject);
      var
        LaserOutput      : single;
        Scaling_Factor  : single;
      begin
        Edit1.Text      := FloatToStr(ScrollBar1.Position/100.0);
        Scaling_Factor := (StrToFloat(Edit1.Text)-9.94);

        LaserOutput      := Scaling_Factor;
        ptAOVoltageOut.chan := 4;
        ptAOVoltageOut.OutputValue := LaserOutput;

        ErrCde := DRV_AOVoltageOut(DeviceHandle, ptAOVoltageOut);

      end;

    procedure TForm1.Button3Click(Sender: TObject);
      Var
        Phase_Length, Pull_Rate1 : double;
        ErrA, ErrB, P : Integer;
        Duration : Variant;
      Begin
        Val(edit5.text, Phase_Length, ErrA);
        Val(PullRate.text, Pull_Rate1, ErrB);
        Duration := ((Phase_Length/Pull_Rate1)/360)*60000;
        Timer4.interval := Duration;
        Timer4.Enabled := True;
        P := 0;

```

```

end;

procedure TForm1.Button4Click(Sender: TObject);
    Var
        ErrA,ErrB : Integer;
        N,O,A : Real;
        BasePower,MaxPower : Double;
        LaserOutput      : single;
        Scaling_Factor  : single;
    begin
        P := P + 1;
        N := P*(PI/180);

        Val(edit4.text,MaxPower,ErrA);
        Val(edit8.text,BasePower,ErrB);

        O := BasePower + ((MaxPower-BasePower)/2);
        O := O + ((MaxPower-BasePower)/2)*Sin(N);
        A := O- 9.94;

        Scaling_Factor      := A;
        LaserOutput          := Scaling_Factor;
        ptAOVoltageOut.chan  := 4;
        ptAOVoltageOut.OutputValue := LaserOutput;

        ErrCde := DRV_AOVoltageOut(DeviceHandle,ptAOVoltageOut);
        Edit6.text := floattostr(O);
    end;

procedure TForm1.Button5Click(Sender: TObject);
    begin
        Timer4.enabled := false;
    end;

end.

```